TESIS DE LA UNIVERSIDAD DE ZARAGOZA

2025 113

Marta Redrado Domingo

Tailoring Iridium (III) Complexes for Improved Anticancer Activity: The Role of Ligands and the Incorporation of Gold (I) Fragments

Director/es
Gimeno Floria, María Concepción
Fernández Moreira, Vanesa

ISSN 2254-7606

Prensas de la Universidad
Universidad Zaragoza

Universidad de Zaragoza
Servicio de Publicaciones

ISSN 2254-7606

Universidad Zaragoza
1542

Tesis Doctoral

TAILORING IRIDIUM (III) COMPLEXES FOR IMPROVED ANTICANCER ACTIVITY: THE ROLE OF LIGANDS AND THE INCORPORATION OF GOLD (I) FRAGMENTS

Autor

Marta Redrado Domingo

Director/es

Gimeno Floria, María Concepción
Fernández Moreira, Vanesa

UNIVERSIDAD DE ZARAGOZA
Escuela de Doctorado

Programa de Doctorado en Química Inorgánica

2023

Universidad Zaragoza
1542

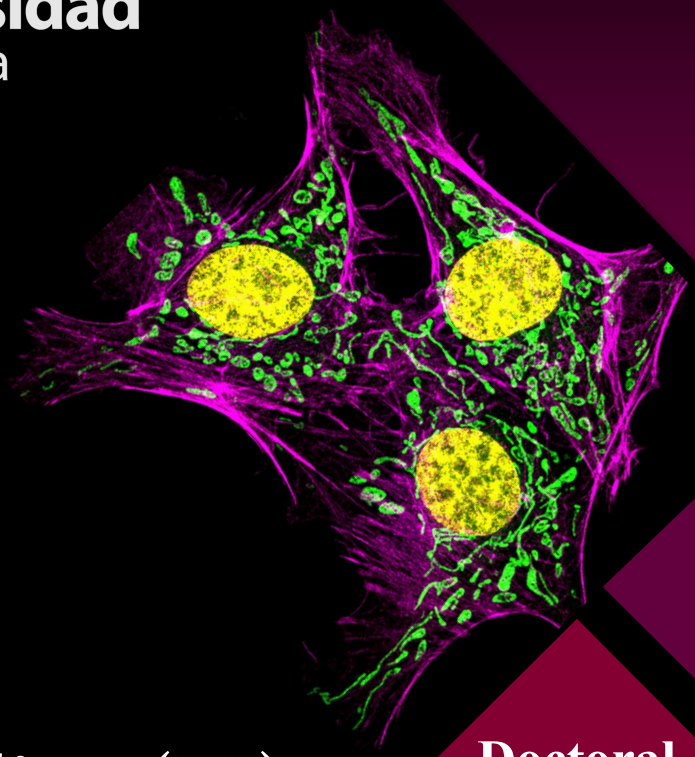

Doctoral Thesis 2023

Tailoring Iridium(III) Complexes for Improved Anticancer Activity: The Role of Ligands and the Incorporation of Gold(I) Fragments

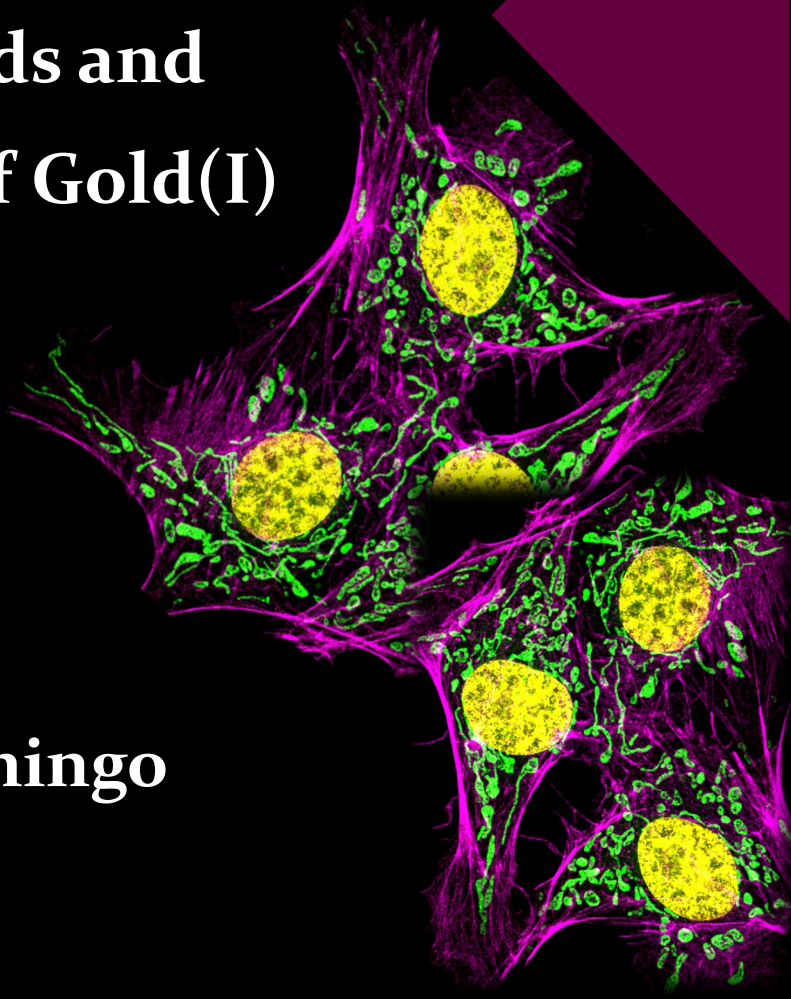

Marta Redrado Domingo

Tailoring Iridium (III) Complexes for Improved Anticancer Activity:

The Role of Ligands and the Incorporation of Gold (I) Fragments

Author

Marta Redrado Domingo

Supervisors

Prof. Maria Concepción Gimeno Floría

Dra. Vanesa Fernández Moreira

Universidad de Zaragoza

Programa de Doctorado en Química Inorgánica

Zaragoza 2023

Universidad de Zaragoza

Departamento de Química Inorgánica

Tailoring Iridium (III) Complexes for Improved Anticancer Activity: The Role of Ligands and the Incorporation of Gold (I) Fragments

Memoria presentada para acceder al título de Doctor por Marta Redrado Domingo

Zaragoza, 2023

CSIC
Consejo Superior de Investigaciones Científicas

iSQCH
Instituto de Síntesis Química y Catálisis Homogénea

María Concepción Gimeno Floría, Profesor de Investigación de Organismo Público de Investigación (Consejo Superior de Investigaciones Científicas) en el Instituto Universitario de Investigación mixto de Síntesis Química y Catálisis Homogénea (ISQCH), y

Vanesa Fernández Moreira, Investigadora Ramón y Cajal (Universidad de Zaragoza) en el Instituto Universitario de Investigación mixto de Síntesis Química y Catálisis Homogénea (ISQCH).

CERTIFICAN

Que la presenta memoria titulada "Tailoring Iridium (III) Complexes for Improved Anticancer Activity: The Role of Ligands and the Incorporation of Gold (I) Fragments" ha sido realizada en el Departamento de Química Inorgánica de la Facultad de Ciencias de la Universidad de Zaragoza, y autorizan su presentación para que sea calificada como Tesis Doctoral.

Zaragoza, Mayo de 2023.

Fdo. Prof. M. Concepción Gimeno Fdo. Dra. Vanesa Fernández Moreira

Puede que nada en este mundo pase por casualidad,

quizás todo ocurre por alguna razón...

Y así, poco a poco nuestro destino va tomando forma...

-Silvers Rayleigh-

Table of contents

En primer lugar, me gustaría dar las gracias a mis directoras de tesis, la Prof. Dr. Mª Concepción Gimeno y a la Dra. Vanesa Fernández Moreira por acogerme desde el primer día y poner a mi alcance todos los medios de los que disponían. Gracias por vuestras ideas, ayuda, palabras de ánimo, disposición, consejos y paciencia infinita. Sin vosotras nada de este trabajo habría sido posible. GRACIAS por darme alas y permitirme aprender a volar. Me habéis hecho crecer tanto profesional como personalmente, y sin lugar a dudas sois una de las principales razones que me animan a seguir en el mundo de la investigación.

En segundo lugar, quiero dar las gracias al Dr. Daniel Muñoz Espín por acogerme en su grupo durante mi estancia predoctoral, poner a mi alcance todos los avances y tecnología de la que disponía, así como iniciarme en el campo de la senescencia y cultivos celulares.

Me gustaría mostrar también mi agradecimiento al resto de miembros de Gimeno's Group. Al Prof. Dr. Antonio Laguna por su alegría y amabilidad; a la Dra. Elena Cerrada por su carisma, alegría desbordante y fidelidad a las pausas de café, en las cuales tan pronto arreglábamos el mundo como lo poníamos del revés; a la Dra. Olga Crespo , guardiana del luminómetro por su disposición en cualquier momento del día; a la Dra. Raquel Pérez, maestra de ceremonias, no volverá a sonar un "cumpleaños feliz" sin que me vengas a la mente; a la Dra. Mamen Blanco por su personalidad arrolladora; a la Dra. Lola Villacampa por enseñarme que hay veces que una reacción "está pura con impurezas, pero lo importante es que ha ido". No me puedo olvidar de los nuevos integrantes los Dres. Jorge y Juanvi, María y Elisa, por transmitirme positividad y tranquilidad.

Mención aparte se merecen mis antiguos compañeros de laboratorio, ellos fueron mentores en la sombra y apoyo incondicional en mis inicios. El Dr. Adrián Alconchel, sin lugar a duda una de las mejores personas que he tenido el gusto de conocer; decidido y luchador como no hay otro. Adri, gracias por espabilarme, por centrarme, por tus palabras de ánimo cuando todo se ponía oscuro, pero sobre todo por acompañarme en este viaje, no habría sido lo mismo sin ti. El Dr. Daniel Salvador, Dani para los amigos. Contigo he compartido desde dramas y

confidencias hasta clases de aquaboard. Eres ejemplo de resiliencia y tesón… ojalá volver a compartir laboratorio contigo. Al Dr. Andrés Luengo, gracias por ayudarme en mis inicios, porque, aunque tenías tu propio método didáctico, siempre estabas dispuesto a échame una mano. Mis queridas Dras. Anabel y. Melanie, dos ejemplos de determinación y carácter, me alegrasteis los días. Y no podía faltar el Dr. Matthias Boege, él me enseñó a valorar mi vida y seguridad en el laboratorio. Gracias a todos.

Y llegaron las nuevas incorporaciones y con ellas la frescura y energía de los inicios. El primer lugar de este agradecimiento lo tenía que ocupar como no podía ser de otro modo mi Javi. Amigo, después de tanto tiempo aquí seguimos, juntos. Eres calma y tempestad, consejero y confidente, eres luz…, madre mía la que vas a liar cuando decidas confiar en ti mismo. Cree en ti, yo ya lo hago. El segundo lugar es para ti, Fanny, impulsiva, emocional, caótica, gracias por mejorar mi mood siempre que estoy contigo. Por otro lado, está mi querida Eva, tú sabes que entre bordes nos entendemos, gracias por estar y dejar que te llorara los dramas, es una maravilla verte crecer cada día. Mención aparte se merece Roberto, Winnie the Pooh con alma de roquero, eres caos magic, pero me encanta el toque rosa que le estás dando al laboratorio. Irati y JC, el radiopatio de Gimeno's Group, capaces de ponerte al día de todas las novedades en cuestión de minutos, qué necesarios sois… Sandra, persona buena y trabajadora como pocas que conozca, siempre dispuesta a ayudar. Raquel y Noelia, chute de energía desde primera hora de la mañana. Por último, Guillermo y Jandro, ellos, ese dúo con humor propio. Gracias chicos.

Gracias también a la gente del departamento de bioquímica, en especial a Andrea. Por formarme, animarme y ayudarme en todo momento.

No puedo olvidarme de Ángel y Raquel, conversación asegurada cada vez que bajas al RMN, gracias por todos vuestros consejos, los carbonos cuaternarios de esta tesis han visto la luz gracias a vosotros.

Manolo, esto ha sido posible gracias a ti, por ser apoyo incondicional, psicólogo 24/7, por tu aporte de energía diario, por tus palabras de ánimo, por enseñarme a

fluir, por estar siempre al pie del cañón, por hacerme reír… Por animarme a perseguir mis sueños, y sobre todo por enseñarme que la vida consiste en ser feliz, así tal cual, que lo importante es el camino y que por mucho que cueste llegar a la cima las vistas, al final son preciosas. Gracias por empujarme a seguir, te prometo que lo haré sin reblar.

El último lugar es para mi familia, papá, mamá, Andrea y Zara. Testigos de todo este proceso. Gracias por animarme y apoyarme, por seguirme allá a donde voy, por estar a mi lado incondicionalmente… Siempre me hacéis la misma pregunta "Y todo esto, ¿para qué?, ¿para qué sirve?, ¿ya hemos curado el cáncer?", aún no puedo responderos a estas preguntas, ojalá pronto sí. Esperadme en Zaragoza, prometo volver.

Abbreviations

2-HE	2-hydroxyethidium
4T1-luc2	Stage IV human breast cancer cells
7-AAD	7-aminoactinomicina D
a.w.	Activation wavelength
A549	Adenocarcinomic human alveolar basal epithelial cells
AAS	Atomic absorption spectroscopy
acac	Acetylacetonate
Ar.	Argon
ATP	Adenosine triphosphate
BC	Before Christ
BODIPY	Dipyrromethene boron difluoride
bzq	benzo[*h*]quinolone
c.a.	“circa”, around
CCDC	Cambridge Crystallographic Data Centre
CDK	Cyclin-dependent kinase
CT	Computed tomography
CTB	CellTracker Blue
DCM	Dichloromethane
DHE	Dihydroethidium
DMEM	Dulbecco's modified eagle medium
DMSO	Dimethyl sulfoxide
DNA	Deoxyribonucleic acid
dpa	2,2’-dipyridylamine
dppm	Bis(diphenylphosphino) methanide

DTNB	5,5’- dithiobis(2-nitrobenzoic acid)
ECFCs	Endothelial colony forming cells
em	Emission
EMA	European Medicines Agency
exc	Excitation
FBS	Fetal bovine serum
FDA	Food and drug administration
FITC	Fluorescein isothiocyanate
FLIM	Fluorescence lifetime imaging microscopy
GAPDH	Glyceraldehyde-3-phosphate dehydrogenase
HeLa	Cervical cancer cells
Hep3B	Human hepatocellular carcinoma cells
HPD	Haematoporphyrin derivative
HRMS	High resolution mass spectrometry
HTS	High throughput screening
IC_{50}	Inhibitory concentration 50%
ICP-MS	Inductively-coupled plasma mass spectrometry
IL	Intraligand
IL-10	Interleukin-10
IR	Infrared
ISC	Intersystem crossing
LC	Ligand-centered
LD_{50}	Lethal Dose 50%
LDS	Lysosomal storage diseases
LLCT	Ligand-to-ligand charge transfer
LMCT	Ligand-to-metal charge transfer
LMP	Lysosomal membrane permeation
logP	Partition coefficient octanol/water

LTG	LysoTracker Green
LTR	LysoTracker Red
MC	Metal-centered
MLCT	Metal-to-ligand charge transfer
MMP	mitochondrial membrane potential
MO	Molecular orbital
mpc	Methyl-2-phenylquinoline-4-carboxylate
MRI	Magnetic resonance imaging
MTFR	MitoTracker Far Red
MTR	MitoTracker Red
MTT	(3-(4,5-dimethylthiazol-2-yl)-2,5-diphenyltetrazolium bromide) tetrazolium
NADPH	Nicotinamide adenine dinucleotide phosphate
NHC	N-heterocyclic carbenes
NIR	Near infrared
NMR	Nuclear magnetic resonance
NTB	2-nitro-5-thiobenzoate
OLED	Organic light-emitting diode
PARP	Poly(ADP-ribose) polymerase
PBMCs	Peripheral blood mononuclear cells
PBS	Phosphate buffered saline
PDT	Photodinamic therapy
PET	Positron emission tomography
PFS	Progression-free survival
PI	Phototoxic index
ppy	2-phenyl pyridine
PS	Photosensitizer
r.t.	Room temperature

RNA	Ribonucleic acid
RNase	Ribonuclease
ROS	Reactive oxigen species
SASP	Senescence-associated secretory phenotype
SBLCT	Surface barrier layer capacitor transitions
SK-Mel-103	Human melanoma cells
SK-Mel-28	Melanoma cancer cell line
SnCs	Senescent cells
SPECT	Single photon emission computer tomography
TME	Tumoral microenvironment
TMRE	Tetramethylrhodamine ethyl ester
TNB	2-nitro-5-thiobenzoate anion
Trx	Thioredoxin
TrxR	Thioredoxin reductase
UV	Ultraviolet
VEGF	Vascular endothelial growth factor
ε	Molar extinction coefficient
Φ	Quantum yield
β-Gal	β-galactosidase
τ	Lifetime

Resumen

La presente tesis doctoral está enfocada en la síntesis de complejos monometálicos de Ir^{III} y heterometálicos de Ir^{III}/Au^{I} para su uso como agentes teragnósticos y/o fotosensibilizadores, y el estudio de sus propiedades ópticas y biológicas sobre distintas líneas celulares tumorales. Un centro metálico de iridio (III) con marcadas propiedades luminiscentes y fotobioactivas, será el eje central sobre el que se fundamenten todos los complejos metálicos desarrollados. Posteriormente la incorporación de diversos ligandos tipo quelato o un centro metálico de oro (I) nos permitirá modular su actividad y sus dianas biológicas. En este trabajo se ha realizado un estudio que permite entender los factores clave a tener en cuenta a la hora de diseñar un complejo luminiscente ciclometalado de iridio (III), para ser usado bien como agente teragnóstico o bien en terapia fotodinámica.

En el capítulo 1, se describe la síntesis de un derivado monometálico de iridio (III) y varios bimetálicos de iridio (III)/oro (I), del tipo $[Ir(C\hat{}N)_2(dppm)]^+$ e $[Ir(C\hat{}N)_2(dppmAuX)]^+$, donde C^N representa al ligando ortometalado 2-fenilpiridina (ppy), dppm es el ligando quelado bis(difenilfosfino)metano que servirá después de su desprotonación, como puente entre los dos centros metálicos (Ir^{III}-Au^{I}) y X representa el ligando auxiliar del oro, pudiendo ser cloruro, PPh_3 o tiocitosina. Los complejos obtenidos conservan las propiedades luminiscentes propias de su precursor monometálico de iridio, con una emisión en verde que es independiente de la presencia del fragmento de Au^{I}. De la misma forma, este fragmento de Au^{I} tampoco tiene influencia significativa en la capacidad antiproliferativa de los compuestos, donde la especie monometálica ya presenta un valor IC_{50} en el rango de nanomolar. Sin embargo, sí se ve incrementada la inhibición de la enzima mitocondrial TrxR y, además, se observa un aumento en las especies reactivas de oxígeno (ROS) por la presencia del fragmento de oro (I). En cuanto a su biodistribución y actividad antiangiogénica, todos los complejos tienen un comportamiento similar, siendo la mitocondria su diana final después de un proceso de tráfico intracelular entre los lisosomas y las mitocondrias, así como un marcado potencial antiangiogénico.

En el capítulo 2, se describe la síntesis de complejos monometálicos de iridio (III) y oro (I), del tipo $[Ir(C\hat{}N)_2(N\hat{}N)]^{+/2+}$ y $[Au(NHC)X]^{0/+}$, donde C^N representa al ligando ortometalado 2-fenilpiridina, y N^N o NHC representan las dos posibilidades de coordinación del derivado 3-bencil-1-pentil-imidazo[4,5-f][1,10]fenantrolina, donde el centro de Ir^{III} se coordinará mediante su extremo diimina y el de Au^{I} lo hará mediante un carbeno NHC. Adicionalmente, se han sintetizado dos derivados heterometálicos combinando las dos posibilidades de coordinación que ofrece el citado ligando. Los estudios de luminiscencia han confirmado el desplazamiento de los perfiles de excitación y emisión en función de los sustituyentes (X) unidos al centro de oro, bromuro o JohnPhos. Además, se han estudiado las propiedades antiproliferativas de todos los complejos sintetizados en la linea A549 en diferentes condiciones (oscuridad e irradiando a 405 nm) mostrando en todos los casos unos valores de IC_{50} en el rango bajo de micromolar, potenciándose en condiciones de irradiación en aquellos complejos que contienen un centro de Ir^{III} en su estructura. Este hecho puede ser explicado por la generación de oxígeno singlete vinculada con la presencia de este centro en la molécula. Adicionalmente, se ha podido determinar el tipo de muerte inducida por los mismos, siendo en todos los casos un proceso apoptótico y su biodistribución mediante microscopía confocal de fluorescencia.

El capítulo 3 recoge el diseño de complejos bifuncionales de iridio (III) con un doble perfil de emisión. Por un lado, se combina un fragmento emisor en amarillo/verde a la vez que bioactivo de Ir^{III} de tipo $[Ir(C\hat{}N)_2(N\hat{}N)]^{+}$, donde C^N representa un ligando ortometalado ppy (2-fenilpiridina) o bzq (benzoquinolina) y N^N un ligando diimina modificado con un cromóforo orgánico con emisión en el azul (acridina o antraceno). Este diseño incorporando un cromóforo orgánico en la estructura metálica de Ir^{III} ofrece la posibilidad de rastrear el complejo dentro de las células utilizando una longitud de onda de irradiación diferente a la de activación terapéutica, que es aquella centrada en el fragmento metálico. La capacidad fototerapéutica de los distintos complejos sintetizados fue estudiada en la linea A549, así como sus dianas biológicas, el tipo de muerte celular que inducen

y su capacidad para generar una parada del ciclo celular, obteniéndose en todos los casos unos resultados muy prometedores

El último capítulo amplía la estrategia de sintetizar nuevos agentes fotosensibilizadores, sin embargo, se han realizado ciertas modificaciones respecto a los complejos mencionados anteriormente para mejorar las propiedades de los mismos, tales como sustituir el ligando C^N por metil-2-fenilquinolina-4-carboxilato (mcp) y N^N por diferentes familias de derivados azol. El objetivo es conseguir una mayor solubilidad en medios biológicos y activaciones del PS a mayores longitudes de onda, donde se tenga una mayor penetración en los tejidos y poder acceder así a tumores más grandes e internos. La posibilidad de obtener complejos análogos catiónicos y neutros, mediante la desprotonación del grupo azol coordinado al centro metálico, permite establecer una tendencia de como la carga de los complejos afecta tanto a las propiedades ópticas como biológicas de los mismos. Posteriormente, se llevaron a cabo la evaluación de los complejos sintetizados como agentes quimioterapéuticos y fotosensibilizadores en diversas líneas celulares tales como A549, 4T1-luc2 o B16-F10-luc. También se estudió su biodistribución, su capacidad para generar oxigeno singlete y en consecuencia inducir muerte celular. Una vez completados los estudios, los complejos más prometedores han sido llevados a ensayos *in vivo* tanto de toxicidad como de eficacia para demostrar su potencial como agentes anticancerígenos.

Abstract

The present doctoral thesis focuses on the synthesis of monometallic complexes of Ir^{III} and heterometallic complexes of Ir^{III}/Au^{I} for their use as theranostic agents and/or photosensitizers, and the study of their optical and biological properties on different tumor cell lines. An iridium (III) metal center with luminescent and photobioactive properties will be the central axis on which all the developed metal complexes are based. Subsequently, the incorporation of various chelate ligands or an Au^{I} metal center will allow us to modulate their activity and biological targets. This work allows to understand the key factors to consider when designing a cyclometalated iridium (III) luminescent complex, to be used either as a theranostic agent or in photodynamic therapy.

In chapter 1, the synthesis of a monometallic iridium (III) derivative and three iridium (III)/gold (I) bimetallic complexes are described, These complexes are of type $[Ir(C\text{^}N)_2(dppm)]^+$ and $[Ir(C\text{^}N)_2(dppmAuX)]^+$, where C^N represents the orthometallated ligand 2-phenylpyridine (ppy), dppm is the chelate ligand bis(diphenylphosphino)methane that will be used as linker between the two metal centers (Ir^{III}-Au^{I}), after its deprotonation, and X represents the auxiliary gold ligand, which can be chloride, PPh_3, or thiocytosine. The synthetized complexes retain the luminescent properties characteristic of their iridium monometallic precursor, with a green emission that is independent of the presence of the Au^{I} fragment. Similarly, this Au^{I} fragment does not have a significant influence on the antiproliferative capacity of the compounds, where the monometallic species already presents an IC_{50} value in the nanomolar range. However, the inhibition of the mitochondrial enzyme TrxR is potentiated, and an increase in reactive oxygen species (ROS) production is observed due to the presence of the gold (I) fragment. As for their biodistribution and anti-angiogenic activity, all the complexes have a similar behavior, with the mitochondria being their final target after an intracellular trafficking process between lysosomes and mitochondria, as well as a marked anti-angiogenic potential.

In chapter 2, the synthesis of monometallic iridium (III) and gold (I) complexes of the type $[Ir(C^N)_2(N^N)]^{+/2+}$ and $[Au(NHC)X]^{0/+}$ is described, where C^N represents the orthometallated ligand 2-phenylpyridine, and N^N or NHC represents the two coordination possibilities of the 3-benzyl-1-pentyl-imidazo[4,5-f][1,10]phenanthroline derivate, where the Ir^{III} center will coordinate through the diimine , while the Au^{I} center will do through an NHC carbene. Additionally, two heterometallic derivatives combining the two coordination possibilities offered by the aforementioned ligand have been synthesized. Luminescence studies have confirmed the displacement of excitation and emission profiles depending on the ancillary ligand (X) bonded to the gold center, bromide or JohnPhos. In addition, the antiproliferative properties of all the synthesized complexes have been studied in the A549 line under different conditions (dark and irradiation at 405 nm), showing in all cases IC_{50} values in the low micromolar range, with a potentiation under irradiation conditions in those complexes containing an Ir^{III} center in their structures. This fact can be explained by the generation of singlet oxygen associated to the presence of this center in the molecule. Additionally, the type of induced cell death has been determined, being in all cases an apoptotic process, and their biodistribution was studied through confocal fluorescence microscopy.

Chapter 3 describes the design of bifunctional iridium (III) complexes with a dual emission profile. On the one hand, an emitter fragment in yellow/green of the type $[Ir(C^N)_2(N^N)]^{+}$, where C^N represents an orthometallated ppy (2-phenylpyridine) or bzq (benzoquinoline) ligand is linked through a N^N ligand (diimine ligand) with an organic chromophore with emission in blue (acridine or anthracene). This design incorporating an organic chromophore in the Ir^{III} metal structure offers the possibility of tracking the complex within cells using a different irradiation wavelength than the therapeutic activation wavelength, which is centered on the metal fragment. The phototherapeutic capacity of the different synthesized complexes was studied in the A549 cell line, as well as their biological targets, the type of cell death that they induce, and their ability to generate a cell cycle arrest, obtaining very promising results in all cases.

The last chapter expands on the strategy of synthesizing new photosensitizer agents. However, certain modifications have been made to the complexes mentioned above to improve their properties, such as replacing the C^N ligand with methyl-2-phenylquinoline-4-carboxylate (mcp) and the N^N ligand with different families of azole derivatives. The aim is to achieve greater solubility in biological media and activation of the PS at longer wavelengths, generating greater tissue penetration, thus accessing larger and more internal tumors. The possibility of obtaining analogous cationic and neutral complexes, by deprotonation of the azole coordinated to the metal center, allows to establish a tendency of how the charge of the complexes affects both their optical and biological properties. Subsequently, the synthesized complexes were evaluated as chemotherapeutic and photosensitizer agents in various cell lines such as A549, 4T1-luc2, or B16-F10-luc. Their biodistribution, their ability to generate singlet oxygen, and consequently induce cell death, were also studied. Once the studies were completed, the most promising complexes were tested for both toxicity and efficacy *in vivo* to demonstrate their potential as anticancer agents.

Introduction

I.1 Metals in medicine

Medicinal inorganic chemistry is an area of bioinorganic chemistry that combines traditional inorganic chemistry and biology to design metal complexes for therapeutic or diagnostic applications.[1,2] The field of medicinal inorganic chemistry encompasses the analysis of metalloproteins, the functions of metallic ions at molecular level, their homeostasis in living beings, the design of different metal complexes and the study of their properties.[3,4,5]

The use of metals for therapeutic purposes has been explored since ancient times.[6] For instance, civilizations such as Egyptians used copper for the disinfection of water, while the Chinese and Arabs discovered that gold could be used as a treatment for chronic diseases or that mercury chloride could generate a diuretic effect.[7] Centuries later, in 1912, Paul Ehrlich developed the first metallodrug with therapeutic applications, Salvarsan,[8] and he is nowadays considered "the founder of chemotherapy". Salvarsan is an arsenic-based antimicrobial agent that demonstrated its great effectiveness against syphilis, and opened the door to using other metallic elements into the medicinal area. Since those days, numerous metal complexes with diverse therapeutic properties have been administered,[9] such as platinum and ruthenium complexes as anticancer agents,[10,11] gold compounds as antiarthritic drugs,[12] cobalt species as antiviral[13] and lanthanides complexes as magnetic resonance imaging (MRI) agents (Figure 1).[14,15]

The driving force behind the increasing effort devoted to the delivery of novel metallodrugs relies on the belief that the use of metallic complexes confers additional benefits compared to organic molecules. While small organic drugs are mostly composed by carbon, hydrogen, nitrogen and oxygen, and their geometry is entirely dependent on carbon hybridization, metal-based drug structures are more diverse due to the variety of *d* orbital geometries.[16] Specially, in tetrahedral, pyramidal, trigonal bipyramidal and octahedral structures, higher and more variated ways of coordination allow for the tuning of the chemical reactivity of metal complexes. Additionally, not only does the metal nature play a crucial role, but the coordinated ligands also have a significant impact on biological activity.

Thus, modulation of ligands, counterions, or substituents around the metal center could lead to the recognition of target sites and increase or inhibit the activity of an enzyme, or even influence the mechanism of action of the chemotherapeutic drug itself.[17]

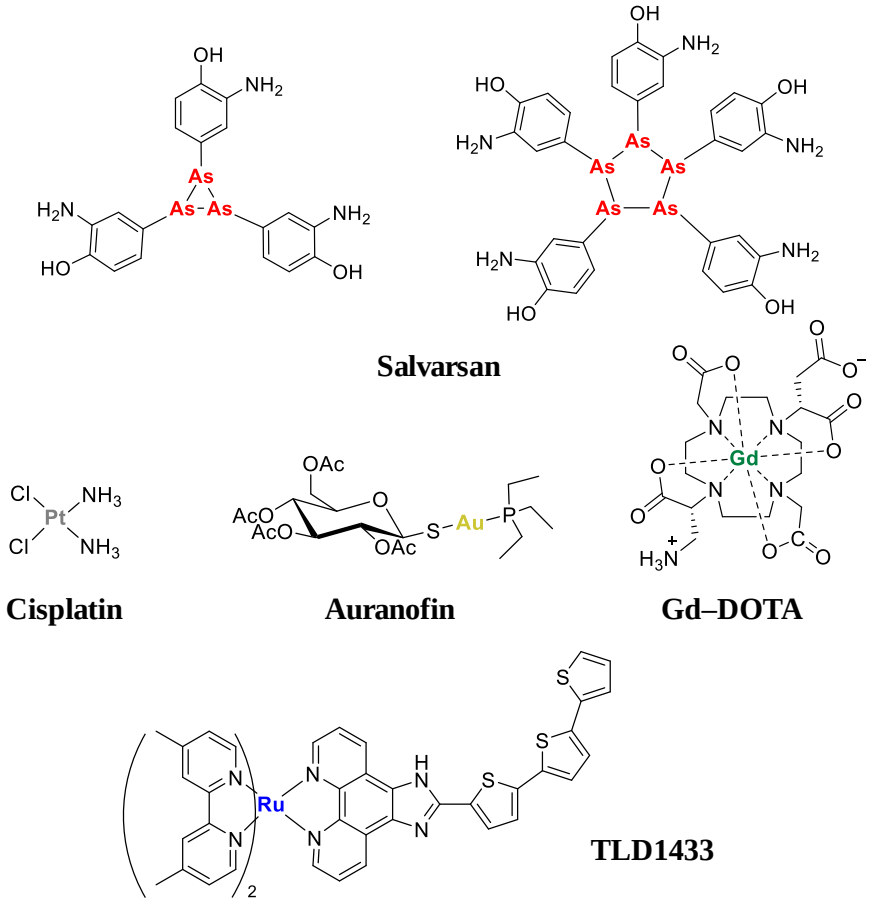

Figure 1. *Examples of metal-based drugs used in therapy and diagnostic applications.*[18]

Despite all the benefits that metallodrugs present, it is important to mention that one of the biggest challenges that these species face is their selective delivery to specific targets. For this reason, a potential metallodrug must demonstrate sufficient reactivity and selectivity towards its biological target. To achieve this purpose, a specific design of the molecule is required to control the thermodynamic and kinetic processes that could occur in the biological environment.

I.2 Cancer and treatments

Cancer is a disease that is defined by an uncontrolled proliferation of cells with the capacity to migrate to other tissues or spread via lymph or blood to other locations in the body.[19] Under normal conditions, cells are constantly engaged in a cell cycle process, where they generate new cells through a mitotic stage. When cells are damaged or due to aging, they die, and new cells replace them. However, sometimes this ideal metabolic order is altered due to stress, external stimuli, or irradiation sources, and abnormal cells instead of dying, undergo continuous cellular division, generating a high concentration of non-normal cells. Accumulation of those cells containing mutations or alterations in their functions, generates tumours. Tumors are defined as benign or malignant based on their capacity to migrate or spread to other parts of the body. A benign tumor grows slowly and does not show a tendency to migrate to other parts of the body. On the other hand, a malignant tumor grows exponentially and can invade other tissues. When a tumor is malignant, it is termed cancer. A minority of cancerous cells do not generate lumps or masses of tissues, such as leukemia, but they are still considered cancer.

Cancer is a genetic illness caused by modifications of genes involved in the correct functions of cells, particularly those related to growth and cell division, stimulate the beginning of this illness. Genetic changes that can cause cancer are quite variated however, most of them happen because of:

a) errors while cells are immersed in a cell division cycle. It is demonstrated that there are at least two mechanisms of cell cycle control. The first type of control involves kinase enzymes.[20] Kinase activation commonly requires the presence of a second subunit that is just expressed at the appropriate time during the cell cycle. Once that both units are associated, they form an active complex known as “cyclin-dependent kinase –cyclin” (CDK-cyclin), turning on the cell cycle progression. The second type of cell cycle regulation is known as checkpoints.[21] When these checkpoints sense flaws in some events as DNA replication or chromosome secretion, they activate

signals that cause a delay in cycle progression until the danger of mutation has been averted. If one of these mechanisms fail, there is an increase in the probability of suffering cancer. Figure 2 shows the cell cycle of a mammalian cell and the checkpoints analyzed in every cell cycle phase (G0, G1, S, G2 and M) including the correspondent kinases implicated. During a cell division cycle, chromosomes are replicated once (DNA synthesis or S-phase) and segregated to create two genetically identical daughter cells (mitosis or M-phase). These events are divided by two steps: the first one of growth and, the second one of reorganization (gap phases G1 and G2, respectively). Cells can stop cycling after division, entering a state of quiescence (G0). Progress through the cycle is accomplished by the regulated activity of complexes CDK–cyclin, as reported in Figure 2.[22]

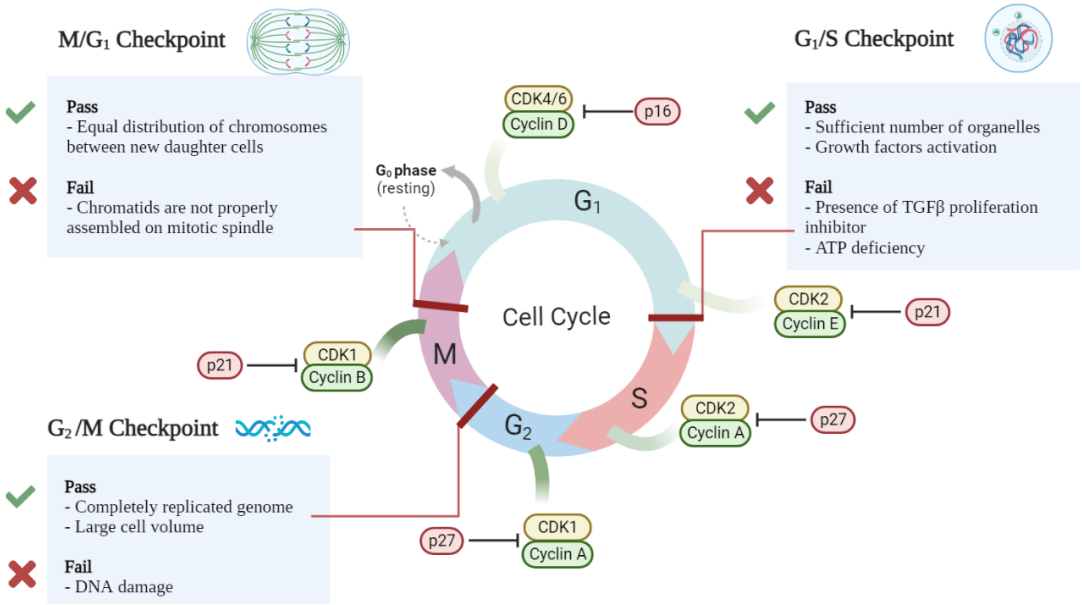

Figure 2. *Schematic representation of mammalian cell cycle and checkpoints.*

b) damage to DNA generated. Endogenous cellular processes and the effects of exogenous agents, such as exposue to UV irradiation, inappropriate diet, consumption of drugs, alcohol, or tobacco, and occupational exposures to harmful substances, constantly alter DNA.[23] These adverse outcomes generate 70,000 distinct damage events in a cell each day, contributing to the distortion of DNA structure. If left unrepaired, these events can

potentially stall replication or impact gene expression, ultimately leading to the generation of abnormal cells, as shown in Figure 3.[24]

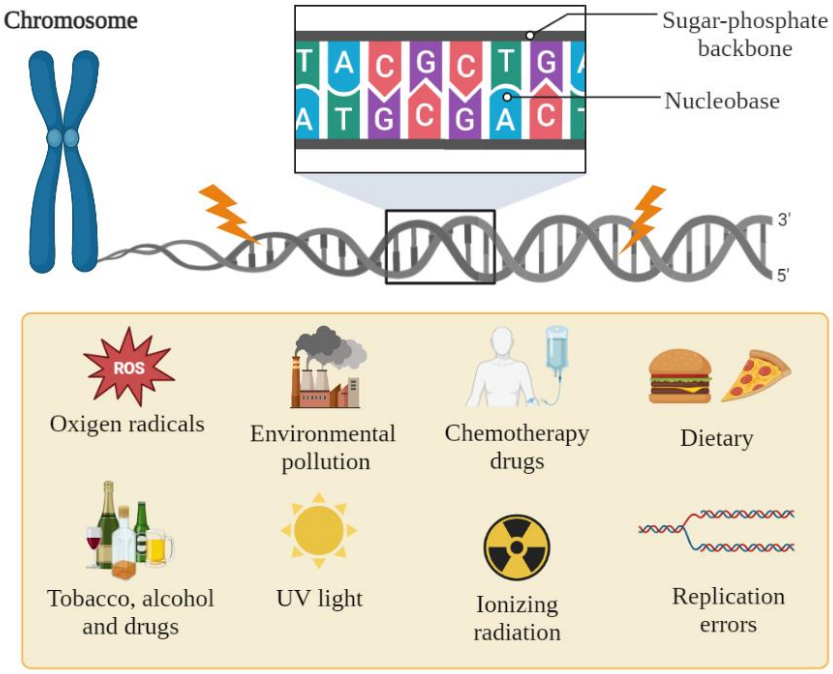

Figure 3. *Overview of the difference sources and exogenous exposures leading to DNA damage that contributes to generate cancer.*

c) heritance from our ancestors.[25] Recent studies have revealed that germline p53 mutations contributed to an increased predisposition to cancer.[26] This protein, known as guardian of the genome, plays a crucial role in cell cycle arrest, specifically by blocking the cycle at the beginning of DNA replication or before the mitotic stage if rare phenomena are detected.[27] Although inherited mutations can increase the risk of developing cancer, they are a minor cause of this disease.

It has been demonstrated that the body is able to eliminate those cells that suffer mutations in their DNA *via* the immune system. However, the efficacy of this phenomenon decreases with aging or when the number of aberrant cells is too high. Some of them can escape from this elimination process, promoting into a cancerous phenotype. Tumor cells can evade the immune attack using two main mechanisms: avoiding immune recognition or generating an immunosuppressive tumor microenvironment (TME). In the first strategy, cancer cells may lose the

expression of tumor antigens on the cell surface, thus avoiding the recognition by cytotoxic T cells that target those antigens. In the second approach, cancer cell-derived factors instigate an immune-tolerant TME, such as secreting suppressive molecules like IL-10,[28] or V domain immunoglobulin suppressor, which are crucial for T-cells activation.[29] When these strategies are combined, they result in a complex and efficient system for immune evasion.[30]

Sometimes, cancer evolves to metastatic cancer. In metastasis, tumor cells break away from their original tissues and form new tumors in other parts of the body. Metastasis is a multi-step process encompassing (1) the local infiltration of tumor cells, (2) the migration of cancer cells into vessels (a process called intravasation), (3) survival in the circulatory system, (4) extravasation and (5) subsequent proliferation and colonization at distal sites (Figure 4).[31] The velocity and aggressiveness of invasion of metastatic cells depends on the types of cells that are migrating and the cellular microenvironmental conditions. For that reason, new strategies are crucial for targeting cell movements or the adhesion of cancer cells in other tissues, as well as for developing antimetastatic drugs, in order to minimize this phenomenon. Actually, metastasis is the leading cause of cancer mortality.

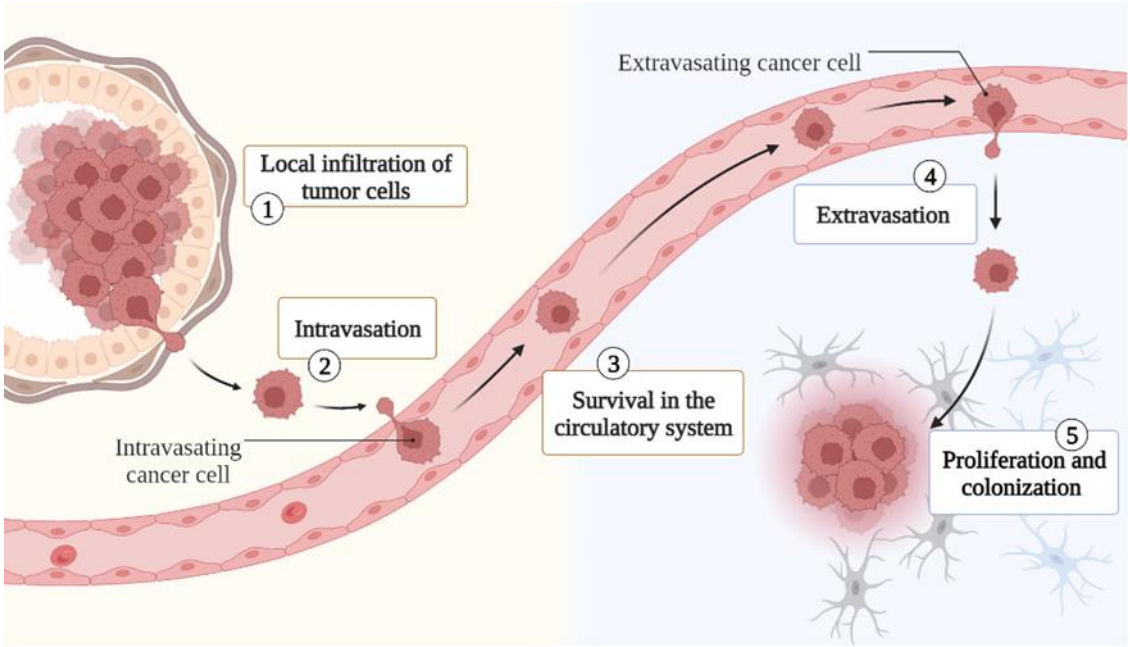

Figure 4. *Schematic representation of a metastatic process.*

Nowadays, more than 100 types of cancer have been described.[32] However, it is possible to categorize cancer based on the type of cells that give rise to them:

a) Carcinoma: This is the most common type of cancer. They are formed by aberrant epithelial cells. These cells cover the inside and outside surfaces of the body. In this group, stands out adenocarcinoma (breast, colon and prostate), basal cell carcinoma (epidermis), squamous cell carcinoma (stomach, intestine, lung, kidney) and transitional carcinoma (ureter, bladder).
b) Sarcoma: Cancer that is formed in bone or soft tissues as muscle, fat, or blood vessels, among others.
c) Leukemia: This type of cancer begins in the blood-forming tissue of the bone narrow. The main characteristic of this cancer is that it do not form solid tumors.
d) Lymphoma: Cancer that starts in lymphocytes (T or B cells), white blood cells that fight diseases and are part of the immune system. In lymphoma, abnormal lymphocytes build up in lymph nodes and lymph vessels, as well as in other organs of the body.
e) Multiple myeloma: Another type of cells that involve immune cells as plasma cells.
f) Melanoma: Most melanomas appears in the skin, but melanomas can also arise in other pigmented tissues, such as the eye.
g) Brain and spinal cord tumors.

The complexity of cancer results from multiple causes, a combination of altered gens, and the different tissues of origin. The main treatment modalities to tackle this illness include surgery, chemotherapy, radiotherapy, transplantation, and more recently, immunotherapy and hormone therapy.[33]

For early stages of tumors, cancer treatment strategies typically involve surgical resection of affected tissues followed by radiotherapy and/or chemotherapy.[34] Although radiotherapy is a powerful tool to destroy cancerous cells, it can also be harmful for healthy cells, organs, and tissues. Similarly, while chemotherapy has

been proven effective in reducing morbidity and mortality, chemotherapeutic agents also damage healthy cells, especially those undergoing rapid division and growth.[35] Drug resistance is a major disadvantage of chemotherapy. This phenomenon occurs wherein cancer cells that initially were eliminated by an anti-cancer drug, and with time are able to develop resistance to the used drug. Other limitations of conventional chemotherapeutic compounds include lack of specificity, rapid drug metabolism, and difficulty in dosage selection, which can lead to harmful side effects such as nephrotoxicity, alopecia, myelosuppression, among others.[36]

Metal-based chemotherapies have gained prominence since the discovery of cisplatin, *cis*-diamminedichloroplatinum(II), by B. Rosenberg in 1965.[37] Among metal-based anticancer drugs, cisplatin is the most used, and effective treatment against solid tumors such as melanoma, cervical, testicular, or ovarian cancers.[38] Currently, this Pt^{II}-complex is being used in combination with other drugs as topoisomerases II inhibitors (doxorubicin or bleomycin), mustards (melphalan) and antimetabolites.[39]As mentioned, one of the main drawbacks of cisplatin is generation of tumor resistance after repeated administration. To overcome this limitation, significant efforts have been made worldwide to develop a new generation of platinum analogues. Among them, carboplatin, a less active but safer drug, and especially oxaliplatin have entered as first-line treatment for colorectal cancers.[40]

Despite all the research that has been made, no success has been achieved in minimizing side effects, systemic toxicity, and the incidence of drug resistance. It is for this reason that non-platinum drugs are emerging as powerful alternatives, due to their different mode of action, biodistribution patterns, and final targets.

Gold, silver, copper, cobalt, zinc, ruthenium or iridium complexes have invoked considerable interest due to their demonstrated antiproliferative effects. These complexes offers the possibility of tuning their properties and mechanisms of action by variating the nature of the ligands.[41]

I.3 Gold (I) complexes: Properties and applications

Throughout the history of civilization, gold has been exploited for its therapeutic properties. It is considered a unique substance that can poison the mind faster than the body, as reflect by the myth of king Midas or more recently, Thesaurus in One Piece. The use of gold in medicine was first reported in China in 2500 BC. In medieval times, alchemists made an elixir known as *aurum potabile*, which was used to treat heart disease, impotence, dementia, and early aging. In the 17th century, Nicholas Culpepper published several pharmacopoeias, where the utilization of a gold cordial helped to cure fevers or melancholy, among other pathologies. Later on, in the 19th century, a mixture of gold and sodium chloride were used to treat syphilis, $Na[AuCl_4]$. The past century, Robert Koch discovered in 1890 the *in vitro* bacteriostatic properties of gold, but doctors largely ignored these findings until the discovery of Salvarsan (around 1910), and its demonstrated efficacy as treatment of rheumatoid arthritis. Other medical use of gold was as application of radioactive gold-198.[42,43]

Focusing in gold (I) complexes, it is known that they exhibit a d^{10} closed-shell configuration, which generally results in linear complexes, the most common disposition, and to a lesser extent, three- or four- coordinates with trigonal and tetrahedral coordination geometries, respectively. Due to its "soft" metal character, gold (I) has a pronounced tendency to form stable complexes with easily polarisable soft donor atoms, such as sulfur and phosphorus. [44]

An important consideration to take into account is that gold (I) exhibits a strong tendency to form linear complexes and presents a moderate capacity for being oxidized to gold (III). These two facts can only be explained by relativistic effects. The majority of late-transition metals, and especially in the case of gold, undergo an intense electrostatic attraction that suffered by *s* and *p* electrons as a results of the 79 protons in the nucleus, that generate an increase in the spinning velocities. Such velocities close to the speed of light can cause a rise in their mass.[45] In consequence, there is a contraction of the orbital, that mainly affects the *s* electrons, and even those in outer shells. However, the outer *d* electrons (*5d*) that

are shielded from the nucleus by the *s* electrons, experience a slight expansion. Consequently, the energy levels of *6s* orbitals decrease, being closer to *5d* orbitals (see Figure 5).

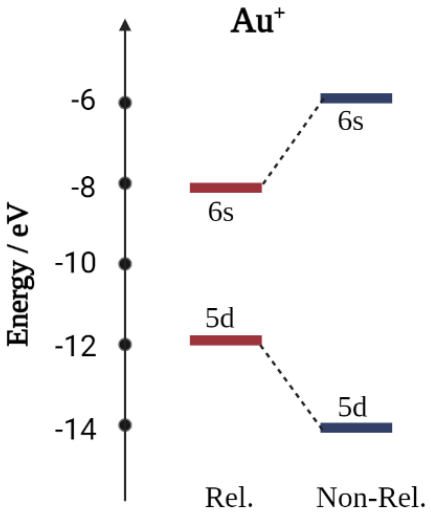

Figure 5. *Calculated relativistic and non-relativistic (n-1)d and ns orbitals for gold (n=6).*

This reduction on the gap of energy is also observed for *s*, *p* and *d* states, leading to the formation of hybrids *sp* or *sd* orbitals. This phenomenon can plausibly explain how d^{10} closed-shell configuration presented in gold (I) center loses its inertness and allows the interaction between two centers with the same charge, Au^{I}-Au^{I}, termed *aurophilicity*.[46] The aforementioned ability of gold (I) centers to interact with other metals as Ir^{III}, Ag^{I}, Cu^{I}, Pt^{II}, or itself is due to the possibility of modulating the energy from its frontier orbitals.[47]

The organometallic chemistry of gold has attracted much attention in the recent years. Many studies aim to increase the knowledge on the basis of the coordination properties of this metal. Initially, organogold complexes were explored merely as laboratory curiosities without any useful applications. However, years later, these complexes demonstrated their potential in a great variety of applications as a result of the exploration of their optical, biological and catalytic properties.[48] The most common uses of gold complexes are summarized in Figure 6, ranging from sensors to catalysts, materials, and drugs.

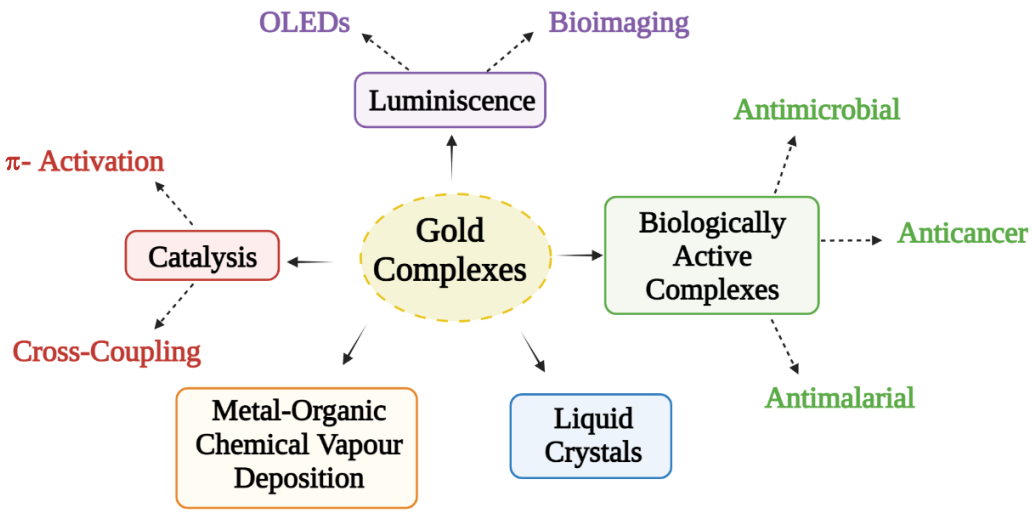

Figure 6. *Summary of applications of gold complexes.*

Gold compounds exhibit a wide range of activities towards several diseases, but they are largely studied for cancer treatment, with several gold complexes and nanoparticles in clinical trials. The design of gold complexes for antitumor activity over the past decades has been based on three pillars: i) Au^{I} drugs present immune-regulatory effects,[49] ii) structural analogies between square planar complexes of Au^{III} and Pt^{II}, and equal electronic configurations d^8, iii) possibility of using gold drugs in combination with other treatments to potentiate their effects.[50]

Focusing on gold (I) complexes with anticancer properties, it can be said that Auranofin is by far the most well-known gold drug used for treatment of cancer and is currently in phase II of clinical trials. The presence of phosphine and thiolate ligands in its structure (Figure 1), helps to stabilize the gold (I) center due to the high strength of Au-P and Au-S bonds.[51] Gold complexes exhibit a proven efficiency inhibiting the function of the mitochondrial thioredoxin system, which is composed by thioredoxin (Trx), thioredoxin reductase (TrxR), and NADPH as the key components, as shown in Figure 7.[52] Thioredoxin system takes part in many cellular processes, such as the reduction of protein disulphide, regulation of ROS species, and in some transcription factors critical for cell proliferation. Cancer cells need to synthetize transcription factors to promote its proliferation and spread. Therefore, the reduction of Trx by TrxR is an essential process for cancer

cells,[53] and thioredoxin system contributes to the propagation of tumor cells and chemoresistance, making it an important target for antitumor compounds.[54]

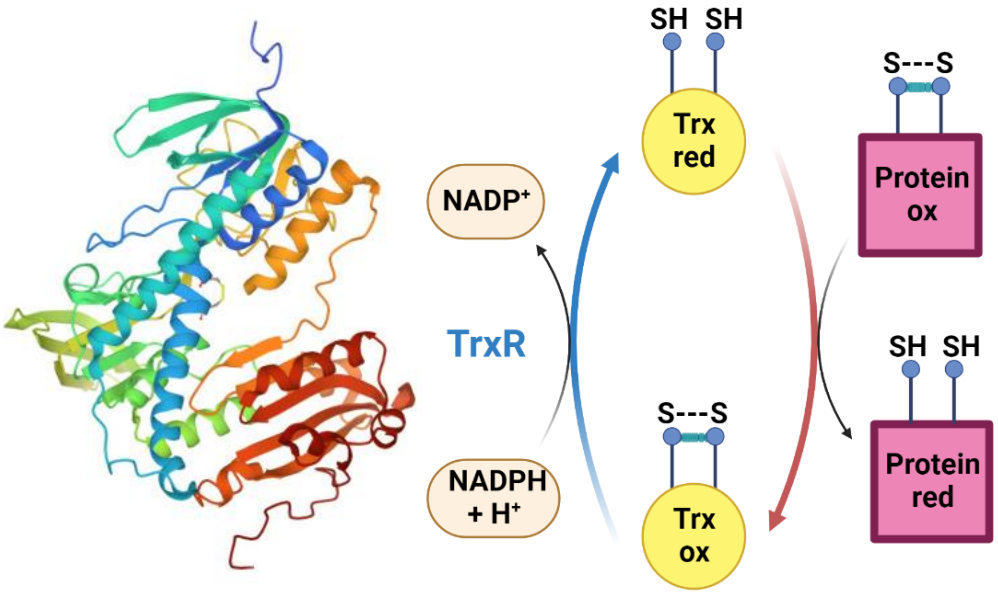

Figure 7. *Schematic representation of reactions that take place in Trx system.*

The thiol group in the reduced form of Trx can bind to soft metal ions like Au^{I}. If gold (I) center binds to Trx, it can block its activity, leading to mitochondrial damage and impairment of Trx enzyme to maintain redox homeostasis, and in last term leading to cell death. Therefore, research into gold (I) anticancer complexes is of great interest within the development of new anticancer drugs.

I.4 Iridium (III) complexes: Applications

The search for an efficient cancer treatment has been ongoing for many years, and humanity has looked for answers in deities as well as the stars. Interestingly, iridium, which is extremely abundant in meteorites, has its origin in this quest. Iridium is one of the less abundant metals of the platinum group, and possesses an electronic configuration of $[Xe]4f^{14}5d^{7}6s^{2}$. It was discovered in 1804 by Smithson Tennat as an impurity in platinum. Iridium is not only the most resistant metals to corrosion but also insoluble in all mineral acids, including *aqua regia*. Futhermore, it has a high melting point and can maintain properties in air at temperatures above

1600 ºC.[55] The chemistry of iridium is extremely varied, exhibiting all oxidation states from -1 to +9, and three coordination numbers (4, 5 and 6), giving several geometries. However, oxidation states +1 and +3 are the most common. In the oxidation state +1, iridium presents a tetra- or penta-coordinate geometry, giving square planar and trigonal bipyramidal complexes, respectively. In contrast, iridium (III) is a $5d^6$ center, and the majority of complexes are hexacoordinated and octahedral disposition.[56] In the last years, iridium (I) and (III) complexes have experienced an incredible increase in their uses and applications, being applied in fields such as catalysis and photocatalysis,[57] in luminescent material such as OLEDs in televisions,[58] or as photosensitizers (PSs)[59] in medicine. As the aim of this thesis is the delivery of novel trackable anticancer agents, the scope of this introduction will be restricted to bioactive and emissive cyclometallated iridium (III) complexes that have demonstrated their great prospect in medicine and bioimaging.

At this point, it is necessary to make special emphasis in the principles that govern the phenomenon of luminescence. Luminescence is defined as "a spontaneous emission of radiation from an electronically excited species or from a vibrational excited species not in thermal equilibrium with its environment".[60] According to the mode of excitation, luminescence can be classify as shown in Table 1.[61]

Table 1. *Origin of the various types of luminescence.*

Phenomenom	**Mode of excitation**
Photoluminiscence	Absorption of light (photons)
Electroluminiscence	Electric field
Chemiluminiscence	Chemical reaction
Bioluminiscence	*In vivo* biological reaction
Radioluminiscence	Ionizing radiation
Thermoluminiscence	Heating after prior storage of energy
Cathodoluminiscence	Cathode rays
Sonoluminiscence	Ultrasound
Triboluminiscence	Frictional and electrostatic forces

Fluorescence and phosphorescence are particular types of luminescence. To describe the differences between both processes, it is convenient to use an energy diagram known as Perrin-Jablonski Diagram. This diagram represents the electronic states of a molecule and indicates the possible transitions, as shown in Figure 8.[62,63]

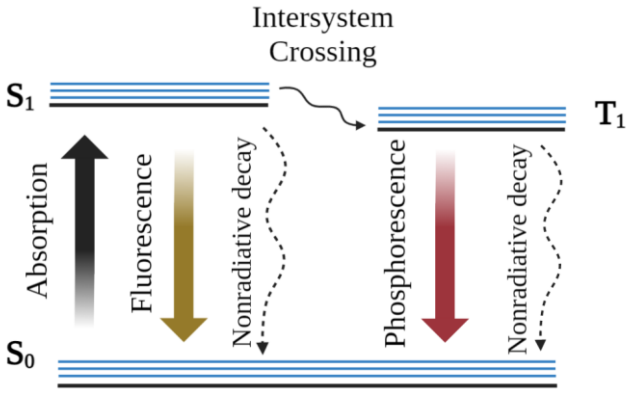

Figure 8. *Simplified Perrin-Jablonski diagram.*

In view of this schematic image, fluorescence could be explained as an emission from the first excited singlet state (S_1) that is reached upon light absorption. On contrary, phosphorescence is an emission from the triplet state (T_1) after a process of intersystem crossing, which is a nonradiative transition between two isoenergic vibrational levels belonging to electronic states of different multiplicities from S1. However, some more appropriate definitions could be:[60]

a) Fluorescence: Spontaneous emission of radiation (luminescence) from an excited molecular entity with retention of spin multiplicity.
b) Phosphorescence: Long-lived luminescence that involves a change in spin multiplicity, typically from singlet to triplet state or vice versa.

Two other important concepts in molecular luminescence are lifetimes and quantum yields. Lifetime is related to the time that a fluorophore remains on average in the excited state before the emission takes place. Commonly, a fluorescence process presents lifetimes between 10^{-10} to 10^{-7} s, while a phosphorescent one exhibits higher values, between 10^{-6} to 10 s. Otherwise, the quantum yield indicates how effective the emissive process is, in other words, it is

the ratio of the number of photons emitted to the number of photons absorbed. Some of absorbed protons are lost in nonradiative pathways that include internal conversion processes as well as nonradiative conversion via intersystem crossing phenomena. (Figure 8).

Coming back to luminescent metal complexes, and focusing on transition metals, four electronic transitions are possible: i) metal-centered (MC), that are influenced by the symmetry of the complex, in the case of iridium *d-d* transitions; ii) MLCT, metal-to-ligand charge transfer; iii) LMCT, ligand-to-metal charge transfer, iv) LC or IL, ligand-centered or intraligand transitions, and v) LLCT, ligand-to-ligand charge transfer.[64] In iridium (III) complexes, the *d* orbitals have strong interactions with the ligands, and there are just a few examples where the metal do not contribute to the emissive process. Therefore, the transition mainly responsible of the phosphorescence in cyclometallated Ir^{III} complexes is originated from ^{3}MLCT state, which is attained by intersystem crossing (ISC) from the higher lying singlet MLCT state, as shown in Figure 9. This fact results in lifetimes in the range of hundreds of nanoseconds.

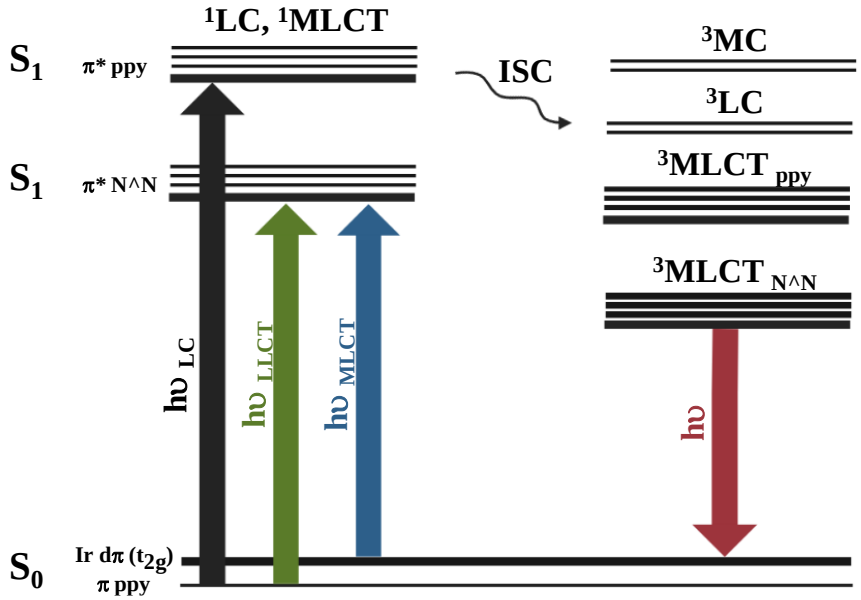

Figure 9. *MO diagram showing transitions for iridium (III) complexes of the type* $[Ir(ppy)_2(N^N)]^{0/+}$.

Specifically, cyclometallated iridium complexes exhibit tuneable emission through the coordination of different ligands, superior photostability, and large Stokes' shifts that can minimize self-quenching processes. In addition, these complexes display a diverse emissive-state character, ^{3}MLCT, ^{3}LC or ^{3}LL'CT.

I.4.1 Iridium (III) complexes as imaging agents

Iridium (III) complexes exhibit many advantageous characteristics for their use in biological applications. For instance, they can be bonded to a wide range of ligands which enables fine tuning of their physical and chemical properties. Regarding the cellular uptake of these complexes, it can be easily quantitated by several techniques as atomic absorption spectroscopy (AAS) or inductively-coupled plasma mass spectrometry (ICP-MS). Many of these complexes, especially those with pyridine-derivated ligands, demonstrate outstanding optical properties, which not only enable tracking of their intracellular trafficking process but also help determine their final biodistribution within cells. These complexes can also be visualized using other techniques as fluorescence confocal microscopy or fluorescence lifetime imaging microscopy (FLIM).[65]

Among these techniques, confocal fluorescence microscopy stands out as an optical method that can provide high-resolution images of fixed and non-fixed cells or tissues.[66] Instead of illuminating the whole sample at once, it uses a laser focused on a specific part of the sample. So the emission of light only came from this point, thanks a pinhole that cuts off signals that are out of focus. In this way only the signals from the illuminated region of the sample are allowed to enter on the detector, as shown Figure 10.

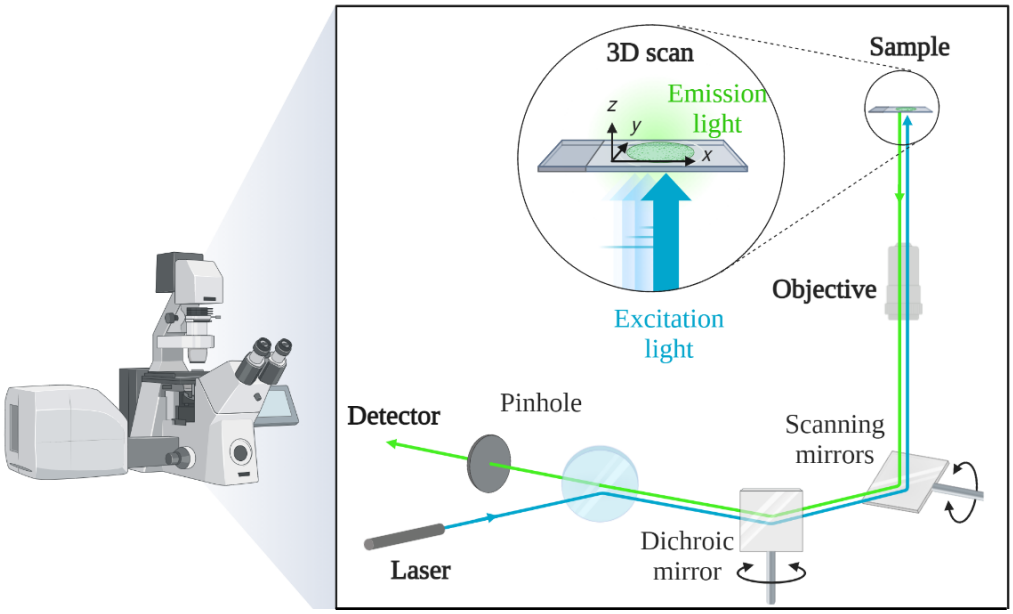

Figure 10. *Schematic representation of excitation and emission light pathways in a fluorescence confocal microscope configuration.*

Although confocal microscopy has mainly been used in research laboratories, its application in clinical settings has also been reported, but it has not yet been globally extended. [67,68] This technique has gained importance in surgical oncology because it offers the possibility to analyze fresh tissues at high resolution, avoiding a tedious tissue processing.[69]

Considering all these facts, it can be said that cyclometallated iridium (III) complexes are appropriate candidates as luminescent biological reagents, as many recent reports have demonstrated.[70] Figure 11 presents a selection of different Ir^{III} complexes that have shown accumulation in either tubuline, lysosome, mitochondria, or endoplasmic reticulum, driven by their different chemical structure.

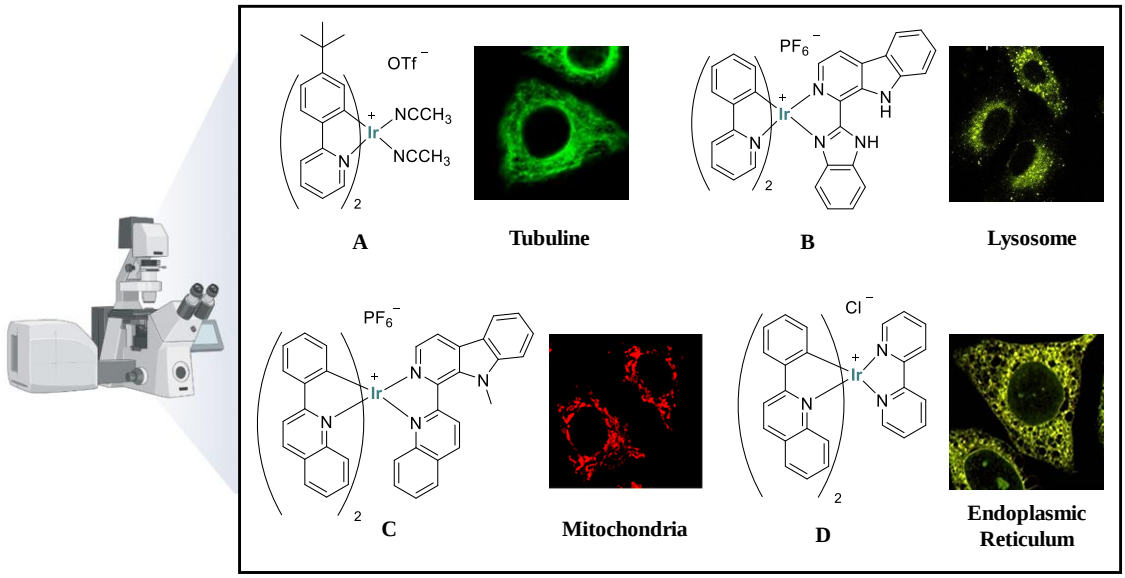

Figure 11. *Cyclometallated Ir^{III} complexes and their biodistribution using confocal microscopy. A) Incubated at 10 μM in HeLa cells;[71] B) Incubated at 10 μM in A549 cells;[72] C) Incubated at 1 μM in A549 cells;[73] D) Incubated at 10 μM in HeLa cells.[74]*

However, cyclometallated iridium (III) complexes are not solely designed as luminescent bioprobes. The need to discover new chemotherapeutic agents with fewer side effects has led to the exploration of other transition metals, different to platinum or gold drugs, for the treatment for malignant tumors. Compared to these metals, iridium complexes possess many excellent features such as high stability, exceptional phosphorescent properties, many possibilities of coordination, easy derivatization of their ligands, which enables modulation of their bioactive and photopysical properties, and increased solubility in biological environments.[75]. Apart from the numerous examples on Ir^{III} complexes reported as visualisation and chemotherapeutic agents, there is a new trend focusing on their excellent prospects as photosensitizers (PSs) for photodynamic therapy (PDT).[76]

I.4.2 The origin of PDT

For ages, PDT has been used as a treatment for several diseases. For instance, in ancient Egypt, India, and China, light was utilized as therapy of skin diseases.[77] In these civilizations, the Sun represented an important part of their cultures, and they firmly believed that sunlight could have associated healing properties.[78] This belief led to the use of the Sun in terms of heliotherapy (use of sunlight or other UV, visible or IR radiation for therapeutic purposes), which was later recorded by Herodotus by ancient Greece.[79] In the 18th and 19th centuries, sunlight gained relevance and was used to treat paralysis, muscle weakness, tuberculosis, and rheumatism.

PDT emerged as a new, globally recognized modality of treatment in the early 20th century. Niels Finsen was a pioneer in this field, having found that exposure to red light could prevent the formation of pustules and reduce skin cancers. In 1903, he was awarded the Nobel Prize for his studies.[80] Since then, many scientists have observed that the combination of light with different chemical reagents could induce cell death. For example, Oscar Raab reported that the combination of acridine with the appropriate wavelengths, could be lethal to infusoria (aquatic micro life found within any aqueous media).[81] The french J. Prime found that epileptic people who was treated with Eosin presented side effects as dermatitis after sun-exposition.[82] Later, H. Von Tappeiner and A. Jesionek demonstrated the efficacy of this compound to treat skin tumours after its activation via white light, and named this phenomenon as "photodynamic action", underlining that light was the basis in this process.[83] However, due to the World Wars I and II, the evolution of this technique was abandoned for nearly 60 years.

In 1960, PDT reintroduced by Richard Lipson and colleagues at the Mayo Clinic.[84] For these studies it was used a compound that was developed by Samuel Schwartz called 'haematoporphyrin derivative' (HPD).[85] HPD preferentially localized in tumors, where it emitted fluorescence, and was considered as a promising diagnosis tool. However, it took a long time for PDT to be implemented therapeutically in oncologic patients. A significant change occurred in 1975 when

Thomas Dougherty and co-workers reported that administration of HPD in combination with red light completely disrupted mammary tumor growth and eliminated bladder carcinoma in mice.[86] The following year, Kelly and co-workers initiated the first human trials with HPD in patients with bladder cancer.[87] After preliminary successes in treating bladder and skin tumors, many researchers started to used PDT to deal with other types of cancer. However, this technique is limited due to the low specificity and potency of photosensitisers (PSs). Since then, more selective and powerful PSs have been developed, many of which are under investigation in clinical trials, as Photofrin (activation wavelength, a.w., 620 nm) for the treatment of cervical, oesophageal, bladder, and gastric cancers, as well as brain tumours or Lutex (a.w. 732 nm) for treatment of cervical, prostate and brain tumors.[88] More recently, Temoporfin and Padeliporfin(not shown) were approved by EMA (European Medicines Agency) for esophageal and prostate cancers, respectively. See Figure 12.

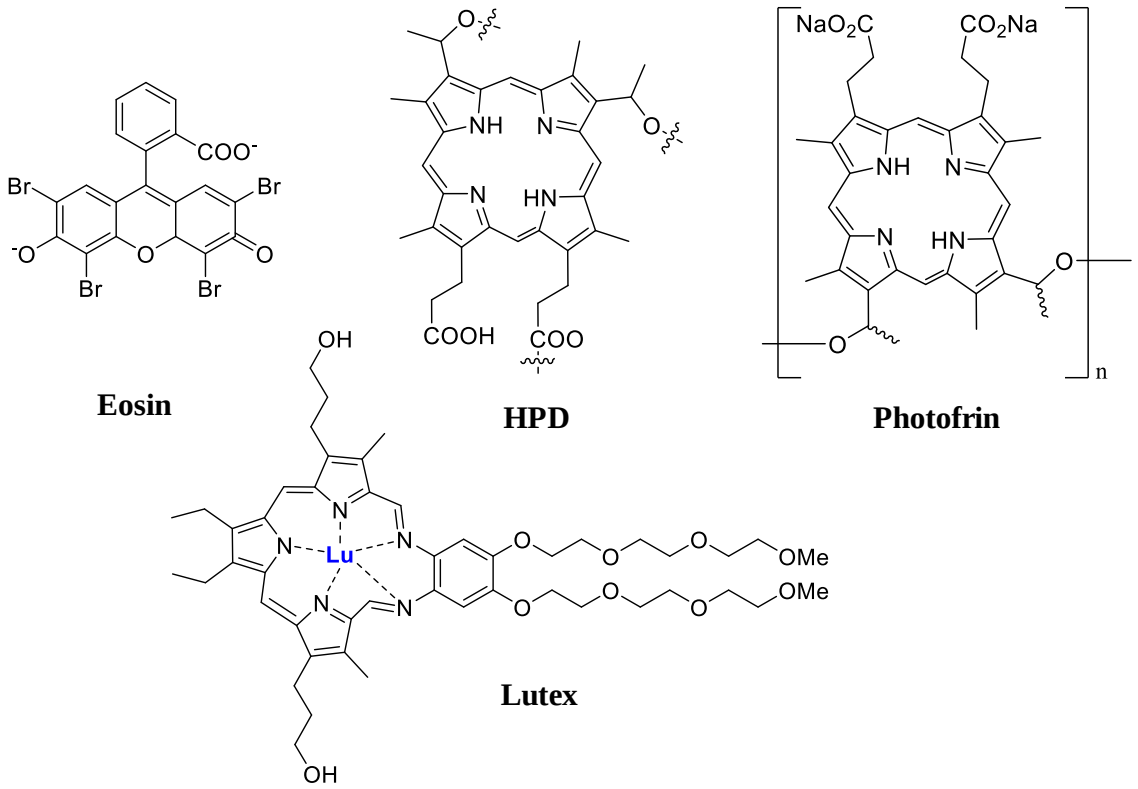

Figure 12. *Chemical structures of the most representative PSs in PDT.*

I.4.2.1 PDT: Mechanism of action

During PDT, a PS is injected either locally or systemically in the patient using a non-toxic dose. The PS is distributed randomly until it accumulates in the target tissue. After the incubation time, which can vary from minutes to hours, the target tissue is irradiated with light using the appropriate wavelength. Therefore, effects of PDT occur only in the region where the PS has been internalized,[89,90,91] as shown Figure 13.

The irradiation wavelength is a crucial factor in PDT. This light is selected based on two criteria: the activation wavelength of PS and the shape and depth of the tumor. Wavelengths between blue and green spectrum, (400-550 nm), present almost no penetration into the tissue due to scattering effects of light. However, the use of higher wavelengths in the red or near infrared region ($\lambda_{irr.}$ >700 nm) allows deeper tissue penetration.[92]

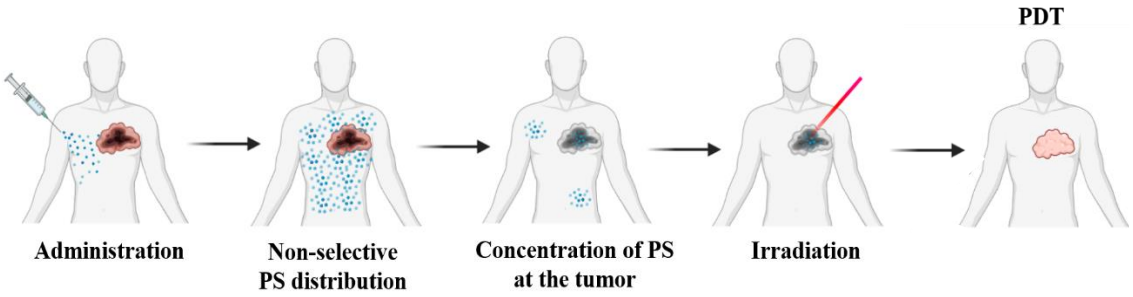

Figure 13. *Clinical PDT procedure.*

Upon irradiation, the PS follows a photophysical mechanism in which an electron is excited from its ground state to the singlet excited state. Thereafter, it could suffer an intersystem crossing process (ICS) to a triplet excited state. From this level, the excited PS can release the energy via decay to the ground state through a radiative process or interact with the biological environment by two different pathways: Type I or Type II, as shown in Figure 14. In the Type I mechanism, several biomolecules including water are oxidized generating ROS (reactive oxygen species), such as hydroxyl or superoxide radicals. On the other hand, the Type II mechanism involves the transfer of energy to molecular oxygen ($^3O_2$) to

form highly cytotoxic singlet oxygen species ($^1O_2$).[93,94] It is generally accepted that Type II mechanism is the predominant pathway for most of the currently approved PSs.[95]

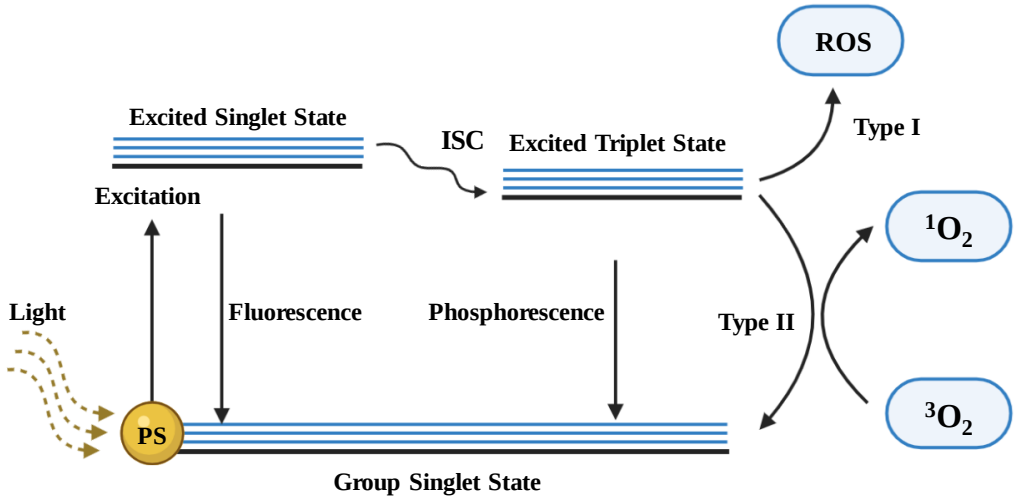

Figure 14. *Mechanism of action of PDT on tumors.*

In view of the limitations and characteristics of PDT, an optimum PS should have some common features, such as: (a) strong absorption in the red/near infrared (NIR) region of the electromagnetic spectrum to allow the treatment of inner tumors; (b) a high quantum yield of the triple excited state to efficiently populate the excited state, (c) a long excited state lifetime, which facilitates the generation of ROS; (d) being innocuous in dark, which generates a high spatiotemporal control and low systemic toxicity of the treatment; (e) fast clearance from the body, decreasing the possibility of suffering side effects, and (f) a short and highly yielding synthetic route.[96]

I.4.2.2 Therapeutic applications of photodynamic therapy

As previously mentioned, PDT has several indications in different cancer types, for instance, esophageal cancer, non-small-cell lung cancer, prostate cancer, and superficial basal cell carcinoma.[97,98,99] Clinically, the most commonly used PSs are derivatives of porphyrin, as shown in Figure 12. However, these organic PSs have some drawbacks, such as poor water solubility and low tissue penetration, making

them unsuitable for the treatment of inner cancers. To overcome such limitations and fulfill the characteristics described in the previous section, late transition metals such as ruthenium, osmium or iridium have been extensively investigated. The use of these late transition metal complexes is increasing due to the intrinsic properties based on the metal atom, such as the partially filled *d* subshell, the possibility to give rise to cations with an incomplete *d* subshell.[100,101] This characteristic provides attractive photophysical and chemical properties, including strong luminescence, chemical and photophysical stability, high yielding singlet oxygen production upon light irradiation due to spin–orbit coupling, which leads the ultrafast and efficient generation of population of triplet excited states, and[102,103] consequently, such efficient population of the triplet excited state will render high yields for the generation of ROS. Moreover, these metal complexes have demonstrated therapeutic capacity in PDT.[104,105] As previously mentioned, the generation of $^1O_2$ is responsible for the oxidation of different cellular components, subsequently generating cell death. However, the specific molecular mechanisms that generate metal-based PDT cytotoxicity vary depending on the metal and their biodistribution. Some transition metals interact with DNA, generating DNA damage, while others provoke cell death via mitochondria or endoplasmic reticulum stress, as shown in Figure 15.

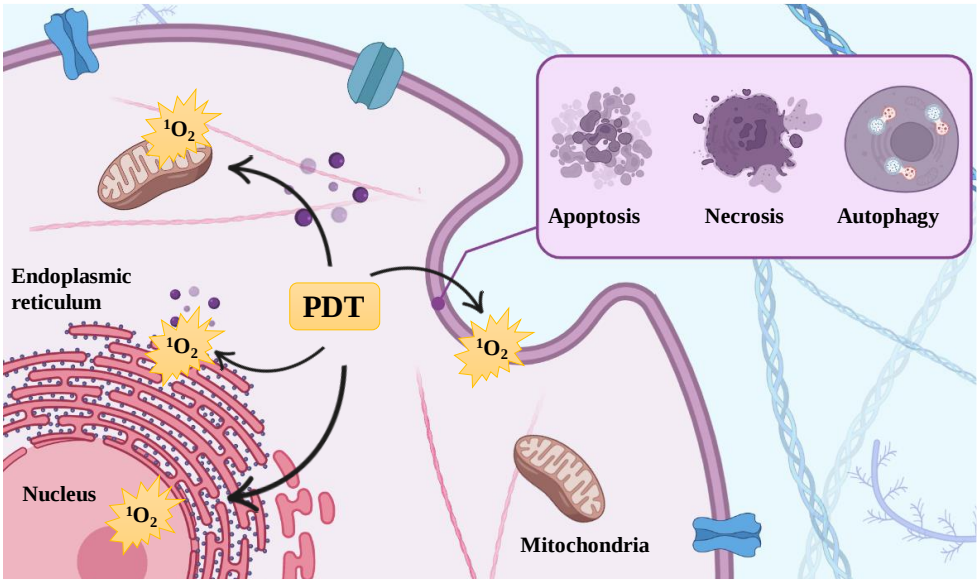

Figure 15. *Representation of cellular damage generated by PDT and the different cell death pathways induced.*

TLD1433 is the first metal-based PS that was entered clinical trial for the treatment of bladder cancer with PDT (Figure 1). This Ru^{II} complex was developed by Prof. McFarland and coworkers, and its good perspective in PDT has stimulated further investigation in this field.[99] Additionally, Ir^{III} complexes have demonstrated their capacity as PSs. Most of them present high quantum yields in the triplet excited state, enabling an efficiently production of ROS.[106] Recent publications suggest that these complexes have the tendency to accumulate in mitochondria and lysosomes, which are key organelles in the fight against cancer.[107,108]

If accumulation occurs in mitochondria, it can induce mitochondrial damage and highly ROS production, resulting in cytochrome *c* release, caspase-3 and PARP cleavage, and apoptotic cell death without disruptioning the cell cycle or causing genotoxicity.[109] Furthermore, singlet oxygen production in the mitochondrial region could be more efficient than in other parts of the cell due to the higher concentration of oxygen, resulting in more toxicity. The crucial role of mitochondria in regulating different cellular functions, such as cellular energy production or the control of apoptotic factors, among others, makes that many efforts in PDT are devoted to the design of mitochondria selective PSs.[110] Alternatively, if accumulation occurs in lysosomes, multiple cellular functions could also be affected, such as the catabolism of complex substrates, nutrient digestion, and signalling pathways involved in cell metabolism and growth. These alterations are known as lysosomal storage diseases (LSDs), and they are directly connected with an apoptotic cell death mechanism.[111]

Considering the importance of the organelle accumulation, being able to elucidate the biodistribution of the drug to ensure its trafficking into mitochondria or lysosomes prior to photoactivation could be crucial for increasing therapeutic potential of PSs.

I.4.3 Theranostic complexes

Despite significant efforts devoted to understand cancer cell biology and the development of anticancer drugs, this disease continues being an important cause of mortality. Statistics are not optimistic; they predict that the number of people diagnosed with cancer will increase by 60% within following two decades.[112] Besides, the widely used treatments for cancer were surgery, radiotherapy and chemotherapy and, some new modalities such as hormone-based therapy, stem cell therapy, immunotherapy[113] there is an emerging modality in the last years called theranosis.

In 1998, John Funkhouser reported the term theranostic agent, that was used to describe those materials that combine properties of therapy and diagnostic imaging. However, the concept of theranosis comes from nuclear medicine. In the 1940s, radioactive iodine $^{123}I^-$ was used for both, treatment of thyroid cancers and its diagnose.[114] Nowadays, the concept of theranostic agent is commonly used to describe those drugs that combine in a unique system therapeutic and diagnostic properties (Figure 16).

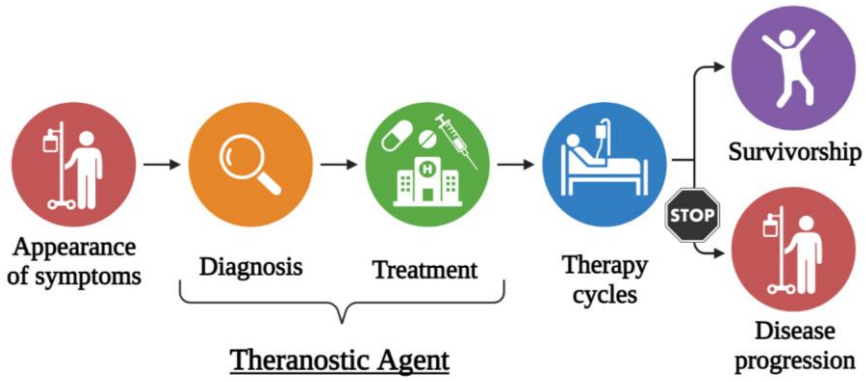

Figure 16. *Stages of cancer treatment. Application of theranostic agents.*

Thus, theranosis encompasses diagnostic and therapeutic functions in a single system, allowing to monitoring the response at the same time.[115] Among the most relevant non-invasive techniques used for monitoring the response or visualizing the trafficking of drugs, the following can be found:

- Positron emission tomography (PET). It measures, in a quantitative way, the physiological function by looking parameters as blood flow, metabolism, neurotransmitters, and radiolabelled drugs. This technique allows monitoring changes over time as a disease process evolves or in response to a specific stimulus.[116]

- Single photon emission computer tomography (SPECT). This technique is a nuclear imaging modality used frequently in diagnosis. It produces a 3-dimensional image of the distribution of a radioactive tracer injected into the bloodstream and subsequently taken up by certain tissues. SPECT allows the clinician to assess the functionality of specific tissues.[117]

- Computed tomography (CT). It combines a series of X-ray images taken from different angles around your body and uses computer processing to create cross-sectional images (slices) of the bones, blood vessels and soft tissues inside the body.[118]

- Magnetic resonance imaging (MRI). A visualization technique that uses normally paramagnetic species such as Gd^{3+} complexes or supramagnetic iron species to produce detailed images from any part of the body. For this purposes the hydrogen nucleus (proton) is used due to its abundance in water and fat.[119]

- Fluorescence microscopy. This is used for rapid medical diagnosis and relies in fluorochromes that are specific for an infecting agent, cell organelle, or cellular type.[120]

It is important to note that all mentioned-techniques are not exempted from disadvantages in terms of tissue penetration, resolution, or applicability.[121] Sometimes it is difficult to select the appropriate one to obtain the desired diagnosis.[122] However, considering the high cost of some of these techniques (such as MRI, CT, PET, and SPECT) together with the necessity of using radionuclides or isotopes (in MRI, PET and SPECT), makes fluorescence microscopy a good alternative for drug visualization. In particular, this technique has key features,

including sensitivity, real-time visualization and non-ionization safety, which make the delivery of novel optical probes very appealing.

Taking into account the advantages displayed by this technique, and the importance at the stage of drug design of knowing the pathway that a drug follows into cells for addressing more effective treatments, it seems like a great idea to combine a bioprobe with a luminescent fragment to function as tracking tag. Thus, the design of metallic bifunctional bioprobes is based on the combination of a selective metallic drug with a visualization agent. The trackable metallic bioprobe can have different nature, and its design could be conceived also in several ways. For instance, type 1) the introduction of an organic chromophore in the structure of a metal-based drug, type 2) the synthesis of luminescent metal-based drug with anticancer properties, or type 3) combining two different metal fragments in the same molecule, one of them providing the optical properties and the other the therapeutic ones (Figure 17).[123]

Within type 1 theranostic agents, traditionally, organic chromophores as acridine, anthracene, coumarine, or BODIPY have been used as optical probes for the development of trackable drugs. However, these organic molecules present some limitations in their optical properties when they are used as tags in fluorescence microscopy, such as short lifetimes, difficult emission tuning, or easy photobleaching processes. Instead, metal-based optical probes (type 2) have been proven as excellent candidates in fluorescence visualization techniques due to their phosphorescent emission nature and their robustness towards photobleaching processes.

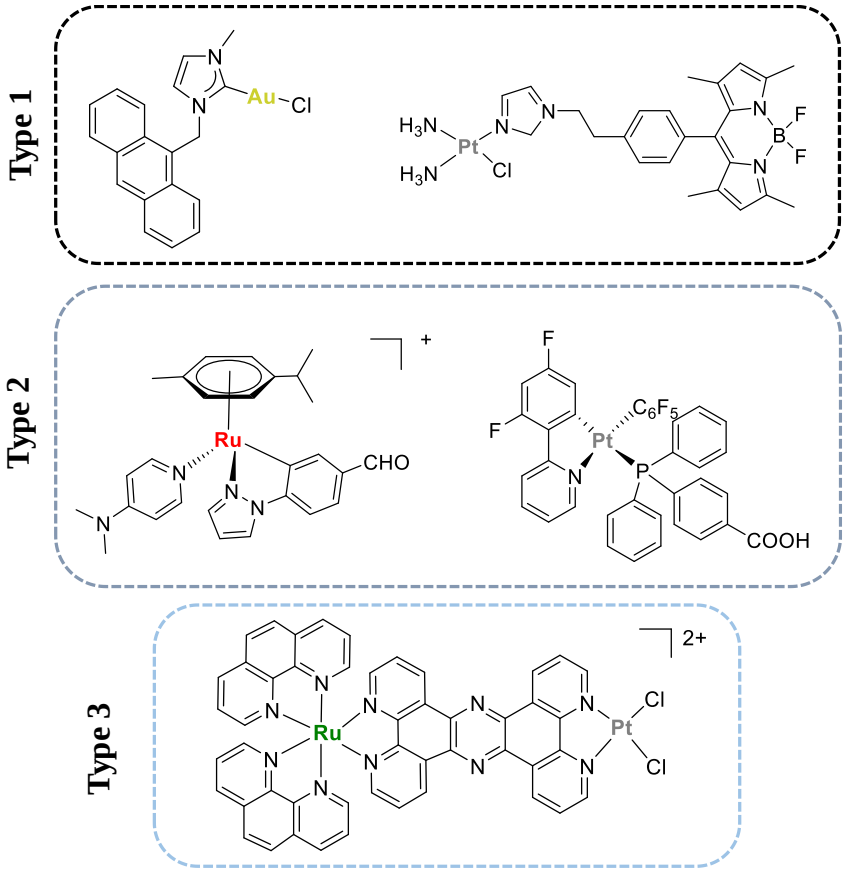

Figure 16. *Example of theranostic agents. Type 1, metallodrugs that contain in their structures a chromophore;*[124,125] *type2, luminescent metallodrugs;*[126,127] *type 3, bimetallic complexes.*[128]

Finally, the third type of theranostic agents are those based on heterobimetallic complexes. It has been proven that the presence of two different metallic fragments with inherent bioactive and emissive properties respectively fragments can generate a synergic effect. Therefore, the luminescent metallic fragment not only allows the tracking of the of the complex, but also in many occasions is able to increase the cytotoxic potential, in comparison with that of the mononuclear species.[129,127]

The design of these complexes starts with the selection of the appropriate fragments that should be connected by strong bonds in order to avoid their disruption. So, the selection of a ditopic ligand that could connect both metallic fragments could be considered a key feature for this type of theranostic agents. In this context, several examples have been reported, confirming the effectiveness of this modality of bimetallic complexes. For instance: in 2014, the first bimetallic

d^6-d^{10}, Re^I-Au^I, trackable complex was synthetized by Fernández-Moreira and Gimeno.[130] The authors used pyridine ligands functionalized with an alkynyl group as linker between both metal centers. Thus, the Re^I fragment was easily coordinated to the nitrogen atom of the pyridine, whereas the Au^I fragment was introduced within the alkynyl moiety upon deprotonation. (Figure 18). It was verified that the cytotoxic activity of the bimetallic species was much higher (IC_{50}: 4.4-19 μM) than the mono metallic Re^I ones (IC_{50}: 150-200 μM) in lung cancer cell line, A549. In addition, the presence of the gold fragment not only increased the cytotoxic potential, but also drove a completely different cellular biodistribution pattern. So, the presence of the bioactive gold center directs the bioaccumulation of the complex from the mitochondria to the nucleus, acting as a vector to target different organelles. (Figure 18).

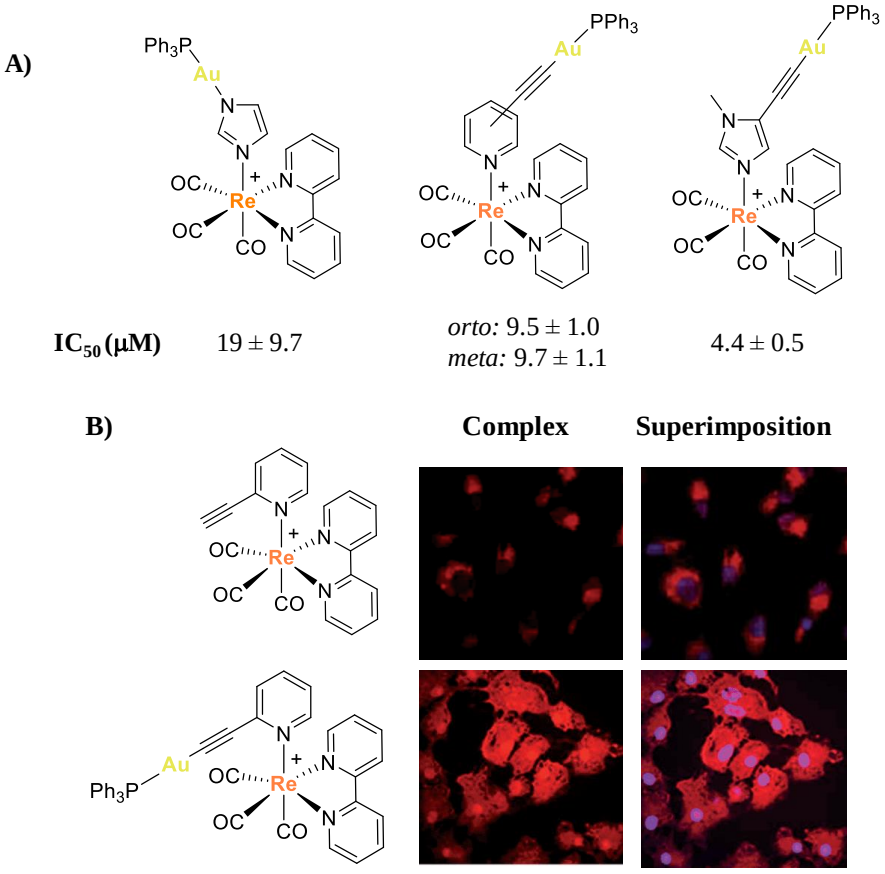

Figure 18. *A) Reported examples of Re^I-Au^I theranostic agents. B) Biodistribution profiles of monometallic and heterobimetallic complexes in A549 cells at 150 and 10 μM, respectively, after 4 hours of incubation. (Red colour: emission from the synthesised complexes, blue colour: emission from DRAQ5).*

One year later, the first example of heterometallic emissive Ru^{II} and a bioactive Au^{I} species was described by Hemmert and Gornitzka.[131] They funtionalized the typical emissive $[Ru(bipy)_2(N\text{^}N)]_2^+$ core, where N^N represents a diimine ligand derivatized with an imidazole ring that was used as linker for binding the Au^{I} fragment. The correspondent heterometallic Ru^{II}-Au^{I}-NHC complexes obtained exhibited high cytotoxicity in human hepatocellular carcinoma cells (Hep3B), and thanks to the optical properties conferred by the Ru^{II} fragment, it was possible to observe their biodistribution using fluorescence confocal microscopy. As it is shown in Figure 19, these complexes localize in the cytoplasm, mainly in the peripheral area of the nuclei of liver cancer cells Hep3B.

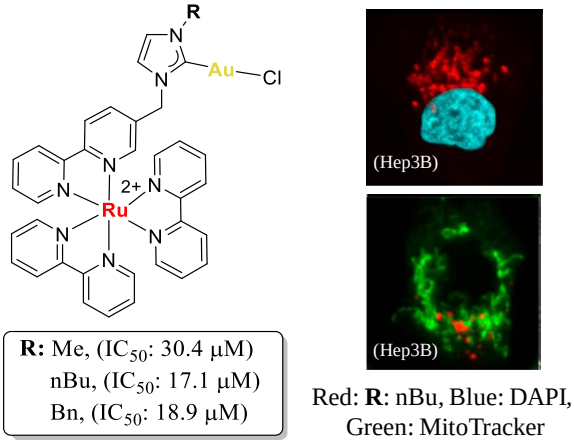

Figure 19. *IC_{50} values of depicted complexes in human hepatocellular carcinoma cells (Hep3B), and cellular biodistribution of Ru^{II}-Au^{I} (R: nBu), using fluorescence confocal microscopy.*

In the same line, Ir^{III} complexes bearing cyclometallated ligands exhibit well-known optical properties,[132] with capability for being used in cellular imaging, as well as, a great stability in biological media. In 2020, Fernández-Moreira and Gimeno synthetized the first example of heterobimetallic Ir^{III}-Au^{I} complexes that can be used as theranostic agents.[133] In this article, the authors used peptide bioconjugates as linker between the two metal centers. The aim of the peptide was to improve water solubility and, at the same time, to facilitate cell recognition of the complex. The introduction of the gold fragment was achieved by coordination through different groups (alkynyl or sulfur) included in the design of the peptides. Fluorescence microscopy confirmed a lysosomal accumulation for all the

synthetized complexes. The cytotoxicity of all species was conditioned by the strength of the Au-ligand bond. While Au^{I}-S(cysteine) bond was more readily cleaved in a biological environment, rendering therefore a high toxicity, the Au^{I}-C(triazole) bond was more stable, forcing the gold fragment to stay trapped in the lysosome and eventually hindering its cytotoxicity (Figure 20).[134]

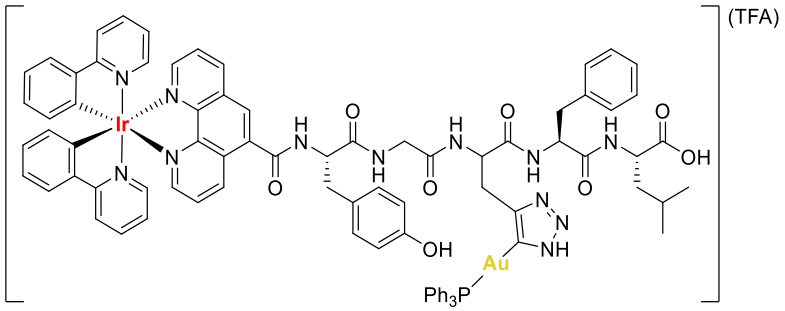

IC_{50}(A549, 24 h): >50 μM

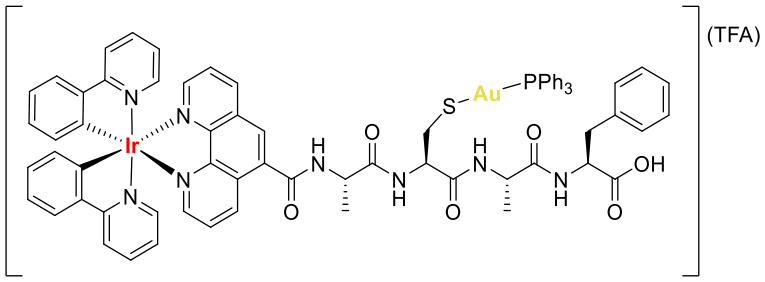

IC_{50}(A549, 24 h): 12.3±1.83 μM

Figure 20. *Chemical structures of binuclear Ir^{III}-Au^{I} complexes and their IC_{50} values measured in A549 cells after 24 h of incubation.*

In general, the lack of information regarding the action mechanism of drugs is one of the main deficiencies encountered in the development of new treatments. Therefore, having the possibility of tracking a drug in cells by non-invasive fluorescence techniques could give crucial information for better drug design. The use of d^6 metallic fragment over traditional organic chromophore for the imaging process, overcomes problems related with photostability. As a consequence of the increment of photostability, transition metal complexes enable their application in monitoring processes that occurs in living biological systems. Even though sometimes the synthetic pathway for developing metallic theranostic agents is more tedious, their final properties make this effort profitable, as it has been demonstrated by the reported examples.

[1] K.D. Mjos, C. Orvig, *Chem. Rev.* **2014**, *114*, 4540-4563.
[2] E.J. Anthony, E.M. Bolitho, H.E. Bridgewater, O.W.L. Carter, J.M. Donnelly, C. Imberti, E.C. Lant, F. Lermyte, R.J. Needham, M. Palau, P.J. Sadler, H. Shi, F.-X. Wang, W.-Y. Zhang, Z. Zhang, *Chem. Sci.* **2020**, *11*, 12888-12917.
[3] T. Failes, C. Cullinane, C. Diakos, N. Yamamoto, J. Lyons, T. Hambley, *Chem. Eur. J.* **2007**, *13*, 2974-2982.
[4] F.E. Jacobsen, J.A. Lewis, S.M. Cohen, *ChemMedChem* **2007**, *2*, 152-171.
[5] E.L. Que, D.W. Domaille, C.J. Chang, *Chem. Rev.* **2008**, *108*, 1517-1549.
[6] H.T. Chifotides, K.R. Dunbar, *Acc. Chem. Res.* **2005**, *38*, 146-156.
[7] C. Beers, A. Mousavi, *Toxicol. Environ. Chem.* **2013**, *95*, 207-213.
[8] P. Ehrlich, A. Bertheim, *Ber. Dtsch. Chem. Ges.* **1912**, *45*, 756-766.
[9] S.P. Fricker, *Dalton Trans.* **2007**, 4903-4917.
[10] R.W.Y. Sun, D.L. Ma, E.L.M. Wong, C.M. Che, *Dalton Trans.* **2007**, *43*, 4884-4892.
[11] M.S. Costa, Y.G. Gonçalves, B.C. Borges, M.J.B. Silva, M.K. Amstalden, T.R. Costa, L.M.G. Antunes, R.S. Rodrigues, V.M. Rodrigues, E.F. Franca, M.A.P. Zoia, T.G. de Araújo, L.R. Goulart, G. Von Poelhsitz, K.A.G. Yoneyama, *Sci. Rep.* **2020**, *10*, 15410-15431.
[12] C.F. Shaw, *Chem. Rev.* **1999**, *99*, 2589-2600.
[13] J.B. Delehanty, J.E. Bongard, D.C. Thach, D.A. Knight, T.E. Hickey, E.L. Chang, *Bioorg. Med. Chem.* **2008**, *16*, 830-837.
[14] A. de Almeida, B.L. Oliveira, J.D.G. Correia, G. Soveral, A. Casini, *Coord. Chem. Rev.* **2013**, *257*, 2689-2704.
[15] S. Lacerda, É. Tóth, *ChemMedChem* **2017**, *12*, 883-894.
[16] E. Meggers, *Curr. Opin. Chem. Biol.* **2007**, *11*, 287-292.
[17] I. Romero–Canelon, P.J. Sadler, *Inorg. Chem.* **2013**, *52*, 12276-12291.
[18] S. Monro, K.L. Colón, H. Yin, J. Roque, P. Konda, S. Gujar, R.P. Thummel, L. Lilge, C.G. Cameron, S.A. McFarland, *Chem. Rev.* **2019**, *119*, 797-828.
[19] https://www.cancer.gov/
[20] D.O. Morgan, *Nature* **1995**, *374*, 131-134.
[21] S.J. Elledge, *Science* **1996**, *274*, 1664-1672.
[22] K. Collins, T. Jacks, N.P. Pavletich, *PNAS* **1997**, *94*, 2776-2778.
[23] A. Tubbs and A. Nussenzweig, *Cell* **2017**, *168*, 644-656.
[24] C. Mingard, J. Wu, M. McKeague, S.J. Sturla, *Chem. Soc. Rev.* **2020**, *49*, 7354-7377.
[25] M. Růžička, P. Kulhánek, L. Radová, A. Čechová, N. Špačková, L. Fajkusová, K. Réblová, *PLoS ONE* **2017**, *12*, e0182377.
[26] S.J. Hwang, L.S. Cheng, G. Lozano, C.I. Amos, X. Gu, L.C. Strong. *Hum Genet.* **2003**, *113*, 238-243.
[27] D. Lane, *Nature* **1992**, *358*, 15-16.
[28] J.P. Böttcher, E. Bonavita, P. Chakravarty, H. Blees, M. Cabeza-Cabrerizo, S. Sammicheli, N.C. Rogers, E. Sahai, S. Zelenay, C.S. Reis, *Cell* **2018**, *172*, 1022-1037.
[29] C. Böger, H.M. Behrens, S. Krüger, C. Röcken, Oncoimmunology **2017**, *6*, e1293215.
[30] H.Gonzalez, C. Hagerling, Z. Werb, *Genes Dev.* **2018**, *32*,1267-1284.
[31] F. van Zijl, G. Krupitza, W. Mikulits, *Mutat Res.* **2011**, *728*, 23-34.

[32]https://www.cancer.gov/about-cancer/understanding/what-is cancer#:~:text=Cancer%20is%20a%20disease%20caused,are%20also%20called%20genetic%20changes.

[33] D.T. Debela, S.G. Muzazu, K.D. Heraro, M.T. Ndalama, B.W. Mesele, D.C. Haile, S.K. Kitui, T. Manyazewal, *SAGE Open Med*. **2021**, *9*, 20503121211034366.

[34] M. Arruebo, N. Vilaboa, B. Sáez-Gutierrez, J. Lambea, A. Tres, M.Valladares, Á. González-Fernández, *Cancers* **2011**, *3*, 3279-3330.

[35] M.A. Moses, H. Brem, R. Langer, *Cancer Cell* **2003**, *4*, 337-341.

[36] S. Zimmermann, R. Dziadziuszko, S. Peters, *Cancer Treat. Rev.* **2014**, *40*, 716-722.

[37] B. Rosenberg, L. Vancamp, J.E. Trosko, V.H. Mansour, *Lett. Nature* **1969**, *222*, 385-386.

[38] N.J. Wheate, S. Walker, G.E. Craig, R. Oun, *Dalton Trans.* **2010**, *39*, 8113-8127.

[39] Robert Buckingham, *Martindale: The complete drug reference*, 40th edn., S.C. Sweetman (Ed.), Pharmaceutical Press, London, **2020**.

[40] L. Kelland, *Nat. Rev. Cancer* **2007**, *7*, 573-584.

[41] Q. Peña, A. Wang, O. Zaremba, Y. Shi, H.W. Scheeren, J.M. Metselaar, F. Kiessling, R.M. Pallares, S. Wuttke, T. Lammers, *Chem. Soc. Rev.* **2022**, *51*, 2544-2582.

[42] S.P. Pricker, *Gold Bull.* **1996**, *29*, 53-60.

[43] G.J. Higby, *Gold Bull.* **1982**, *15*, 130-140.

[44] E.R.T. Tiekink, *Crit. Rev. Oncol. Hematol.* **2002**, *42*, 225-248.

[45] M. Bardají, A. Laguna, *J. Chem. Educ.* **1999**, *76*, 201-203.

[46] H. Schmidbaur, A. Schier, *Chem. Soc. Rev*. **2012**, *41*, 370-412.

[47] H. Schmidbaur, A. Schier, *Chem. Soc. Rev.* **2008**, *37*, 1931-1951.

[48] R.P. Herrera, M.C. Gimeno, *Chem. Rev.* **2021**, *121*, 8311-8363.

[49] C. Nardon, N. Pettenuzzo, D. Fregona, *Curr. Med. Chem*. **2016**, *23*, 3374-3403.

[50] F.H. Abdalbari, C.M. Telleria, *Discover. Oncology* **2021**, *12*, 42-60.

[51] B. Bertrand, A. Casini, *Dalton Trans.* **2014**, *43*, 4209-4219.

[52] K. Fritz-Wolf, S. Kehr, M. Stumpf, S. Rahlfs, K. Becker, *Nat. Commun.* **2011**, *2*, 383-391.

[53] S. Park, H.B. Kim, C. Piao, M.Y. Kang, S. Park, S.W. Kim, J. Lee, *Biochem. Biophys. Res. Commun.* **2016**, *482*, 706-712.

[54] C.I. Yeo, K.K. Ooi, E.R.T. Tiekink, *Molecules* **2018**, *23*, 1410-1436.

[55] L. B. Hunt, *Platinum Metals Rev.* **1987**, *31*, 32-41.

[56] E. Longhi, L. De Cola, Iridium(III) Complexes for OLED Application. In Iridium(III) in Optoelectronic and Photonics Applications, **2017**. Chapter 6, E. Zysman-Colman (Ed.).

[57] D.N. Tritton, F.-K. Tang, G.B. Bodedla, F.-W. Lee, C.-S. Kwan, K.C.-F. Leung, X. Zhu, W.-Y. Wong, *Coord. Chem. Rev.* **2022**, *459*, 214390-214408.

[58] H. Amouri, *Chem. Rev.* **2023**, *123*, 230-270.

[59] L.C.-C. Lee, K. K.-W. Lo, *J. Am. Chem. Soc.* **2022**, *144*, 14420-14440.

[60] S.E. Braslavsky, *Pure Appl. Chem.* **2007**, *79*, 293-465.

[61] B. Valeur, M.N. Berberan-Santos, *Molecular Fluorescence: Principles and applications*, **2013**, Wiley-VCH, 2nd Edition, Germany.

[62] J. Perrin, *Trans. Faraday Soc.* **1922**, *17*, 546-572.

[63] A. Jablonski, *Z. Phys.* **1935**, *94*, 38-46.

[64] Balzani, V., Bergamini, G., Campagna, S., Puntoriero, F. (**2007**). *Photochemistry and Photophysics of Coordination Compounds: Overview and General Concepts. In: Balzani, V., Campagna, S. (eds) Photochemistry and Photophysics of Coordination Compounds I. Topics in Current Chemistry*, vol 280. Springer, Berlin, Heidelberg.
[65] K.K.-W. Lo, K.Y. Zhanga, *RSC Adv.* **2012**, *2*, 12069-12083.
[66] R.H. Webb, G.W. Hughes, F.C. Delori, *Appl. Opt.* **1987**, *26*, 1492-1499.
[67] S. El Hallani, C.F. Poh, C.E. Macaulay, *Oral Oncol.* **2013**, *49*, 582-590.
[68] C. Longo, I. Zalaudek, G. Argenziano, G. Pellacani, *Dermatol. Clin.* **2012**, *30*, 799-814.
[69] M. Ragazzi, S. Piana, C. Longo, F. Castagnetti, M. Foroni, G. Ferrari, G. Gardini, G. Pellacani, *Mod. Pathol.* **2014**, *27*, 460-471.
[70] C. Caporale, M. Massi, *Coord. Chem. Rev.* **2018**, *363*, 71-91.
[71] C. Li, Y. Liu, Y. Wu, Y. Sun, F. Li, *Biomaterials* **2013**, *34*, 1223-1234.
[72] L. He, Y. Li, P. Tan, R. Ye, H. Chen, J. Cao, N. Ji, W. Mao, *Chem. Sci.* **2015**, *6*, 5409-5418.
[73] W.-W. Qin, Z.-Y. Pan, D.-H. Cai, Y. Li, L. He, *Dalton Trans*. **2020**, *49*, 3562-3569.
[74] J.S. Nam, M.-G. Kang, J.Kang, S.-Y.Park, S.J.C. Lee, H.-T. Kim, J.K. Seo, O.-H. Kwon, M.H. Lim, H.-W. Rhee, T.-H. Kwon, *J. Am. Chem. Soc.* **2016**, *138*, 10968-10977.
[75] J. Pracharova, G. Vigueras, V. Novohradsky, N. Cutillas, C. Janiak, H. Kostrhunova, J. Kasparkova, J. Ruiz, V. Brabec, *Chem. Eur. J.* **2018**, *24*, 4607-4619.
[76] H. Huang, S. Banerjee, P.J. Sadler, *ChemBioChem* **2018**, *19*, 1574-1589.
[77] R. Roelandts, *Photodermatol. Photoimmunol Photomed.* **1991**, *8*, 184-189.
[78] A. Grzybowski, J. Sak, J. Pawlikowski, *Clin. Dermatol.* **2016**, *34*, 532-537.
[79] D. Mitton, R. Ackroyd, *Photodiagnosis Photodynamic Ther*. **2008**, *5*, 103-111.
[80] N.R. Finsen, *Phototherapy* (Edward Arnold, London, **1901**).
[81] O. Raab, *Zeitung Biol*. **1900**, *39*, 524-526.
[82] J. Prime, *Les accidents toxiques par l'eosinate de sodium* (Jouve and Boyer, Paris, **1900**).
[83] H. von Tappeiner, A. Jesionek, *Muench Med. Wochenschr*. **1903**, *47*, 2042-2044.
[84] R.L. Lipson, E.J. Baldes, *Arch. Dermatol.* **1960**, *82*, 508-516.
[85] S.K. Schwartz, K. Abolon, H. Vermund, *Univ. Minn. Med. Bull*. **1955**, *27*, 7-8.
[86] T.J. Dougherty, G.B. Grindey, R. Fiel, K.R. Weishaupt, D.G. Boyle, *J. Natl. Cancer Inst.* **1975**, *55*, 115-121.
[87] J.F. Kelly, M.E. Snell, *J. Urol.* **1976**, *115*, 150-151.
[88] D. Dolmans, D. Fukumura, R. Jain, *Nat. Rev. Cancer* **2003**, *3*, 380-387.
[89] H. Shi, P.J. Sadler, *Br. J. Cancer* **2020**, *123*, 871-873.
[90] A.P. Castano, P. Mroz, M.R. Hamblin, *Nat. Rev. Cancer* **2006**, *6*, 535-545.
[91] K. Plaetzer, B. Krammer, J. Berlanda, F. Berr, T. Kiesslich, *Lasers Med. Sci.* **2009**, *24*, 259-268.
[92] U.O. Nseyo, J. DeHaven, T.J. Dougherty, W.R. Potter, D.L. Merrill, S.L. Lundahl, D.L. Lamm, *J. Clin. Laser Med. Surg.* **1998**, *16*, 61-68.
[93] S. Callaghan, M. O. Senge, *Photochem. Photobiol. Sci.* **2018**, *17*,1490-1514.
[94] J. Karges, *ChemBioChem* **2020**, *21*, 3044-3046.

[95] S. Monro, K.L. Colón, H. Yin, J. Roque III, P. Konda, S. Gujar, R.P. Thummel, L. Lilge, C.G. Cameron, S.A. McFarland, *Chem. Rev.* **2019**, *119*, 797-828.
[96] A.C. Jung, F. Moinard-Butot, C. Thibaudeau, G. Gasser, C. Gaiddon, *Pharmaceutics* **2021**, *13*, 1788-1805.
[97] I.B. Tan, G. Dolivet, P. Ceruse, V.V. Poorten, G. Roest, W. Rauschning, *Head Neck* **2010**, *32*, 1597-1604.
[98] A.R. Azzouzi, S. Vincendeau, E. Barret, A. Cicco, F. Kleinclauss, H.G. van der Poel, C.G. Stief, J. Rassweiler, G. Salomon, E. Solsona, A. Alcaraz, T.T. Tammela, D.J. Rosario, F. Gomez-Veiga, G. Ahlgren, F. Benzaghou, B. Gaillac, B. Amzal, F.M. Debruyne, G. Fromont, *Lancet. Oncol.* **2017**, *18*, 181-191.
[99] A.H. Arits, K. Mosterd, B.A. Essers, E. Spoorenberg, A. Sommer, M.J. De Rooij, H.P. van Pelt, P.J. Quaedvlieg, G.A. Krekels, P.A. van Neer, J.J. Rijzewijk, A.J. van Geest, P.M. Steijlen, P.J. Nelemans, N.W. Kelleners-Smeets, *Lancet. Oncol.* **2013**, *14*, 647-654.
[100] L.K. McKenzie, H.E. Bryant, J.A. Weinstein, *Coord. Chem. Rev.* **2019**, *379*, 2-29.
[101] V. Novohradsky, A. Rovira, C. Hally, A. Galindo, G. Vigueras, A. Gandioso, M. Svitelova, R. Bresolí-Obach, H. Kostrhunova, L. Markova, J. Kasparkova, S. Nonell, J. Ruiz, V. Brabec, V. Marchán, *Angew. Chem. Int. Ed. Engl.* **2019**, *58*, 6311-6315.
[102] L. Zeng, P. Gupta, Y. Chen, E. Wang, L. Ji, H. Chao, Z.-S. Chen, *Chem. Soc. Rev.* **2017**, *46*, 5771-5804.
[103] J.D. Knoll, C. Turro, *Coord. Chem. Rev*. **2015**, *282-283*, 110-126.
[104] L.B. Josefsen, R.W. Boyle, *Met.-Based Drugs* **2008**, *2008*, 276109-276132.
[105] O.J. Stacey, S.J.A. Pope, *RSC Adv.* **2013**, *3*, 25550-25564.
[106] C. Caporale, M. Massi, *Coord. Chem. Rev.* **2018**, *363*, 71-91.
[107] Y. Li, C.-P. Tan, W. Zhang, L. He, L.-N. Ji, Z.-W. Mao, *Biomaterials* **2015**, *39*, 95-104.
[108] J. Zhou, J. Li, K.Y. Zhang, S. Liu, Q. Zhao, *Coord. Chem.Rev.* **2022**, *453*, 214334-214357.
[109] S.M. Mahalingam, J.D. Ordaz, P.S. Low, *ACS Omega* **2018**, *3*, 6066-6074.
[110] M.T. Jeena, S. Kim, S. Jin, J.-H. Ryu, *Cancers* **2020**, *12*, 4-24.
[111] T. Corrêa, B.C. Feltes, R. Giugliani, U. Matte, *WIREs Mech. Dis*. **2021**, *13*, e1521.
[112] R.L. Siegel, K.D. Miller, H.E. Fuchs, A. Jemal, *CA Cancer J. Clin.* **2022**, *72*, 7-33.
[113] V. Schirrmacher, *Int. J. Oncol*. **2019**, *54*, 407-419.
[114] E.M. Chapman, *JAMA* **1983**, *25*, 2042-2044.
[115] S. S. Kelkar, T. M. Reineke, *Bioconjugate Chem.* **2011**, *22*, 1879-1903.
[116] A. Berger, *BMJ* **2003**, *326*, 1449-1450.
[117] R.J. Jaszczak, R.E. Coleman, C.B. Lim, *IEEE Trans. Nucl. Sci.* **1980**, *27*, 1137-1153.
[118] T. Buzug, *Computed Tomography: From Photon Statistics to Modern Cone-Beam CT*, ed. 1, **2008**, Springer-Verlag Berlin Heidelberg.
[119] A. Berger, *BMJ* **2002**, *324*, 35-36.
[120] J. Lichtman, J.A. Conchello, *Nat Methods* **2005**, *2*, 910-919.
[121] A.R. Kherlopian, T. Song, Q. Duan, M.A. Neimark, M.J. Po, J.K. Gohagan, A.F. Laine, *BMC Syst. Biol.* **2008**, *2*, 74-92.
[122] M. Baker, *Nature* **2010**, *463*, 977-979.
[123] V. Fernández-Moreira, M.C. Gimeno, *Chem. Eur. J.* **2018**, *24*, 3345-3353.

[124] A. Citta, E. Schuh, F. Mohr, A. Folda, M.L. Massimino, A. Bindoli, A. Casini, M.P. Rigobello, *Metallomics* **2013**, 1006-1015.
[125] M.K. Raza, S. Gautam, A. Garai, K. Mitra, P. Kondaiah, A.R. Chakravarty, *Inorg. Chem.* **2017**, *56*, 11019-11029.
[126] F.J. Ballester, E. Ortega, V. Porto, H. Kostrhunova, N. Davila-Ferreira, D. Bautista, V. Brabec, F. Domínguez, M.D. Santana, J. Ruiz, *Chem. Commun.* **2019**, *55*, 1140-1143.
[127] G. Millán, N. Giménez, R. Lara, J.R. Berenguer, M.T. Moreno, E. Lalinde, E. Alfaro-Arnedo, I.P. López, S. Piñeiro-Hermida, J.G. Pichel, *Inorg. Chem.* **2019**, *58*, 1657-1673.
[128] P.J. Jarman, F. Noakes, S. Fairbanks, K. Smitten, I.K. Griffiths, H.K. Saeed, J.A. Thomas, C. Smythe, *J. Am. Chem. Soc.* **2019**, *141*, 2925-2937.
[129] F. Pelletier, V. Comte, A. Massard, M. Wenzel, S. Toulot, P. Richard, M. Picquet, P. Le Gendre, O. Zava, F. Edafe, A. Casini, P.J. Dyson, *J. Med. Chem.* **2010**, *53*, 6923-6933.
[130] V. Fernández-Moreira, I. Marzo, M.C. Gimeno, *Chem. Sci.* **2014**, *5*, 4434-4446.
[131] L. Boselli, M. Carraz, S. Mazères, L. Paloque, G. González, F. Benoit-Vical, A. Valentin, C. Hemmert, H. Gornitzka, *Organometallics* **2015**, *34*, 1046-1055.
[132] C. Caporale, C.A. Bader, A. Sorvina, K.D.M. MaGee, B.W. Skelton, T.A. Gillam, P.J. Wright, P. Raiteri, S. Satgni, J.L. Morrison, S.E. Plush, D.A. Brooks, M. Massi, *Chem. Eur. J.* **2017**, *23*, 15666-15679.
[133] A. Luengo, I. Marzo, M. Reback, I.M. Daubit, V. Fernández-Moreira, N. Metzler-Nolte, M.C. Gimeno, *Chem. Eur. J.* **2020**, *26*,12158-12167.
[134] H.-T. Liu, X.-G. Xiong, P.D. Dau, Y.-L. Wang, D.-L. Huang, J. Li, L.-S. Wang, *Nat. Commun.* **2018**, *9*, 16200-16211.

Chapter 1

1.1 Introduction

The initial discovery of cisplatin in 1965 by Dr. Rosenberg[1] was followed by clinical trials that demonstrated its efficacy in several cancer types, as testicular, bladder or advanced ovarian cancer.[2] However, its considerable side effects and nephrotoxicity,[3] as well as the indiscriminate attack on healthy rapidly dividing cells,[4] limited it use and forced the development of a new generation of metallodrugs, as it has been previously mentioned in the introduction section.

In such manner, Au^{I} complexes aroused as a great alternative to circumvent the disadvantages of platinum-based drugs. This is due to the different mechanism of action exhibited by gold drugs. These complexes are able to inhibit thiol enzymes, specifically the mitochondrial enzyme thioredoxin reductase TrxR,[5] which is overexpressed in cancer cells.[6] Among the Au^{I} complexes, Auranofin stands out as a particularly effective drug. This gold-based drug consists of a Au^{I} center coordinated to a thiosugar (2,3,4,6-tetra-O-acetyl-1-thio-β-D-glucopyranose) and triethylphosphine, and it was initially approved by FDA in 1985 as treatment for rheumatoid arthritis. Nowadays auranofin is emerging as a promising agent for cancer therapy in a repurposing program,[7] especially as a treatment for ovarian cancer, and is currently undergoing clinical trials.[8] Therefore, huge efforts are being devoted to developing novel Au^{I} complexes with different S, C, P-donor ligands to increase the range of cancer diseases that can be treated with them.[9]

Alternatively, cyclometallated Ir^{III} complexes have been used in many fields due to their exceptional optical properties. In this sense, their applications as chemosensors, bioimaging probes, or light emitting devices are outstanding.[10] The typical structure of these emissive Ir^{III} complexes contains two bidentate cyclometallated ligands, C^N, and a bidentate diimine ligand, N^N, rearranged in an octahedral fashion around the metal center, $[Ir(C^N)_2(N^N)]^{0/+}$. Modification of these ligands allows for the tuning of the properties of the final complex, finding the right combination for each particular application. In this regard, the selection of the different ligands that are involved in the coordination sphere is key to

selectively targeting a specific organelle. For instance, many Ir^{III} complexes have been described to specifically localize in lysosomes,[11] mitochondria,[12] or nuclei[13] among other inner compartments, by simple modification of their ligand scaffolds. However, Ir^{III} complexes containing a diphosphine (P^P) instead of diimine ligands, i.e. $[Ir(C^N)_2(P^P)]^{0/+}$, are by far less studied as bioprobes.[14]

As commented in the introduction section, among the different strategies to deliver a new generation of metallodrugs, the combination of two different metallic fragments in a single molecule is underdeveloped (theranostic agent type 3). This strategy gives the possibility of joining the diverse intrinsic properties of each metal fragment, trying to get a synergistic effect that will improve their therapeutic potential.

For the time being, the use of heterobimetallic complexes in the field of theranosis is still in its infancy.[15] In most of heterometallic drugs reported (see Figure 1.1), the initial hypothesis was based on the fact that the combinations of two metals could enhance the cytotoxic capabilities , however none of them made emphasis in the possibility of tracking their pathway by visualization techniques. Thus, species containing fragments derived from Ru^{II}, Pt^{II}, Au^{I}, Ti^{IV}, Cu^{II}, Ag^{I}, Ir^{III} or Fe^{II}, among others, were combined with some analogous chemotherapeutic-metallic drugs, such as cisplatin, RAPTA-T or Auranofin.[16]

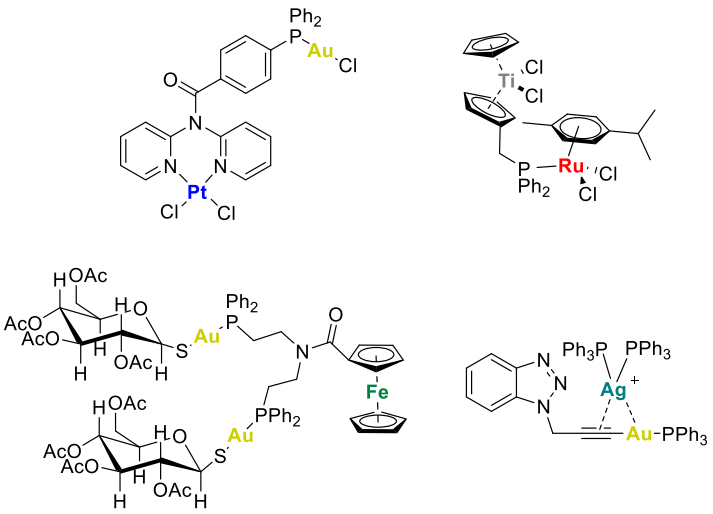

Figure 1.1. *Examples of heterobimetallic complexes that can be used as bioprobes, but their mechanism of action were not studied by visualization techniques.*[16,17,18,19]

Alternatively, among the published bimetallic complexes used as theranostic agents, only one species based on the combination of Ir^{III}-Au^{I} centers has been reported by our research group on 2020.[11] This complex contains a cyclometallated Ir^{III} core of the type $[Ir(ppy)_2(N\hat{}N)]^+$, where the N^N ligand has been bioconjugated with a peptide. Different peptide functionalization groups allowed for the subsequent coordination of the Au^{I} fragment, as shown in Figure 1.2. This single publication highlights the novelty of this type of heterometallic complexes opening the door for the synthesis of novel and promising compounds based on Ir^{III}-Au^{I}.

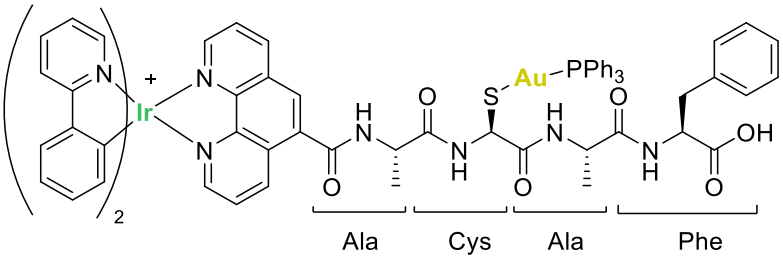

Figure 1.2. *Chemical structure of the single example of Ir^{III}-Au^{I} published.*

In an attempt to widen the scope of these promising heterobimetallic Ir^{III}-Au^{I} complexes and since $[Ir(C\hat{}N)_2(P\hat{}P)]^+$ complexes have been barely used for biological applications, a new approach has been incorporated.[14] This time diphosphine ligands have been used as linker between the optical and therapeutic fragments. Therefore, three new heterobimetallic complexes have been synthetized by combining a cytotoxic and emissive fragment, $[Ir(ppy)_2(P\hat{}P)]^+$, with different Au^{I} substrates. The expected synergy between the metal centers could enhance the antitumoral properties and allow to track the inner interplay, and identify their final targets. A thorough study was conducted on the antiproliferative activity, cytotoxicity, capacity to generate reactive oxygen species (ROS), effect on the mitochondrial membrane potential, and biodistribution on lung cancer cells (A549) for a series of diphosphine-based Ir^{III}-Au^{I} complexes. Moreover, their antiangiogenic properties were examined using endothelial colony forming cells (ECFCs) for evaluating their possible use as antimetastatic agents.

1.2 Objectives and methodology

In this chapter, the development of bimetallic Ir^{III}-Au^{I} complexes as potential theranostic agents is described. These complexes combine two different metallic cores in a single molecule, separated by a linker, to generate a synergistic effect between the metal centers. This approach enhances not only the therapeutic activity driven by the gold (I) fragment but also the luminescent properties of the cyclometallated iridium core, facilitating the traceability of these drugs.

The initial step in developing the desired heterobimetallic probes is to synthesize the cyclometallated emissive Ir^{III} species $[Ir(C\text{^}N)_2(dppm)]^+$, where C^N represents an orthometallated phenylpyridine ligand (ppy) and dppm is the bis(diphenylphosphino)methane that will serve as the bridge ligand between the two metal centers. Subsequently, different Au^{I} substrates were added in the presence of an intrinsic or extrinsic base to form the bimetallic complexes with a diphosphino-methanide bridging ligand, as shown in Scheme 1.1. Moreover, the use of different Au^{I} fragments (triphenylphosphine, chloride or thiocytosine) enables tuning of the biological properties, including ROS generation, mitochondrial transmembrane potential or the inhibition of thioredoxin reductase, among others features.

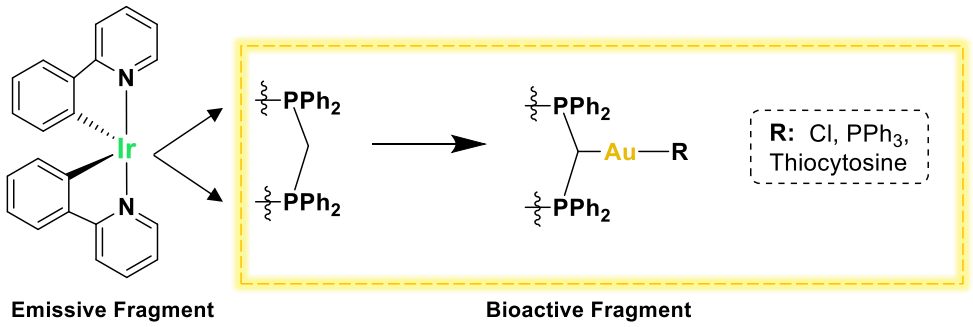

Scheme 1.1. *Depiction of developed bimetallic Ir^{III}-Au^{I} complexes.*

1.3 Synthesis and characterization

The synthetic approach for obtaining heterobimetallic Ir^{III}-Au^{I} theranostic agents requires the use of a diphosphine as linker between the metal centers. In this work, we selected bis(diphenylphosphino)methane, also known as dppm, as the linker ligand due to its ability to provide a robust and simple coordination between the two metallic fragments. The two phosphorous atoms in dppm could easily bind to the iridium center in a chelated fashion, while the gold fragment can be directly coordinated to the methanide carbon upon deprotonation.

The first step was the synthesis of the cyclometallated Ir^{III} precursor, $[Ir(ppy)_2(\mu\text{-}Cl)]_2$, following a slightly different methodology that the one described in published procedures.[20] Specifically, $IrCl_3 \cdot nH_2O$ was dissolved in a solution of 2-ethoxyethanol which contained 2-phenylpyridine. Then, water was added in a proportion 1:3 (water:2-ethoxiethanol) and the mixture was refluxed at 115 ºC for 24 h affording the precipitation of the desired product. The dimer precursor, $[Ir(ppy)_2(\mu\text{-}Cl)]_2$, was filtered and washed with water, ethanol and acetone to finally obtain a high yield (87%) of a yellow solid product (see Scheme 1.2).

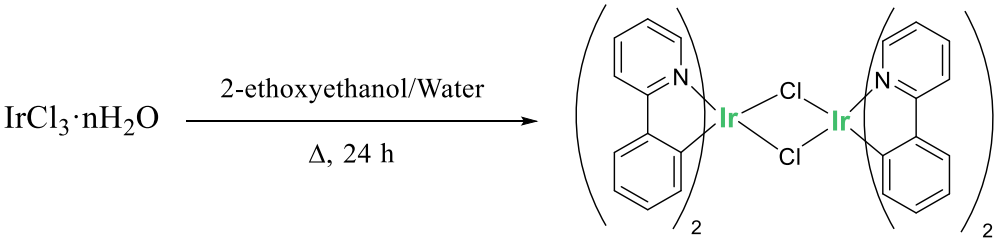

Scheme 1.2. *Synthetic procedure of* $[Ir(ppy)_2(\mu\text{-}Cl)]_2$.

Once that the dimer precursor was attained, it was refluxed with two equivalents of dppm in dry and degassed methanol for 12 h. Afterwards, methanol was replaced by dichloromethane giving rise to a bright yellow solution, which was stirred at room temperature with and excess of KPF_6 for 30 minutes. Finally, hexane was added affording the desired complex **1.1** by precipitation, which was filtered, washed with ether and dried under vacuum.

Complexes **1.2** and **1.3** were obtained by adding either [Au(acac)PPh_3] or [AuCl(tht)] in dichloromethane to complex **1.1**, in the presence of an intrinsic, acetylacetonate (acac), or extrinsic base, Cs_2CO_3. respectively, after 24 h of reaction at room temperature (r.t.), as shown Scheme 1.3. The last step in this synthetic pathway involved a ligand exchange reaction to obtain complex **1.4**. In this reaction, the chloride ligand was substituted by a deprotonated thiocytosine, which is going to be exclusively coordinated to the gold center through the sulfur atom. Therefore, starting from a solution of complex **1.3** in dichloromethane and adding an excess of five equivalents of Cs_2CO_3 and an equimolar amount of thiocytosine, it was possible to isolate complex **1.4** as a pale-yellow solid after its precipitation with diethyl ether. All complexes were synthetized in high to moderate yields. Complex **1.1** was obtained in 85%, **1.2** in 91%, **1.3** in 70% and **1.4** in 92% yield. The reduction in yield for complex **1.3** could be attributed to the low stability of the Au^I precursor, [AuCl(tht)], in basic conditions.

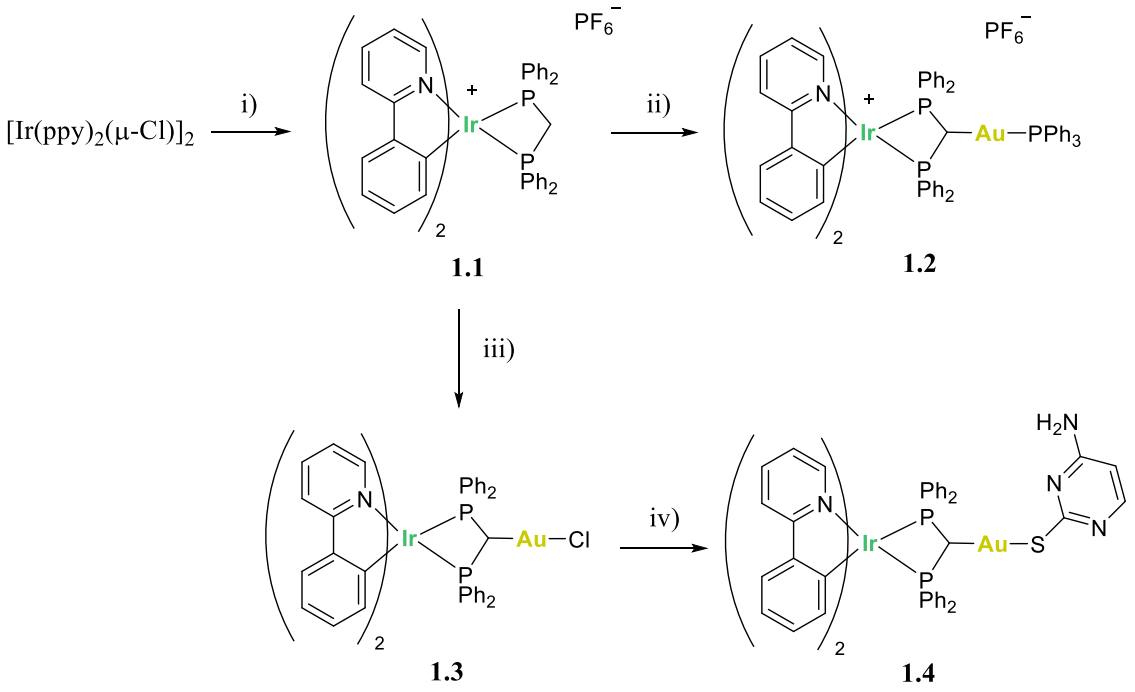

Scheme 1.3. *Synthetic pathway of complexes* ***1.1-1.4****. i)* $[Ir(ppy)_2(\mu\text{-}Cl)]_2$*, dppm,* KPF_6*, MeOH, reflux, 12 h; ii)* ***1.1****,* [Au(acac)PPh_3]*,* CH_2Cl_2*, r.t., 24 h; iii)* ***1.1****,* [AuCl(tht)]*,* CH_2Cl_2*, r.t., 24 h; iv)* ***1.3****, thiocytosine,* Cs_2CO_3*,* CH_2Cl_2*, r.t., 24 h.*

The successful synthesis of these complexes was confirmed by NMR spectroscopy using ^{1}H, APT and $^{31}P\{^{1}H\}$ experiments. Moreover, IR spectroscopy and high resolution mass spectrometry (HRMS) were used as additional characterization techniques to confirm the formation of the complexes.

For the characterization of these species, it was particularly relevant $^{31}P\{^{1}H\}$-NMR spectroscopy. In the free ligand dppm, the singlet peak appears at -22.6 ppm, but in complex **1.1**, the same peak was observed at -56 ppm, indicating a shift to high field. The high displacement observed, which is contrary to the expected shift towards a lower field, is due to the formation of a four-membered ring. Upon synthesizing complex **1.2**, the $^{31}P\{^{1}H\}$ spectrum revealed that the singlet had become a doublet of doublets centered at -46 and -49 ppm, due to the loss of symmetry within the Ir^{III} complex. Additionally, a triplet at 38 ppm appeared corroborating the presence of the PPh_3 ligand bonded to the gold center (see Figure 1.3). This pattern suggests an inequivalence in the phosphorus atoms, which was later confirmed by X-Ray diffraction.

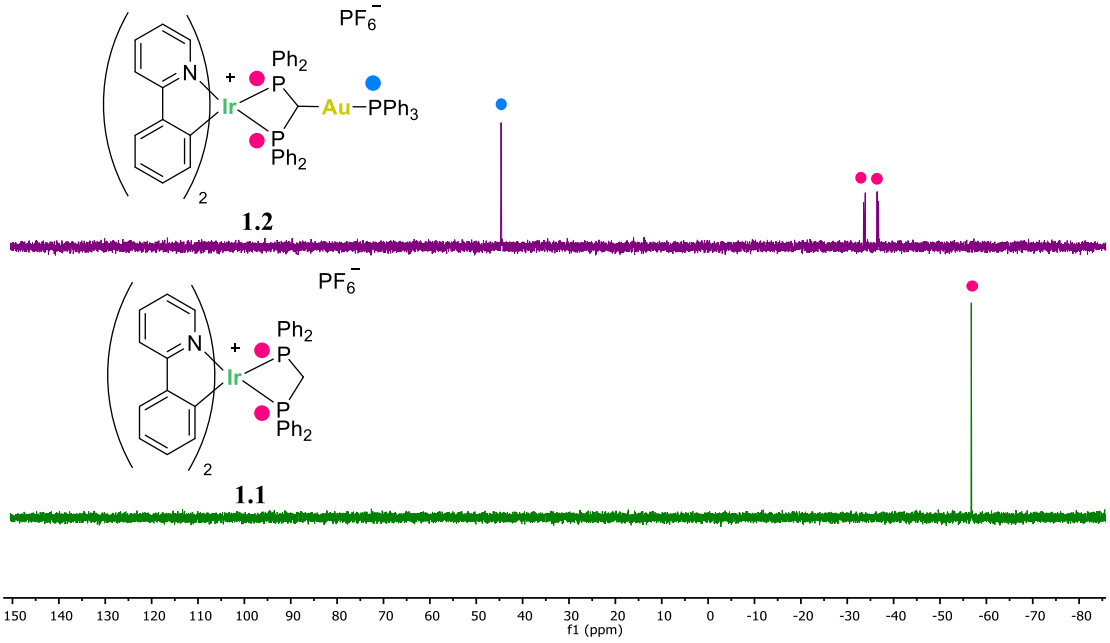

Figure 1.3. *Comparison between $^{31}P\{^{1}H\}$-NMR (400 MHz) spectra of complex* ***1.1*** *and complex* ***1.2****. Solvent: CD_2Cl_2.*

^{1}H-NMR spectroscopy also showed the typical shift for the protons and carbons of the cyclometallatated ligand upon coordination of the dppm to form **1.1**, being particularly relevant the shift of proton in *ortho* to the nitrogen atom of the pyridine ring from 9.25 in the dimer precursor to 8.15 ppm (see Figure 1.4). The presence of the different gold fragments in complex **1.2**, **1.3** and **1.4** barely altered the proton chemical shifts of the ppy.

Moreover, the coordination of the gold fragment can be clearly confirmed by the shift observed by the methylene proton, as well as the loss of symmetry in the ^{1}H-NMR spectra. In the initial complex **1.1**, the methylene protons appeared as a triplet at 5.42 ppm as a result of phosphorus coupling and integrated for two protons. After the deprotonation process and subsequent coordination of the Au^{I} fragment, this signal shifted to 5.49 ppm. This relevant signal appeared at 5.38 and 5.35 ppm as a doublet for complexes **1.3** and **1.4** respectively, integrating now for a single proton.

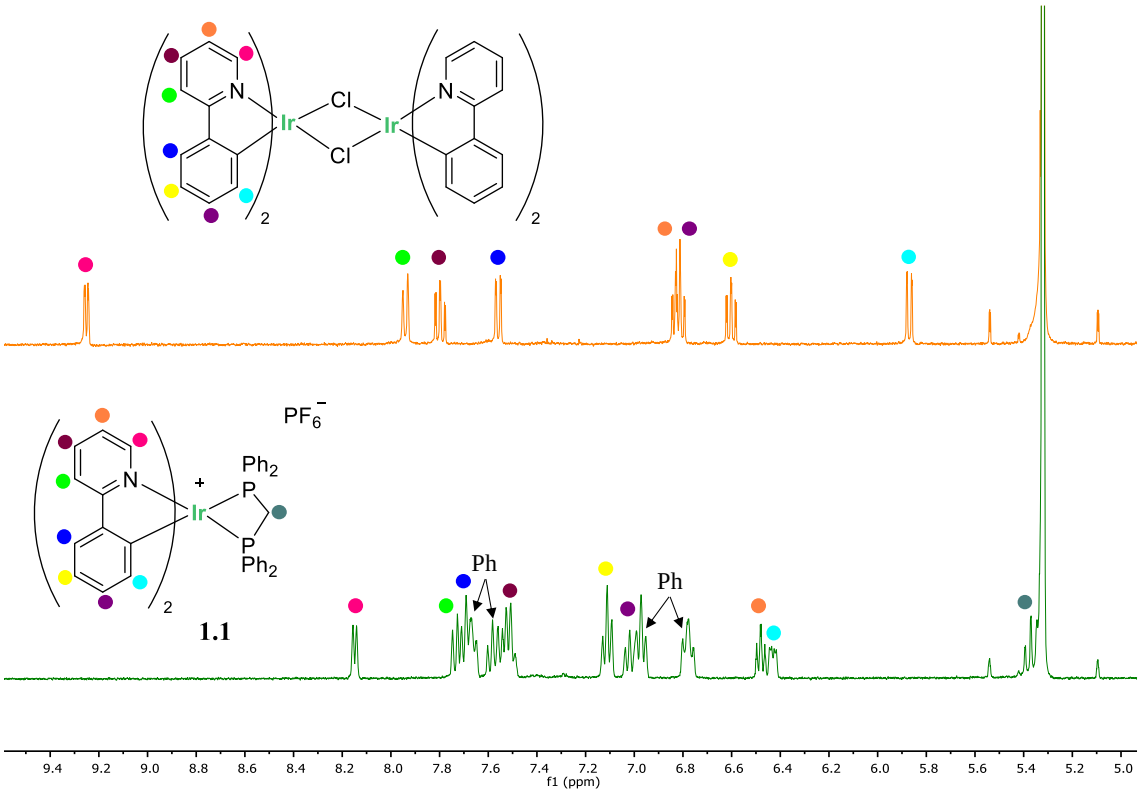

Figure 1.4. *Comparison between ^{1}H-NMR (400 MHz) spectra of complex **1.1** and [Ir(ppy)$_2$(μ-Cl)]$_2$. Solvent: CD_2Cl_2.*

IR spectroscopy was key in characterizing complex **1.3**. This technique enabled visualization of the typical absorption band at 335 cm^{-1}, corresponding to the stretching vibration of the Au-Cl bond, i.e. υ(Au-Cl), as it has been reported for similar gold complexes.[21] This signal indicated the successful coordination of the gold center to the deprotonated dppm ligand.

Additionally, it was possible to isolate crystals of complex **1.2** for X-Ray diffraction. They were obtained as bright yellow needles by slow diffusion of diethyl ether into a dichloroethane solution of **1.2**. The analysis of their X-Ray structure indicates that this asymmetric molecule crystallizes in a P-1 space group. The unit cell is formed by two independent molecules of the Λ enantiomer and three molecules of dichloroethane, which is the crystallization solvent.

The crystalline structure exhibits the typical spatial distribution for this type of cyclometallated Ir^{III} complexes, where ligands adopt an octahedral disposition around the metal center. As it was expected, the pyridyl nitrogen atoms of the orthometalled ligand, ppy, coordinate to the iridium center *trans* to each other. Furthermore, they present an angle N-Ir-N of 165.8(6)º or 166.1(3)º in the molecules **1.2a** and **1.2b**, respectively. This disposition forces that phenyl groups of ppy to be displayed in *trans* configuration to the diphosphine ligand. Both molecules have similar bond distances and angles, which are analogous to those reported for other diphosphine Ir^{III} complexes.[14] The main difference observed in complex **1.2**, in comparison with the reported analogue, is that the P-Ir-P bite angle is slightly smaller at 68.77º compared to 76.11º. This could be due to the constriction around the Ir^{III} center caused by the gold coordination to the dppm ligand, leading to a shorter bite angle. In addition, in Figure 1.5, it is possible to appreciate how the Au^{I} fragment is coordinated to the methanide carbon. The Au^{I} center displays a linear disposition with the phosphorus and the carbon atoms, as it is expected for this type of complexes.[22] The most significant bond distances and angles are collected in Figure 1.5.

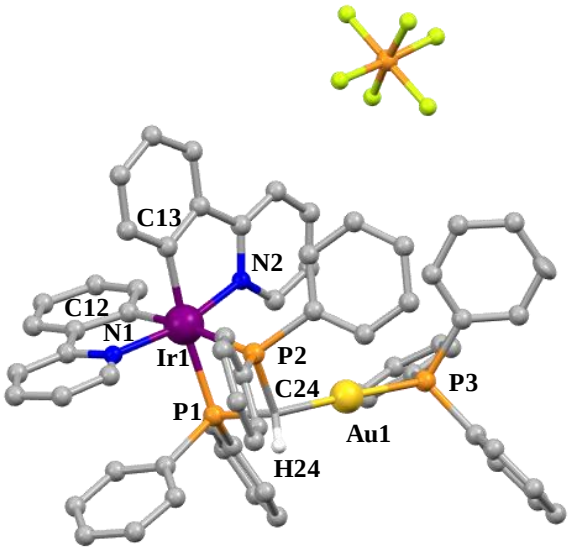

Bond Lenghts (Å)	**Ir1-C12**	2.063(7)
	Ir1-C13	2.059(7)
	Ir1-N1	2.079(6)
	Ir1-P1	2.388(5)
	Ir1-P2	2.421(2)
	Au1-C24	2.109(7)
	Au1-P3	2.274(1)
Angles °	**C24-Au1-P3**	177.9(2)
	P2-Ir1-P1	68.77(6)
	N2-Ir1-N1	165.8(6)
	P1-C24-P1	96.0(3)

Figure 1.5. *Mercury representation of the crystal structure of complex* ***1.2*** *(hydrogen atoms have been omitted for clarity, except hydrogen 24) and table with the most significant bond lengths and angles.*

1.4 Optical properties

Photophysical properties of complexes **1.1** to **1.4** were measured in aerated DMSO solution at room temperature. The most relevant data are collected in Table 1.1.

Table 1.1. *Luminescent properties of complexes* ***1.1-1.4****.*

	UV/vis·10^3 (ε[$dm^3mol^{-1}cm^{-1}$])	**λ_{em} (λ_{exc}) [nm]**	**ζ [ns]**	**Φ (%)**
1.1	265 (9.5), 304 (3.9), 384 (1.2)	526 (425)	181	1.6
1.2	265 (10.1), 305 (4.5), 382 (1.5)	528 (446)	160	5.1
1.3	260 (10.2), 300 (4.9), 374 (1.6)	527 (415)	234	2.7
1.4	263 (10.6), 303 (4.5), 385 (1.2)	529 (407)	184	1.2

The UV-Visible spectra for all the complexes show intense absorption bands below 300 nm that can be assigned, based on published studies, to ligand-centered spin-allowed $\pi \rightarrow \pi^*$ transitions (see Figure 1.6).

Additional bands with lower intensity appeared between 280 and 350 nm. Those bands could be attributed to forbidden intraligand $^{3}\pi\rightarrow\pi^{*}$ and ^{1}MLCT transitions. Over 380 nm, it is appreciable a long tail that is typically associated in this type of complexes with a ^{3}MLCT transition.[23]

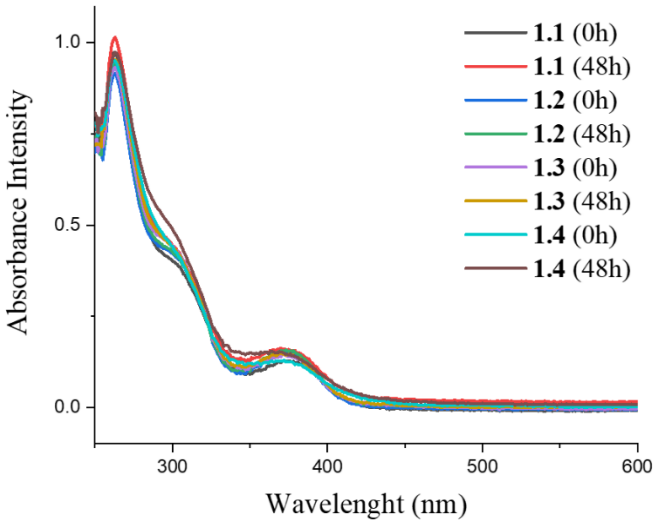

Figure 1.6. *Absorption spectra in DMSO solution of complexes* ***1.1-1.4*** *and their stabilities at 48 hours, 310 K and using a concentration of [5·10^{-5}M].*

Regarding their emission spectra, complexes **1.1-1.4** present a structureless emission centered at 530 nm, as it can be seen in Figure 1.7. Such emission maximum is completely independent of the presence of the Au^{I} fragment and its multiple ancillary ligands. These emissions bands could be assigned mainly to ^{3}MLCT and with lower contributions of ^{3}LC transitions.[24] This origin assignation was made based on the fact that emission bands from charge transfer processes are generally featureless, however those more structured are originated by ligand-centered transitions (LC) for these type for complexes.[25]

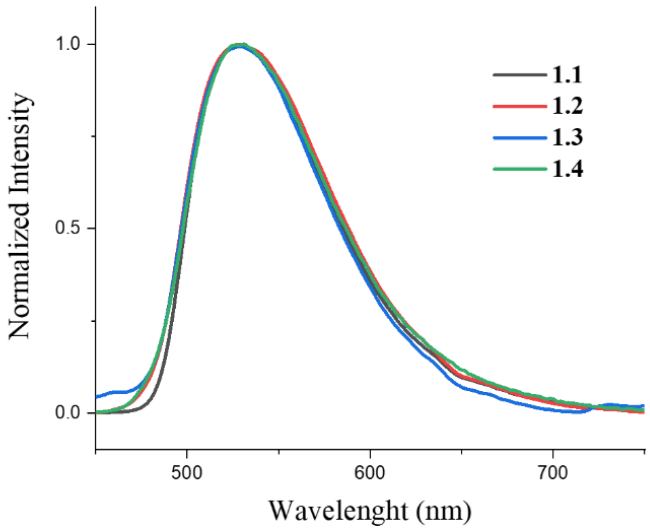

Figure 1.7. *Emission spectra in DMSO solution of complexes* ***1.1-1.4*** *at 298 K and [10^{-3}M].*

Regarding their lifetimes, all values ranged between 160 to 234 ns, corroborating the phosphorescent nature of the emission. Quantum yield values were also measured in aerated DMSO solution. Complex **1.2** exhibits the highest quantum yield of all the series (Φ = 5.2%) and complex **1.4** the lowest (Φ = 1.2%), suggesting that the gold ancillary ligand helps to tune the emission efficiency to some extent.

In addition, the stability of the complexes was studied by UV-vis spectroscopy in DMSO and in a mixture of DMSO/PBS (final DMSO concentration < 5%; supplementary material) during 48 h at 310 K. As it can be seen in Figure 1.6, no changes were observed in their absorption band patterns, confirming their structural stability under those conditions. It is important to notice that the selection of the specific conditions to perform the stability assay is not performed randomly. The main objective is to corroborate the stability of the complexes in similar conditions to those used for the biological assays.

1.5 Antiproliferative activity

The antiproliferative activity of complexes **1.1** to **1.4**, as well as, their dimer precursor, $[Ir(ppy)_2(\mu\text{-}Cl)]_2$, was determined by MTT assays in A549 cell line (lung carcinoma cells). The MTT (3-(4,5-dimethylthiazol-2-yl)-2,5-diphenyltetrazolium bromide) tetrazolium reduction assay was the first cell proliferation assay suitable for high throughput screening (HTS).[26]

24 h before starting with the MTT assay, 10,000 cells/well were seeded in 96-well plates (100 µL/well) using DMEM (10% FBS) as culture media and allowed to attach prior to the addition of complexes. For the addition of complexes **1.1** to **1.4**, a stock solution [0.1 M] of each one using DMSO as solvent was prepared. From this stock solution, serial dilutions were made using DMEM. Working solutions of the complexes were prepared at different concentrations from 100 to 0.2 µM. Cells were incubated with complexes **1.1** to **1.4** (100 µL/well) of each working concentration in quadruplicate, as shown Figure 1.8 for 24 h. The scheme 1.4 summarizes all this process.

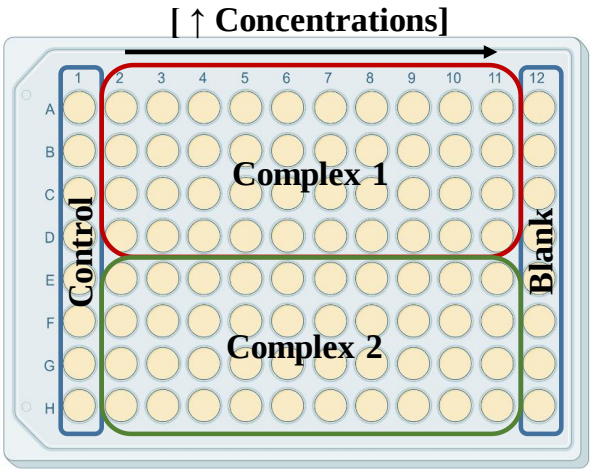

Figure 1.8. *Schematic representation of the disposition of studied complexes in 96-well plate.*

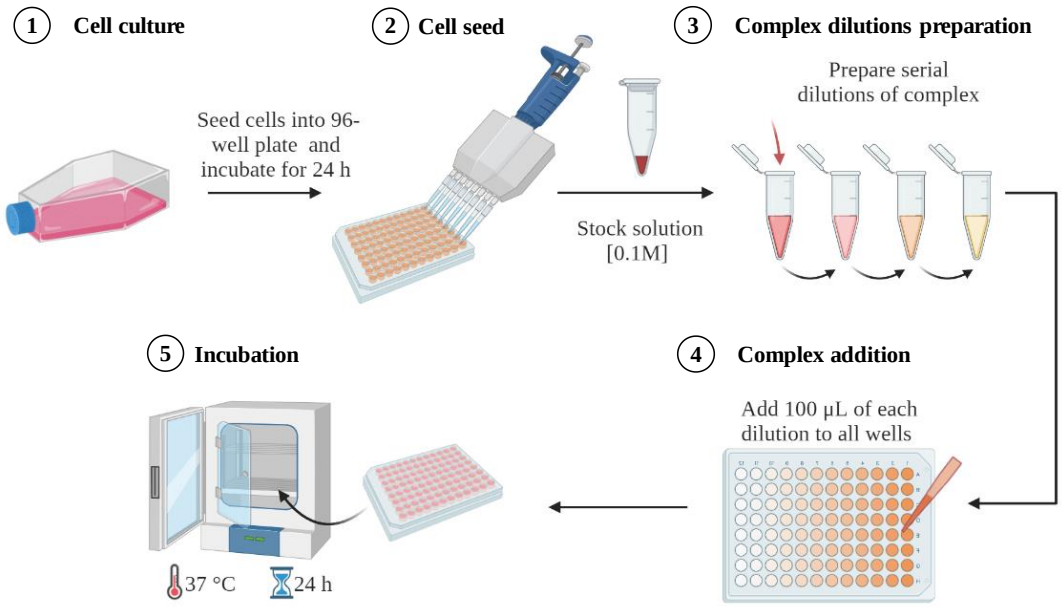

Scheme 1.4. *Schematic representation of a MTT assay protocol (from cell culture to complex incubation).*

After this time, 10 µL MTT substrate (PBS solution at a final concentration of 5 mg/ml) was added to each well and incubated for 2 hours. Viable cells with active metabolism are able to convert MTT into purple formazan crystals. However, when cells die, they lose the ability to convert MTT into formazan. Thereafter removal of the cell culture medium, the addition of 100 µL of DMSO to each well solubilizes the formazan crystals rendering a purple colour only in those wells where there are alive cells. The concentration of formazan was measured by recording absorbance at 550 nm using a plate reading spectrophotometer. The quantity of formazan could be estimated as directly proportional to the number of viable cells, giving an estimation of the cytotoxicity of a complex[27] (Scheme 1.5).

The IC_{50} values are calculated as the mean of three independent experiments using GraphPad Prism software. It is important to note that in each experiment, the viability of the cells is assessed not only for the complexes but also for a control experiment containing the higher concentration of DMSO used during the assay. DMSO can cause cell death at high concentrations, so it is crucial to determine that its quantity does not affect cellular viability. Additionally, a blank column is included in the experiment to account for the absorption of the 96-well plate and all reagents (such as DMEM) used during the experiment.

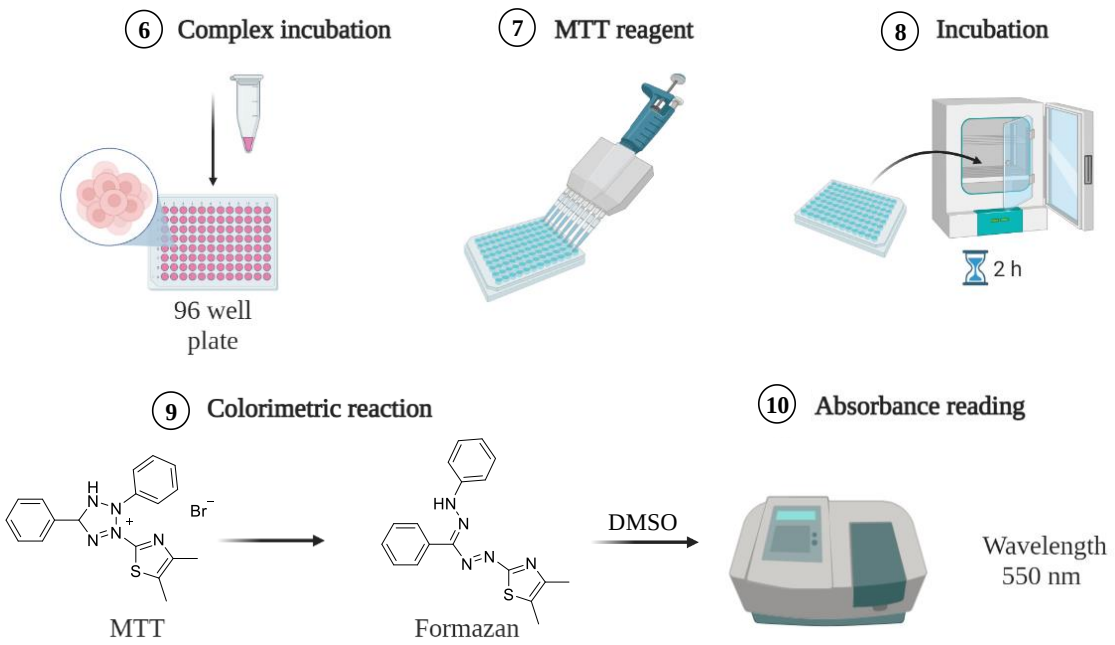

Scheme 1.5. *Schematic representation of a MTT assay protocol (from complex incuation to absorbance reading).*

Focusing on the complexes developed in this chapter, it can be said that all complexes exhibit significant cytotoxic behaviour, with IC_{50} values ranging between 0.6 and 1.7 μM, while their precursor, $[Ir(ppy)_2(\mu\text{-}Cl)]_2$, does not show any alteration to cell proliferation. As shown in Table 1.2, the heterobimetallic Ir^{III}-Au^{I} complexes **1.2** and **1.4** generate an increase in the sensitivity of A549 cells compared to the monometallic Ir^{III} complex **1.1**. This finding confirms the initial hypothesis suggesting that the combination of two different metals can generate a synergistic effect to enhance therapeutic properties. However, the bimetallic complex **1.3** does not follow the same trend, exhibiting the highest IC_{50} value among all the complexes. This result could be due to its non-balanced lipo-hydrophilicity or its lower capacity to permeate the cell membrane, as seen later by confocal fluorescence microscopy.

In addition, cisplatin was also tested in the same conditions as a positive control of the MTT assay. As shown in Table 1.2, the IC_{50} value of cisplatin is much higher than that of the studied complexes, indicating a weaker antiproliferative character for cisplatin compared to complexes **1.1**-**1.4**, and all of them being more cytotoxic.

Table 1.2. *IC_{50} values of complexes **1.1**-**1.4**, $[Ir(ppy)_2(\mu\text{-}Cl)]_2$ dimer precursor and cisplatin incubated in A549 cells for 24 h.*

Complex	IC_{50} (μM)
$[Ir(ppy)_2(\mu\text{-}Cl)]_2$	>50
1	1.0 ± 0.08
2	0.8 ± 0.06
3	1.7 ± 0.08
4	0.6 ± 0.06
cisplatin	20.8 ± 2.1

1.6 Cell death mechanism

Considering the IC_{50} values obtained for the different complexes, it was decided to investigate the cell death mechanism of the monometallic complex **1.1** and the bimetallic complex **1.4** to determine whether the presence of the gold fragment could induce a different cell death pathway. The analysis was performed by flow cytometry using specific fluorescent markers, Annexin V-DY634 and 7-AAD. Annexin V-DY634 is used to identify cells undergoing apoptosis, as it binds to phosphatidylserine exposed on the extracellular side of their plasma membranes. In healthy live cells, phosphatidylserine is located within the inner leaflet of the plasma membrane and is completely inaccessible to Annexin V. However, during programmed cell death (apoptosis), the plasma membranes lose their asymmetry, and phosphatidylserine is translocated from the inner to the outer leaflet of the membrane, allowing Annexin V to bind to the residue. Annexin V is commonly conjugated with a fluorophore, such as FITC or DY634, in order to facilitate the detection of apoptotic cells by flow cytometry. [28] 7-AAD, 7-amino actinomycin D is an additional fluorescent marker typically used in these assays. It is a dye that cannot permeate membrane of viable cells. However, it binds to double-stranded DNA by intercalating between base pairs in guanine or cytosine-rich regions once the cell collapses as a consequence of necrotic cell death pathway, thus working as an indicator of necrotic death mechanism, as shown in Figure 1.9.[29]

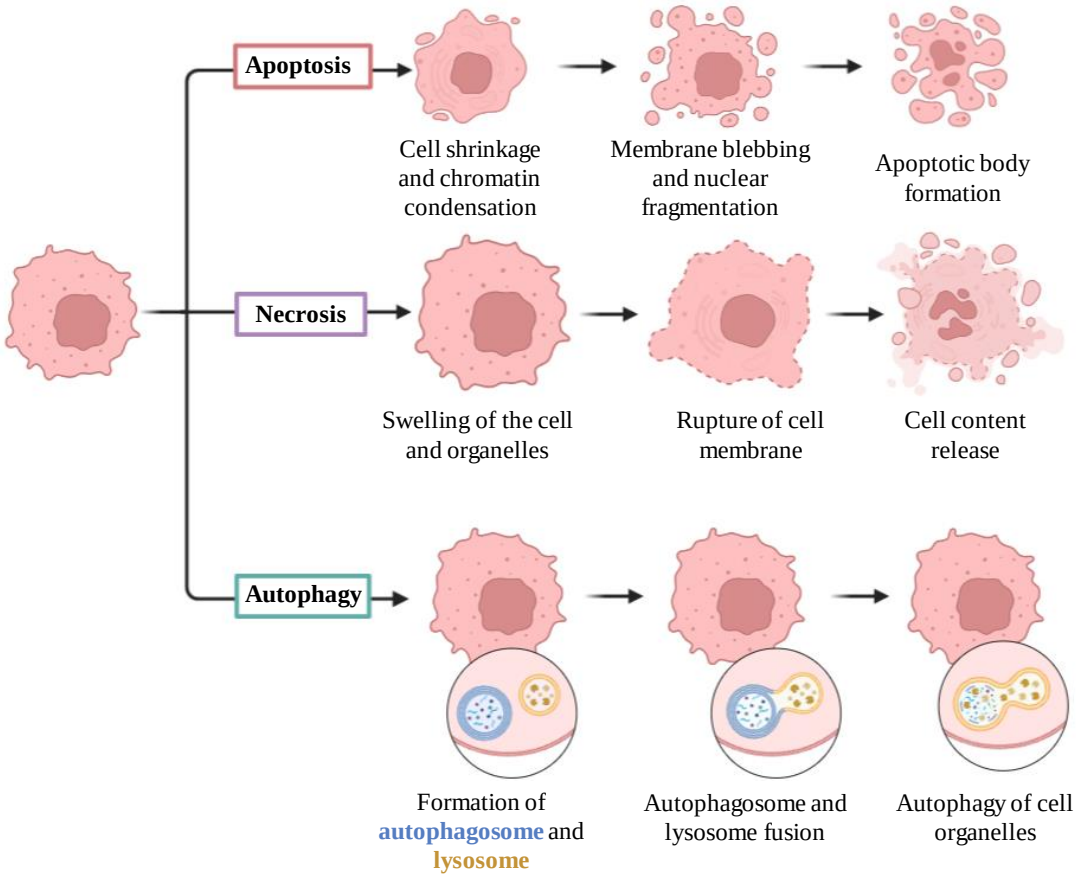

Figure 1.9. *Schematic representation of types of cell death.*

The cell death mechanisms induced by complexes **1.1** and **1.4** after 24 h of incubation in A549 cells were studied using three different concentrations ($1/2IC_{50}$, IC_{50} and $2IC_{50}$ values), to determine how the concentration of complex affects the cell death pathway. As shown in Figure 1.10, three populations of cells could be distinguished for complexes **1.1** and **1.4**. A) Annexin V-DY634 positive and 7-AAD negative cells, indicate an apoptotic death. B) Annexin V-DY634 negative and 7-AAD positive cells show a necrotic cell death pathway, and C) cells positive for Annexin V-DY634 and 7-AAD suggesting a late apoptotic stage. This last scenario is especially common in *in vitro* assays. When cells enter in an apoptotic cell death pathway, the absence of macrophages block the elimination of the cells, forcing them to enter in the stage of late apoptosis that finally leads to necrosis.

Therefore, in this specific assay, it can be said that both complexes present an apoptotic cell death mechanism. In both cases the main cell population displayed a positive response for Annexin V-DY634 whereas 7-AAD remains negative. Moreover, this is a concentration dependent process. In view of the similar results obtained for **1.1** and **1.4**, it is suggested that these outcomes could be extended to **1.2** and **1.3** due to their structural similarity.

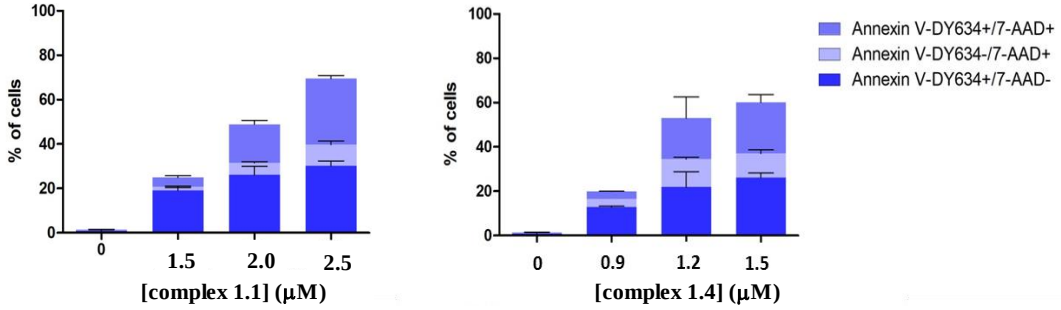

Figure 1.10. *Study of cell death mechanism in A549 cell line, induced by complexes **1.1** and **1.4** at different concentrations, after 24 h of incubation.*

1.7 Study of cell morphology

Inverted microscope was used to visualize A549 cells in the presence and absence of complexes **1.1** and **1.4**, in order to track any morphological changes or behavioral modifications. Control cells (untreated cells) grew normally and presented a healthy morphology. However, those cells that were exposed to complexes **1.1** or **1.4**, exhibited a high population of cytoplasmic vacuoles, the size and quantity of which increased with the time and dose of complexes. In fact, the little black triangles in Figure 1.11 clearly show that 48 h after the addition of the complexes, vacuoles occupied almost all of the cytoplasm. In addition to highly vascularized cells, there were also dying cells present. Black arrows point to those cells suffering an apoptotic cell death, and to a lesser extent blue arrow indicate necrotic cells. The microscopy images in Figure 1.11 are in concordance with the results mentioned in the previous section obtained by flow cytometry, in which the predominant cell death mechanism was apoptosis.

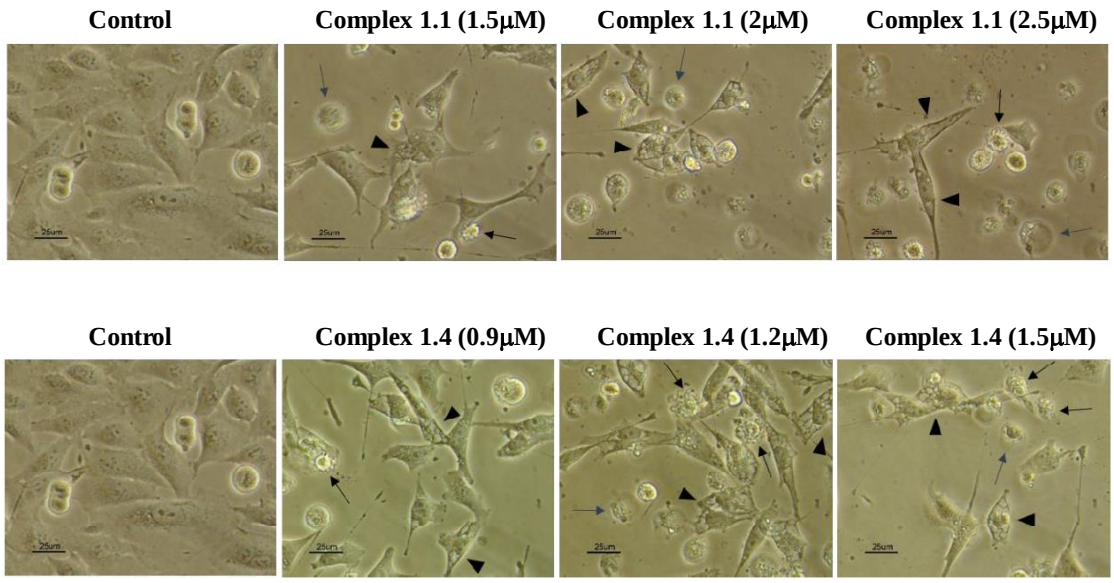

Figure 1.11. *Phase contrast microscopy images of A549 cells treated with complexes **1.1** and **1.4** at different concentrations after 48 h. Black and blue arrows point to examples of apoptotic and necrotic cells, respectively. Little black triangles show cells containing cytoplasmic vacuoles.*

The results obtained from the microscopy images and the study of cell death mechanism suggest that the studied complexes may present a complementary cell death pathway called paraptosis, which is characterized by cytoplasmic vacuolation and is independent of caspase activation. This is in line with the morphological changes observed in the cells treated with complexes **1.1** and **1.4.** Therefore, it is suggested that these complexes can induce paraptosis followed by apoptotic cell death. These findings may also be applicable to complexes **1.2** and **1.3** due to their structural similarity.

1.8 Cellular biodistribution

Fluorescence confocal microscopy assays were performed to elucidate the biodistribution of complexes **1.1-1.4** in A549 cells. The compounds were incubated at a concentration of 2 μM in A549 cells for 24 h. After this time, organelle-selective commercial dyes were added to the wells, and fluorescence microscopy was used to evaluate their internalization. IBIDI plates were used for

this biodistribution study, and the experimental setup is depicted in Figure 1.12. Well 1 represents the control for the tracker, which is used to select the microscope laser parameters and confirm that the marker has been properly internalized into the cells. Wells 2-4 contain the complexes together with the tracker, and where colocalization analysis is performed. Well 5 is the negative control, containing only cells without any complex or tracker, which is used to regulate the laser parameters and avoid autofluorescence interferences. Wells 6-8 are negative controls for the complexes, used to check the internalization rate and signal of the complexes within the cells.

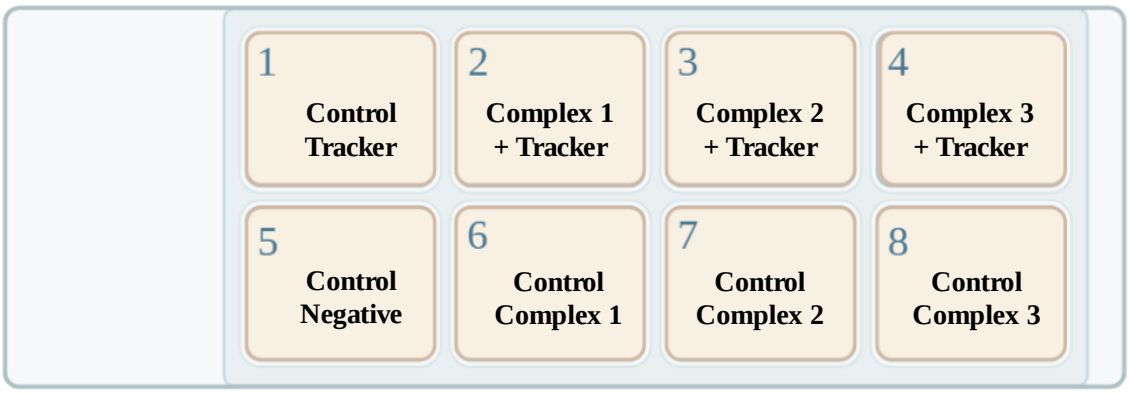

***Figure 1.12**. Depiction of well distribution in 8-well plate for confocal microscopy assay.*

The trackers used for this confocal microscopy assay were MitoTracker Red (MTR), a commercial dye that selectively stains mitochondria, and LysoTracker Red (LTR), a tracker that selectively stains lysosomes. These trackers were incubated at 75 nM for MTR and 250 nM for LTR for 30 and 60 minutes, respectively. The excitation lasers used were 559 nm for both trackers and 473 nm for the complexes. Figure 1.13 displays a simulation of emission and excitation spectra of both trackers and the complexes, which is important for selecting commercially dyes for the biodistribution experiment, and the excitation and emission parameters for collecting confocal images. It was also important for the emission pattern not to be similar, but this was less problematic if the excitation of the complexes and trackers occurred in different areas of the spectrum.

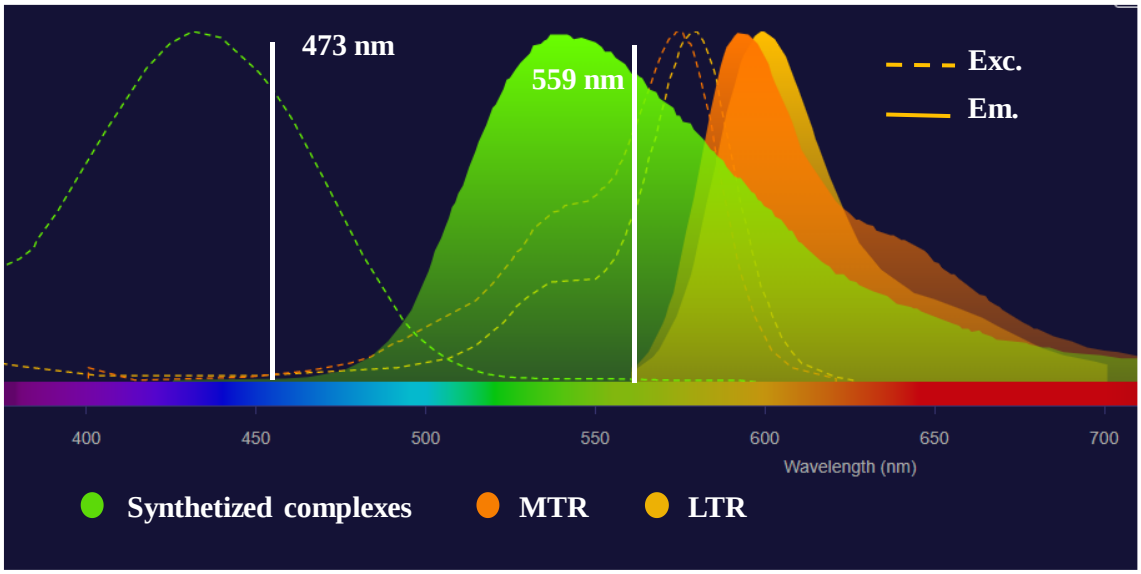

Figure 1.13. *Simulation of the different excitation and emissive profiles of studied complexes (**1.1-1.4**) and comercial trackers (MTR and LTR) used in the biodistribution assay.*[30]

The first attempt to know the final target of these complexes was performed using MTR as selective dye. For this aim, 10,000 cells/well were seeded in complete medium (200 µL/well) and left 24 h to be attached to the bottom. Then, 100 µL of culture medium was removed and 100 µL of a solution of the corresponding complexes (**1.1**-**1.4**) were added to a final concentration of 2 µM. The complexes were incubated with the cells for 24 h. Thereafter, MTR was added, and cells were incubated additionally for 30 min. Then, the medium was replaced with fresh medium without phenol red (200 µL), in order to eliminate any precipitate that could be on the well and to avoid possible emissive interferences coming from the phenol red. Images were collected in a sequential mode in a FluoView FV10i confocal microscope using 60 oil immersion lenses, and later they were processed using FV10-ASW 3.1 Viewer Software.

Focusing on images collected in Figure 1.14, where in green is observed the emission coming from complex **1.2** (top row) and **1.3** (bottom row) and in red that of MTR, it can be said that all complexes were able to internalize into the cells and they were distributed through the cytoplasm. In addition, superimposition images (Figure 1.14 C and D) suggest a partial mitochondrial localization, however it is clear that they were also accumulated in other organelles.

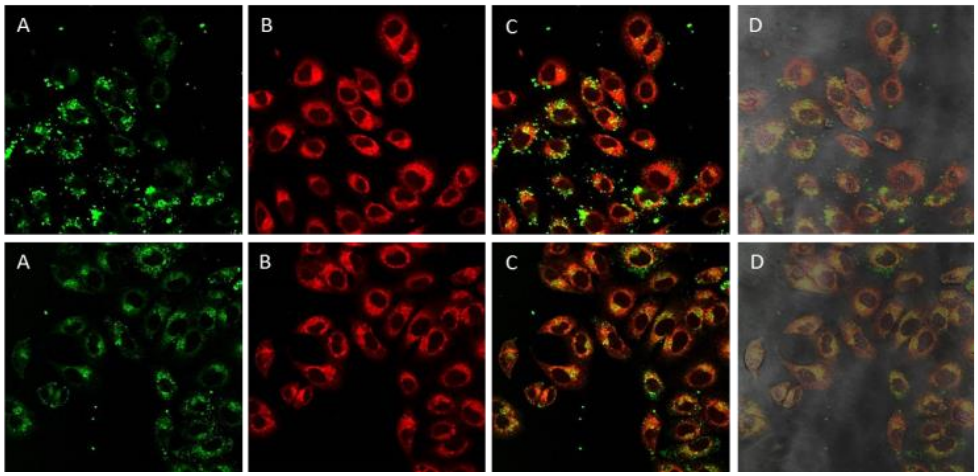

Figure 1.14. *Fluorescence confocal microscopy images of A549 cells incubated with* ***1.2*** *(top row),* ***1.3*** *(bottom row) for 24 h and stained with MTR (30 min, 75 nM). Images after irradiation at (A) 473 nm; (B) 598 nm; (C) superimposition pictures of A, B; (D) superimposition with phase contrast. Green: complexes* ***1.2*** *and* ***1.3****, Red: MitoTracker Red.*

Complex **1.1** also presented an abnormal biodistribution pattern with round spots near the nucleus, see Figure 1.15. However, a cross section intensity profile revealed that those spots are mitochondria as MTR is also localized there together with **1.1** (Figure 1.15 B). A partial mitochondrial localization is suggested.

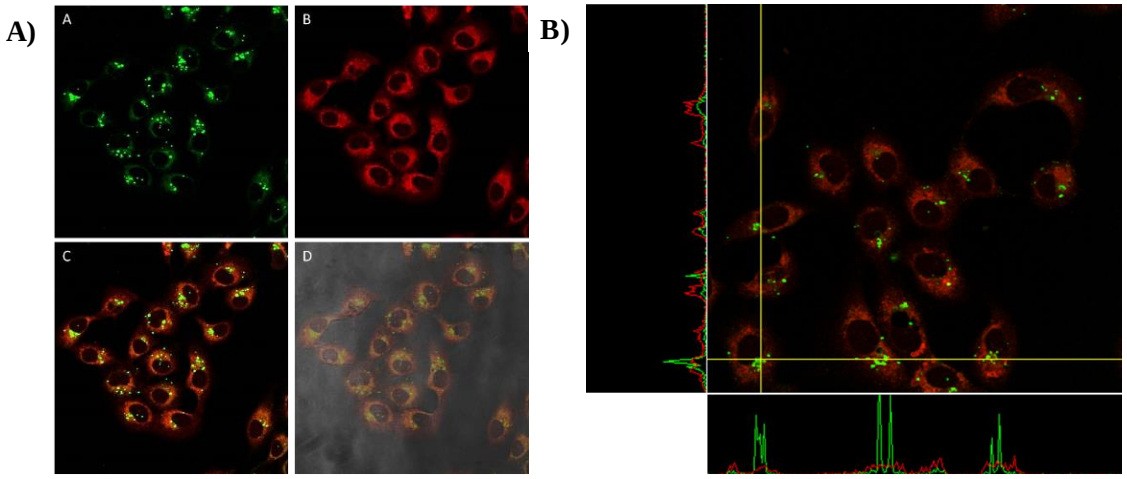

Figure 1.15. *A) Fluorescence confocal microscopy images of A549 cells incubated with complex* ***1.1*** *for 24 h and stained with MTR. (A) Image after irradiation at 473 nm; (B) after irradiation at 598 nm; (C) superimposition picture of A, B; (D) superimposition with phase contrast. Green: complex* ***1.1****, Red: MTR. B) Superimposition of pictures A, B and cross-section of their intensities.*

In an attempt to assess the global biodistribution, and knowing that similar Ir^{III} complexes presented a dual mitochondria-lysosomal biodistribution,[14] an additional confocal microscopy study was carried out. This time using LTR as internal standard and lowering incubation times for the complexes from 24 to 18 hours. As expected, superimposition images in Figure 1.16 (C and D) revealed that complex **1.4** accumulate in lysosomes, as well as in others cytoplasmic organelles.

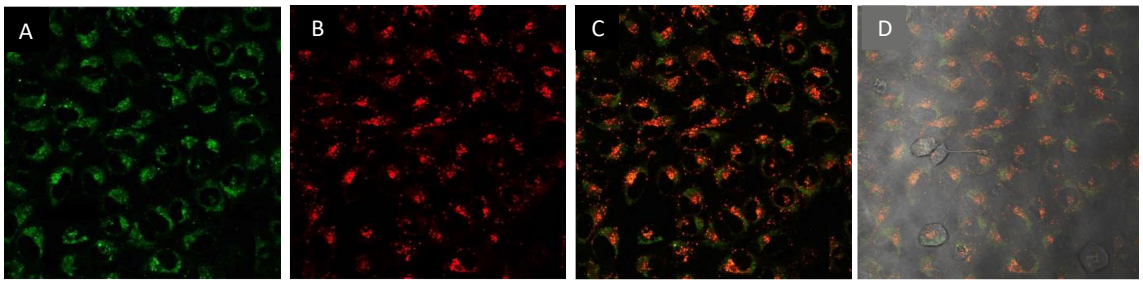

Figure 1.16. *Images of complex **1.4** after incubation with A549 for 18 h and LTR (15 min). Image after irradiation at (A) 473 nm; (B) 598 nm; (C) superimposition picture of A, B; (D) superimposition with bright field image. Green: complex **1.4**, Red: LysoTracker Red.*

Similar behaviour can be described for complexes **1.2** and **1.3**, being the localization of complex **1.2** slightly more diffuse in comparison with its analogous **1.3**. Based on the cross section of the intensity for this complex and LTR in Figure 1.18 C, the partial lysosomal localization can be confirmed, Figure 1.17.

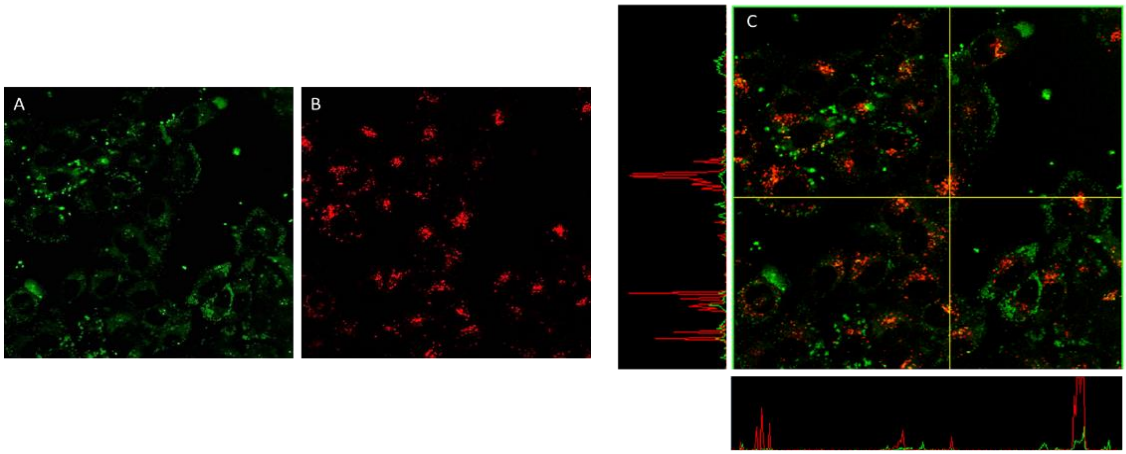

Figure 1.17. *Confocal microscopy images of complex **1.2** after incubation with A549 and LysoTracker Red. Image after irradiation at (A) 473 nm; (B) 598 nm; (C) superimposition of pictures A, B and cross-section of their intensities. Green: complex **1.2**, Red: LTR.*

Once, that this lysosomal accumulation was confirmed, one last biodistribution assay was performed just to explain the duality observed. For this purpose, complex **1.4** was incubated for just 2 h, and LTR were added. In view of images collected in Figure 1.18, it can be said that at low incubation time these complexes accumulate only in the lysosomes. Therefore, initially, complexes enter the cells and accumulate in the lysosomes and thereafter they are able scape and internalize in the mitochondria, their final targets.

To conclude, it can be said that synthetized complexes exhibit a dual biodistribution pattern, in which a trafficking process from lysosomes to mitochondria could be taking place, being these organelles their final targets.[31]

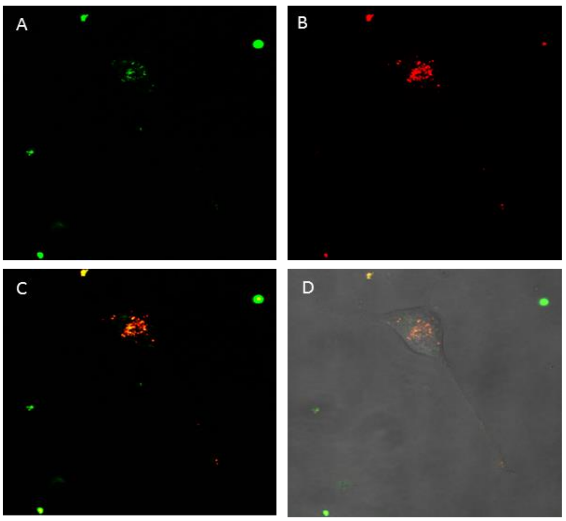

Figure 1.18. *Fluorescence confocal microscopy images of A549 cells incubated with* ***1.4*** *(2 h) and stained with LTR. (A) Image after irradiation at 473 nm; (B) after irradiation at 598 nm; (C) superimposition picture of A, B; (D) superimposition with phase contrast. Green: complex* ***1.4****, Red: LTR.*

1.9 Analysis of mitochondrial transmembrane potential

Mitochondria are considered as the synthesizers of cellular energy. In all eukaryotes cells, mitochondria are the main source of adenosine triphosphate (ATP), a compound crucial for cell functions. Its functions include cell division, biosynthesis, folding and degradation of proteins, and the generation and maintenance of membrane potentials. Mitochondrial transmembrane potentials are directly associated with the integrity and well-function of mitochondria. If a severe change of this potential takes place, the generation of ATP is limited and in consequence cells die in the majority of cases following an apoptotic pathway,[32,33] see Figure 1.19.

Therefore, the partial mitochondrial localization detected by fluorescence confocal microscopy, in addition with the apoptotic cell death mechanism induced for all complexes **1.1**-**1.4**, forces the analysis of the mitochondrial integrity. For this purpose, TMRE (tetramethylrhodamine ethyl ester) probe was used to study the mitochondrial transmembrane potential using flow cytometry. TMRE is a cell permeant, positively-charged with a red-orange emission that accumulates in active mitochondria due to their relative negative charge. On the contrary, depolarized or inactive mitochondria fail to sequester TMRE. Additionally, S63845 was used as positive control. This reagent is a selective inhibitor of the Mcl-1 antiapoptotic protein that is involved in the regulation of mitochondrial apoptotic pathway. 50,000 A549 cells/well were seeded in complete medium in flat-bottom using 12-well plates (1 mL/well) and allowed to attach for 24 h. Cells were treated for 48 h with compound **1.4** using a concentration of 0.9 μM. Then, cells were trypsinized, resuspended in 500 μL of medium. TMRE were added for a final concentration of 60 nM and the mixture was incubated at 37 ºC in the dark for further 20 minutes. Finally, a total of 10,000 cells were acquired on a FACS CaliburTM flow cytometer and data were analysed using CellQuest Pro, FlowJo 7.6.1 and GraphPad Prism software.

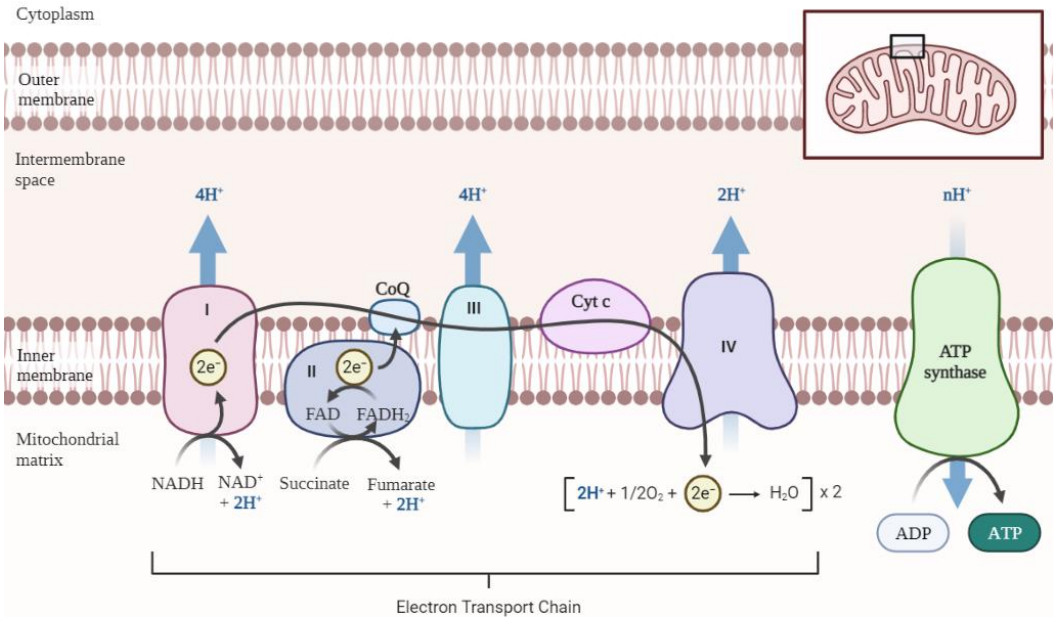

Figure 1.19. *Schematic representation of electron transport chain presents in mitochondria, and main responsible of the generation of mitochondrial transmembrane potential.*

In view of the results shown in the graph in Figure 1.20, where there is a shift in the staining pattern of TMRE of the cells incubated with complex **1.4**, in comparison with that of untreated cells, it can be said that this complex generates a completely disruption in the mitochondrial transmembrane potential. This means, that mitochondrial integrity is totally compromized in presence of **1.4**, which is in concordance with the mitochondrial localization and the apoptotic cell death mechanism observed previously.

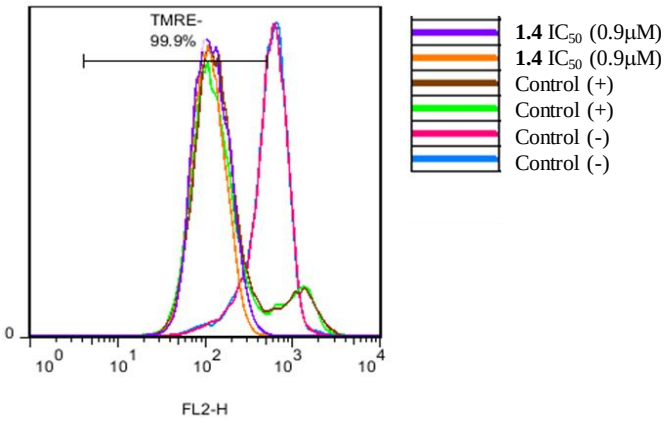

Figure 1.20. *Disruption of mitochondrial transmembrane potential induced by complex **1.4**. Negative control: Untreated cells; positive control: cells treated with S63845.*

1.10 Generation of ROS

Reactive oxygen species (ROS) are radicals, ions or molecules that have a single unpaired electron in their outermost shell of electrons. Due to this fact, ROS are highly reactive. ROS can be categorized into two groups: free oxygen radicals (superoxide ($O2•^-$), hydroxyl radical (•OH), nitric oxide (NO•)), and non-radical ROS (hydrogen peroxide (H_2O_2), singlet oxygen ($^1O_2$), among others).[34]

The fact of having a clear disruption of the mitochondrial membrane potential might suggest that ROS species are being generated. The induction capability of reactive oxygen species (ROS) was analyzed by flow cytometry using CellROX™ assay kit. This cell-permeant dye is weakly fluorescent in a reduced state, however, exhibits bright fluorescence upon oxidation by reactive oxygen species (ROS) and subsequent binding to DNA. Complexes **1.1** and **1.4** were selected for this assay to see how the presence of gold fragment could modulate the ROS production. For this purpose, 50,000 cells/well were seeded in complete medium in flat-bottom 6-well plates (3 mL/well) and allowed to attach for 24 h prior to addition of the compounds. Complexes **1.1** and **1.4** were added to cells and incubated for 24 h. Subsequently, cells were trypsinized and the CellROX®Green Flow cytometry assay kit (C10492) was used to evaluate the generation of ROS. Analysis was performed in a Gallios Flow Cytometer using Kaluza v2.1 software for data analysis.

Incubation of the complexes was made using a lower concentration to that of their IC_{50} values (**1.1:** 0.8 μM and **1.4:** 0.48 μM) in order to prevent cell death and verifying the ROS production without causing a severe damage. For both complexes, there was a clear dose-dependent generation of ROS in A549 cells. However, complex **1.4** was able to induce a much higher level of ROS than **1.1**, which was revealed by the higher shift of fluorescence in FL1 channel, as shown in Figure 1.21. Such increment could be explained by the presence of the gold fragment in the molecule, which has been reported in previous studies to induce oxidative cellular stress.[35]

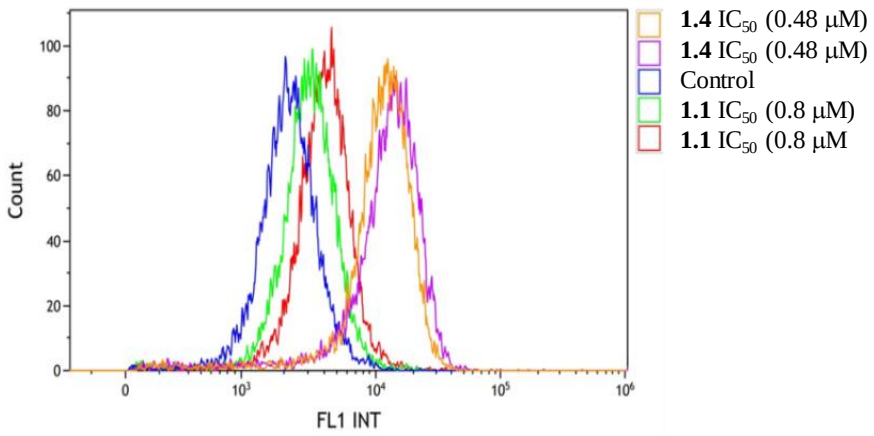

Figure 1.21. *ROS production induced by* ***1.1*** *and* ***1.4*** *in A549 cells.*

1.11 Thioredoxin reductase inhibition

As mentioned at the introduction section, gold complexes are well known for their capability to target enzymes, especially those that contain thiols. This targeting feature is attributed to the strong affinity of Au^{I} for binding thiols. Most of the thiol-containing enzymes, such as TrxR, thioredoxin reductase, are overexpressed in cancer cells, therefore, they are believed to be good biological targets to deal with this disease.[36] Hence, the interaction capacity of complexes **1.1** and **1.4** with the enzyme TrxR was studied by UV-Visible spectroscopy. This assay would allow to know if inhibition of this enzyme is taking place, and additionally, if complex **1.4** containing a gold fragment is able to enhance such inhibition as expected in comparison with the monometallic Ir^{III} complex **1.1**.

The mentioned complexes were incubated with cells at their IC_{50} values (**1.1**: 1 μM; **1.4**: 0.6 μM) for 24 h. After that, a total protein extraction protocol was followed to remove all proteins from the cells and to determinate the specific activity of TrxR. Thus, 5,5'- dithiobis(2-nitrobenzoic acid) (DTNB) was added to the different protein extracts in presence of NADPH and subsequent measurements of absorption intensity at 412 nm were performed for 5 min by absorption spectroscopy. It is known that DTNB rapidly evolves to 2-nitro-5-thiobenzoate anion (TNB) if no-inhibition of the thioredoxin reductase enzyme has occurred,

affording a yellow solution that absorbs specifically at 412 nm.[37] In view of the plotting of the evolution of TNB over time for **1.1**, **1.4** and a control experiment, shown in Figure 1.22, it can be said that both complexes display lower slope values (**1.1**: 0.00192; **1.4**: 0.00183) in comparison with that of the control (0.00211) suggesting a moderate TrxR inhibition. Additionally, it is worth mentioning that complex **1.4**, as expected, is the one affecting the activity of the TrxR to a greater extent, possibly due to the presence of gold fragment within the molecule.

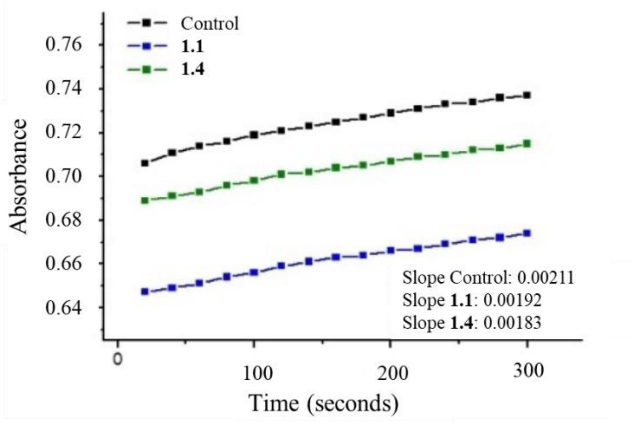

Figure 1.22. *Inhibition of the enzyme Thioredoxin Reductase (TrxR) for complexes* ***1.1*** *and* ***1.4****. Representation of the evolution of the absorbance intensity of TNB at 412 nm over 5 minutes.*

1.12 Antiangiogenic activity assay

The term angiogenesis is referred to the formation of new blood vessels. This process involves the migration, growth, and differentiation of endothelial cells. Angiogenesis is controlled by chemical signals in the body, such as vascular endothelial growth factor (VEGF), proteins that bind to receptors on the surface of normal endothelial cells.[38] When VEGF and other endothelial growth factors bind to their receptors on endothelial cells, signals within these cells are initiated promoting the growth and survival of new blood vessels. However, other chemical signals, called angiogenesis inhibitors, disrupt blood vessel formation. Antiangiogenic drugs targeting the VEGF pathway have slowed metastatic disease

progression in some patients, leading to progression-free survival (PFS) and overall survival benefits compared with controls.[39]

The effect of the synthesized compounds on *in vitro* angiogenesis was investigated using Cultrex hydrogel matrix. It was found that incubation of compounds **1.1**, **1.2** and **1.4** at 0.25 μM for 20 h with endothelial forming colony cells (ECFCs) inhibited vessel generation. As is shown in Figure 1.23, complexes **1.1** and **1.4** once again, produced larger effect than complex **1.2**, suggesting a better antiangiogenic character and ultimately a possible antimetastatic character.

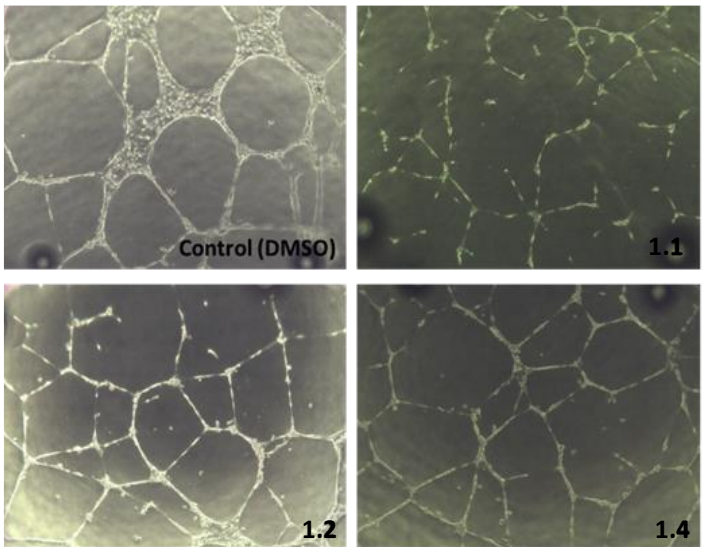

Figure 1.23. *Images of in vitro antiangiogenic activity assays in ECFCs cells incubated with complexes* ***1.1****,* ***1.2*** *and* ***1.4*** *for 20 h at 0.25 μM.*

1.13 Conclusions

In this chapter, one cyclometallated Ir^{III} complex (**1.1**) and three hetero-bimetallic Ir^{III}-Au^{I} complexes (**1.2**-**1.4**) containing a bis(diphenylphosphino)methanide ligand as linker between the metal fragments have been synthetized. All of them exhibited great bioactive and emissive properties. These complexes showed emissions that are dominated by the iridium fragment over the gold one, whose origin is due to ^{3}MLCT transitions mainly from the Ir^{III} core to the diphosphine ligand. As consequence, no relevant shift of their emission maxima has been observed with the different Au^{I} ancillary ligand. Additionally, antiproliferative MTT assays, revealed that A549 cells showed high sensitivity for all complexes (IC_{50} values 0.6-1.7 μM), especially those containing the gold center linked to a triphenylphosphine (**1.2**) or a thiocytosine group (**1.4**). Interestingly, complex **1.4** containing a gold fragment prompted greater ROS generation, at the same time that generated bigger TrxR inhibition in comparison with the monometallic Ir^{III} analogue (**1.1**); even though, both complexes rendered a completely disruption of the mitochondrial transmembrane potential in A549 cells. Moreover, microscopy images and cell death analysis performed by flow cytometry revealed massive cytoplasmic vacuolization and apoptotic body formations, which tended to indicate an apoptotic cell death pathway. Focusing on the biodistribution studies performed in A549 cells, complexes **1.1**-**1.4** seemed to exhibit a partial dual localization in lysosomes and mitochondria. Fluorescence microscopy analysis performed at different incubation times suggested a time-dependant trafficking process from the lysosomes to the mitochondria.

Moreover, all synthetized complexes displayed antiangiogenic properties in endothelial cells. Specifically, complexes **1.1** and **1.4** presented the highest inhibition of angiogenesis, revealing themselves as potential antimetastatic species.

In view these results, it could be said that these bimetallic complexes might be potential candidates for further studies as promising antitumour agents due to their

proven ability for disrupting mitochondria membrane potential, being efficient ROS generators, their high cytotoxic potential in cancer cells and antimetastatic activity.

1.14 General synthetic procedures

The starting material $[Ir(ppy)_2(\mu\text{-}Cl)]_2$ was prepared according to published procedures.[40] Other reagents and solvents were commercially available from Sigma-Aldrich, and used without further purification. Manipulations were performed under argon atmosphere and using dry solvents.

Instrumentation

Mass spectra were recorded on a BRUKER ESQUIRE 3000 PLUS, with the electrospray (ESI) technique. ^{1}H, $^{13}C\{^{1}H\}$ and $^{31}P\{^{1}H\}$ NMR, including 2D experiments, were recorded at room temperature on a BRUKER AVANCE 400 spectrometer (^{1}H, 400 MHz, ^{13}C, 100.6 MHz, $^{31}P\{^{1}H\}$, 162 MHz) with chemical shifts (δ, ppm) reported relative to the solvent peaks of the deuterated solvent.[41] Steady-state photoluminescence spectra were recorded with a Jobin-Yvon-Horiba fluorolog FL-3-11 spectrometer using band pathways of 3 nm for both excitation and emission. UV/vis spectra were recorded with 1 cm quartz cells on an Evolution 600 spectrophotometer. Quantum yields were measured using an absolute method provided by Hamamatsu Photonics Quantaurus-QY C11347-11. Specifically, each sample was measured using the excitation scanning mode in aerated DMSO solution at RT. Excitation of the samples was made from 370 to 470 nm in 10 nm intervals. The quantum yield value given is the one obtained at maxima intensity excitation, that is, **1.1** (425 nm), **1.2** (446 nm), **1.3** (415 nm), **1.4** (405 nm). The experiment was repeated three times to ensure reproducibility.

Synthetic Procedure of Complex 1.1

The synthesis of **1.1** was accomplished by the treatment of two equivalents of ligand dppm (bis(diphenhylphophino)methane) (35.9 mg, 0.094 mmol) with one equivalent of $[Ir(ppy)_2(\mu\text{-}Cl)]_2$ (50 mg, 0.047 mmol) in methanol, under reflux for 12 hours. Once the reaction was completed, the solvent was evaporated under vacuum and the slurry was dissolved in the minimum amount of dichloromethane. KPF_6 was added and the mixture was stirred at room temperature for 30 minutes.

Finally, hexane was added to obtain **1.1** as a pale yellow solid by precipitation, which was filtered and washed with ether (82.7 mg, 0.08 mmol, 85%).

^{1}H NMR (400 MHz, CD_2Cl_2) δ 8.15 (d, J = 5.4 Hz, 1H), 7.86 (dt, J = 10.8, 4.8 Hz, 2H), 7.79 – 7.68 (m, 2H), 7.64 – 7.55 (m, 1H), 7.55 – 7.46 (m, 3H), 7.16 – 6.90 (m, 7H), 6.49 – 6.38 (m, 2H), 5.42 (t, J = 9.8 Hz, 1H) ppm. ^{13}C NMR (101 MHz, CD_2Cl_2) δ 156.6, 155.7, 153.6, 143.4, 138.4, 132.5, 132.3, 132.3, 131.6, 131.1, 130.6, 130.4, 130.3, 129.8, 129.5, 129.4, 129.3, 128.1, 125.5, 124.1, 120.9, 34.9 ppm. ^{31}P NMR (162 MHz, CD_2Cl_2) δ -56.11 ppm. ^{19}F NMR (376 MHz, CD_2Cl_2) δ -72.05, -73.94 ppm. ESI-HRMS (m/z): 885.2139 M^+, $C_{47}H_{38}IrN_2P_2$ (885.1889).

Synthetic Procedure of Complex 1.2

A mixture of complex **1.1** (10 mg, 0.01 mmol) and [Au(acac)PPh_3] (5.42 mg, 0.01 mmol) in dry dichloromethane (5 mL) was stirred for 24 hours under argon atmosphere. The resultant solid was filtered, washed with ether and dried under vacuum, affording complex **1.2** as yellow solid. (13.56 mg, 0.009 mmol, 91%).

^{1}H NMR (400 MHz, CD_2Cl_2) δ 9.54 (d, *J* = 5.6 Hz, 1H), 7.97 (d, *J* = 7.6 Hz, 1H), 7.83 – 7.71 (m, 5H), 7.63 (dd, *J* = 11.8, 7.6 Hz, 2H), 7.55 – 7.31 (m, 16H), 7.23 – 7.05 (m, 6H), 7.01 – 6.79 (m, 15H), 6.64 (td, *J* = 7.9, 2.3 Hz, 2H), 6.46 – 6.32 (m, 1H), 6.28 – 6.19 (m, 1H), 6.03 – 5.97 (m, 1H), 5.49 (m, 1H) ppm. ^{13}C NMR (101 MHz, CD_2Cl_2) δ 143.4, 142.6, 137.8, 137.6, 136.8, 136.6, 133.7, 133.6, 132.6, 132.5, 131.9, 131.6, 130.8, 130.7, 130.6, 130.4, 130.3, 130.1, 129.8, 129.7, 129.4, 129.3, 129.2, 128.6, 128.5, 128.1, 128.0, 127.9, 127.8, 124.6, 124.2, 123.2, 123.1, 122.7, 121.9, 119.9, 119.1, 34.3 ppm. ^{31}P NMR (162 MHz, CD_2Cl_2): δ=38.62 (t, J= 9.5 Hz), −45.79 (dd, J= 37.8, 9.4 Hz), −48.73 (dd, J= 37.7, 9.7 Hz) ppm. ESI-HRMS (m/z): 1343.2638 M^+, $C_{65}H_{52}AuIrN_2P_3$ (1343.2615).

Synthetic Procedure of Complex 1.3

50 mg (0.05 mmol) of **1.1**, 15.51 mg (0.05 mmol) of [AuCl(tht)], 15 mg of Cs_2CO_3 and 10 mL of dry dichloromethane were placed in a 50 mL round bottom flask. The mixture was stirred for 24 hours at room temperature. The reaction was monitored by TLC (dichloromethane / hexane 9:1). After the reaction was

completed, diethyl ether was added to the mixture affording the precipitation of a yellow solid, complex **1.3**, which was filtered, washed with ether and dried under vacuum. (38.79 mg, 0.034 mmol, 70%).

^{1}H NMR (400 MHz, CD_2Cl_2) δ 8.15 (d, J = 5.6 Hz, 1H), 7.77 – 7.63 (m, 4H), 7.55 (dt, J = 16.6, 8.0 Hz, 4H), 7.10 (d, J = 7.5 Hz, 2H), 7.05 – 6.94 (m, 3H), 6.79 (d, J = 10.2 Hz, 2H), 6.52 – 6.45 (m, 1H), 6.45 – 6.40 (m, 1H), 5.38 (d, J = 7.3 Hz, 1H) ppm. ^{13}C NMR (101 MHz, CD_2Cl_2) δ 153.0, 147.2, 141.9, 140.5, 131.9, 131.7, 131.1, 130.5, 130.3, 130.0, 129.8, 129.3, 129.0, 128.8, 128.7, 124.9, 123.5, 123.4, 122.9, 122.3, 120.3, 118.7, 34.4 ppm. ^{31}P NMR (162 MHz, CD_2Cl_2) δ -56.85 ppm. IR: υ(Au-Cl): 335 cm^{-1}.

Synthetic Procedure of Complex 1.4

25 mg (0.02 mmol) of complex **1.3** were dissolved in 10 mL of dry dichloromethane and 5 equivalents of Cs_2CO_3 were added. The mixture was stirred for 15 min at room temperature. Then, thiocytosine (2.60 mg, 0.02 mmol) was added and the reaction mixture was stirred for 24 hours. Once the reaction was completed, the solvent was evaporated to a minimum volume and the addition of diethyl ether afforded the precipitation of a pale yellow solid, which was filtered, washed with hexane and dried under vacuum. (22.37 mg, 0.018 mmol, 92%). ^{1}H NMR (400 MHz, CD_2Cl_2) δ 8.15 (d, *J* = 5.3 Hz, 1H), 7.78 – 7.63 (m, 5H), 7.55 (m, 5H), 7.11 (t, *J* = 7.5 Hz, 2H), 6.99 (dt, *J* = 13.6, 7.4 Hz, 3H), 6.79 (t, *J* = 9.1 Hz, 2H), 6.48 (ddd, *J* = 7.5, 6.0, 1.5 Hz, 1H), 6.43 (dd, *J* = 7.5, 2.9 Hz, 1H), 5.35 (d, *J* = 9.4 Hz, 1H) ppm. ^{13}C NMR (101 MHz, CD_2Cl_2) δ 153.6, 148.3, 147.8, 141.3, 140.6, 138.9, 137.0, 134.6, 133.5, 133.1, 132.5, 132.3, 131.8, 130.9, 130.4, 129.8, 129.5, 127.3, 126.3, 125.5, 124.1, 123.8, 121.4, 120.9, 119.3, 117.99, 35.0 ppm. ^{31}P NMR (162 MHz, CD_2Cl_2) δ -56.71 ppm. ESI-HRMS (m/z): 1117.1760 M^+, $C_{47}H_{41}AuIrN_2P_2S$ (1117.1403).

1.15 Materials and methods

Cell culture

A549 (human lung carcinoma) cell line was routinely cultured in high glucose DMEM medium supplemented with 5% fetal bovine serum (FBS), L-glutamine and penicillin/streptomycin. Endothelial colony forming cells (ECFC) were isolated from umbilical cord blood from healthy births (ucb-ECFCs) following the method described by Ingram.[42] All cultures were maintained at 37 °C in a humidified atmosphere of 95% air/5% CO_2.

Antiproliferative activity assays

The MTT-reduction assay was used to analyse cell metabolic activity as an indicator for cell sensitivity to the complexes in A549 cell line. 10^5 cells/ml were seeded in complete DMEM (10% FBS) medium in flat-bottom, 96-well plates (100 µL/well) and allowed to attach for 24 h prior to addition of compounds. Cells were incubated with complexes **1.1**-**1.4** for 24 h and then 10 µL of MTT (5 mg/mL in PBS) were added to each well and plates were incubated for 2 h at 37 °C. Finally, culture medium was removed and DMSO (100 µL/ well) was added to dissolve the formazan crystals. The optical density was measured at 550 nm using a 96-well multiscanner autoreader (ELISA) and IC_{50} was calculated using GraphPad Prims 5 software. Each compound was analyzed at least in three independent experiments.

Cell death mechanism assays

Apoptotic and necrotic cell death was determined by measuring phosphatidylserine exposure on cell surface and cell membrane permeabilization, respectively, in A549 cells. $5{\cdot}10^5$ cells/well were seeded in complete medium in flat-bottom, 12-well plates (1 mL/well) and left overnight to be attached to the bottom. Cells were treated for 48 h with compounds **1.1** and **1.4** at concentrations of: 1, 1.5, 2, 2.5 µM (**1.1**), 0.6, 0.9, 1.2, 1.5 µM (**1.4**) in duplicate. For apoptosis inhibition evaluation, cells were preincubated for 1 h with the pan-caspase inhibitor Z-VAD-fmk (30 µM) prior to the addition of the compounds and it was

renovated 24 h later. After treatments, cells were trypsinised, resuspended in 100 µl of a mixture of Annexin-binding buffer (ABB; 140 mM NaCl, 2.5 mM $CaCl_2$, 10 mM HEPES/NaOH pH 7.4), DY634-conjugated Annexin V and 7-amino-actinomycin D (7-AAD) and incubated at room temperature in the dark for 15 minutes. Finally, cells were diluted to 500 µL with ABB and a total of 10,000 cells were acquired on a FACSCaliburTM flow cytometer. Cell death was analyzed using CellQuest Pro, FlowJo 7.6.1 and GraphPad Prism 5 software.

ROS production measurement

$5 \cdot 10^5$ A549 cells/well were seeded in complete medium in flat-bottom, 6-well plates (3 mL/well) and allowed to attach for 24 h prior to addition of the compounds. Complexes **1.1** and **1.4** were dissolved in DMSO, (stock solution, 0.1 µM), and subsequent dilution were made for adding them to cells up to concentration of 80% their IC_{50} values in duplicate. Cells were incubated with the complexes for 24 h and subsequently, they were trypsinized and the CellROX®Green Flow cytometry assay kit (C10492) was used to evaluate the generation of ROS in a Gallios Flow Cytometer using Kaluza v2.1 software for data analysis.

Mitochondrial transmembrane potential analysis

Integrity of the mitochondrial outer membrane was evaluated by measuring disruption of mitochondrial transmembrane potential. For this assay, $50 \cdot 10^5$ A549 cells/mL were seeded in complete medium in flat-bottom, 12-well plates (1 mL/well) and allowed to attach for 24 h prior to addition of compounds. Cells were treated for 48 h with compound **1.4** at 0.9 µM in duplicate. Then, they were trypsinized, resuspended in 500 µL of containing of complete medium and 60 nM of the tetramethylrhodamine ethyl ester (TMRE) probe and incubated at 37 ºC in the dark for further 20 minutes. Finally, a total of 10,000 cells were acquired on a FACSCaliburTM flow cytometer and data were analyzed using CellQuest Pro, FlowJo 7.6.1 and GraphPad Prism 5 software.

Tube formation assay

Endothelial cells (10^4cells/well) were suspended in cell culture medium containing complexes **1.1**, **1.2** or **1.4** at 0.25 μM (DMSO) for 20 hours. Thereafter, they were seeded over Cultrex® Reduced Growth Factor Basement Membrane Matrix gelled (37 °C for 30 min) in wells of μ-Slide Angiogenesis coverslips. Images were acquired with a Moticam 3 digital camera system through a CK40 inverted microscope using a 10x objective.

Fluorescence confocal microscopy

$8 \cdot 10^3$ A549 cells/well were seeded in complete medium in μ-slide 8 well (300 μL/well) and left 24 h to be attached to the bottom. Then, 200 μL of culture medium was removed and 100 μL of a solution of the corresponding complexes (**1.1**-**1.4**) were added to a final concentration of 2 μM. The complexes were incubated with the cells for 2 h, 18 h or 24 h depending on the specific experiment. Thereafter, MitoTracker Red (MTR) at 75 nM or LysoTracker Red-DND-99 (LTR) at 250 nM was added. They were incubated with the cells for 30 min (MitoTracker) or 60 min (LysoTracker) at room temperature. Eventually the medium was replaced with fresh medium without phenol red. Images were collected in a sequential mode in a FluoView FV10i confocal microscope with a 60 oil immersion lens, a line average of 4, and a format of 1024x1024 pixels using excitation wavelength of either 473 nm or 559 nm. The confocal pinhole was 1 Airy unit. Images were analyzed with FV10-ASW 3.1. Viewer software.

Crystal structure analysis

Crystals were mounted in inert oil glass fibres and transferred to the cold gas stream of a SMART APEX Duo diffractometer equipped with a low-temperature attachment. Data were collected using monochromated Mo Kα radiation (λ = 0.71073 Å). Scan type ω. Absorption corrections based on multiple scans were applied with the program SADABS. The structures were solved by direct methods and refined on F2 using the program SHELXL-2016. All non-hydrogen atoms were refined anisotropically. Hydrogen atoms were included in calculated

positions and refined using a riding model. CCDC deposition number 2052537 contains the supplementary crystallographic data. These data can be obtained free of charge by The Cambridge Crystallography Data Centre.

[1] C. Barnard, *Johnson Matthey Technol. Rev.* **2017**, *61*, 52-59.
[2] P.J. Loehrer, L.H. Einhorn, *Ann. Intern. Med.* **1984**, *100*, 704-713.
[3] P.J. O'Dwyer, J.P. Stevenson, S.W. Johnson, *Clinical Status of Cisplatin, Carboplatin, and Other Platinum-Based Antitumor Drugs. In Cisplatin*, B. Lippert (Ed.), Denmark, **1999**.
[4] R. Oun, Y.E. Moussa, N.J. Wheate, *Dalton Trans.* **2018**, *47*, 6645-6653.
[5] L. Ortego, F. Cardoso, S. Martins, M.F. Fillat, A. Laguna, M. Meireles, M.D. Villacampa, M.C. Gimeno, *J. Inorg. Biochem.* **2014**, *130*, 32-37.
[6] P.Y. Gasdaska, J.E. Oblong, I.A. Cotgreave, G. Powis, *Biochim. Biophys. Acta*. **1994**, *1218*, 292-296.
[7] C. Roder, M.J. Thomson, *Drugs R. D.* **2015**, *15*, 13-20.
[8] S.J. Weir, L.J. DeGennaro, C.P. Austin, *Cancer Res.* **2012**, *72*, 1055-1058.
[9] E. Cerrada, V. Fernández-Moreira, M.C. Gimeno, *Adv. Organomet. Chem.* **2019**, *71*, 227-258.
[10] C. Caporale, M. Massi, *Coord. Chem. Rev.* **2018**, *363*, 71-91.
[11] A. Luengo, I. Marzo, M. Reback, I.M. Daubit, V. Fernández-Moreira, N. Metzler-Nolte, M.C. Gimeno, *Chem. Eur. J.* **2020**, *26*, 12158-12167.
[12] M. Ouyang, L. Zeng, H. Huang, C. Jin, J. Liu, Y. Chen, L. Jia, H. Chao, *Dalton Trans.* **2017**, *46*, 6734-6744.
[13] S. Liu, H. Liang, K.Y. Zhang, Q. Zhao, X. Zhou, W. Xua, W. Huang, *Chem. Commun.* **2015**, *51*, 7943-7946.
[14] L. Hao, Z.-W. Li, D.-Y. Zhang, L. He, W. Liu, J Yang, C.-P. Tan, L.-N. Ji, Z.-W. Mao, *Chem. Sci.* **2019**, *10*, 1285-1293.
[15] M. Redrado, V. Fernández-Moreira, M.C. Gimeno, *ChemMedChem* **2021**, *16*, 932-941.
[16] F. Pelletier, V. Comte, A. Massard, M. Wenzel, S. Toulot, P. Richard, M. Picquet, P. Le Gendre, O. Zava, F. Edafe, A. Casini, P.J. Dyson, *J. Med. Chem.* **2010**, *53*, 6923-6933.
[17] H. Goitia, Y. Nieto, M.D. Villacampa, C. Kasper, A. Laguna, M.C. Gimeno, *Organometallics* **2013**, *32*, 6069-6078.
[18] A. Johnson, I. Marzo, M.C. Gimeno, *Dalton Trans.* **2020**, *49*, 11736-11742.
[19] F. Pelletier, V. Comte, A. Massard, M. Wenzel, S. Toulot, P. Richard, M. Picquet, P. Le Gendre, O. Zava, F. Edafe, A. Casini, P. J. Dyson, *J. Med. Chem.* **2010**, *53*, 6923-6933.
[20] A. Auffrant, A. Barbieri, F. Barigelletti, J. Lacour, P. Mobian, J.-P. Collin, J.-P. Sauvage, B. Ventura, *Inorg. Chem*. **2007**, *46*, 6911-6919.
[21] R. Usón, A. Laguna, M. Laguna, M.N. Fraile, P.G. Jones, G.M. Sheldrick, *Dalton Trans.* **1986**, 291-296.
[22] E.J. Fernández, M.C. Gimeno, P.G. Jones, A. Laguna, M. Laguna, E. Olmos, *Inorg. Chim. Acta* **1995**, *238*, 173-177.
[23] P. Alam, I.R. Laskar, C. Climent, D. Casanova, P. Alemany, M. Karanam, A.R. Choudhury, J.R. Butcher, *Polyhedron* **2013**, *53*, 286-294.
[24] Y. Chi, S.F. Wang, P. Ganesan, *Chem. Rec.* **2019**, *19*, 1644-1666.

[25]V. Thamilarasan, P. Karunakaran, N. Kavitha, C. Selvaraju, N. Sengottuvelan, *Polyhedron* **2016**, *118*, 12-24.
[26] T. Mosmann, *J. Immunol. Meth.* **1983**, *65*, 55-63.
[27] F.M. Freimoser, C.A. Jakob, M. Aebi, U. Tuor, *Appl. Environ. Microbiol.* **1999**, *65*, 3727-3729.
[28] M. van Engeland, L.J. Nieland, F.C. Ramaekers, B. Schutte, C.P. Reutelingsperger, *Cytometry* **1998**, *31*, 1-9.
[29] N. C. Zembruski, V. Stache, W.E. Haefeli, J. Weiss, *Anal. Biochem.* **2012**, *429*, 79-81.
[30] https://www.thermofisher.com/order/fluorescence-spectraviewer#!/
[31]F. Schibilla, A. Holthenrich, B. Song, A.L.L. Matos, D. Grill, D.R. Martir, V. Gerke, E. Zysman-Colman, B.J. Ravoo, *Chem. Sci.* **2018**, *9*, 7822-7828.
[32] W. Kühlbrandt, *BMC Biol.* **2015**, *13*, 89-100.
[33] S.W. Perry, J.P. Norman, J. Barbieri, E.B. Brown, H.A. Gelbard, *BioTechniques* **2011**, *50*, 98-115.
[34] G.-Y. Liou, P. Storz, *Free Radic. Res.* **2010**, *44*, 479-496.
[35] I. Mármol, M. Virumbrales-Muñoz, J. Quero, C. Sánchez-de-Diego, L. Fernández, I. Ochoa, E. Cerrada, M.J.R. Yoldi, *J. Inorg. Biochem.* **2017**, *176*, 123-133.
[36] M.M. Mohamed, B.F. Sloane, *Nat. Rev. Cancer* **2006**, *6*, 764-775.
[37] B. Cunniff, G.W. Snider, N. Fredette, R.J. Hondal, N.A.H. Heintz, *Anal. Biochem.* **2013**, *443*, 34-40.
[38] J. Ebos, R. Kerbel, *Nat. Rev. Clin. Oncol.* **2011**, *8*, 210-221.
[39] B. Czakó, L. Kürti, A. Mammoto, D.E. Ingber, E.J. Corey, *J. Am. Chem. Soc.* **2009**, *131*, 9014-9019.
[40] S. Sprouse, K.A. King, P.J. Spellane, R.J. Watts, *J. Am. Chem. Soc.* **1984**, *106*, 6647-6653.
[41] G.R. Fulmer, A.J.M. Miller, N.H. Sherden, H.E. Gottlieb, A. Nudelman, B.M. Stoltz, J.E. Bercaw, K.I. Goldberg, *Organometallics* **2010**, *29*, 2176-2179.
[42] D.A. Ingram, L.E. Mead, H. Tanaka, V. Meade, A. Fenoglio, K. Mortell, K. Pollok, M.J. Ferkowicz, D. Gilley, M.C. Yoder, *Blood* **2004**, *104*, 2752-2760.

Chapter 2

2.1 Introduction

Heterometallic complexes have garnered growing interest across a range of research fields, including catalysis,[1] material science,[2] and medicine.[3] In medical applications, various metallic combinations have been investigated. The first approaches relied in combining two bioactive metallic fragments, such as Fe^{II} with Au^{I}, Ru^{II} with Pt^{II}, Ti^{IV} with Au^{I}, or Cu^{I}/Ag^{I} with Au^{I} (depicted in Figure 2.1). Later on, some combinations even pair emissive metallic fragments with antiproliferative ones. For example, mixtures of d^6 complexes with noble metals have gained increasing attention in recent years. In this way, Re^{I} or Ir^{III} complexes combined with Au^{I} species have been designed as theranostic agents, where the d^6 metallic core typically provides the emissive properties for cell imaging, and the Au^{I} fragment acts as the therapeutic component. These complexes offer large Stokes' shifts and relatively long lifetimes, making them favorable for bioimaging purposes.

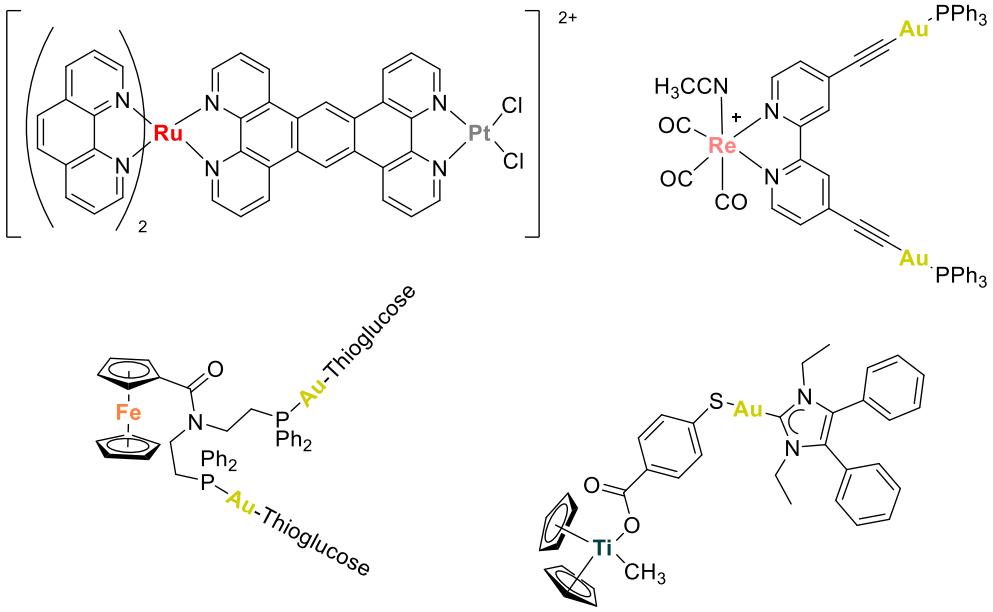

Figure 2.1. *Depiction of heterometallic Ru^{II}/Pt^{II},[4] Re^{I}/Au^{I},[5] Ti^{IV}/Au^{I},[6] and Fe^{II}/Au^{I} [7] complexes.*

Iridium (III) complexes of the type $[Ir(C\text{^}N)_2(N\text{^}N)]^{0/+}$, where C^N represents a cyclometallated ligand, and N^N a chelate ligand, exhibit a phosphorescent emission in the majority of the cases due to a metal-to-ligand charge transfer (^{3}MLCT) and ligand-to-ligand charge transfer (^{3}LLCT) transition involving the

orbitals of C^N and N^N ligand.[8] It is for this reason that is easy to tune their optical properties by varying the chelated ligands. The introduction of rigidity or increasing the aromaticity can generate an emissive shift to lower energies.[9] Alternatively, gold (I) complexes have been utilized as anti-inflammatory drugs in the form of gold thiolates, such as the disodium aurothiomalate salt or aurothioglucose, among others, for the treatment of rheumatoid arthritis.[10] Recently, gold (I) complexes have gained significance in the development of anticancer agents, particularly since auranofin, which was initially used as an antiarthritic drug, has entered in phase four of clinical trials for the treatment of chronic lymphocytic leukaemia (NCT01419691 and NCT01747798), ovarian cancer (NCT03456700), and lung cancer (NCT01737502).[11] Additionally, several studies have demonstrated that a careful ligand selection can produce gold complexes with antiproliferative activity against a wide variety of cancer cell lines.[12]

The pursuit of enhancing the anticancer properties of gold (I) complexes has led to the emergence of N-heterocyclic carbene (NHC) compounds as a promising new class of ligands in the field of medicine.[13] These gold carbene bonds exhibit a high σ-donating capacity, comparable to that of phosphines which are key in the drug auranofin.[14] In 2004, the group of Berners-Price and Day discovered the anticancer activity of Au^{I} N-heterocyclic carbenes (NHC) (Figure 2.2A) when evaluating the mitochondrial swelling capabilities of a series of bis-NHC Au^{I} derivatives.[15] This initial finding, along with the convenient functionalization of NHCs, spurred more research into this type of organometallic complexes. For instance, Che and co-workers combined NHC and phosphine ligands to report on dinuclear Au^{I} complexes (Figure 2.2B) that not only exhibited significant anticancer effects *in vivo* but also antiangiogenic effects in tumor models and inhibition of sphere formation of cancer stem cells *in vitro*. The dinuclear complex, formed by the careful combination of the mentioned ligands, maintained favourable stability in the presence of thiol groups and inhibited the enzyme TrxR.[16]

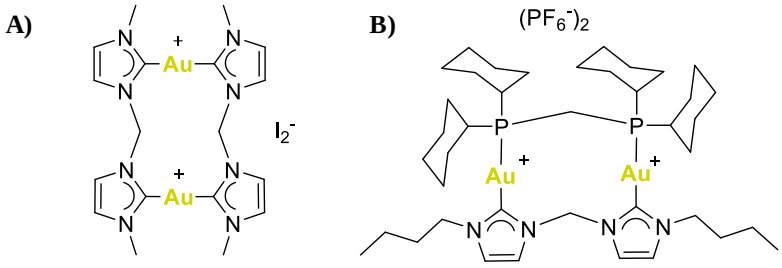

Figure 2.2. *Chemical structures of some Au^I-NHC complexes reported by A) Berners-Price and Day,[15] and B) Che and coworkers.[16]*

Many other examples were reported by our research group, such as Au^I-NHC complexes bearing acridine as a wingtip group (Figure 2.3), for creating new theranostic compounds.[17] This time, the trackable function is provided by an organic chromophore instead of a d^6 metal complex. Their luminescence, cytotoxicity, and biodistribution of these compounds have been examined in A549 cells, revealing a peculiar biodistribution, with the complexes mainly localized in lysosomes and to a lesser extent in the nucleus.

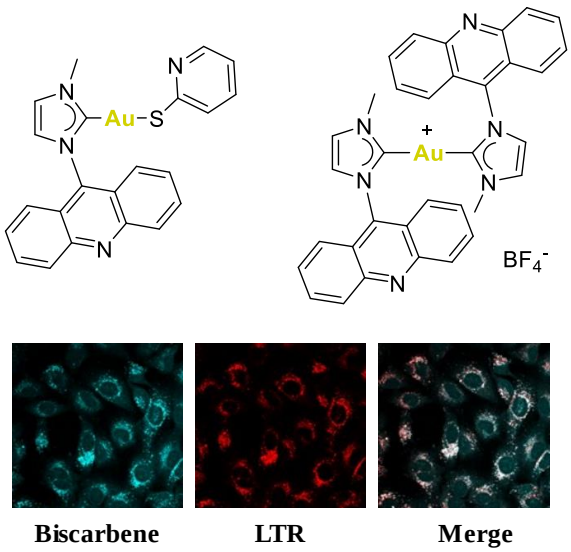

Figure 2.3. *Chemical structures of some Au^I-NHC complexes reported by Gimeno and co-workers and the biscarbene confocal images on A549 cells, confirming their partial lysosomal-nuclear distribution.*

The use of cyclometalated iridium (III) N-heterocyclic carbene complexes as anticancer agents has not been widely explored. However, in the recent years, some promising examples have emerged, such as the ones reported by Li and Mao.[18] These cyclometalated Ir^{III} complexes containing N-heterocyclic carbene

ligands have been investigated as anticancer drugs and PSs. It has been demonstrated that they are more cytotoxic than cisplatin against different tumor cell lines, can quickly penetrate into cells, and mainly localize in the mitochondria. Mechanism studies show that these complexes exert their anticancer efficacy by increasing the intracellular ROS level, reducing the mitochondrial membrane potential (MMP), and inducing apoptosis. Figure 2.4 illustrates some of their structures.

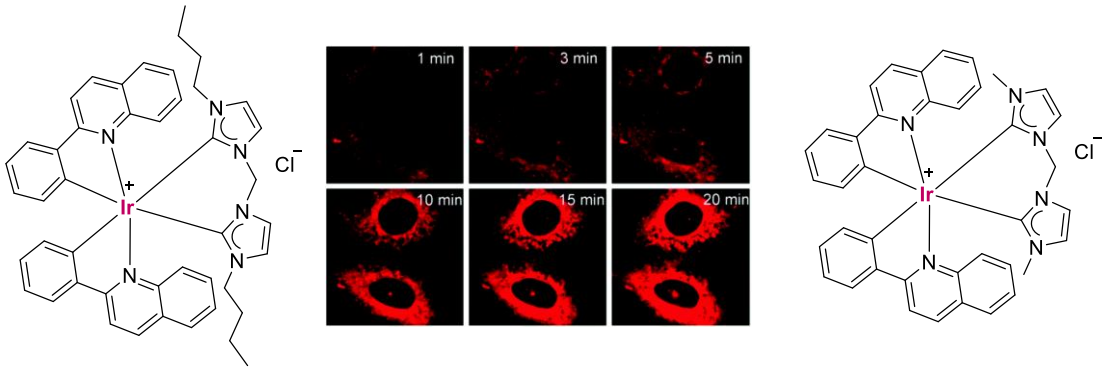

Figure 2.4. *Chemical structures of some Ir^{III}-NHC complexes reported by Li and Mao,[18] and real-time tracking of mitochondria in A549 cells stained with the first complex for different time intervals.*

In this sense, the possibility of unifying an Au^{I}-NHC complex with a cyclometallated Ir^{III} complex through multidentate fused imidazole [4,5,f]-1,10-phenanthroline derivatives could be thought as a great ally in bringing together a luminescent Ir^{III} fragment and therapeutic Au^{I} species, generating novel theranostic agents. Some examples using this type of linker have been reported in the literature, confirming that the imidazo[4,5-f]-1,10-phenanthroline ligand has a tremendous synthetic versatility, as shown in Figure 2.5.

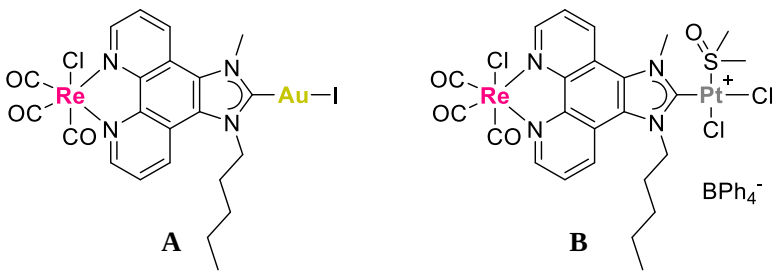

Figure 2.5. *Reported chemical examples of bimetallic complexes containing imidazo[4,5-f] 1,10-phenanthroline fragment in their structure. A) Re^{I}/Au^{I};[19] B) Re^{I}/Pt^{II}.[20]*

2.2 Objectives and methodology

In this chapter, the synthesis of a group of heterobimetallic Ir^{III}-Au^{I} complexes, coordinated through a fused imidazo[4,5-f]-1,10-phenanthroline core is reported.

The cyclometallated Ir^{III} center coordinates to the two nitrogen atoms of the phenanthroline in a bidentate fashion, while the Au^{I} metal binds to the carbene carbon of the fused imidazolium, resulting in cationic complexes with a general formula of $[Ir(ppy)_2(N\text{^}N\text{^}C\text{-}AuR)]^+$, where R can be bromide, or the phosphine JohnPhos. (Figure 2.6)

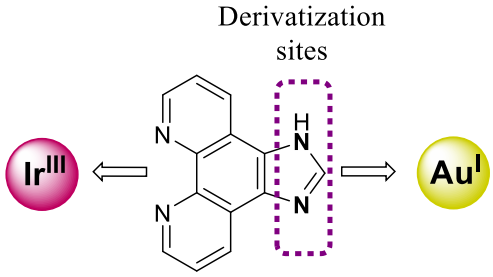

Figure 2.6. *Synthetic versatility offered by of imidazo[4,5-f]-1,10-phenanthroline ligand.*

The initial step in developing the desired heterobimetallic probes is to synthesize the imidazo[4,5-f]-1,10-phenanthroline derivate, by functionalization of its imidazolyl nitrogens with two different residues. In this case, a pentyl and benzile group were selected due to their capacity for tuning solubility in biological media and the luminescence in the final complex. Subsequently, the coordination of the iridium (III) center took place, followed by the addition of different Au^{I} substrates in the presence of an extrinsic base to form the bimetallic complexes.

The aim of this work is to pave the way for the design of new Ir^{III}-Au^{I} species that contain imidazo[4,5-f]-1,10-phenanthroline derivate as linker, offering the possibility of a synergistic effect between both metallic fragments. Their emissive properties, photocytotoxic activity in tumor cell lines (A549), cell distribution, mechanism of death, as well as their singlet oxygen production, have been thoroughly investigated.

2.3 Synthesis and characterization

The synthetic approach for obtaining heterobimetallic Ir^{III}-Au^{I} theranostic agents requires the use of an imidazo[4,5-f]-1,10-phenanthroline derivate as a linker between the metal centers. This ligand was selected due to its tremendous synthetic versatility, allowing to coordinate the iridium center in a chelated fashion, while the gold fragment can be directly coordinated to the carbene carbon upon deprotonation.

The synthesis starts refluxing the commercial 1,10-phenanthroline-5,6-dione with NH_4OAc and formaldehyde in 10 mL of glacial acetic acid at 110°C for 4 hours. Thereafter, the reaction was cooled, and NH_3 was added until a pH between 8-9 was reached, affording imidazo[4,5-f]-1,10-phenanthroline (**L2.1**). The next step was the functionalization of one imidazolyl nitrogen. For this purpose, an excess of iodopentane (5 eq.) was added to a basic solution of NaOH containing **L2.1** in DMSO (1 mL), and the mixture was stirred at 40ºC for 24 h, giving **L2.2** as a pale brown solid. The last step for obtaining the imidazolium salt is the functionalization of the resting imidazolyl nitrogen. This reaction took place by refluxing **L2.2** with bromobenzyl in dry acetonitrile for 24 h. The resulting suspension was filtered, and the filtrate was evaporated to dryness. The residue was dissolved in DCM/water, and several extractions were carried out. The aqueous phases were collected, and the evaporation of this phase afforded the desired ligand **L2.3** as a fine pale-yellow solid. Once that all ligands were obtained (**L2.1**: 87%; **L2.2**: 81%, and **L2.3**: 63%), the coordination of Ir^{III} core to them took place. $[Ir(ppy)_2(\mu\text{-}Cl)]_2$ (prepared following slightly different methodology that the one described in published procedures[21]) was refluxed with the corresponding ligand in a mixture DCM/MeOH (2:1) for 12 hours, giving the desired complexes **2.1**, **2.2,** and **2.3**, respectively. In all cases, it was necessary to purify the final complex using a chromatographic column with DCM as eluent first and thereafter a mixture of DCM:MeOH (9:1). The Scheme 2.1 collect all the synthetic procedure.

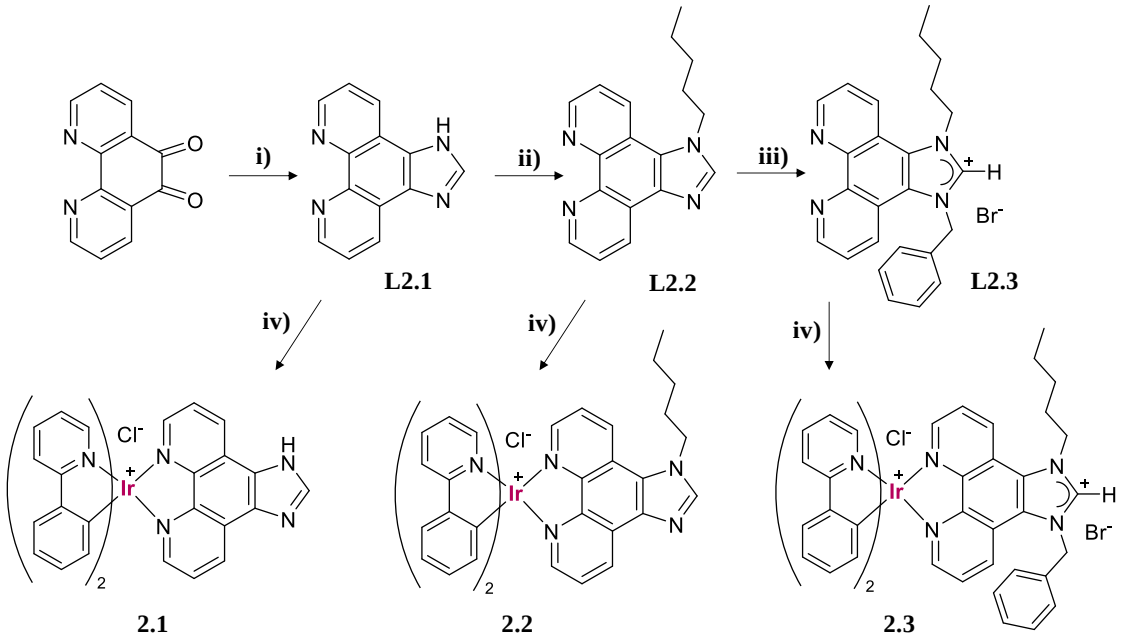

Scheme 2.1. *Synthetic route for obtaining ligands* ***L2.1-L2.3*** *and complexes* ***2.1-2.3****. (i)* NH_4OAc*, formaldehyde, acetic acid glacial, 110°C, 4 h; Addition NH3(aq) to pH 8-9;(ii) Iodopentane, NaOH, DMSO, 40ºC, 24 h; (iii) Bromobenzyl,* CH_3CN *(dry), 85°C, 24 h; (iv).* $[Ir(ppy)_2(\mu\text{-}Cl)]_2$*, DCM:MeOH (2:1), 45ºC, 12 h.*

The successful synthesis of these ligands and their respective Ir^{III} complexes was confirmed by NMR spectroscopy using ^{1}H-NMR, APT and bidimensional experiments. On top of that, high resolution mass spectrometry (HRMS) was used as additional characterization techniques to confirm their formation.

For characterizing these species, ^{1}H-NMR spectroscopy was particularly relevant. The complexes (**2.1**-**2.3**) spectra were collected in Figure 2.7, where it is shown, that the protons in the imidazolyl ring undergo the most significant changes. It is possible to observe how after the coordination of the pentyl group, (N-C*H*$_2$(CH$_2$)$_3$CH$_3$: 4.83 ppm, **2.2**) the imidazolyl proton (-(pent)NC*H*NH-) shifted upfield going from 9.52 ppm in complex **2.1** to 8.30 ppm in complex **2.2**. The coordination of the second residue (benzyl) generating the imidazolium salt (N-C*H*$_2$(CH$_2$)$_3$CH$_3$: 5.25 ppm; N-C*H*$_2$Ph: 6.70 ppm), produced downfield shift of the imidazolyl proton (-(pent)NC*H*NBz-). In complex **2.3**, it can be assigned to the singlet that appeared at 11.30 ppm.

In the free ligands these signals appeared as singlets 8.46 (**L2.1**), 8.00 (**L2.2**), and 10.39 (**L2.3**) ppm.

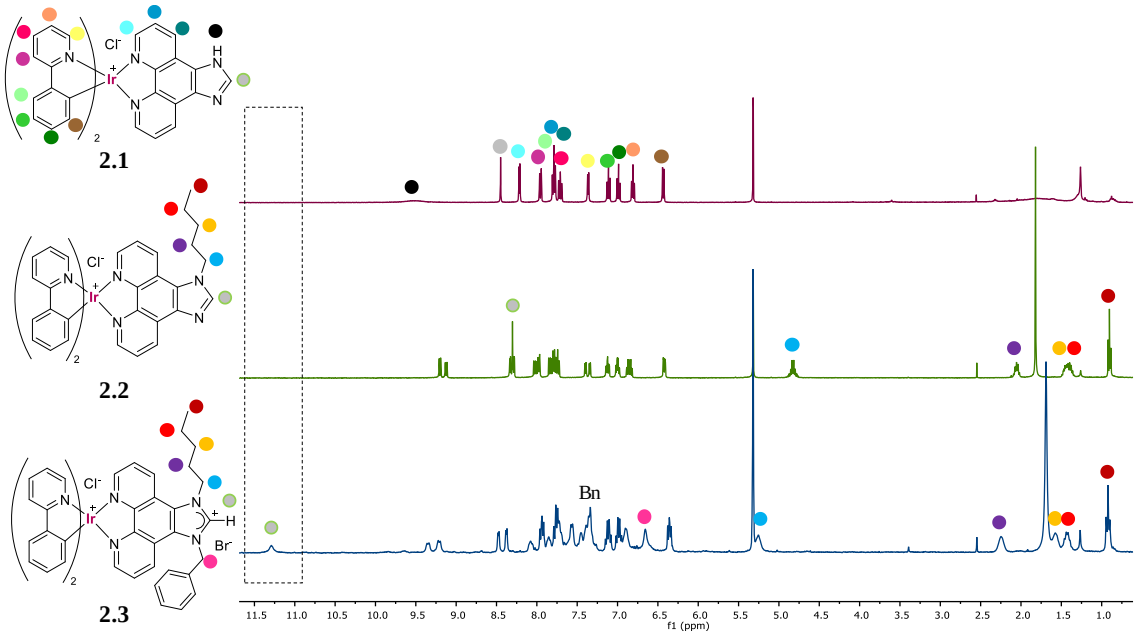

Figure 2.7. *Comparison between ^{1}H-NMR (400 MHz) spectra of complexes* ***2.1****,* ***2.2*** *and* ***2.3****. Solvent: CD_2Cl_2.*

For the correct synthesis of heterobimetallic complexes **2.5** and **2.7**, it was necessary to isolate their Au^{I}-NHC precursors **2.4** and **2.6** prior to coordinating them to $[Ir(ppy)_2(\mu\text{-}Cl)]_2$, as shown in Scheme 2.2. Starting from **L2.3**, which was dissolved in DCM (5 mL), [AuCl(tht)] or [AuCl(JohnPhos)] were added in presence of K_2CO_3 (2 eq.). After 6 hours of reaction, the suspension was filtered through celite, and the volume of DCM was reduced to a minimum, followed by the addition of diethyl ether, resulting in complexes **2.4** and **2.6**, respectively. Subsequently, the complexes were dissolved in a mixture of DCM:MeOH (1:1) (5 mL), and $[Ir(ppy)_2(\mu\text{-}Cl)]_2$ was added. The mixture was stirred for 20 hours at room temperature in order to avoid the decomposition of gold complex. The solvents were evaporated until a minimum volume, and pentane was added affording the desired heterobimetallic Ir^{III}-Au^{I} complexes in low yield (**2.5** (Br, 51%); **2.7** (JohnPhos; 43%)).

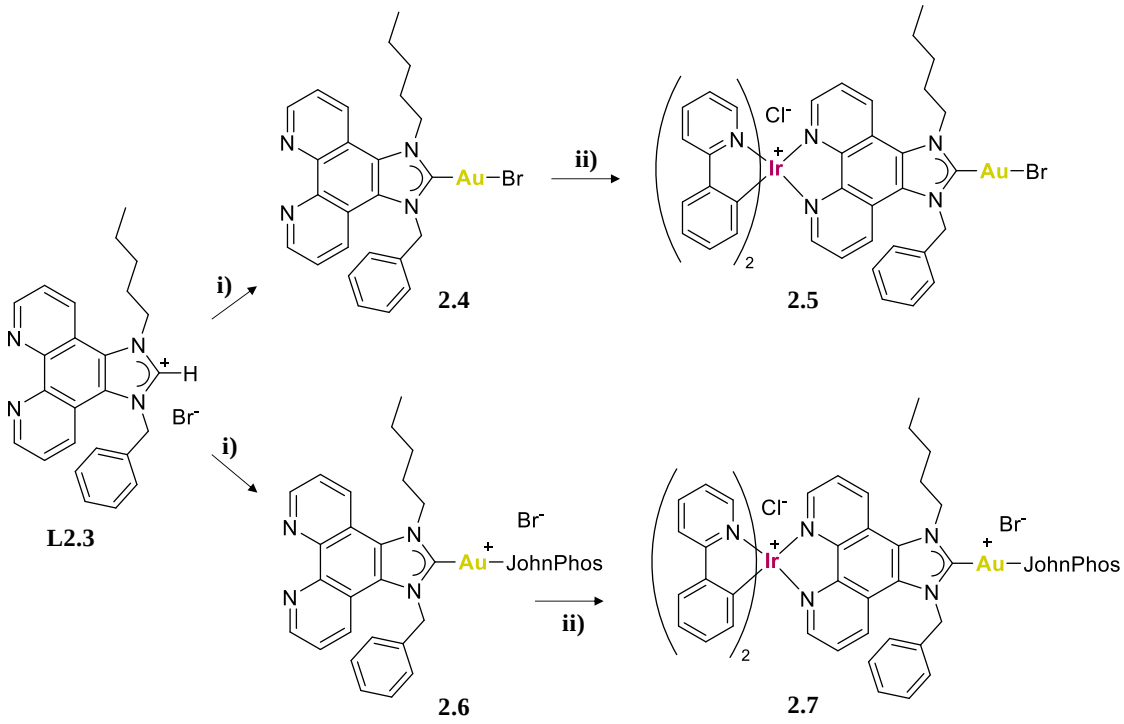

Scheme 2.2. *Synthetic route for the obtention of AuI-NHC complexes* ***2.4*** *and* ***2.6****, and their respective heterobimetallic complexes* ***2.5*** *and* ***2.7****. (i) [AuCl(tht)] or [AuCl(JohnPhos)], K_2CO_3, DCM, 6 h, r.t.; ii) $[Ir(ppy)_2(\mu\text{-}Cl)]_2$, DCM:MeOH (1:1), 20 h, r.t.*

The progress of these reactions can be easily monitored by ^{1}H-NMR. The disappearance of the imidazolyl proton at 10.39 ppm in **L2.3**, along with the observed shift for the aromatic protons upon coordination are indicative of the accomplishment of the reaction (Figure 2.8). In addition, ^{31}P-NMR also confirmed de coordination of gold (I) center to the imidazolium salt, as a singlet appeared at 63.72 and 63.85 ppm for complexes **2.6** and **2.7**, respectively. Furthermore, ESI mass spectrometry corroborated the correct synthesis of desired complexes.

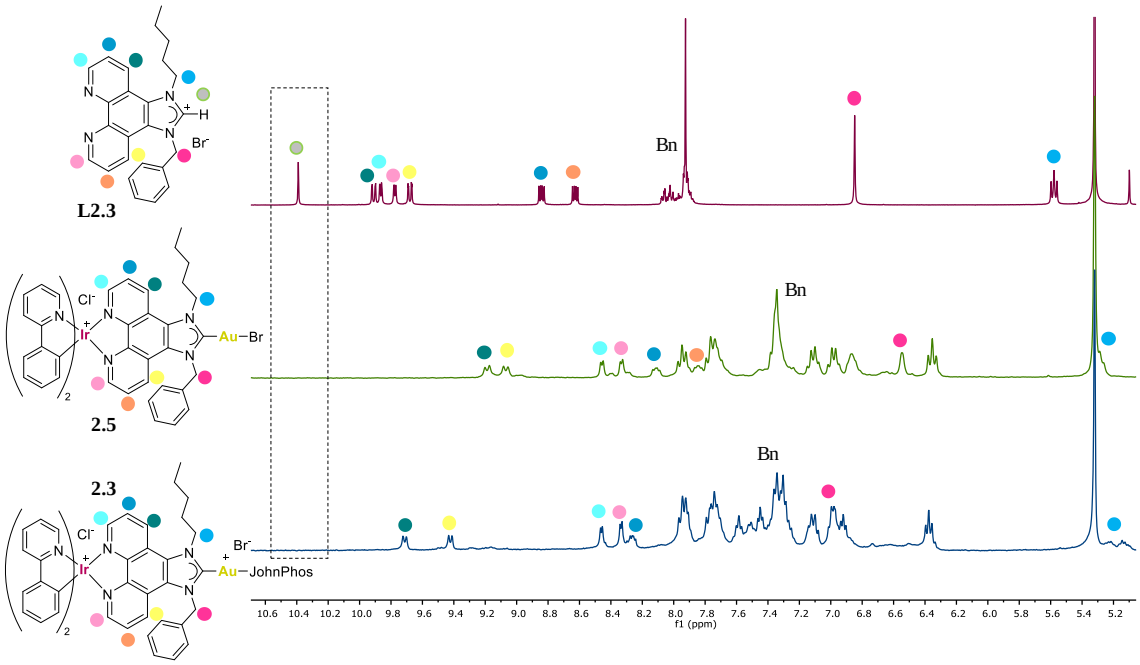

Figure 2.8. *Comparison between ^{1}H-NMR (400 MHz) spectra of ligand* ***L2.3****, and complexes* ***2.5*** *and* ***2.7****. Solvent: CD_2Cl_2.*

Additionally, crystals of complexes **2.1** and **2.4** were isolated for X-Ray diffraction analysis. The crystals of complexes **2.1** were obtained as bright yellow needles by slow diffusion of pentane into a dichloromethane solution of **2.1**. The X-ray analysis showed that this asymmetric molecule crystallizes in the $P2_1/n$ space group. The unit cell is formed by one independent molecule crystalizing with two molecules of dichloromethane, which is the crystallization solvent.

The crystalline structure exhibits the typical spatial distribution for this type of cyclometallated Ir^{III} complexes, where ligands adopt an octahedral disposition around the metal center. As expected, the pyridyl nitrogen atoms of the orthometalled ligand, ppy, coordinate to the iridium center *trans* to each other. Furthermore, they present an angle N-Ir-N of 174.0(2) º. This disposition forces that phenyl groups of ppy to be displayed in *trans* configuration to ligand **L2.1**. The most significant bond distances and angles are collected in Figure 2.9.

Regarding, the crystalline structure of complex **2.4**, collected in Figure 2.10, it can be said that crystallizes in the P-1 space group, and it exhibits a linear geometry around the gold center, with an angle of 178.2(1)°. The Au-C distance for the NHC

carbon atom is 2.005(4) Å, and 2.3796(8) Å for Au-Br. These distances and angles are in concordance with similar NHC-Au^{I}-Br complexes reported in literature.[22]

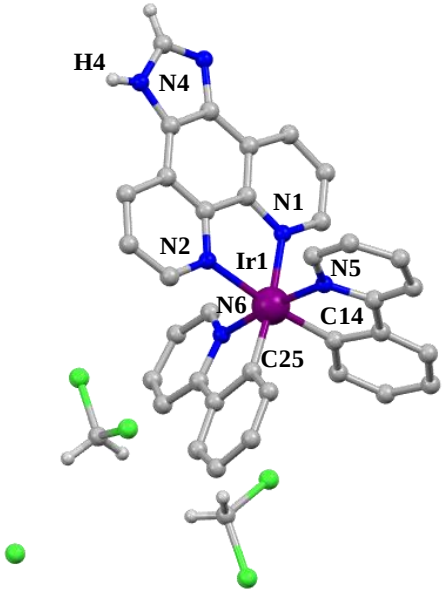

Bond Lenghts (Å)	**Ir1-C14**	2.003(5)
	Ir1-C25	1.997(5)
	Ir1-N1	2.133(4)
	Ir1-N2	2.145(4)
	Ir1-N5	2.042(4)
	Ir1-N6	2.030(4)
	N4-H4	0.860
Angles °	**N1-Ir1-N2**	78.1(1)
	N5-Ir1-N6	174.0(2)

***Figure 2.9**. Mercury representation of the crystal structure of complex **2.1** (hydrogen atoms have been omitted for clarity, except hydrogen 4 and 5) and table with the most significant bond lengths and angles.*

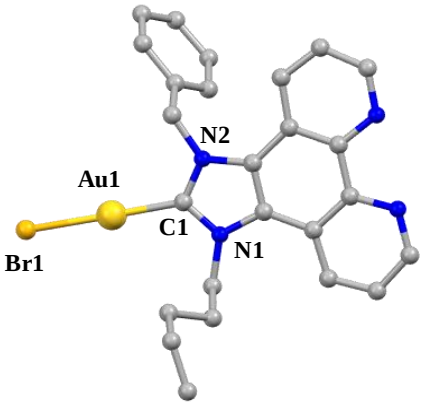

Bond Lenghts (Å)		**Angles °**	
Au1-C1	2.005(4)	**C1-Au1-Br1**	178.2(1)
Au1-Br1	2.3796(8)		

***Figure 2.10**. Mercury representation of the crystal structure of complex **2.4** (hydrogen atoms have been omitted for clarity) and table with the most significant bond lengths and angles.*

2.4 Optical Properties

Photophysical properties of the synthetized complexes (**2.1**-**2.7**) were measured in aerated DMSO solution at room temperature. The most relevant data are collected in Table 1.1.

Table 1.1. *Luminescent properties of complexes **2.1**-**2.7** in DMSO.*

	UV/vis·10^3 (ε[$dm^3mol^{-1}cm^{-1}$])	**λ_{em} (λ_{exc})[nm]**	**ζ[ns]**	**Φ [%]**
2.1	280 (73.0), 374 (19.8), 394 (21.6)	606 (425)	421	4.7
2.2	260 (55.0), 296 (37.3), 393 (7.6)	610 (450)	392	6.2
2.3	259 (69.0), 269 (65.0), 285 (13.0)	660 (450)	360	5.8
2.4	264 (95.0), 310 (15.8), 349 (3.4)	-	-	-
2.5	270 (76.5), 286 (10.4)	533 (425)	397	10.9
2.6	264 (67.1), 275 (61.5), 310 (15.7)	381 (300)	576	7.9
2.7	268 (63.6), 291 (40.1), 386 (8.9)	637 (450)	469	1.2

The UV-Visible spectra of all the complexes exhibit intense absorption bands below 300 nm, which can be assigned to ligand-centered spin-allowed π→π* transitions based on published studies (see Figure 2.11). Additional bands with lower intensity appear between 280 and 350 nm, which could be attributed to forbidden intraligand ^{3}π→π* and ^{1}MLCT transitions. In iridium-containing complexes (**2.1**-**2.3**, **2.5**, and **2.7**), a long tail is observed over 350 nm, which is typically associated with a ^{3}MLCT transition.[23]

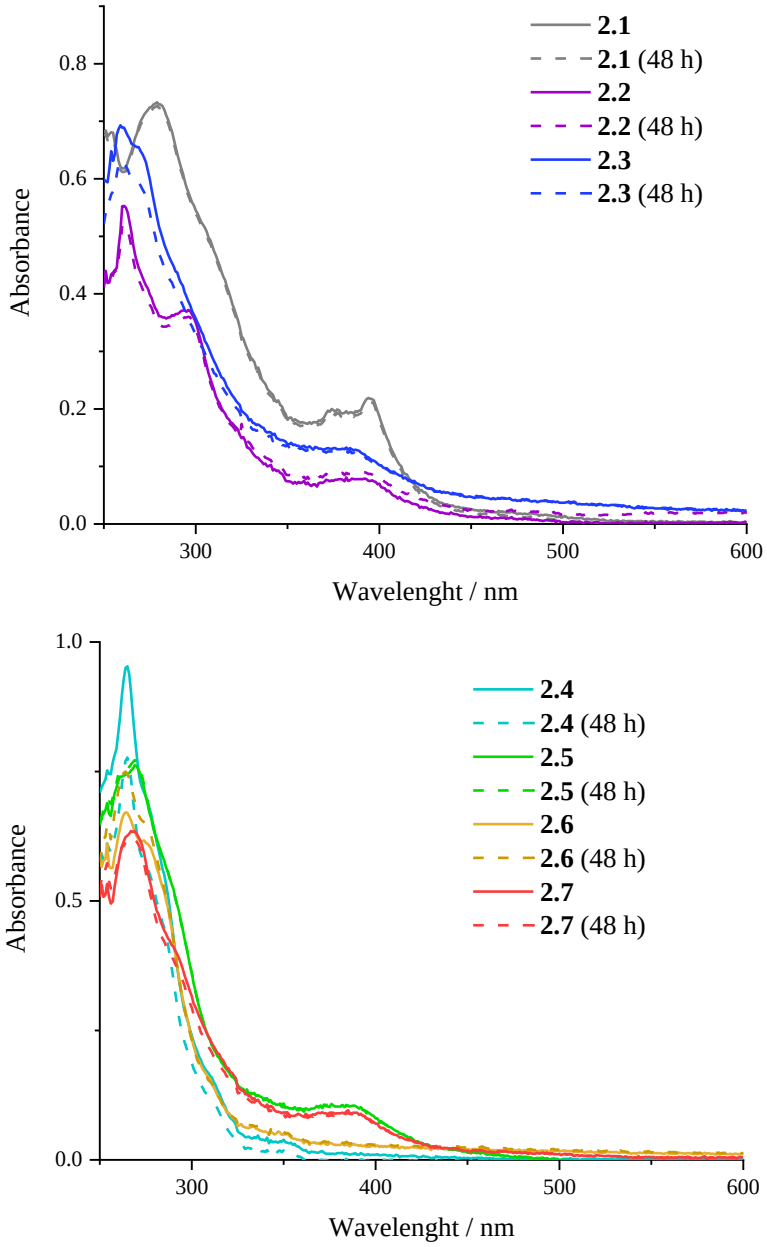

Figure 2.11. *Absorption spectra in DMSO:PBS (1:1) solution of complexes* ***2.1-2.7*** *and their stabilities at 48 hours, 310 K and using a concentration of [10^{-5}M].*

Focusing on their emission spectra, complexes **2.1-2.7** present a structureless emission, as it can be seen in Figure 2.12. Emission maximum is completely dependent of the presence of the Au^{I} fragment and the residues coordinated to the imidazolyl ring. Complexes **2.1** and **2.2**, exhibit emission centered on 605 nm, showing that the incorporation of the pentyl group to the imizadolyl ring does not generate any changes in the emission spectra, however, complex **2.3**, which contains the imidazolium salt in its structure, presents an emission shifted to higher wavelengths (660 nm), confirming that the incorporation of benzyl residue is not

innocent. Regarding the emission maximum of bimetallic complexes **2.5** and **2.7** at 533 and 637 nm, respectively, it can be said that they are directly related with the nature of the Au^{I} fragment coordinated. If it presents Au-Br the emission shifts to more energetic wavelengths, on contrary, the presence of Au-JohnPhos changes this emission to higher wavelengths. The additional cationic character provided by the metal center of Au^{I}-JohnPhos in complex **2.7** reduces the energy difference between the HOMO and LUMO orbitals, contributing to make this transition less energetic. These emissions bands could be assigned mainly to ^{3}MLCT.[24] This origin assignation was made because emission bands from charge transfer processes are generally featureless; however, additional computational studies should be made to confirm their origin and percentage of contribution.

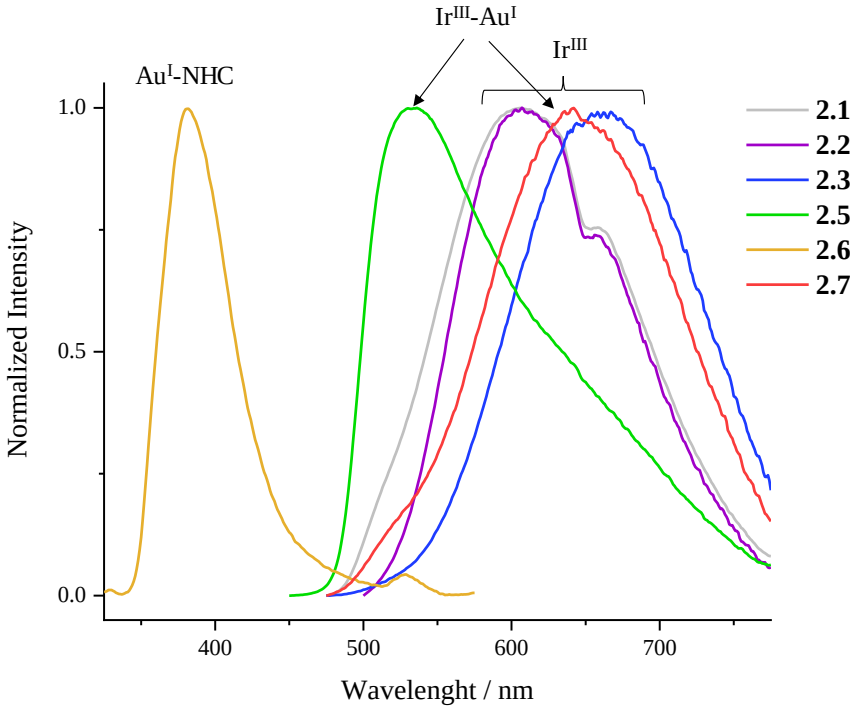

Figure 2.12. *Normalized emission spectra in DMSO solution of complexes* ***2.1-2.7*** *(except* ***2.4****) using a concentration of [10^{-3}M].*

Focusing on their lifetimes, all values ranged between 360 to 470 ns for iridium-containing complexes, corroborating the phosphorescent nature of the emission.[25] Meanwhile, the lifetime for the Au^{I}-carbene (**2.6**) is slightly higher, 576 ns. Quantum yield values were also measured in aerated DMSO solution. The heterobimetallic complexes, **2.5** exhibits the highest quantum yield of all the series

(Φ = 10.9%) and complex **2.7** the lowest (Φ = 1.2%), suggesting that the gold ancillary ligand is key for tuning the emission efficiency.

2.5 Antiproliferative properties

The antiproliferative activity of complexes **2.1** to **2.7**, as well as their ligand precursors **L2.1-L2.3**, was determined by MTT assays in A549 cell line (lung carcinoma cells). These assays were performed in dark conditions for all compounds and, dark and irradiation at 405 nm for 10 minutes for all complexes.

Based on the data collected in Table 2.2, it can be said that ligands **L2.1** and **L2.2** do not exhibit antiproliferative properties. However, the imidazolium salt (**L2.3**) shows moderate activity with IC_{50} value of 10.4 μM. In contrast, complexes exhibit significant antiproliferative behaviour, with IC_{50} values ranging between 9.1 to 1.34 μM in dark conditions. The Au^{I}-NHC-JohnPhos complex (**2.6**) is the most active in these conditions. In general, the antiproliferative properties of all the complexes increase when they are irradiated with a source of 405 nm. It is noteworthy that only Ir^{III}-containing complexes exhibit phototoxicity, this could be attributed to the absorption band previously observed for these complexes at 405 nm, however these absorptions appeared for Au^{I} complexes (**2.4** and **2.6**) at lower wavelenghts.

***Table 2.2**. IC_{50} values of ligands **L2.1-L2.3**, and complexes **2.1-2.7**, in A549 cells for 48 h, in dark and under irradiation conditions at 405 nm.*

	Dark	**Irrad. (405 nm)**	**PI**
L2.1	>50	-	-
L2.2	>50	-	-
L2.3	10.4 ± 0.41	-	-
2.1	4.20 ± 0.17	2.94 ± 0.37	1.3
2.2	3.24 ± 0.20	2.46 ± 0.05	0.8
2.3	6.13 ± 0.34	2.49 ± 0.33	1.3
2.4	7.23 ± 0.22	7.10 ± 0.24	1.0
2.5	4.27 ± 0.35	0.49 ± 0.03	8.7
2.6	1.34 ± 0.13	1.23 ± 0.08	1.1
2.7	9.11 ± 0.12	0.34 ± 0.18	8.8

As shown in Table 2.2, the heterobimetallic Ir^{III}-Au^{I} complexes (**2.5** and **2.7**) increase the sensitivity of A549 cells compared to the monometallic Ir^{III} complexes (**2.1**-**2.3**) once that they have been activated through irradiation. This finding confirms the initial hypothesis suggesting that the combination of two different metals can generate a synergistic effect to enhance therapeutic properties.

2.6 Cell death mechanism

In view of the IC_{50} values obtained for the different complexes, it was decided to investigate the cell death mechanism of the monometallic complex **2.3** and the bimetallic complexes **2.5** and **2.7** to determine whether the presence of the gold fragment could induce a different cell death pathway. The analysis was performed by flow cytometry using a specific apoptosis fluorescent marker, Annexin V-FITC, which labels phosphatidylserine sites on the membrane surface and is conjugated with fluorescein isothiocyanate (FITC).[26]

The cell death mechanisms induced by complexes **2.3**, **2.5** and **2.7** after 48 h of incubation in A549 cells were studied at their IC_{50} values. Half on the samples were incubated in dark conditions, while the rest were irradiated after 24 h for 10 min at 405 nm in order to replicate the conditions of the antiproliferative assays. As shown in Figure 2.13, it can be said that all complexes (monometallic and bimetallic) induced an apoptotic cell death mechanism. In all cases, almost hundred per cent of cell population, displayed a positive response for Annexin V-FITC, confirming the apoptotic pathway. Additionally, the influence of the incubation conditions (dark and under irradiation) was studied, and it can be confirmed that the induction of an apoptotic cell death mechanism is due to the complex, not the conditions. This is demonstrated in Figure 2.13, where no differences can be observed for irradiated and dark samples.

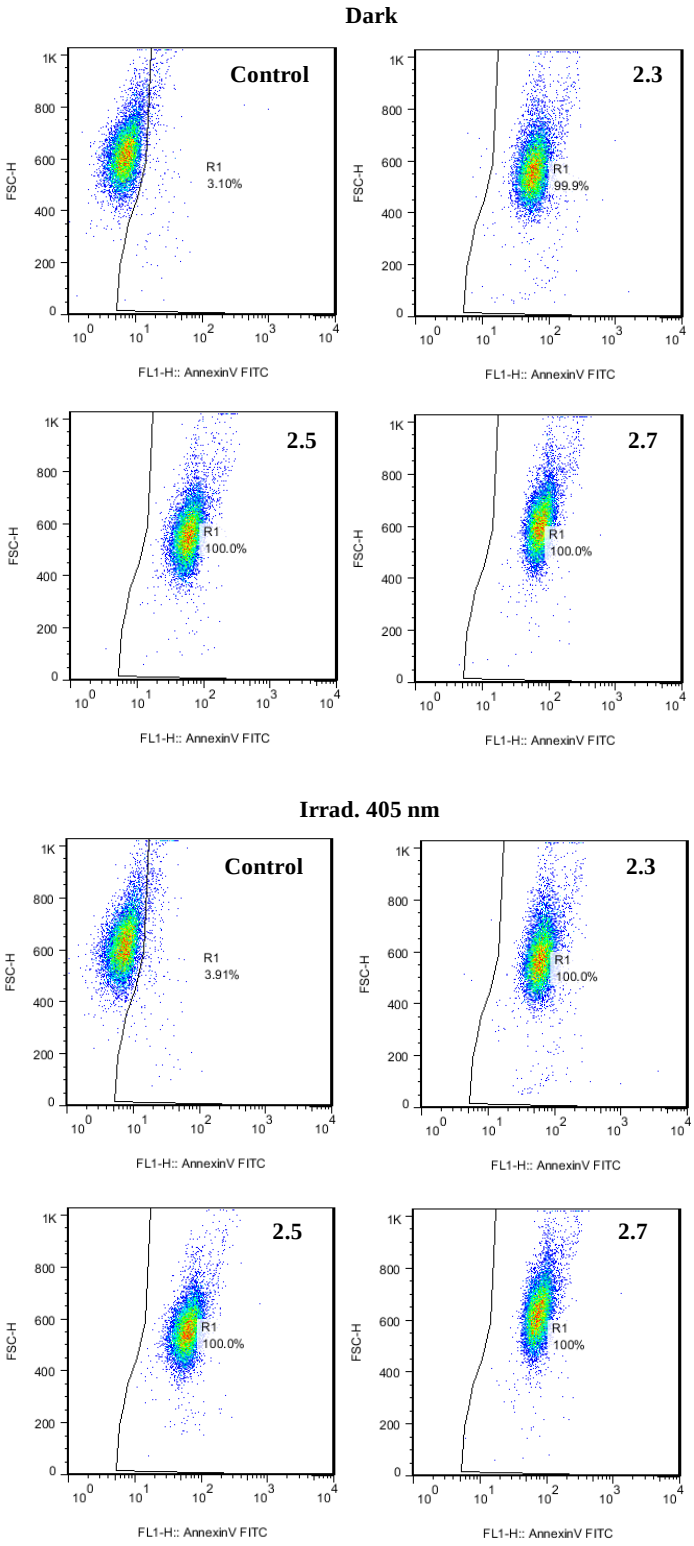

Figure 2.13. *Study of cell death mechanism in A549 cell line, induced by complexes* ***2.3***, ***2.5*** *and* ***2.7*** *at their* IC_{50} *values, after 48 h of incubation under irradiation at 405 nm (10 min), or in dark conditions.*

2.7 Study of cell morphology

An inverted microscope was used to visualize A549 cells in the presence and absence of complexes **2.3**, **2.5**, and **2.7** to track any morphological changes that can help to elucidate how, the presence of different metal centers in the molecule and/or the different incubation conditions (dark and irradiated at 405 nm) could induce cellular changes. Control cells (untreated cells) grew normally and presented a healthy morphology. However, those cells that were exposed to complexes (**2.3**, **2.5** or **2.7**), exhibited a high population of cytoplasmic vacuoles, and clearly showed sing of apoptotic cell death. This fact is even more evident in the cells were exposed to the irradiation source. As collects Figure 2.14, black arrows point to those cells suffering an apoptotic cell death, and, to a lesser extent, blue arrows indicate necrotic cells. These microscopy images are in concordance with the results obtained by flow cytometry, in which the predominant cell death mechanism was apoptosis.

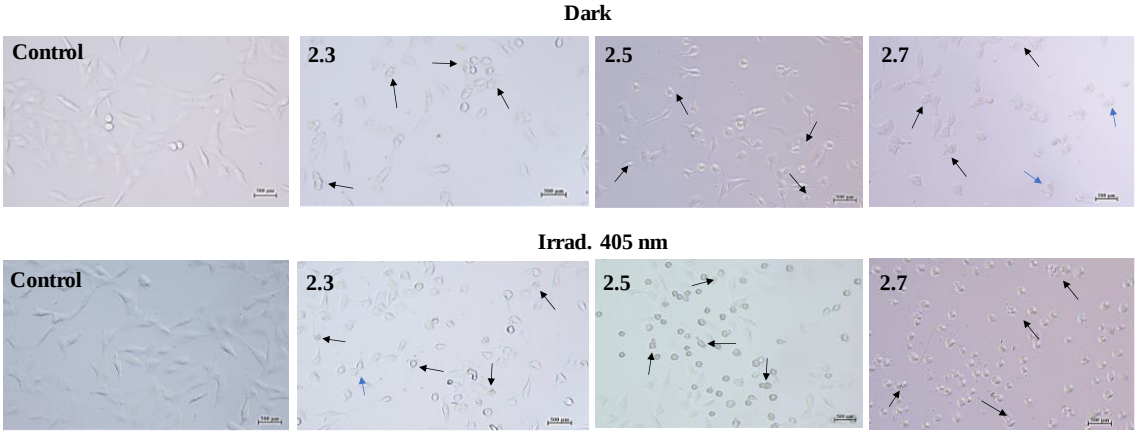

Figure 2.14. *Phase contrast microscopy images of A549 cells treated with complexes* ***2.3****,* ***2.5*** *and* ***2.7*** *at (4 μM) after 25 h of incubation (1 hour later the irradiation). Black and blue arrows point to examples of apoptotic and necrotic cells, respectively.*

2.8 Cellular biodistribution

Fluorescence confocal microscopy assays were performed to elucidate the biodistribution of complexes **2.3**, **2.5** and **2.7** in A549 cells. The compounds were incubated at a concentration of 4 μM in A549 cells for 2 h. After this time, lysosomal-selective commercial dye, LysoTracker Green (LTG), 500 nM incubated for 45 minutes, was added to the wells, and fluorescence microscopy was used to evaluate their internalization.

The excitation lasers used were 559 nm for both trackers and 473 nm for the complexes. Figure 2.15 displays a simulation of emission and excitation spectra of studied complexes and LTG tracker.

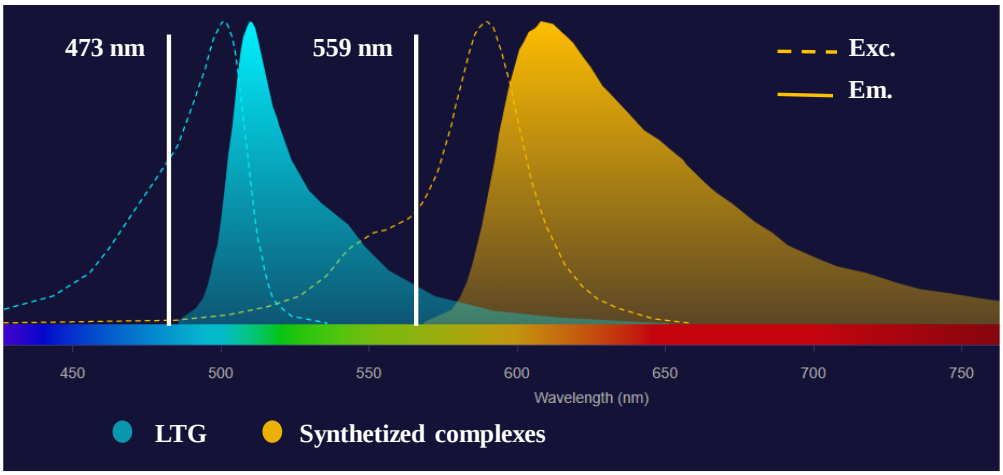

Figure 2.15. *Simulation of the different excitation and emissive profiles of studied complexes (**2.3**, **2.5** and **2.7**) and the comercial tracker LTG used in the biodistribution assay.*[27]

Focusing on the images collected in Figure 2.16, where the emission from complexes **2.3** (top row) and **2.5** (bottom row) is observed in red, and that of LTG in green, it can be concluded that all complexes were able to internalize into the cells and were distributed throughout the cytoplasm. Additionally, superimposition images suggest that complex **2.3** does not localize in lysosomes, meanwhile a partial lysosomal localization can be suggested for **2.5**. However, it is clear that they were also accumulated in other organelles, with patterns that resemble mitochondrial distribution.

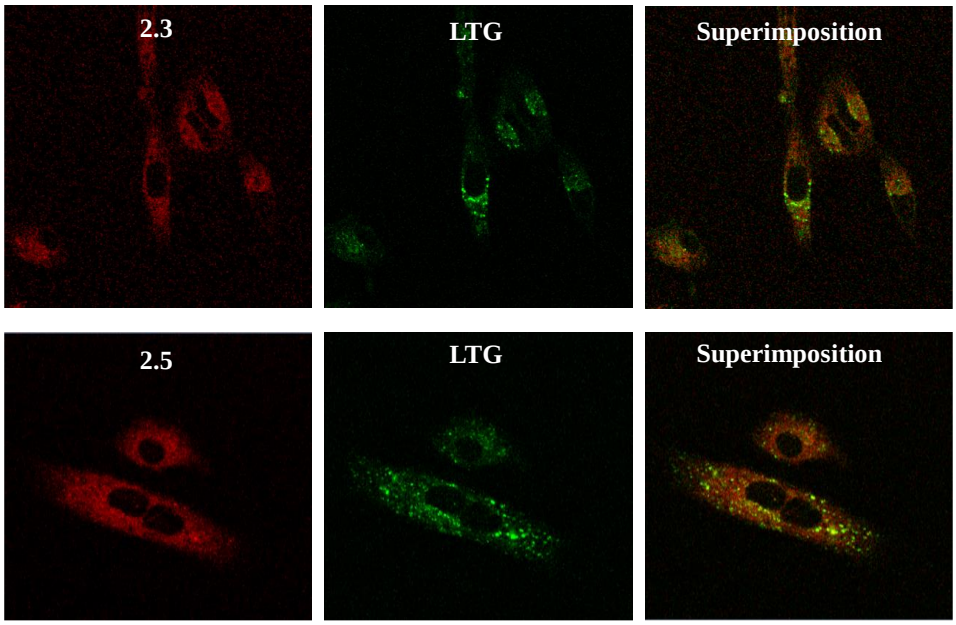

Figure 2.16. *Fluorescence confocal microscopy images of A549 cells incubated with* ***2.3*** *(top row),* ***2.5*** *(bottom row) stained with LTG (45 min, 500 nM).*

Regarding complex **2.7**, its confocal microscopy images exhibit a less clear pattern due to its low quantum yield (1.2). However, it is plausible to suggest a lysosomal localization as can be seen in Figure 2.17.

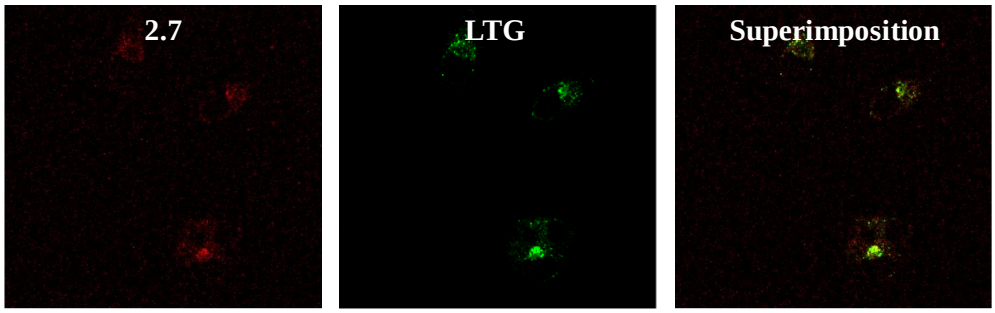

Figure 2.17. *Fluorescence confocal microscopy images of A549 cells incubated with* ***2.7*** *(2 h, 4 μM)stained with LTG (45 min, 500 nM).*

Based on these results, the complexes display different distribution patterns. Complex **2.3** localizes in other organelles rather than lysosomes, while complex **2.5** shows partial lysosomal distribution. However, the bimetallic analogue **2.7** targets lysosomes as its primary site, indicating that the presence of the Au^{I} residue can modulate their distribution. Nevertheless, further confocal microscopy experiments are necessary to identify any other targets of these complexes.

2.9 Measurement of singlet oxygen production

After observing the increase on the antiproliferative activity of complexes upon irradiation at 405 nm, as described in previous section 2.5, and considering that this increment could be due to the presence of intracellular reactive oxygen species (ROS),[28] the generation of singlet oxygen ($^1O_2$) was specifically measured. It is known that phosphorescence of $^1O_2$ appears at 1270 nm; therefore, if it is produced upon irradiation, an emission band should be visible in the NIR.[29] Direct measurement of emission of $^1O_2$ was then undertaken by steady state fluorescence spectroscopy for synthetized complexes (**2.3-2.7**), irradiating an acetonitrile solution of complexes with a 450 nm picosecond pulsed diode laser. Additionally, a parallel experiment was performed just measuring the solvent in absence of complexes to corroborate that band observed at 1270 nm was not a mere artefact from the spectrometer.

As shown Figure 2.18, only iridium-containing complexes (**2.3**, **2.5** and **2.7**) generate singlet oxygen upon irradiation, this fact is in concordance with the results observed in the antiproliferative assays, where the best photocytotoxic index were reported for these complexes; PI: 1.3, 8.7 and 8. 8, respectively.

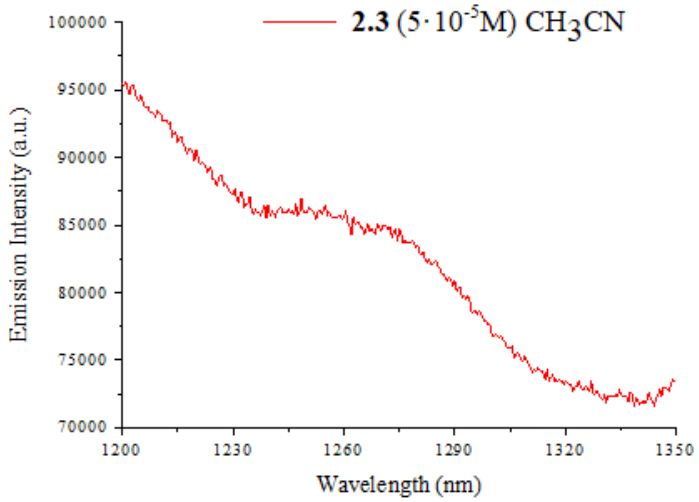

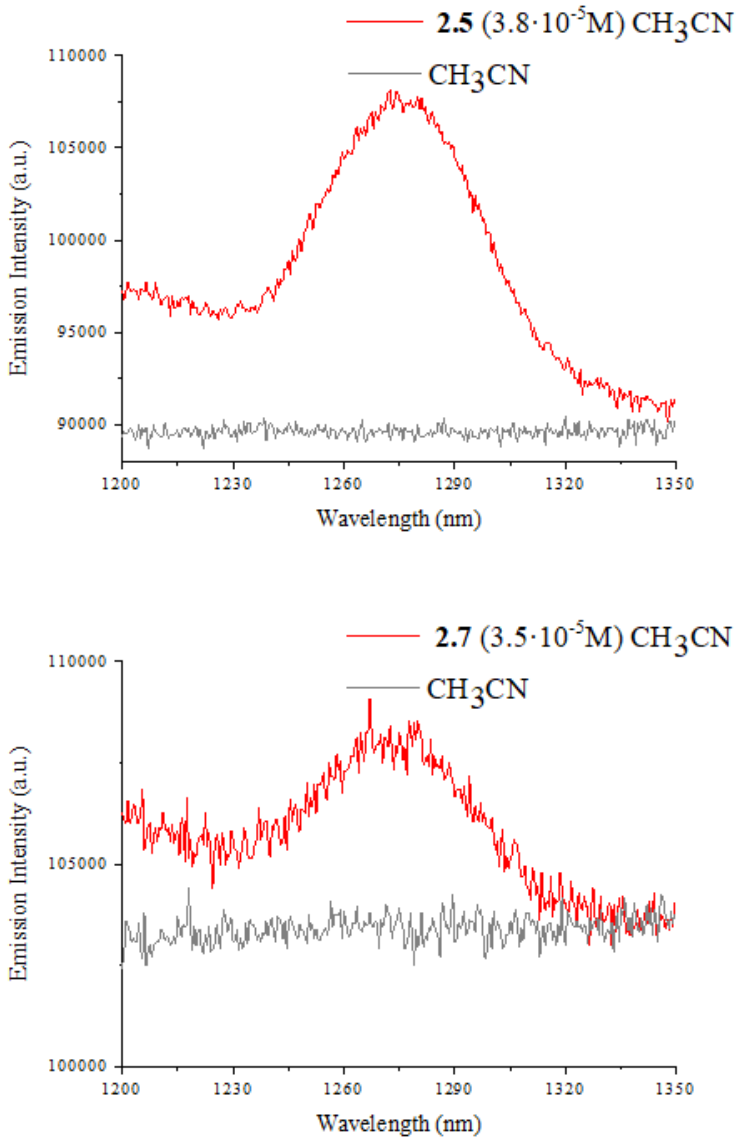

Figure 2.18. *Measurement of singlet oxygen production of complex* ***2.3, 2.5*** *and* ***2.7*** *when they are irradiated with a diode laser of 450 nm. Emission recorder at 1270 nm.*

2.10 Conclusions

In this chapter, a series of complexes containing fused imidazo[4,5-f]-1,10-phenanthroline ligand (NHC) was synthetized. It was possible to isolate and study the antiproliferative properties of three organic-based NHC ligands (**L2.1**-**L2.3**), as well as the biological and photophysical properties of three cyclometallated Ir^{III}-NHC complexes (**2.1** -**2.3**), two Au^{I}-NHC complexes (**2.4** and **2.6**) and two hetero-bimetallic Ir^{III}-Au^{I} complexes (**2.5** and **2.7**) containing a ligand **L2.3** as linker between the metal fragments. All complexes exhibited antiproliferative properties on A549 cells, that can be enhanced upon irradiation at 405 nm, being bimetallic complexes the best PSs (PI: **2.5**:8.7 and **2.7**: 8.8). Interestingly, this fact could be explained due to the singlet oxygen production detected for all iridium containing complexes, that it is in concordance with the IC_{50} values calculated. Additionally, iridium-containing complexes showed emissions that are dominated by the iridium fragment. However, the presence the gold residue in complexes **2.5** and **2.7** generates a relevant shift of their emission maxima. In all cases the emission origin is assigned to ^{3}MLCT transitions mainly from the Ir^{III} core to the diimine NHC ligand. Moreover, microscopy images and cell death analysis performed by flow cytometry revealed apoptotic body formations, which tended to indicate an apoptotic cell death pathway. Focusing on the biodistribution studies performed in A549 cells, complexes **2.3**, **2.5** and **2.7** seemed to exhibit a completely different distribution. While complex **2.3** does not localized in lysosomes, complex **2.5** inhibits a partial localization in these organelles, and **2.7** presents a lysosomal biodistribution.

In view these results, it could be said that these bimetallic complexes (**2.5** and **2.7**) might be potential candidates for further studies as promising PS agents due to their proven generation of singlet oxygen, their high cytotoxic potential in cancer cells upon irradiation, their controlled apoptotic cell death mechanism and the traceability using non-invasive techniques.

2.11 General synthetic procedures

The starting material $[Ir(ppy)_2(\mu\text{-}Cl)]_2$,[30] [AuCl(tht)],[31] and [AuCl(JohnPhos)][32] were prepared according to published procedures. Other reagents and solvents were commercially available from Sigma-Aldrich and used without further purification. The synthesis of **L2.3** was performed under argon atmosphere and using dry solvents.

Instrumentation

Mass spectra were recorded on a BRUKER ESQUIRE 3000 PLUS, with the electrospray (ESI) technique. ^{1}H, $^{13}C\{^{1}H\}$ and $^{31}P\{^{1}H\}$ NMR, including 2D experiments, were recorded at room temperature on a BRUKER AVANCE 400 spectrometer (^{1}H, 400 MHz, ^{13}C, 100.6 MHz, $^{31}P\{^{1}H\}$, 162 MHz) with chemical shifts (δ, ppm) reported relative to the solvent peaks of the deuterated solvent.[33] Steady-state photoluminescence spectra were recorded with a Jobin-Yvon-Horiba fluorolog FL-3-11 spectrometer using band pathways of 3 nm for both excitation and emission. UV/vis spectra were recorded with 1 cm quartz cells on an Evolution 600 spectrophotometer. Quantum yields were measured using an absolute method provided by Hamamatsu Photonics Quantaurus-QY C11347-11.

Synthetic procedure of ligand L2.1

A mixture of 1,10-phenanthroline-5,6-dione (0.525 g, 2.5 mmol), ammonium acetate (3.85 g, 50 mmol), formaldehyde (0.26 mL of 36% solution, 3.5 mmol), and glacial acetic acid (12 mL) was refluxed for 4 h. Then, the reaction mixture was cooled to room temperature and poured into water (10 mL). The solution was neutralized with a NH_3 aqueous solution (pH 7-8), affording the desired product as a pale solid that was filtered and washed with diethyl ether. (2.17 mmol, 87%).

^{1}H NMR (400 MHz, DMSO-d_6) δ 9.03 (dd, J = 4.3, 1.8 Hz, 2H), 8.82 (dd, J = 8.1, 1.6 Hz, 2H), 8.46 (s, 1H), 7.82 (dd, J = 8.1, 4.3 Hz, 2H) ppm.^{13}C NMR (101 MHz, DMSO-d_6) δ 154.1, 147.8, 143.5, 140.9, 132.3, 129.5, 123.3.ppm.

Synthetic procedure of ligand L2.2

A 25 mL round-bottom flask was loaded with **L2.1** (800 mg, 3.63 mmol), sodium hydroxide (157 mg, 3.93 mmol), and DMSO (2 mL). The solution was stirred for 30 minutes at room temperature, after which 1-iodopentane was added (500 μL, 3.82 mmol), and the solution was heated to 40ºC for 24 hours. The resulted suspension was cooled, filtered, washed with water (3 x 5 mL), and diethyl ether (3 x 5 mL), and dried. The resulting solid was the ligand **L2.2** as a pale brown solid. (2.94 mmol, 81%).

^{1}H NMR (400 MHz, $CDCl_3$) δ 9.16 (d, J = 8.0 Hz, 2H), 9.00 (dd, J = 8.1, 1.8 Hz, 1H), 8.57 (dd, J = 8.4, 1.6 Hz, 1H), 8.02 (s, 1H), 7.77 (dd, J = 8.1, 4.4 Hz, 1H), 7.63 (dd, J = 8.4, 4.4 Hz, 1H), 4.64 (t, J = 7.2 Hz, 2H), 2.08 (m, 2H), 1.47 (m, 4H), 0.95 (t, J = 14.1 Hz, 3H) ppm. ^{13}C NMR (101 MHz, $CDCl_3$): δ 148.6, 147.7, 144.5, 143.9, 142.6, 137.3, 130.0, 128.0, 124.2, 123.5, 123.3, 122.4, 119.6, 47.8, 29.5, 28.5, 22.0, 13.7 ppm. HRMS (ESI): m/z (calcd.) = 291.1610, m/z (found) = 291.1605.

Synthetic procedure of ligand L2.3

50 mg (0.17 mmol) of **L2.2**, was dissolved in 3 mL of dry acetonitrile, and 50 μL (0.34 mmol) of bromobenzyl were added. The solution was refluxed for 24 h at 85ºC. The resulting suspension was filtered, and the filtrate was evaporated to dryness. The residue was solved in DCM/water and several extractions were carried out, collecting the aqueous phases. The evaporation of this phase afforded the desired ligand **L2.3** as a fine pale-yellow solid. (0.11 mmol, 63%).

^{1}H NMR (400 MHz, Methanol-d_4) δ 9.94 (s, 1H), 9.46 (d, J = 8.7 Hz, 1H), 9.42 (d, J = 4.8 Hz, 1H), 9.33 (d, J = 3.7 Hz, 1H), 9.23 (d, J = 8.6 Hz, 1H), 8.39 (dd, J = 8.6, 4.9 Hz, 1H), 8.18 (dd, J = 8.6, 4.8 Hz, 1H), 7.64 – 7.44 (m, 7H), 6.40 (s, 3H), 5.20 – 5.07 (m, 3H), 2.25 (t, J = 7.6 Hz, 3H), 1.56 (ddd, J = 37.3, 15.4, 8.0 Hz, 7H), 1.01 (t, J = 7.2 Hz, 4H) ppm. ^{13}C NMR (101 MHz, Methanol-d_4) δ 191.1, 149.5, 144.6, 140.9, 140.8, 136.5, 136.5, 134.3, 133.6, 132.0, 131.3, 130.9, 130.5, 130.4, 128.8, 128.5, 127.7, 127.4, 127.3, 127.2, 121.1, 120.7, 55.0, 52.3, 29.5, 23.3, 14.2 ppm. HRMS (ESI): m/z (calcd.) = 381.2079, m/z (found) = 381.2098.

Synthetic procedure of complexes 2.1 to 2.3

25 mg (0.02 mmol) of $[Ir(ppy)_2(\mu\text{-}Cl)]_2$ were solved in a mixture DCM/MeOH (4:2 mL), thereafter ligands **L2.1**, **L2.2** or **L2.3** were added (0.04 mmol). The mixture was refluxed for 12 hours to 45ºC. Then, solvents were evaporated to dryness, and a minimum volume of dichloromethane (1 mL) was added, and the addition of petroleum ether afforded the desired complexes, **2.1**, **2.2** and **2.3**, respectively. It was necessary to purify the final complexes using a chromatographic column with DCM as the eluent, which was later changed to a mixture of DCM:MeOH (9:1).

2.1: (0.030 mmol, 77%) ^{1}H NMR (400 MHz, Methylene chloride-d_2) δ 8.45 (s, 1H), 8.21 (dd, J = 5.1, 1.4 Hz, 2H), 7.96 (d, J = 8.0 Hz, 2H), 7.82 -7.75 (m, 4H), 7.75-7.68 (m, 2H), 7.36 (d, J = 5.2 Hz, 2H), 7.15-7.08 (m, 2H), 6.99 (td, J = 7.5, 1.4 Hz, 2H), 6.85-6.77 (m, 2H), 6.43 (d, J = 6.7 Hz, 2H) ppm. ^{13}C NMR (101 MHz, Methylene chloride-d_2) δ 168.5, 150.9, 149.1, 145.2, 144.5, 143.5, 138.6, 132.4, 126.8, 125.4, 123.7, 123.2, 120.3 ppm.

2.2: (0.033, 82%) ^{1}H NMR (400 MHz, Methylene chloride-d_2) δ 9.20 (dd, J = 8.3, 1.5 Hz, 1H), 9.12 (dd, J = 7.4, 1.2 Hz, 1H), 8.43-8.17 (m, 3H), 8.16-7.93 (m, 3H), 7.85-7.68 (m, 5H), 7.40 (d, J = 5.1 Hz, 1H), 7.34 (d, J = 5.1 Hz, 1H), 7.11 (t, J = 6.7 Hz, 2H), 7.00 (t, J = 4.1 Hz, 2H), 6.91-6.79 (m, 2H), 6.42 (d, J = 7.5 Hz, 2H), 4.83 (m, J = 8.0 Hz, 2H), 2.06 (3, 2H), 1.40 (m, 4H), 0.90 (t, J = 7.1 Hz, 3H) ppm. ^{13}C NMR (101 MHz, Methylene chloride-d_2) δ 168.5, 168.4, 150.8, 150.4, 149.9, 149.5, 149.2, 149.0, 146.2, 145.5, 145.2, 144.4, 144.4, 138.9, 138.7, 138.7, 133.1, 132.4, 132.3, 132.3, 131.4, 131.3, 127.7, 127.5, 127.3, 125.7, 125.6, 125.5, 123.8, 123.6, 123.4, 123.3, 123.3, 120.5, 120.4, 49.0, 30.2, 29.2, 22.8, 14.2 ppm. HRMS (ESI): m/z (calcd.) = 791.2469, m/z (found) = 791.2454.

2.3: (0.024, 59%) ^{1}H NMR (400 MHz, Methylene chloride-d_2) δ 11.29 (s, 1H), 9.34 (s, 1H), 9.21 (d, J = 8.2 Hz, 1H), 8.48 (d, J = 4.4 Hz, 1H), 8.38 (d, J = 4.5 Hz, 1H), 8.06 (d, J = 7.9 Hz, 1H), 7.94 (dd, J = 8.2, 5.6 Hz, 2H), 7.84 (d, J = 6.0 Hz, 1H), 7.74 (dt, J = 13.9, 7.3 Hz, 4H), 7.57 (d, J = 6.6 Hz, 2H), 7.46-7.27 (m, 5H), 7.12 (m, 2H), 7.03-6.84 (m, 4H), 6.66 (s, 2H), 6.40-6.29 (m, 2H), 5.25 (m, 2H), 2.25 (m, 2H) 1.57 (m, 2H), 1.42 (m, 2H), 0.92 (t, 3H) ppm.^{13}C NMR (101 MHz, Methylene chloride-d_2) δ 207.2, 167.8, 151.8, 150.0, 149.7, 149.6, 143.7, 142.6,

141.4, 138.6, 137.1, 136.5, 134.6, 134.1, 132.9, 132.1, 131.1, 129.9, 129.3, 129.2, 128.6, 128.2, 128.1, 127.2, 127.1, 125.3, 124.2, 123.4, 122.3, 122.0, 120.2, 118.4, 40.8, 29.3, 28.9, 22.7, 14.1 ppm. HRMS (ESI): m/z (calcd.) = 441.1505, m/z (found) = 441.1494 M^{2+}.

Synthetic procedure of complexes 2.4 and 2.6

25 mg (0.05 mmol) of **L2.3** were solved in DCM (5 mL), and then [AuCl(tht)] or [AuCl(JohnPhos)] (0.05 mmol) and an excess of K_2CO_3 (0.1 mmol) were added. The colourless solutions were stirred at room temperature for 6 hours. The resulting suspensions were filtered through celite, and the volume of DCM was reduced to a minimum. The addition of diethyl ether (10 mL) afforded complexes **2.4** and **2.6**, respectively as white solids, which were filtered and dried.

2.4: (0.042 mmol, 84%) ^{1}H NMR (400 MHz, Methylene chloride-d_2) δ 9.22 (d, J=1.2 Hz, 1H), 9.10 (d, J=1.2 Hz, 1H), 8.73 (d, J = 8.2 Hz, 1H), 8.47 (d, J = 8.2 Hz, 1H), 7.86 (m, 1H), 7.57 (m, 1H), 7.44-7.14 (m, 5H), 6.36 (s, 2H), 5.17 (m, 2H), 2.13 (m, 2H), 1.54-1.24 (m, 4H), 0.96 (t, J = 6.9 Hz, 3H) ppm. ^{13}C NMR (101 MHz, Methylene chloride-d_2) δ 200.2, 184.5, 170.6, 150.2, 150.1, 145.6, 136.6, 136.5, 135.0, 130.3, 130.1, 123.0, 129.9, 129.0, 126.7, 126.3, 124.7, 124.6, 124.3, 123.9, 119.0, 118.7, 30.2, 29.2, 22.9, 14.8, 14.3 ppm. ESI-HRMS (m/z): 957.3677 $[M]^+$ (Au-BisNHC).

2.6: (0.038 mmol, 76%) ^{1}H NMR (400 MHz, Methylene chloride-d_2) δ 8.83 (dd, J = 8.5, 1.6 Hz, 1H), 8.56 (dd, J = 8.5, 1.6 Hz, 1H), 8.03-7.93 (m, 2H), 7.71-7.62 (m, 3H), 7.51-7.28 (m, 7H), 7.16-7.11 (m, 2H), 6.89 (tt, J = 7.3, 1.3 Hz, 1H), 6.14 (s, 2H), 4.92-4.78 (m, 2H), 2.18-1.96 (m, 2H), 1.56-1.44 (m, 4H), 1.39 (d, J = 15.5 Hz, 21H), 0.98 (t, J = 7.2 Hz, 3H) ppm. ^{13}C NMR (101 MHz, Methylene chloride-d_2) δ 191.8, 165.3, 161.5, 150.4, 145.7, 144.1, 142.1, 140.7, 137.3, 134.8, 134.3, 134.2, 133.7, 133.6, 133.0, 132.7, 132.5, 132.2, 131.7, 130.9, 130.2, 130.1, 129.8, 129.8, 129.5, 129.0, 128.4, 128.1, 128.1, 127.8, 127.1, 125.8, 125.6, 124.4, 124.1, 118.6, 118.3, 38.3, 38.1, 31.0, 30.5, 29.4, 22.9, 14.2 ppm. ^{31}P NMR (121 MHz, Methylene chloride-d_2) δ 63.72 ppm. HRMS (ESI): m/z (calcd.) = 875.3511, m/z (found) = 875.3522.

Synthetic procedure of complexes 2.5 and 2.7

20 mg of complexes **2.4** or **2.6** were solved in a mixture 1:1 DCM:MeOH (3 mL). Then, $[Ir(ppy)_2(\mu\text{-}Cl)]_2$ (0.01 mmol) was added, and the yellow solutions were stirred for 20 hours at room temperature. After that, solvents were evaporated until minimum volume, and pentane (10 mL) was added to afford the desired heterobimetallic complexes **2.5** and **2.7**, respectively, as orange-brown solids, which were filtered and dried.

2.5: (0.005 mmol, 51%) ^{1}H NMR (400 MHz, Methylene chloride-d_2) δ 9.21 (d, J = 8.9 Hz, 1H), 9.10 (d, J = 8.9 Hz, 1H), 8.46 (d, J = 4.8 Hz, 1H), 8.33 (d, J = 4.7 Hz, 1H), 8.11 (m, 1H), 7.95 (t, J = 8.9 Hz, 2H), 7.84 (s, 2H), 7.80-7.69 (m, 4H), 7.35 (q, J = 8.6, 6.7 Hz, 6H), 7.16-7.07 (m, 2H), 7.04-6.93 (m, 2H), 6.95-6.83 (m, 2H), 6.56 (s, 1H), 6.42-6.33 (m, 2H), 5.33-5.23 (m, 2H), 2.12 (m, 2H), 1.64 (d, J = 7.4 Hz, 2H), 1.45 (q, J = 7.4 Hz, 2H), 0.94 (t, J = 7.3 Hz, 3H) ppm. ^{13}C NMR (101 MHz, Methylene chloride-d_2) δ 205.1, 184.9, 168.2, 151.5, 150.3, 149.4, 144.5, 144.1, 139.0, 136.9, 134.4, 133.9, 133.8, 133.2, 132.1, 131.5, 130.1, 129.3, 128.4, 127.8, 127.5, 126.7, 125.6, 123.9, 123.7, 121.8, 120.6, 36.0, 30.2, 29.2, 23.0, 14.3. HRMS (ESI): m/z (calcd.) = 652.8516, m/z (found) = 653.1851 $[M]^{3+}$, σ (CH_3CN, 10^{-5}M): 116.32 mS/cm.

2.7: (0.004 mmol, 43%) ^{1}H NMR (400 MHz, Methylene chloride-d_2) δ 9.71 (d, J = 8.6 Hz, 1H), 9.42 (d, J = 8.7 Hz, 1H), 8.46 (d, J = 5.1 Hz, 1H), 8.34 (d, J = 4.9 Hz, 1H), 8.26 (dd, J = 8.7, 5.0 Hz, 1H), 8.01-7.87 (m, 5H), 7.75 (ddd, J = 17.2, 12.0, 7.8 Hz, 7H), 7.64-7.23 (m, 16H), 7.21-7.06 (m, 3H), 7.06-6.85 (m, 5H), 6.37 (q, J = 8.2 Hz, 2H), 5.25-5.04 (m, 2H), 2.07 (d, J = 18.8 Hz, 2H), 1.59 (m, 2H), 1.46-1.16 (m, 25H), 0.91 (t, J = 7.3 Hz, 3H) ppm. ^{13}C NMR (101 MHz, Methylene chloride-d_2) δ 212.0, 168.3, 165.0, 153.6, 151.5, 150.5, 150.0, 149.7, 149.5, 149.3, 146.1, 145.9, 144.30, 138.9, 138.8, 135.2, 134.8, 134.5, 133.9, 132.2, 132.0, 131.4, 130.9, 130.4, 130.3, 129.7, 129.1, 129.1, 128.6, 128.4, 128.2, 126.7, 126.0, 125.6, 124.2, 123.5,

121.8, 120.7, 38.5, 38.2, 31.3, 30.8, 29.7, 23.2, 14.4 ppm. ^{31}P NMR (162 MHz, Methylene chloride-d_2) δ 63.85 ppm. HRMS (ESI): m/z (calcd.) = 688.2224, m/z (found) = 688.2226 M^{2+}.

2.12 Materials and methods

Cell culture

A549 (human lung carcinoma) cell line was routinely cultured in high glucose DMEM medium supplemented with 10% fetal bovine serum (FBS), L-glutamine and penicillin/streptomycin. All cultures were maintained at 37 °C in a humidified atmosphere of 95% air/5% CO_2.

Antiproliferative Activity Assays

The MTT-reduction assay was used to analyze cell metabolic activity as an indicator for cell sensitivity to the complexes in A549 cell line. 8,500 cells/well were seeded in complete DMEM (10% FBS) medium in flat-bottom, 96-well plates (100 µL/well) and allowed to attach for 24 h prior to addition of compounds. Cells were incubated with synthetized compounds (**L2.1**-**L2.3** and **2.1**-**2.7**) for 48 h. For those studies performed under irradiation conditions, cells were incubated with the complexes for 24 h, irradiated at 405 nm for 10 min, and incubated for other 24 h. After 48 h of incubation, 10 µL of MTT (5 mg/mL in PBS) were added to each well and plates were incubated for 2 h at 37 °C. Finally, culture medium was removed and DMSO (100 µL/ well) was added to dissolve the formazan crystals. The optical density was measured at 550 nm using a 96-well multiscanner autoreader (ELISA) and IC_{50} was calculated using GraphPad Prims 9 software. Each compound was analyzed at least in three independent experiments.

Cell Death Mechanism Assays

Apoptotic cell death pathway was determined by measuring phosphatidylserine exposure on cell surface in A549 cells. With this purpose, 10^5 cells/well were seeded in complete medium in flat-bottom, 12-well plates (1 mL/well) and left

overnight to be attached to the bottom. Cells were treated for 48 h with compounds **2.3**, **2.5** and **2.7**, in dark and under irradiation conditions (405 nm for 10 min) at concentrations of their IC_{50} values in duplicate. After the incubation time, cells were washed with PBS (1 mL/well), trypsinised (0.5 mL/well), and resuspended in 100 μL of a mixture of Annexin-binding buffer (ABB; 140 μM NaCl, 2.5 μM $CaCl_2$, 10 μM HEPES/NaOH pH 7.4), and FITC-conjugated Annexin V. They were incubated at room temperature in the dark for 15 minutes. Finally, cells were diluted to 500 μL with PBS and a total of 10,000 cells were acquired on a FACSCaliburTM flow cytometer. Cell death was analyzed using CellQuest Pro, FlowJo 7.6.1 and GraphPad Prism 9 software.

Singlet Oxygen Production Measurement

Singlet oxygen emission spectra were measured on a PicoQuant, FT300 fluorescence spectrometer equipped with a Hamamatsu H10330 A-45 thermoelectric cooled NIR-PMT unit with a spectral range of 950 nm to 1400 nm. The compounds **L2.3**, **2.3**-**2.7** (10 μM in CH_3CN) were excited with a 450 nm picosecond pulsed diode laser (P-C-450, PicoQuant) with 80 MHz repetition rate. Signals were digitised with a Time Harp 260 PCI card (PicoQuant). Spectra were recorded in the custom measurement mode of EasyTau software.

Fluorescence Confocal Microscopy

10^4 A549 cells/well were seeded in complete medium in μ-slide 8 well (300 μL/well) and left 24 h to be attached to the bottom. Then, 200 μL of culture medium was removed and 100 μL of a solution of the corresponding complexes (**2.3**, **2.5** and **2.7**) were added to a final concentration of 4 μM. The complexes were incubated with the cells for 2 h. Thereafter, LysoTracker Green (LTG) at 500 nM was added. They were incubated together with the cells for 45 min. Eventually the medium was replaced with fresh medium. Images were collected in a sequential mode in a ZEISS LSM 880 confocal microscope with a 60 oil immersion lens, a line average of 4, and a format of 1024x1024 pixels using excitation wavelength of either 473 nm or 559 nm. The confocal pinhole was 1 Airy unit. Images were analyzed with Zen Blue Little software.

Crystal Structure Analysis

Crystals were mounted in inert oil glass fibres and transferred to the cold gas stream of a SMART APEX Duo or a Bruker Venture diffractometer equipped with a low-temperature attachment. Data were collected using monochromated Mo Kα radiation (λ = 0.71073 Å). Scan type ω. Absorption corrections based on multiple scans were applied with the program SADABS. The structures were solved by direct methods and refined on F^2 using the program SHELXL-2016. All non-hydrogen atoms were refined anisotropically. Hydrogen atoms were included in calculated positions and refined using a riding model. These data can be obtained free of charge by The Cambridge Crystallography Data Center.

[1] J.A. Mata, F.E. Hahn, E. Peris, *Chem. Sci.* **2014**, *5*, 1723-1732.

[2] M. Hardy, A. Lützen, *Chem. Eur. J.* **2020**, *26*, 13332-13346.

[3] M. Redrado, V. Fernández-Moreira, M.C. Gimeno, *ChemMedChem* **2021**, *16*, 932-941.

[4] P.J. Jarman, F. Noakes, S. Fairbanks, K. Smitten, I.K. Griffiths, H.K. Saeed, J.A. Thomas, C. Smythe, *J. Am. Chem. Soc.* **2019**, *141*, 2925-2937.

[5] A. Luengo, M. Redrado, I. Marzo, V. Fernández-Moreira, M.C. Gimeno, *Inorg. Chem* **2020**, *59*, 8960-8970.

[6] N. Curado, N. Giménez, K. Miachin, M. Aliaga-Lavrijsen; M.A. Cornejo, A.A. Jarzecki, M. Contel, *ChemMedChem* **2019**, 14, 1086-1098.

[7] H. Goitia, Y. Nieto, M.D. Villacampa, C. Kasper, A. Laguna, M.C. Gimeno, *Organometallics* **2013**, *32*, 6069-6078.

[8] J. Zhou, J. Li, K.Y. Zhang, S. Liu, Q. Zhao, *Coord. Chem. Rev.* **2022**, *453*, 214334-214357.

[9] L.C.-C. Lee, K.K.-W. Lo, *Chem. Asian J.* **2022**, *17*, e202200840.

[10] P.J. Sadler, *Gold Bull.* **1976**, *9*, 110-118.

[11] L.F. Boullosa, J.V. Loenhout, T. Flieswasser, J. De Waele, C. Hermans, H. Lambrechts, B. Cuypers, K. Laukens, E. Bartholomeus, V. Siozopoulou, W.H. De Vos, M. Peeters, E.L.J. Smits, C. Deben, *Redox Biol.* **2021**, *42*, 101949-101966.

[12] V. Fernández-Moreira, R.P. Herrera, M.C. Gimeno, *Pure Appl. Chem*. **2019**, *91*, 247-269.

[13] M. Mora, M.C. Gimeno, R. Visbal, *Chem. Soc. Rev.* **2019**, *48*, 447-462.

[14] G. Moreno-Alcántar, P. Picchetti, A. Casini, *Angew. Chem. Int. Ed.* **2023**, https://doi.org/10.1002/ange.202218000.

[15] P.J. Barnard, M.V. Baker, S.J. Berners-Price, D.A. Day, *J. Inorg. Biochem*. **2004**, *98*, 1642-1647.

[16] T. Zou, C.T. Lum, C.N. Lok, W.P. To, K.H. Low, C.M. Che, *Angew. Chem. Int. Ed.* **2014**, *53*, 5810-5814.

[17] R. Visbal, V. Fernández-Moreira, I. Marzo, A. Laguna, M.C. Gimeno, *Dalton Trans.* **2016**, *45*, 15026-15033.

[18] Y. Li, B. Liu, X.-R. Lu, M.-F. Li, L.-N. Ji, Z.-W. Mao, *Dalton Trans.* **2017**, *46*, 11363-11371.

[19] A. Luengo, I. Marzo, V. Fernández-Moreira, M.C. Gimeno, *Appl. Organomet. Chem.* **2022**, e6661.

[20] A.A. Webster, S.K.K. Prasad, J.M. Hodgkiss, J.O. Hoberg, *Dalton Trans.* **2015**, *44*, 3728-3736.

[21] A. Li, M. Yu, Y. Sun, Y. Wu, C. Huang, F. Li, *J. Am. Chem. Soc.* **2011**, *133*, 11231-11239.

[22] A. Johnson, M.C. Gimeno, *Organometallics* **2017**, 36, 1278-1286.

[23] K. Hasan, A.K. Bansal, I.D.W. Samuel, C. Roldán-Carmona, H.J. Bolink, E. Zysman-Colman, *Sci. Rep.* **2015**, *5*, 12325-12341.

[24] Q. Zhao, S. Liu, M. Shi, F. Li, H. Jing, T. Yi, C. Huang, *Organometallics* **2007**, *26*, 5922-5930.

[25] W. Wang, Z. Mao, M. Wang, L.-J. Liu, D.W.-J. Kwong, C.-H. Leung, M. Dik-Lung, *Chem. Commun.* **2016**, *52*, 3611-3614.

[26] M. van Engeland, L.J. Nieland, F.C. Ramaekers, B. Schutte, C.P. Reutelingsperger, *Cytometry* **1998**, *31*, 1-9.

[27] https://www.thermofisher.com/order/fluorescence-spectraviewer#!/

[28] L. Wang, S. Monro, P. Cui, H. Yin, B. Liu, C.G. Cameron, W. Xu, M. Hetu, A. Fuller, S. Kilina, S.A. McFarland, W. Sun, *ACS Appl Mater. Interfaces* **2019**, *11*, 3629-3644.

[29] A.A. Gorman, M.A.J. Rodgers, *J. Photochem. Photobiol. B.* **1992**, *14*, 159-176.

[30] S. Sprouse, K.A. King, P.J. Spellane, R.J. Watts, *J. Am. Chem. Soc.* **1984**, *106*, 6647-6653.

[31] R. Usón, A. Laguna, M. Laguna, D.A. Briggs, H.H. Murray, J.P. Fackler Jr. *Inorganic Syntheses*, Ed. H.D. Kaesz, **1989**, 85-90.

[32] L.K. Batchelor, E. Paunescu, M. Soudani, R. Scopelliti, P.J. Dyson, *Inorg. Chem*. **2017**, 56, 9617-9633.

[33] G.R. Fulmer, A.J.M. Miller, N.H. Sherden, H.E. Gottlieb, A. Nudelman, B.M. Stoltz, J.E. Bercaw, K.I. Goldberg, *Organometallics* **2010**, *29*, 2176-2179.

Chapter 3

3.1 Introduction

Traditional cancer treatment modalities are based on a combination of techniques. In most cases, the first approach involves surgical removal of the tumor, followed by treatment with chemotherapy, radiotherapy or immunotherapy, among others.[1] Although the combination of these techniques has produced successful results, it should be noted that their use can lead to severe side effects such as alopecia, anemia, nausea, fatigue, concentration problems, pain, and more. Additionally, there is a worryingly increment of metastatic tumors and drug resistance.[2] For these reasons, many efforts have been devoted to developing new treatment modalities to overcome these challenges.

Among other underdeveloped cancer treatment techniques, photodynamic therapy (PDT) has emerged as a promising alternative, due to its capacity to destroy tumors, reduce the vascularization around tumoral area, and stimulate immune response.[3,4] As mentioned in the introduction section on PDT, an optimum photosensitizer (PS) should possess some common characteristics as: (a) a high singlet oxygen ($^1O_2$) quantum yield, (b) near-infrared (NIR) absorption, (c) a large Stokes shift, (d) specific organelle targeting, (e) high PDT efficiency, and (f) good biocompatibility and photostability.[5] These characteristic can be easily unified in metallic complexes thanks their ability to tune their properties by varying their ligand scaffolds. Many metal-based tetrapyrrolic derivate containing Ru^{II}, Os^{II} or Re^{I} have attracted attention for being used as PSs.[6] Remarkably, it is the Ru^{II} complex TLD-1433 reported by the group of McFarland that recently has entered in clinical trials for bladder cancer (Figure 3.1).[7] However, those Ru^{II} polypyrirdyl complexes generally present a low cellular uptake, and long internalization times for therapeutical applications. Cyclometallated Ir^{III} complexes are a good alternative to circumvent the disadvantages of Ru^{II} complexes,[8] and they have experimented an incredible boost in the last years. The positive charge on many Ir^{III} cyclometallated complexes can increase their solubility in physiological conditions compared to organic PSs as porphyrins or phthalocyanines.[9] These species also exhibit excellent energy transfer activity, making them efficient type

II PSs that can generate $^1O_2$ in high yields. Remarkably, Ir^{III} complexes also display high chemical and photochemical stability, avoiding the photobleaching suffered by some organic PSs.[10] All these characteristic make Ir^{III} species a great alternative to traditional photosensitizers. The cellular targets of Ir^{III} PSs are quite variated, including several organelles as mitochondria, lysosomes, nucleus endoplasmic reticulum, among others, and some proteins crucial in the cell cycle.

For instance, Huang and co-workers reported an Ir^{III} complex, which had as target the mitochondria, and was able to reduce the respiration rate of HeLa cells under hypoxia, and using PDT (475 nm) induced cell apoptosis, indicating its potential for treating hypoxic tumors. (Figure 3.1A).[11] The presence of PPh_3^+ group in the molecule resulted key for mitochondrial localization. In contrast, Mao and collaborators reported an Ir^{III}-β-carboline complex that could selectively stain in lysosomes, and induced caspase-dependent apoptosis through lysosomal damage on A549 cells upon irradiation (425 nm), and singlet oxygen production (Figure 3.1B).[12] Less extended are nucleus-targeting Ir^{III} complexes. Titan and collaborators, reported a complex able to generate ROS that induce DNA and nuclear damage, and the released from the nucleus to finally localize in mitochondria, generating a secondary damage under continued irradiation. (Figure 3.1C). [13]

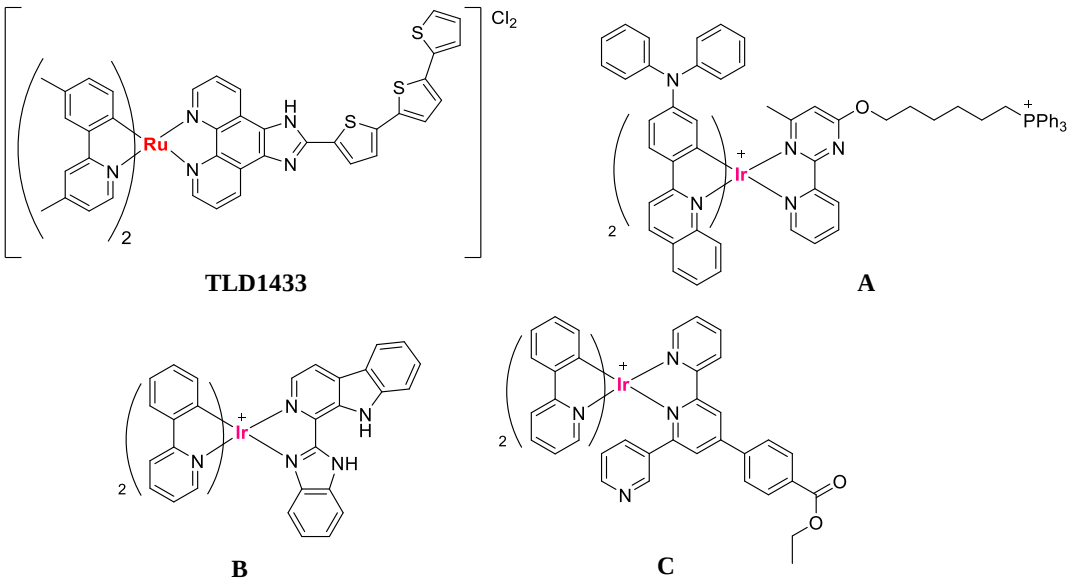

Figure 3.1. *Structures of Ir^{III} and Ru^{II} photosensitizers used in PDT.*

3.2 Objectives and methodology

This chapter describes the development of bifunctional iridium (III) complexes that can be independently activated as photosensitizer (PS) or cell imaging agent by varying the applied irradiation wavelength. The design of these complexes is based on incorporating a luminescent tag (organic chromophore) to an Ir^{III} PS, both having distinct optical properties enabling activation of the tracking or visualization individually from that of therapy function.

To develop the initial prototypes for obtaining bifunctional Ir^{III} complexes, the initial step is to connect a bioactive Ir^{III} yellow/green emissive fragment of the type $[Ir(C\text{^}N)_2(N\text{^}N)]^+$, where C^N represents an orthometallated ligand ppy, (2-phenyl pyridine) or bzq (benzo[*h*]quinolone) and N^N a diimine ligand, with a blue emissive organic chromophore (acridine or anthracene). The combination of both fragments will be made through the diimine ligand 2,2'-dipyridylamine (dpa), that offers great synthetic versatility and allows an easy coupling.

In this way, an organic chromophore can be incorporated to Ir^{III} metallic scaffold, offering the possibility of tracking the complex within the cells using a different irradiation wavelength from that of therapy activation. Moreover, the use of different cyclometallated ligands (ppy or bzq) enables tuning the metal based optical properties for delivering upgraded PS.

The aim of this work is to deliver the first synthetic steps towards designing bifunctional metalloprobes within photodynamic therapy (PDT) and cell imaging agents, as shown in Figure 3.2.

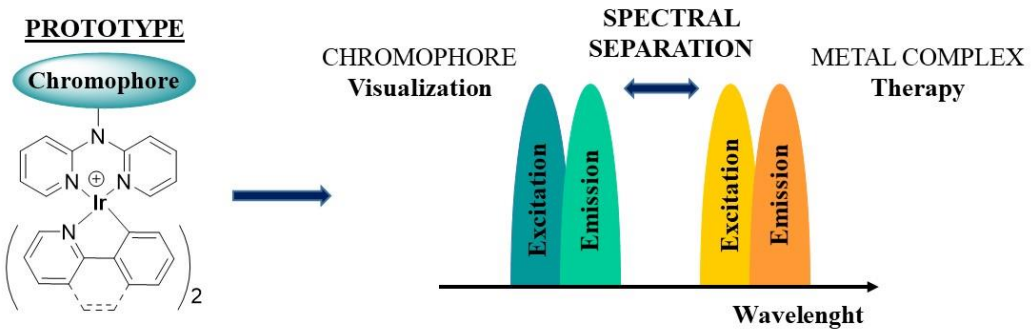

Figure 3.2. *Depiction of developed bifunctional Ir^{III} complexes.*

3.3 Synthesis and characterization

The synthetic procedure for developing the bifunctional cyclometallated Ir^{III} complexes starts with the synthesis of ligands **L3.1** and **L3.2**. These ligands were synthetized using 2,2'-dipyridylamine (dpa) as a linker between the iridium (III) center and the organic chromophore. Specifically, 9-bromoanthracene and 9-chloroacridine were chosen as blue organic chromophores due to their easy coupling reaction with amines, as has been previously described by Zhu and collaborators.[14] Moreover, both chromophores present similar chemical structure, differing only by nitrogen atom in the aromatic scaffold, thus offering the possibility of analyzing the influence of such nitrogen in the modulation of the optical and biological properties. Additionally, it is expected that these chromophores would allow tracking the complex within the cells using a completely different irradiation wavelength from that of PS activation.

The first step to obtain the mentioned ligands was the deprotonation of dpa in a reflux of toluene, using ^{t}BuOK as extrinsic base, followed by the addition of the correspondent halogen chromophore precursors, 9-bromoanthracene or 9-chloroacridine. The reaction mixture was refluxed for 16 hours under argon atmosphere, see Scheme 3.1. Once the reaction was finished, the volume of toluene was reduced, yielding the desired ligands as off-white solids. These were filtered, cleaned with dichloromethane to eliminate the excess of base, and dried. No additional purification technique was necessary. Both ligands were obtained in high yields. **L3.1**: 80% and **L3.2**: 96%.

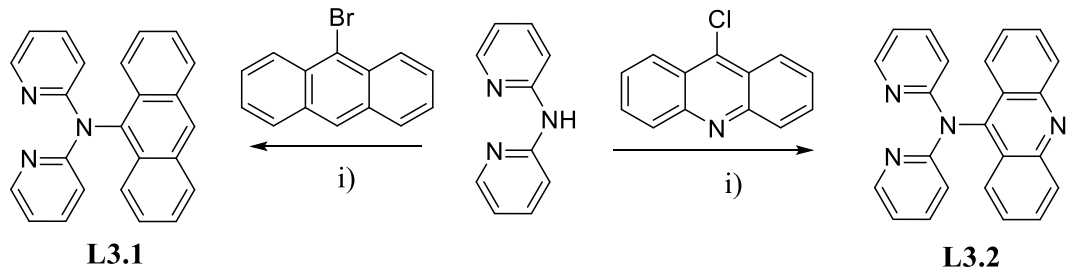

Scheme 3.1. *Synthetic pathway for the synthesis of **L3.1** and **L3.2**. Reaction conditions as follow: (i) ^{t}BuOK, toluene, reflux, Ar. Atmosphere, 16 h.*

The next step in obtaining the desired complexes with dual emission properties was to incorporate **L3.1** and **L3.2** as a diimine ligand to an cyclometallated iridium (III) fragment. For that purpose, it was decided to use two different metallic precursors, $[Ir(ppy)_2(\mu\text{-}Cl)]_2$ and $[Ir(bzq)_2(\mu\text{-}Cl)]_2$. The main differences between them are the increment of the aromaticity and rigidity of the cyclometalled ligand, which will surely affect the photophysical properties of the iridium complex.

Once ligands **L3.1** and **L3.2** were synthetised, the complexes **3.1-3.4** were obtained by refluxing the correspondent ligand with stechoimetric amounts of iridium dimmer precursors, $[Ir(ppy)_2(\mu\text{-}Cl)]_2$ or $[Ir(bzq)_2(\mu\text{-}Cl)]_2$ in methanol under inert conditions, see Scheme 3.2. After 15 hours of reaction, resultant mixtures were cooled, and products were isolated as yellow-orange solids, upon filtration and washing with ether, and dried under vacuum. All complexes, were obtained in high to moderate yields. **3.1**: 92%; **3.2**: 94%; **3.3**: 61% and **3.4**: 99%.

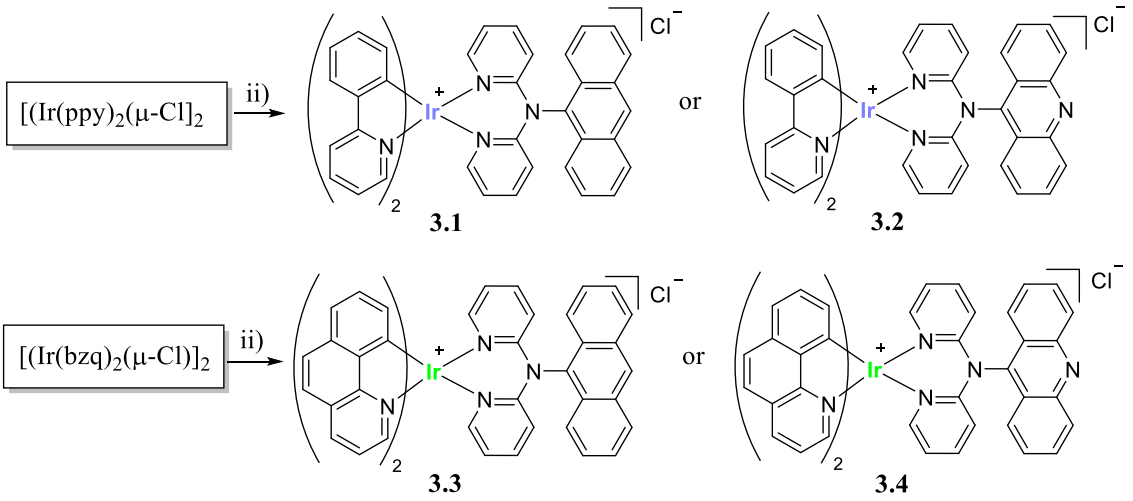

Scheme 3.2. *Synthetic pathway for the synthesis of complexes* ***3.1-3.4****. Reaction conditions as follow: (ii)* ***L3.1*** *or* ***L3.2****, MeOH, reflux, 15 h, Ar. Atmosphere.*

Complexes **3.1-3.4** and ligands **L3.1** and **L3.2**, were characterized using various techniques including ^{1}H, $^{13}C\{^{1}H\}$ spectroscopy and mass spectrometry (HRMS). ^{1}H-NMR spectra were well-defined for all syntethized molecules. Moreover, it was possible to observe the typical pattern for the dipyridylamine derivatives coordinated to a cyclometallated Ir^{III} center. Specifically, the pyridine protons of the N^N ligands appeared at lower field in comparison with those of the free ligand.

Therefore, Figure 3.3 clearly shows the doublet of doublet peak at 7.65 ppm corresponding to H_{para} in the free ligand **L3.2**, shifting to 7.24 and 7.01 ppm in complexes **3.2** and **3.4**, respectively. Following the same trend, also cyclometallated protons are affected by the coordination of diimine ligands. Figure 3.3 also shows that H_{orto} of pyridine (pink dots) shift to lower ppm , meanwhile H_{orto} of phenyl group (light blue dots) of ppy shifted to higher ppm compared to its dimmer precursor, after the coordination of ligands. Moreover, a set of eight resonances (each integrating as 2 protons) was observed for the two orthometallated ligands. This pattern could be explained by the C2 symmetric nature of these complexes. Furthermore, an additional set of four resonances was observed for the two pyridyl rings present in the N^N ligand, as was reported previously for similar complexes.[15] Analogous shifts and ^{1}H-NMR patterns were found for complexes **3.1** and **3.3**.

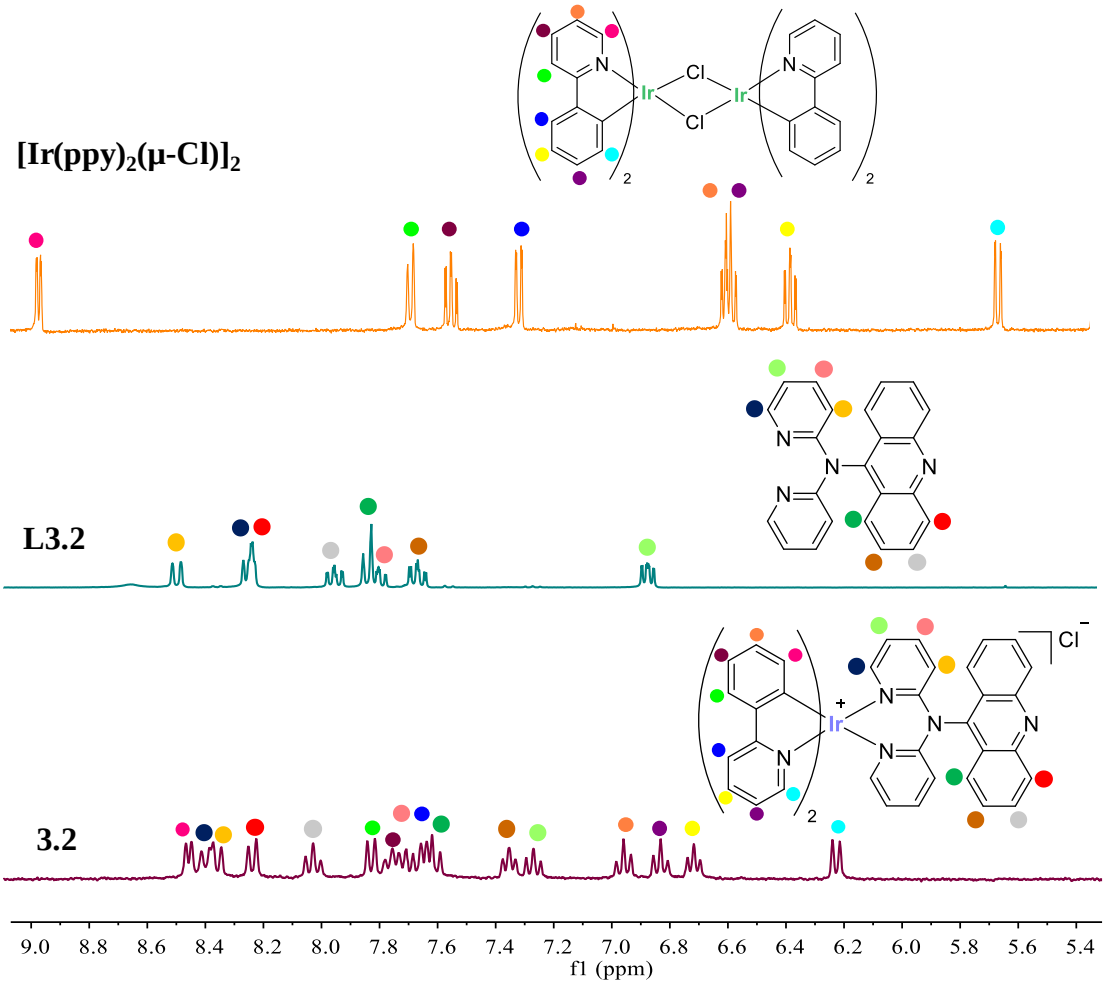

Figure 3.3. *^{1}H-NMR spectra of dimmer **L3.2** and complex **3.2**, in CD_2Cl_2.*

3.4 Photophysical properties

Optical properties of complexes **3.1**-**3.4**, as well as ligands **L3.1** and **L3.2** were measured in DMSO solution under standard conditions. Absorption UV-visible spectra were measured at [$2 \cdot 10^{-5}$ M] for the ligands and [10^{-5} M] for the complexes **3.1**-**3.4**. The most relevant data are depicted in Table 3.1.

Table 3.1. *UV-visible data of **L3.1**, **L3.2** and **3.1-3.4** measured in aerated DMSO solution.*

	UV-vis ($\times 10^3$ ε/dm^3 mol^{-1} cm^{-1})/nm
L3.1	260 (47.5), 318 (8.7), 355 (3.4), 373 (5.2), 394 (4.5)
L3.2	260 (47.5), 270 (30.7), 317 (16.2), 350 (7.5), 362 (9.8), 388 (5.4)
3.1	260 (94.4), 320 (14.5), 354 (10.0), 375 (10.7), 395 (8.9), 424 (3.9)
3.2	260 (87.5), 273 (68.1), 310 (25.4), 380 (20.2), 400 (22.1), 427 (6.5)
3.3	260 (43.4), 324 (9.4), 353 (6.7), 374 (5.5), 394 (3.9), 423 (1.8)
3.4	260 (39.1), 271 (35.1), 308 (12.9), 380 (10.1), 398 (11.5), 425 (3.2)

The synthesized complexes show a dominant band around 260 nm, which could be assigned to a spin allowed ligand centered (^{1}LC, $\pi \rightarrow \pi^*$) transition, as well as, others with less intensity, between 350-450 nm, which correspond to ^{1}MLCT and ^{1}LLCT transitions. A weak long tail over 450 nm is also observed, which is assigned to spin forbidden ^{3}MLCT, ^{3}LLCT and ^{3}LC transitions. These transitions occur due to the high spin-orbit coupling of the iridium metal, see Figure 3.4.[16] The absorption at lower energies will be used in PDT assays to activate the complex with more penetrating irradiation wavelengths.

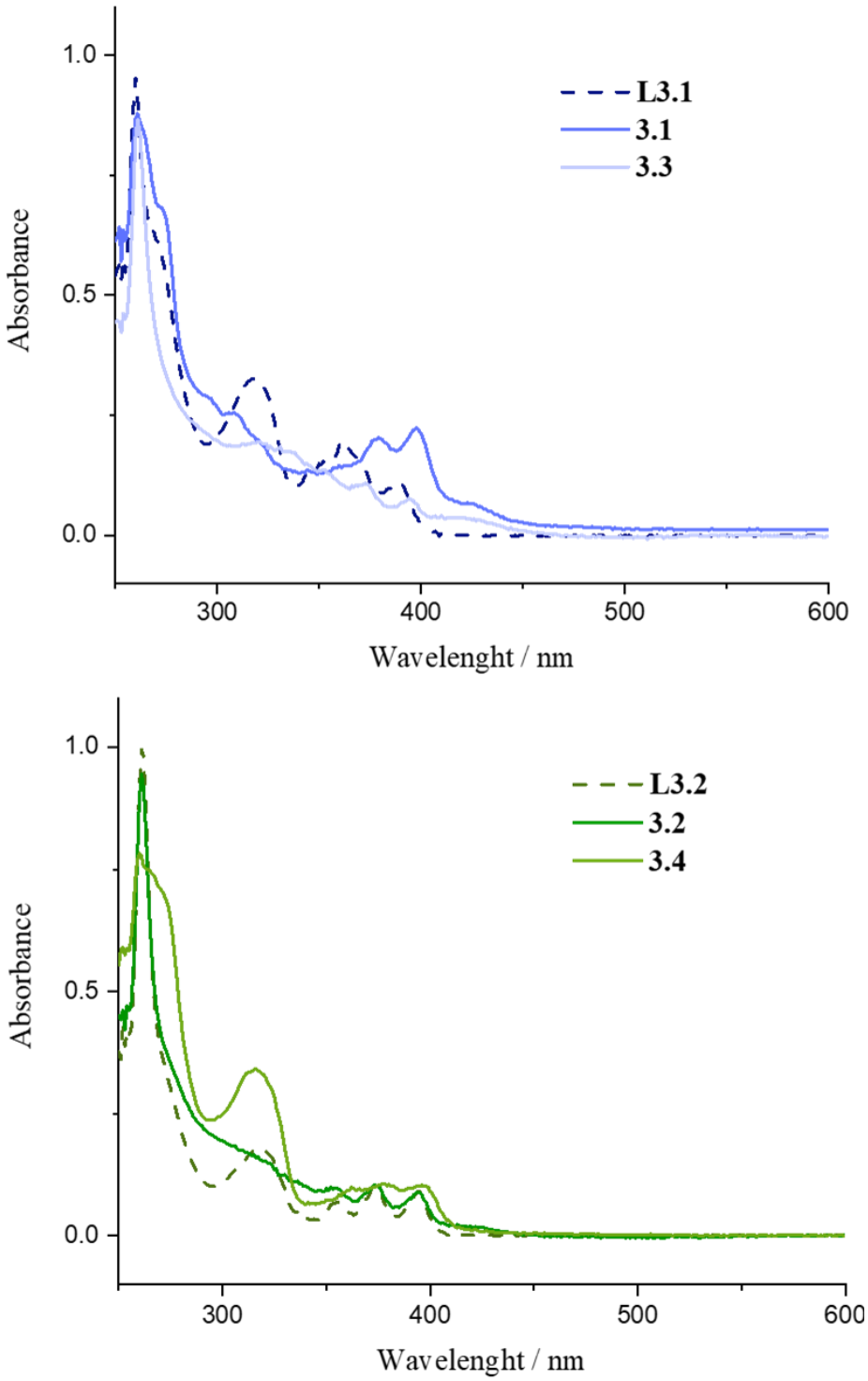

Figure 3.4. *Absorption spectra in DMSO solution at room temperature. Up:* ***L3.1*** *at [2·10^{-5}M] and complexes* ***3.1*** *and* ***3.3*** *at [10^{-5}M]. Down:* ***L3.2*** *at [2·10^{-5}M] and complexes* ***3.2*** *and* ***3.4*** *at [10^{-5}M].*

Furthermore, the emissive properties were measured, in aerated DMSO solution at room temperature, all relevant data were collected in Table 3.2.

Table 3.2. *Luminescent data of* ***L3.1*** *and* ***L3.2*** *and complexes* ***3.1-3.4****.*

	λ_{em} [λ_{exc}] (nm)	τ (ns)	Φ (%)
L3.1	405, 422, 448 [375]	-	-
L3.2	409, 431, 557 [400]	-	-
3.1	486, 515s, 551 [437]	186	8.3
3.2	485, 514 [433]	210	8.4
3.3	521s, 551s [432]	242	6.4
3.4	521s, 547s	451	10

The studied complexes displayed a strong emission band between 485 and 515 nm (**3.1** and **3.2**) and between 521 and 551 nm (**3.3** and **3.4**), as shown in Figure 3.5, upon excitation at 450 nm. This emission can be assigned to a mixture of ^{3}MLCT and ^{3}LLCT transitions.[17] It is important to highlight how the increment in the aromaticity of the cyclometallated ligand, from ppy to bzq, generates a small red shift in the emission spectra. This behaviour is associated to the destabilization of HOMO orbitals, which are the highest-occupied molecular orbitals, resulting from a mixture of Ir dπ orbitals and the π orbitals of the cyclometallated ligand.

Moreover, it is especially remarkable that when the complexes are irradiated between 375 and 400 nm, an additional emissive band with emission maxima around 400 nm can be observed (Figure 3.6A). This secondary band can be attributed to a ^{1}LC transition within the chromophore, and its structured pattern resembles that of free anthracene or acridine. ^{1}LC emission was more easily observed in the case of complexes **3.3** and **3.4**, due to the fact that their ^{3}MLCT transition is red shifted (c.a. 521 nm) in comparison with that of complexes **3.1** and **3.2** (c.a. 486 nm). Figure 3.6A clearly shows the great dependence of the emission pattern on the irradiation wavelength applied. This confirms the initial idea that it was possible to individually excite one part of the molecule or the other by varying the excitation wavelength. Figure 3.6B revealed the main excitation pattern for each fragment of complex **3.4**.

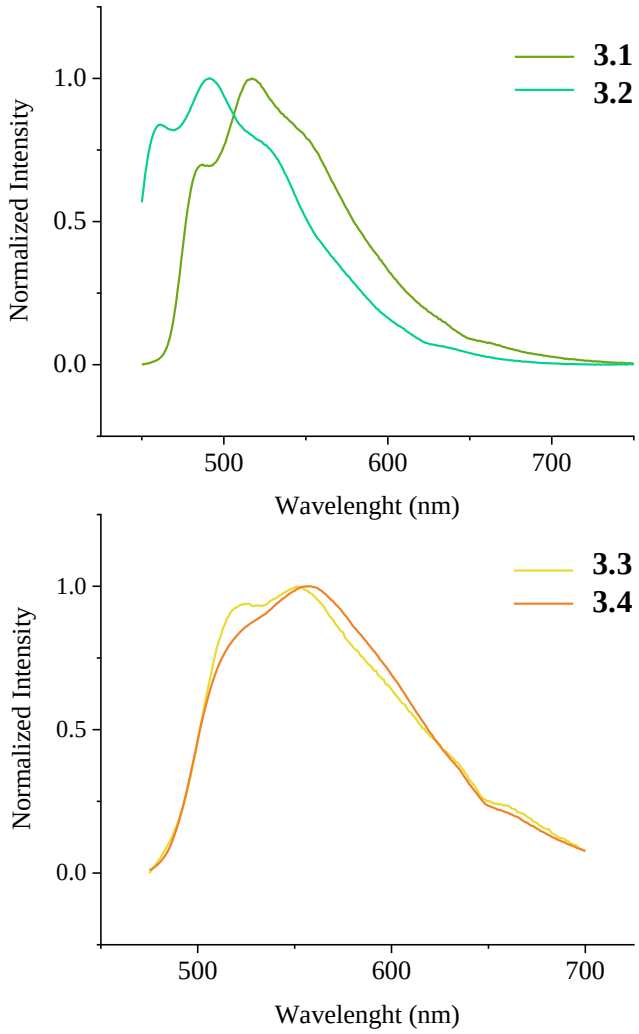

Figure 3.5. *Emission spectra of complexes* ***3.1-3.4*** *in DMSO solution at 298 K.*

Focusing on the lifetimes of the different complexes for their excited states, it is possible to conclude that all complexes present lifetime values between 186-451 ns, indicating a phosphorescence process. This result is in concordance which others previously reported in the literature for similar Ir^{III} complexes.[17] Additionally, their quantum yields were measured in aerated DMSO displaying moderated values between 6.5% to 10%.

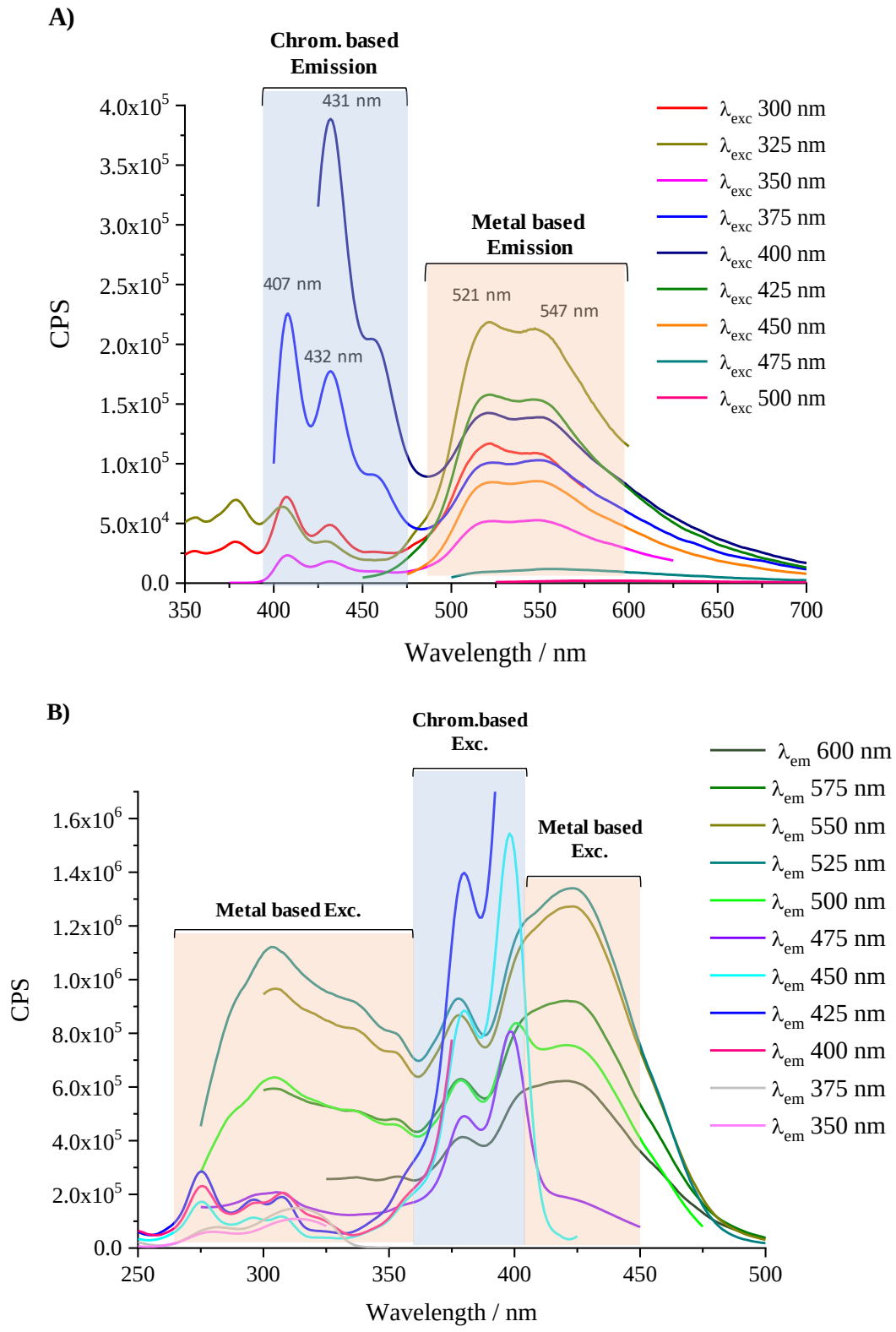

Figure 3.6. *Emission spectra (A) of complex* ***3.4*** *for the different emission profiles and the correspondent excitation spectra (B) upon excitation at different wavelengths.*

3.5 Antiproliferative activity

In vitro sensibility to ligands **L3.1** and **L3.2**, as well as, complexes **3.1**-**3.4**, was determined by MTT assay for to A549 cell line after a period of exposure to the treatment of 24 hours, following the methodology explained in Chapter 1. The ligand precursors, **L3.1** and **L3.2**, present IC_{50} values over 50 μM. On the contrary, neither of their resultant complexes follow a similar behaviour. Complexes **3.1**-**3.3** display a moderate antiproliferative activity, with IC_{50} values between 13.6 and 19.6 μM, followed by complex **3.4**, which IC_{50} value is 43.38 μM. These results might suggest that bioactivity falls into the metallic fragment.

In parallel, PDT studies were performed. This time, cells were irradiated for 10 min after 5 hours of incubation with the different complexes, and kept in culture for futher 19 h. For these assays, two different irradiation wavelenghts were used, 405 and 470 nm, with the main purpose of confirming the suitability of these complexes as photosensitizers. IC_{50} data is collected in Table 3.3.

Analysis of the IC_{50} values revealed that when a 405 nm irradiation source was used, the antiproliferative activity for all complexes increased at least 7 times compared to that displayed in dark conditions. However, irradiation at 470 nm gave a considerable increase of the antiproliferative capacity. The IC_{50} values for the studied complexes dropped to the nanomolar range, which was especially remarkable in the case of complex **3.4**, where its IC_{50} value was reduced 110 times compared to dark conditions. Therefore, complex **3.4**, is proposed to be the best PS agent from the developed complexes **3.1**-**3.4** due to its superior performance under irradiation conditions ($IC_{50\ (dark)}$: 43.4 ± 0.14 μM; $IC_{50\ (470\ nm)}$: 0.39 ± 0.09μM, PI: 111).

The diverse bioactivity displayed by complexes upon the different irradiation source at 405 or 470 nm could be explained by the varied nature of the excited states implicated in the process. Thus, when an irradiation of 405 nm is applied, the organic chromophore is the main fragment excited. However, changing this irradiation to 470 nm, makes the iridium fragment the one that is preferably

excited. This assumption is made based on the analysis of the photophysical properties previously described. Figure 3.6 clearly showed the different effect on the emissive properties upon irradiating at 405 vs 470 nm, with a main emission band centered at 437 nm and 535 nm respectively, and affecting either the chromophore (^{1}LC) or the Ir^{III} fragment (^{3}MLCT). As result, it can be suggested that theses complexes present a higher PDT character upon activation of the metallic fragment over the chromophore.

Table 3.3. *IC_{50} values (μM) of **L3.1** and **L3.2** and complexes **3.1-3.4** incubated for 24 h in A549 cells.*

	IC_{50} (DARK)	**$^1IC_{50}$ (λexc 405 nm)**	**PI**	**$^1IC_{50}$ (λexc 470 nm))**	**PI**
L1	>50	-		-	
L2	>50	-		-	
1	13.6 ± 0.08	1.16 ± 0.06	11.7	0.18 ± 0.05	75.5
2	19.6 ± 0.68	2.54 ± 0.08	7.7	0.34 ± 0.06	57.6
3	18.9 ± 0.12	1.35 ± 0.08	14.0	0.40 ± 0.08	47.2
4	43.4 ± 0.14	>5		0.39 ± 0.09	111.2

[1] 10 min of irradiation after 5 hours of incubation. (PI: Phototoxic index).

3.6 Cell morphology alterations

Changes in cell morphology as a consecuence of treatment with syntethized complexes were analized using an inverted microscope. Control cells (neat cells) grew exponentially, as expected. Additionally, cells treated with **L3.1** and **L3.2** had a similar morphology to that of the control cells. In those wells cells were dividing, and no apoptotic or necrotic cells were detected. On the contrary, cells underwent modifications in their morphology when they were exposed to complexes **3.1-3.4**. In all the studied conditions, it was possible to observe cytoplasmic vesicle formations, which were especially remarkable for **3.3** and **3.4**, complexes containing the cyclometallated bzq ligand. Moreover, cell cycle arrest was not detected, and cells division still took place in all the cases. Overall, the

formation of apoptotic bodies (black arrows in Figure 3.7) was observed, leading us to suggest an apoptotic cell death mechanism.

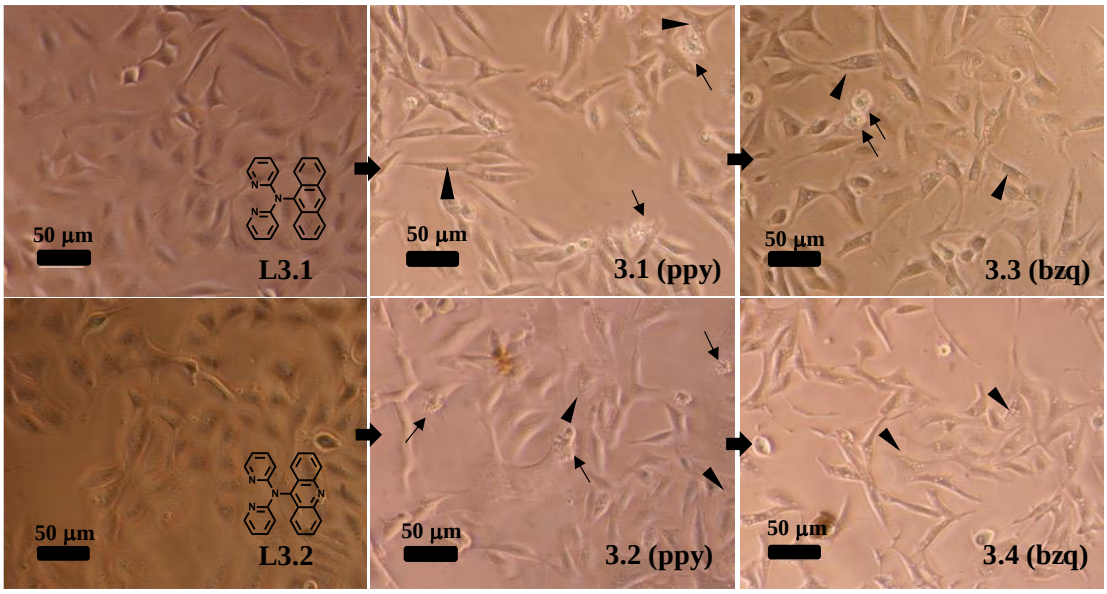

Figure 3.7. *Images of A549 cells treated with compounds* ***L3.1***, ***L3.2*** *(20 µM) and* ***3.1-3.4*** *(10 µM) for 20 h. Black arrows point to apoptotic cells. Black triangles show examples of cells containing cytoplasmic vesicles.*

3.7 Study of cytotoxic activity and cell cycle arrest

As previously indicated, when cells are treated with complexes **3.1**-**3.4**, they undergo morphological changes, including cytoplasmic vascularization, which are indicative of an apoptotic cell death mechanism. To confirm the cell death mechanism, complex **3.4**, the most promising PS complex, was analized by flow cytometry using simultaneous double staining of Annexin V-DY634 (apoptotic cell death) and 7-AAD (necrotic cell death), in both dark and under 470 nm irradiation. Therefore, A549 cells were treated with complex **3.4**, in a range of concentration going from its IC_{50} to ½·(IC_{50}) and ¼·(IC_{50}) values for 24 h.

As shown in Figure 3.8, complex **3.4** displays cytotoxic activity directly correlated with its concentration. Thus, the higher the concentration, the highest toxicity prompted. Although in both conditions, dark and irradiated, it was possible to observe cell death, their mechanism seemed to differ. When cells were treated with

complex **3.4** in dark, especially at high concentrations, they reached a similar distribution of early (Annexin-V-DY634 (+) and 7ADD (-)) and late apoptosis (Annexin-V-DY634 (+) and 7ADD (+)). However, at low concentration their main state was that of early apoptosis. On the contrary, irradiated cells reached mainly the late apoptotic state for all concentration ranges. Therefore, these results suggest that complex **3.4** follows and apoptotic cell death mechanism under irradiation. In addition, the high number of vesicles found in the cytoplasm by microscopy at the morphology analysis seem to indicate that paraptosis, another type of programmed cell death, could coexist with apoptosis.[18]

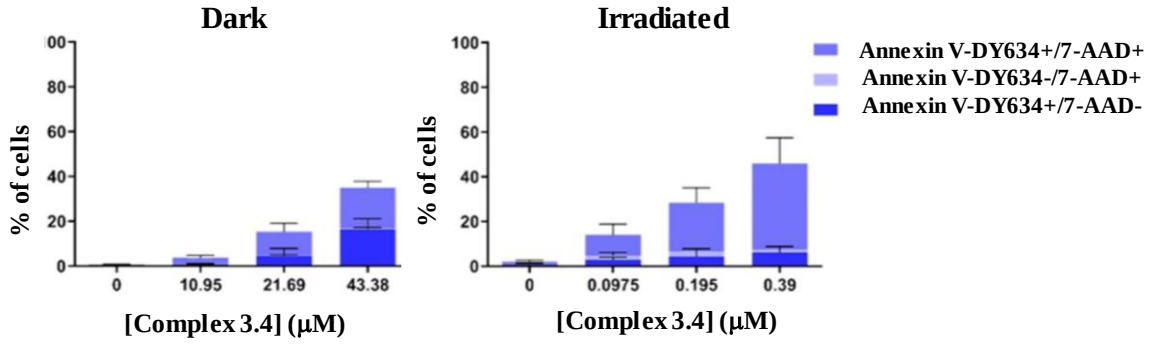

Figure 3.8. *Cytotoxicity assays of complex **3.4** after 24 h of incubation in A549 cells. In dark (left); Under 10 minutes irradiation at 470 nm (right).*

To dig into the mechanism of action of this complex, the next step was to study if complex **3.4** was able to modify or interrupt the cell cycle. The cell cycle could be described as a series of growth and development steps that a cell undergoes from its formation and division to eventually produce two identical cells. Specifically, the cell cycle involves as a sequence of four phases: During G1 phase, cells grow and are metabolically active, through phase S cells duplicate their DNA and became ready for dividing in phase G2, and finally they get divided resulting in two cells during phase M. It is at this point when the daughter cells carry out their own cell cycle.[19]

The study of cell cycle was performed in dark and upon irradiation conditions. The aim of this experiment was to elucidate whether the antiproliferative behavior previously reported for complex **3.4** could be related with a cell cycle arrest at any of the phases. Thus, complex **3.4** was incubated in A549 cells ($4 \cdot 10^5$ cells/well) at

¼ IC_{50} value for 24 h. Then, propidium iodide and RNase were added as fluorescent markers and, finally, cells were analyzed by flow cytometry. Figure 3.9 indicates that in both conditions, cells exhibited the typical cell cycle pattern for healthy cells. Most of them were in G0/G1 phase, in the growing step. In addition, the cell distribution at the different phases was barely disrupted with respect to the respective controls (neat cells). In consequence, it can be concluded, that complex **3.4** was not capable to stop the cell cycle at any of its phases, neither in dark or under irradiation conditions.

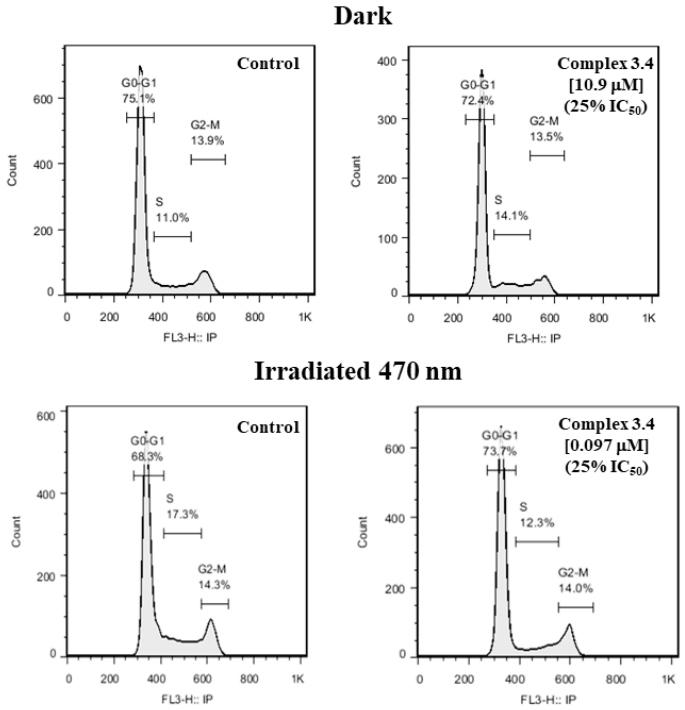

Figure 3.9. *Cell cycle analysis after treatment with complex* ***3.4*** *in dark (top graphs) and under irradiation at 470 nm (bottom graphs).*

3.8 Determination of partition coeficient octanol/water: logP

The partition coefficient octanol/water, $logP_{(oct/W)}$, was determined for synthetized complexes **3.1**-**3.4**, as well as their ligand precursors, **L3.1** and **L3.2**. This value, logP, indicates the ratio liphophilicity/hydrophilicity of a drug. The liphophilicity of a compound is an essential information to predict its physicochemical behavior *in vivo* and its drug-likeness. It can be measured by several experimental methods

as the sake flash method among others.[20] A depiction of this method is collected in Figure 3.10.

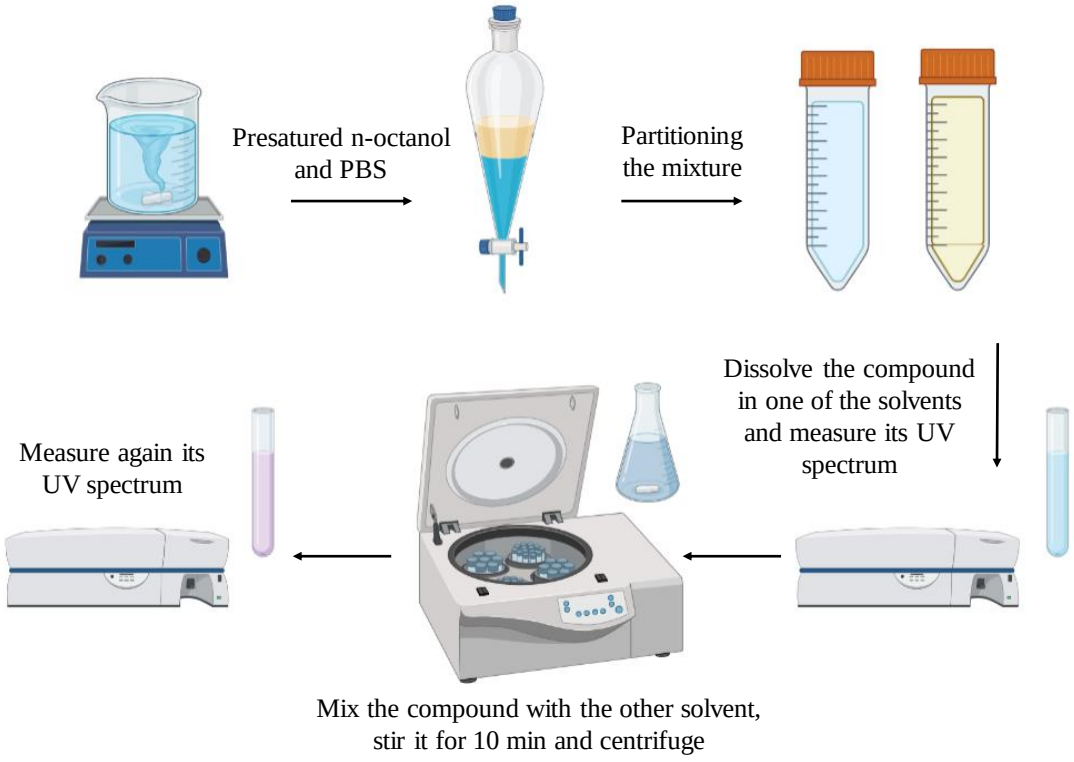

Figure 3.10. *Schematic protocol of the shake flash method for the calculation of logP.*

Specifically, to perform this assay, it was necessary the preparation of PBS solution that contain: 800 mL of Mili-Q Water, 8 g NaCl, 0.2 g KCl, 1.44 g Na_2PO_4 and 0.24 g KH_2PO_4. The mixture was stirred until it was completely dissolved, and its pH was adjusted between 7.2-7.4 using diluted solutions of HCl or NaOH. 72 h prior to starting the assay, 500 mL of n-octanol with 500 mL of PBS were mixed to achieve the saturation of both. After this time, a liquid-liquid extraction was carried out, and the two phases were stored in separate falcons. On the day of measurement: a) a known amount of the complex was dissolved in the solvent with higher solubility (saturated octanol or saturated PBS), to prepare a solution of an exact concentration ($5 \cdot 10^{-5}$M), b) its Vis-UV absorption spectrum was collected, after recording the baseline in the same solvent. The absorbance should not exceed 1. In this way, the absorption coefficient, ε, of the studied compound can be determined for the chosen solvent, d) 3 mL of this solution of known concentration

was mixed with another 3 mL of the other solvent (either n-octanol or PBS) and stirred energetically for 10 min ensuring the mixture of phases, e) the mixture was centrifuged for 10 min at 3,000 rpm to separate both phases, f) Vis-UV absorption spectrum of the phase of which ε is known was measured, g) the following equation 1 was applied to calculate logP.

$$logP = \frac{Initial\ concentration}{|Initial\ concentration - Final\ concentration|}$$

Equation 1. *Determination of logP.*

Table 3.4 displays all the logP values measured for **L3.1** and **L3.2** as well as for **3.1**-**3.4**. In particular, logP values range from 0.28 in case of complex **3.2**, being the least lipophilic, to 1.73 for complex **3.3**. These results are in concordance with the higher lipophilicity of ligand **L3.1** compared to **L3.2,** added to the more lipophilic nature of the orthometallated bzq in complexes **3.3** and **3.4** compared to ppy in **3.1** and **3.2**.

Table 3.4. *logP values for synthetized compounds at pH=7.4 and 298 K.*

	logP (Oct/W)
L3.1	1.20
L3.2	0.59
3.1	0.75
3.2	0.28
3.3	1.73
3.4	1.24

3.9 Cellular biodistribution

To elucidate de biodistribution that these complexes have in A549 cell line, fluorescence confocal microscopy assays were performed. Complexes **3.2**-**3.4** were incubated in A549 cells for 2 hours and Mitotracker Red (MTR) was added as internal standard. After 15 min of incubation and the renewal of the cell medium, the cells were visualized by a fluorescence microscope using different irradiation wavelengths (458 nm for activating the complexes and 598 for the tracker). Figure 3.11 shows a schematic representation of the different excitation and emissive profiles of studied complexes (**3.2**-**3.4**) and Mitrotracker Red used in biodistribution assay.

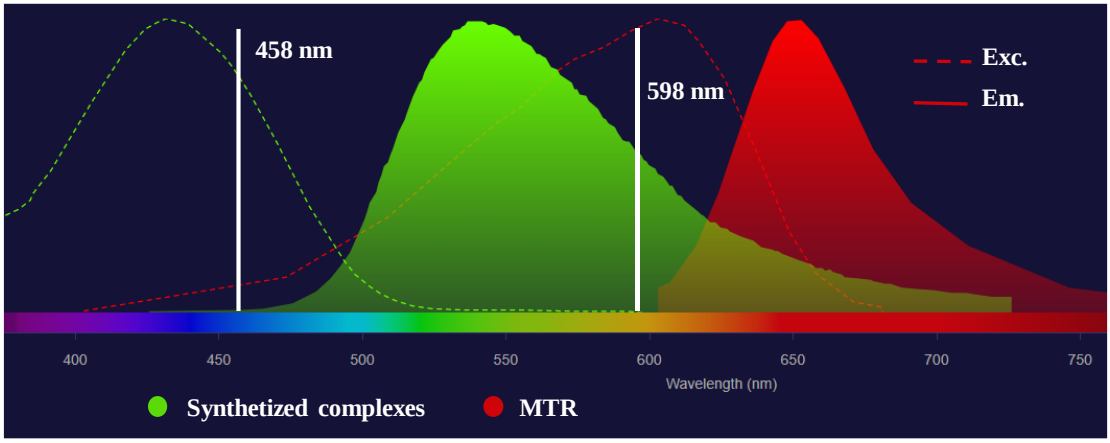

Figure 3.11. *Simulation of the emission and excitation pattern of MTR and the selected excitation lasers.*[21]

All complexes were able to enter the cell without permeating the nucleus, see Figure 3.12. However, they showed slightly different patterns. Complex **3.3** fully colocalized with MTR, indicating a mitochondrial localization, whereas complexes **3.2** and **3.4**, in addition to mitochondrial localization, showed an additional biodistribution in areas near the nucleus.

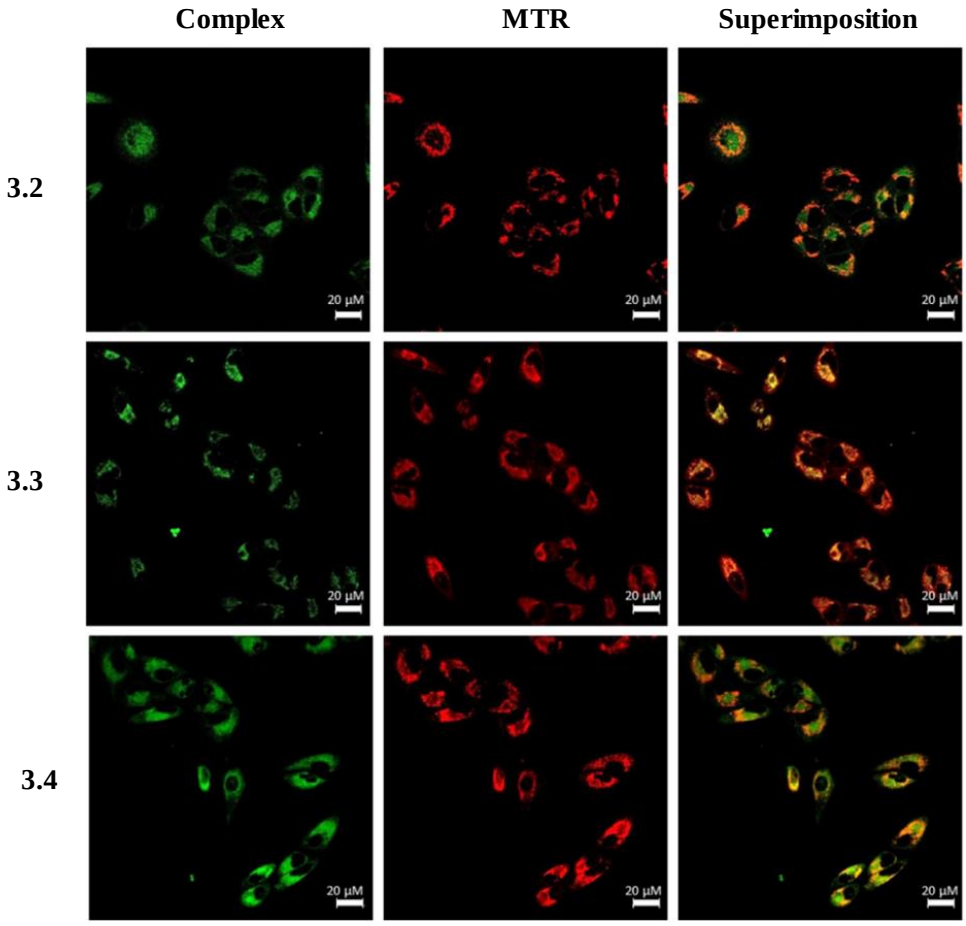

Figure 3.12. *Fluorescence confocal microscopy images of A549 cells incubated with complexes **3.2**, **3.3** and **3.4** (2 h) and stained with MTR (30 min). Image after irradiation at 458 (green) and 598 nm (red).*

The different distribution pattern for the complexes **3.2** and **3.4** in comparison with that of **3.3**, see Figure 3.13, could be explained because of the nature of the organic chromophore. Thus, it can be suggested that variations on the chromophore from anthracene to acridine led to an alternative biodistribution from neat mitochondrial to mitochondrial and an additional organelle accumulation. In fact, Zhao and coworkers[22] also described some Ir^{III} complexes containing an anthracene moiety, which has a selective accumulation in mitochondria. Based on the results, it can be hypothesized that the presence of the nitrogen atom within the chromophore is the source for the alternative accumulation.

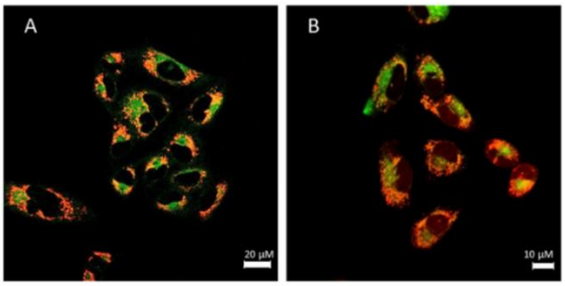

Figure 3.13. *Superimposition images in A549 cells of complexes* ***3.2*** *(A) and* ***3.4*** *(B) incubated 2 h and stained with MitoTracker Red (MTR).*

3.10 Generation of reactive oxygen species

Reactive oxygen species (ROS) could be generated as result of phototherapeutic effect that the probe may exert upon irradiation. It is known that complex **3.4** reduces its IC_{50} value up to 110 times when is irradiated at 470 nm, ($IC_{50\ (dark)}$: 43.4 µM; $IC_{50\ (470\ nm)}$: 0.39 µM), and a plausible explanation could be driven by the generation of ROS species. To confirm this ROS generation, an assay was performed by flow citometry using DHE (dihydroethidium) as fluorescent probe. In presence of the supeoxide ion and hidrogen peroxide, DHE would be oxidazed to 2-HE (2-hydroxyethidium). The assay was carried out for complex **3.4** incubated at different concentrations in dark and under irradiation conditions, and the results are depicted in Figure 3.14.

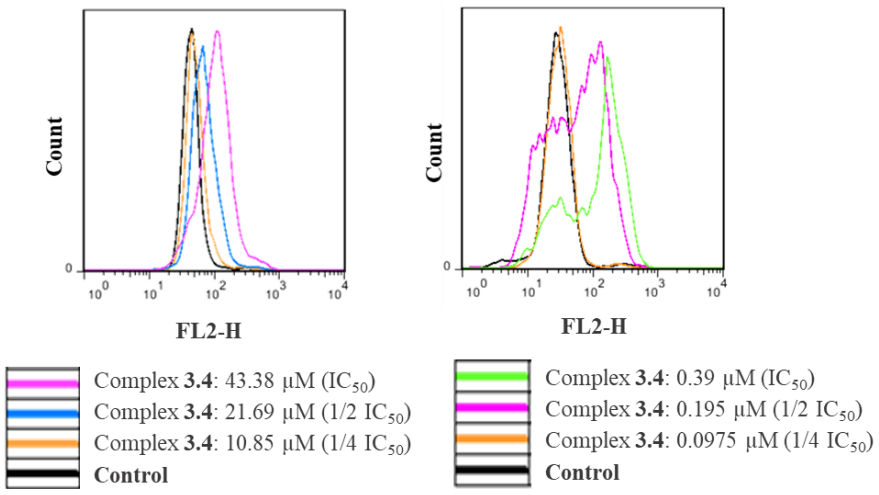

Figure 3.14. *ROS generation induced by complex* ***3.4*** *at increasing concentrations in dark (left graph) and upon irradiation at 470 nm for 10 min (right graph).*

As shown above, complex **3.4** displayed a concentration-dependant ROS generation in both conditions; however, the production of ROS is higher under irradiation conditions, as expected. Surprisingly, each condition generates different profiles. When the assays were performed in dark, a single peak shifted to the right was observed because of ROS production. In contrast, under irradiation using ½ IC_{50} or higher concentration, two peaks appeared. One of them was in the same position as the control, while the other was right shifted. This behavior could suggest that a fraction of cells has overactivated their ROS production mechanism, whereas the rest maintain production levels similar to control cells. These higher levels of ROS generation might be a result of the photoactivation of the iridium complex that enables to reach the iridium complexes a triplet excited state. At this point an electron transfer process (PDT type I) and/or energy transfer process (PDT type II) takes places, generating the highly cytotoxic ROS.[23] In conclusion, it could be said that A549 cells enhanced ROS production after exposition to complex **3.4** in non-irradiated and, to a greater extent, under irradiated conditions.

3.11 Conclusions

In this chapter, two ligands derived of 2,2'-dipyridylamine, **L3.1** and **L3.2,** have been synthetized. **L3.1** contains anthracene while **L3.2** contains acridine. Additionally, four Ir^{III} complexes have been obtained combining two different cyclometallated ligands, ppy (**3.1** and **3.2**) or bzq (**3.3** and **3.4**), in order to tune the metal based optical properties for delivering upgraded PS.

The optical properties of all the complexes showed an excitation dependent emissive pattern, which was more evident in the case of complex **3.4**. Specifically, this complex showed that the main emissive band was due to the organic chromophore, acridine, (LC transition) when the irradiation was performed between 374 and 400 nm, with a structured band between 407 and 450 nm. When irradiated at different wavelength ranges, the main emission was centered at approximately 525 nm, which was due to the iridium fragment (^{3}MLCT and ^{3}LLCT transition).

The difference in the emissive origin could also be observed in the photocytotoxic properties upon incubation with A549 cells. All the complexes displayed moderate antiproliferative activity, showing IC_{50} values between 13.6-43.4 μM, with complex **3.4** being the least potent. However, under irradiation conditions, their bioactivity increased, especially when the irradiation affected the metal-based core. Thus, complex **3.4** revealed an IC_{50} value of 43.38 ± 0.14 μM in dark, IC_{50} > 5 μM upon irradiation for 10 min at 405 nm and IC_{50} of 0.39 ± 0.09 μM upon irradiation for 10 min at 470 nm. These results highlight the importance of the intrinsic photophysical properties of Ir^{III} fragment over those of organic chromophores for PDT.

Furthermore, microscopy analysis revealed cytoplasmic vacuolization and typical apoptotic and necrotic features, which were confirmed by cytotoxicity assays, suggesting that complex **3.4** induces an apoptotic cell death.

Confocal fluorescence microscopy studies revealed that complex **3.3** localized in mitochondria; however, complexes **3.2** and **3.4** were only partly localized in these

organelles and presented other subcellular distribution. This difference within cellular localization could be attributed to the role of chromophore, as both complexes **3.2** and **3.4** contain the same chromophore, acridine. Moreover, no cell cycle alterations were detected, but a greater ROS generation was observed under irradiation conditions compared to dark conditions.

3.12 General synthetic procedures

The starting material $[Ir(ppy)_2(\mu\text{-}Cl)]_2$ and $[Ir(bzq)_2(\mu\text{-}Cl)]_2$, were prepared according to published procedures.[24] Other reagents and solvents were commercially available from Sigma-Aldrich and used without further purification. Manipulations were performed under argon atmosphere.

Instrumentation

Mass spectra were recorded on a BRUKER ESQUIRE 3000 PLUS, with the electrospray (ESI) technique. ^{1}H, $^{13}C\{^{1}H\}$ and $^{31}P\{^{1}H\}$ NMR, including 2D experiments, were recorded at room temperature on a BRUKER AVANCE 300 spectrometer (^{1}H, 300 MHz, ^{13}C, 75 MHz) with chemical shifts (δ, ppm) reported relative to the solvent peaks of the deuterated solvent.[25] Steady-state photoluminescence spectra were recorded with a Jobin-Yvon-Horiba fluorolog FL-3-11 spectrometer using band pathways of 3 nm for both excitation and emission. UV/vis spectra were recorded with 1 cm quartz cells on an Evolution 600 spectrophotometer. Quantum yields were measured using an absolute method provided by Hamamatsu Photonics Quantaurus-QY C11347-11.

Synthetic procedure of ligands L3.1 and L3.2

An equimolar mixture of 2,2'-dipyridylamine (100 mg; 0.584 mmol) and 9-bromoanthracene (**L3.1**) (151.7 mg; 0.584 mmol) or 9-chloroacridine (**L3.2**) (128.52 mg; 0.584 mmol) was dissolved in 5 mL of toluene, thereafter potassium tert-butoxide (77 mg; 0.65 mmol) was added to the solution. The reaction mixture was refluxed overnight. The volume of toluene was reduced under vacuum, affording a off-white solid, which was filtered and dried affording **L3.1** (162.2 mg; 80% yield) or **L3.2** (196.76 mg; 96% yield).

L3.1: ^{1}H NMR (300 MHz, Acetone-d_6) δ 8.69 (s, 1H), 8.50 (d, J = 8.9 Hz, 2H), 8.22 (d, J = 3.9 Hz, 2H), 8.16 (d, J = 8.4 Hz, 2H), 7.82 (d, J = 8.4 Hz, 2H), 7.74–7.56 (m, 6H), 6.89–6.80 (m, 2H) ppm. ^{13}C NMR (75 MHz, Acetone-d_6) δ 149.6, 148.40, 140.8, 138.2, 137.5, 129.8, 128.6, 128.5, 127.9, 126.9, 126.8, 116.8, 112.6, 103.0 ppm.

L3.2: ^{1}H NMR (300 MHz, Acetone-d_6) δ 8.48 (d, J = 8.8 Hz, 2H), 8.25–8.20 (m, 4H), 7.96–7.90 (m, 2H), 7.84–7.75 (m, 4H), 7.68–7.61 (m, 2H), 6.85 (ddd, J = 7.2, 5.0, 1.0 Hz, 2H) ppm. ^{13}C NMR (75 MHz, Acetone-d_6) δ 148.4, 138.2, 131.6, 130.9, 128.4, 125.1, 116.8, 112.6, 110.4, 110.4 ppm. HRMS (ESI): m/z calcd. for $C_{23}H_{16}N_4$ 348.1375; found: 349.1453 (**L3.2** + H).

Synthetic procedure of complexes 3.1 and 3.2

$[Ir(ppy)_2(\mu\text{-}Cl)]_2$ (50 mg, 0.046 mmol) was dissolved in 5 mL of MeOH, then **L3.1** or **L3.2** was added to the solution in an equimolar proportion (**L3.1**, 32.38 mg or **L3.2**, 32.47 mg). The reaction mixture was refluxed for 15 h under argon atmosphere. The resultant suspension was cooled, and the yellow solid was isolated by filtration affording 40.4 mg of **3.1** (92% yield) or 41.19 mg of **3.2** (94% yield) respectively.

Complex **3.1**: ^{1}H NMR (300 MHz, CD_2Cl_2) δ 8.43 (dd, J = 9.1, 0.9 Hz, 3H), 8.13 (ddd, J = 5.8, 1.6, 0.8 Hz, 2H), 7.98–7.94 (m, 2H), 7.85 (ddd, J = 8.4, 1.5, 0.8 Hz, 2H), 7.73 (ddd, J = 8.2, 7.3, 1.5 Hz, 2H), 7.60–7.39 (m, 12H), 7.04 (ddd, J = 7.4, 5.8, 1.5 Hz, 2H), 6.89 (ddd, J = 7.8, 7.3, 1.3 Hz, 2H), 6.74 (td, J = 7.4, 1.4 Hz, 2H), 6.42 (t, J = 6.5 Hz, 2H), 6.08 (ddd, J = 7.5, 1.3, 0.5 Hz, 2H) ppm. ^{13}C NMR (75 MHz, CD_2Cl_2) δ 168.3, 168.3, 163.0, 152.9, 150.0, 150.0, 149.8, 149.8, 144.5, 144.5, 138.8, 138.8, 138.5, 138.5, 132.3, 132.3, 130.8, 130.8, 129.2, 129.2, 127.9, 127.9, 127.8, 127.8, 127.77, 127.7, 126.3, 126.3, 125.2, 125.2, 123.4, 123.4, 122.7, 122.7, 120.2, 120.2, 117.9 ppm.

Complex **3.2**: ^{1}H NMR (300 MHz, CD_2Cl_2) δ 8.46–8.30 (m, 6H), 8.21 (d, J = 8.2 Hz, 2H), 8.00 (t, J = 7.7 Hz, 2H), 7.84–7.52 (m, 10H), 7.33 (dd, J = 7.4, 5.8 Hz, 2H), 7.25 (dd, J = 8.2, 6.8 Hz, 2H), 6.94 (t, J = 7.5 Hz, 2H), 6.81 (t, J = 7.4 Hz, 2H), 6.69 (t, J = 6.5 Hz, 2H), 6.20 (d, J = 7.6 Hz, 2H) ppm. ^{13}C NMR (75 MHz, CD_2Cl_2) δ 167.7, 152.1, 152.0, 150.4, 149.4, 149.3, 149.2, 143.9, 138.5, 138.0, 133.4, 131.7, 130.3, 126.5, 124.7, 122.9, 122.2, 121.5, 119.7, 118.4, 117.3, 116.9 ppm. HRMS (ESI): m/z calcd. For $C_{45}H_{32}IrN_6$ 849.2318; found: 872.5459 (**3.2** + Na).

Synthetic procedure of complexes 3.3 and 3.4

$[Ir(bzq)_2(\mu\text{-}Cl)]_2$ (50 mg, 0.043 mmol) was dissolved in 5 mL of MeOH, then **L3.1** or **L3.2** was added to the solution in an equimolar proportion (**L3.1**, 29.72 mg or **L3.2**, 29.94 mg). The reaction mixture was refluxed for 15 h under argon atmosphere. The resultant suspension was cooled, and the yellow solid was isolated by filtration affording 24.6 mg of **3.3** (61% yield) or 40.08 mg of **3.4** (99% yield) respectively.

Complex **3.3**: ^{1}H NMR (300 MHz, CD_2Cl_2) δ 8.59–8.47 (m, 5H), 8.38–8.31 (m, 2H), 8.25 (d, J = 8.6 Hz, 2H), 8.04 (dd, J = 8.4, 1.3 Hz, 2H), 7.83 (d, J = 8.8 Hz, 2H), 7.72 (d, J = 8.8 Hz, 2H), 7.67–7.48 (m, 8H), 7.41 (dd, J = 8.0, 0.9 Hz, 2H), 7.03 (dd, J = 7.9, 7.2 Hz, 2H), 6.45–6.39 (m, 2H), 6.08 (dd, J = 7.2, 0.9 Hz, 2H) ppm. ^{13}C NMR (75 MHz, CD_2Cl_2) δ 171.9, 149.7, 148.7, 146.9, 145.9, 140.7, 138.5, 137.0, 129.7, 129.4, 129.0, 128.6, 127.4, 127.3, 127.2, 125.7, 123.8, 121.9, 120.2, 118.3, 117.0, 111.8, 105.7 ppm.

Complex **3.4**: ^{1}H NMR (300 MHz, CD_2Cl_2) δ 8.54 (d, J = 5.3 Hz, 2H), 8.47 (t, J = 9.5 Hz, 4H), 8.33 (d, J = 8.1 Hz, 2H), 8.25 (d, J = 1.2 Hz, 2H), 7.86–7.82 (m, 4H), 7.71–7.68 (m, 4H), 7.60–7.49 (m, 6H), 7.39 (d, J = 7.8 Hz, 2H), 7.04 (t, J = 7.5 Hz, 2H), 6.46–6.38 (m, 2H), 6.08 (d, J = 7.1 Hz, 2H) ppm. ^{13}C NMR (75 MHz, CD_2Cl_2) δ 152.3, 149.7, 149.0, 148.7, 138.6, 137.1, 134.3, 132.7, 130.6, 129.7, 129.4, 129.0, 127.4, 123.8, 121.8, 120.2, 118.3, 116.9 ppm. HRMS (ESI): m/z calcd. for $C_{49}H_{32}IrN_6$ 897.2318; found: 906.8221 (**3.4** + Li-H).

3.13 Materials and methods

Cell culture

Human lung carcinoma A549 cell line was cultured in high glucose Dubecco's Modified Eagle's Medium (DMEM) supplemented with 5% fetal bovine serum (FBS) as well as L-glutamine and penicillin/streptomycin at 37 ºC in a humidified atmosphere of 95% air and 5% CO_2.

Cell viability assays

Cell metabolic activity was analysed by an MTT-reduction assay to assess the A549 cell sensitivity to the complexes. Thus, 10^5 cells/mL were seeded in flat-bottom 96-well plates (100 µL/well) in complete medium and allowed to attach for 24 h. A stock solution of the complexes was prepared in DMSO 0.1 M. Subsequent dilutions of the different stock solutions from the complexes using DMEM were prepared. 100 µL/well were added to the cells, in concentrations ranging from 0.2 to 50 µM. Each concentration was performed by quadruplicate. After 5 h of incubation with the complexes, duplicates of each concentration were irradiated with an LED lamp upon 405 and 470 nm with a light dose of 6.5 and 15.1 J/m^2, respectively, for 10 min. Before irradiation, culture medium was replaced with fresh medium in order to avoid interference with non-internalized complexes. Cells were cultured for a further 19 h. Then, 10 µL of MTT (5 mg/mL in PBS) were added to each well and then further 2 h incubation was allowed at 37 ºC. Finally, after removing the culture medium, DMSO (100 µL/well) was added to dissolve the formazan crystals. Multiskan EX 96-well multiscanner autoreader was used to determine the optical density at 550 nm and IC_{50} was calculated. Each experiment was repeated at least three independent analyses.

Cytotoxicity assays

Necrotic and apoptotic cell death was determined by measuring cell membrane permeabilization and phosphatidylserine exposure on cell surface in A549 cells, respectively. 10^5 cells/well were seeded in flat-bottom, 12-well plates (1 mL/well) in complete medium and left 12 h to attach to the plates. Cells were incubated with

complex **3.4** for 5 h, at concentrations of the IC_{50}, 1/2 IC_{50} and 1/4 IC_{50} in quadruplicate before changing culture medium and irradiating at 470 nm of half of the experimental points. After 19 h, cells were trypsinized and thereafter re-suspended in 50 µL of a mixture of DY634-conjugated Annexin V, Annexin-binding buffer (ABB; 140 mM NaCl, 2.5 mM $CaCl_2$, 10 mM HEPES/NaOH pH 7.4) and 7-amino-actinomycin D (7-AAD). After incubation for further 15 min at room temperature in dark, cells were diluted to 300 µL with ABB. A total of 10,000 cells were acquired on a FACSCalibur™ flow cytometer and cell death analysis was performed using Flowjo 7.6.1, CellQuest Pro and GraphPad Prism 8 software.

ROS production measurement

A549 cells ($4 \cdot 10^5$ cells/well) were seeded in flat-bottom, 6-well plates (3 mL/well) in complete medium and allowed attaching for 24 h. Thereafter a DMSO solution of complex **3.4** added to cells up to concentration of IC_{50}, 1/2 IC_{50} and 1/4 IC_{50} in duplicate. Cells were incubated with the complex for 5 h and subsequently half of the experimental points were irradiated at 470 nm after replacing culture medium. Upon 19 h, cells were trypsinised, re-suspended in 100 µL of a mixture of PBS and 2 µM of the dihydroethidium (DHE) probe, incubated at 37 ºC in the dark for 15 min and diluted to 300 µL with PBS. Lastly, a total of 10,000 events were acquired on a FACSCalibur™ flow cytometer and data were analysed using the aforementioned software.

Cell cycle analysis

$4 \cdot 10^5$cells/well (A549) were seeded in complete medium in flat-bottom, 6-well plates (3 mL/well), left overnight to be attached to the bottom and incubated with complex **3.4** at the concentration of 1/4 IC_{50} for 5 h in quadruplicate. Thereupon, cell culture was changed, and half of the experimental points were irradiated at 470 nm. After 19 h in culture, cells were trypsinized, washed twice with PBS, fixed with cold 70% ethanol (v/v) by vortexing and stored at -20 ºC for at least 24 h. After that, cells were washed with cold PBS and stained with 500 µL of a solution of propidium iodide (PI) and RNase for 20 min at room temperature in the dark.

Finally, a total of 10,000 cells were acquired on a FACSCalibur™ flow cytometer and data were analysed using the software mentioned above.

Fluorescence confocal microscopy assay

A549 cells ($8 \cdot 10^3$ cells/well) were seeded in µ-slide 8 well (300 µL/well) in complete medium and left 24 h to get attached to the bottom of the slide. After removing 200 µL of culture medium from each well, 100 µL of a solution of the corresponding complexes were added reaching a final concentration of 2 µM. The complexes were incubated with the cells for 24 h, and thereafter, the internal standard MitoTracker Red (MTR) was added to a final concentration of 15 nM. MTR was incubated with the cells for further 15 min at room temperature. Finally, the medium of each well was replaced with fresh medium phenol red free. Images were collected in a ZEISS LSM 880 confocal microscope in a sequential mode with a 40 oil immersion lens. Specifically, it was used a line average of 4, a format of 1024 × 1024 pixels and an excitation wavelength of either 458 nm or 588 nm with a confocal pinhole of 1 Airy unit. Images were analysed ZEISS ZEN lite (blue edition) a free software.

Distribution coefficient ($logP_{7.4}$) measurement

The n-octanol-water coefficient of complexes **3.1**-**3.4** and **L3.1** and **L3.2** were determined using a shake-flask method.[26] A mixture of buffered-saline distilled water (100 mL, phosphate buffer [PO_4^{3-}] = 10 mM, [NaCl] = 0.15 M, pH 7.4) and n-octanol (100 mL) was shaken for 72 h to allow saturation of both phases. Approximately 0.5 mg of the complexes or ligands were dissolved in 3 mL of the aqueous phase and 3 mL of the organic phase were added, mixing them for 10 min. The resulting emulsion was centrifuged to separate the phases. The concentration of the compounds in each phase was determined using UV absorbance spectroscopy at 298 K. $logP_{7.4}$ was defined as log{[compound(organic phase)]/[compound(aqueous phase)]}.

[1] A. Seluanov, V.N. Gladyshev, J. Vijg, V. Gorbunova, *Nat. Rev. Cancer* **2018**, *18*, 433-441.
[2] C. Holohan, S. Van Schaeybroeck, D.B. Longley, P.G. Johnston, *Nat. Rev. Cancer* **2013**, *13*, 714-726.
[3] C. Abels, *Photochem. Photobiol. Sci.* **2004**, *3*, 765-771.
[4] A.P. Castano, P. Mroz, M.R. Hamblin, *Nat. Rev. Cancer* **2006**, *6*, 535-545.
[5] A.C. Jung, F. Moinard-Butot, C. Thibaudeau, G. Gasser, C. Gaiddon, *Pharmaceutics* **2021**, *13*, 1788-1805.
[6] F. Heinemann, J. Karges, G. Gasser, *Acc. Chem. Res*. **2017**, *50*, 2727-2736.
[7] G. Shi, S. Monroa, R. Hennigar, J. Colpitts, J. Fong, K. Kasimova, H. Yina, R. DeCoste, C. Spencer, L. Chamberlaina, A. Mandel, L. Lilgec, S.A. McFarland, *Coord. Chem. Rev.* **2015**, *282*, 127-138.
[8] A. Frei, R. Rubbiani, S. Tubafard, O. Blacque, P. Anstaett, A. Felgentrager, T. Maisch, L. Spiccia, G. Gasser, *J. Med. Chem*. **2014**, *57*, 7280-7292.
[9] L. Flamigni, A. Barbieri, C. Sabatini, B. Ventura, F. Barigelletti, *Photochemistry and Photophysics of Coordination Compounds II*, Springer, Berlin, **2007**, 143-203.
[10] C. Jin, J. Liu, Y. Chen, R. Guan, C. Ouyang, Y. Zhu, L. Ji, H. Chao, *Sci. Rep.* **2016**, *6*, 22039-22052.
[11] W. Lv, Z. Zhang, K.Y. Zhang, Y, Zhang, H.R. Yang, S.J. Liu, A. Xu, S. Guo, Q. Zhao, W. Huang, *Angew. Chem. Int. Ed*. **2016**, *55*, 9947-9951.
[12] L. He, Y. Li, C.-P. Tan, R.-R. Ye, M.-H. Chen, J.-J. Cao, L.-N. Ji, Z.-W. Mao, *Chem. Sci.*, **2015**, *6*, 5409-5418.
[13] X. Tian, Y. Zhu, M. Zhang, L. Luo, J. Wu, H. Zhou, L. Guan, G. Battaglia, Y. Tian, *Chem. Commun.* **2017**, *53*, 3303-3306.
[14] Y. Xie, Y. Ding, X. Li, C. Wang, J.P. Hill, K. Ariga, W. Zhang, W. Zhu, *Chem. Commun.* **2012**, *48*, 11513-11515.
[15] M. Vaquero, A. Ruiz-Riaguas, M. Martínez-Alonso, F.A. Jalón, B.R. Manzano, A.M. Rodríguez, G. García-Herbosa, A. Carbayo, B. García, G. Espino, *Chem. Eur. J.* **2018**, *24*, 10662-106673.
[16] R.D. Costa, E. Ortí, H.J. Bolink, F. Monti, G. Accorsi, N. Armaroli, *Angew. Chem. Int. Ed.* **2012**, *51*, 8178-8211.
[17] S.S. Bhat, V.K. Revankar, R.V. Pinjari, S. Naveen, N.K. Lokanath, V. Kumbar, K. Bhate, D.G. Kokarea, *New J. Chem.* **2018**, *42*, 16846-16854.
[18] S. Sperandio, K.S. Poksay, B. Schilling, D. Crippen, B.W. Gibson, D.E. Bredesen, *J. Cell. Biochem.* **2010**, *111*, 1401-1412.
[19] G.J. Kops, B.A. Weaver, D.W. Cleveland, *Nat. Rev. Cancer* **2005**, *5*, 773-785.
[20] C.A. Lipinski, F. Lombardo, B.W. Dominy, P.J. Feeney, *Adv. Drug Deliv. Rev.* **2001**, *46*, 3-26.
[21] https://www.thermofisher.com/order/fluorescence-spectraviewer#!/
[22] X. Liu, P. Dai, T. Gu, Q. Wu, H. Wei, S. Liu, K.Y. Zhang, Q. Zhao, *J. Inorg. Biochem*. **2020**, *209*, 111106-111116.
[23] H. Huang, S. Banerjee, P.J. Sadler, *ChemBioChem* **2018**, *19*, 1574-1589.

[24] S. Sprouse, K.A. King, P.J. Spellane, R.J. Watts, *J. Am. Chem. Soc.* **1984**, *106*, 6647-6653.
[25] G.R. Fulmer, A.J.M. Miller, N.H. Sherden, H.E. Gottlieb, A. Nudelman, B.M. Stoltz, J.E. Bercaw, K.I. Goldberg, *Organometallics* **2010**, *29*, 2176-2179.
[26] E. García-Moreno, E. Cerrada, M.J. Bolsa, A. Luquin, M. Laguna, *Eur. J. Inorg. Chem.* **2013**, *2013*, 2020-2030.

Chapter 4

4.1 Introduction

Heterocycles are an important class of compounds widely distributed in nature. These compounds make up the majority of known organic molecules and exhibit a diverse range of properties. For instance, they play a key role in metabolism, being part of the structure of several hormones, vitamins, and antibiotics.[1,2] In view of this biological compatibility, heterocycles have been investigated as pharmacophores with the aim of developing novel and more selective drugs for different illnesses. Among all heterocyclic compounds, those five-membered heterocycles which contain nitrogen atoms in their structures, known as azoles, exhibit a tendency to be biologically active and open the door for being used in several disciplines, such as biochemistry, or medicine.[3]

In 1944, the antifungal activity of an azole derivate, benzimidazole, was reported for the first time.[4] However, it was not until 1958 that the scientific community became interested in the activity of these heterocycles, thanks the introduction of clotrimazole, a topical drug to treat fungal skin infections. Since this pioneer example, many others have followed. Pfizer developed a broad-spectrum triazole with antifungal properties, Fluconazole, which was approved in 1990 for its use in the treatment of oesophageal, vaginal, and genitourinary infections.[5] Maintaining a similar structural pattern, several analogues were developed, such as Voriconazole, or Ravuconazole (see Figure 4.1).

In view of the good results previously mentioned, azole derivate seem to be an indispensable starting point in drug discovery. A plausible reason for explaining their great biological properties could be due to their small and stable cyclic ring structure, in which the nitrogen atoms can act both, as hydrogen bond donor and acceptors at the active site of the receptor, allowing for stronger and more selective interactions. In addition, it has been reported that triazoles show a tendency to be involved in other interactions, such as coordination with metals at the receptor sites of some enzymes for instance, tirosynase,[6] and undergo π-πstacking interactions.[7]

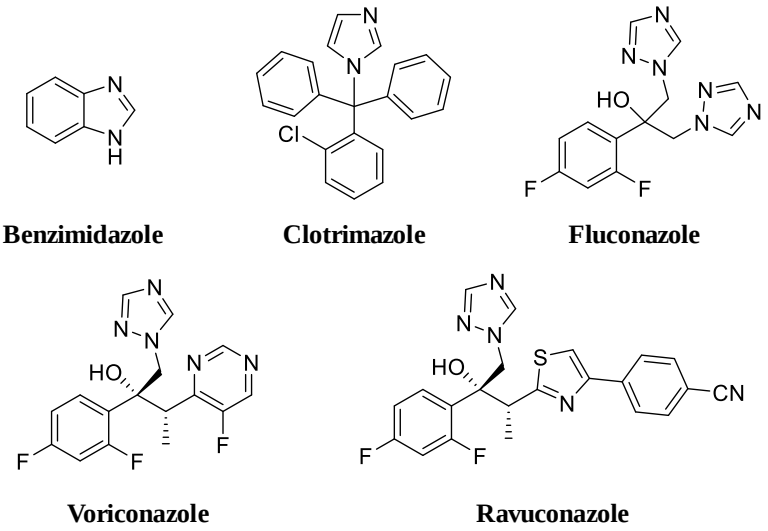

Figure 4.1. *Chemical structures of azole-derivate used as antifungals over the years.*

However, because of the excessive use of these compounds as antifungals, resistance to them were acquired. Therefore, it is vital to synthetize novel azole derivates than can circumvent this resistance problem. For this purpose, medicinal inorganic chemistry is devoted huge effort in the development of metallic complexes which contain azole derivate in their structure in aim of modulating their properties, minimizing their side-effects, and opening the door for their use in other medical areas as could be antibiotics, antipyretic, or anticancer compounds.[8,9] Ir^{III} complexes have attracted much attention as plausible PSs due to their tuneable properties that can enhance water solubility and photostability compared to traditional PSs. Several examples of cyclometallated Ir^{III} complexes containing azole derivate in their structures have been reported in the recent years.[10] Most of them exhibit a clear tendency to internalize in lysosomes as have been demonstrated through techniques as confocal microscopy, FLIM or ICP-mass spectrometry.[11]

Lysosomes are acidic organelles, with a pH between 4.5 and 5.5, that contain hydrolytic enzymes able to degrade most biomolecules. A severe disruption of the lysosomes can generate lysosomal membrane permeation (LMP),[12] that in last term induce cell death via apoptosis. As lysosomes are involved in cell death mechanism, they are emerging as potential targets for targeted cancer therapy.[13,14]

In 2015, Mao and collaborators reported some Ir^{III} complexes acid-sensitive with β-carbonile groups for targeting the lysosomes.[15] These complexes showed lysosome-targeted pH-responsive singlet oxygen production and high phototoxicity. Their phosphorescent properties were used to track the lysosomal integrity after PDT treatment, thereby providing a method for monitoring *in situ* the therapeutic effect of PDT. Further studies demonstrated that these complexes induce caspase-dependant apoptosis through lysosomal damage after irradiation (a.w. 425 nm). In Figure 4.2 the structure of the most active complex of the series and its lysosomal biodistribution in A549 cell line are shown.

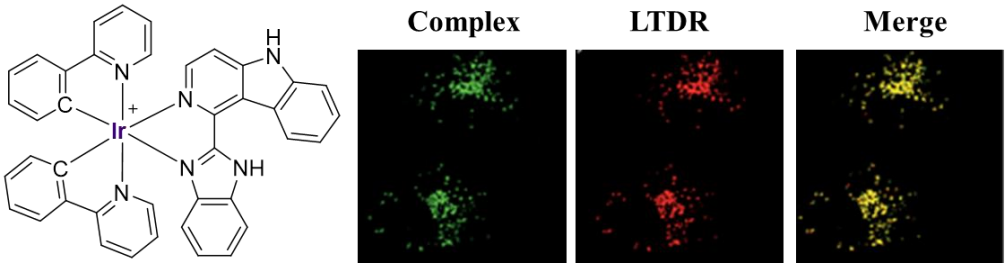

Figure 4.2. *Chemical structure of complex developed by Mao and coworkers, and its biodistribution in A549 cells, using LysoTracker Deep Red (LTDR) as a marker of lysosomes.*[15]

The good results obtained inspired many research groups to develop further series of Ir^{III} complexes containing benzimidazole derivates as lysosome-targeted PDT.

In this context, Espino and collaborators also reported cyclometallated Ir^{III} complexes containing benzimidazolyl fragments, as shown Figure 4.3.[16] Biological studies revealed that these complexes have a moderate cytotoxicity in the dark against different human cancer cell lines. Surprisingly, these complexes exhibited mitochondrial accumulation, something less common for iridium complexes bearing azole ligands, and, upon photoactivation, the complexes induced mitochondrial membrane depolarization and DNA damage, thus triggering cell death, mainly by apoptosis.

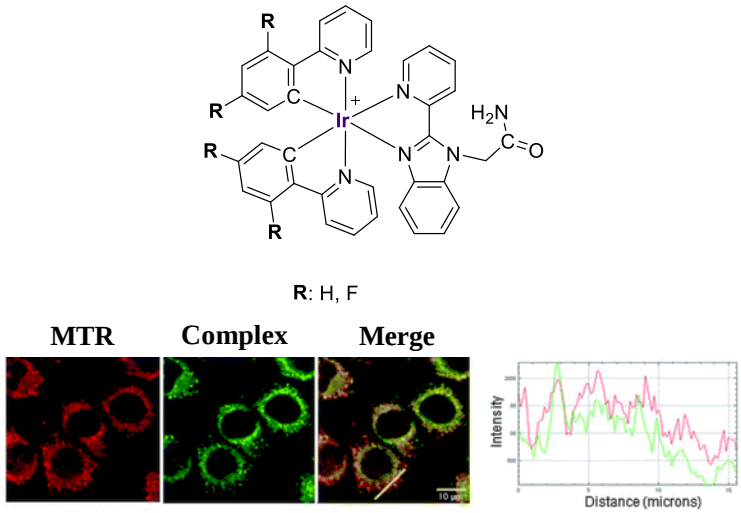

Figure 4.3. *Chemical structures of complexes reported by Espino and coworkers, and biodistribution for complex containing R:H on SK-Mel-28 cells (melanoma cancer cell line), using MitoTracker Red (MTR) as a marker of mitochondria.*[16]

Among the published Ir^{III} complexes containing azole moieties as auxiliary ligands, some examples have been reported by our research group on 2022.[17] Their antiproliferative activity against lung cancer A549 cells increased up to 15 times upon irradiation conditions, reaching IC_{50} values in the nanomolar range and pointing them as good PSs candidates for photodynamic therapy via $^1O_2$ generation. Their cellular biodistribution analysis by fluorescence microscopy and FLIM techniques suggested the lysosomes as accumulation organelle. (Figure 4.4)

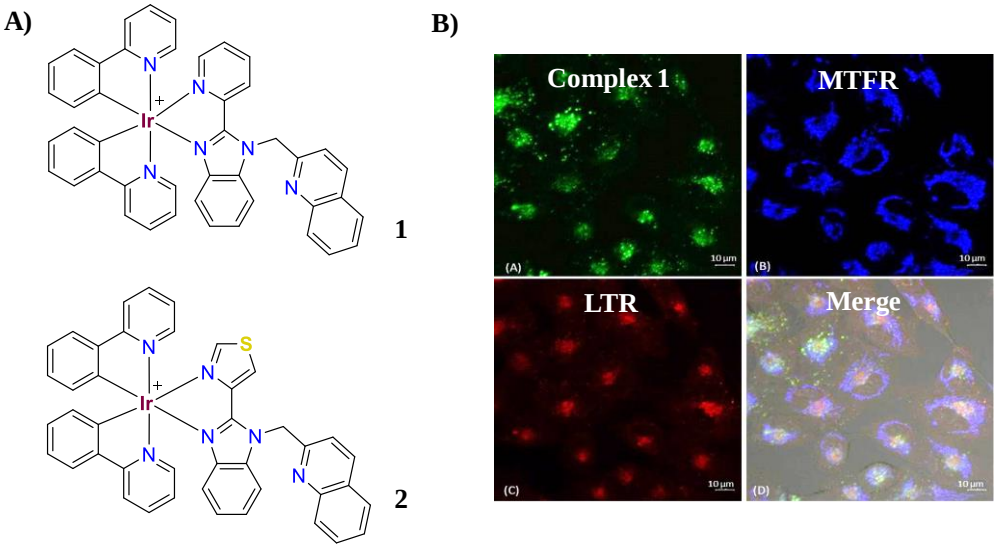

Figure 4.4. *A) Chemical structures of complexes reported; B) biodistribution or complex 1 in A549 cells, using MitoTracker Far Red (MTFR) as a marker of mitochondria, LysoTrakcer Red (LTR) for staining lysosomes.*[17]

4.2 Objectives and methodology

This chapter describes the development of a new class of emissive cyclometallated iridium (III) complexes with general structure of the type $[Ir(C\hat{}N)_2(N\hat{}N)]^{+/0}$, where C^N is methyl-2-phenylquinoline-4-carboxylate (mpc) and N^N are different families of the azole derivates. Then, evaluation of the complexes as both, chemotherapeutic and PS agents, are thoroughly addressed.

In the context of PDT, the initial step is to develop an Ir^{III} complex containing cyclometallated ligands capable of shifting the absorption pattern of these complexes to higher wavelengths to allow treating tumors in deeper tissues.[18] Additionally, increasing the solubility in physiological media is also extremely important for the good performance of any drug. A good cylometallated ligand design could be key for achieving these features. Later, the addition of the different azole derivates in presence or absence of an extrinsic base afforded the final complexes.

On top of that, these Ir^{III} complexes offer the possibility of tracking them into cells using fluorescence confocal microscopy and providing information on their biological interplay and final targets.

As previously mentioned, azole compounds have been used in medicine as treatment of several diseases. In this chapter, not only the azole-containing complexes will be evaluated as anticancer agents, but also as senolytic probes. For that purpose, cytotoxicity, ficoll, senescence induction, stability, and *in vivo* assays, among others, will be performed, while the entire process can be tracked thanks to the emissive capacity of cyclometalled Ir^{III} complexes.

4.3 Synthesis and characterization

The synthetic approach for obtaining the desired Ir^{III} PS agents requires, in the first instance, an appropriate design of the cyclometallated ligand that must assist the Ir^{III} to fulfil certain characteristics as being water-soluble, photostable and capable to be activated by low energy irradiation in order to treat inner tumors, among others. For this purpose, a derivate of 2-phenylpyridine, the 2-phenylquinoline-4-carboxylic acid, was chosen. This molecule exhibits higher aromaticity and less flexibility than its analogous 2-phenylpyridine, two conditions that force a redshift of the emission when cyclometallated to a Ir^{III} core.[19] Additionally, the presence of a carboxylic group in the cyclometallated ligand allows for easy functionalization of its structure. This carboxylic group was changed to a methyl ester group, by a protection step, in order to avoid undesirable side reactions. The final cyclometallated ligand that is going to be used throughout this chapter is methyl-2-phenylquinoline-4-carboxylate (mpc), as shown in Figure 4.5.

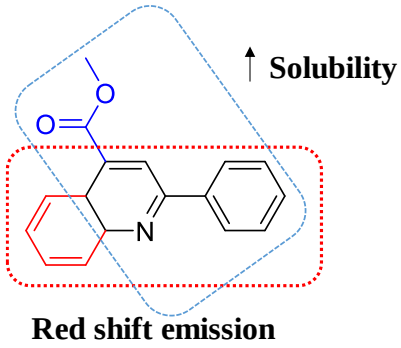

Figure 4.5. *Explained depiction of the designed cyclometallated ligand.*

The first step then, prior to the synthesis of the Ir^{III} dimer precursor involves protecting 2-phenylquinoline-4-carboxylic acid. This ligand is refluxed in thionyl chloride for two hours, resulting in the corresponding highly reactive acylchloride. The excess of thionyl chloride is neutralized using ammonia, and methanol is immediately added. The mixture is stirred for 4 hours at room temperature, yielding the desired compound in high yield. The next step is the preparation of the correspondent dimer, $[Ir(mpc)_2(\mu\text{-}Cl)]_2$, which is prepared by refluxing methyl-2-phenylquinoline-4-carboxylate with $IrCl_3 \cdot nH_2O$ using 2-ethoxyethanol as a

solvent. After 24 h a dark red-black suspension appears. The solid is isolated by filtration and washed with water, ethanol, and acetone, affording the desired dimer in moderate yield (64%) as a garnet solid. (Scheme 4.1).

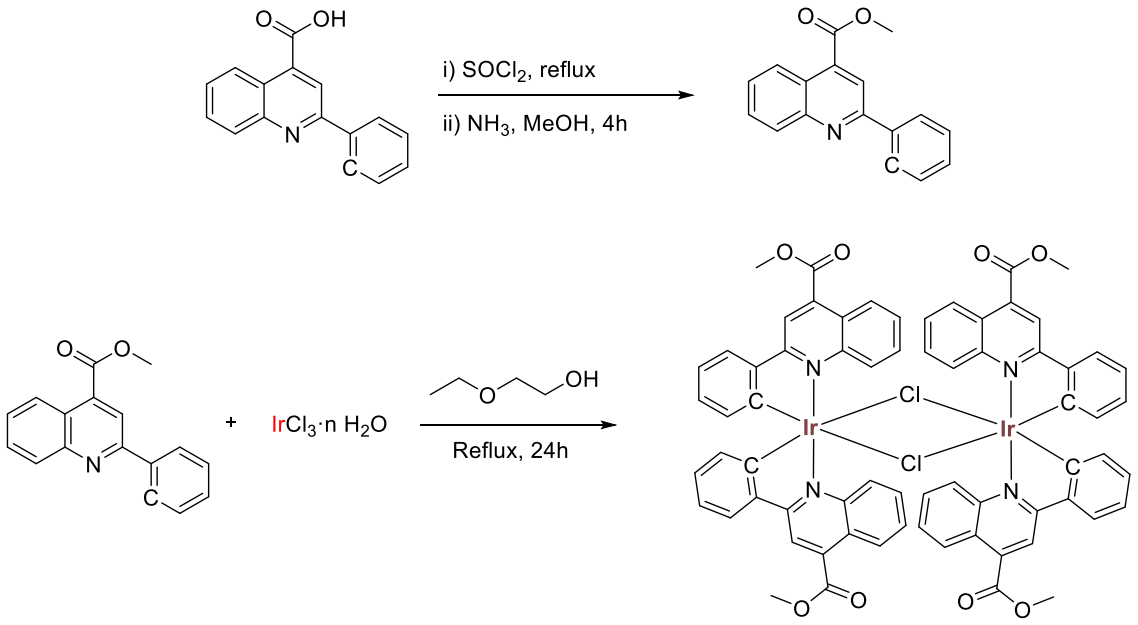

Scheme 4.1. *Synthetic pathway for the synthesis of iridium (III) dimer precursor.*

Once that the precursor was obtained, it was refluxed with two equivalents of the different azole derivates. The choice of azoles as N^N ligands was not made randomly. As discussed in the introduction section, azole derivatives have been widely employed due to their outstanding properties in the field of medicine.

Recently, the use of metal complexes containing these derivatives in their structure has experienced a strong increase, due to their promising anticancer properties and the possibility of using them as PSs. With this aim, it was decided to use azoles with different structures in order to try to control their properties. The complexes of the first two families contain, 2-(2-pyridyl)benzimidazole (**4.1** and **4.2**) and 2-(4-thiazolyl)benzimidazole (**4.3** and **4.4**), respectively, to determine how the properties of the iridium complexes can be modified with the change of the pyridyl group for the thiazolyl group (Figure 4.6). In the case of the third (**4.5** and **4.6**) and fourth (**4.7** and **4.8**) families, the goal is to understand how increasing the number of nitrogen atoms present in the azole ring can modulate the final properties of the complexes, for which the ligands, 3-(2-pyridyl)pyrazole, 2-(1H-1,2,4-triazol-3-

yl)-pyridine, and 2-(2H-tetrazol-5-yl)pyridine will be used. Additionally, considering that previous publications have shown that complexes containing azoles exhibit a high dependence on the pH of the medium, cationic, and neutral complexes have been sought for all the families.

Refluxing $[Ir(mpc)_2(\mu\text{-}Cl)]_2$ in dry dichloromethane with two equivalents of the desired azole in presence of an extrinsic base, Cs_2CO_3, for 20 h gave rise to neutral complexes, **4.1**, **4.3**, **4.5** and **4.7**, as red suspensions, which were filtered, washed with pentane, and dried. On contrary, for the synthesis of their cationic analogues (**4.2**, **4.4**, **4.6**, and **4.8**), a mixture of dry solvents, DCM:MeOH (1:1), was required. After 20 hours of reflux, the reaction was complete. To isolate these complexes, the volume of solvents had to be reduced to a minimum and pentane was added, affording the desired complexes (Figure 4.6). In all cases, it was necessary to use a chromatographic column to purify the complexes, using a mixture of DCM:MeOH (9:1) as the eluent. Complexes were obtained in moderate to good yields (64-82%), due to yield loss during the purification steps.

All their structures were characterized using different techniques, such as ^{1}H, $^{13}C\{^{1}H\}$ spectroscopy, mass spectrometry (HRMS- ESI), and in some cases, X-Ray diffraction.

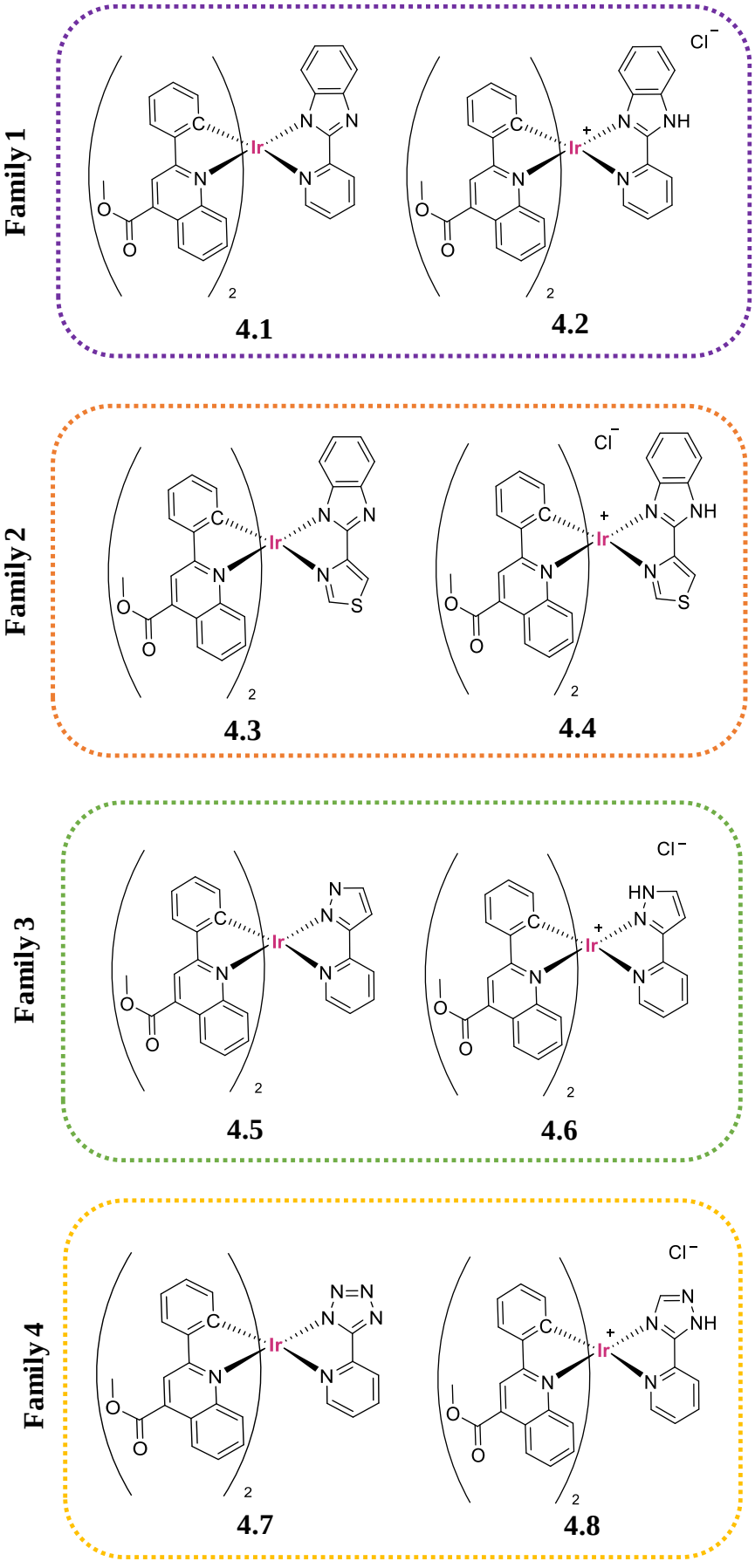

Figure 4.6. *Chemical structures of synthetized families of complexes.*

^{1}H-NMR spectra were well-defined for all synthetized complexes, and the typical pattern for these asymmetric derivatives could be observed. In particular, the methyl ester protons that appeared as a singlet in the dimer precursor, unfold in two different singlets, corroborating the coordination of azole-derivates to the iridium center (blue dots), as well as, the asymmetry of the final complexes. This fact was also verified by the singlet of cyclometallated ligand that was integrated by two protons (green dot) that evolves in two singlets integrating by one proton each, in the final complexes. Figure 4.7 shows the ^{1}H-NMR spectra of $[Ir(mpc)_2(\mu\text{-}Cl)]_2$, as well as complex **4.3**, where not only the shift for all the mpc protons are observed upon coordination of 2-(4-thiazolyl)benzimidazole, but also the different proton integration in because the inequivalence of both cyclometallated ligands in **4.3**.

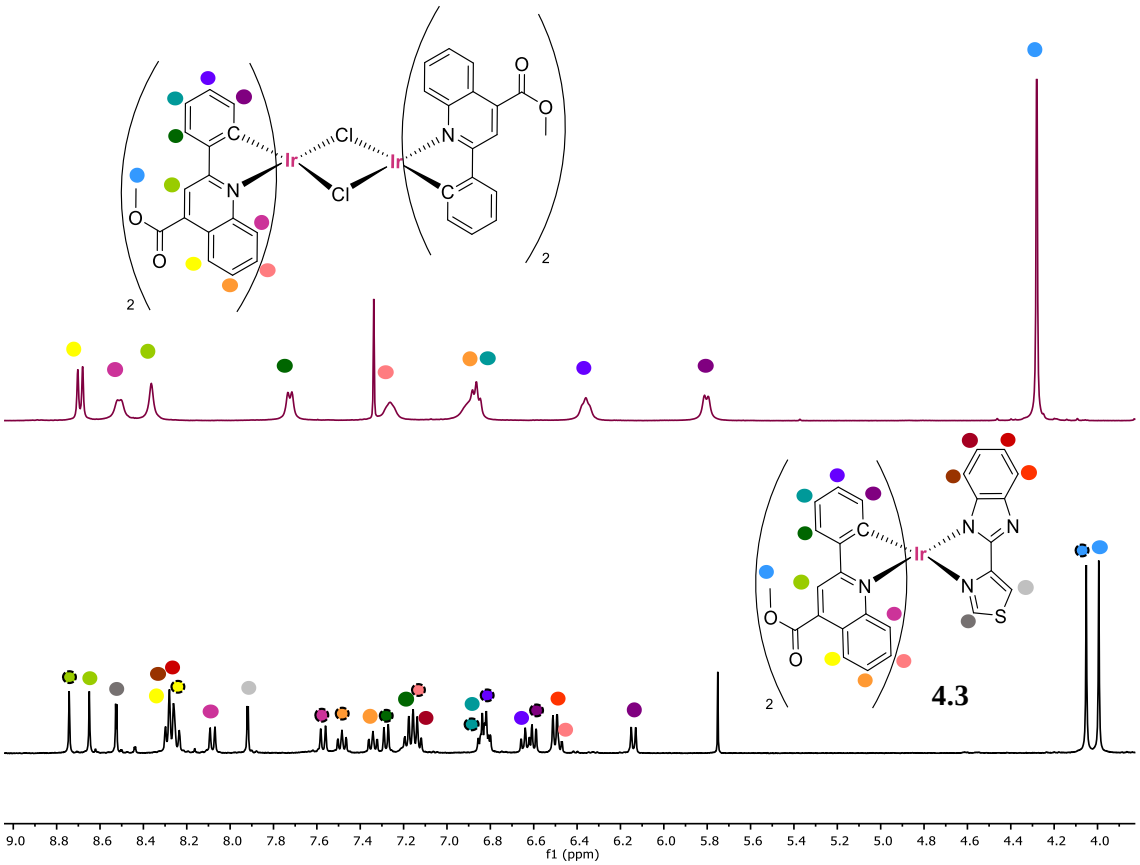

Figure 4.7. *Comparative ^{1}H-NMR (400 MHz) spectra of $[Ir(mpc)_2(\mu\text{-}Cl)]_2$ and complex **4.3**. Solvent: $CDCl_3$ (dimer), DMSO (**4.3**).*

Focusing on the different pairs, the main different between the complexes relies on the presence of the amine proton upshifted if the complex is cationic and its absence if the complex is neutral. In the particular case of complexes **4.5** and **4.6**, this proton appears at 13.95 ppm for cationic complex **4.6** (purple dot), which disappears in neutral complex **4.5**, as shown in Figure 4.8. The same behavior was observed for **4.1**, **4.4**, and **4.8**, which resonances appeared at 12.94, 12.97 and 13.17 ppm, respectively. In addition, the characteristic singlet protons of methyl 2-phenylquinoline-4-carboxylate (green and blue dots) of cyclometallated ligand mpc, changes and appeared as two singlets as a consequence of the asymmetry in the final complex following the same trend previously seen for complex **4.3** (Figure 4.7).

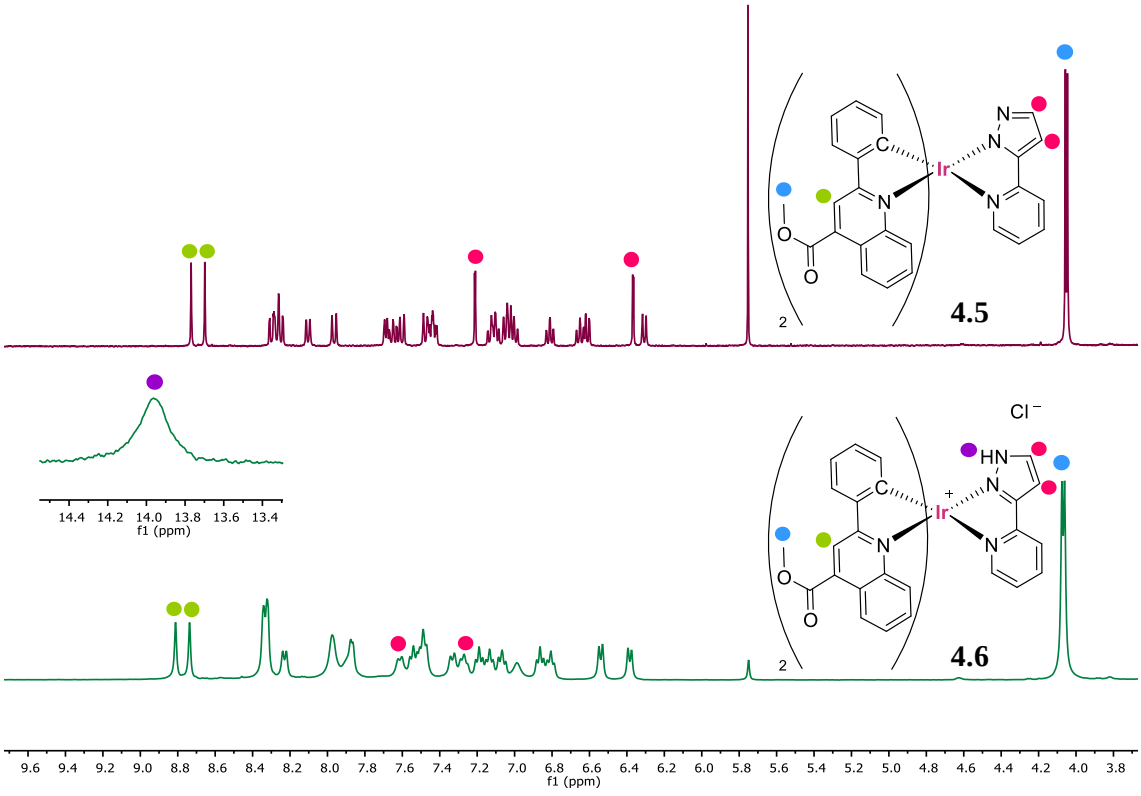

Figure 4.8. *Comparative ^{1}H-NMR (400 MHz) spectra of complexes **4.5** and **4.6**. Solvent: DMSO.*

Furthermore, all complexes were characterized using $^{13}C\{^{1}H\}$ spectroscopy and HRMS-ESI, corroborating once again their successful synthesis. However, the neutral complexes (**4.1**, **4.3**, **4.5** and **4.7**), appear protonated as $M+H^{+}$, in their mass

spectra as a consequence of the energetic technique (ESI) used for characterizing them.[20]

In addition, crystals of complex **4.4** and **4.7** were isolated and measured by X-Ray diffraction. They were obtained as bright dark red needles by slow diffusion of pentane into a dichloromethane solution of **4.4**. The analysis of their X-Ray structure indicates that this asymmetric molecule crystallizes in a monoclinic P2(1)/c space group. The unit cell is formed by two independent molecules of the Λ enantiomer and two molecules of dichlorometane. As shown in Figure 4.9, the crystalline structure exhibits the typical spatial distribution for this type of cyclometallated Ir^{III} complexes, where ligands adopt an octahedral disposition around the metal center. As it was expected, the pyridyl nitrogen atoms of the orthometallated ligand, mpc, are coordinated to the iridium centre in *trans* to each other, and the angles are close to the ideal octahedral disposition of 180º. In addition, the diamine ligand bite angle (N3-Ir1-N4) is smaller 75.6(2)º, than the ones of cyclometallated ligands, 93.4(3) and 92.8(2)º, respectively. No relevant non-covalent interactions have been observed between molecules.

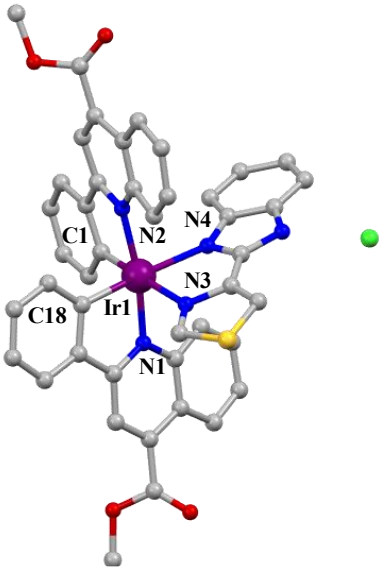

Bond Lenghts (Å)	**Ir1-N1**	2.107(5)
	Ir1-N2	2.079(6)
	Ir1-N3	2.190(5)
	Ir1-N4	2.190(6)
	Ir1-C1	1.991(7)
	Ir1-C18	1.998(6)
Angles º	**N1-Ir1-N2**	170.5(2)
	N2-Ir1-C1	93.4(3)
	N1-Ir1-C18	92.8(2)
	N3-Ir1-N4	75.6(2)

Figure 4.9. *Mercury representation of the crystalline structure of complex* ***4.4*** *(hydrogen atoms have been omitted for clarity) and table with the most significant bond angles (°) and bond distances (Å).*

Regarding complex **4.7**, it crystalized as dark red cubes by slow diffusion of pentane into a dichloromethane solution of the complex. The analysis of X-Ray structure of this complex revealed that crystalized in monoclinic P2(1)/c space group. The unit cell is formed by a molecule of Λ enantiomer of complex **4.7** and a molecule of dichloromethane, the crystallization solvent.

Once again, its crystalline structure exhibits the typical spatial distribution for octahedral complexes, with the pyridyl nitrogen atoms of the mpc ligand in *trans* to each other. As its previously analogue **4.4**, this structure presents an angle N1-Ir1-N2 of 174.1(1)º, very close to the ideal, 180º, expected for an octahedral complex. The main difference that can be observed for the bite angles of cyclometallated ligands 95.7º and 96.0º, respectively, and the much smaller 75.3º, which correspond to the diimine ligand. The most significant bond distances and angles are collected in Figure 4.10. No relevant non-covalent interactions have been observed.

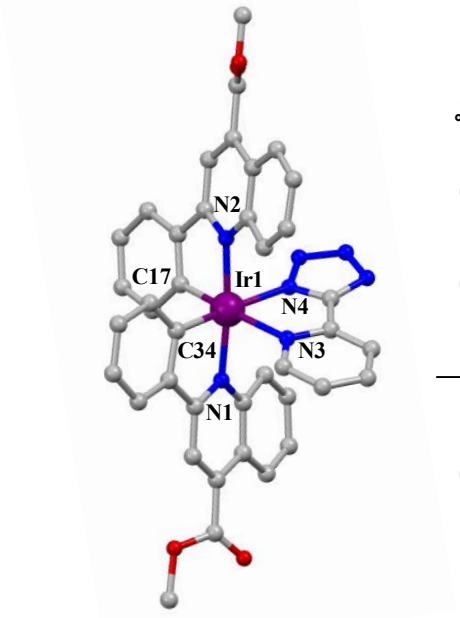

Bond Lenghts (Å)	**Ir1-N1**	2.084(3)
	Ir1-N2	2.086(4)
	Ir1-N3	2.198(3)
	Ir1-N4	2.120(3)
	Ir1-C17	1.996(4)
	Ir1-C34	1.996(3)
Angles º	**N3-Ir1-N4**	75.3(1)
	N2-Ir1-C17	95.7(1)
	N1-Ir1-C34	96.0(1)
	N1-Ir1-N2	174.1(1)

Figure 4.10. *Mercury representation of the crystalline structure of complex* ***4.7*** *(hydrogen atoms have been omitted for clarity) and table with the most significant bond angles (°) and bond distances (Å).*

4.4 Optical properties

Photophysical properties of complexes **4.1** to **4.8** were measured in DMSO solution at room temperature. The most relevant data are collected in Table 4.1.

Table 4.1. *Luminescent properties of complexes **4.1**-**4.8**.*

	UV/vis·10^4 (ε[$dm^3mol^{-1}cm^{-1}$])	**λ_{em} (λ_{exc}) [nm]**	**ζ^a [ns]**	**Φ^a**	**Φ^b**
4.1	273 (8.8), 354 (7.1), 466 (0.8)	715 (590)	60	20.3	32.3
4.2	269 (7.2), 292 (6.3), 313 (5.9), 327 (6.0), 349 (4.9), 463 (0.6)	702 (590)	260	19.2	27.5
4.3	273 (8.7), 315 (5.9), 356 (3.8), 471(0.8)	725 (600)	54	13.7	36.9
4.4	271 (8.7), 294 (7.3), 355 (3.8), 469 (0.7)	690 (592)	257	21.1	40.6
4.5	273 (9.1), 357 (4.2), 461 (1.1)	720 (590)	50	19.7	41.6
4.6	271 (6.9), 259 (6.0), 355 (3.3), 464 (0.6)	690 (610)	265	23.6	56.1
4.7	271 (6.7), 293 (5.6), 357 (3.1), 482 (0.5)	690 (573)	188	20.6	45.8
4.8	270 (7.2), 292 (5.5), 357 (7.1), 466 (0.8)	698 (585)	166	19.4	47.2

[a] Aerated DMSO solution. [b] Deoxygenated DMSO solution

UV/vis spectra and quantum yields collected in DMSO solution at [10^{-5}M], luminescent properties and lifetimes measured in DMSO solution at [10^{-3}M].

UV-Visible spectra for all the complexes shows intense absorption bands bellow 300 nm that can be assigned based on published studies to ligand centered spin-allowed $\pi \rightarrow \pi^*$ transitions.[21,22] See Figure 4.11. In addition, other bands with lower intensity appeared between 280 and 400 nm. Those bands could be attributed to forbidden intraligand $^3\pi \rightarrow \pi^*$ and ^{1}MLCT transitions. Over 400 nm, it is appreciable a long tail that is typically associated in this type of complexes with a forbidden ^{3}MLCT transition.[23]

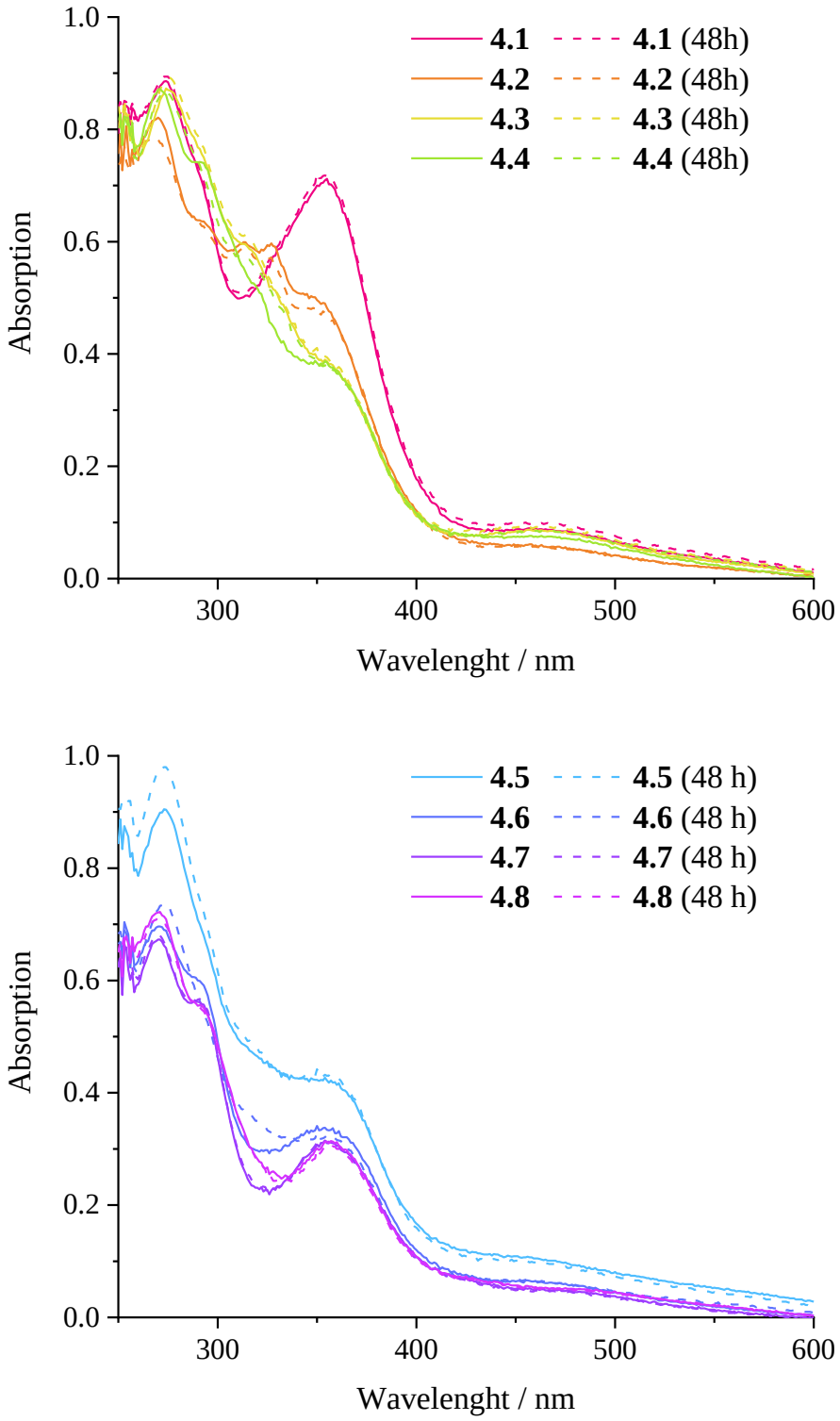

Figure 4.11. *Absorption spectra in DMSO:PBS (1:1) solution at [10^{-5}M] of complexes* ***4.1-4.8*** *and their stabilities at 48 hours and 310 K.*

In addition, the stability of the complexes was studied by UV spectroscopy in both, DMSO and in a mixture of DMSO/PBS (1:1) during 48 h at 310 K. As seen in Figure 4.11, no changes were observed in their absorption band patterns, confirming their structural stability under these conditions. It is important to note that the selection of the specific conditions for the stability assay was not random, but rather aimed to corroborate the stability of the complexes under conditions similar to those used for the biological assays.

Regarding their emission spectra, complexes **4.1**-**4.8** present a structureless emission, which maximum are in a range of 690 to 725 nm, as it can be seen in Figure 4.12. These emissions bands could be assigned mainly to ^{3}MLCT/^{3}LLCT.[24] This origin assignation is in concordance with that made for similar complexes reported in the literature.[25,26] An important consideration is that emission maximum is dependent of the charge of complexes. Focusing on the different family pairs, neutral complex **4.1** exhibits a maximum emission (715 nm) less energetic than its cationic analogous, **4.2** (702 nm). The same tendency is observed for complexes of families 2 and 3, where neutral complexes **4.3** and **4.5**, exhibit less energy maximum emissions (725, 720 nm, respectively) in comparison with their cationic analogues **4.4** and **4.6** (690 nm in both cases). This trend could be explained as a consequence of the modification of frontier orbitals. As expected, cationic species have their maxima blue-shifted in comparison with their neutral counterparts due to the less electron density on the metal center that ultimately stabilizes the HOMO orbitals.[27]

A titration experiment was performed to monitor the change of emission of complexes **4.5**-**4.6** at different pH levels, Figure 4.13. For this purpose and using as starting material complex **4.5**, subsequent additions of a diluted solution of HCl [10^{-5} M] were added, affording the modulation of pH until the total conversion of **4.5** to **4.6**. In parallel titration assay was performed using 2 mL of a solution of complex **4.5** [10^{-5} M], and drop-by-drop HCl [10^{-5} M] was added in order to reproduce the conditions of luminometer assay, for controlling de pH variations, after each addition, a pH-meter was used, the setup of this assay is collected in

Figure 4.14. The estimated value of pK_a was 5.17, which is useful for biological purpose. pH lower than 6.0 are usually associated with tumour tissues or hypoxia. Then, this pH- dependency could help to target the complexes to cancer cells.[28]

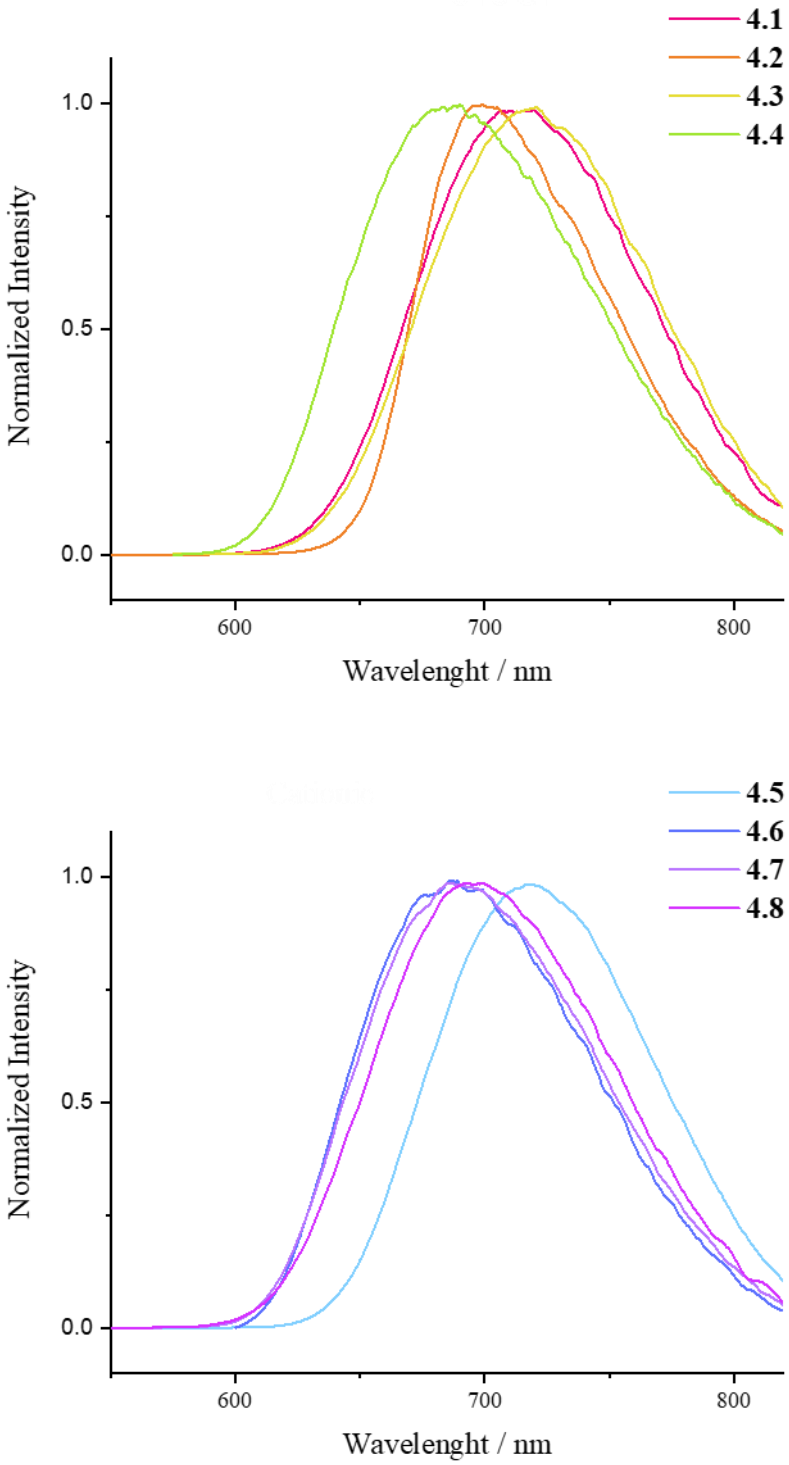

Figure 4.12. *Emission spectra in DMSO solution of complexes* ***4.1-4.8*** *at 298 K.*

In regard to their lifetimes, all values ranged between 50 to 260 ns, corroborating the phosphorescent nature of the emission. Neutral complexes exhibit lower lifetimes than their cationic analogues. Quantum yield values were also measured in aerated and deaerated DMSO solutions. All of them exhibit excellent quantum yields in aerated solutions, with values around 20%. These values experience a considerable increase in deaerated solution. It is especially remarkable the case of complex **4.8**, which quantum yield goes from 23.6 to 56.1% as result of the deoxygenation. See Table 4.1.

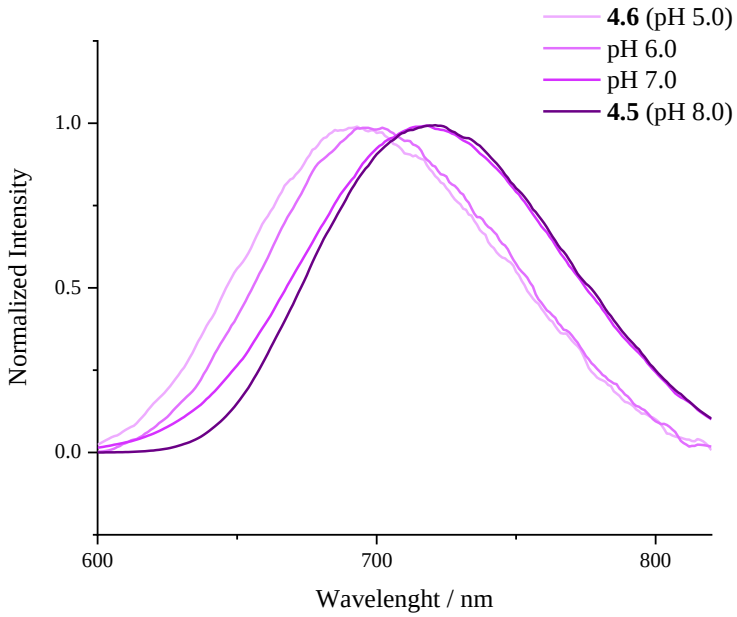

Figure 4.13. *Change on emission maximum of complex* ***4.5*** *at different pH, until total conversion to complex* ***4.6****.*

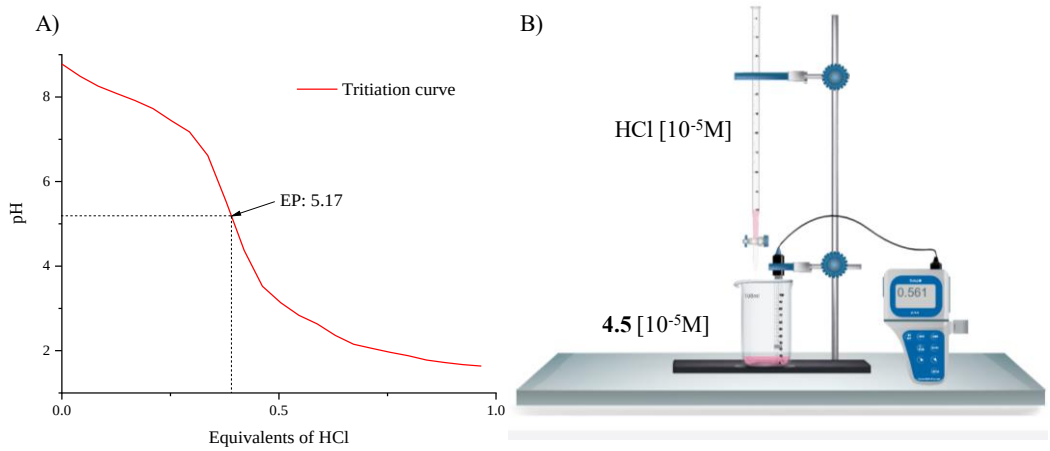

Figure 4.14. *Titration experiment of complex* ***4.5****. A) Estimation of its* pK_a *using a solution of HCl [*10^{-5} *M], B) Experimental setup of titration assay.*

4.5 Biological properties

At this point, complexes are going to be divided in pairs, (**4.1**-**4.2**; **4.3**-**4.4**; **4.5**-**4.6**), in order to study their biological properties more deeply, and how these are affected by the different coordination of the azole derivate rendering a neutral or a cationic complex. In the case of complexes **4.7** and **4.8**, the focus will be set on how the increment of nitrogen atoms in the azole ring could tune the final biological properties.

4.5.1 Biological properties of complexes 4.1 and 4.2

In this section, the antiproliferative properties and biodistribution pattern of complexes **4.1** and **4.2** in A549 cells were studied, as well as a study of cellular morphology alteration and an estimation of their cell death pathway that these cells suffer when they are incubated with these complexes. (Figure 4.15)

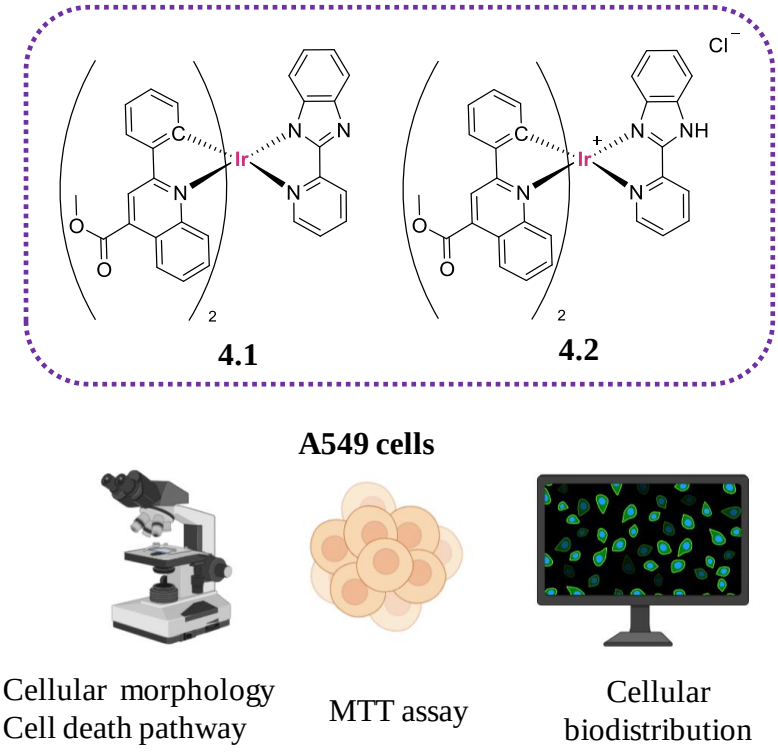

Figure 4.15. *Depiction of biological assays performed using complexes **4.1** and **4.2**.*

4.5.1.1 Antiproliferative properties

The antiproliferative activity of complexes **4.1** to **4.2**, was determined by MTT assays in A549 cell line. Complexes were evaluated using a range of concentrations from 0.2 to 100 μM using the serial dilutions method, starting from a stock solution of 0.1 μM in DMSO. These assays were performed using different conditions: no irradiation (dark) and irradiation at 470 or 525 nm for ten minutes. The selection of the irradiation wavelength was made based on their absorption spectra. Complexes **4.1** and **4.2** have an absorption band at 463 nm with a long tail, and as it has been previously mentioned, this could be attributed to $^{3}\pi\rightarrow\pi^{*}$ and ^{1}MLCT transitions.

The IC_{50} values collected in Table 4.2, suggest a high antiproliferative character of these two complexes under irradiation conditions, with greater effectiveness observed when they are activated by a 470 nm source (IC_{50}: 1.2 ± 0.3 μM (**4.1**) and 0.8 ± 0.1 μM (**4.2**)). This fact can be explained due to a bigger absorption at this wavelength in comparison with the one at 525 nm. It is noteworthy that no antiproliferative character has been observed when complexes are incubated in A549 cells under dark conditions at 200 μM.

Therefore, it can be said that the cytotoxicity of these complexes is directly associated to the activation of the iridium center that acts as PS, generating a PDT effect. Additionally, it is notable that complex **4.2**, the cationic one of the pair, shows a slightly greater antiproliferative effect compared to its deprotonated analogue, the neutral complex. This difference in behavior can be attributed to the higher solubility and hydrophilicity that charged complexes present, as well as the better cell membrane permeability of cationic species over neutral species.

Table 4.2. *IC_{50} values (μM) of complexes **4.1** and **4.2** incubated in A549 cell line for 24h.*

	$IC_{50,\ dark}$	**$IC_{50,\ 470\ nm}$**	**$IC_{50,\ 525\ nm}$**
4.1	> 200	1.2 ± 0.3	1.6 ± 0.1
4.2	> 200	0.8 ± 0.1	1.0 ± 0.2

4.5.1.2 Microscopy analysis: Cell death mechanism and morphological changes

The visualization of A549 cells upon 24 h in presence and absence of complexes **4.1** and **4.2**, was performed using an inverted microscope to elucidate the effect of the different irradiation source into the cell death mechanism and/or cell morphology. The aim of this experience is to track the morphological changes that could be taking place as a consequence of PDT as well as the cell death mechanism. Cell were visualized after irradiation at both, either 470 or 525 nm for 10 min.

Untreated cells were growing normally and all presented a healthy morphology. When cells are incubated with complexes **4.1** and **4.2** in the dark, no relevant effect was observed, and the cells continued to be alive and exhibit healthy morphology. However, those cells that were exposed to complexes **4.1** or **4.2** under irradiation conditions, exhibited a high population of death cells or dying cells. In fact, black arrows in Figure 4.16 point to those cells that are suffering an apoptotic cell death, while the blue arrows indicate a necrotic pathway.

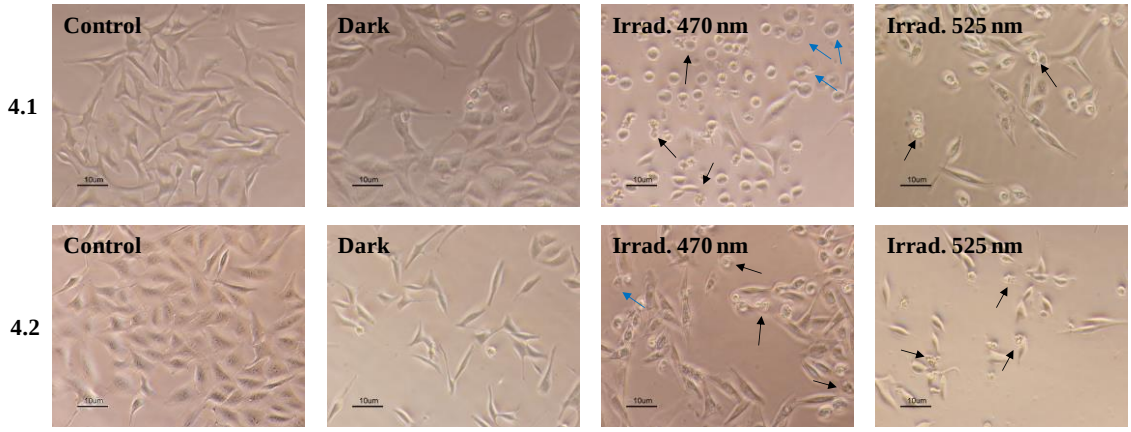

Figure 4.16. *Phase contrast microscopy images of A549 cells treated with complexes **4.1** and **4.2** at 1.5 μM after 24 h. Black and blue arrows point to examples of apoptotic and necrotic cells, respectively.*

It is worth noting that cells exposed with more energetic irradiation at 470 nm exhibit a combination of cell death mechanism, whereas those exposed to a 525 nm irradiation seems to follow an apoptotic cell death pathway. Nevertheless, further experiments would be necessary to verify the exact cell death mechanism.

4.5.1.3 Cellular biodistribution

Fluorescence confocal microscopy assays were conducted to investigate the biodistribution of the complexes in A549 cells. However, this assay was only performed for complex **4.2**, since both complexes have similar antiproliferative effects and provide comparable morphological analysis. Thus, compound **4.2** was incubated at 2 μM in A549 cells for 2 hours, then organelle selective trackers were added. The trackers that were used for this confocal microscopy assay were CellTracker Blue (CTB), a commercial dye designed to freely pass through cell membranes into cells, allowing to track the internalization process, and LysoTracker Green (LTG), a tracker selective for lysosomes. These trackers were incubated for 30 and 45 min respectively, using concentrations of 500 nM for CTB and 250 nM for LTG. Excitation lasers of 405 and 473 nm were used for CTB and LTG, respectively, and a laser of 561 nm was selected for activating complex **4.2**. Figure 4.17 shows the simulation of emission and excitation patterns of tracker with complexes, along with the selected excitation lasers.

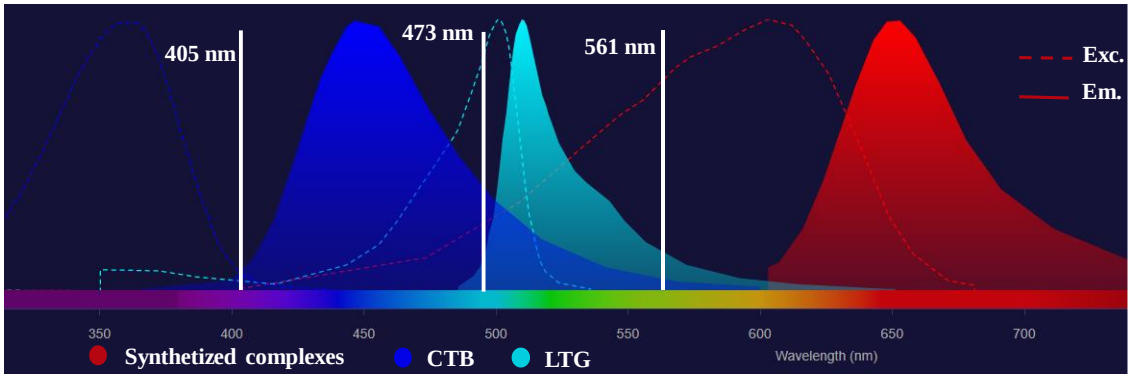

Figure 4.17. *Schematic representation of the different excitatory and emissive profiles of complex* ***4.2*** *and comercial trackers (CTB and LTG) used in biodistribution assay.*[29]

Focusing on images collected in Figure 4.18, where in red is observed complex **4.2** and in blue the CTB (top row). At bottom row, complex **4.2** was incubated with LTG, unfortunately no signal has been observed for this tracker so it could be suggested a quenching process of the emission of LTG by **4.2**, since the positive LTG control possess the expected lysosome emission pattern. The quenching

process will be explained in more detail for complexes **4.5** and **4.6** in section 4.5.3.5.

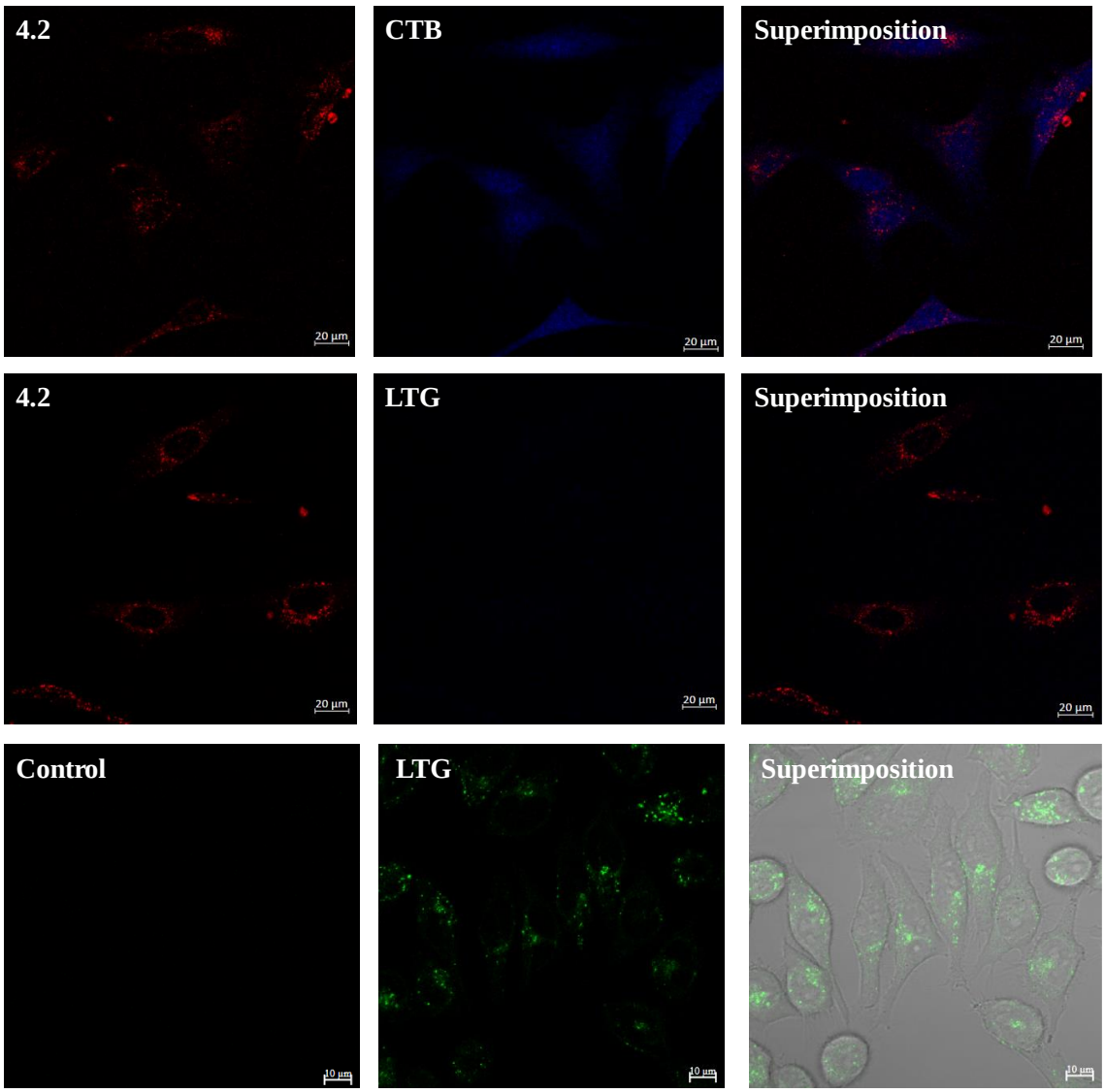

Figure 4.18. *Confocal images of complex **4.2** incubated in A549 cells. Top row: **4.2** with CTB; Middle row: **4.2** with LTG; Bottom row: Positive control LTG.*

In view of images collected in Figure 4.18, it can be said that complex **4.2**, and for extension complex **4.1**, are able to internalize into the cells and they were distributed through the cytoplasm, in a pattern that remember a lysosomal disposition. In addition, the superimposition image collected in top row suggests that complex **4.2** could be internalized by an endocytosis process. (Figure 4.19)

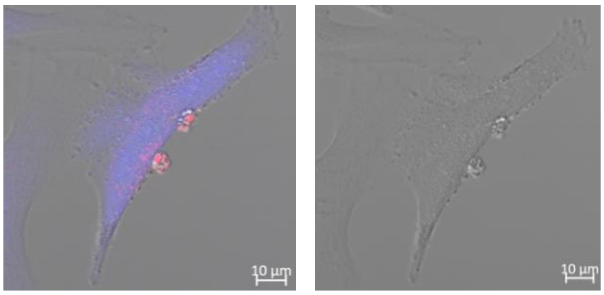

Figure 4.19. *Amplification section. Complex* ***4.2*** *internalizating in A549 cell line. Red: Complex* ***4.2****; Blue: CTB.*

Endocytosis is a cellular process characterized for the production of internal membranes from the plasma membrane lipid bilayer. The cell membrane is naturally impermeable to complexes larger than 1 kDa; however, cells exhibit a variety of active internalization mechanisms to allow the entry of large molecular complexes.[30] Here, the cell membrane will invaginate to engulf molecules and extracellular fluid in an intracellular membrane-bound vesicle, or endosome, that will subsequently traffic through the cell. [31]. Figure 4.20 shows a schematic representation of internalization process of complexes and how in last term endosomes fused with lysosomes, being these organelles the final targets of internalized complexes. In the present case, the bright red dots seen in Figure 4.19 resemble intracellular vesicles or endosomes that have been incorporated to the cell carrying complex **4.2**.

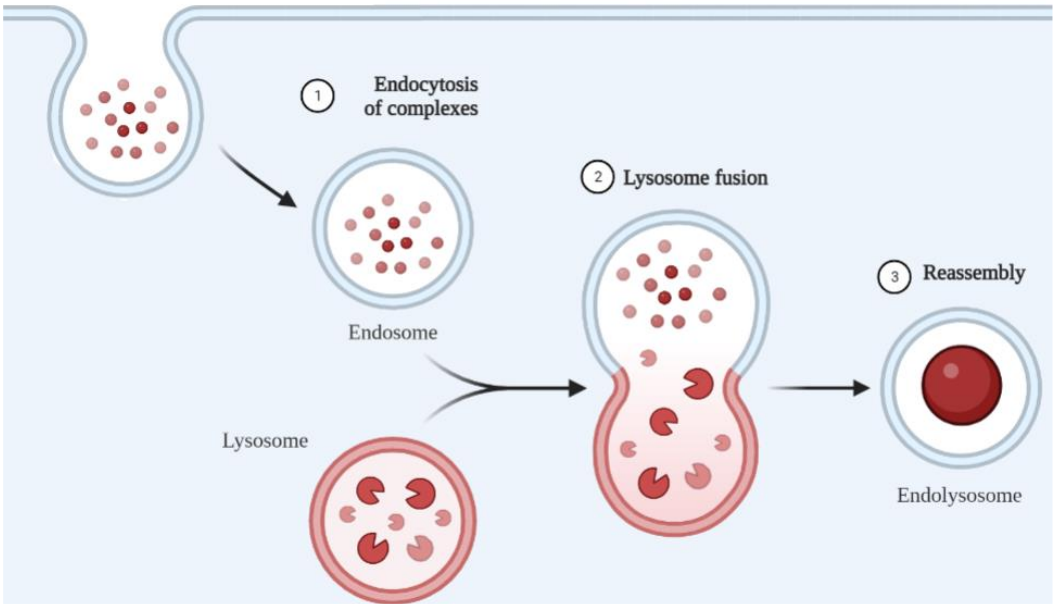

Figure 4.20. *Representation of an endocytosis process.*

4.5.2 Biological properties of complexes 4.3 and 4.4

In this section, we will address the capacity of complexes **4.3** and **4.4** to destroy A549 and SK-Mel-103 (human melanoma cells), as well as their senescent versions using PDT. Before presenting the data gathered, we will describe the origin, nature and implication of senescent cells in cancer in order to contextualize the interest aroused by this cellular stage within cancer therapy. Figure 4.21. Part of this work was performed during a short-stay at Cambridge University, in the group head by Dr. Daniel Muñoz Espín.

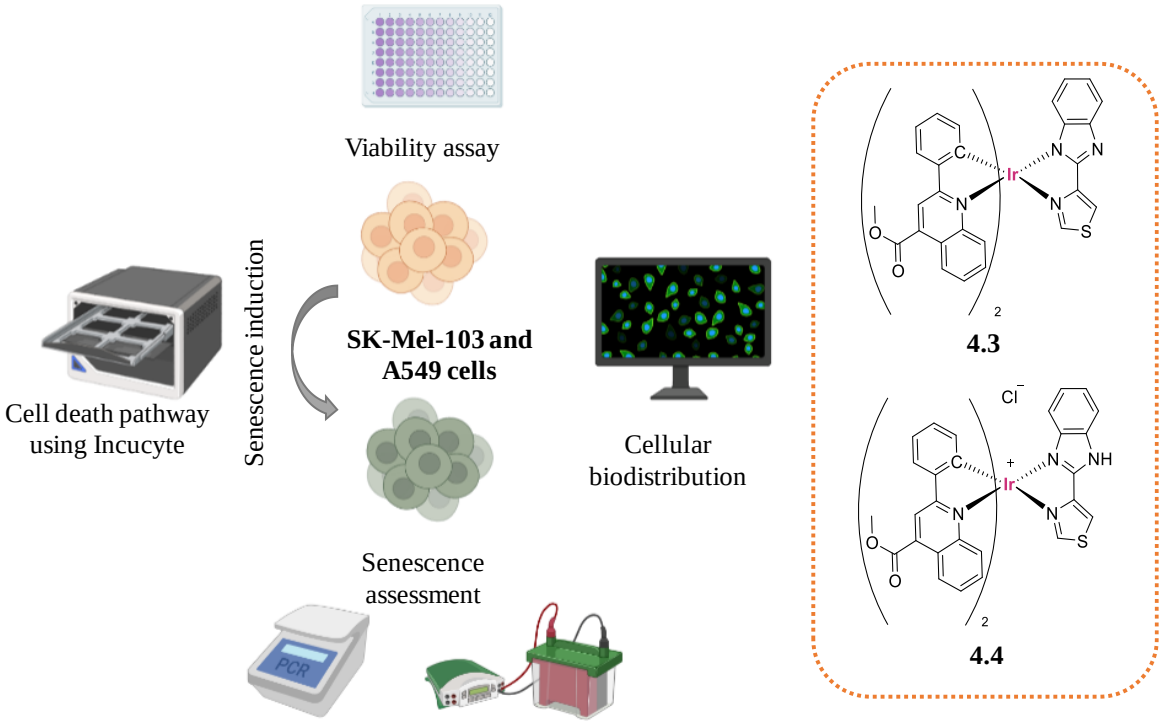

Figure 4.21. *Depiction of biological assays performed using complexes* ***4.3*** *and* ***4.4****.*

4.5.2.1 Introduction to senescence

The phenomenon of senescence was discovered by Hayflick and Moorhead in 1961. They demonstrated that normal cultured cells have a finite number of cell divisions before they enter a permanent cell cycle arrest in which they remain viable.[32] This phenomenon is characterized by high lysosomal activity, increased secretion of chemokines, cytokines and growth factors[33] as well as upregulation of anti-apoptotic mechanisms, changes in cell morphology, heterochromatin[34] and

finally an increase in β-galactosidase activity.[35] Cellular senescence is a highly heterogeneous state triggered by various factors such as DNA damage, oncogene activation, telomere shortening[36] or cellular stress.[37]

Diseases related to ageing and cancer metastasis or progression are closely associated with cells entering this stage of cell cycle arrest.[38,39] In addition, senescent cells (SnCs) can be artificially generated after treatment with certain types of chemotherapy or radiation sources.[40] For example, Wang and co-workers reported that treatment of nasopharyngeal carcinoma with cisplatin caused the cells to enter a stage of senescence,[41] and later studies confirmed that other drugs used in chemotherapy such as hydroxyurea, doxorubicin or camptothecin also promote similar behaviour, Figure 4.22.[42]

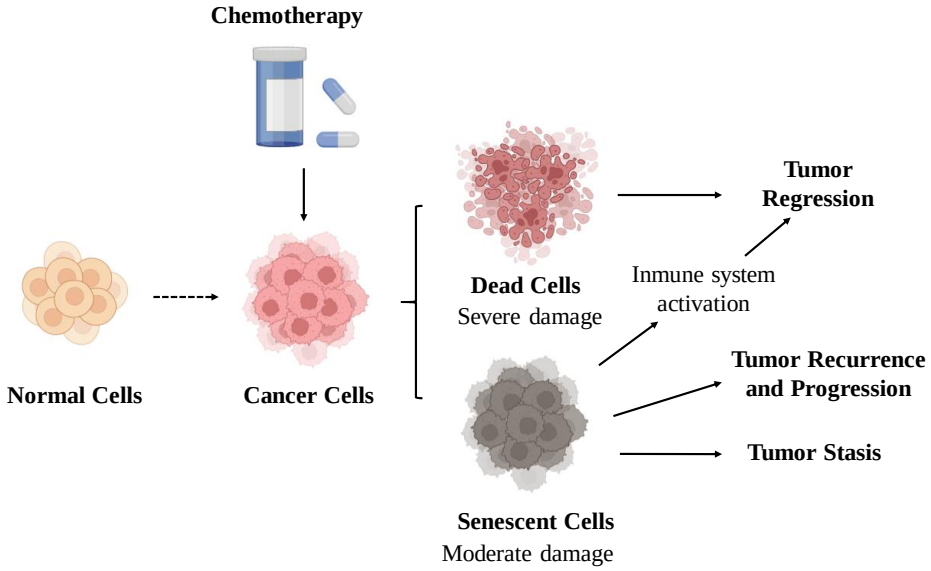

Figure 4.22. *Schematic illustration of chemotherapy's effects in cancer cells.*

Senescence plays a dual role in regulating cancer: it provides patients with an additional time frame and enables the use of novel therapies for cure. Specifically, senescence acts as a barrier that prevents the division of cells with active oncogenes, the promoters of cancer cells. Activation of tumor suppression genes such as p53/$p21^{CIP1}$ and $p16^{INK4a}$/RB[43] is critical in promoting cell cycle arrest and senescence. Consequently, the immune system is also activated, encouraging the elimination of SnCs.[44] Despite the good prospects of inducing senescence in cancer

therapy, the accumulation of SnCs may increase the likelihood of recurrence and metastasis. SnCs acquire the senescence-associated secretory phenotype known as SASP, secrete high levels of various proteins and contribute to the development of chronic inflammation in the cellular microenvironment. As a result, the likelihood of suffering from age-related diseases and tumor growth increases.[45]

For the last fifty years, senescence has been considered a double-edged sword for controlling and eliminating cancer cells. On the one hand, it can prevent the malignant transformation of the cells by permanently arresting the cell cycle, and on the other hand, it can promote the activation of the immune system. However, as mentioned earlier, the accumulation of these cells is also undesirable, as it may eventually promote tumor recurrence when the cell cycle is reactivated.[46] It seems clear that there is a fine line between the advantages and disadvantages of senescence that needs to be addressed. As a result, there is growing interest in developing new drugs that can selectively induce (pro-senescence drugs or senescence inducers) or destroy (senolytics) SnCs, most of which are organic compounds (Figure 4.23). Pro-senescence drugs include doxorubicin,[47] palbociclib[48] or camptothecin,[42] all typical drugs for the treatment of various cancers.

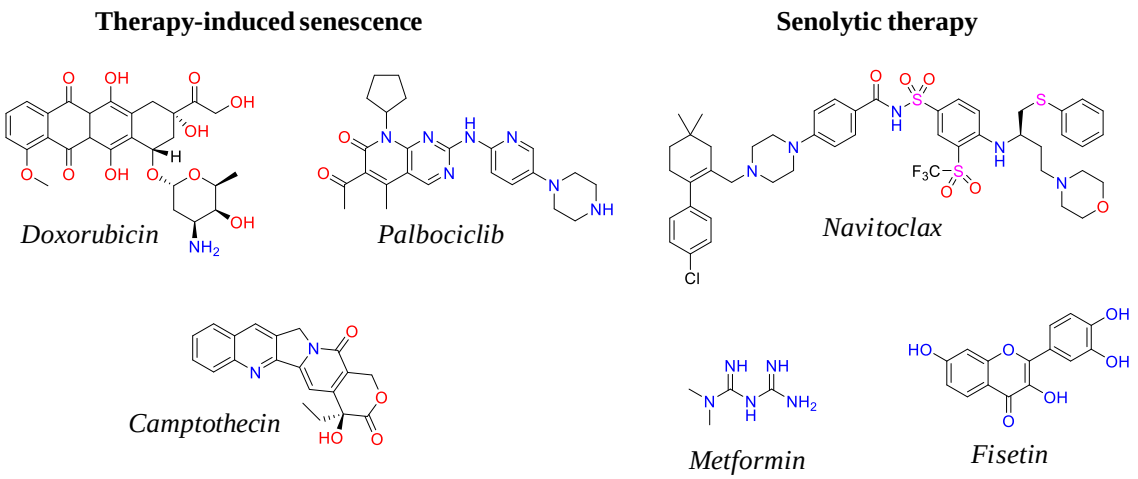

Figure 4.23. *Examples of organic drugs with application in senescence.*

Instead, drugs such as Navitoclax (antidiabetic),[49] Metformin (anticancer)[50] and Fisetin (antioxidant)[51] have shown their ability as senolytic destroyers of SnCs. So,

having seen the multitude of drugs that have a completely opposite effect, much work remains to be done to identify the specific features of an agent that turn it from a pro-senescence drug to a senolytic. Metal-based drugs such as cisplatin or carboplatin are also used as pro-senescence drugs in senotherapy.[52,53] However, this field is still in its infancy as most studies focus on organic compounds.

4.5.2.2 In situ induction of SnCs

The conditions required for the generation of senescence differ from the cellular line used. For senescence induction of A549 cell line, the cells must be placed in a petri dish or flask until a confluency percentage of around 80%. Then, they are treated with a concentration of 15 µM of cisplatin for 10 days, without changing the media. On contrary for the senescence induction of SK-MEL-103 cells, they were treated with 5 µM of palbociclib for 7 days. However, it is crucial to renew the media and the treatment after 2 days, for obtaining them successfully. It can be observed that during this process cells are still viable, but they suffer morphological alterations, such as a noticeable increment in size. After this time, assessment assay should be done to confirm the senescence induction, and cells can be handled normally (see Figure 4.24).

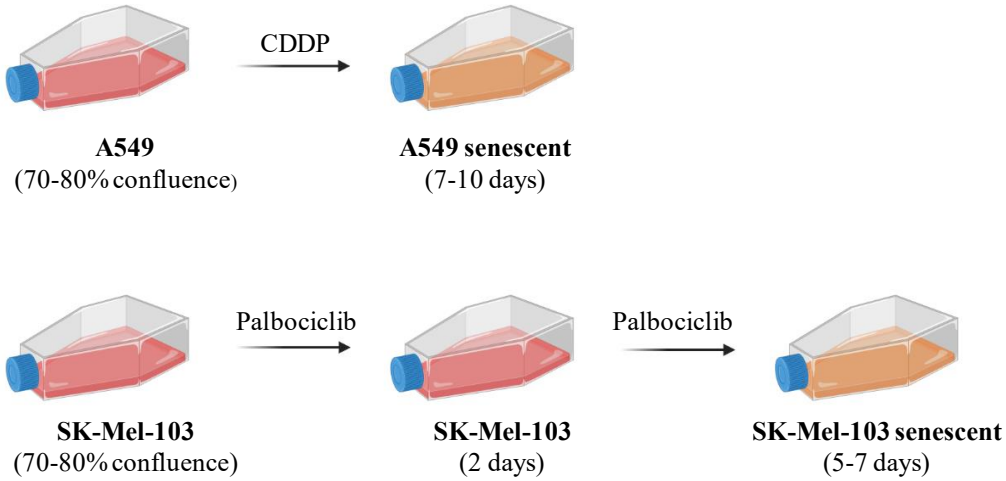

Figure 4.24. *Schematic representation of senescence induction.*

4.5.2.3 Assessment of senescence

As mentioned in the previous section, senescence is a highly heterogeneous phenomenon that involves many cellular changes, such as overexpression of proteins, modifications of cellular morphology, β-galactosidase activity, oxidative stress, among others. However, not all of them need to take place simultaneously for a cell entering in a senescent stage. The lack of a global maker is the main limitation when targeting SnCs. To confirm senescence induction, it is mandatory the identification of at least three of the hallmarks previously described. The most commonly used for assessing an ongoing senescence stage are described below.

A) The permanent cell cycle arrest could be easily detected by flow cytometry or by optical microscopy with the corroboration of a constant percentage of cellular confluency over time.

B) Optical microscopy can also be used to detect changes in the cellular morphology. Generally, SnCs increase their size at least twice times.

C) Determination of an increment of a β-galactosidase activity (SA-β-gal) by a staining assay. In fact, the simplicity of this assay led many research groups dealing with SnCs to incorporate it in their daily work.[54]

D) The overexpression of some proteins such as p16, p21 or p53 could be determined by Western Blot analysis or flow cytometry. These proteins are involved in the cell cycle progression, and their overexpression could lead to a cell cycle arrest and thus, to cellular senescence.

E) Detection of SASP. SnCs secret numerous proteins as cytokines, chemokines and proteinases that, overall, generate inflammation in the cellular microenvironment.[55]

Among all the methodologies described for the confirmation of senescence, four of them were chosen. The first and easiest one was the study of confluency over the time using an inverted microscope. In Figure 4.25, it can be seen how non-

senescent cell undergo cellular division over time, however senescent maintain their percentage of confluency, confirming their permanent cell cycle arrest.

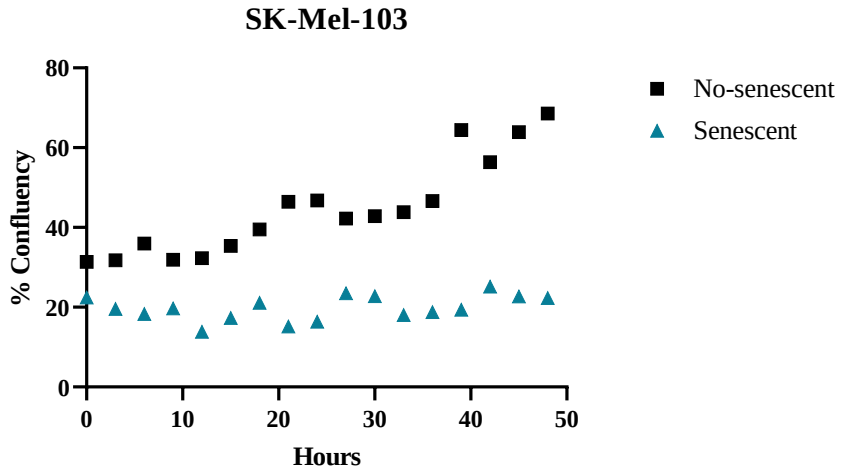

Figure 4.25. *Study of percentage of confluency over time for SK-Mel-103 cells.*

Secondly, RNA was extracted from senescent and non-senescent cells, and a PCR assay was performed to detect how senescence can modify the expression of some genes. From the graph collected in Figure 4.26, it can be seen that senescent cells undergo an overexpression of GLB1, the galactosidase β1 gene, which provides instructions for producing the enzyme β-galactosidase. As previously mentioned, this enzyme is overexpressed in senescent cells. Additionally, there is an overexpression of CDKN2A, the cyclin-dependent kinase inhibitor 2A gene, which is involved in the generation of proteins such as p16. On the contrary, LMNB1, the Lamin B1 gene, which is essential in the mitotic process for cellular division, is underexpressed and could be associated with a cell cycle arrest.

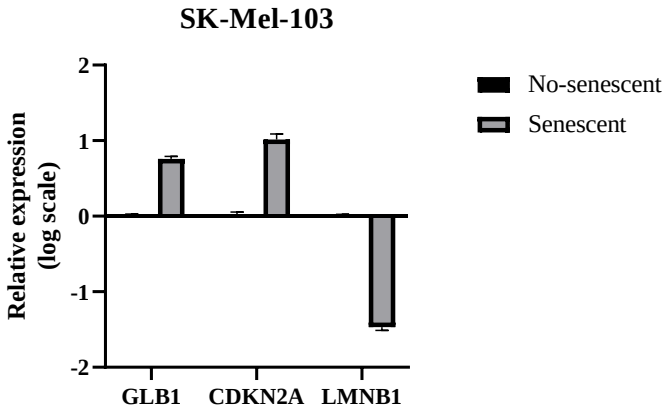

Figure 4.26. *Expression of genes in SK-Mel-103 perfomed at SK-Mel-103 cells.*

Additionally, Western Blot assays were performed to identify the proteins associated with the senescent stage. Western Blot technique is often used in to separate, identify proteins and quantify the expression of proteins. In this technique a mixture of proteins is separated based on their molecular weights, and thus by type, through gel electrophoresis. These results are then transferred to a membrane producing a band for each protein. The membrane is then incubated with labeled antibodies specific to the protein of interest. The last step is the quantification of proteins using a chemiluminescent reactive, the darkest is the band, the bigger is the quantity of protein.[56]

In this case, p-Rb, p53, p21 and GAPDH were analysed. p-Rb or, retinoblastoma protein, is critical in cell cycle regulation. The underexpression of this protein generates a cell cycle disruption. As shows Figure 4.27, senescence cells exhibit lower quantity of this protein confirming a disruption of cell cycle. On contrary, proteins p53 and p21 play central roles in regulating the cell division cycle. Their overexpressions are directly related with tumor suppression actions, blocking the cell cycle progression. It is for this reason that they are overexpressed on senescent cells. Finally, GAPDH, glyceraldehyde-3-phosphate dehydrogenase, controls the energy production pathway. There are no relevant differences are observed in the expression of this protein between senescent or non-senescent cells, as shown in the bottom row of Figure 4.27.

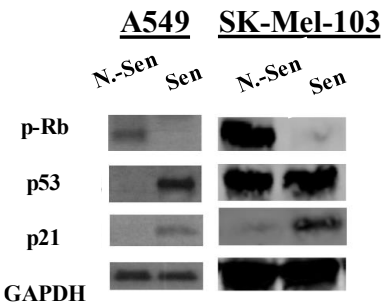

Figure 4.27. *Western Blot assays of protein expression of A549 and SK-Mel-103 cells.*

Finally, the increase of a β-galactosidase activity was checked by a staining assay, using a commercial kit (senescence β-galactosidase staining kit #9860).[57] For this purpose, senescent and non-senescent cells were placed in a 6-well plate, three

wells of each, and allowed to attach for 24 h before performing the test. Images collected in Figure 4.28 were obtained using an inverted microscope. It can be seen that senescent cells have increased their size at least twice in comparison with their non-senescent counterparts. Additionally, some of them exhibit multiple nuclei, and it can be appreciated a clear blue coloration, that is directly correlated with an increment β-galactosidase activity and, in consequence, with a senescence stage.

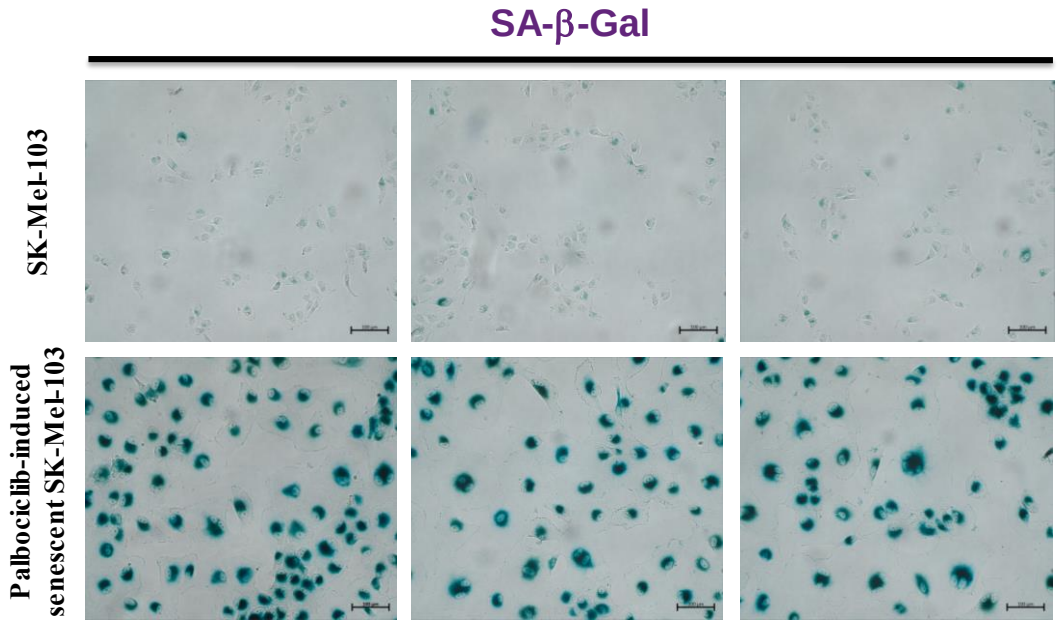

Figure 4.28. *SA-β-Gal staining test for SK-Mel-103 cells.*

4.5.2.4 Photoactivity of complexes 4.3 and 4.4

The first step to study the efficacy of complexes **4.3** and **4.4** in PDT is to demonstrate that the irradiation source itself does not have influence on cell viability. With this aim an analysis of cell viability was performed on senescent and non-senescent cells for both cell lines. Thus, senescent and non-senescent (control) SK-Mel-103 and A549 cells were irradiated with a 470 nm lamp for ten minutes without the presence of any complex. The graphs collected in Figure 4.29, show that this irradiation source does not have effect on the viability of the cells by itself. Therefore, all viability alterations in the following assays are going to be due to the used complexes.

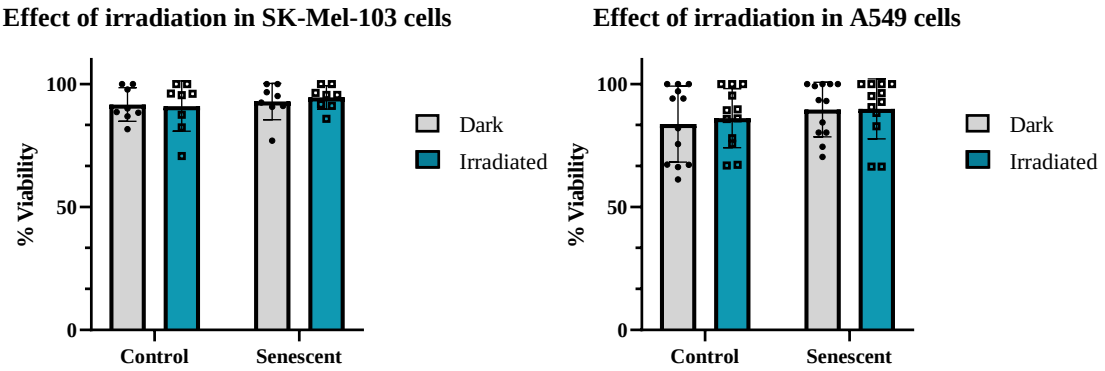

Figure 4.29. *Effect on cell vialibity generated by 470 nm irradiation source.*

After that, viability test, this time in presence of complexes **4.3** and **4.4** was perfomed using CellTiter-Blue, a fluorescent method for monitoring cell viability quantitatively, without necesity of using flow cytometry. This assay is based on the ability of living cells to convert a redox dye (resazurin) into a fluorescent product (resorufin). Non-viable cells rapidly lose metabolic capacity and thus do not generate a fluorescent signal.[58] For the experiment, 6,500 cells/well were seeded in flat-bottom-clear 96-well pates. The following day, complexes **4.3** and **4.4** were incubated in A549 and SK-Mel-103 cells, senescent and non-senescent for 48 h. The range of studied concentrations was from 100 μM to 50 nM, using serial dilutions. Twenty-four hours after complexes were added, media was replaced, and the half of plates were irradiated at 470 nm for 10 minutes, while the others were incubated in dark conditions. Once the 48 hours of incubation had elapsed, 10 μL of CellTiter-Blue were added in each well. The cells were incubated for an additional 2 hours, and the fluorescence in each well was meaused using VICTOR Multilabel Plate Reader (Pelkin Elmer), and GraphPad Prism as analysis sotfware. The data collected in Table 4.3 show the viability of A549 and SK-Mel-103, senescent and non-senescent cells after their treatment with **4.3** and **4.4** by means of LD_{50} dose, the quantity of compound that should be added to cells to promote cell death in halft of the population.

In view of LD_{50} data, it can be said that complexes **4.3** and **4.4** exhibit great activity as PS agents. In all cases, their cytotoxicity is potentiated as consequence of the irradiation with PI from 9.33 to 114.2. Complex **4.3** and **4.4** shows the capacity to

induce cell death in both studied-cell lines. Focusing on its PDT properties, it can be said that complex **4.3** presents high phototoxic index (PI), with the highest values for the SK-Mel-103 cells. Its cytotoxicity increases 85.5 (LD_{50}(470 nm): 0.19 ± 001 µM) and 114.2 (LD_{50}(470 nm): 0.19 ± 001 µM) times, for non-senescent and senescent cells, respectively, once it is activated with 470 nm light source. Regarding its protonated analogous, complex **4.4** follows the same tendency as complex **4.3**. However, it exhibits higher toxicity in dark conditions for all studied cells, so its potential as PS agent is smaller, PI: 46.8 (no-senescent cells) and 29.3 (senescent cells).

Table 4.3. *LD_{50} values (µM) of complexes **4.3** and **4.4** incubated in A549 and SK-Mel-103 cell lines, senescent and non-senescent for 48 h, using PDT (470 nm).*

	A549	**Dark**	**Irrad. (470 nm)**	**PI**
4.3	*No-Senescent*	23.4 ± 0.32	1.25 ± 0.02	18.7
	Senescent	28.3 ± 0.61	2.37 ± 0.03	11.9
4.4	*No-Senescent*	23.8 ± 0.5	0.64 ± 0.03	37.2
	Senescent	12.7 ± 0.48	1.36 ± 0.10	9.33

	SK-Mel-103	**Dark**	**Irrad. (470 nm)**	**PI**
4.3	*No-Senescent*	21.7 ± 0.90	0.19 ± 0.01	114.2
	Senescent	24.8 ± 0.76	0.29 ± 0.03	85.5
4.4	*No-Senescent*	10.3 ± 0.23	0.22 ± 0.03	46.8
	Senescent	9.36 ± 0.55	0.32 ± 0.07	29.3

It is necessary to point out that even though both complexes present high photocytotoxicity in A549 cells and SK-Mel-103, the latter is the most sensitive to the complexes, reaching LD_{50} values in the nanomolar range.

4.5.2.5 Cell death pathway

In view of the LC_{50} values obtained for complexes **4.3** and **4.4** in the studied cell lines, it was decided to study the cell death mechanism of both complexes. The analysis was performed using Incucyte. This equipment is designed to capture live cellular changes meanwhile cells are in the incubator. Additionally, it is equipped with lasers of different wavelengths, allowing for high-resolution fluorescence and bright field images to be captured and data to be recorded in real time over hours, days, or weeks.

For these assays, cells (both cell lines, senescent and non-senescent) were seeded in 96-well plates, and complexes were added. Immediately after the addition, 100 μL/well of IncuCyte® Annexin V Green Reagent were added to cells and placed on the Incucyte, capturing images every 2 hours using a x20 objective and an irradiation source of 420 nm. This reagent allows detecting apoptotic cells through the emitted fluorescence, as shown in Figure 4.30.

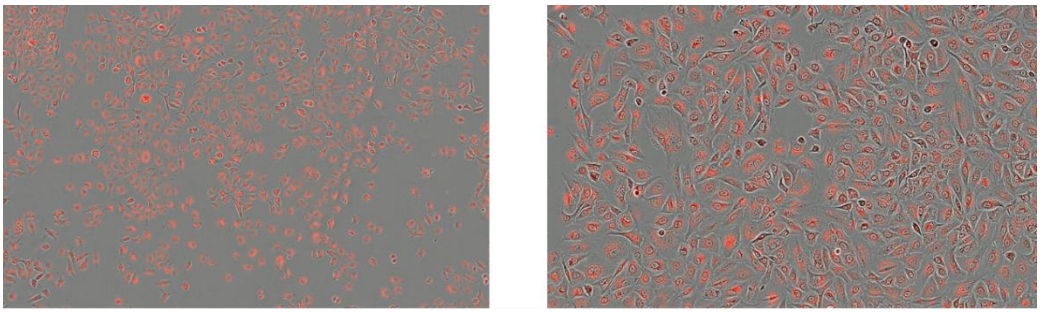

Figure 4.30. *Incucyte images of A549 senescent and non-senescent cells, after their treatment with complex* ***4.4*** *with PDT (470 nm), and IncuCyte® Annexin V Green Reagent.*

It could be said that the fluorescence emitted from cells confirms an apoptotic cell death mechanism for senescence and non-senescent cells. These results have also been confirmed for complex **4.3** and for SK-Mel-103 cell line using the same assay. Therefore, it can be concluded, that complexes **4.3** and **4.4** are able to induce apoptotic death in the studied cell lines.

4.5.2.6 Biodistribution assays

Fluorescence confocal microscopy assays were performed to elucidate the biodistribution of complex **4.4** in A549 and SK-Mel-103 cells senescent and non-senescent. Compound **4.4** was incubated at a concentration of 2 μM in both cell lines for 30 minutes, then, organelle selective trackers were added. The trackers used for these confocal microscopy assays were Hoechst 33342, a fluorescent stain for labelling DNA, and LysoTracker Green (LTG). These trackers were incubated for 30 and 5 min respectively, using concentrations of 500 nM for Hoechst and 250 nM for LTG. Based on the photophysical properties of **4.4** and the trackers, see simulation in Figure 4.31, the selected excitation lasers were these of 365 and 473 nm for Hoechst and LTG, respectively, and a laser of 561 nm for complex **4.4**.

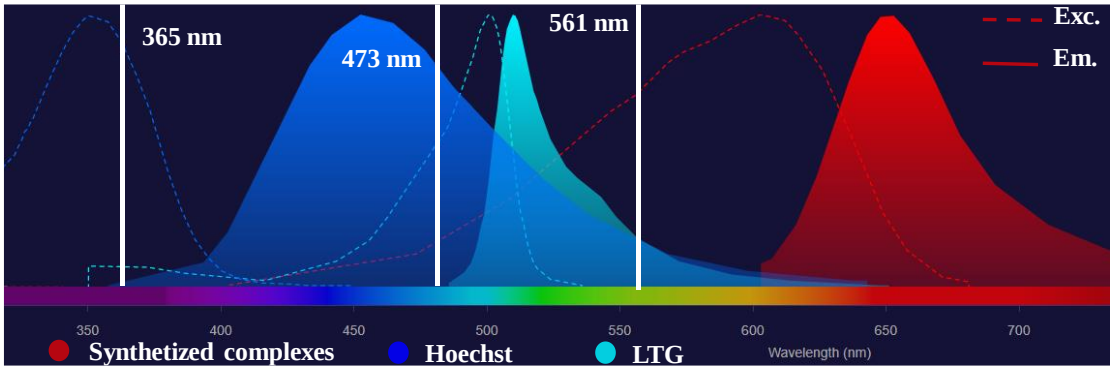

Figure 4.31. *Schematic representation of the different excitation and emissive profiles of complex* ***4.4*** *and comercial trackers (Hoechst and LTG) used in biodistribution assay.*

Focusing on the images collected in Figure 4.32, where the nuclear dye Hoechst is observed in blue, LTG in green, and the emission coming from complex **4.4** in red, it can be said that complex **4.4** was able to internalize in A549 cells. The superimposed images suggest a lysosomal localization of this complex in both senescent and non-senescent cells.

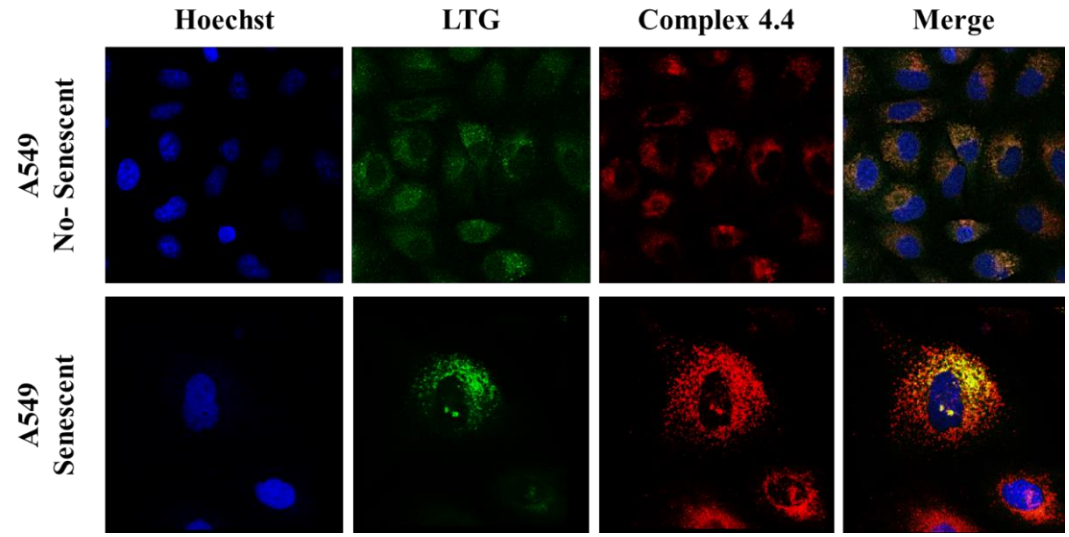

Figure 4.32. *Confocal images of complex* ***4.4*** *incubated in A549 cells. Top row: Senescent cells; Bottom row:Non-senescent cells. Objetive x40.*

A similar pattern is observed when complex **4.4** was incubated with SK-Mel-103 (Figure 4.33). Once again, a lysosomal accumulation is observed, with no nuclear permeabilization.

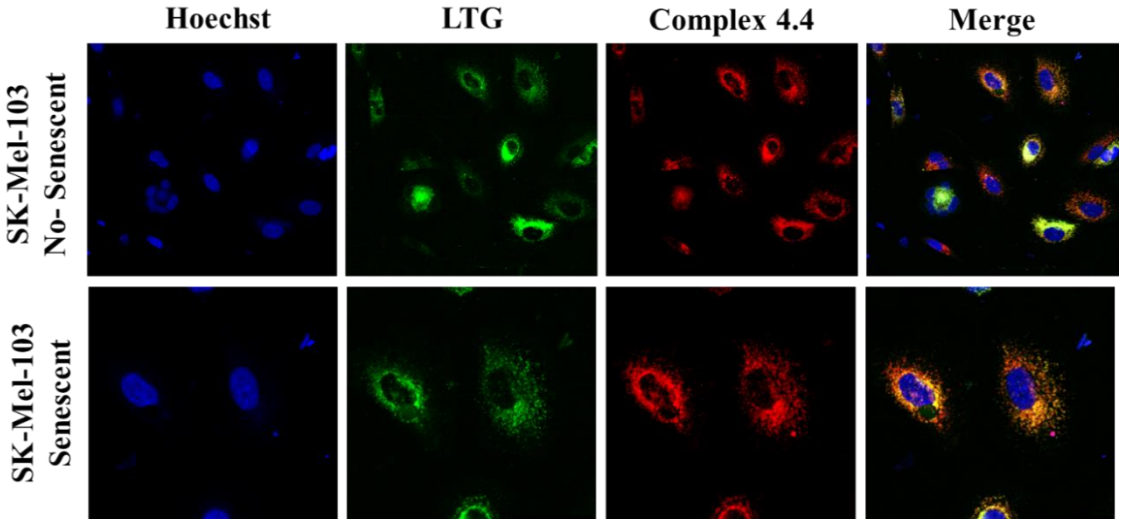

Figure 4.33. *Confocal images of complex* ***4.4*** *incubated in SK-Mel-103 cells. Top row: Senescent cells; Bottom row:Non-senescent cells. Objetive x40.*

In conclusion, it can be said that synthetized complex **4.4** exhibits a lysosomal biodistribution pattern, with these organelles being their final targets. Additionally, it could be suggested that the same biodistribution occurs for complex **4.3** as a consequence of its structural analogy.

4.5.3 Biological properties of complexes 4.5 and 4.6

The capacity of complexes **4.5** and **4.6** to be used as chemotherapeutic or PS agents, depending on the type of tumor cell line that needs to be treated, will be explored in this section. For this purpose, *in vitro* studies have been conducted on different cell lines to determine the selectivity of these complexes for tumor cells. In this specific case, lung A549 and breast 4T1-luc2 cancerous cell lines were selected as targets. Later, their mechanism of action, cellular biodistribution and the generation of ROS were studied. The non-toxic effect on healthy cells was also explored, leading to promising *in vivo* assays. Figure 4.34.

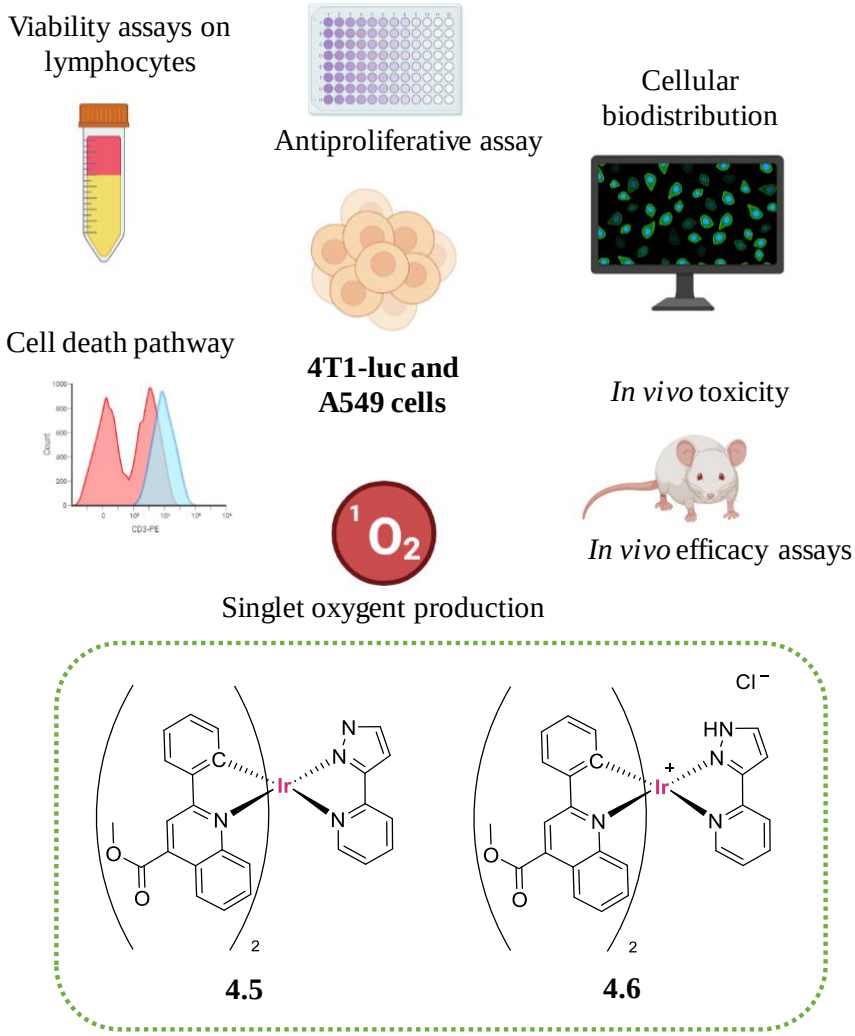

Figure 4.34. *Depiction of biological assays performed using complexes* ***4.5*** *and* ***4.6****.*

4.5.3.1 Antiproliferative properties

The antiproliferative activity of complexes **4.5** and **4.6** was determined by MTT assays in A549 and 4T1-luc2 cell lines. 4T1-luc2 cell line is a murine luciferase-expressing cell line, that mimics a stage IV human breast cancer. The complexes were evaluated using a range of concentrations from 0.2 to 100 μM, and following the conventional serial dilution method starting from a stock solution of 0.1 μM in DMSO as in the previous sections and chapters. These assays were performed under different conditions, including no irradiation and irradiation at 470 nm for ten minutes.

The IC_{50} values collected in Table 4.4 suggest that for A549 cell line, complexes **4.5** and **4.6** do not exhibit antiproliferative character when they are incubated without irradiation (dark conditions, IC_{50}(**4.5**) > 200 μM, IC_{50}(**4.6**): 67.2 ± 1.2 μM). However, if these complexes are exposed to an irradiation source of 470 nm for 10 min, their antiproliferative potential undergoes a considerable increment, PI: > 86.9 and 39.5, respectively. The incubation time also plays a key role in this assay, as reflex their IC_{50} values. When complexes are incubated for 48 h at A549 cells instead of 24 h, they exhibit a moderate antiproliferative character even in dark conditions IC_{50}(**4.5**): 22.2 ± 0.9 μM, IC_{50}(**4.6**): 58.0 ± 1.6 μM). Once again, their best IC_{50} values are obtained after 10 minutes of irradiation with PI of 25.8 and 62.4 for **4.5** and **4.6**, respectively and reaching IC_{50} values in the nanomolar range (IC_{50}(**4.5**): 0.86 ± 0.05 μM, IC_{50}(**4.6**): 0.93 ± 0.07 μM).

Table 4.4. *IC_{50} values (μM) of complexes **4.5** and **4.6** incubated in A549 and 4T1-luc2 cell lines for 24, 48 h, or 72 h, in dark and under irradiation conditions.*

	A549	**Dark**	**Irrad. (470 nm)**	**PI**
4.5	*24 h*	>200	2.3 ± 0.2	86.9
	48h	22.2 ± 0.9	0.86 ± 0.05	25.8
4.6	*24 h*	67.2 ± 1.2	1.7 ± 0.3	39.5
	48h	58.0 ± 1.6	0.93 ± 0.07	62.4

	4T1-luc2	Dark	Irrad. (470 nm)	PI
4.5	*24 h*	21.8 ± 0.8	19.6 ± 1.3	1.1
	48 h	0.22 ± 0.05	-	-
	72 h	0.14 ± 0.09	-	-
4.6	*24 h*	4.6 ± 0.4	2.1 ± 0.7	2.2
	48h	0.27 ± 0.08	-	-
	72 h	0.22 ± 0.03	-	-

Focusing on the results for 4T1-luc2 cells, complex **4.5** presents a moderate cytotoxicity (21.4 ± 0.8 μM), while its analogue **4.6** exhibits higher activity with a IC_{50} value of 4.6 ± 0.4 μM. The antiproliferative character of these complexes exhibit a clear dependency with the incubation time. At 48 h of incubation their IC_{50} values drop to nanomolar range (IC_{50}(**4.5**): 0.22 ± 0.05 μM, IC_{50}(**4.6**): 0.27 ± 0.08 μM) and maintain this tendency at 72 h (IC_{50}(**4.5**): 0.14 ± 0.09 μM, IC_{50}(**4.6**): 0.22 ± 0.03 μM). No irradiation is necessary to induce antiproliferactive activity for these complexes on 4T1-luc2 cell line.

This change of behavior between the pair could be explained as a consequence of the difference hydro-lypophilicity. Meanwhile complex **4.5** has a $K_{o/w}$ of 2.157, complex **4.6** exhibits a lower $K_{o/w}$ value, 0.132, suggesting its greater hydrophilicity. This fact could explain the higher cytotoxicity displayed by **4.6** not only in 4T1-luc, but also in A549 cell line in comparison with these of **4.5**. In contrast with the increased antiproliferative activity displayed by both complexes in A549 upon irradiation, activation of those with a 470 nm source does not generate a relevant change in photocytotoxicity against 4T1-luc with PI values of just 1.1 (**4.5**) and 2.2 (**4.6**).

Therefore, it could be suggested that there is a change in selectivity depending on the incubation conditions. In 4T1-luc these complexes are active in dark conditions, but in A549 cell line, it is necessary to photoactivate them to observe cytotoxic behavior.

4.5.3.2 Cytotoxic activity and cell death mechanism

Considering the IC_{50} values obtained for complexes **4.5** and **4.6**, it was decided to investigate their cell death mechanism to determine whether the charge of the complex, either neutral or cationic, or the different incubation conditions could induce a different cell death pathway. The analysis was performed by flow cytometry using specific fluorescent markers, Annexin V-FITC and PI. Annexin V-FITC is used to identify cells undergoing apoptosis,[59] while propidium iodide (PI) is a fluorescent DNA-binding dye, that freely penetrates cell membranes of dead or dying cells via necrosis.[60] The cell death mechanisms induced by complexes **4.5** and **4.6** once that they have been irradiated in A549 cells after 24 hours of incubation were studied using two different concentrations, 200 and 400 μM for **4.5** and at 67.2 and 135 μM for **4.6** corresponding to the IC_{50} and $2{\cdot}IC_{50}$ value of each complex. As shown in Figure 4.35, three populations of cells could be distinguished for complexes **4.5** and **4.6**. A) Annexin V-FITC positive and PI negative cells, indicative of an apoptotic death; B) Annexin V-FITC negative and PI positive cells showing a necrotic cell death pathway, and C) cells positive for Annexin V-FITC and PI suggesting a late apoptotic stage. The ratio between the cell populations each marker shows that both complexes induce cell death via an apoptotic pathway. Besides, this cell death mechanism seems to be concentration independent.

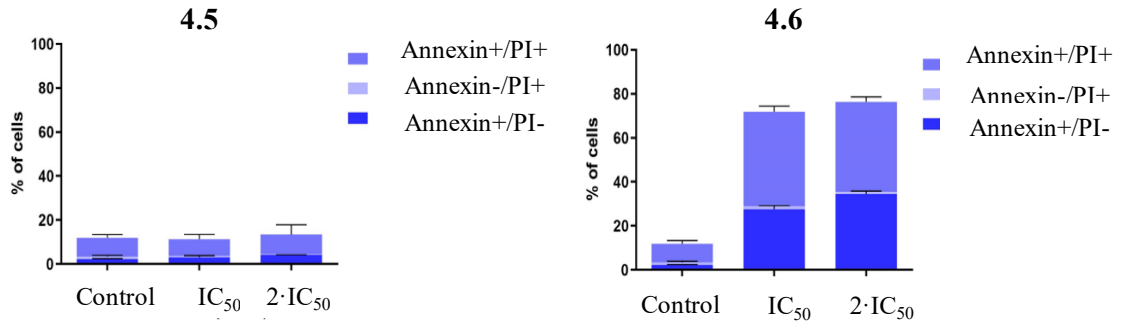

Figure 4.35. *Cytotoxicity assays of complex **4.5** and **4.6**, incubated in A549 cell line for 24 h, in a range of concentration between their IC_{50} and $2{\cdot}IC_{50}$ values, under irradiation at 470 nm.*

4.5.3.3 Cell morphology analysis

An inverted microscope was used to visualize A549 cells in the presence and absence of complexes **4.5** and **4.6** under irradiation conditions, in order to track any morphological changes. The control cells, which were untreated with the complexes, grew normally and presented a healthy morphology. However, some of the cells exposed to complexes **4.5** or **4.6**, exhibited cytoplasmic vacuoles, the size and quantity of which increased with the dose of complexes. In fact, the little black triangles in Figure 4.36 clearly show that 24 hours after the addition of the complexes, vacuoles occupied almost all the cytoplasm of cells, and this effect is potentiated as a consequence of complexes concentration. In addition, it can be observed cells dying. Black arrows point to those cells suffering an apoptotic cell death, and to a lesser extent blue arrow indicate necrotic cells. Thus, the microscopy images in Figure 4.36 are in concordance with the results mentioned in the previous section obtained by flow cytometry, in which the predominant cell death mechanism was via apoptosis.

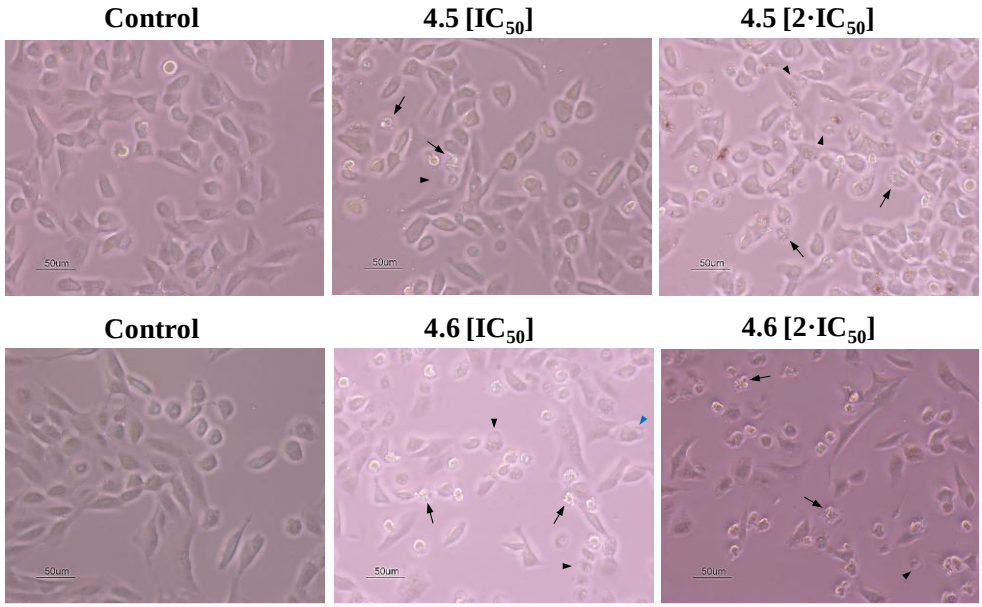

Figure 4.36 *Phase contrast microscopy images of A549 cells treated with complexes* ***4.5*** *and* ***4.6*** *at different concentrations after 24 h. Black and blue arrows point to examples of apoptotic and necrotic cells, respectively. Little black triangles show cells containing cytoplasmic vacuoles.*

4.5.3.4 Measurement of singlet oxygen production

After observing the increase in the antiproliferative activity of complexes **4.5** and **4.6** upon irradiation on A549 cells, and considering that this increment could be due to the generation of intracellular reactive oxygen species (ROS),[61] production of singlet oxygen ($^1O_2$) was specifically addressed. It is known that emission of $^1O_2$ appears at 1270 nm, therefore, if it is produced upon irradiation, an emission band should be visible in the NIR.[62] Direct measurement of emission of $^1O_2$ was then undertaken by steady state fluorescence spectroscopy for synthetized complexes **4.5** and **4.6**, as shown Figure 4.37. Irradiation of an acetonitrile solution of complexes with a 450 nm picosecond pulsed diode laser, rendered a band centered at 1270 nm, indicative of $^1O_2$ generation. An additional experiment was performed to corroborate that band observed at 1270 nm was not a mere artefact from the spectrometer, measuring the neat solvent (CH_3CN) in absence of complexes. So, it could be said that complex **4.5** and **4.6** can induce singlet oxygen production, which is surely one of the factors implicated in their photocytotoxic character.

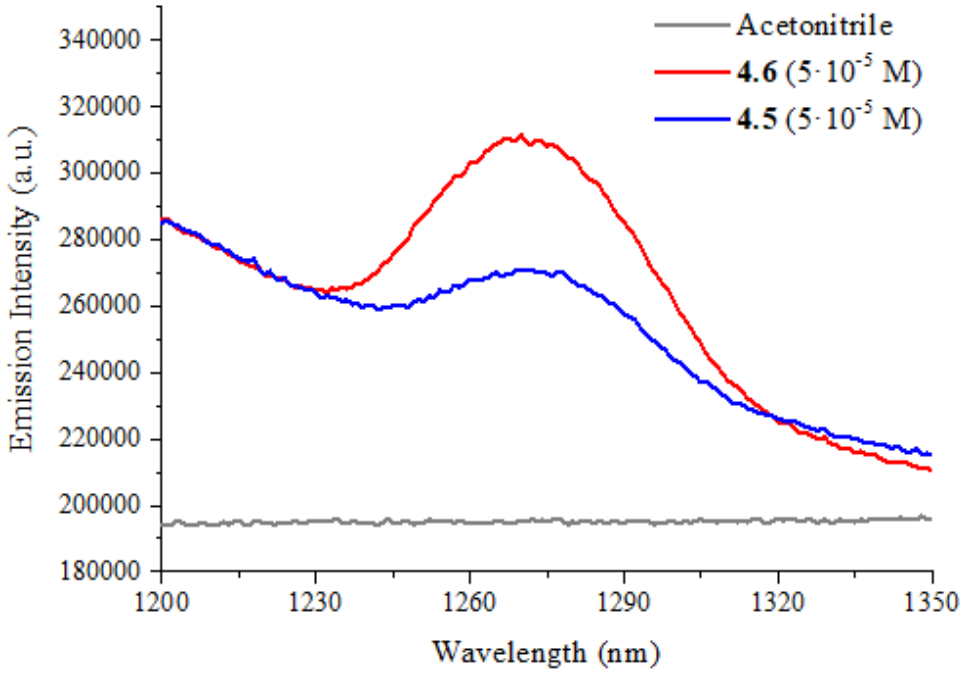

Figure 4.37. *Measurement of singlet oxygen production of complex* ***4.5*** *and* ***4.6*** *when it is irradiated with a diode laser of 450 nm. Emission maximum at 1270 nm.*

4.5.3.5 Biodistribution assays

Fluorescence confocal microscopy assays were performed to elucidate the biodistribution of complex **4.6** on A549 (Figure 4.38) and 4T1-luc2 cells (Figure 4.40). The same biodistribution could be expected for complex **4.5** as a consequence of its structural analogy with complex **4.6**. The complex was incubated at 2 μM in both cell lines for 2 hours, then commercial trackers have been added. The trackers that were used for these confocal microscopy assays were either CellTracker Blue or LysoTracker Green (LTG). These trackers were incubated for 30 and 45 min respectively, using concentrations of 500 nM for CTB and 250 nM for LTG. Following the assistance of the emission simulation provided in Figure 4.17, the excitation lasers used were those of 405 and 473 nm for CBT and LTG, respectively, and that of of 561 nm for activating **4.6**. (Figure 4.38)

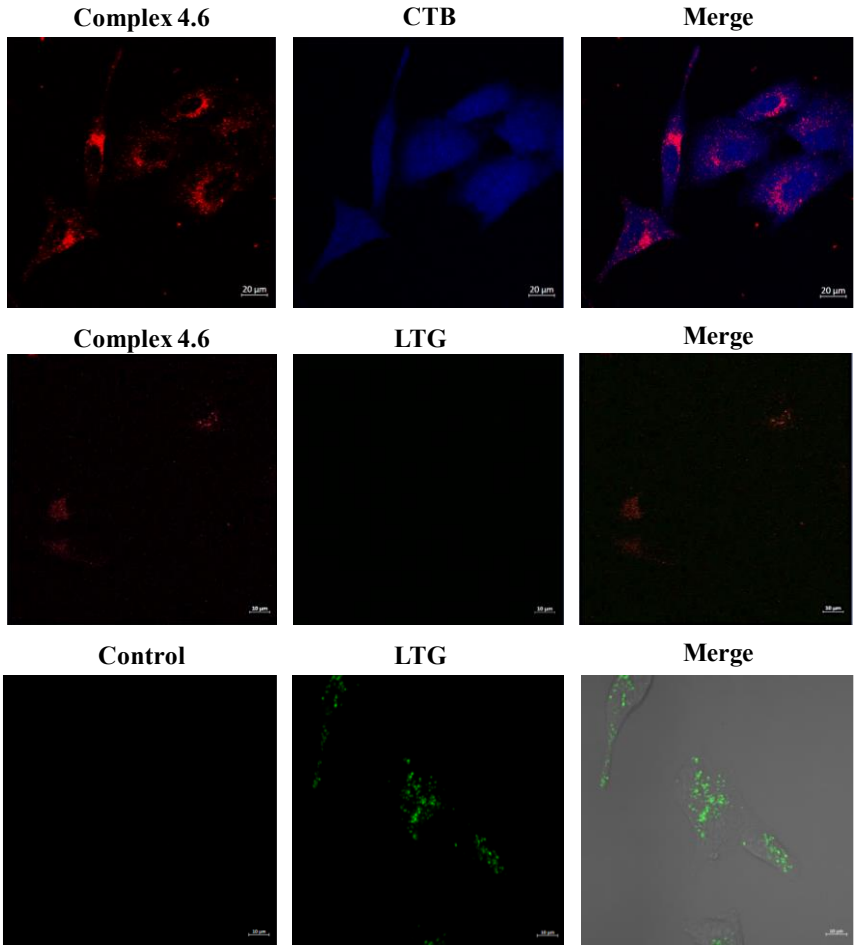

Figure 4.38. *Confocal images of complex **4.6** in A549 cells. Top row: CTB; Middle row: LTG; Bottom row: Control LTG (without **4.6**)*

Fluorescence confocal images collected in Figure 4.38, where in blue is observed the nuclear dye CTB and in red the emission coming from complex **4.6**, show that **4.6** was able to internalize A549 cells (top row).

However, no biodistribution pattern could be suggested for the parallel asay, where the **4.6** was incubated with A549 together with LTG. It can be suggested then that emission from LTG is somehow quenched by the presence of **4.6** and that of the **4.6** has also decreased. The middle row of Figure 4.38 clearly showed a faint emission of complex **4.6** and the one coming from LTG is nonexistent. In bottom row of Figure 4.38 is collected the positive control of LTG, where cells are only incubated with LTG, to confirm its emision in absence of complex **4.6**. To verify the hypotesis of a quenching effect between complex **4.6** and LTG, an additional experiment was performed using fluorescence spectroscopy. First, emission of a DMSO solution of LTG was collected, and then 0.5 mL of a DMSO solution of complex **4.6** [2 μM] was added. Then, emission spectra were recorded over time upon the addition of **4.6** (at 0 min, 10 min and 20 min). Figure 4.39 shows how the intensity of the emission of LTG at 511 nm decreases over time when exposed to complex **4.6**. In fact, only 20 min after addition of **4.6**, the emission of LTG is quenched completelly suggeting that the same process might be taken place *in vitro*, and thus preventing the clear assesment of the biodistrubion of **4.6** by fluorescence microscopy. Besides the confirmation of a quenching process between **4.6** and LTG, this assay gave us the final proof for elucidating the biodistribution of **4.6** in A549 cell. It can be said that **4.6** accumulates in the lysosomes, otherwise, the emission from the LTG would not have been quenched. Both species would be located within the same organelle, and as LTG is a lysosome selective dye, it is clear that **4.6** accumulates within the same organelle.

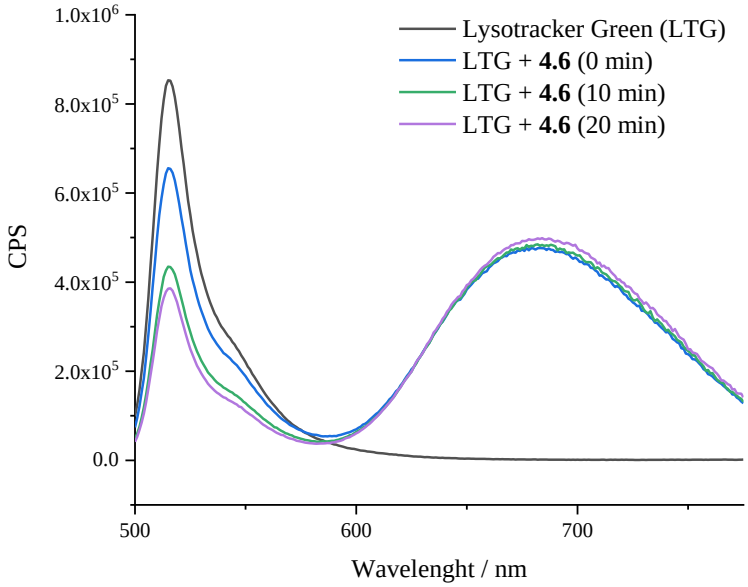

Figure 4.39. *Quenching assay of LTG when is mixtured with complex* ***4.6****.*

Once it was known that 20 min were enough for **4.6** to quench the emission of the LTG, a different approach was undertaken to elucidate the biodistribution of this complex within 4T1-luc2 cells by fluorescence microscopy. This time, LTG was added immediately before starting to collect the confocal images to avoid the loss of its emission intensity. Figure 4.40 collects confocal images obtained, and it can be said that complex **4.6** clearly internalizes in lysosomes, as confirmed by the superimposition images.

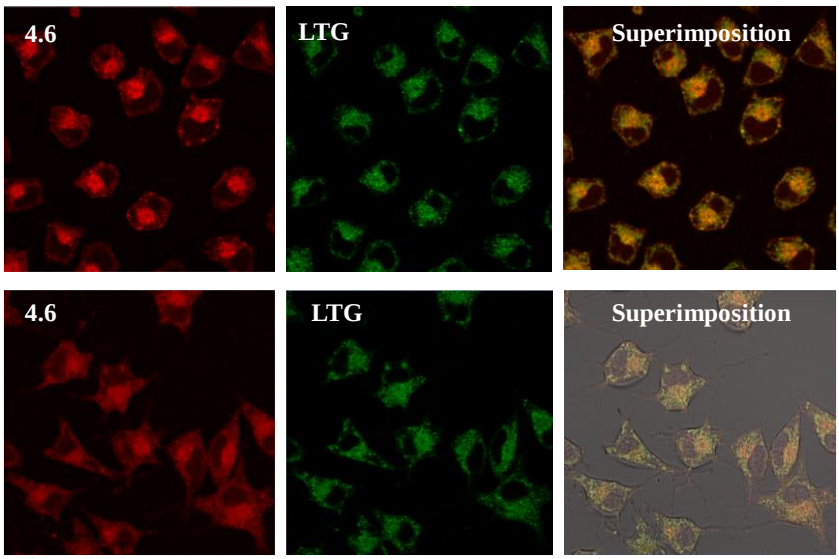

Figure 4.40. *Confocal images of complex* ***4.6*** *in 4T1-luc2 cells for 2 hours (2 μM). LTG: 500 nM, 2 min.*

4.5.3.6 Antiproliferative and cytotoxic activity in lymphocytes

In view of the completely different activity and selectivity that complexes **4.5** and **4.6** exhibit in lung and breast cancer cell lines, it is crucial to check if these complexes induce cytotoxicity in healthy cells. With this end, Ficoll gradient centrifugation was carried out in order to extract the lymphocytes from blood.

In first attempt, 15 mL of Ficoll-Paque were placed in a 50 mL falcon, carefully 25 mL blood (from a blood bank not older than 8 hours) were added. Specifically, the Ficoll reagent is used for isolation of lymphocytes in high yield from peripheral blood using a simple and rapid centrifugation procedure. Therefore, the mixture was centrifuged at 1,000 rpm for 30 minutes at 20ºC affording four layers, plasma on top, following peripheral blood mononuclear cells (PBMCs) and platelets, then next Ficoll Paque reagent (colorless) and red blood cells together with polymorphonuclear cell at the bottom. Thereafter, the upper layer was aspirated, without disturbing the interphase (Figure 4.41). The white central interface (PBMC) was carefully transferred to a new 50 mL conical tube, and 40 mL of PBS were added, mixed and centrifuged at 1,000 rpm for additional 10 minutes. The supernatant was eliminated, and the resultant pellet was once again suspended in 40 mL of PBS and centrifuged for 10 minutes, twice. In this way, most of the platelets will remain in the supernatant upon centrifugation. So, the supernatant was removed, and the pellet was solved in DMEM. The extracted lymphocytes were counted and placed in both 96-well plates (12,000 cells/well) for the antiproliferative assay and in 6-well plates (50,000 lymphocytes/well) for the cytotoxicity assays.

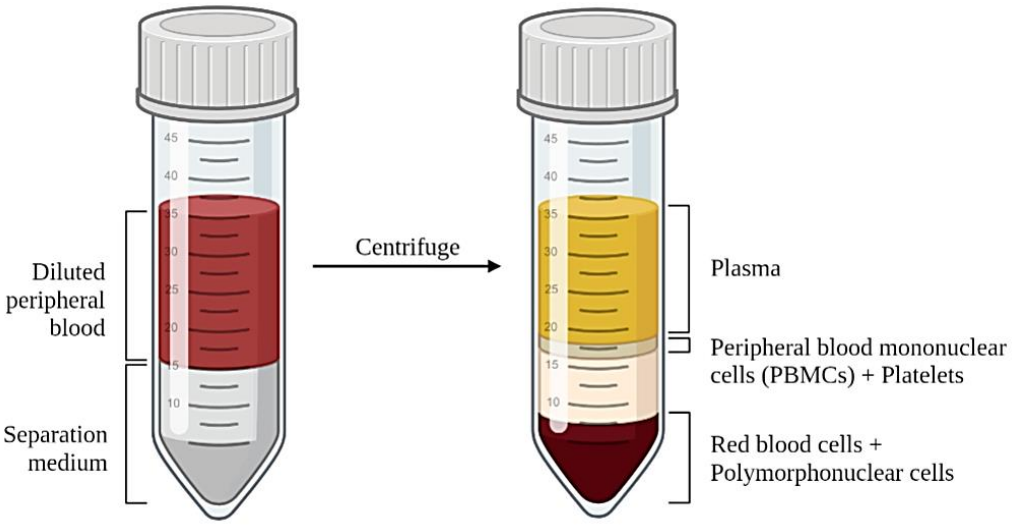

Figure 4.41. *Schematic representation of the isolation of lymphocytes from blood.*

The MTT antiproliferative assays performed using the standard protocole demostrated that complexes **4.5** and **4.6** had no effects on the lymphocytes after been incubated for 24 or 72 h, in dark and under irradiation conditios (470 nm), as shown their IC_{50} values collected in Table 4.5.

Table 4.5. *IC_{50} values (μM) of complexes **4.5** and **4.6** incubated in lymphocytes for 24 or 72 h, in dark and under irradiation conditions. One independent assay.*

Lymphocytes	Dark 24 h	Irrad. 24 h	Dark 72 h	Irrad. 72 h
4.5	>100	>100	98.6 ± 0.17	83.6 ± 0.27
4.6	>100	>100	96.3 ± 0.28	81.9 ± 0.30

In view of these promising results obtained in the proliferation test, a flow cytometry assay was performed to further confirm that these complexes do not induce cell death in healthy cells. For this aim the previously seeded 6-well plates were incubated for 12 hours, thereafter complexes were added. After 5 hours, cells were irradiated at 470 nm for 10 minutes, and incubated again until 24 hours. After this time, Annexin V-FITC was added and cells were analyzed. Figure 4.42 collects the graphs obtained by flow cytometry, confirming that no cell death has occurred upon 24 h. Control cells exhibit the same pattern that those cells treated with the complexes, in both non-irradiated and irradiated conditions. These results

suggest that complexes **4.5** and **4.6** have a selective cytotoxicity towards tumoral cells.

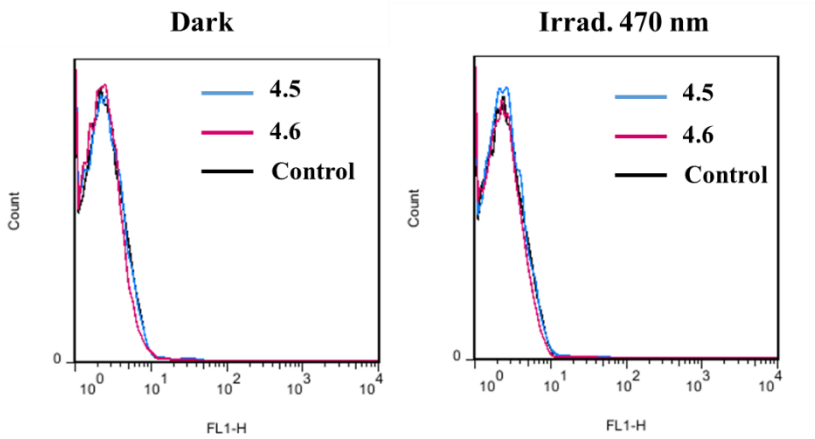

Figure 4.42. *Cell death study at lymphocytes induced by complexes* ***4.5*** *and* ***4.6****.*

4.5.3.7 In vivo assays: Toxicity and efficacy

Having confirmed the promising anticancer potential of lysosome-selective complexes **4.5** and **4.6** in A549 and 4T1-Luc cell lines, and observing their lack of toxicity towards healthy cells, we were encouraged to continue studying their properties *in vivo*. Therefore, toxicity and efficacy of complexes **4.5** and **4.6** to deal with breast cancer at stage IV using 4T1-luc cells *in vivo* was addressed.

In vivo toxicity

To evaluate the toxicity of complexes **4.5** and **4.6**, an acute oral toxicity test was performed based on the OECD Test No. 425: Acute Oral Toxicity: Up-and-Down Procedure.[63] The highest dose tested was 175 mg/kg and the starting dose was 17.5 mg/kg, applying a slope of 2· The test was performed on 6 RjOrl: SWISS mice of 10-11 weeks with dosing intervals of 48 h. Then, toxicity was evaluated after each single administration.

Each compound was prepared in a saline buffer solution which contained 5% of DMSO. Dilution of complexes **4.5** and **4.6** were administered at 10 mL/kg of body weight. The health of the animals was measured by weighting them and assessing their general status, spontaneous and provoked behaviour through an evaluation

scale stablished by Morton and Griffiths.[64] These data were collected daily for a total of 14 days. (Figure 4.43)

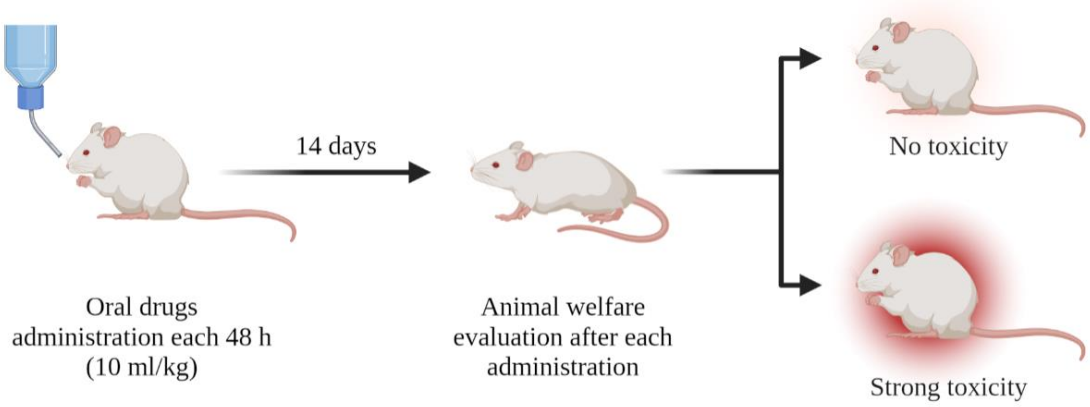

Figure 4.43. *Schematic representation of in vivo toxicity assay performed.*

Interestingly, no loss of animal welfare was detected in any of the mice during the 14 days after the administration of complexes, demonstrating their lack of toxic effects.

In vivo efficacy assays

Once it was observed that no toxic effects occurred following treatment of mice with complexes **4.5** and **4.6**, the next step was to evaluate their chemotherapeutic effect. To achieve this goal, two different assays were conducted. The first assay measured the bioluminescence of tumor cells to determine whether our complexes could reduce breast tumors in their early stages. This assay was based on the bioluminescence generated by the reaction luciferine-luciferase. The second assay involved the assessment of the performance of our complexes into well-established and vascularized tumors. This experiment was based in the measurement of the tumor size and weight. On top of that, the increment of the survival probability was also addressed.

For the assay of early tumors stage, 4T1-luc2 murine mammary tumor cells expressing luciferase were implanted subcutaneously in mice and visualized using optical imaging to monitor tumor growth non-invasively in a longitudinal study. A total of 36 BALB/cByJRj strain (Janvier Labs) mice were used in this assay, distributed in four different groups, (a) control (non-treated), (b) treated with **4.5**

or (c) **4.6**, and (d) positive control (treated with 5-fluorouracil, a chemotherapeutic drug used as treatment for several cancer as breast tumors). [65] On day 0, 4T1-luc cells were implanted subcutaneously in the lumbar region of all mice. The following day, after optical imaging follow-up, the experimental groups (a-d) were established and those mice within group b, c and d were treated with the correspondent compound, either **4.5**, **4.6** or 5-fluoroacil respectively. At that time, the mean radiance of each experimental group was set between 9,62 x 10^7 and 1,06 x 10^8 photon/sec/cm^2/sr. This first assay had a total duration of 11 days from the day of inoculation of the tumor cells. Optical imaging follow-up, mice weight measurements and treatment were performed on days 1, 5, 7, and 11, as shown in Figure 4.44. In all cases, complexes **4.5** and **4.6** were administered orally to conscious mice using a concentration of 1 mg/kg body weight as a suspension in physiological saline buffer contained 5% DMSO.

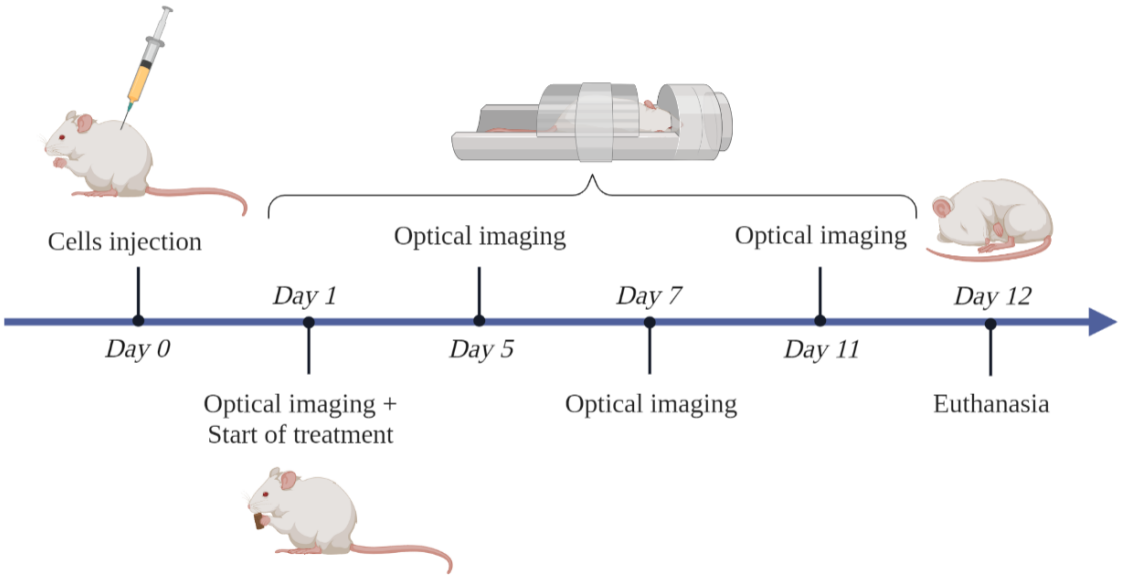

Figure 4.44. *Schematic representation of in vivo efficacy assay in 4T1-luc2 tumors at early stage.*

Based on the graph collected in Figure 4.45 displaying the bioluminescence intensity at different days of the assay it can be concluded that complexes **4.5** and **4.6** are effective in controlling the expansion of 4T1-luc2 during the early stages of tumor growth. Bioluminescence imaging showed almost no emission in mice treated with the complexes, whereas a significant increase in emission intensity

was observed in the control mice and those treated with 5-fluorouracil, indicative of higher tumor growth.

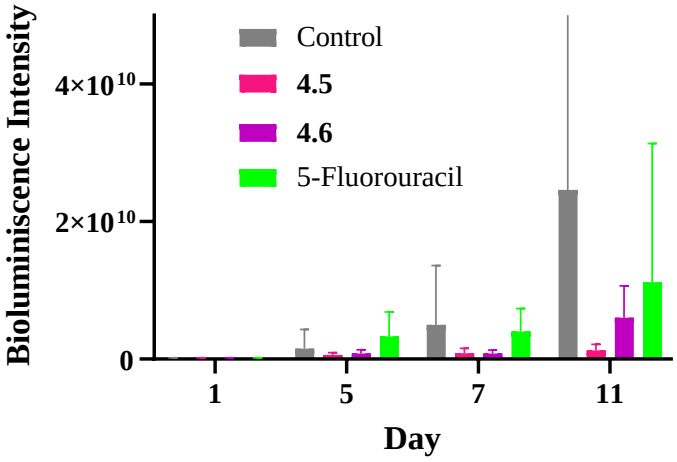

Figure 4.45. *Bioluminiscence intensity collected from mice at different days.*

This data can be corroborated with the bioluminescence scan images (Figure 4.46), where the lower bioluminescence intensity comes from the mice treated with complex **4.5**, follows for the treated with **4.6** and the highest emission intensity, that represents a bigger tumor, comes from control mice.

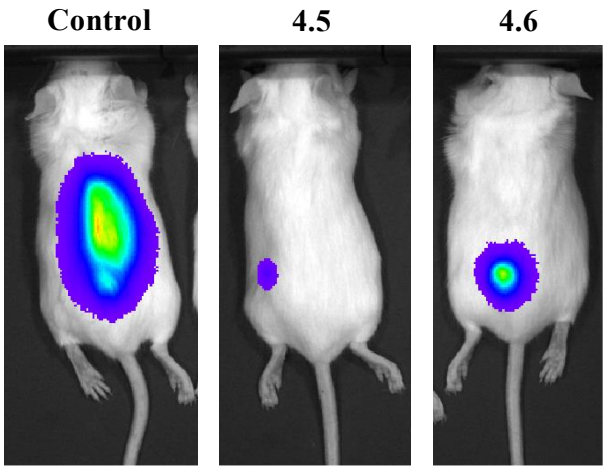

Figure 4.46. *Bioluminiscence scan images at day 11, of a mouse control, and those treated with complexes **4.5** and **4.6**.*

For the second experiment, tumors were treated upon they were well-organized and vascularized. Therefore, even though tumor cells were injected on day 0, the mice were not treated until day 14, and from that point, they were monitored until day 32. So, once again, 4T1-luc2 cells were implanted subcutaneously into 21 mice

(BALB/c AnNRj and BALB/c JRj) at day 0, and their tumor growth was not monitored in a longitudinal study through calliper measurements until day 14. On day 14, the 21 mice were divided into two different experimental groups: (a) control (10 mice) and (b) those treated with complex **4.5** (11 mice). For this experiment only complex **4.5** was selected as it presented the best antitumoral prospects. As before, Treatment with complex **4.5** was performed orally administered at a concentration of 1 mg/kg, as a suspension in physiological buffer saline which containing 5% of DMSO. Calliper and weight measurement as well as treatment administration, were performed on days 14, 18, 21, 25, and 32, as shown Figure 4.47. Through the calliper measurements, the mean tumor volume was calculated with the following formula tumor volume = ½ (length × width·2).[66]

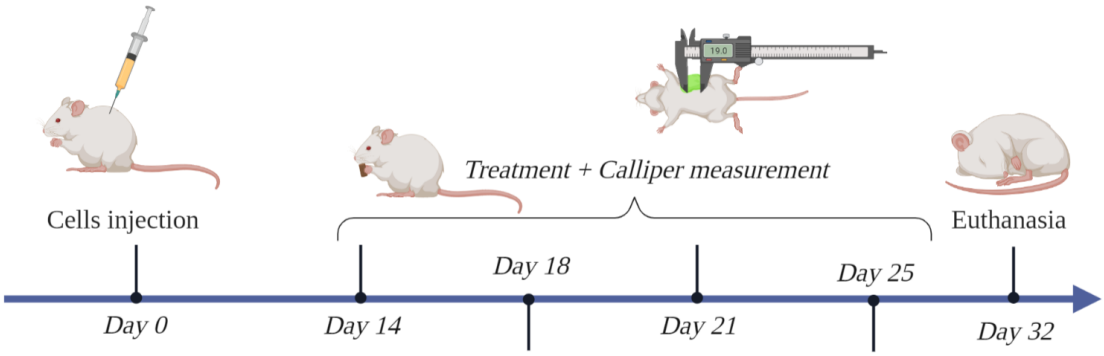

Figure 4.47. *Schematic representation of in vivo efficacy assay in 4T1-luc2 tumors at late stage.*

Figure 4.48A shows the evolution over time of the tumor volume for the two experimental groups (a) and (b). The top graph clearly shows that the experimental group treated with complex **4.5** present clear a reduction of the tumor size from day 14, reaching at day 32 half of the volume in comparison with that of the control mice. Moreover, graph B, which displays the weight of the tumor on the euthanasia day (day 32), corroborates the size reduction for the mice treated with complex **4.5**. Additionally, Figure 4.49 presents a picture of one selected tumor from each experimental group to demonstrate, in a more visual manner, the potential of complex **4.5** to reduce the size of breast tumor in an advance and vascularized stage.

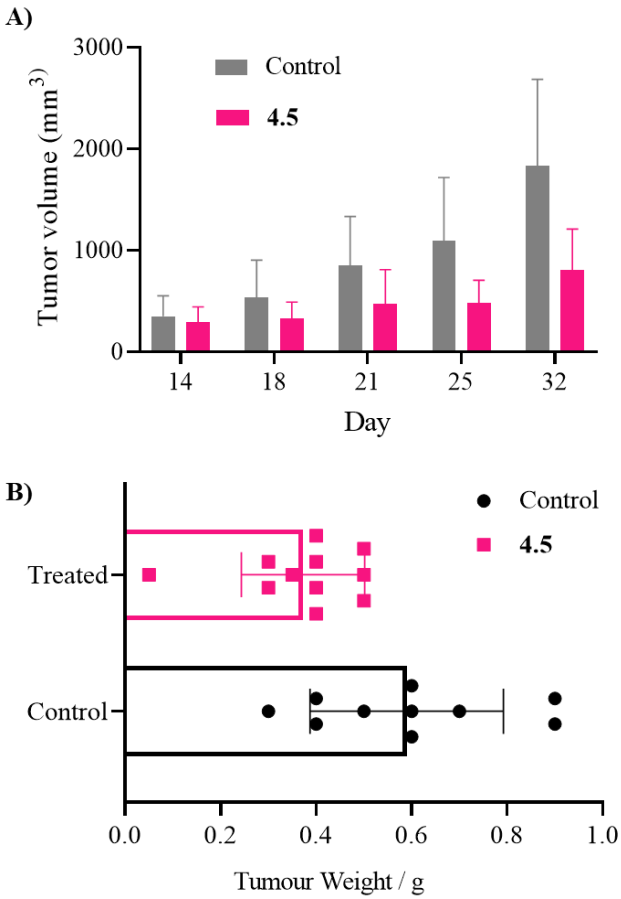

Figure 4.48. *A)Tumor volume variation trough the days; B) Comparative graph of tumor weight on day 32.*

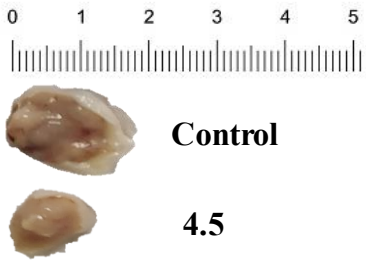

Figure 4.49. *Size analysis (cm) between control and tumors treated with* ***4.5****.*

Finally, a Kaplan-Meire curve was plotted to check the mice survival probability at day 32 (Figure 4.50). Analysis of the data shows that there is a remarkable increase in the suvival probabiblity of treated mice in comparision with that of non treated mice, raising from a 10% to 73 %. Therefore, it can be reasonably surmised that complex **4.5** and **4.6** exhibit a remarkable ability to decelerate the progresion

of breast cancer at early stages. Furthermore, complex **4.5** was found to effectivelly reduce the tumor size while increasing the survival probability in organized and vascularized tumors.

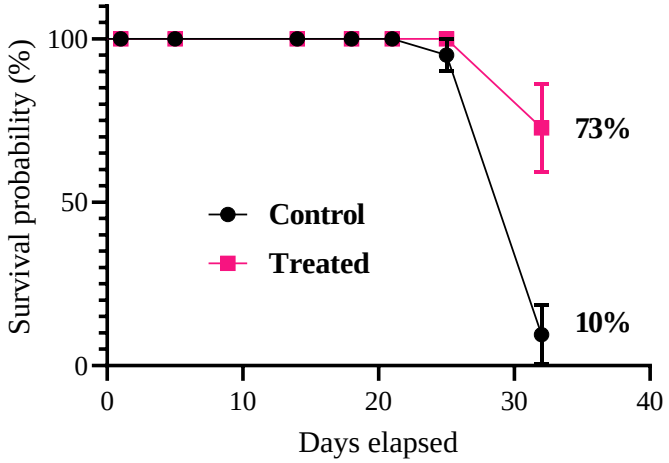

Figure 4.50. *Graph of the survival probability of mice treated and non-treated.*

4.5.4 Biological properties of complexes 4.7 and 4.8

In this section, it will be explored the capacity of complexes **4.7** and **4.8** to be used as PS agents. For this purpose, *in vitro* studies have been conducted on different cell lines such as lung cancer (A549), breast cancer (4T1-luc2) and melanoma (B16-F10-luc), to determine the selectivity of these complexes for a tumor cell line. Later, their cell death mechanism, cellular biodistribution, morphological changes, and the generation of singlet oxygen were studied. Additionally, their toxicity and the PSs properties were studied more deeply in *in vivo* assays. Figure 4.51.

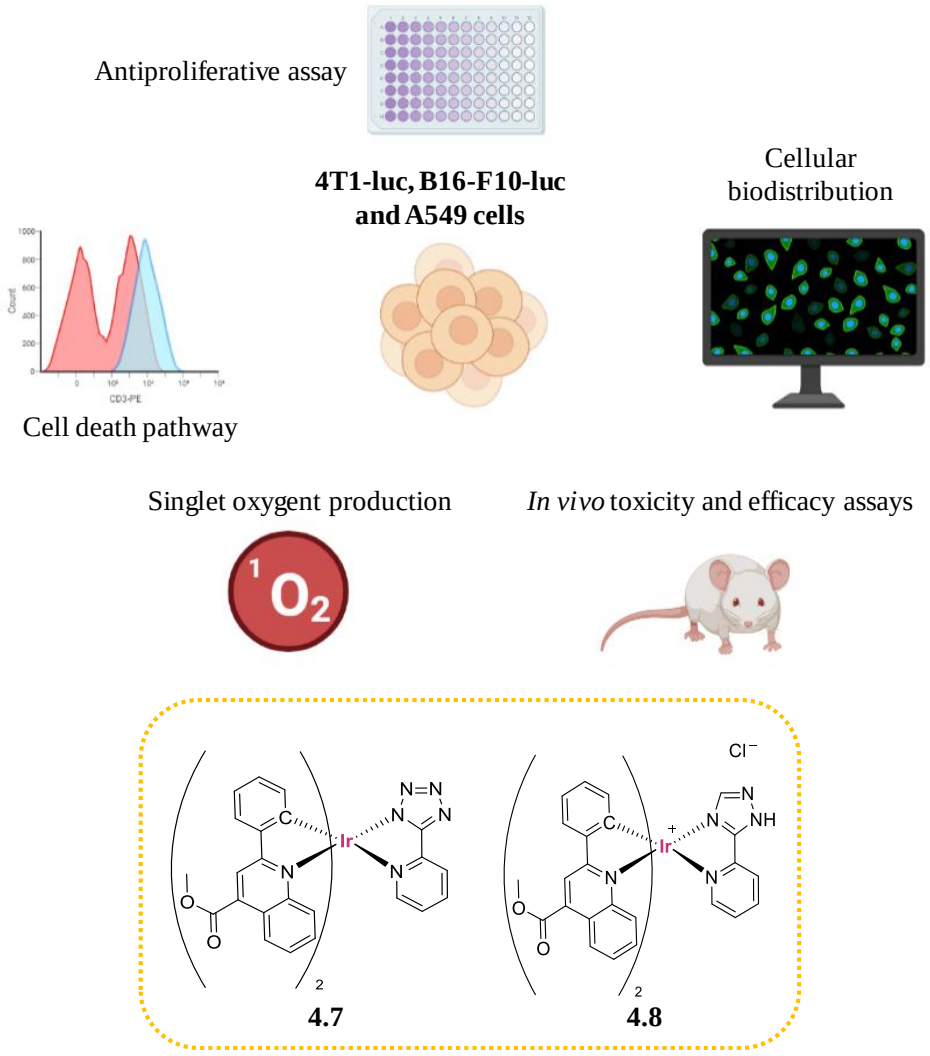

Figure 4.51 *Depiction of biological assays performed using complexes* ***4.7*** *and* ***4.8****.*

4.5.4.1 Antiproliferative properties

The antiproliferative activity of complexes **4.7** and **4.8** was determined by MTT assays in A549, and 4T1-luc2 cell lines as well as in B16-F10-luc. In particular, B16-F10-luc is a murine luciferase-expressing cell line like 4T1-luc2, but in this case mimics a human melanoma instead of breast cancer. It was now incorporated to this screening as melanoma is the typical cancer treated with PDT. Thus, the complexes were evaluated using a range of concentrations from 0.2 to 250 μM, using the serial dilution method starting from a stock solution of 0.1 μM in DMSO, and they were incubated for 48 h. These assays were performed with no irradiation

and irradiation at 470 nm for ten minutes after 24 h of incubation, and maintained for further 24 h in dark.

Focusing the IC_{50} values displayed by the complexes **4.7** and **4.8**, it can be said that both of them exhibit significant photocytotoxic behavior in A549 and 4T1-luc2 cell lines (Table 4.6). Their IC_{50} values drop from 200 μM, when incubated in dark conditions, to the nanomolar range when they are irradiated for 10 minutes at 470 nm (0.93 ± 0.1 (**4.7**), 0.97 ± 0.03 (**4.8**) The remarkably high photocytotoxic index displayed, c.a 200 for **4.7** and 500 for **4.8**, suggests that both of them could be extraordinary candidate as PS for PDT. However, their photocytotoxic potential diminishes when it comes to deal with B16-F10-luc cells, showing PI values of 11 and 36, respectively, as both complexes present moderate cytotoxicity already in dark conditions, (IC_{50}: (5.7 ± 0.3 (**4.7**), 23.5 ± 0.5 (**4.8**)).

Analysis of the ratio between the lipo-hydrophilicity of complexes **4.7** and **4.8** revealed values of a $K_{o/w}$ of 0.472 for **4.7** and -0.193 for **4.8**, showing the higher hydrophilic character of complex **4.7** at neutral pH.[67,68]

Table 4.6. *IC_{50} values (μM) of complexes **4.7** and **4.8** incubated in A549, B16-F10-luc and 4T1-luc2 cell lines for 48 h, in dark and under irradiation conditions.*

	Cell Line	Dark	Irrad. (470 nm)	PI
4.7	*A549*	215 ± 2.1	0.93 ± 0.1	231
	B16-F10-luc	5.7 ± 0.3	0.50 ± 0.08	11
	4T1-luc2	201 ± 1.2	0.97 ± 0.03	207
4.8	*A549*	207 ± 0.8	0.35 ± 0.05	591
	B16-F10-luc	23.5 ± 0.5	0.66 ± 0.06	36
	4T1-luc2	187 ± 0.9	0.34 ± 0.02	550

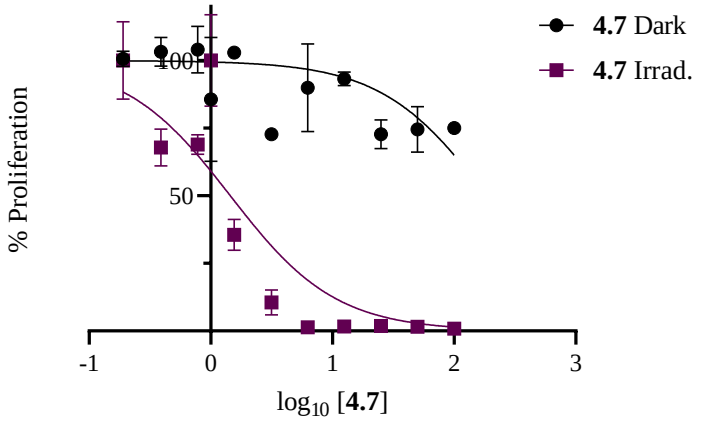

Figure 4.52. *Graph of the percentage of proliferation of 4T1-luc2 cells when they are incubated with complex* ***4.7*** *for 48 h.*

It is worth mentioning that the varying antiproliferative character observed in dark conditions among the three cell lines is notable, as the IC_{50} of both complexes is roughly 200 μM in A549 and 4T1-luc2 cell lines, but falls to below 20 μM in B16-F10-luc cells. The distinct values suggest the potential of these complexes to function as both chemotherapeutic agents for combating melanoma (B16-F10-luc) and as photosensitizer for treating lung or breast tumors (A549 and 4T1-luc2, respectively).

4.5.4.2 Cell morphology analysis

Inverted microscope was used to visualize A549 cells in the presence and absence of complexes **4.7** and **4.8**, in order to track any morphological changes as a consequence of irradiation. There is a remarkable phototoxic change when these complexes are irradiated in this cell line with PI of 231 and 591, respectively. For this assay, A549 cells were incubated with complexes at 200 μM in dark, and at 0.5 μM if they were irradiated at 470 nm. As shown in Figure 4.53, control cells grew normally and presented a healthy morphology in both studied conditions. However, those cells that were exposed to complexes **4.7** or **4.8** in dark started showing some apoptotic signals (presence of blebs, cytoplasmic vacuoles, and generation of apoptotic bodies).[69] Under irradiation conditions, cells presented even clearer those signs described previously, indicative of an apoptotic cell death mechanism. In addition, the microscopy images revealed that complex **4.8** induced, to a lesser extent, necrotic cells when PDT was activated, while in dark

the induction of apoptosis is majority in comparison with complex **4.7** (see Figure 4.53, blue arrows).

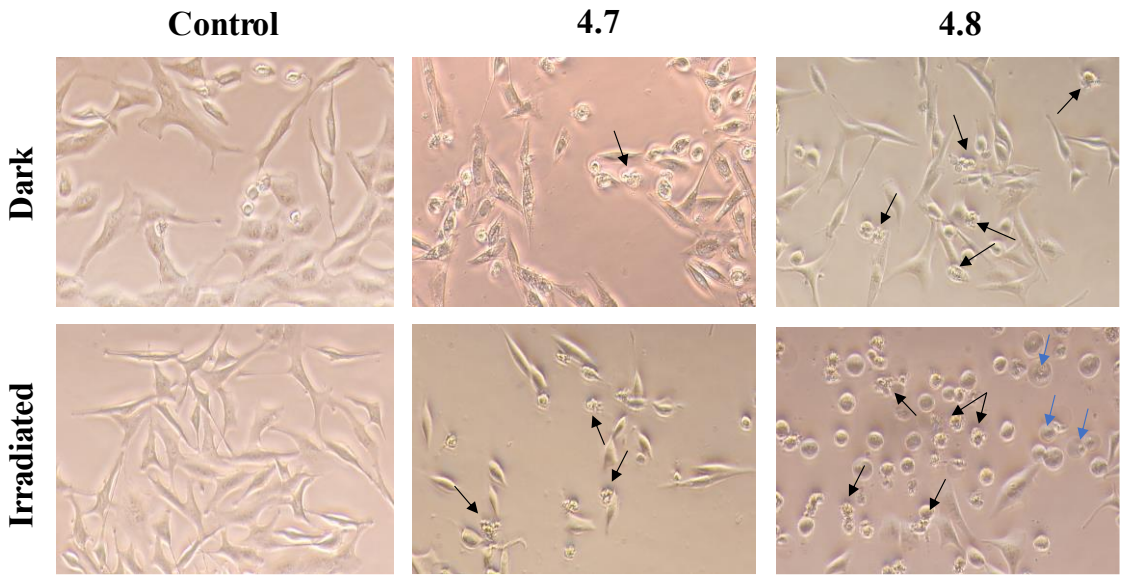

Figure 4.53. *Phase contrast microscopy images of A549 cells treated with complexes **4.7** and **4.8** in drak or irradiated 10 minutes at 470 nm, after 48 h of incubation. Black and blue arrows point to examples of apoptotic and necrotic cells, respectively.*

4.5.4.3 Cell death mechanism analysis

Considering the excellent IC_{50} values revealed by **4.7** and **4.8** under irradiation conditions, it was decided to investigate their cell death mechanism to determine whether the presence of and additional nitrogen in the azole ring (tetrazole in **4.7** and triazole in **4.8**) could induce a different cell death pathway. The analysis was performed by flow cytometry using Annexin V-FITC as fluorescent marker to identify cells undergoing apoptosis. The cell death mechanism induced by complexes **4.7** and **4.8** once that they have been irradiated in 4T1-luc2 cells after 48 hours of incubation (dark and irradiation at 470 nm). For this assay two different concentrations (IC_{50} and $2{\cdot}IC_{50}$ values, respectively) were used in order to determine if concentration of complex affects the cell death pathway. Figure 4.54 illustrates the results obtained. It can be confirmed that no apoptotic death is observed in control samples as expected. Focusing on those cells that were incubated in dark conditions (left column), it can be said that complex **4.7** does not

generate apoptosis, meanwhile complex **4.8** (triazole containing) induces a moderate apoptotic death, 64.3% of cells are Annexin positive, this value is incremented until 70.2% using a higher concentration of this complex.

Regarding those cells that were incubated with complexes under irradiation conditions (right column). It can be appreciated that the majority of cells follow an apoptotic cell death pathway (**4.7**: 78%; **4.8**: 96%), and this value is slightly increased with the concentration, but this fact is not relevant.

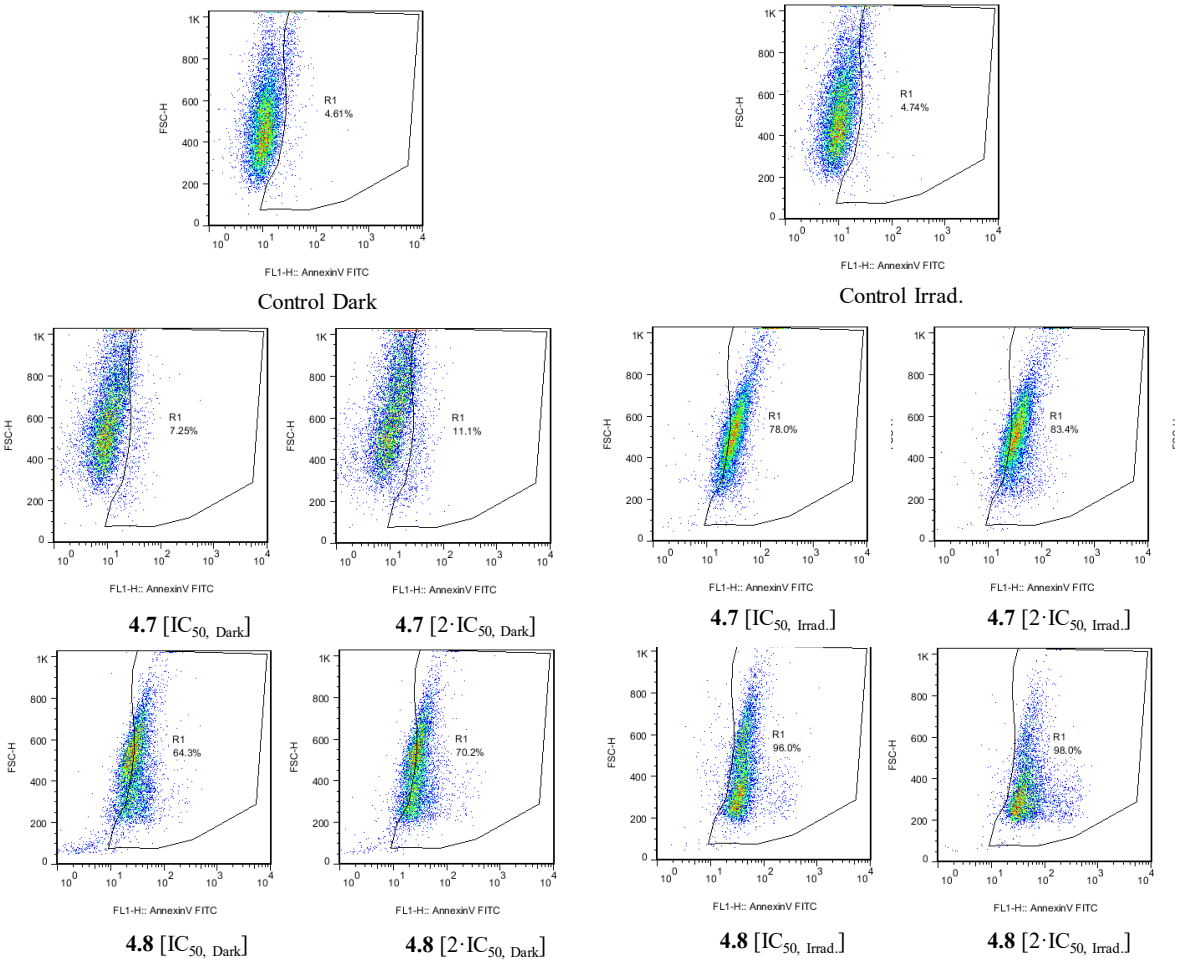

Figure 4.54. *Flow cytometry analysis of apoptotic cell death induced by complexes **4.7** and **4.8**, in dark or irradiation at 470 nm, at their IC_{50} and $2{\cdot}IC_{50}$ concentrations.*

It could be concluded that irradiation plays a key role for the induction of apoptosis on A549 cells when they are exposed to complexes **4.7** and **4.8**. On contrary in dark conditions the presence of a minor number of nitrogens in azole ring (**4.8**) could suggest a tendency for an apoptosis induction.

4.5.4.4 Measurement of singlet oxygen production

Observing the photocytotoxic effects of **4.7** and **4.8** on A459 and 4T1-luc2, prompted us to explore the photocytotoxic mechanism and determine if irradiation was producing singlet oxygen ($^1O_2$). Fluorescence spectroscopy was then used to assess such generation. Irradiation of an acetonitrile solution of complexes **4.7** and **4.8** ($5 \cdot 10^{-5}$ M) with a 450 nm picosecond pulsed diode laser, rendered a band centered at 1270 nm, indicative of $^1O_2$ generation. An additional experiment was performed to corroborate that band observed at 1270 nm was not a mere artefact from the spectrometer, measuring the neat acetonitrile, in absence of complexes.

As shown in Figure 4.55, it could be said that complexes **4.7** and **4.8** can induce singlet oxygen production, being this generation at least one of the causes of the cytotoxicity observed after irradiation.

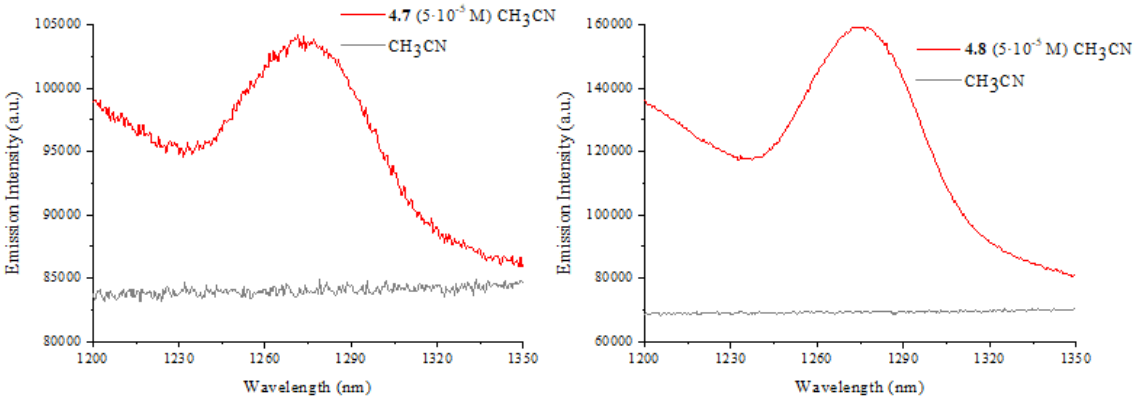

Figure 4.55. *Measurement of singlet oxygen production of complexes **4.7** and **4.8** when it is irradiated with a diode laser of 450 nm. Emission maximum at 1270 nm.*

4.5.4.5 Cellular biodistribution

Fluorescence confocal microscopy assays were performed to elucidate the biodistribution of complexes **4.7** and **4.8** in 4T1-luc2 cells. The compounds were incubated at a concentration of 4 μM in 4T1-luc2 cells for 2 h. After this time, lysosome-selective commercial dye LysoTracker Green (250 nM), was immediately added to the wells prior to collecting confocal images, in order to

avoid a possible quench as it was previously seen for complexes **4.2** and **4.6**. Excitation lasers of 473 nm for LTG and 561 nm for activating complexes were used.

Focusing on images collected in Figure 4.56, where green represents the lysosomal dye LTG, and red the emission coming from complex **4.8**. It can be said that complex **4.8** was able to internalize 4T1-luc2 cells. Additionally, the superimposed images show colocalization of this complex within the lysosomes, confirming the same biodistribution as their analogues.

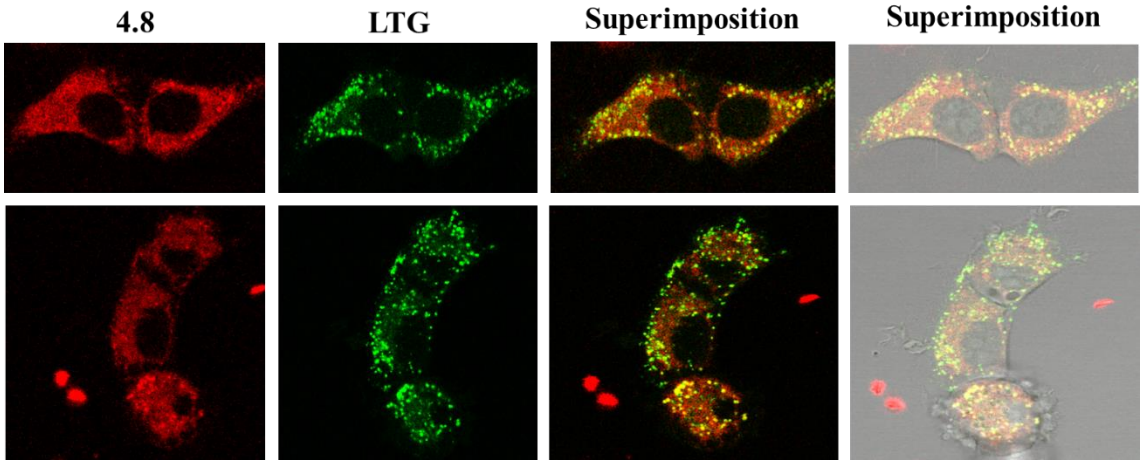

Figure 4.56. *Confocal images of complex 4.6 when it is incubated in 4T1-luc2 cells for 2 hours (2 μM). LTG: 500 nM, 2 min.*

Surprisingly, no confocal images of complex **4.7** could be obtained due to a total quench of its emission in the presence of LTG, even using short incubation times. However, given the similarity in structure with all the complexes shown in this chapter, a lysosomal biodistribution could be suggested.

4.5.3.6 In vivo assays: Toxicity

After studying the different activities of complexes **4.7** and **4.8** in diverse cell lines, and knowing their final targets to be lysosomes and that they exhibit ability to induce an apoptotic cell death pathway, these promising results encouraged us to further study their properties in *in vivo* assays.

In vivo toxicity

To evaluate the toxicity of complexes **4.7** and **4.8**, an acute oral toxicity test was performed based on the OECD Test No. 425: Acute Oral Toxicity: Up-and-Down Procedure.[70] The highest dose tested was 175 mg/kg and the starting dose was 1.75 mg/kg, applying a slope of 2. The test was performed in 6 RjOrl: SWISS mice of 10-11 weeks with dosing intervals of 48 h. Toxicity was evaluated after each single administration. Each compound was prepared in a saline buffer solution which contained 5% of DMSO. Dilutions of complexes **4.5** and **4.6** were administered at 10 mL/kg of body weight. The health of the animals was measured by weighting them and assessing their general status, spontaneous and provoked behaviour through an evaluation scale stablished by Morton and Griffiths.[71] These data were collected daily for a total of 14 days.

Interestingly, no loss of animal welfare was detected in any of the mice during the 14 days after the administration of complexes, demonstrating their non-toxic effect. (Figure 4.57).

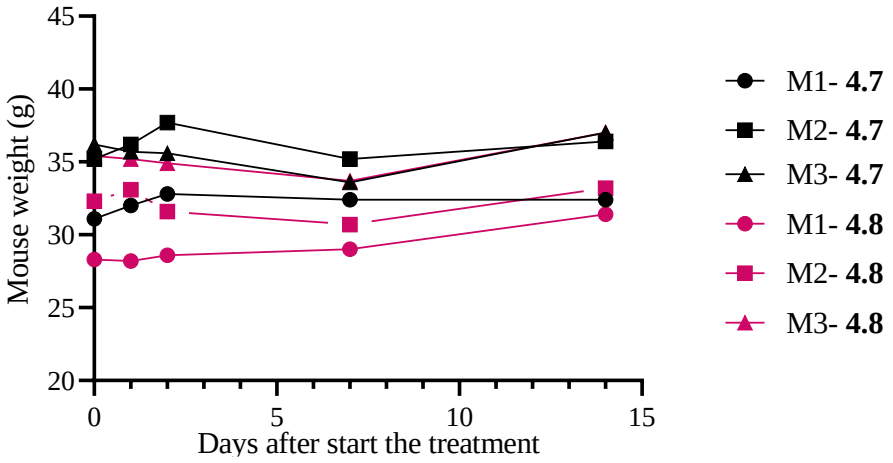

Figure 4.57. *Evolution of mice weight.*

4.6 Conclusions

In this chapter, a series of complexes $[Ir(mcp)_2(N\hat{}N)]^{+/0}$, were the cyclometallated ligand has been introduced in order to increase the solubility in biological media, and red shift the emission maxima. The N^N ligand represents different azole derivatives. The selection of these azole derivatives allows to tailor the properties of final complexes and establish a ratio between their charge and number of heteroatoms present in the fused ring. It was possible to isolate eight different complexes which contain, 2-(2-pyridyl)benzimidazole (**4.1** and **4.2**) and 2-(4-thiazolyl)benzimidazole (**4.3** and **4.4**), 3-phenyl-1H-pyrazole (**4.5** and **4.6**) and, 2-(1H-1,2,4-triazol-3-yl)-pyridine and 2-(2H-tetrazol-5-yl)pyridine (**4.7** and **4.8**), in their deprotonated an protonated form respectively.

Regarding their optical properties, all the complexes in this chapter exhibit emissions around 700 nm that can be attributed to ^{3}MLCT transitions, and show excellent quantum yields in absence of oxygen (27.5-56.1%). Focusing on the different family pairs, neutral complexes **4.1**, **4.3** and **4.5** exhibit in all cases a maximum emission less energetic than in the case of their cationic analogous **4.2**, **4.4** and **4.6**, that can be explained as a consequence of the modification of the energy of frontier orbitals. The synthesized complexes were evaluated as chemotherapeutic agents and photosensitizers in various cell lines such as A549, 4T1-luc2, or B16-F10-luc. Their biodistribution was also studied using fluorescence confocal microscopy, and in all cases, they showed lysosomal accumulation. By activating them using a 470 nm irradiation source, their ability to generate singlet oxygen was activated, inducing cell death via apoptotic pathway and reaching PI values close to 550 in the most promising case (**4.8**). Interestingly, senescence was induced in the A549 and SK-Mel-103 cell lines, showing that the synthesized complexes **4.3** and **4.4** can not only act on cancer cells but also on senescent cells, revealing a promising capacity to be used as photochemotherapeutic and photosenolitic agents. Once the biological studies were completed, the most promising complexes (**4.5**-**4.8**) were tested for both *in vivo* toxicity and efficacy assay demonstrating their potential as anticancer agents.

4.7 General synthetic procedure

All chemicals were purchased as reagent grade from Sigma-Aldrich and used without further purification.

Instrumentation

Mass spectra were recorded on a BRUKER ESQUIRE 3000 PLUS, with the electrospray (ESI) technique. ^{1}H, ^{13}C-{^{1}H} and ^{31}P-{^{1}H} NMR, including 2D experiments, were recorded at room temperature on a BRUKER AVANCE 400 spectrometer (^{1}H, 400 MHz, ^{13}C, 100.6 MHz) with chemical shifts (δ, ppm) reported relative to the solvent peaks of the deuterated solvent. Steady-state photoluminescence spectra were recorded with a Jobin-Yvon-Horiba fluorolog FL-3-11 spectrometer using band pathways of 3 nm for both excitation and emission. UV/vis spectra were recorded with 1 cm quartz cells on an Evolution 600 spectrophotometer. Quantum yields were measured using an absolute method provided by Hamamatsu Photonics Quantaurus-QY C11347-11.

Synthesis of $[Ir(mpc)_2(\mu\text{-}Cl)]_2$

2-Phenylquinoline-4-carboxylic acid (5.4 mmol) was dissolved in methanol (10 mL) and cooled to 0-5 °C. Thionyl chloride (8.2 mmol) was added dropwise under stirring. Once the addition was over, the reaction mixture was refluxed for 2 h, affording a yellow solution. The methanol and the excess of thionyl chloride were removed under vacuum. The residue was neutralized using a solution of sodium bicarbonate (50 mL). The aqueous layer was extracted with chloroform (3 × 20 mL); the combined organic layer was dried over anhydrous sodium sulphate and dried to get the desired compound as pale-yellow solid (1.12 g, 85%).

Once the ligand (methyl-2-phenylquinoline-4-carboxylate) was obtained, 200 mg (0.67 mmol) were dissolved in the minimum volume of 2-etoxiethanol (5 mL) and $IrCl_3 \cdot nH_2O$ (0.34 mmol) was added. The reaction mixture was refluxed at 383 K for 24 h. The resultant suspension was cooled and filtered affording the desired complex as a dark garnet solid, it was washed with water, ethanol, and acetone, and dried under vacuum. (164 mg; 0.11 mmol; 64 %).

Synthesis of complexes 4.1, 4.3, 4.5 and 4.7

50 mg of $[Ir(mpc)_2(\mu\text{-}Cl)]_2$, (0.033 mmol) were disolved in 5 mL of dry dichloromethane. Once all the dimmer has been solubilized, 0.066 mmol of correspondent azole derivate and 15 mg of Cs_2CO_3 were added. The resultant dark red suspension was stirred and refluxed at 318 K for 20 h. The bright red residue was filtered through celite, and the filtered was collected and dried. The red solid obtained was purified by column chromatography using as eluents a mixture of DCM/MeOH (9/1).

4.1: (0.045 mmol; 79%) ^{1}H NMR (400 MHz, DMSO-d_6) δ 8.77 (s, 1H), 8.63 (s, 1H), 8.31 – 8.21 (m, 3H), 8.04 (d, J = 8.9 Hz, 1H), 7.97 (d, J = 7.9 Hz, 1H), 7.87 (t, J = 7.7 Hz, 1H), 7.83 (d, J = 5.5 Hz, 1H), 7.51 (d, J = 9.0 Hz, 1H), 7.48 – 7.43 (m, 1H), 7.42 – 7.31 (m, 3H), 7.17 (dt, J = 11.8, 7.3 Hz, 2H), 7.07 – 7.00 (m, 1H), 6.86 (dt, J = 17.7, 7.6 Hz, 3H), 6.72 – 6.65 (m, 1H), 6.56 – 6.45 (m, 3H), 6.15 (d, J = 8.2 Hz, 1H), 4.05 (s, 3H), 3.99 (s, 3H) ppm. ^{13}C NMR (101 MHz, DMSO-d^6) δ 171.2, 170.7, 166.4, 166.1, 150.9, 149.3, 149.2, 147.6, 147.1, 147.0, 138.5, 138.1, 137.6, 135.5, 135.3, 131.2, 130.9, 130.7, 130.4, 128.5, 128.1, 127.7, 127.6, 127.0, 126.9, 126.5, 126.1, 125.0, 124.9, 124.6, 122.8, 122.7, 121.8, 119.5, 119.0, 118.9, 115.3, 53.7, 53.6 ppm. HRMS (ESI): m/z (calcd.) = 911.0186, m/z (found, **4.1**+H) = 912.2166.

4.3: (0.048 mmol; 73%) ^{1}H NMR (400 MHz, DMSO-d_6) δ 8.74 (s, 1H), 8.65 (s, 1H), 8.53 (d, J = 2.1 Hz, 1H), 8.33 – 8.22 (m, 4H), 8.11 – 8.06 (m, 1H), 7.92 (d, J = 2.1 Hz, 1H), 7.57 (d, J = 9.0 Hz, 1H), 7.48 (ddd, J = 8.2, 6.9, 1.2 Hz, 1H), 7.37 – 7.31 (m, 1H), 7.31 – 7.26 (m, 1H), 7.16 (dtd, J = 15.3, 7.2, 6.6, 1.2 Hz, 3H), 6.88 – 6.78 (m, 3H), 6.69 – 6.57 (m, 2H), 6.54 – 6.46 (m, 2H), 6.14 (d, J = 8.1 Hz, 1H), 4.05 (s, 3H), 3.99 (s, 3H) ppm. ^{13}C NMR (101 MHz, DMSO-d_6) δ 170.5, 170.0, 165.6, 165.4, 163.9, 154.9, 153.9, 151.4, 150.3, 148.1, 147.5, 147.2, 146.7, 146.4, 142.1, 138.3, 138.2, 134.4, 134.4, 130.5, 130.4, 129.8, 127.6, 127.5, 127.4, 127.0, 126.1, 125.4, 125.3, 123.4, 123.2, 122.3, 121.9, 120.0, 119.3, 118.1, 118.1, 117.5, 116.6, 113.5, 53.3, 53.2 ppm. HRMS (ESI): m/z (calcd.) = 917.0320, m/z (found, **4.3**+H) = 918.1708.

4.5: (0.054 mmol; 82 %) ^{1}H NMR (400 MHz, DMSO-d_6) δ 8.73 (s, 1H), 8.66 (s, 1H), 8.31 – 8.23 (m, 3H), 8.12 – 8.09 (m, 1H), 7.96 (d, J = 8.9 Hz, 1H), 7.70 – 7.58 (m, 3H), 7.51 – 7.41 (m, 3H), 7.21 (d, J = 1.9 Hz, 1H), 7.11 (dddd, J = 8.6, 7.2, 6.4, 1.3 Hz, 2H), 7.07 – 6.98 (m, 3H), 6.81 (td, J = 7.4, 1.2 Hz, 1H), 6.67 – 6.59 (m, 2H), 6.37 (d, J = 1.9 Hz, 1H), 6.31 (dd, J = 7.8, 1.2 Hz, 1H), 4.05 (d, J = 4.6 Hz, 6H) ppm. ^{13}C NMR (101 MHz, DMSO-d_6) δ 195.0, 185.5, 170.5, 170.0, 165.7, 165.7, 158.9, 155.0, 152.6, 148.3, 148.2, 147.7, 146.5, 146.3, 145.7, 140.0, 138.5, 138.2, 137.5, 135.2, 133.4, 130.5, 130.2, 130.0, 129.4, 127.5, 127.2, 126.7, 125.8, 125.7, 125.1, 123.2, 123.0, 121.9, 121.1, 119.1, 118.0, 117.8, 103.5, 54.9, 53.81 ppm. HRMS (ESI): m/z (calcd.) = 860.9569, m/z (found, **4.5**+H) = 862.1988.

4.7: (0.042 mmol; 64%) ^{1}H NMR (400 MHz, DMSO-d^6) δ 8.80 (s, 1H), 8.72 (s, 1H), 8.34 (d, J = 8.0 Hz, 1H), 8.32 – 8.25 (m, 2H), 8.23 – 8.16 (m, 1H), 8.01 – 7.90 (m, 2H), 7.92 – 7.85 (m, 1H), 7.79 (d, J = 9.0 Hz, 1H), 7.52 (ddd, J = 7.3, 5.7, 1.5 Hz, 1H), 7.46 (dddd, J = 9.7, 8.2, 6.8, 1.1 Hz, 2H), 7.37 (d, J = 8.9 Hz, 1H), 7.23 – 7.15 (m, 1H), 7.17 – 7.00 (m, 3H), 6.87 (td, J = 7.4, 1.3 Hz, 1H), 6.77 (td, J = 7.4, 1.3 Hz, 1H), 6.65 (dd, J = 7.7, 1.2 Hz, 1H), 6.42 (dd, J = 7.8, 1.1 Hz, 1H), 4.05 (d, J = 1.2 Hz, 6H) ppm. ^{13}C NMR (101 MHz, DMSO-d^6) δ 170.2, 169.7, 165.5, 162.5, 153.8, 147.9, 147.8, 147.5, 147.1, 146.2, 145.9, 140.2, 138.7, 138.3, 135.0, 133.9, 130.9, 130.7, 130.4, 130.1, 128.8, 127.8, 127.5, 127.1, 127.0, 126.6, 126.4, 126.1, 125.8, 125.1, 123.3, 123.2, 122.6, 122.2, 121.8, 118.2, 118.0, 53.3, 53.2 ppm. HRMS (ESI): m/z (calcd.) = 862.9260, m/z (found, **4.7**+H) = 864.1873.

Synthesis of complexes 4.2, 4.4, 4.6 and 4.8

50 mg of $[Ir(mpc)_2(\mu\text{-}Cl)]_2$, (0.033 mmol), and 0.066 mmol of correspondent azole derivative were dissolved in 5 mL of a mixture of dry dichloromethane / methanol (1/1). The mixture was stirred at r.t. for 2 h. The resultant bright red solution was refluxed at 325 K for 20 h. The solvents were removed under vacuum until minimum volume, and the product was precipitated with cool pentane, affording a red solid which was filtered and dried. Column chromatography using as eluents a mixture of DCM/MeOH (9/1) was performed to purify the final complexes.

4.2: (0.044 mmol; 68%) ^{1}H NMR (400 MHz, DMSO-d_6) δ 13.09 (s, 1H), 8.82 (s, 1H), 8.64 (s, 1H), 8.38 – 8.31 (m, 1H), 8.30 (dd, J = 8.5, 1.5 Hz, 2H), 8.26 (dd, J = 8.5, 1.4 Hz, 1H), 8.22 (d, J = 7.9 Hz, 1H), 8.13 (t, J = 7.7 Hz, 1H), 8.03 (d, J = 5.6 Hz, 1H), 7.88 (d, J = 9.0 Hz, 1H), 7.66 (d, J = 6.3 Hz, 1H), 7.08 (ddd, J = 8.7, 6.9, 1.5 Hz, 2H), 6.90 (dtd, J = 12.0, 7.5, 1.3 Hz, 2H), 6.71 – 6.60 (m, 1H), 6.63 – 6.56 (m, 1H), 6.55 (dd, J = 7.7, 1.2 Hz, 1H), 6.33 (d, J = 8.4 Hz, 1H), 4.06 (s, 3H), 3.99 (s, 3H). ^{13}C NMR (101 MHz, DMSO-d_6) δ 214.3, 213.8, 170.3, 170.2, 169.8, 165.4, 165.3, 147.6, 147.4, 147.2, 146.6, 145.7, 140.7, 140.2, 138.9, 138.8, 134.5, 134.1, 131.1, 130.9, 130.8, 130.3, 128.0, 127.3, 127.2, 126.3, 126.1, 124.8, 123.45 122.8, 118.4, 117.6, 53.4, 53.3 ppm. HRMS (ESI): m/z (calcd.) =912.0127, m/z (found) = 912.2152.

4.4: (0.047 mmol; 71%) ^{1}H NMR (400 MHz, DMSO-d_6) δ 12.97 (s, 1H), 8.80 (s, 1H), 8.71 (d, J = 1.9 Hz, 1H), 8.67 (s, 1H), 8.44 (d, J = 2.7 Hz, 1H), 8.35 – 8.25 (m, 5H), 7.88 (d, J = 8.9 Hz, 1H), 7.52 (t, J = 7.6 Hz, 2H), 7.46 (d, J = 9.0 Hz, 1H), 7.40 (dd, J = 8.5, 6.9 Hz, 1H), 7.29 – 7.16 (m, 4H), 7.06 (t, J = 7.8 Hz, 1H), 6.95 – 6.85 (m, 2H), 6.70 – 6.60 (m, 2H), 6.54 (d, J = 7.6 Hz, 1H), 6.34 (d, J = 8.3 Hz, 1H), 4.06 (s, 3H), 4.00 (s, 3H) ppm. ^{13}C NMR (101 MHz, DMSO-d_6) δ 170.4, 169.7, 165.5, 165.3, 147.8, 147.1, 146.7, 145.8, 138.9, 138.8, 134.7, 134.4, 131.0, 130.9, 130.1, 129.0, 127.9, 127.8, 127.3, 127.3, 126.4, 126.1, 124.7, 123.5, 123.4, 122.9, 122.8, 118.5, 117.6, 115.3, 53.4, 53.3 ppm.

4.6: (0.05 mmol; 76 %) ^{1}H NMR (400 MHz, DMSO-d_6) δ 13.96 (s, 1H), 8.81 (s, 1H), 8.74 (s, 1H), 8.38 – 8.30 (m, 3H), 8.23 (d, J = 8.0 Hz, 1H), 8.01 – 7.85 (m, 4H), 7.65 – 7.45 (m, 5H), 7.31 (dd, J = 21.1, 8.5 Hz, 1H), 7.19 (t, J = 7.6 Hz, 1H), 7.13 (t, J = 7.5 Hz, 1H), 7.07 (t, J = 7.9 Hz, 1H), 6.99 (s, 1H), 6.86 (t, J = 7.5 Hz, 1H), 6.81 (t, J = 7.6 Hz, 1H), 6.54 (d, J = 7.9 Hz, 1H), 6.38 (d, J = 7.7 Hz, 1H), 4.07 (d, J = 5.9 Hz, 6H) ppm. ^{13}C NMR (101 MHz, DMSO-d^6) δ 186.5, 170.3, 169.6, 165.5, 165.4, 151.2, 147.3, 147.2, 146.8, 145.9, 145.8, 145.6, 139.9, 139.0, 138.7, 134.3, 133.9, 131.1, 131.0, 130.7, 130.6, 128.0, 127.8, 126.3, 126.1, 124.9, 123.4, 123.2, 122.9, 122.6, 118.3, 118.0, 111.9, 105.2 53.4, 53.4 ppm. HRMS (ESI): m/z (calcd.) =862.2011, m/z (found) = 862.1979.

4.8: (0.044 mmol; 67%) ^{1}H NMR (400 MHz, CD_2Cl_2) δ 8.63 (s, 1H), 8.61 – 8.56 (m, 2H), 8.52 (dd, J = 8.5, 1.4 Hz, 1H), 8.11 (dd, J = 7.9, 1.3 Hz, 1H), 8.03 – 7.99 (m, 2H), 7.94 – 7.88 (m, 2H), 7.63 (ddd, J = 8.9, 6.5, 1.6 Hz, 1H), 7.55 (d, J = 9.3 Hz, 2H), 7.40 (dddd, J = 15.5, 8.4, 6.8, 1.2 Hz, 3H), 7.23 – 7.07 (m, 5H), 6.96 (ddd, J = 8.6, 6.9, 1.5 Hz, 1H), 6.87 – 6.78 (m, 4H), 6.53 (dd, J = 7.9, 1.1 Hz, 1H) ppm. 13C NMR (101 MHz, CD_2Cl_2) δ 170.7, 170.5, 166.4, 166.2, 162.1, 156.6, 152.4, 149.5, 149.5, 148.9, 148.2, 147.1, 146.9, 146.6, 138.8, 138.2, 137.8, 136.3, 135.3, 131.4, 131.1, 130.8, 130.6, 128.3, 127.9, 127.8, 127.6, 127.0, 126.6, 126.3, 124.9, 124.9, 124.6, 122.8, 121.6, 119.3, 119.1, 118.9, 53.6, 53.5 ppm. HRMS (ESI): m/z (calcd.) = 863.1952, m/z (found) = 863.1941.

4.8 Materials and methods

Instrumentation

Mass spectra were recorded on a BRUKER ESQUIRE 3000 PLUS, with the electrospray (ESI) technique. ^{1}H and ^{13}C{^{1}H} NMR, including 2D experiments, were recorded at room temperature on a BRUKER AVANCE 400 spectrometer (^{1}H, 400 MHz, ^{13}C, 100.6 MHz) with chemical shifts (δ, ppm) reported relative to the solvent peaks of the deuterated solvent.[72] Steady-state photoluminescence spectra were recorded with a Jobin-Yvon-Horiba fluorolog FL-3-11 spectrometer using band pathways of 3 nm for both excitation and emission. UV/vis spectra were recorded with 1 cm quartz cells on an Evolution 600 spectrophotometer. Quantum yields were measured using an absolute method provided by Hamamatsu Photonics Quantaurus-QY C11347-11. Specifically, each sample was measured using the excitation scanning mode in aerated and deaerated DMSO solution at RT, after recording a reference sample (neat aerated DMSO at r.t.).

Cell culture

A549 (human lung carcinoma), SK-Mel-103 (human melanoma) and B16-F10-luc (murine melanoma) cell lines were routinely cultured in high glucose DMEM medium supplemented with 10% fetal bovine serum (FBS), L-glutamine and penicillin/streptomycin. 4T1-luc2 cells were cultured in high glucose RPMI medium supplemented with 10% FBS without antibiotics. Senescent cell cultures were cultured in DMEM medium supplement with 10% FBS without antibiotics. All cultures were maintained at 37 °C in a humidified atmosphere of 95% air/5% CO_2.

Senescence induction

A549 cells were treated with 15 µM of cisplatin for 10 days. SK-MEL-103 cells were treated with 5 µM of palbociclib for 7 days. For experiments with cells, cisplatin was reconstituted in sterile PBS, and palbociclib in DMSO.

Antiproliferative activity assays

The MTT-reduction assay was used to analyse cell metabolic activity as an indicator for cell sensitivity to the complexes in A549 cell line. 10^5 cells/mL were seeded in complete DMEM (0.5% FBS) medium in flat-bottom, 96-well plates (100 µl/well) and allowed to attach for 24 h prior to addition of compounds. Cells were incubated with complexes **4.1**-**4.8** for 24 or 48 h and then 10 µl of MTT (5 mg/mL in PBS) were added to each well and plates were incubated for 2 h at 37 °C. For PDT, the irradiation took place 5 or 24 hours after the addition of complexes, depending on the final incubation time, 24 or 48 hours, respectively. Finally, culture medium was removed and DMSO (100 µl/ well) was added to dissolve the formazan crystals. The optical density was measured at 550 nm using a 96-well multiscanner autoreader (ELISA) and IC_{50} was calculated using GraphPad Prims 5 or 9 software. Each compound was analyzed at least in three independent experiments.

Cytotoxicity activity assays

The CellTiter- Blue cytotoxicity assay was used to analyze cell cytotoxic activity of synthetized complexes in A549 and SK-Mel-103 cell lines, senescent and non-senescent. 10^5 cells/mL were seeded in complete DMEM (0.5% FBS) medium in flat-bottom, 96-well plates (100 µl/well) and allowed to attach for 24 h prior to addition of compounds. Cells were incubated with complexes **4.3** and **4.4** for 24 h, then they were irradiated at 470 nm for 10 minutes, and incubated again for additional 24 hours. Then 10 µl of CellTiter-Blue were added to each well and plates were incubated for 2 h at 37 °C. Finally, the fluorescence was measured using an Infinite 200 PRO Multimode Spectrophotometer (TECAN), and LC_{50} was calculated using GraphPad Prims 9 software. Each compound was analyzed at least in three independent experiments.

Cell death mechanism assays

Apoptotic cell death pathway was determined by measuring phosphatidylserine exposure on cell surface in A549 cells. With this purpose, 10^5 cells/well were seeded in complete medium in flat-bottom, 6-well plates (2 mL/well) and left overnight to be attached to the bottom. Cells were treated for 48 h with synthetized complexes (**4.5**-**4.8**) in dark and under irradiation conditions (405 nm for 10 min) at concentrations of their IC_{50} and $2 \cdot IC_{50}$ values in duplicate. After the incubation time, cells were washed with PBS (1 mL/well), trypsinized (0.5 mL/well), and resuspended in 100 µL of a mixture of Annexin-binding buffer (ABB 140 µM; NaCl 2.5 µM; $CaCl_2$ 10 µM; HEPES/NaOH pH 7.4), and FITC-conjugated Annexin V (**4.5**-**4.7**) and PI (**4.5** and **4.6**). They were incubated at room temperature in the dark for 15 minutes. Finally, cells were diluted to 500 µL with PBS and a total of 10,000 cells were acquired on a FACSCaliburTM flow cytometer. Cell death was analyzed using CellQuest Pro, FlowJo 7.6.1 and GraphPad Prism 9 software.

Singlet oxygen production measurement

Singlet oxygen emission spectra were measured on a PicoQuant, FT300 fluorescence spectrometer equipped with a Hamamatsu H10330 A-45 thermoelectric cooled NIR-PMT unit with a spectral range of 950 nm to 1400 nm. The complexes **4.5**, **4.7**, and **4.8** (in CH_3CN) were excited with a 450nm picosecond pulsed diode laser (P-C-450, PicoQuant) with 80 MHz repetition rate. Signals were digitised with a Time Harp 260 PCI card (PicoQuant). Spectra were recorded in the custom measurement mode of EasyTau software

Distribution coefficient ($logP_{7.4}$) measurement

The n-octanol-water coefficient of complexes were determined using a shake-flask method. A mixture of buffered-saline distilled water (100 mL, phosphate buffer $[PO_4^{3-}]$ = 10 mM, [NaCl] = 0.15 M, pH 7.4) and n-octanol (100 mL) was shaken for 72 h to allow saturation of both phases. Approximately 0.5 mg of the complexes or ligands were dissolved in 3 mL of the aqueous phase and 3 mL of the organic phase were added, mixing them for 10 min. The resulting emulsion was centrifuged to separate the phases. The concentration of the compounds in each phase was determined using UV absorbance spectroscopy at 298 K. $logP_{7.4}$ was defined as log{[compound(organic phase)]/[compound(aqueous phase)]}.

Fluorescence confocal microscopy

10^4 cells/well (A549, SK-Mel-103 or 4T1-luc2 cells) were seeded in complete medium in µ-slide 8 well (300 µl/well) and left 24 h to be attached to the bottom. Then, 200 µl of culture medium was removed and 100 µl of a solution of the corresponding complexes (**4.1**-**4.8**) were added to a final concentration of 2 µM. The complexes were incubated with the cells for 2 hours. Thereafter, LysoTracker Green (LTG) at 500 nM, CellBlue Tracker at 500 nM and Hoechst at 500 nM were added. They were incubated with the cells for 45 min LTG and 30 min Hoechst and CBT, at room temperature. In those cases, where complexes suffered a quenching with the tracker, these were added just before starting the fluorescence microscopy visualization. Eventually the medium was replaced with fresh

medium. Images were collected in a sequential mode in a ZEISS LSM 880 confocal microscope with a 60x oil immersion lens, a line average of 4, and a format of 1024x1024 pixels using excitation wavelength of either 405 (CBT), 473 nm (LTG) or 561 nm (complexes). The confocal pinhole was 1 Airy unit. Images were analyzed with Zen Blue Little software.

The biodistribution of complexes **4.3** and **4.4** was studied using Leica TCS SP5 confocal microscope, with a 60x oil immersion lens, a line average of 4, and a format of 1024x1024 pixels using excitation wavelength of either 365 (Hoechst), 473 nm (LTG) or 561 nm (complexes). The confocal pinhole was 1 Airy unit. Images were analyzed with LAS X software.

Crystal Structure Analysis

Crystals were mounted in inert oil glass fibres and transferred to the cold gas stream of a Bruker Venture diffractometer equipped with a low-temperature attachment. Data were collected using monochromated Mo Kα radiation (λ = 0.71073 Å). Scan type ω. Absorption corrections based on multiple scans were applied with the program SADABS. The structures were solved by direct methods and refined on F2 using the program SHELXL-2016. All non-hydrogen atoms were refined anisotropically. Hydrogen atoms were included in calculated positions and refined using a riding model.

***In vivo* assays**

All experiments were conducted following the Project License PI87/ 20 approved by the Ethic Committee for Animal Experiments from the University of Zaragoza. The care and use of animals were performed accordingly with the Spanish Policy for Animal Protection RD53/2013, which meets the European Union Directive 2010/63 on the protection of animals used for experimental and other scientific purposes. Adults female RjOrl: SWISS mice (10-11 weeks) were used. Mice were purchased from Janvier Laboratories. The animals were housed at a maximum of five per cage (30 × 20 × 15 cm) with ad libitum access to food and water. They were kept at a controlled temperature of 23 ± 1ºC on a 12 h light/ dark cycle (lights

on at 7:00 a.m.). Drugs were delivered by the intra- peritoneal route in conscious mice and a standard volume of 10 mL/kg body weight was injected. All compounds were dissolved in water Milli-Q + DMSO 5%, which was the maximum DMSO concentration in solutions delivered to animals.

Animals were observed individually at least once during the first 30 min after dosing, periodically during the first 24 h (with special attention given during the first 4 h), and daily thereafter, for a total of 14 days. The health status of the animals was monitored using an evaluation scale based on the one proposed by Morton and Griffiths.

[1] B. Eftekhari-Sis, M. Zirak, A. Akbari, *Chem. Rev.* **2013**, *113*, 2958-3043.
[2] Y. Ju, R.S. Varma, *J. Org. Chem.* **2006**, *71*, 135-141.
[3] X. Li, L. He, H. Chen, W. Wu, H. Jiang, *J. Org. Chem.* **2013**, *78*, 3636-3646.
[4] DW Woolley, *J. Biol. Chem.* **1944**, *152*, 225-232.
[5] J.A. Maertens, *Clin. Microbiol. Infect.* **2004**, *10*, 1-10.
[6] O. Kleifeld, A. Frenkel, J. Martin, *Nat. Struct. Mol. Biol.* **2003**, *10*, 98-103.
[7] E. Salah, E. Ugochukwu, A.J. Barr, F. Von Delft, S. Knapp, J.M. Elkins, *J. Med. Chem.* **2011**, *54*, 2359-2367.
[8] V. Kumar, K. Kaur, G.K. Gupta, A.K. Sharma, *Eur. J. Med. Chem.* **2013**, *69*, 735-753.
[9] R. Kaur, A.R. Dwivedi, B. Kumar, V. Kumar, *Anticancer Agents Med. Chem.* **2016**, *16*, 465-489.
[10] H. Huang, S. Banerjee, P.J. Sadler, *ChemBioChem* **2018**, *19*, 1574-1589.
[11] L. He, Y. Li, P. Tan, R. Ye, H. Chen, J. Cao, N. Ji, W. Mao, *Chem. Sci*. **2015**, *6*, 5409-5418.
[12] P. Boya, G. Kroemer, *Oncogene* **2008**, *27*, 6434-6451.
[13] P. Saftig, K. Sandhoff, *Nature* **2013**, *502*, 312-313.
[14] M.T. Gyparaki, A.G. Papavassiliou, *Trends Mol. Med*. **2014**, *20*, 239-241.
[15] L. He, Y. Li, C.P. Tan, R.R. Ye, M. Chen, J. Cao, L. Ji, Z.W. Mao, *Chem. Sci.* **2015**, *6*, 5409-5418.
[16] E. Zafon, I. Echevarría, S. Barrabés, B.R. Manzano, F.A. Jalón, A.M. Rodríguez, A. Massaguer, G. Espino, *Dalton Trans.* **2022**, *51*, 111-128.
[17] M. Redrado, M. Miñana, M.P. Coogan, M.C. Gimeno, V. Fernández-Moreira, *ChemMedChem* **2022**, *17*, e202200244.
[18] M.M. Kim, A. Darafsheh, *Photochem. Photobiol.* **2020**, *96*, 280-294.
[19] T.M. Stonelake, K.A. Phillips, H.Y. Otaif, Z.C. Edwardson, P.N. Horton, S.J. Coles, J.M. Beames, S.J.A. Pope, *Inorg. Chem.* **2020**, 59, 2266-2277.
[20] C.S. Ho, C.W. Lam, M.H. Chan, R.C. Cheung, L.K. Law, L.C. Lit, K.F. Ng, M.W. Suen, H.L. Tai, *Clin. Biochem. Rev.* **2003**, *24*, 3-12.
[21] R. Bevernaegie, S.A.M. Wehlin, E.J. Piechota, M. Abraham, C. Philouze, G.J. Meyer, B. Elias, L. Troian-Gautier, J. Am. Chem. Soc. **2020**, *142*, 2732-2737.
[22] B. Liu, L. Lystrom, C.G. Cameron, S. Kilina, S.A. McFarland, W. Sun, *Eur. J. Inorg. Chem*. **2019**, *2019*, 2208-2215.
[23] F.Lafolet, S. Welter, Z. Popovića, L. De Cola, *J. Mater. Chem*. **2005**, *15*, 2820-2828.
[24] C. Caporale, M. Massi, *Coord. Chem. Rev.* **2018**, *363*, 71-91.
[25] T.M. Stonelake, K.A. Phillips, H.Y. Otaif, Z.C. Edwardson, P.N. Horton, S.J. Coles, J.M. Beames, S.J.A. Pope, *Inorg. Chem.* **2020**, *59*, 2266-2277.
[26] J. Zhou, J. Li, K.Y. Zhang, S. Liu, Q. Zhao, *Coord. Chem. Rev.* **2022**, *453*, 214334-214357.
[27] A. Luengo, M. Redrado, I. Marzo, V. Fernández-Moreira, M.C. Gimeno, *Inorg. Chem.* **2020**, *59*, 8960-8970.
[28] K.A. White, B.K. Grillo-Hill, D.L. Barber, *J. Cell Sci*. **2017**, *130*, 663-669.
[29] https://www.thermofisher.com/order/fluorescence-spectraviewer#!/
[30] L.M. Bareford, P.W. Swaan, *Adv. Drug Deliv. Rev.* **2007**, *59*, 748-758.

[31] G.J. Doherty, H.T. McMahon, *Annu. Rev. Biochem*. **2009**, *78*, 31.1-31.46.
[32] L. Hayflick, P.S. Moorhead, *Exp. Cell Res.* **1961**, *25*, 585-621.
[33] V. Gorgoulis, P.D. Adams, A. Alimonti, D.C. Bennett, O. Bischof, C. Bishop, J. Campisi, M. Collado, K. Evangelou, G. Ferbeyre, J. Gil, E. Hara, V. Krizhanovsky, D. Jurk, A.B. Maier, M. Narita, L. Niedernhofer, J.F. Passos, P.D. Robbins, C.A. Schmitt, Demaria, *Cell* **2019**, *179*, 813-827.
[34] D.J. Baker, B.G. Childs, M. Durik, M.E. Wijers, C.J. Sieben, J. Zhong, R.A. Saltness, K.B. Jeganathan, G.C. Verzosa, A. Pezeshki, K. Khazaie, J.D. Miller, J.M. van Deursen, *Nature* **2016**, *530*, 184-189.
[35] B.Y. Lee, J.A. Han, J.S. Im, A. Morrone, K. Johung, E.C. Goodwin, W.J. Kleijer, D. DiMaio, E.S. Hwang, *Aging Cell* **2006**, *5*, 187-195.
[36] A. Bernadotte, V.M. Mikhelson, I.M. Spivak, *Aging* **2016**, *8*, 3-11.
[37] D. Muñoz-Espín, M. Serrano, *Nat. Rev. Mol. Cell Biol.* **2014**, *15*, 482-496.
[38] E. Prasnikar, J. Borisek, A. Perdih, *Ageing Res. Rev.* **2021**, *66*, 101251-101284.
[39] M. Borghesan, W.M.H. Hoogaars, M. Varela-Eirin, N. Talma, M. Demaria, *Trends Cell Biol.* **2020**, *30*, 777-791.
[40] J.A. Ewald, J.A. Desotelle, G. Wilding, D.F. Jarrard, *JNCI* **2010**, *102*, 1536-1546.
[41] X. Wang, S.C. Wong, J. Pan, S.W. Tsao, K.H. Fung, D.L. Kwong, J.S. Sham, J.M. Nicholls, *Cancer Res.* **1998**, *58*, 5019-5022.

[42] A) J.I. Park, J.S. Jeong, J.Y. Han, D.I. Kim, Y. H. Gao, S.C. Park, G.P. Rodgers, I.H. Kim, *J. Cancer Res. Clin. Oncol.* **2000**, *126*, 455-460. B) R.H. te Poele, A.L. Okorokov, L. Jardine, J. Cummings, S.P. Joel, *Cancer Res.* **2002**, *62*, 1876-1883. C) Z. Han, W. Wei, S. Dunaway, J.W. Darnowski, P. Calabresi, J. Sedivy, E.A. Hendrickson, K.V. Balan, P. Pantazis, J.H. Wyche, *J. Biol. Chem.* **2002**, *277*, 17154-17160.

[43] M. Lee, J.S. Lee, *BMB Rep.* **2014**, *47*, 51-59.
[44] P. Hari, F.R. Millar, N. Tarrats, J. Birch, A. Quintanilla, C.J. Rink, I. Fernández-Duran, M. Muir, A.J. Finch, V.G. Brunton, J.F. Passos, J.P. Morton, L. Boulter, J.C. Acosta, *Sci. Adv.* **2019**, *5*, eaaw0254.
[45] M. Lee, J.S. Lee, *BMB Rep*. **2014**, *47*, 51-59.
[46] N.E. Sharpless, C.J. Sherr, *Nat. Rev. Cancer* **2015**, *15*, 397-408.
[47] J.G. Jackson, V. Pant, Q. Li, L.L. Chang, A. Quintás-Cardama, D. Garza, O. Tavana, P. Yang, T. Manshouri, Y. Li, A.K. El-Naggar, G. Lozano, *Cancer Cell* **2012**, *21*, 793-806.
[48] A. Yoshida, E.K. Lee, J.A. Diehl, *Cancer Res.* **2016**, *76*, 2990-3002.
[49] Y. Zhu, T. Tchkonia, H. Fuhrmann-Stroissnigg, H.M. Dai, Y.Y. Ling, M.B. Stout, T. Pirtskhalava, N. Giorgadze, K.O. Johnson, C.B. Giles, J.D. Wren, L.J. Niedernhofer, P.D. Robbins, J.L. Kirkland, *Aging cell* **2016**, *15*, 428-435.
[50] O. Moiseeva, X. Deschênes-Simard, E. St-Germain, S. Igelmann, G. Huot, A. E. Cadar, V. Bourdeau, M.N. Pollak, G. Ferbeyre, *Aging Cell* **2013**, *12*, 489-498.
[51] P. Maher, *Front. Biosci.* **2015**, *7*, 58-82.
[52] K. Fang, C.C. Chiu, C.H. Li, Y.T. Chang, H.T. Hwang, *Oncol. Res.* **2007**, *16*, 479-488.
[53] A.R. Özeş, D.F. Miller, O.N. Özeş, F. Fang, Y. Liu, D. Matei, T. Huang, K.P. Nephew, *Oncogene* **2016**, *35*, 5350-5361

[54] D. Zhou, M. Borsa, A.K. Simon, *Aging Cell.* **2021**, *20*, e13316.

[55] C.D. Wiley, M.C. Velarde, P. Lecot, S. Liu, E.A. Sarnoski, A. Freund, K. Shirakawa, H.W. Lim, S.S. Davis, A. Ramanathan, A.A. Gerencser, E. Verdin, J. Campisi, *Cell Metab.* **2016**, *23*, 303-314.

[56] T. Mahmood, C. Yang, *Am. J. Med. Sci.* **2012**, *4*, 429-434.

[57] https://www.cellsignal.com/products/cellular-assay-kits/senescence-b-galactosidase-staining-kit/9860

[58] https://www.promega.es/products/cell-health-assays/cell-viability-and-cytotoxicity-assays/celltiter_blue-cell-viability-assay/?catNum=G8080#specifications

[59] M. van Engeland, L.J. Nieland, F.C. Ramaekers, B. Schutte, C.P. Reutelingsperger, *Cytometry* **1998**, *31*, 1-9.

[60] E. Brauchle, S. Thude, S.Y. Brucker, K. Schenke-Layland, *Sci. Rep.* **2014**, *4*, 4698.

[61] L. Wang, S. Monro, P. Cui, H. Yin, B. Liu, C.G. Cameron, W. Xu, M. Hetu, A. Fuller, S. Kilina, S.A. McFarland, W. Sun, *ACS Appl Mater. Interfaces* **2019**, *11*, 3629-3644.

[62] A.A. Gorman, M.A.J. Rodgers, *J. Photochem. Photobiol. B* **1992**, *14*, 159-176.

[63] OECD (2022), *Test No. 425: Acute Oral Toxicity: Up-and-Down Procedure*, OECD Guidelines for the Testing of Chemicals, Section 4, OECD Publishing, Paris, https://doi.org/10.1787/9789264071049-en.

[64] D.B. Morton, P.H. Griffiths, *Vet. Rec.* **1985**, *116*, 431-436.

[65] D. Longley, D. Harkin, P. Johnston, *Nat. Rev. Cancer* **2003**, *3*, 330-338.

[66] D.M. Euhus, C. Hudd, M.C. LaRegina, F.E. Johnson, *J. Surg. Oncol.* **1986**, *31*, 229-234.

[67] N.G.M. Schipper, T. Österberg, U. Wrange, C. Westberg, A. Sokolowski, R. Rai, W. Young, B. Sjöström, *Pharm. Res.* **2001**, *18*, 1735-1741.

[68] A.M. Seddon, D. Casey, R.V. Law, A. Gee, R.H. Templer, O. Ces, *Chem. Soc. Rev.* **2009**, **38**, 2509-2519.

[69] G. Häcker, *Cell Tissue Res.* **2000**, *301*, 5-17.

[70] Test No. 425: Acute Oral Toxicity: Up-and-Down Procedure. https://www.oecd.org/env/testno425acuteoraltoxicityupanddownprocedure9789264071049 en.htm, 2020

[71] D.B. Morton, P.H. Griffiths, *Vet. Rec.* **1985**, *116*, 431-436.

[72] G.R. Fulmer, A.J.M. Miller, N.H. Sherden, H.E. Gottlieb, A. Nudelman, B.M. Stoltz, J.E. Bercaw, K.I. Goldberg, *Organometallics* **2010**, *29*, 2176-2179.

Conclusiones Generales

En esta tesis doctoral se describe la síntesis de complejos octaédricos ciclometalados de Ir^{III} del tipo $[Ir(C\hat{}N)_2(L\hat{}L)]^{+/0}$, donde C^N representa los ligandos ortometalados 2-fenilpiridina, benzoquinolina o metil-2-fenilquinolina-4-carboxilato y L^L ligandos quelato tipo difosfina o diimina. De este modo se podrá establecer una tendencia de cómo las propiedades de los complejos se ven influenciadas por la presencia de los distintos ligandos quelato coordinados al centro de Ir^{III}. De manera adicional, se han sintetizado complejos bimetálicos Ir^{III}-Au^{I} para determinar la capacidad de modulación de las propiedades ópticas y bioactivas que este segundo fragmento metálico ejerce sobre el del complejo final.

En el primer y segundo capítulo se recoge la síntesis de complejos bimetálicos de Ir^{III}-Au^{I}, usando como ligandos puente entre los centros metálicos un ligando bis(difenilfosfino)metanuro o un derivado tipo NHC de imidazo[4,5-f]-1,10-fenantrolina, respectivamente. En el primer capítulo se puede observar como la incorporación del centro de Au^{I} no genera una modificación importante en las propiedades ópticas, ya que se mantienen los máximos de emisión y los rendimientos cuánticos no sufren grandes variaciones. Sin embargo, la incorporación de este fragmento metálico adicional, sí que ayuda a modular las propiedades biológicas, no tanto en la mejora de la actividad antiproliferativa sobre la línea A549, donde los valores no son significativos, como en el posible mecanismo de actuación, produciendo un gran aumento de ROS y un gran incremento en la inhibición de la enzima TrxR. Todos los complejos recogidos en este capítulo muestran un proceso de tráfico intracelular desde los lisosomas hasta las mitocondrias, siendo estas sus dianas finales, así como una marcada capacidad para prevenir los procesos antiangiogénicos. Por el contario en el capítulo segundo, la incorporación de un centro de Au^{I} al derivado imidazo[4,5-f]-1,10-fenantrolina coordinado al centro de Ir^{III} por su fragmento diimina, provoca una modulación notable de todas sus propiedades, tanto ópticas como biológicas. En relación a sus propiedades emisoras, estas sufren un desplazamiento hipsocrómico a consecuencia de esta coordinación pasando de 660 nm en el complejo

monometálico de Ir^{III}, a 533 y 637 nm en los complejos bimetálicos. Los rendimientos cuánticos también se ven afectados por la incorporación del centro de Au^{I}. En lo relativo a sus propiedades biológicas, estos complejos, tanto mono como bimetálicos, inducen muerte celular *via* apoptótica, y todos ellos exhiben una buena capacidad antiproliferativa, siendo especialmente destacables los buenos valores de los complejos bimetálicos en la línea celular A549 tras ser irradiados a 405 nm (IC_{50}: monometálico: 2,49 μM; bimetálicos: 0,49 y 0,34 μM). Los estudios de biodistribución por microscopía de fluorescencia confocal permitieron observar una acumulación en las mitocondrias y/o lisosomas, en función de si tenemos un complejo monometálico o uno bimetálico.

En el tercer capítulo, se ha explorado la posibilidad de diseñar fotosensibilizadores (FS) duales para terapia fotodinámica (TFD) y bioimagen y se han sintetizado los primeros candidatos. Para ello se han preparado compuestos de Ir^{III} emisores en amarillo o verde del tipo $[Ir(C\hat{}N)_2(N\hat{}N)]^+$, donde C^N es 2-fenilpiridina o benzoquinolina, y N^N un ligando diimina (2,2'-dipiridilamina) modificado con un cromóforo orgánico con emisión en el azul (acridina o antraceno). De esta manera, se puede rastrear el complejo dentro de las células utilizando una longitud de onda de irradiación diferente a la de activación terapéutica para su acción en TFD. Se ha podido comprobar que es posible obtener compuestos con una doble emisión y cuyas propiedades antiproliferativas están relacionadas con la longitud de onda de activación del complejo. En oscuridad, los complejos presentan una actividad moderada, sin embargo, al aplicar una fuente de irradiación se activan sus propiedades citotóxicas. Cuando la irradiación se realiza a 405 nm, se produce la activación mayoritaria del cromóforo orgánico, en consecuencia, aunque podemos ver como el complejo exhibe una mayor capacidad antiproliferativa que en oscuridad. los mejores resultados se obtienen irradiando a 470 nm, longitud de onda a la que se produce la activación del fragmento metálico (bioactivo). Esta activación del fragmento metálico consigue aumentar la capacidad antiproliferativa más de 110 veces en comparación con la administración en oscuridad. Los ensayos de microscopía revelaron una gran vacuolarización citoplasmática, que posteriormente mediante citometría de flujo se pudo confirmar

como una inducción a una muerte apoptótica. Además, se observó una gran producción de ROS y un patrón de biodistribución dependiente del cromóforo orgánico incorporado.

El último capítulo amplía la estrategia de sintetizar nuevos agentes fotosensibizadores para TFD, sin embargo, se han realizado ciertas modificaciones respecto a los complejos mencionados anteriormente para mejorar las propiedades de los mismos, tales como sustituir el ligando C^N por metil-2-fenilquinolina-4-carboxilato (mcp) y N^N por diferentes familias de derivados azol, con el objetivo de conseguir una mayor solubilidad en medios biológicos y activaciones del FS a mayores longitudes de onda. La posibilidad de obtener complejos análogos catiónicos y neutros, mediante la desprotonación del azol coordinado al centro metálico, permite establecer una tendencia de como la carga de los complejos afecta tanto a las propiedades ópticas como biológicas de los mismos. De manera adicional, se puede ver como el tamaño del anillo (piridina o tiazol) o el número y naturaleza de los heteroátomos presentes en el mismo juega un papel importante en la modificación de sus propiedades. En lo relativo a sus propiedades ópticas, todos los complejos de este capítulo presentan emisiones en la zona roja del espectro, en torno a los 700 nm, y exhiben unos excelentes rendimientos cuánticos (27.5-56.1%). Posteriormente, se llevaron a cabo la evaluación de los complejos sintetizados como agentes quimioterapéuticos y fotosensibilizadores demostrando la gran proyección en diversas líneas celulares tales como A549, 4T1-luc2 o B16-F10-luc. También se estudió su biodistribución mediante microscopía confocal de fluorescencia y en todos los casos mostraron una acumulación lisosomal. Mediante la activación de los mismos usando una fuente de irradiación de 470 nm, se consiguió activar su capacidad para generar oxígeno singlete y en consecuencia inducir muerte celular, llegando en los casos más prometedores a PI próximos a 550. Paralelamente, algunos de estos compuestos se ensayaron en células senescentes de las líneas celulares A549 y SK-Mel-103, mostrando que no solo son capaces de actuar sobre células cancerígenas sino también sobre esta variante celular que contiene el ciclo celular parado. La capacidad demostrada tanto a nivel quimioterapéutico como en TFD de inhibir la proliferación de las células en este

estadio abre la puerta a poder minimizar los efectos del cáncer recurrente. Por último, los complejos más prometedores fueron llevados a ensayos *in vivo* tanto de toxicidad como de eficacia para demostrar su potencial como agentes anticancerígenos.

Como conclusión general, se ha observado que es posible la modulación de las propiedades de complejos ciclometalados de Ir^{III} mediante la incorporación de ligandos tipo quelato y centros metálicos adicionales, en concreto de Au^{I}. La combinación en una molécula de un centro de iridio y otro de oro permite obtener potenciales agentes teragnósticos, en donde un balance entre carga y lipofilia resulta clave para aumentar la solubilidad de los mismos en medio biológico y su capacidad de atravesar la membrana celular. La conexión entre ambos metales que más libertad confiere en términos de derivatización, estabilidad y modulación de la luminiscencia es la que tiene lugar por funcionalización del esqueleto diimina (derivado-NHC), que ha mostrado mejores resultados que un quelato de tipo difosfina. De manera adicional, la incorporación de estructuras que mejoren la solubilidad en medio biológico puede constituir una fuente de mejora como ha demostrado la incorporación de un grupo éster en el ligando ciclometalado mcp, aunque hay que encontrar el balance perfecto entre lipofilia e hidrofilia para conseguir una rápida acumulación celular. En relación con los complejos de iridio, se ha comprobado que la presencia de una carga positiva en los mismos favorece la internalización celular, además de dirigirlos a dianas biológicas específicas. Además, los ligandos quelato unidos juegan un papel muy importante en su biodistribución. Los ligandos tipo azol fuerzan una acumulación lisosomal, mientras que con ligandos tipo fenantrolina o difosfina muestran una tendencia a una acumulación mitocondrial.

General Conclusions

This doctoral thesis describes the synthesis of cyclometalated Ir^{III} complexes of the type $[Ir(C\hat{}N)_2(L\hat{}L)]^{+/0}$, where C^N represents the orthometalated ligands 2-phenylpyridine, benzoquinoline, or methyl-2-phenylquinoline-4-carboxylate, and L^L represents chelating ligands of the diphosphine or diimine type. In this way, a trendency can be established for how the properties of the complexes are influenced by the presence of the different chelating ligands coordinated to the center of Ir^{III}. Additionally, Ir^{III}-Au^{I} bimetallic complexes have been synthesized to determine the modulating capacity of the optical and bioactive properties that this second metal fragment exerts on the final complex.

In the first and second chapters, the synthesis of Ir^{III}-Au^{I} bimetallic complexes is described, using a bis(diphenylphosphino)methane or an NHC derivative of imidazo[4,5-f]-1,10-phenanthroline as bridging ligands between the metal centers, respectively. In the first chapter, it can be observed that the incorporation of Au^{I} center does not generate a significant modification in the optical properties, the emission maxima and quantum yields do not undergo significant variations. However, the incorporation of this additional metal fragment helps to modulate the biological properties, not so much in improving the antiproliferative activity on A549 cell line, but in the possible mechanism of action, producing a large increase in ROS production and potentiating inhibition of the TrxR enzyme. The complexes described in this chapter show an intracellular trafficking process from lysosomes to mitochondria, which are their final targets, as well as a marked capacity to prevent anti-angiogenic processes. On the other hand, in the second chapter, the incorporation of an Au^{I} center to the imidazo[4,5-f]-1,10-phenanthroline derivative coordinated to the Ir^{III} center by its diimine fragment, causes a notable modulation of all their properties, both optical and biological. Regarding their emissive properties, they undergo a hypsochromic shift as a consequence of this coordination, going from 660 nm in the monometallic Ir^{III} complex, to 533 and 637 nm in the bimetallic complexes. The quantum yields are also affected by the incorporation of the Au^{I} center. Focusing on their biological properties, both mono

and bimetallic complexes induce apoptotic cell death, and all of them exhibit good antiproliferative capacity, with the bimetallic complexes showing particularly good values in the A549 cell line after being irradiated at 405 nm (IC_{50}: monometallic: 2.49 μM; bimetallic: 0.49 and 0.34 μM). Biodistribution studies by confocal fluorescence microscopy allowed us to observe accumulation in mitochondria and/or lysosomes, depending on whether we have a monometallic or bimetallic complex.

In the third chapter, the possibility of designing dual photosensitizers (PS) for photodynamic therapy (PDT) and bioimaging has been explored. For this purpose, yellow or green emitting Ir^{III} compounds of the type $[Ir(C\text{^}N)_2(N\text{^}N)]^+$ have been prepared, where C^N is 2-phenylpyridine or benzoquinoline, and N^N is a diimine ligand (2,2'-dipyridylamine) modified with an organic chromophore emitting in blue (acridine or anthracene). In this way, the complex can be traced inside the cells using a different irradiation wavelength than the one for therapeutic activation in PDT. It has been found that it is possible to obtain compounds with dual emission and whose antiproliferative properties are related to the activation wavelength of the complex. In dark, the complexes show moderate activity, but when an irradiation source is applied, their cytotoxic properties are activated. When the irradiation is performed at 405 nm, the organic chromophore is predominantly activated, and although the complex exhibits greater antiproliferative capacity than in dark, the best results are obtained by irradiating at 470 nm, the wavelength at which the metal fragment (bioactive) is activated. This activation of the metal fragment increases the antiproliferative capacity more than 110 times compared to administration in dark. Microscopy assays revealed significant cytoplasmic vacuolization, which was later confirmed through flow cytometry as induction of an apoptotic cell death. In addition, a high production of ROS and a biodistribution pattern dependent on the incorporated organic chromophore were also observed.

The last chapter expands the strategy of synthesizing new photosensitizer agents for PDT, however, certain modifications have been made with respect to the

complexes mentioned above to improve their properties, such as replacing the C^N ligand by methyl-2-phenylquinoline-4-carboxylate (mcp) and N^N with different families of azole derivatives, in order to achieve greater solubility in biological media and the activation of the PS at higher wavelengths. The possibility of obtaining analogous cationic and neutral complexes, by deprotonating the azole coordinated to the metal center, allows to establish a trend of how the charge of the complexes affects both their optical and biological properties. Additionally, the size of the ring (pyridine or thiazole) or the number and nature of the heteroatoms present in it, play an important role in the modification of their properties. Regarding their optical properties, all complexes in this chapter exhibit emissions in the red region of the spectrum, around 700 nm, and show excellent quantum yields (27.5-56.1%). Subsequently, the synthesized complexes were evaluated as chemotherapeutic and photosensitizing agents, demonstrating great potential in various cell lines such as A549, 4T1-luc2, or B16-F10-luc. Their biodistribution was also studied using fluorescence confocal microscopy and in all cases, they showed lysosomal accumulation. By activating them using a 470 nm irradiation source, their ability to generate singlet oxygen and consequently induce cell death was achieved, reaching PI values close to 550 in the most promising cases. In parallel, some of these compounds were tested in senescent cells of the A549 and SK-Mel-103 cell lines, showing that they are not only capable of acting on cancerous cells but also on this cell variant that exhibits a permanent cell cycle arrest. The demonstrated ability of these complexes for being used as chemotherapeutic and PSs opens the door to finding novel strategies for minimizing the effects of recurrent cancer. Finally, the most promising complexes were studied in *in vivo* assays, demonstrating their potential as anticancer agents.

As a general conclusion, it has been observed that modulation of the properties of these cyclometalated Ir^{III} complexes is possible by incorporating chelate ligands and additional metal centers, specifically Au^{I}. The combination of an iridium and gold center in a molecule generates a synergic effect that opens the door to the development of novel theranostic agents, in which a balance between charge and lipophilicity is crucial for increasing their solubility in biological media and their

ability to penetrate cell membranes. The connection between both metals that provides the most freedom in terms of derivatization, stability, and modulation of luminescence occurs through functionalization of the diimine skeleton (NHC-derived), which has shown better results than a diphosphine-type. Additionally, incorporating structures that increase the solubility in biological media may provide a source of improvement, as demonstrated by the incorporation of an ester group in the cyclometalated mcp ligand. However, it is necessary to find the perfect balance between lipophilicity and hydrophilicity to achieve a rapid cellular accumulation. With regard to iridium complexes, the presence of a positive charge helps an easier cellular internalization, in addition to directing them to specific biological targets. Moreover, the chelating ligands attached play an important role in their biodistribution. Azole-type ligands force lysosomal accumulation, while diamine or diphosphine-type ligands show a tendency toward mitochondrial accumulation.

Supplementary Material

Table of contents

Chapter 1

NMR spectra of complexes 1.1-1.4

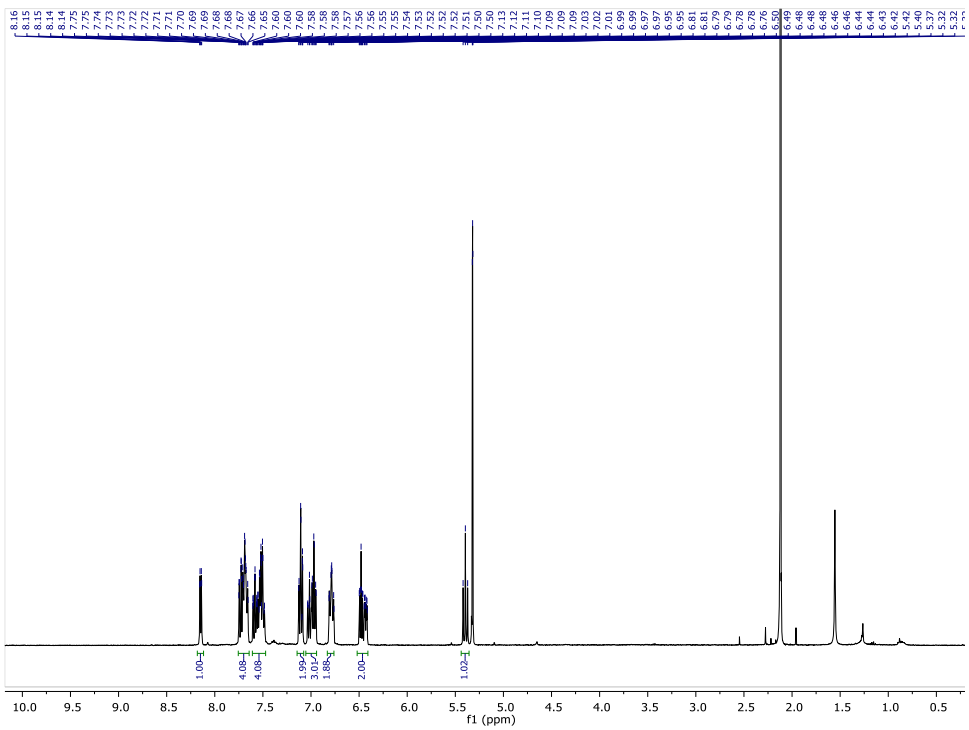

Figure S1.1. ^{1}H-NMR spectrum of complex **1.1**.

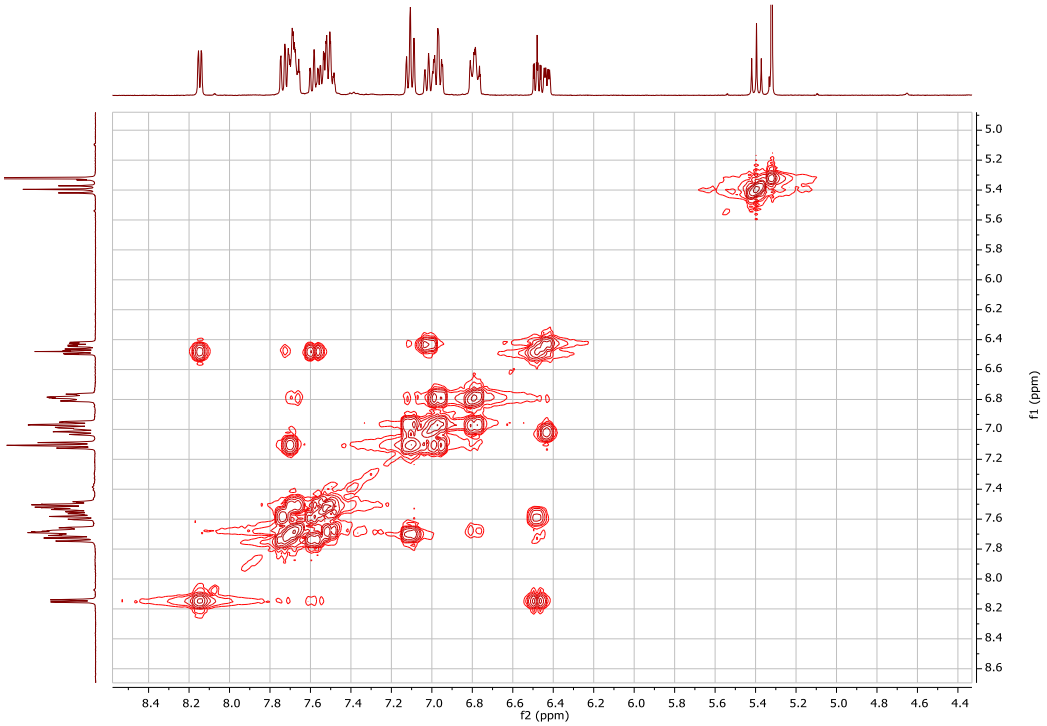

Figure S1.2. COSY-NMR spectrum of complex **1.1**.

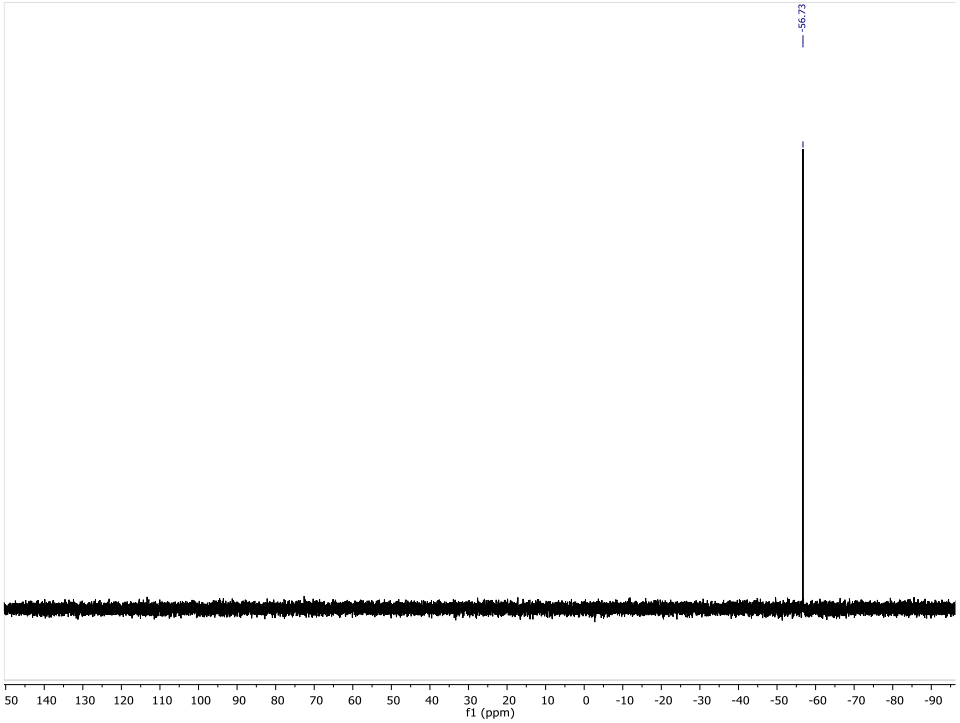

Figure S1.3. ^{31}P-NMR spectrum of complex **1.1**.

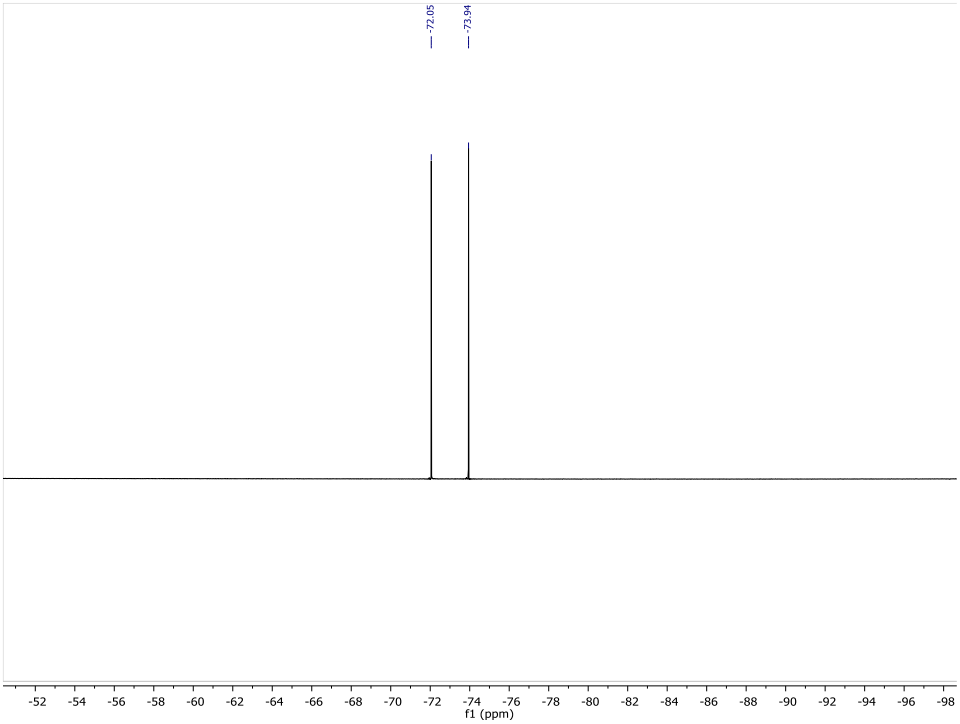

Figure S1.4. ^{19}F-NMR spectrum of complex **1.1**.

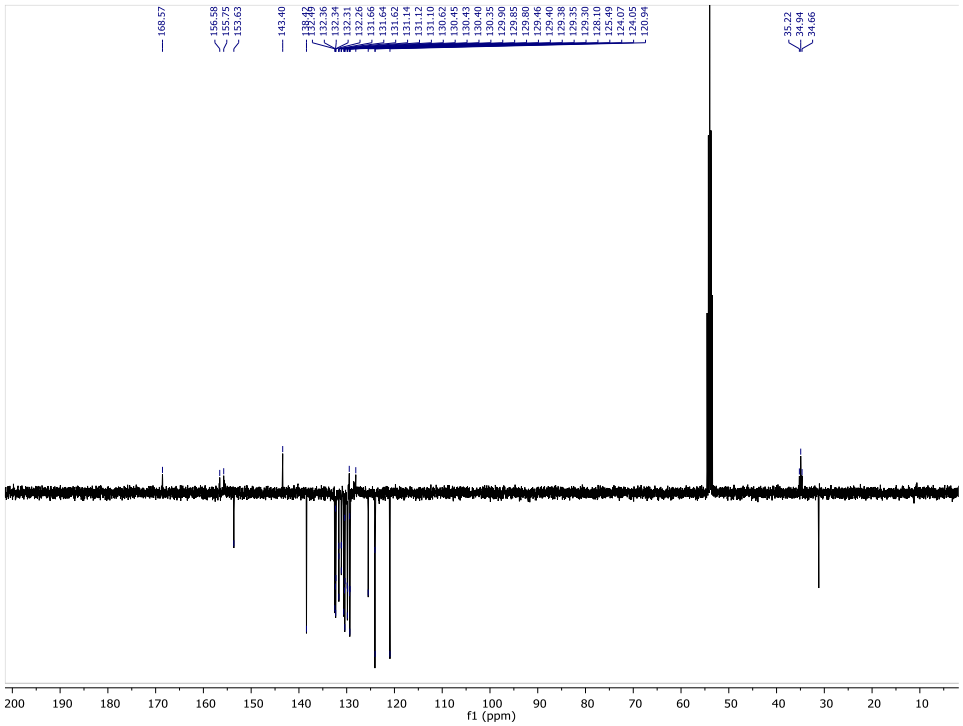

Figure S1.5. APT-NMR spectrum of complex **1.1**.

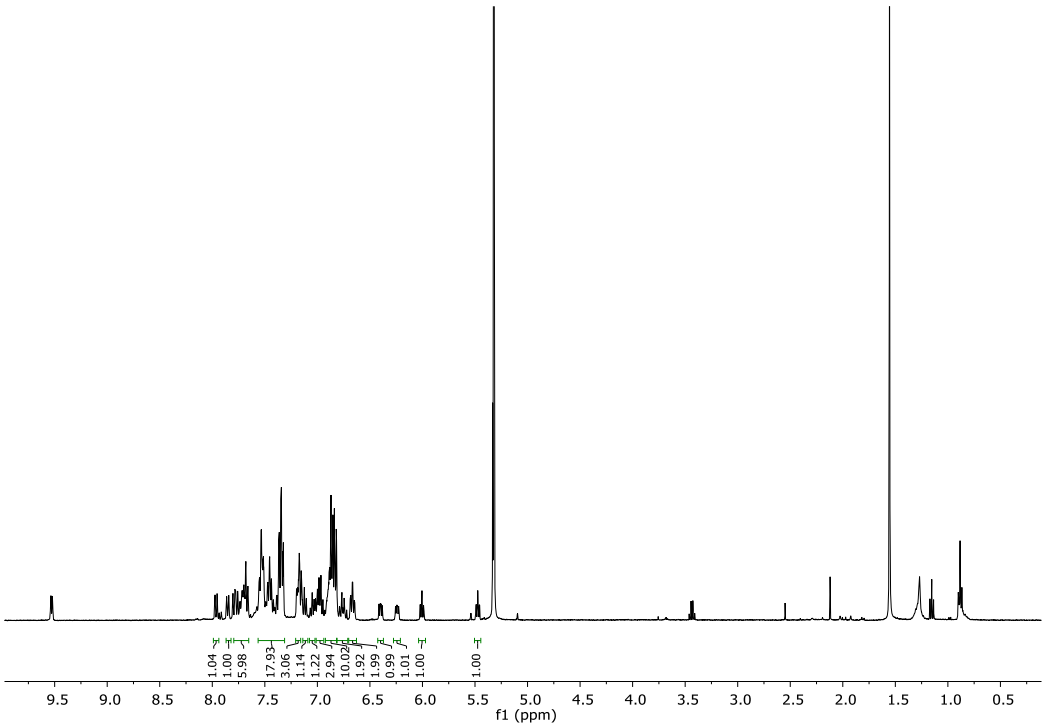

Figure S1.6. [1]H-NMR spectrum of complex **1.2**.

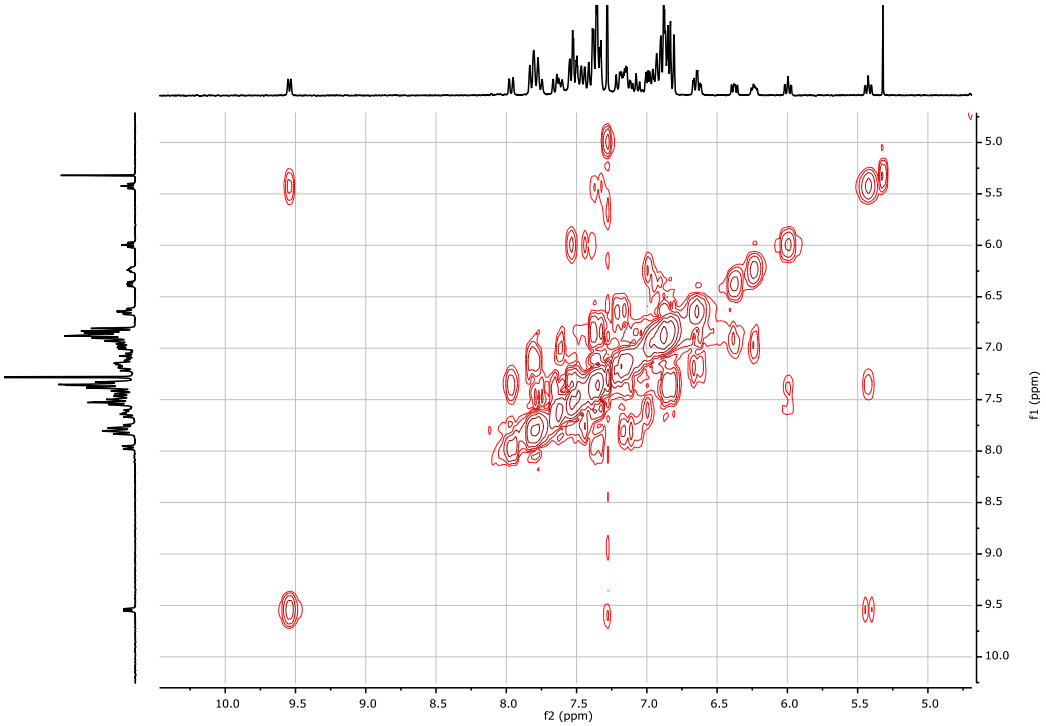

Figure S1.7. COSY-NMR spectrum of complex **1.2**.

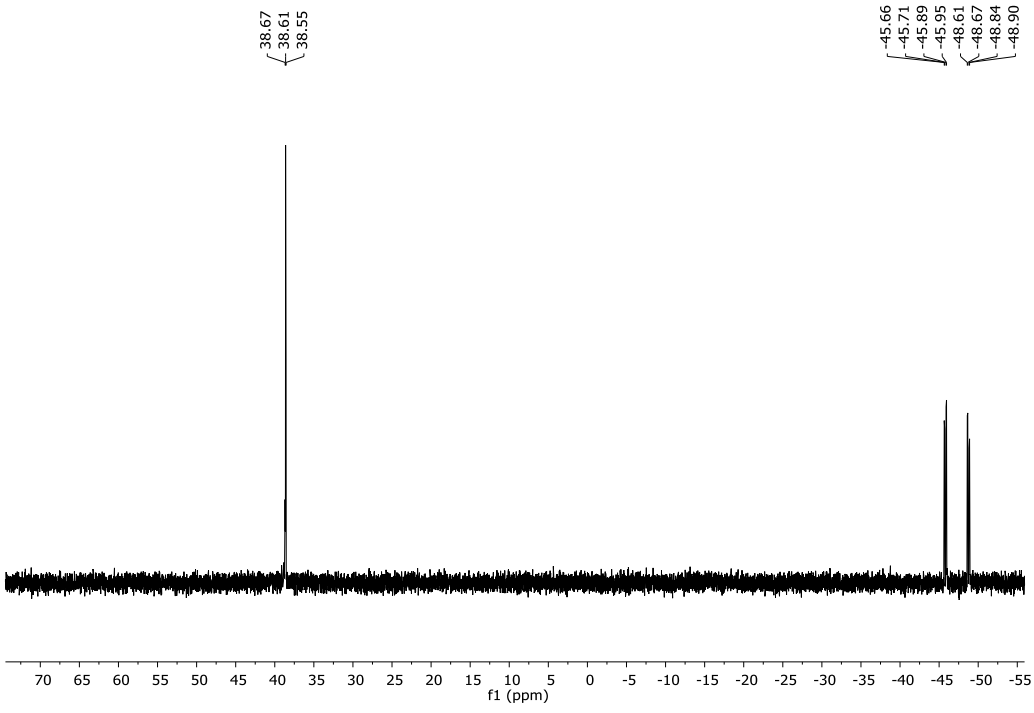

Figure S1.8. ^{31}P-NMR spectrum of complex **1.2**.

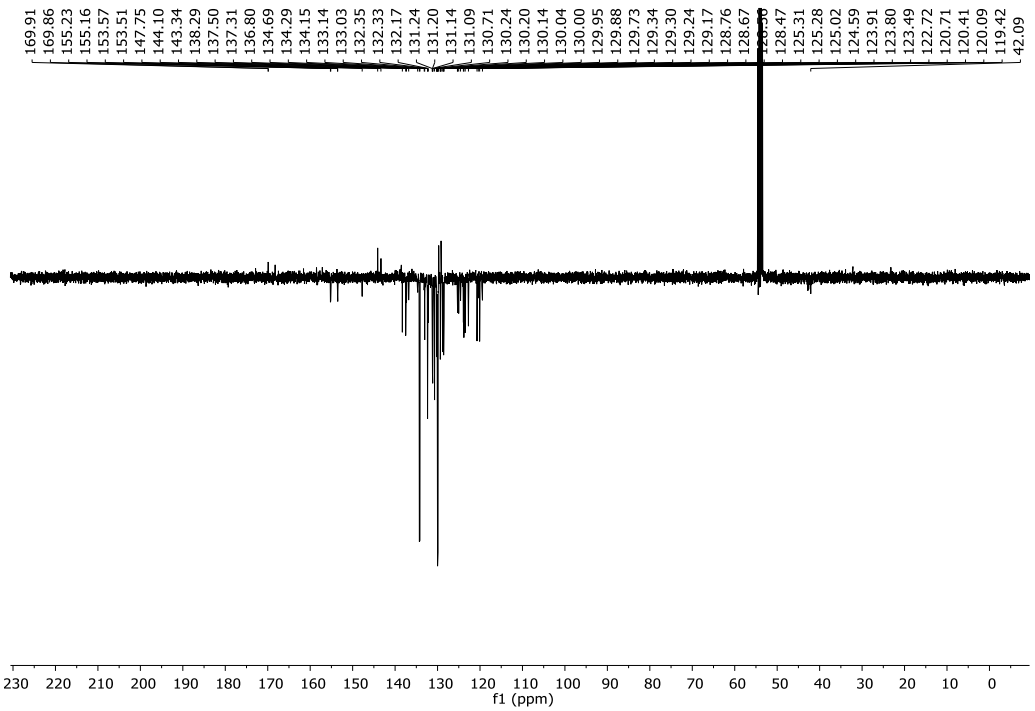

Figure S1.9. APT-NMR spectrum of complex **1.2**.

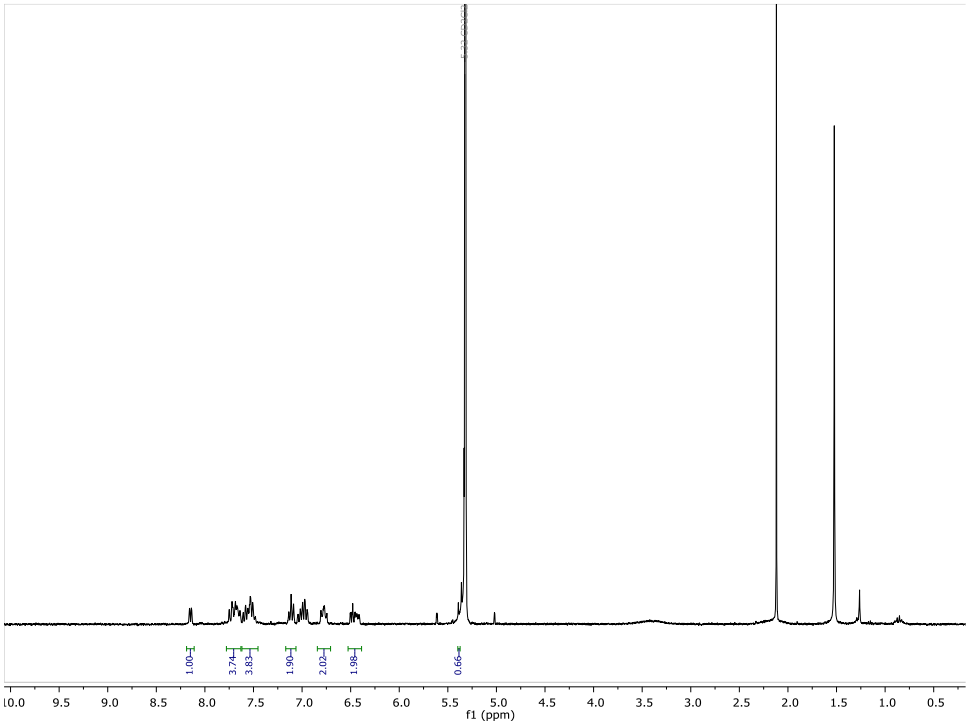

Figure S1.10. ^{1}H-NMR spectrum of complex **1.3**.

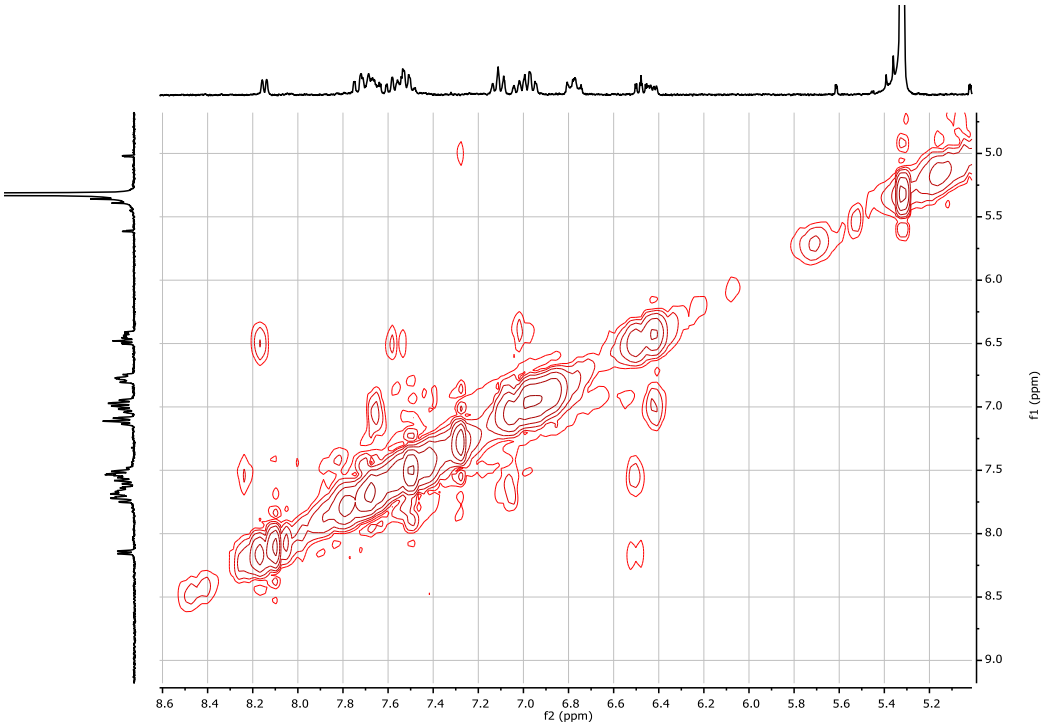

Figure S1.11. COSY-NMR spectrum of complex **1.3**.

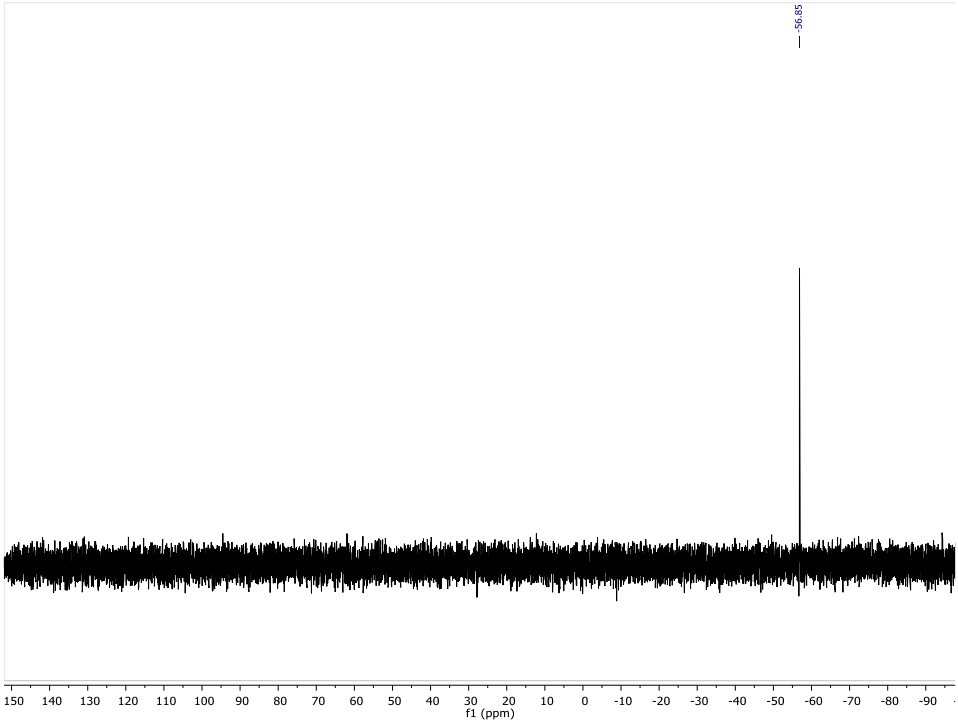

Figure S1.12. ^{31}P-NMR spectrum of complex **1.3**.

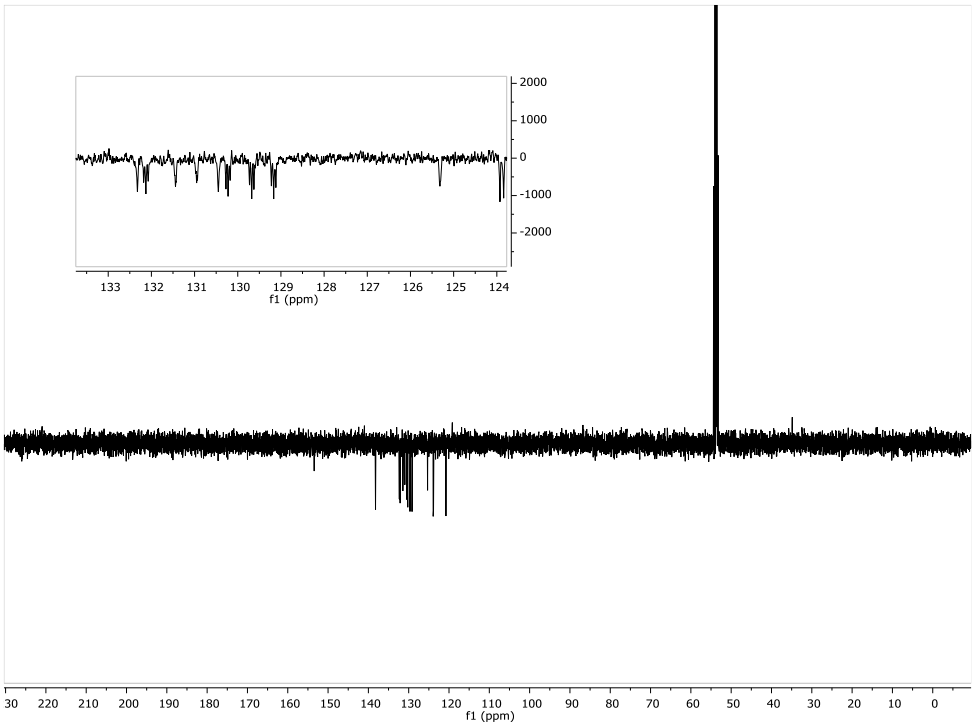

Figure S1.13. APT-NMR spectrum of complex **1.3**.

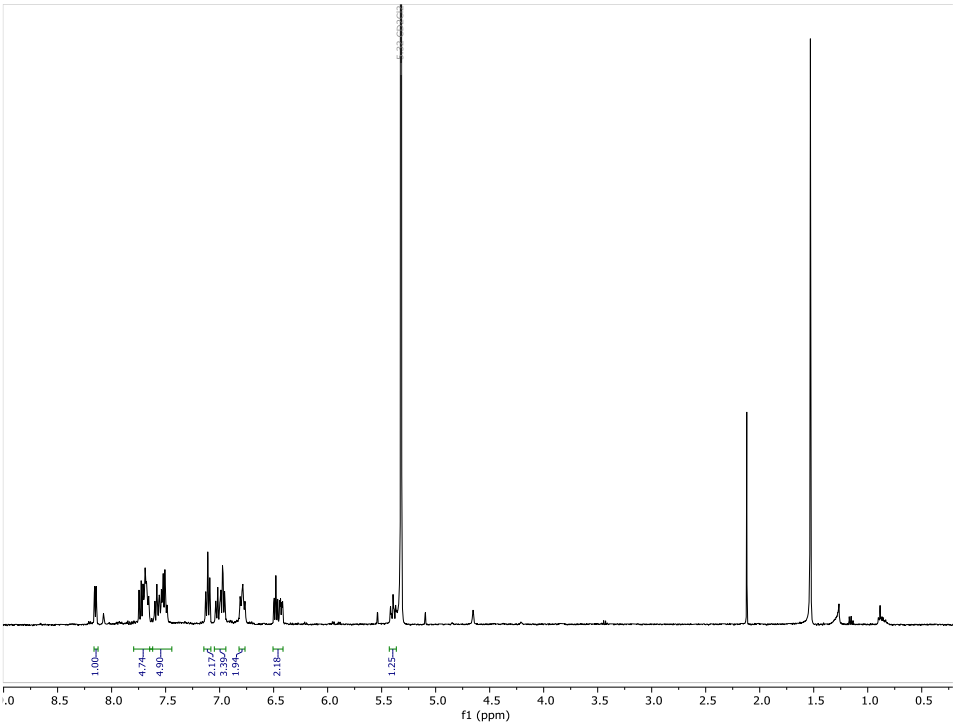

Figure S1.14. ^{1}H-NMR spectrum of complex **1.4**.

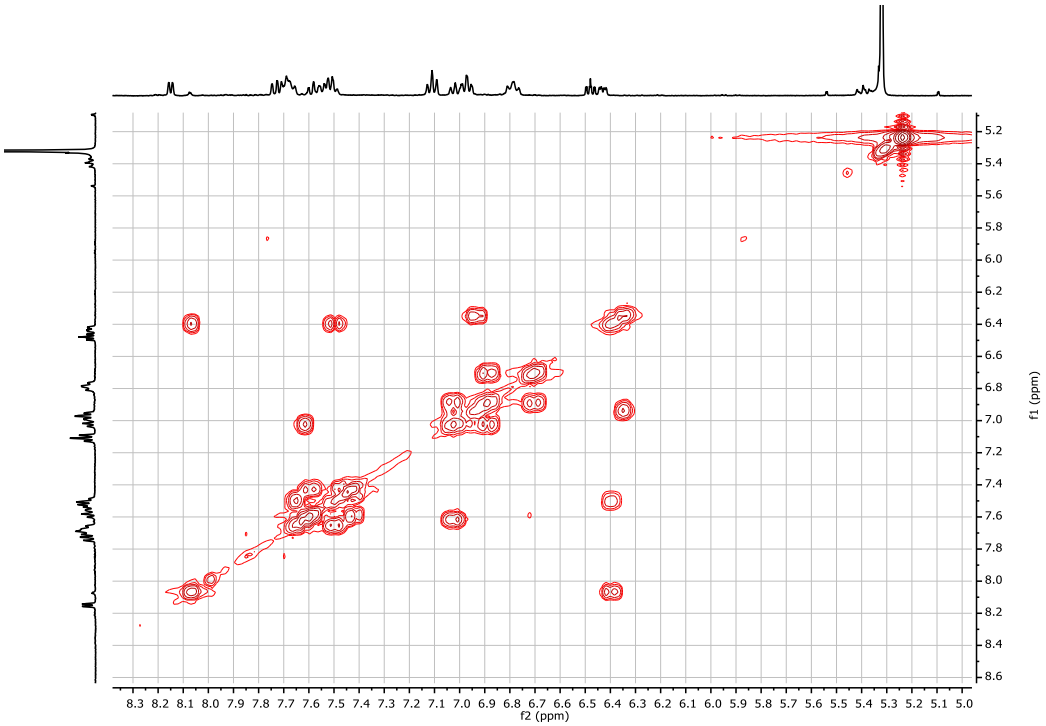

Figure S1.15. COSY-NMR spectrum of complex **1.4**.

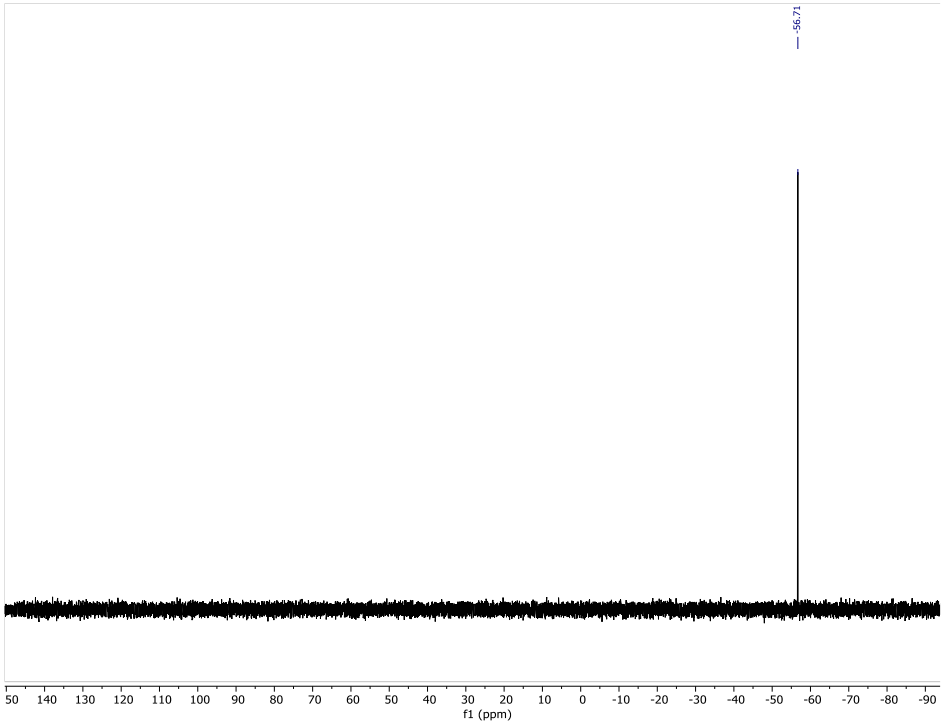

Figure S1.16. ^{31}P-NMR spectrum of complex **1.4**.

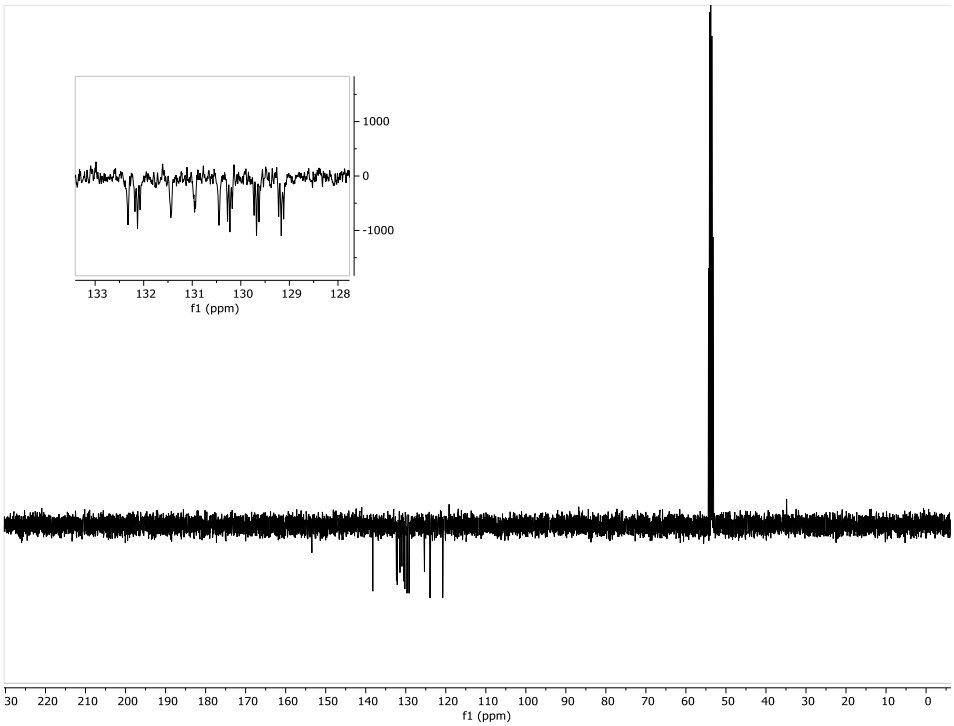

Figure S1.17. APT-NMR spectrum of complex **1.4**.

Mass spectra of compounds 1.1, 1.2 and 1.4

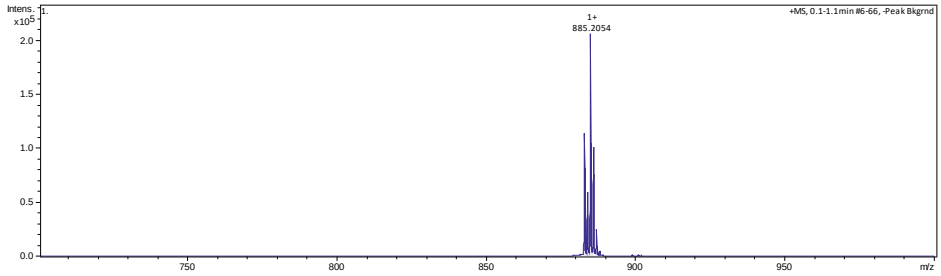

Figure S1.18. ESI-HRMS spectrum of complex **1.1**.

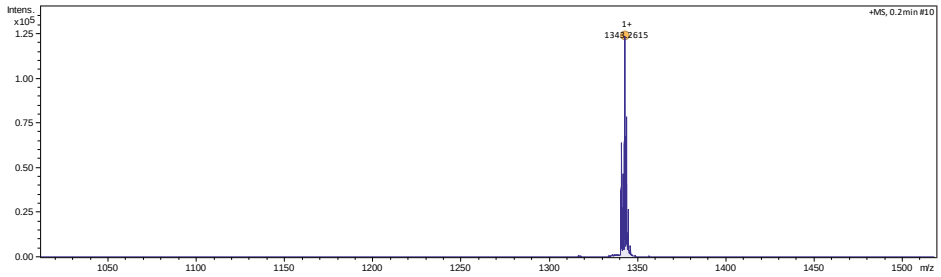

Figure S1.19. ESI-HRMS spectrum of complex **1.2**.

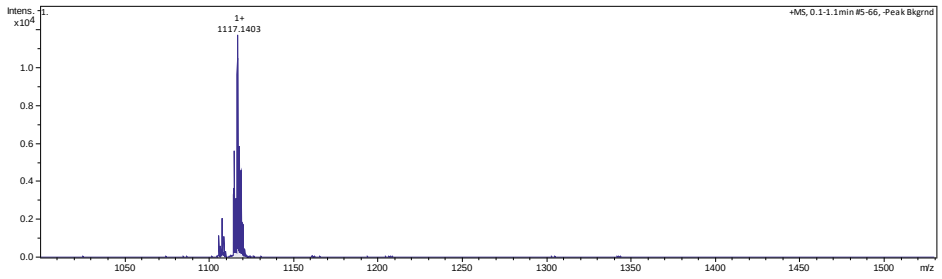

Figure S1.20. ESI-HRMS spectrum of complex **1.4**.

Absorption spectra and stability studies

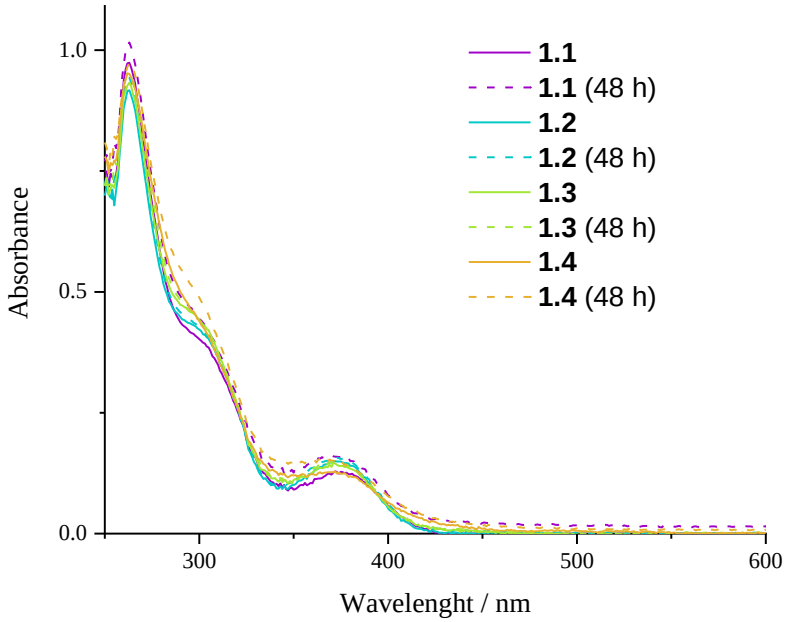

Figure S1.21. Absorption spectra in DMSO/ PBS (<5% DMSO) solution and stability studies at 48 hours.

Emission and excitation spectra of complexes 1.1-1.4

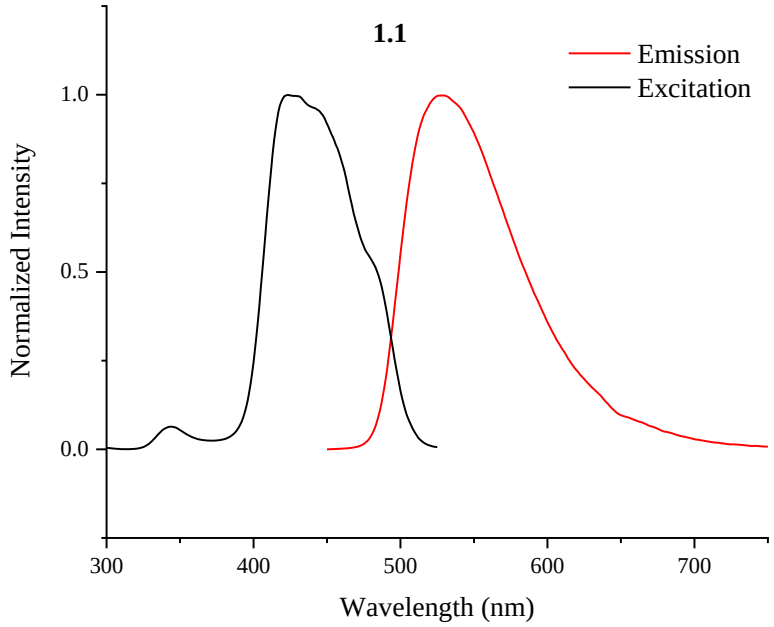

Figure S1.22. Emission-excitation spectra of complex **1.1** measured in DMSO solution.

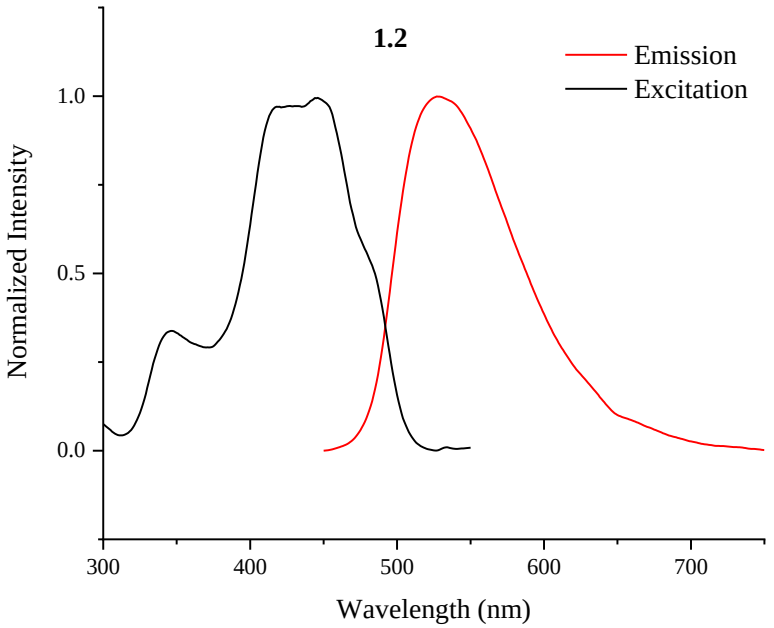

Figure S1.23. Emission-excitation spectra of complex **1.2** measured in DMSO solution.

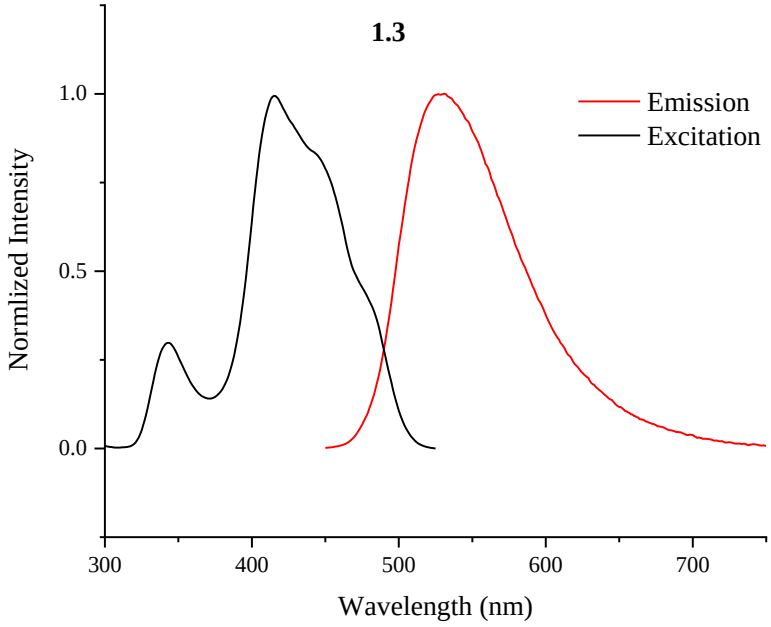

Figure S1.24. Emission-excitation spectra of complex **1.3** measured in DMSO solution.

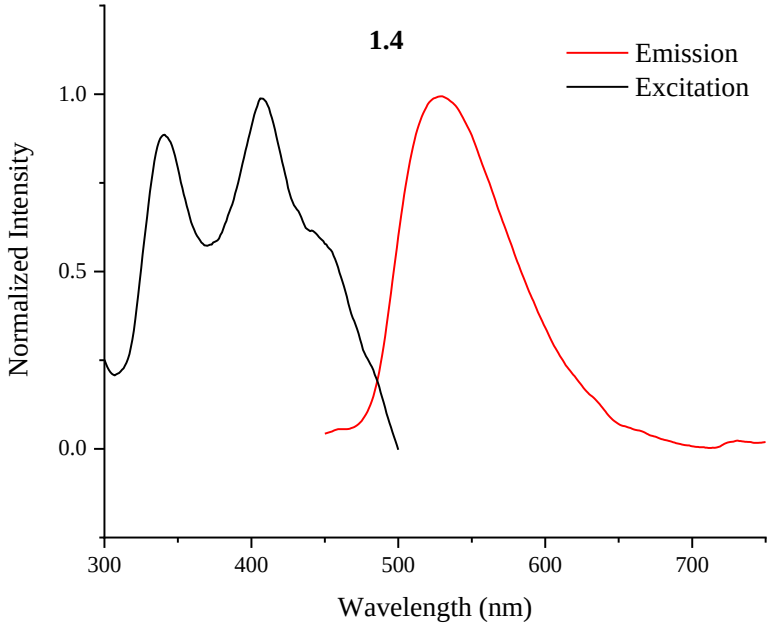

Figure S1.25. Emission-excitation spectra of complex **1.4** measured in DMSO solution.

Chapter 2

NMR spectra of ligand L2.3

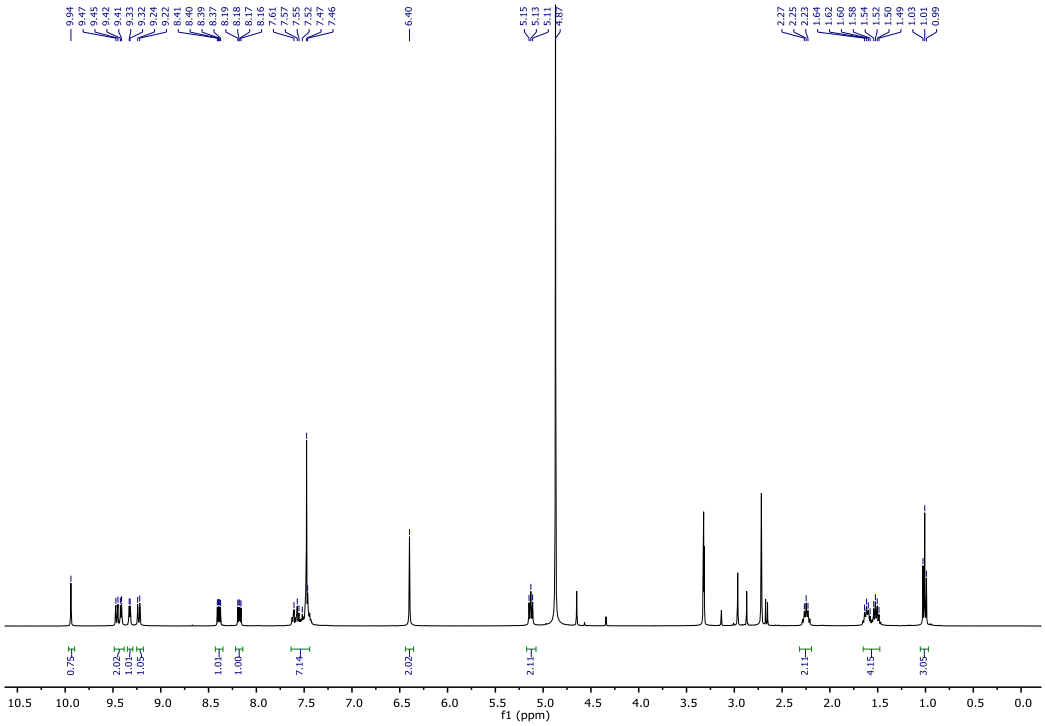

Figure S2.1. ^{1}H-NMR spectrum of ligand **L2.3**.

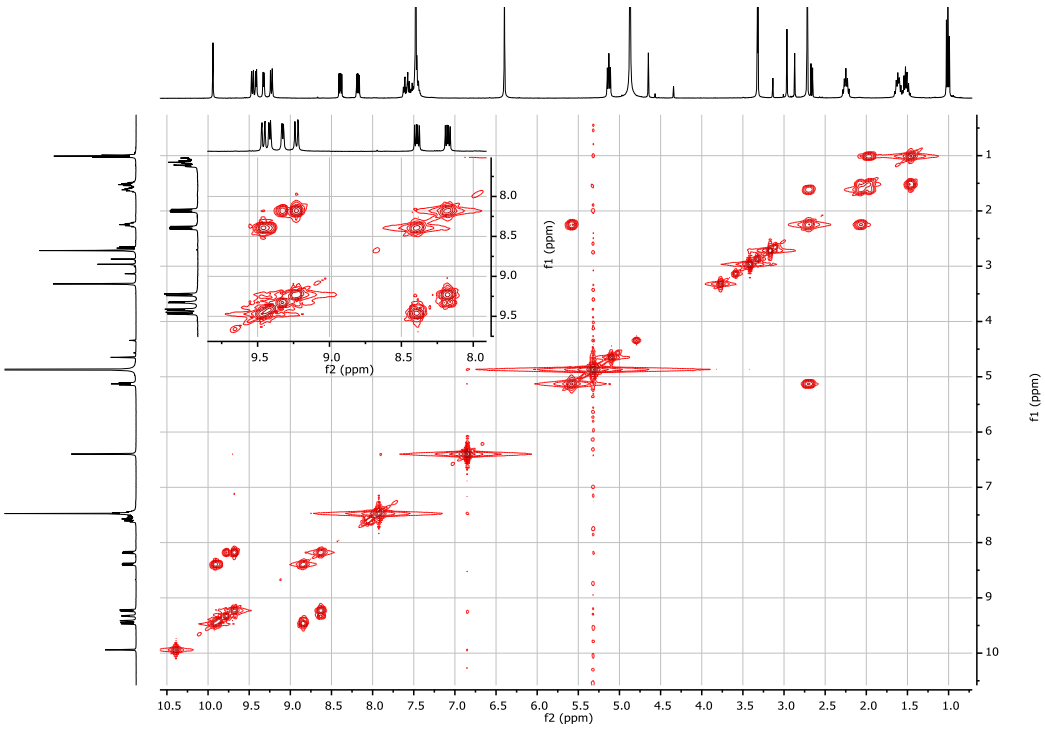

Figure S2.2. COSY-NMR spectrum of ligand **L2.3**.

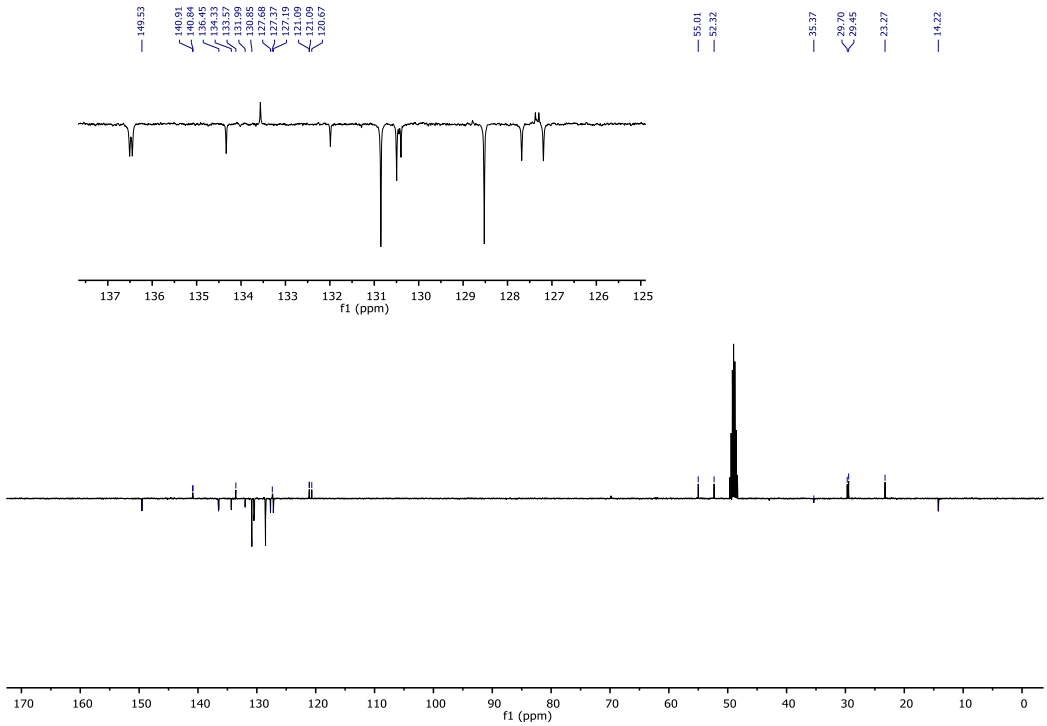

Figure S2.3. APT-NMR spectrum of ligand **L2.3**.

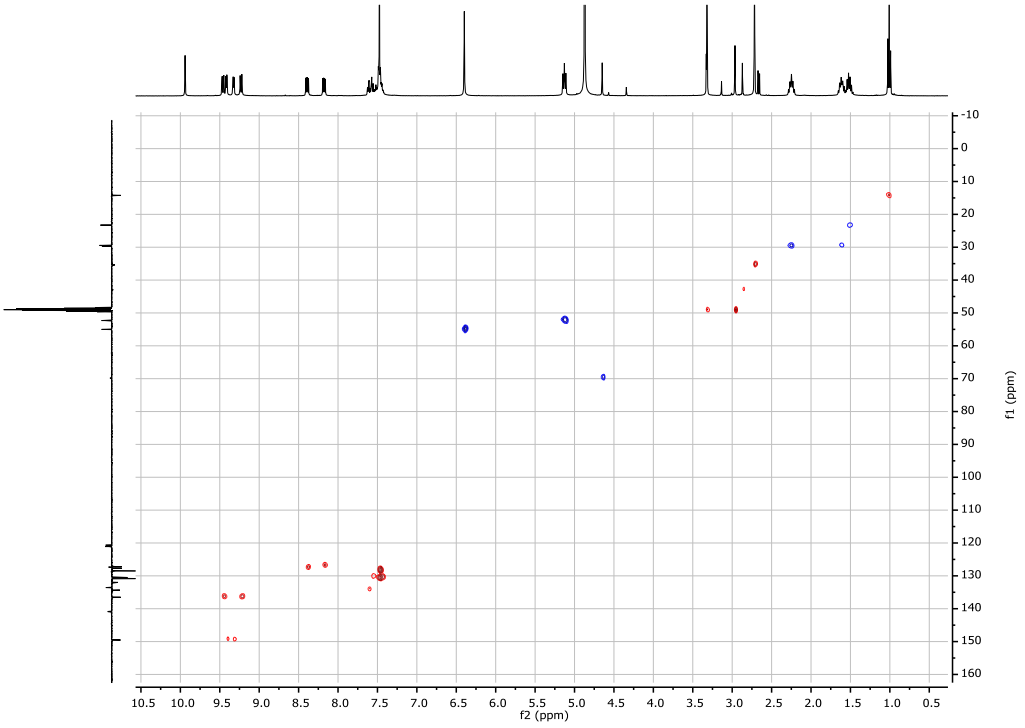

Figure S2.4. HSQC spectrum of ligand **L2.3**.

NMR spectra of complexes 2.1-2.7

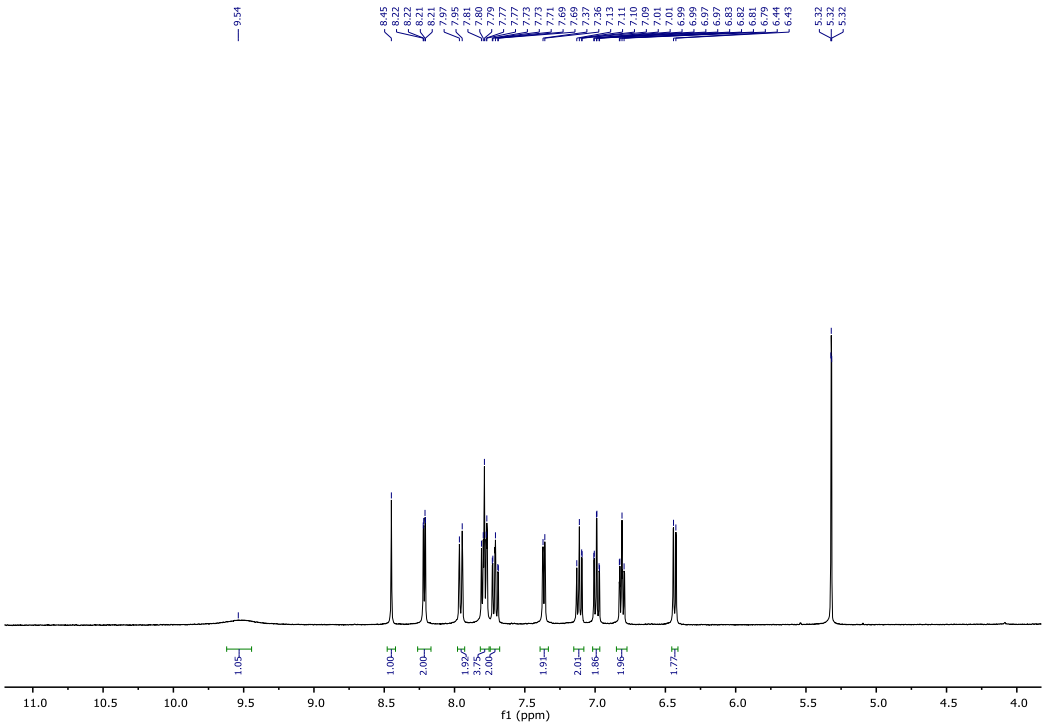

Figure S2.5. ^{1}H-NMR spectrum of complex **2.1**.

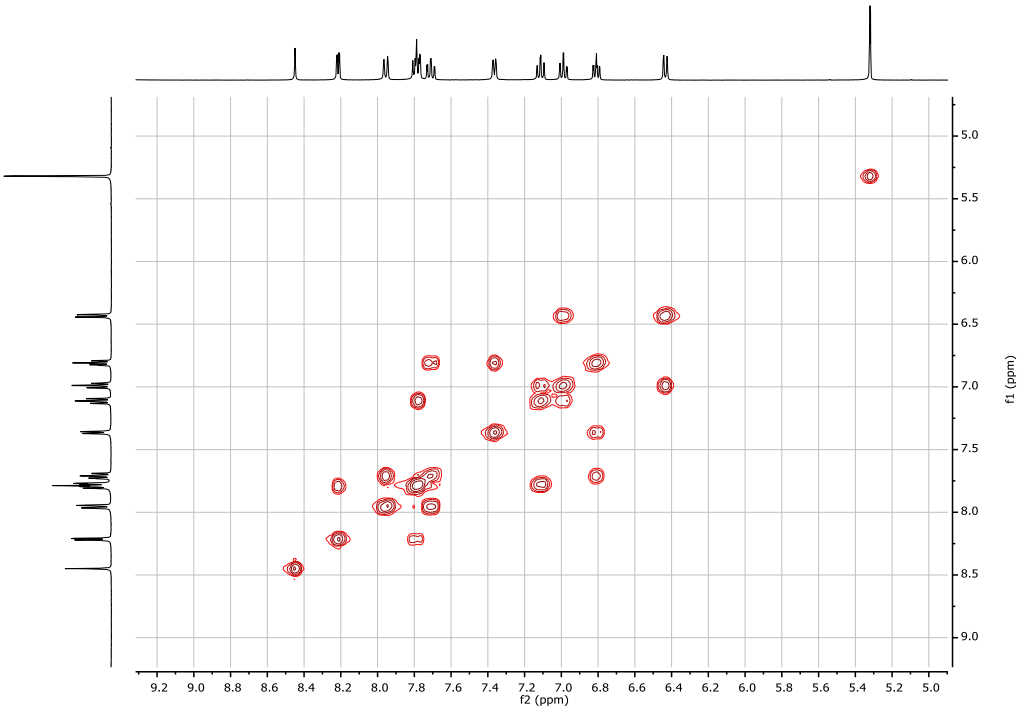

Figure S2.6. COSY-NMR spectrum of complex **2.1**.

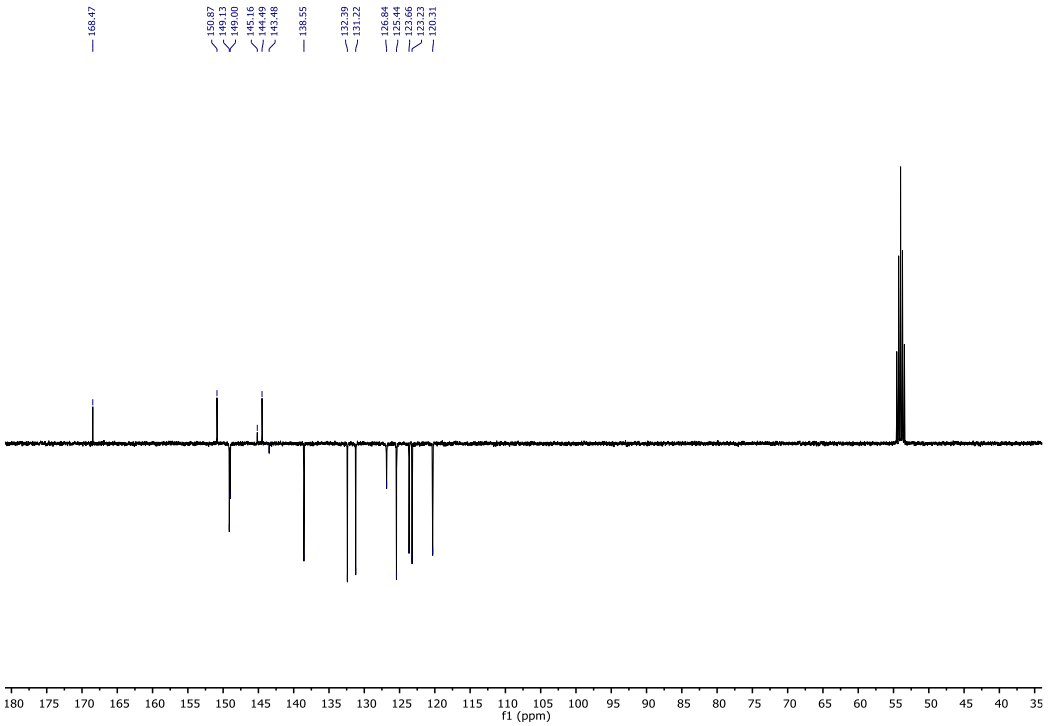

Figure S2.7. APT-NMR spectrum of complex **2.1**.

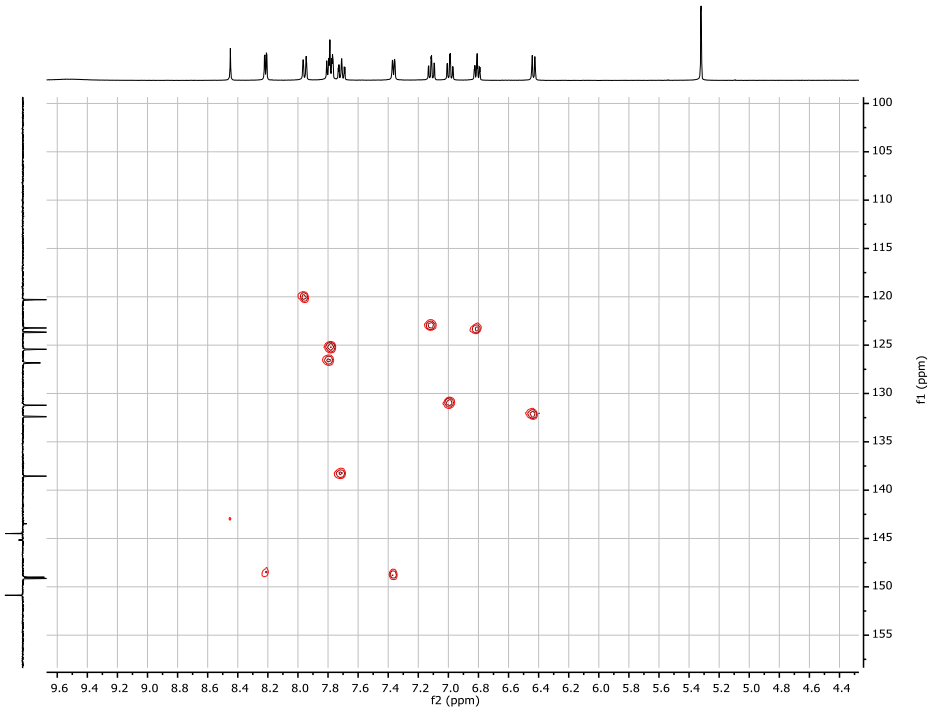

Figure S2.8. HSQC spectrum of complex **2.1**.

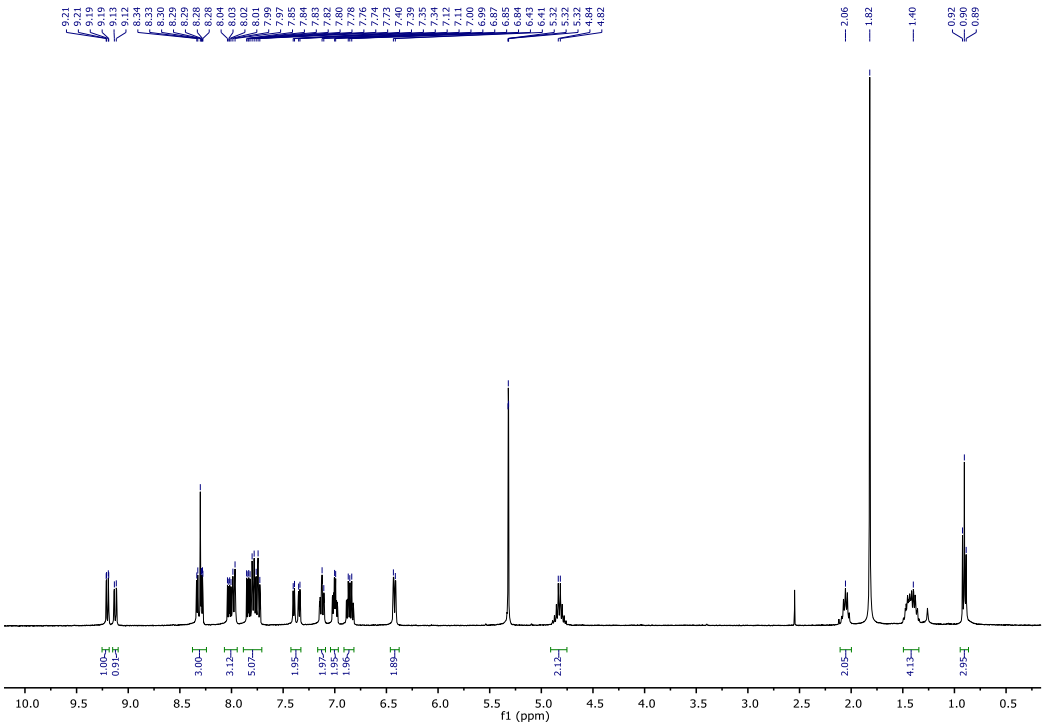

Figure S2.9. ^{1}H-NMR spectrum of complex **2.2**.

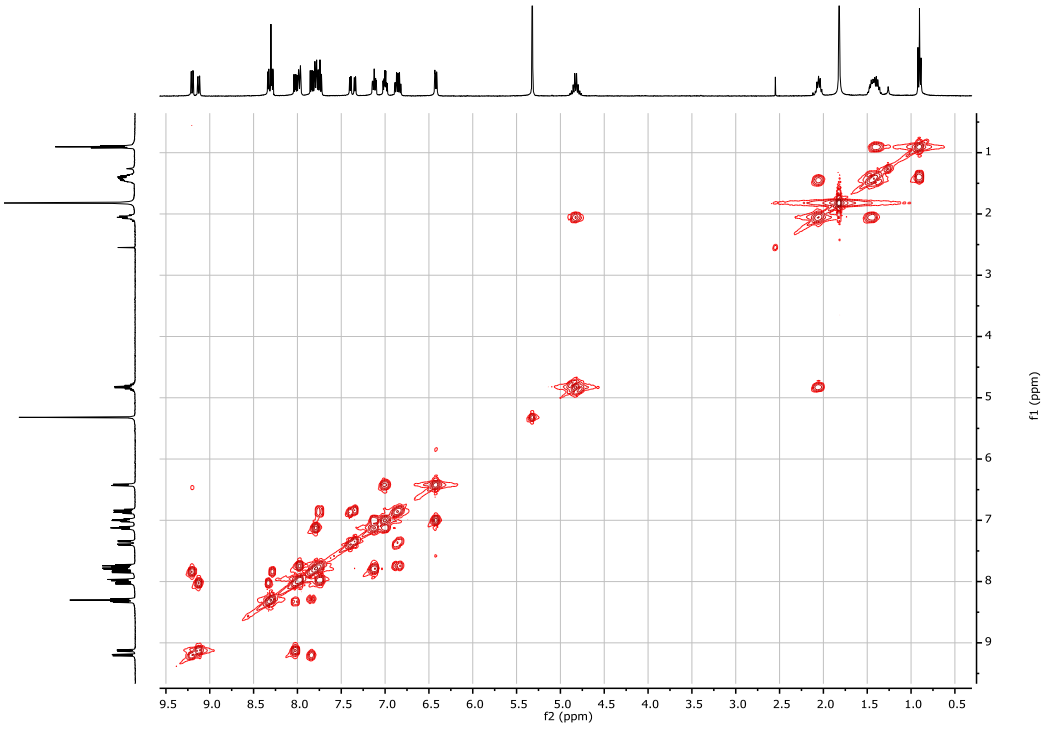

Figure S2.10. COSY-NMR spectrum of complex **2.2**.

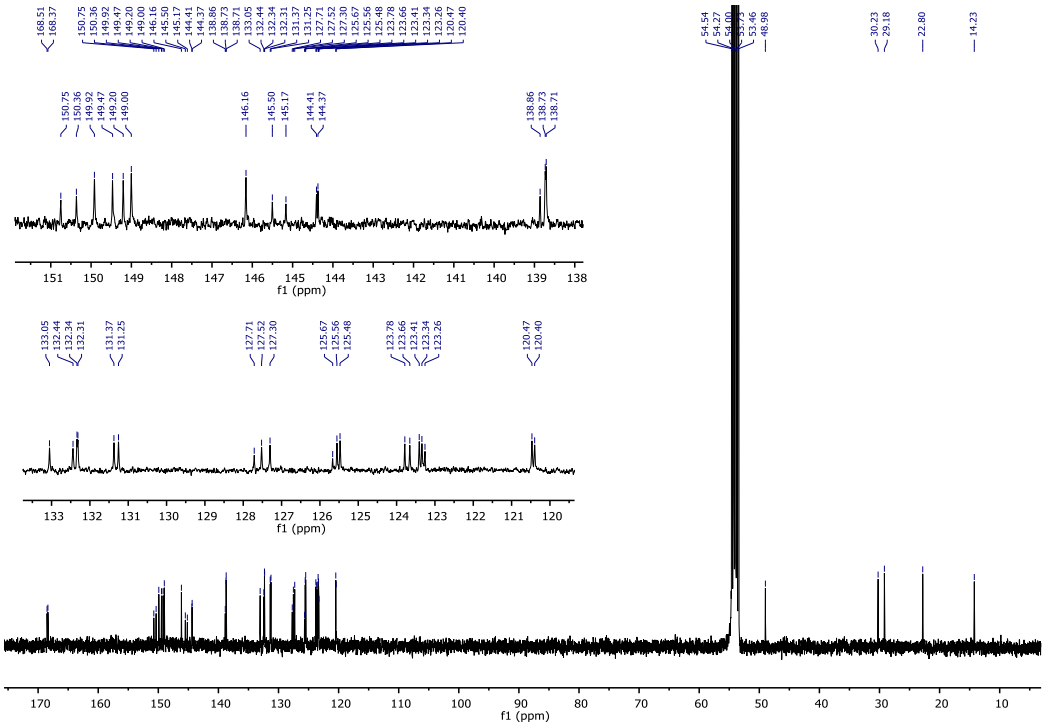

Figure S2.11. ^{13}C-NMR spectrum of complex **2.2**.

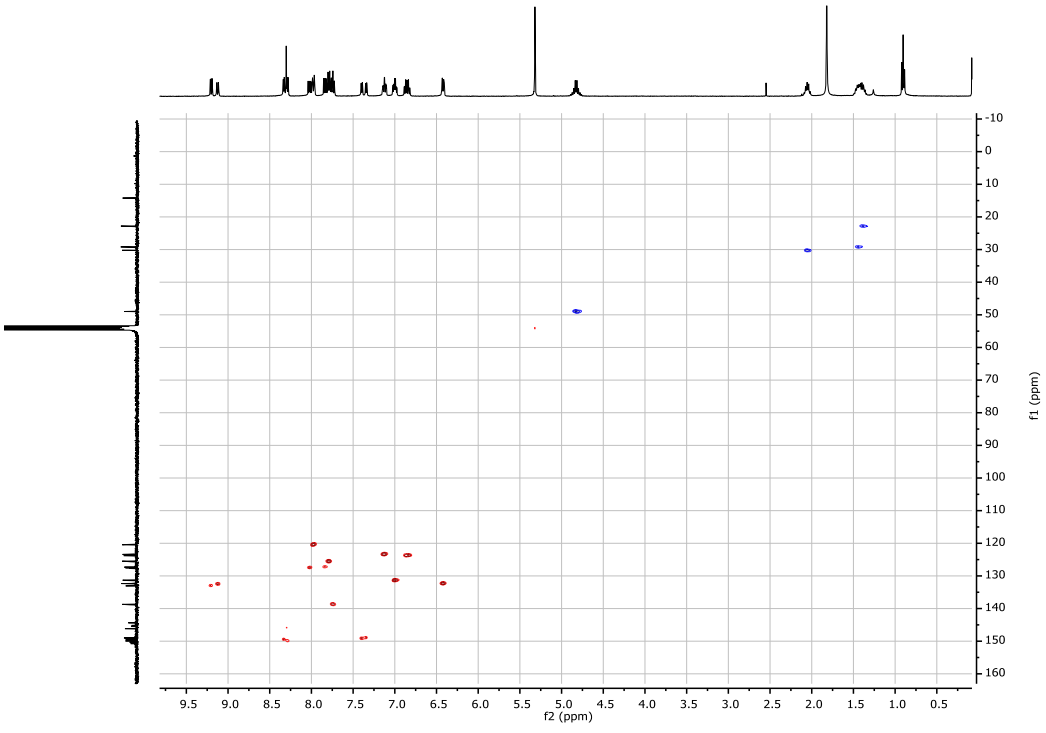

Figure S2.12. HSQC spectrum of complex **2.2**.

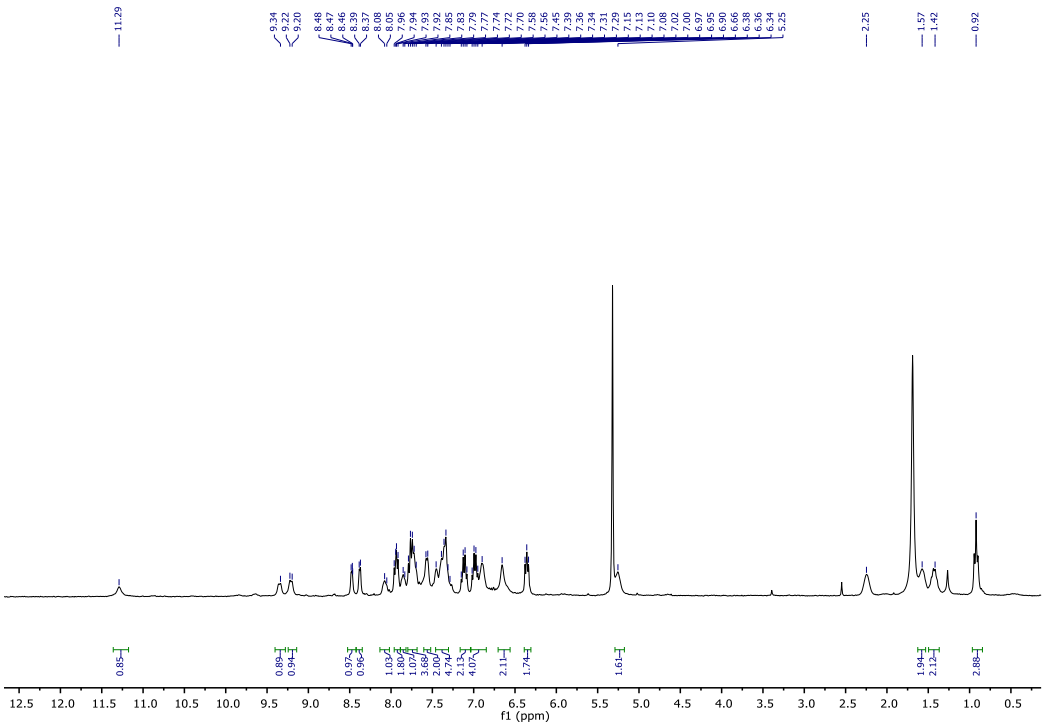

Figure S2.13. [1]H-NMR spectrum of complex **2.3**.

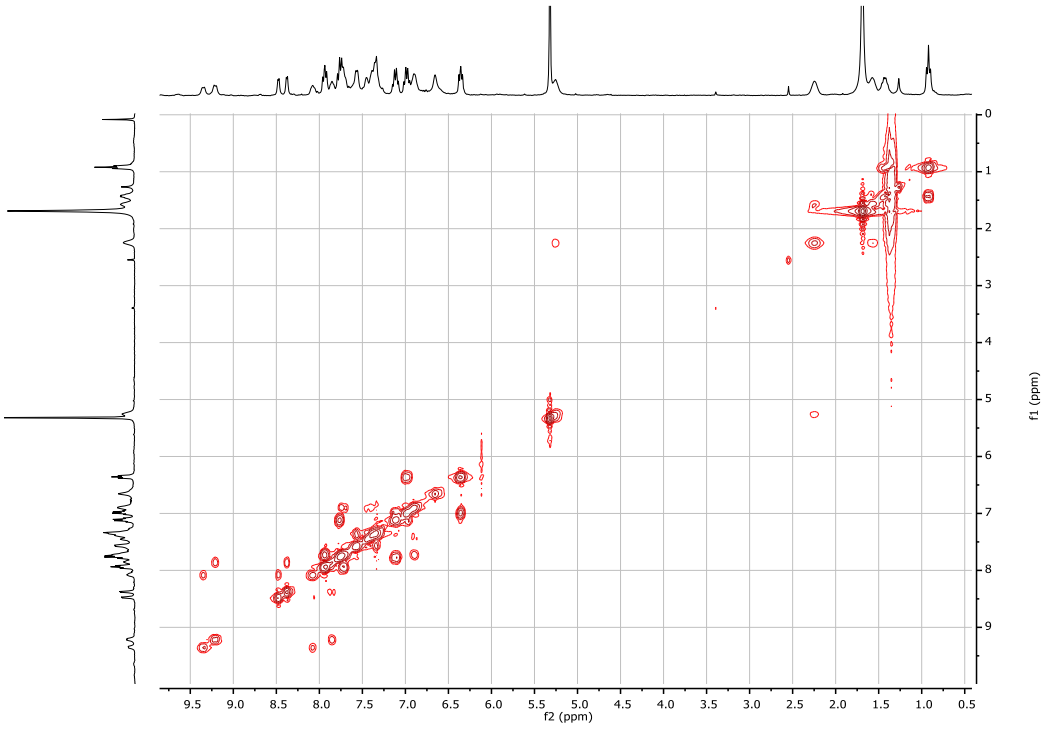

Figure S2.14. COSY-NMR spectrum of complex **2.3**.

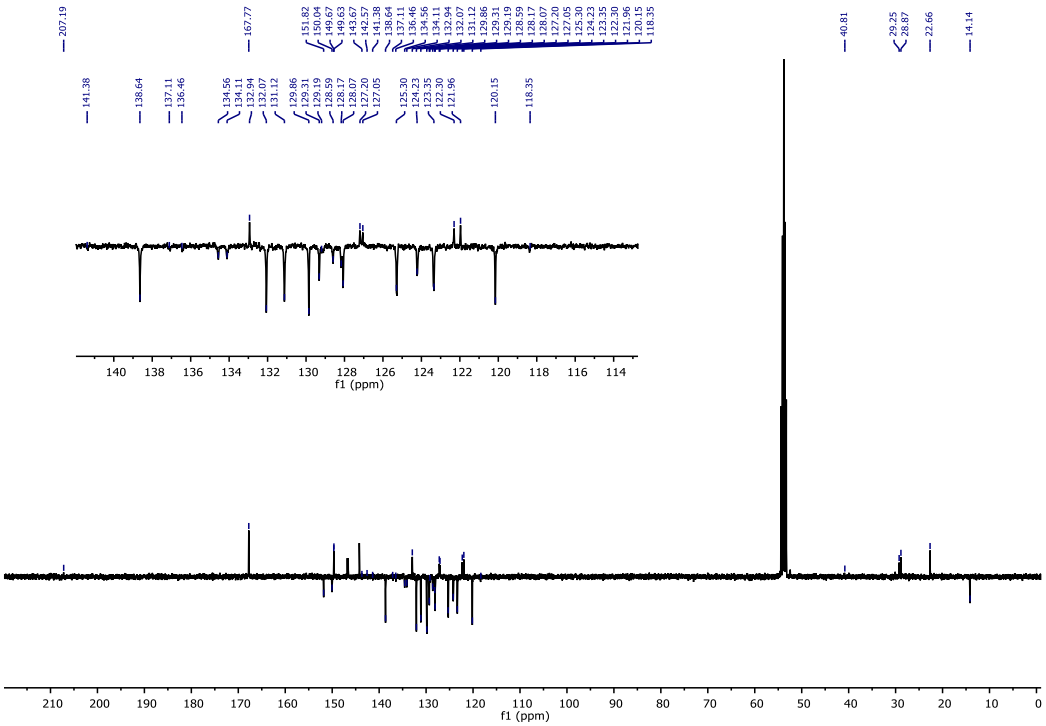

Figure S2.15. APT-NMR spectrum of complex **2.3**.

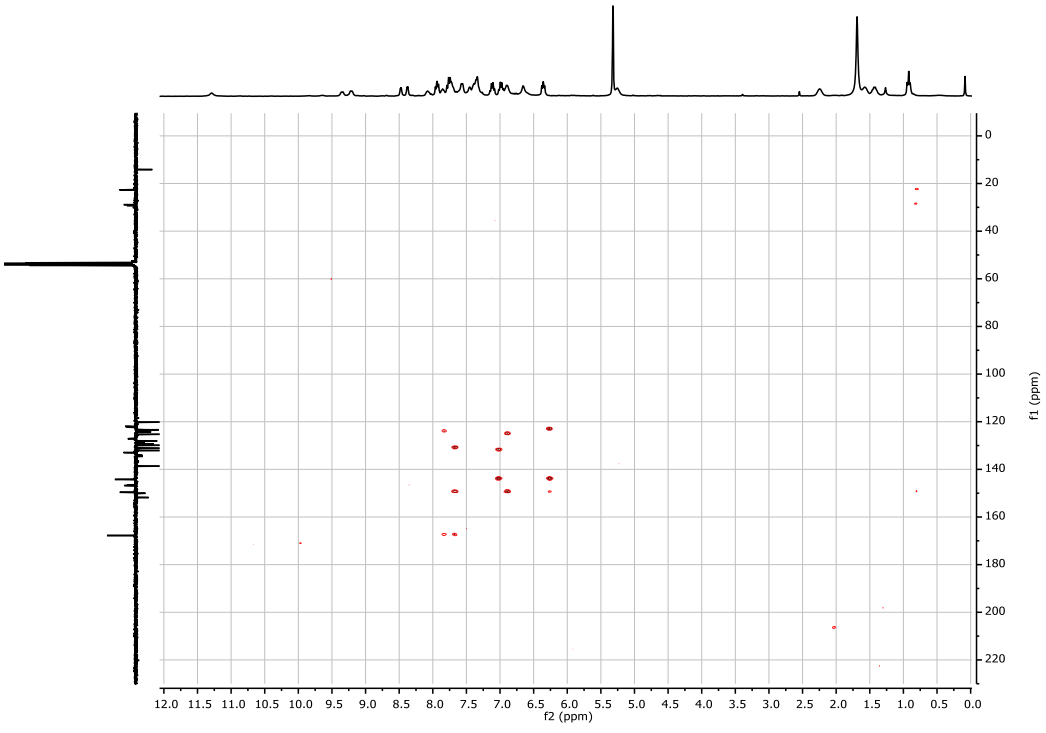

Figure S2.16. HSQC spectrum of complex **2.3**.

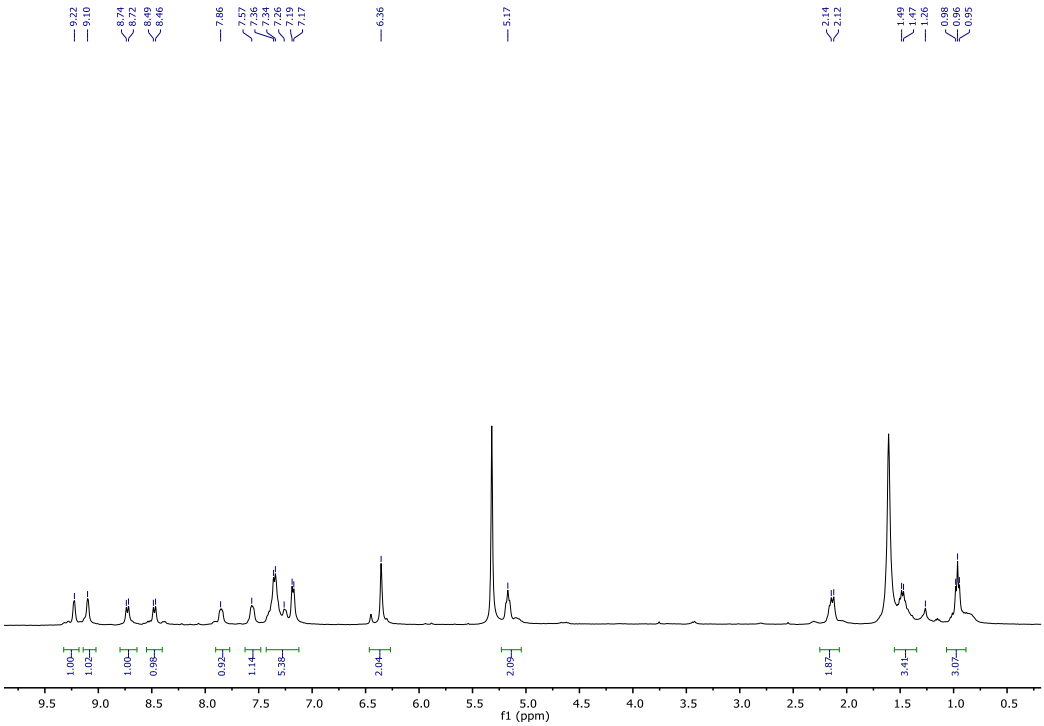

Figure S2.17. ^{1}H-NMR spectrum of complex **2.4**.

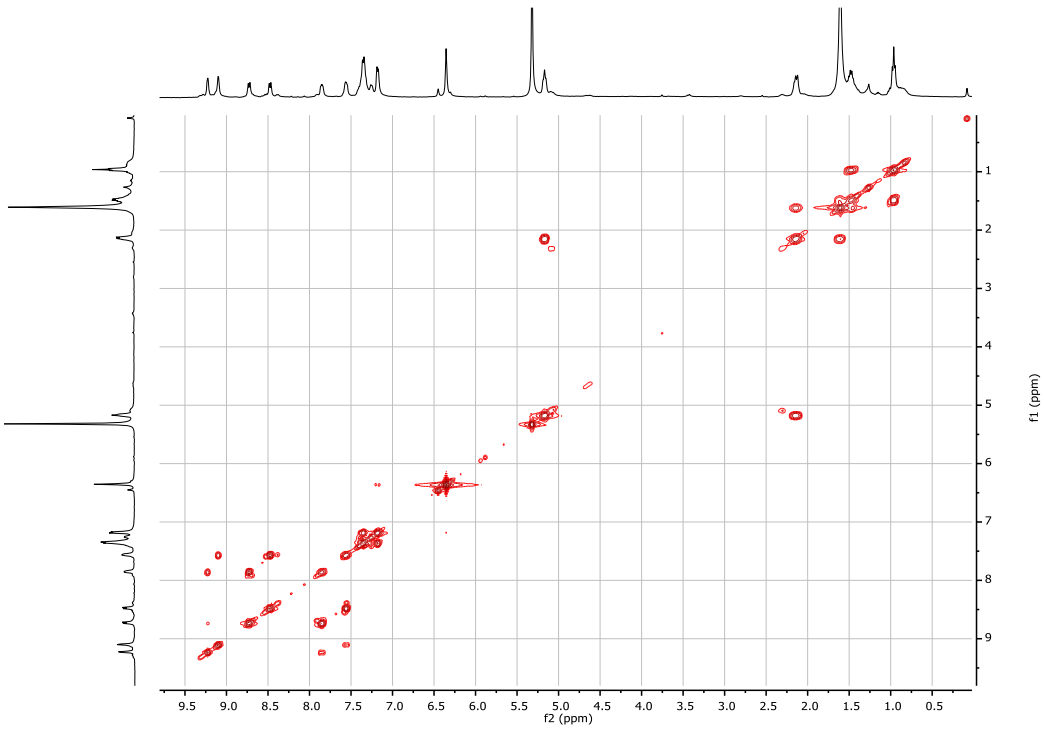

Figure S2.18. COSY-NMR spectrum of complex **2.4**.

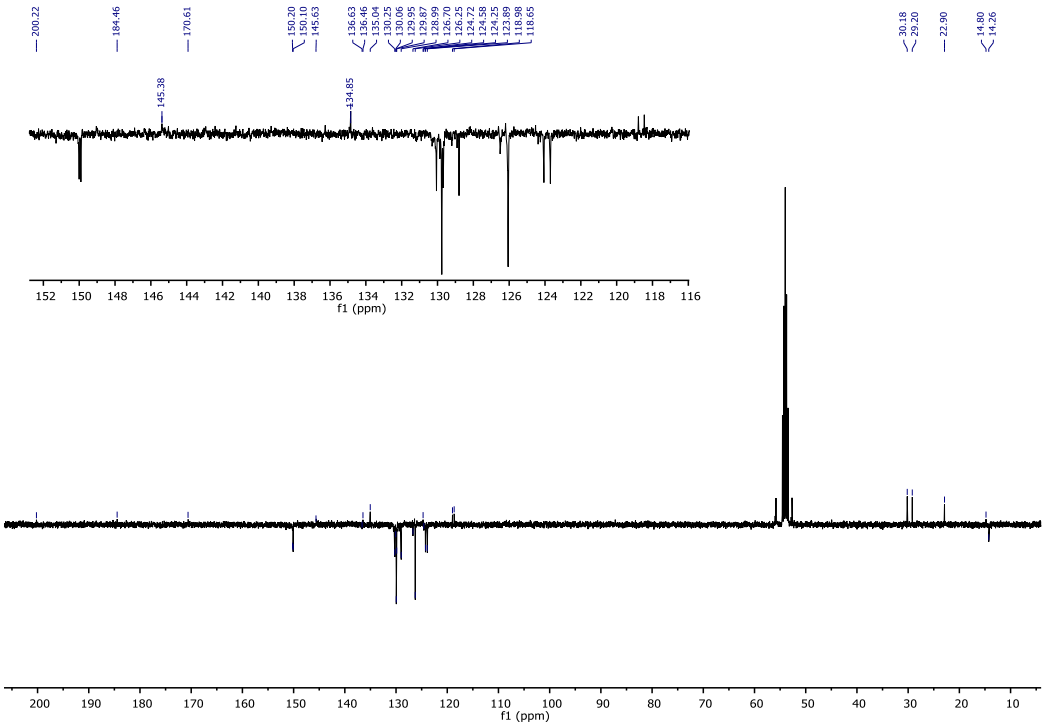

Figure S2.19. APT-NMR spectrum of complex **2.4**.

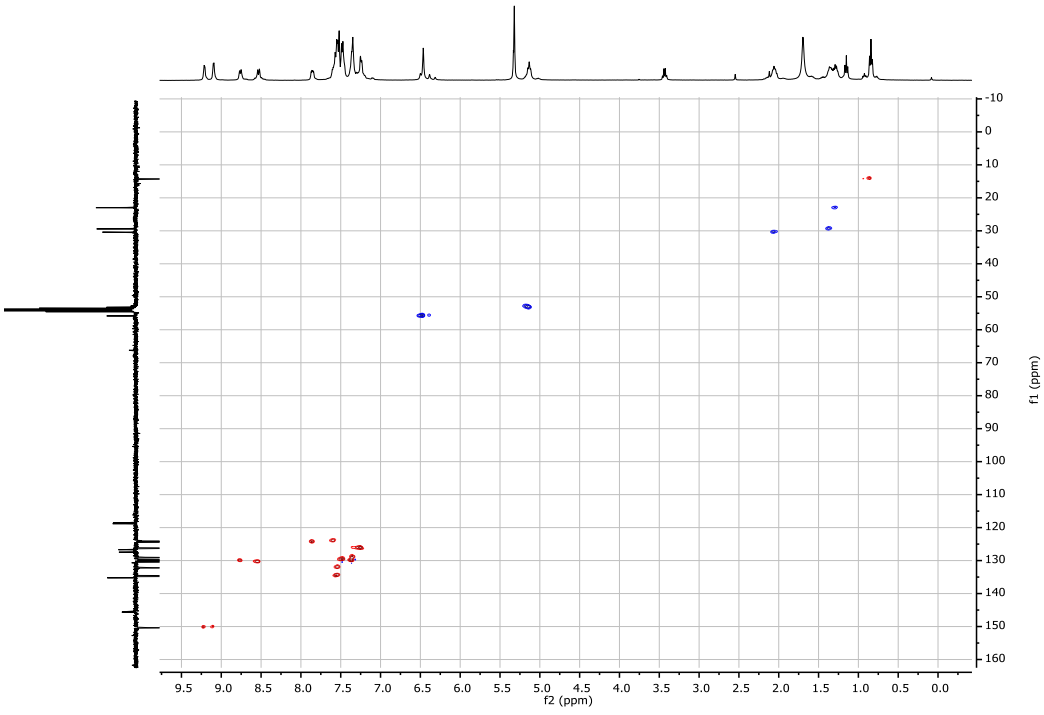

Figure S2.20. HSQC spectrum of complex **2.4**.

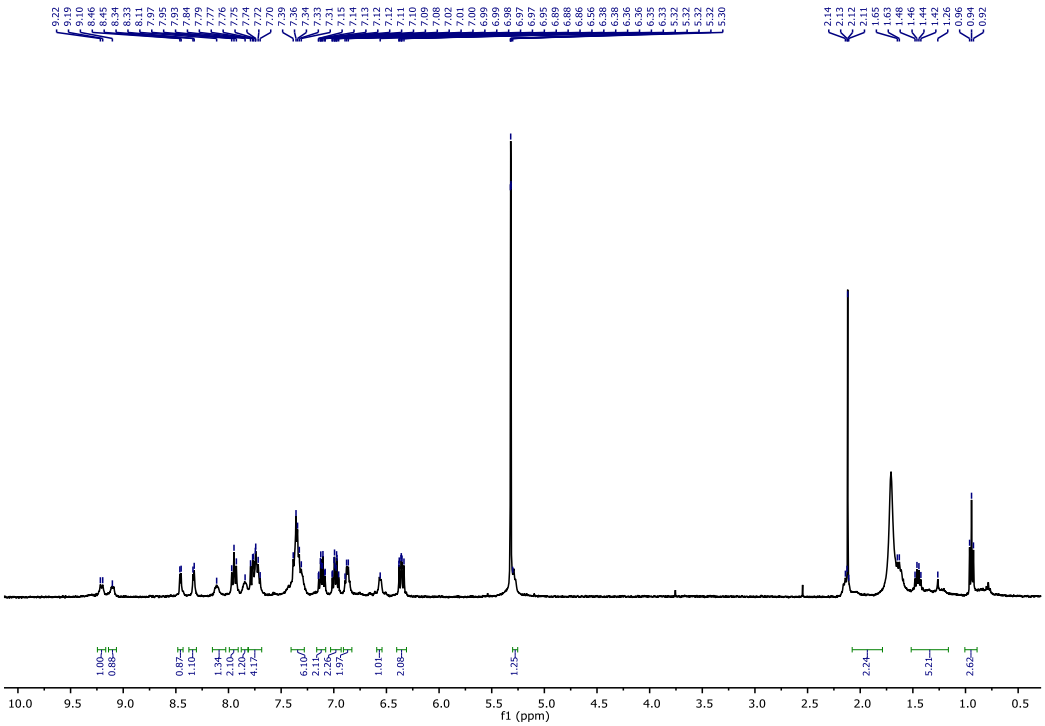

Figure S2.21. ^{1}H-NMR spectrum of complex **2.5**.

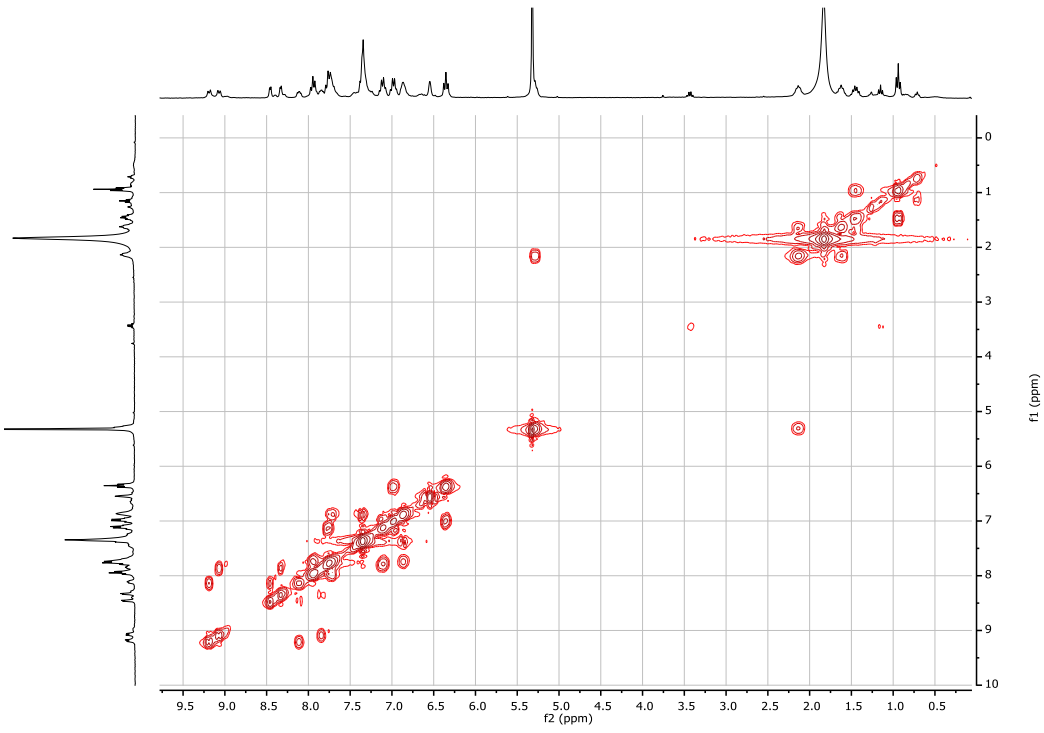

Figure S2.22. COSY-NMR spectrum of complex **2.5**.

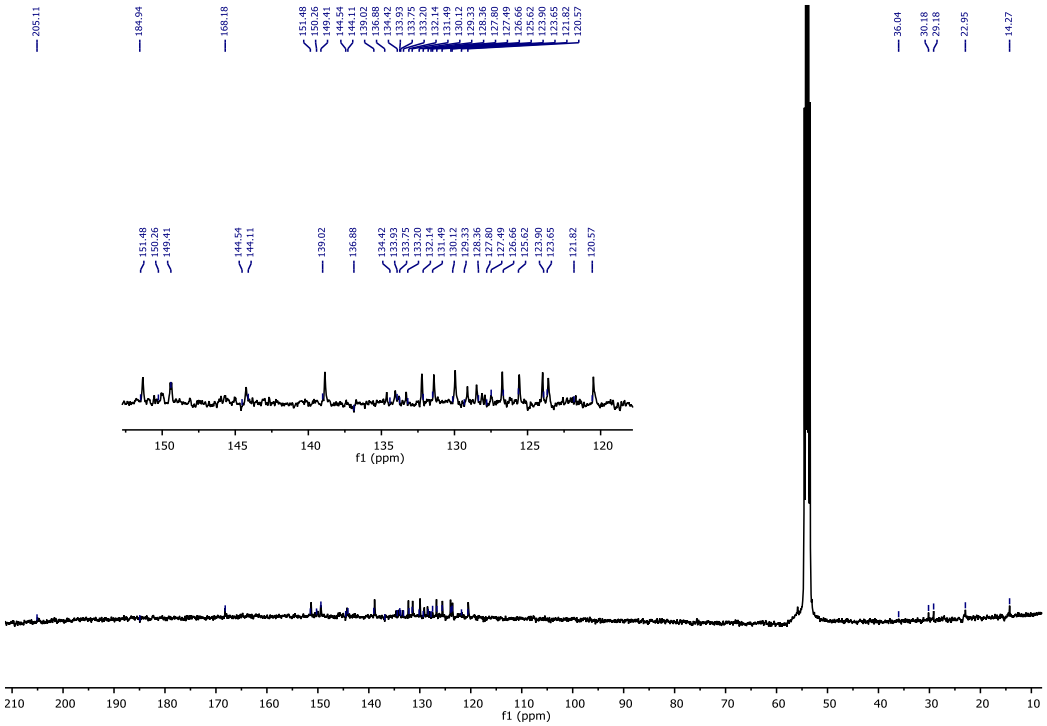

Figure S2.23. ^{13}C-NMR spectrum of complex **2.5**.

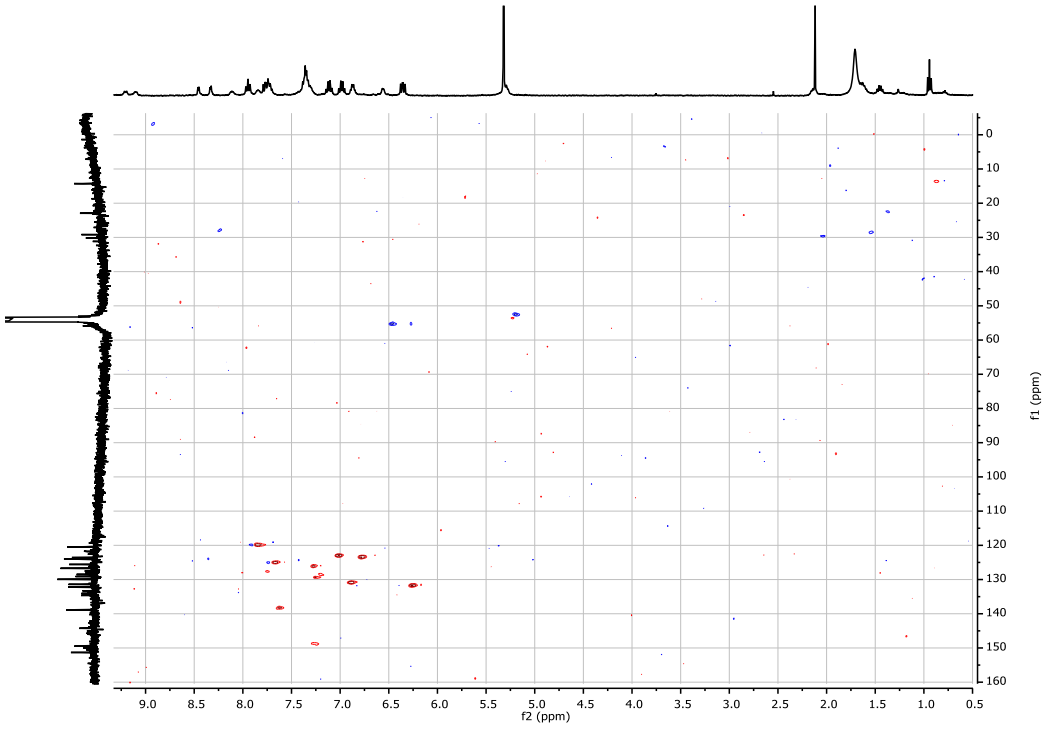

Figure S2.24. HSQC spectrum of complex **2.5**.

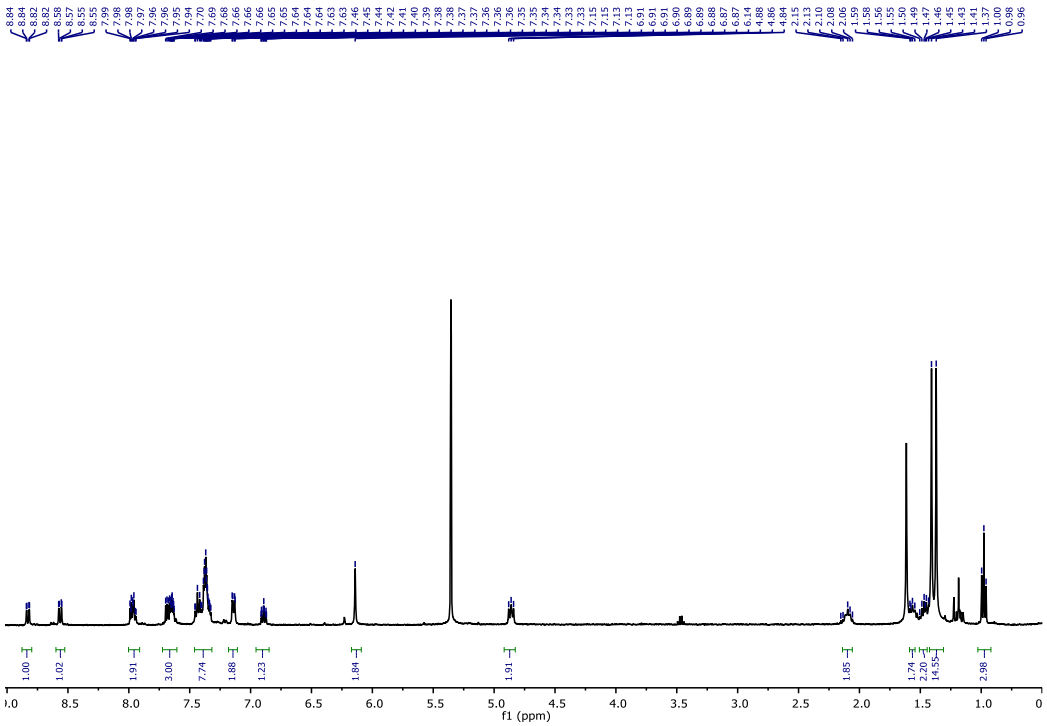

Figure S2.25. ^{1}H-NMR spectrum of complex **2.6**.

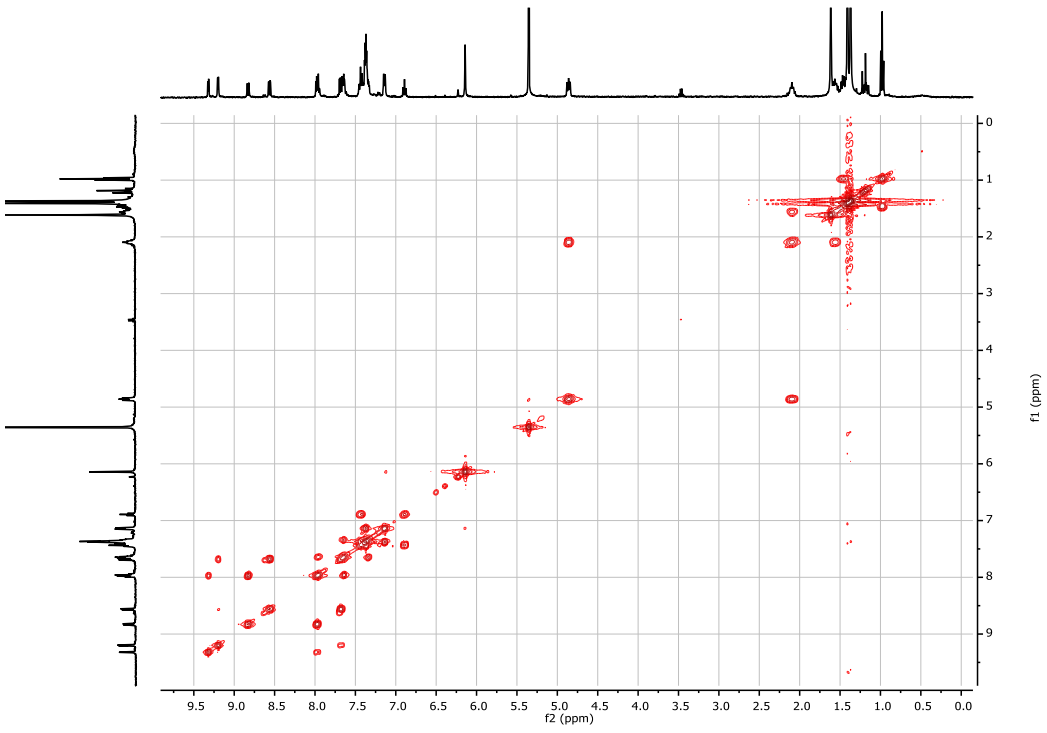

Figure S2.26. COSY-NMR spectrum of complex **2.6**.

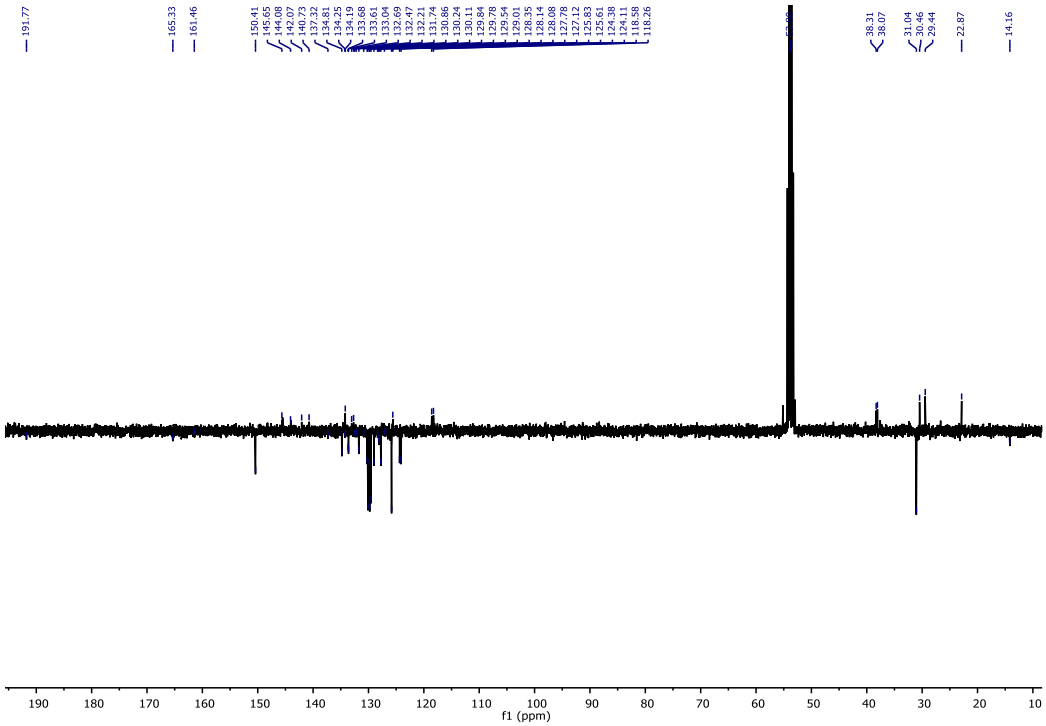

Figure S2.27. APT-NMR spectrum of complex **2.6**.

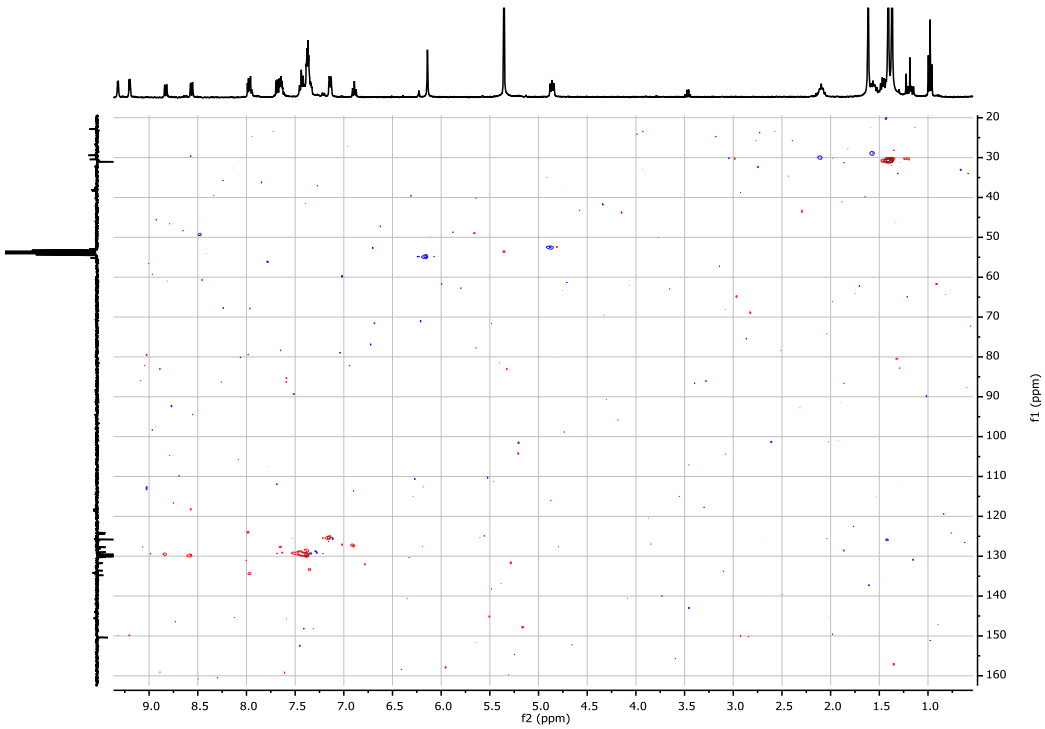

Figure S2.28. HSQC spectrum of complex **2.6**.

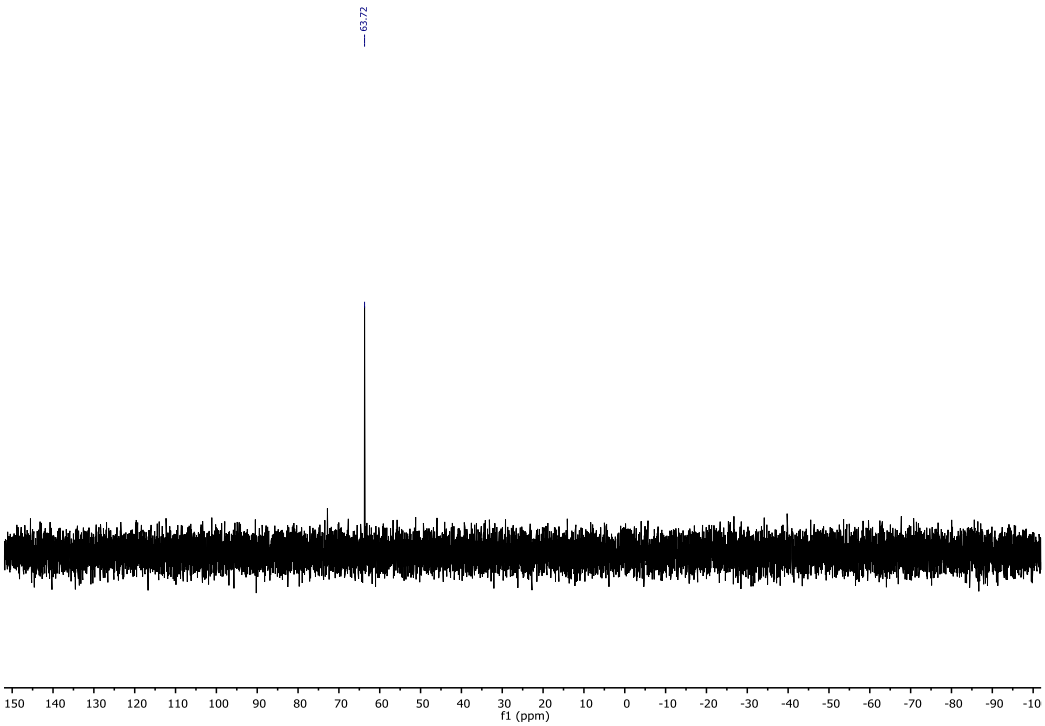

Figure S2.29. ^{31}P-NMR spectrum of complex **2.6**.

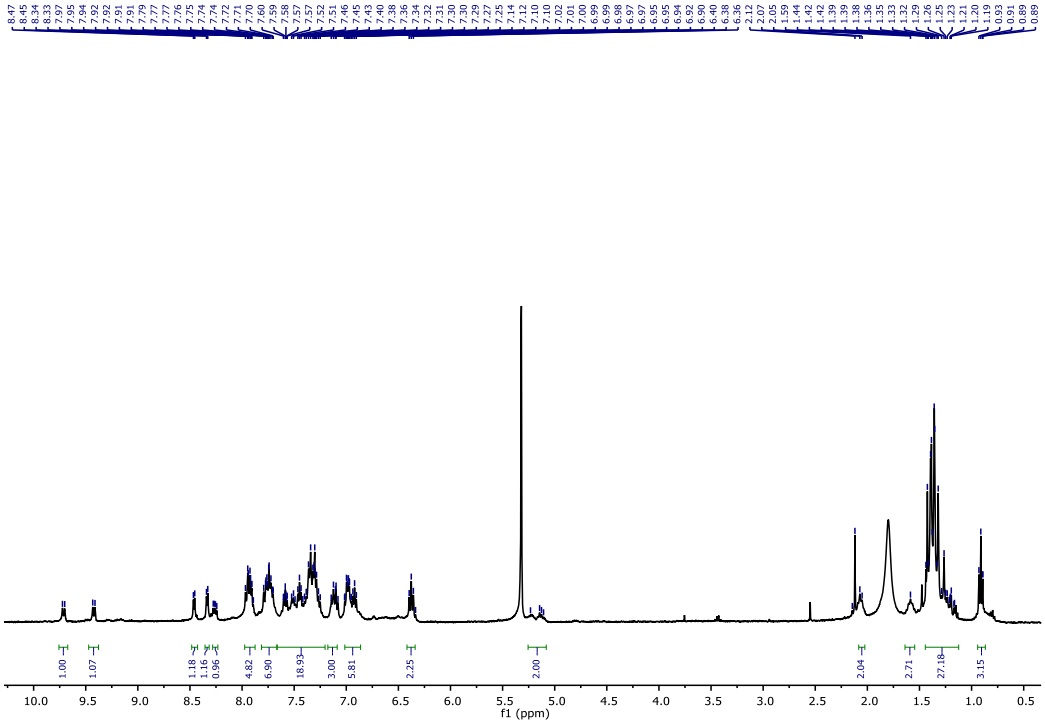

Figure S2.30. ^{1}H-NMR spectrum of complex **2.7**.

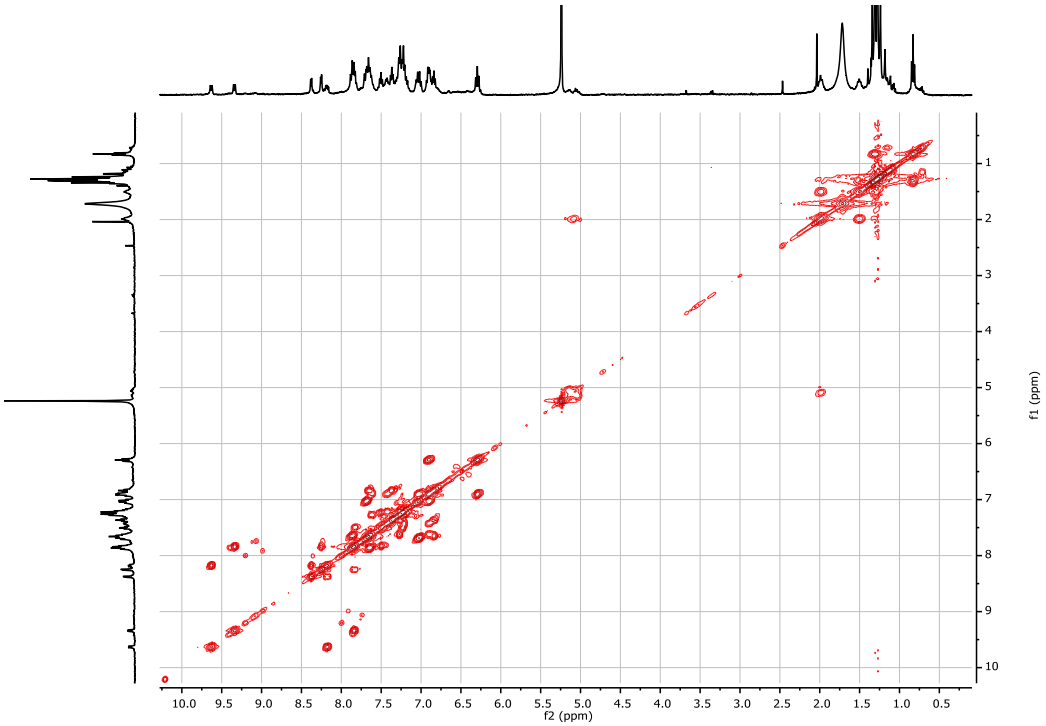

Figure S2.31. COSY-NMR spectrum of complex **2.7**.

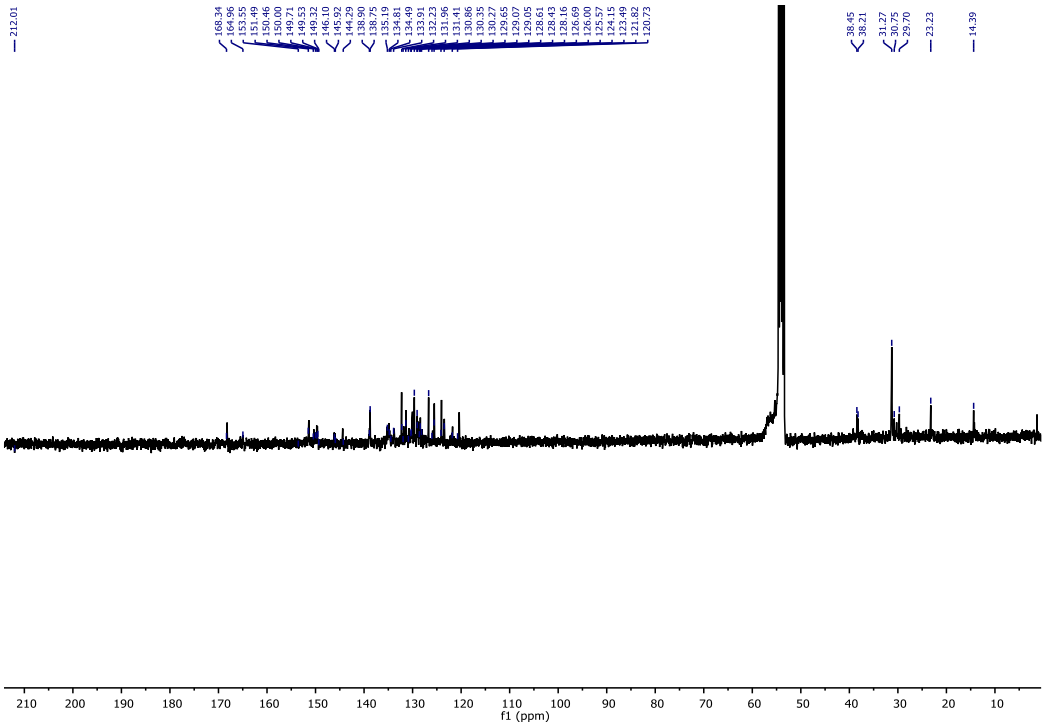

Figure S2.32. ^{13}C-NMR spectrum of complex **2.7**.

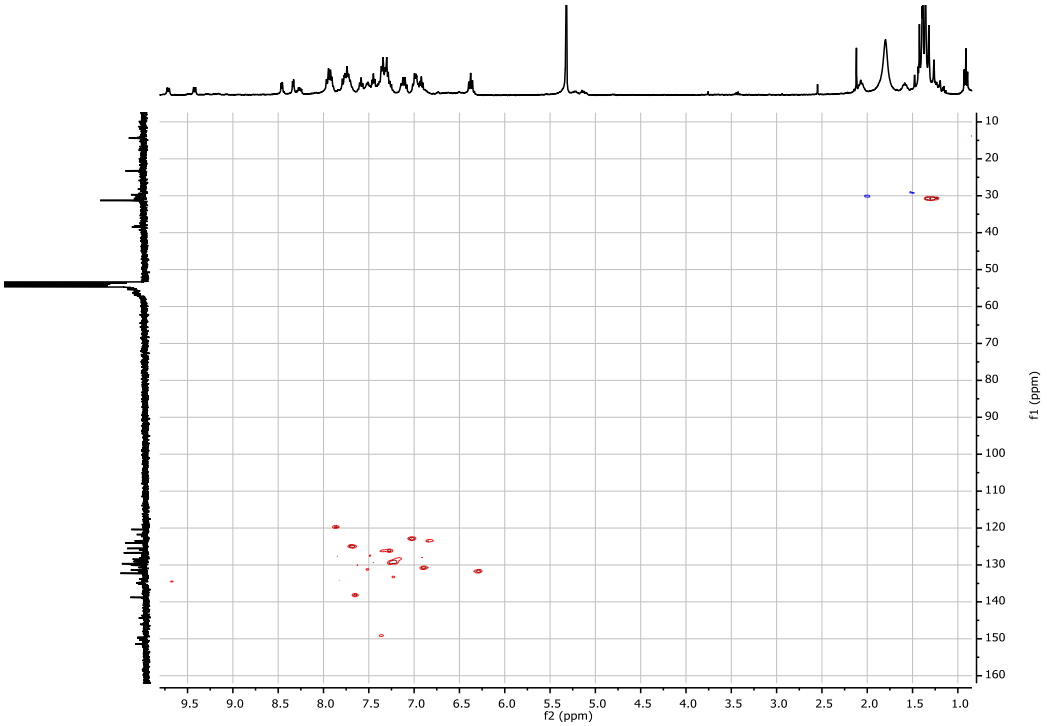

Figure S2.33. HSQC spectrum of complex **2.7**.

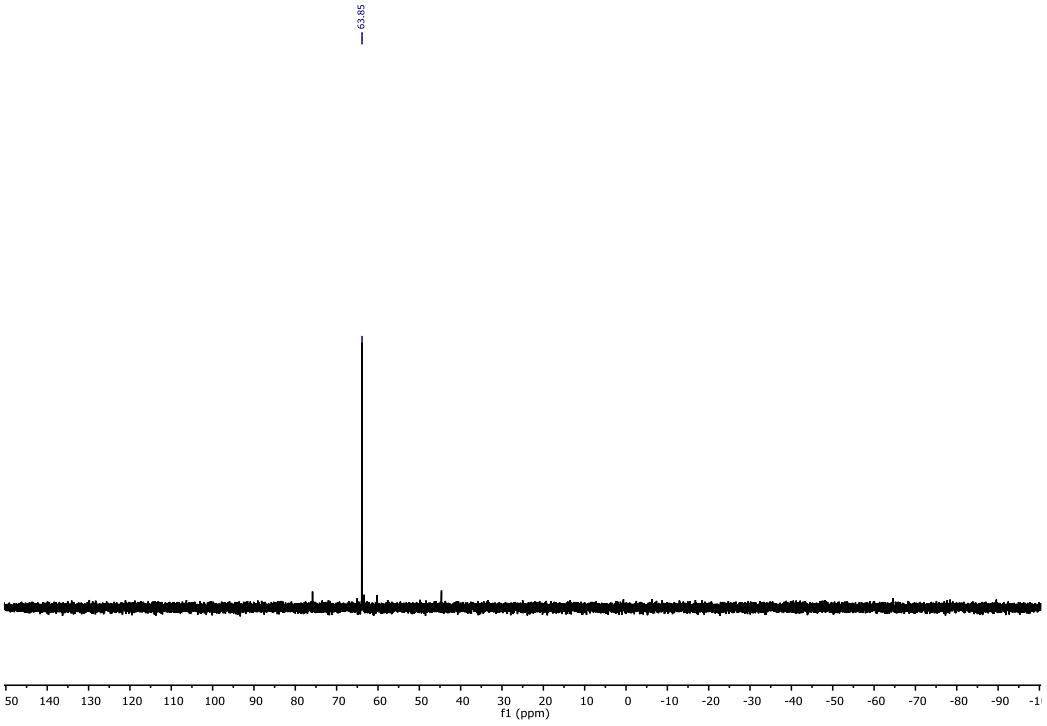

Figure S2.34. ^{31}P-NMR spectrum of complex **2.7**.

Mass spectra of L2.3 and complexes 2.2-2.7

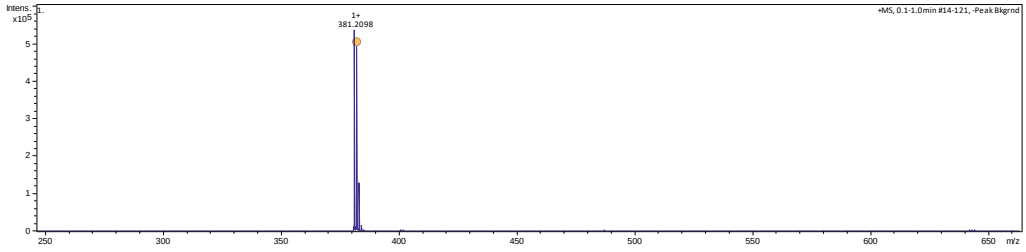

Figure S2.35. ESI-HRMS spectrum of ligand **L2.3**.

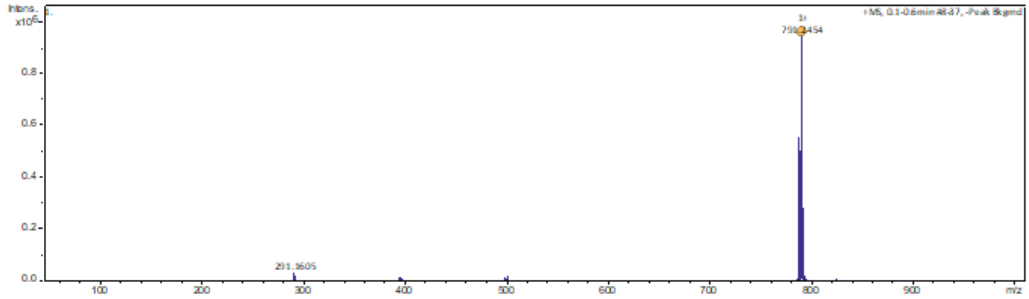

Figure S2.36. ESI-HRMS spectrum of complex **2.2**.

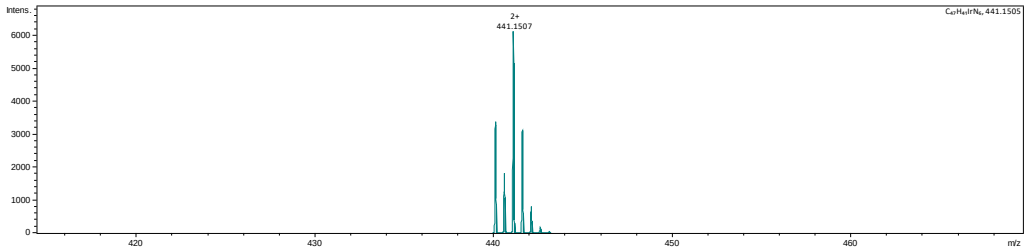

Figure S2.37. ESI-HRMS spectrum of complex **2.3**.

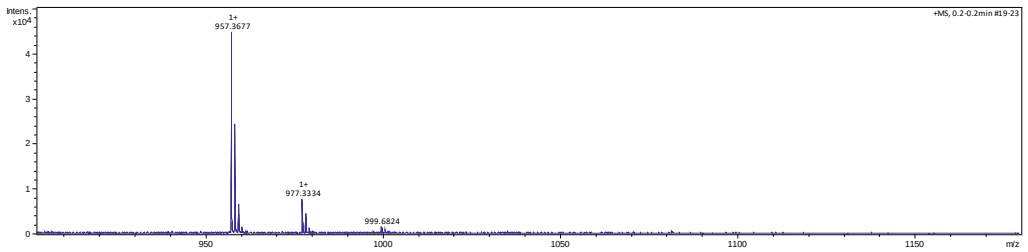

Figure S2.38. ESI-HRMS spectrum of complex **2.4**.

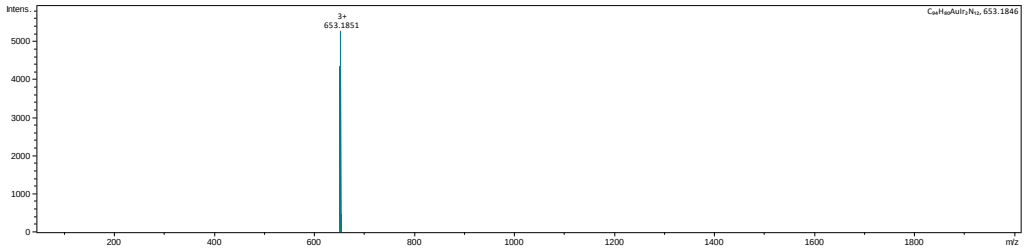

Figure S2.39. ESI-HRMS spectrum of complex **2.5**.

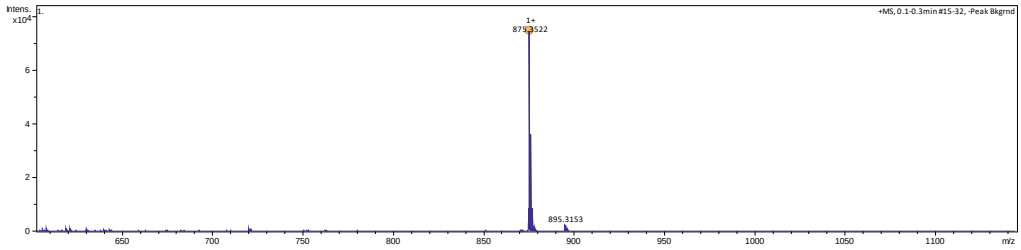

Figure S2.40. ESI-HRMS spectrum of complex **2.6**.

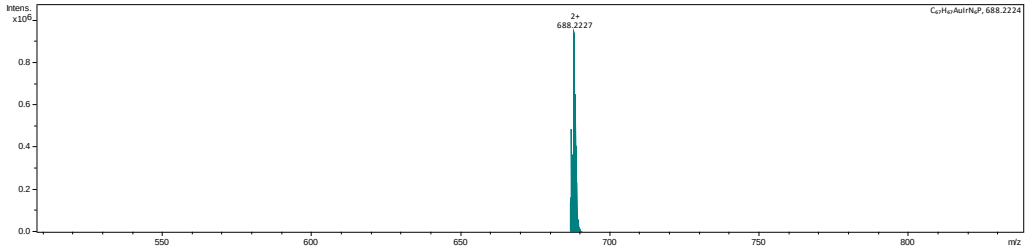

Figure S2.41. ESI-HRMS spectrum of complex **2.7**.

Emission and excitation spectra of complexes 2.1-2.7

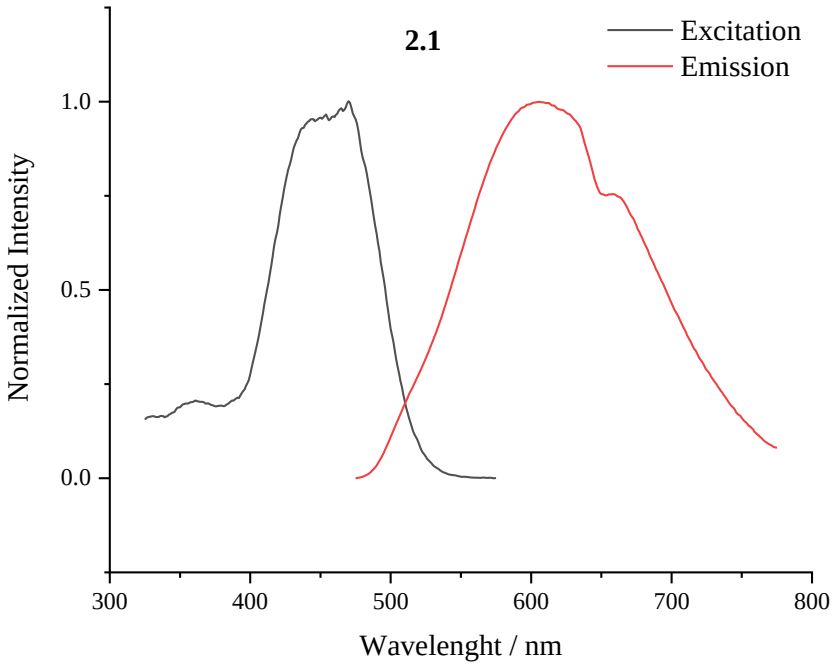

Figure S2.42. Emission-excitation spectra of complex **2.1** measured in DMSO solution.

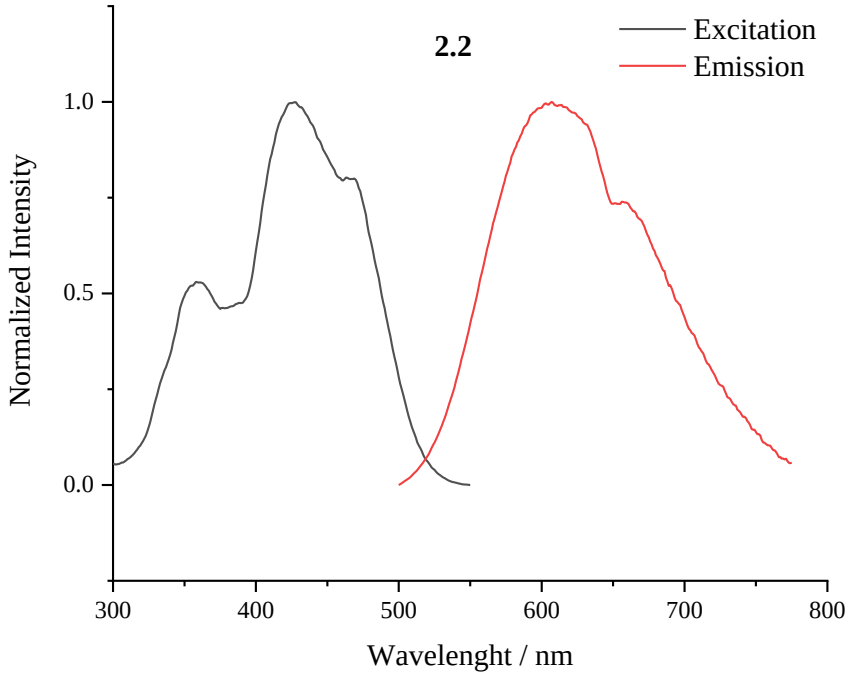

Figure S2.43. Emission-excitation spectra of complex **2.2** measured in DMSO solution.

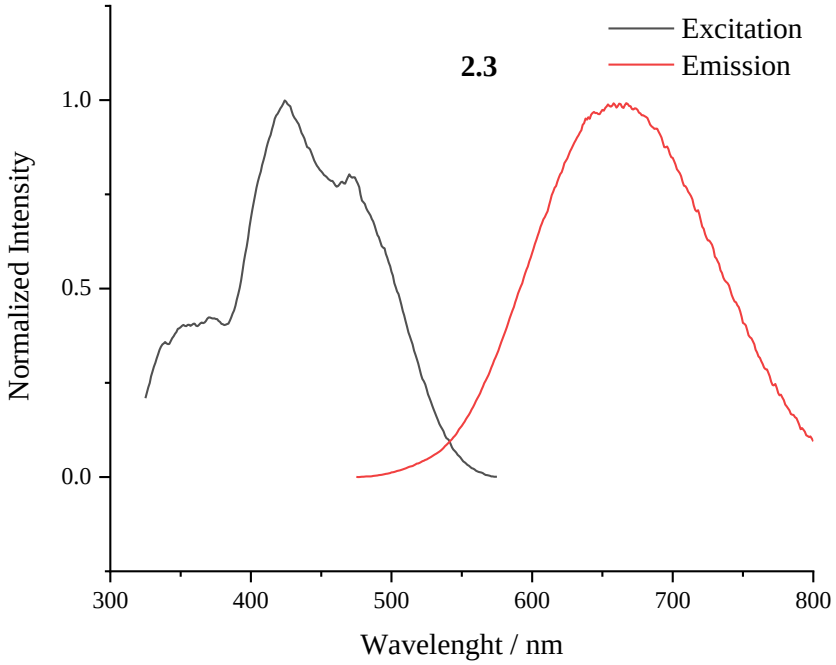

Figure S2.44. Emission-excitation spectra of complex **2.3** measured in DMSO solution.

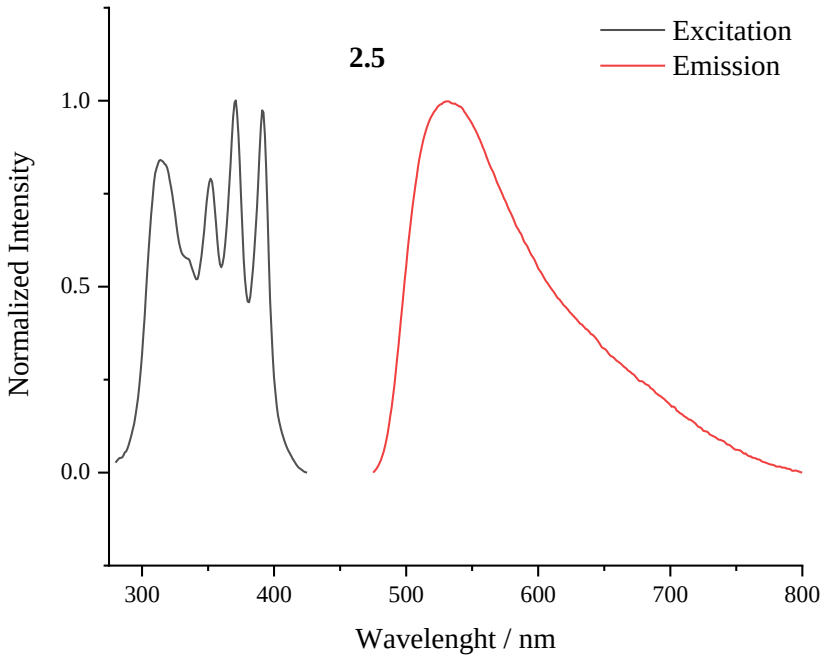

Figure S2.45. Emission-excitation spectra of complex **2.5** measured in DMSO solution.

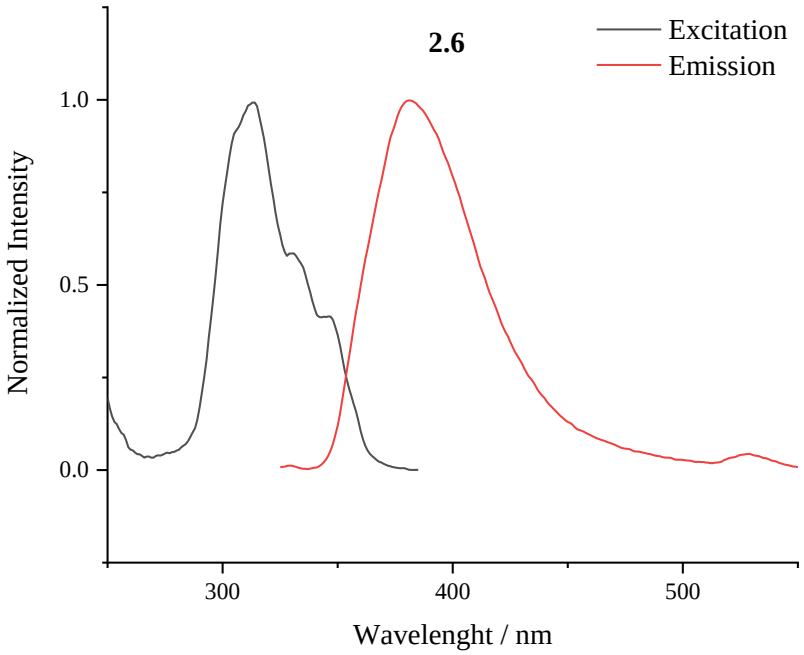

Figure S2.46. Emission-excitation spectra of complex **2.6** measured in DMSO solution.

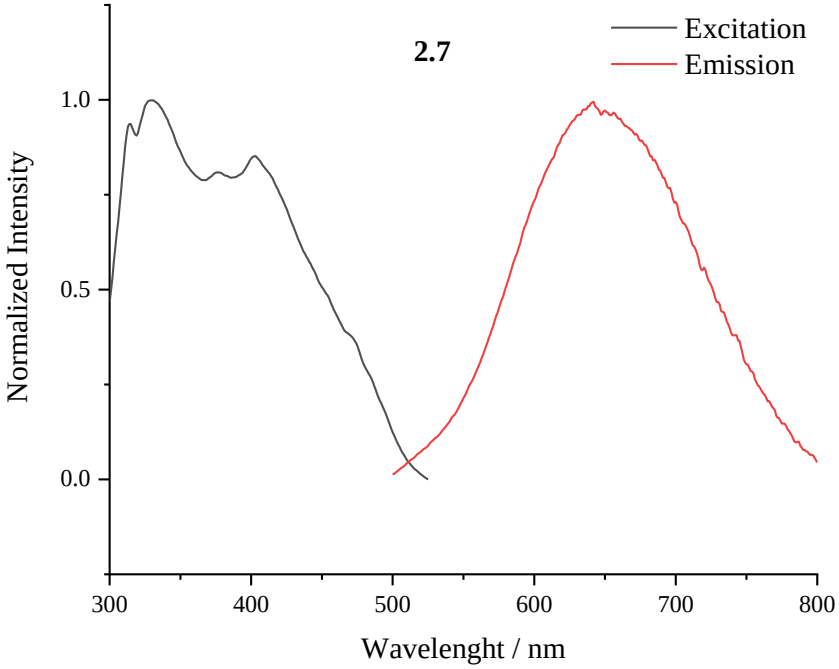

Figure S2.47. Emission-excitation spectra of complex **2.7** measured in DMSO solution.

Chapter 3

NMR spectra of ligands L3.1 and L3.2

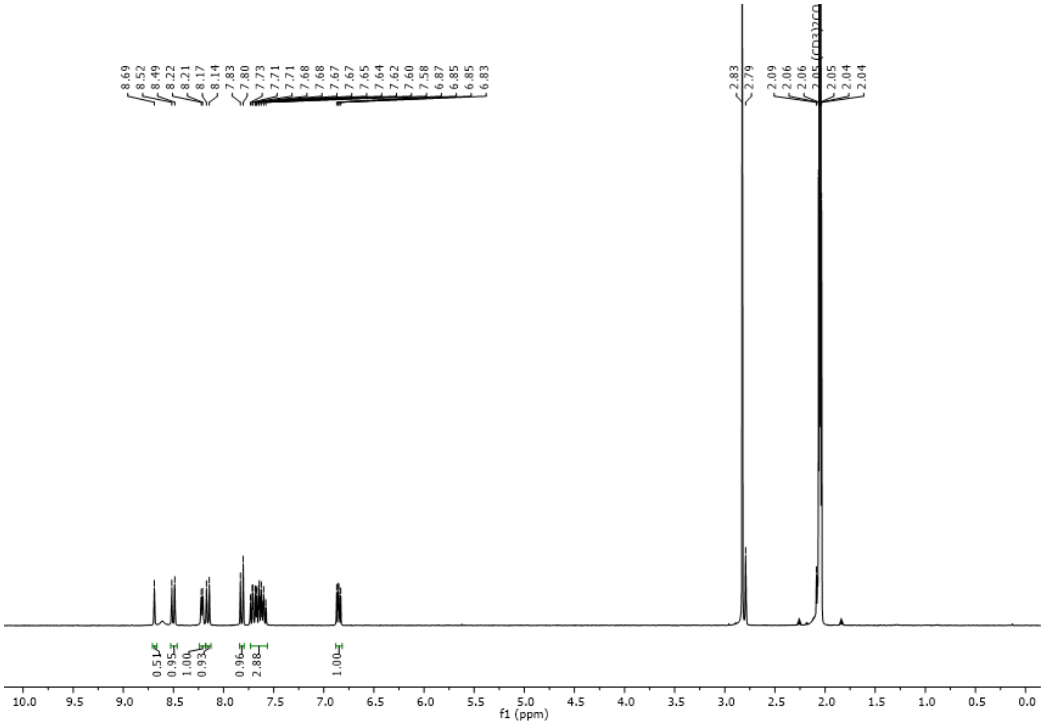

Figure S3.1. ^{1}H-NMR spectrum of ligand **L3.1**.

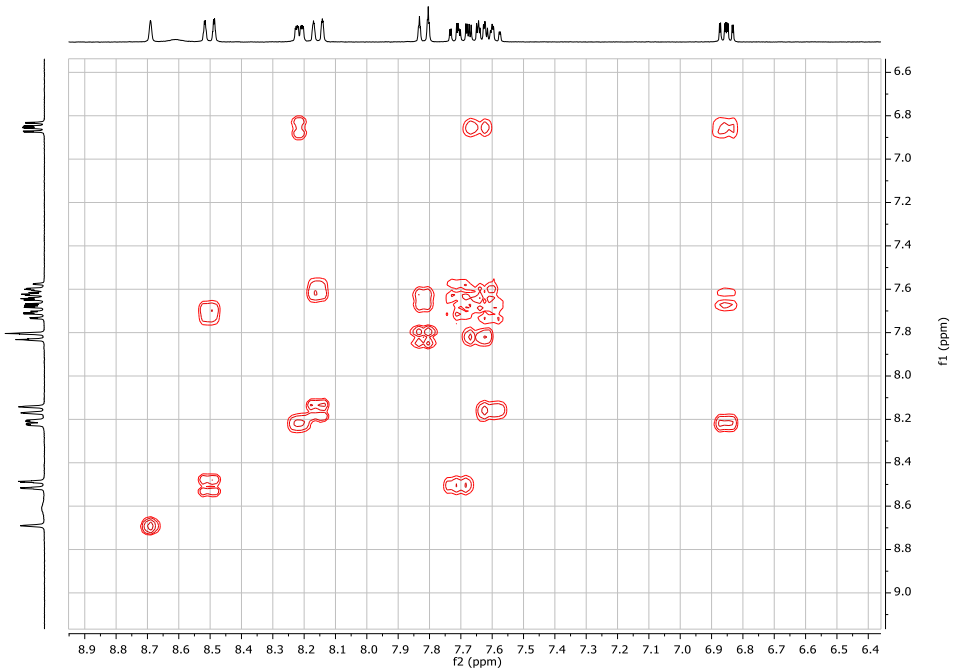

Figure S3.2. COSY-NMR spectrum of ligand **L3.1**.

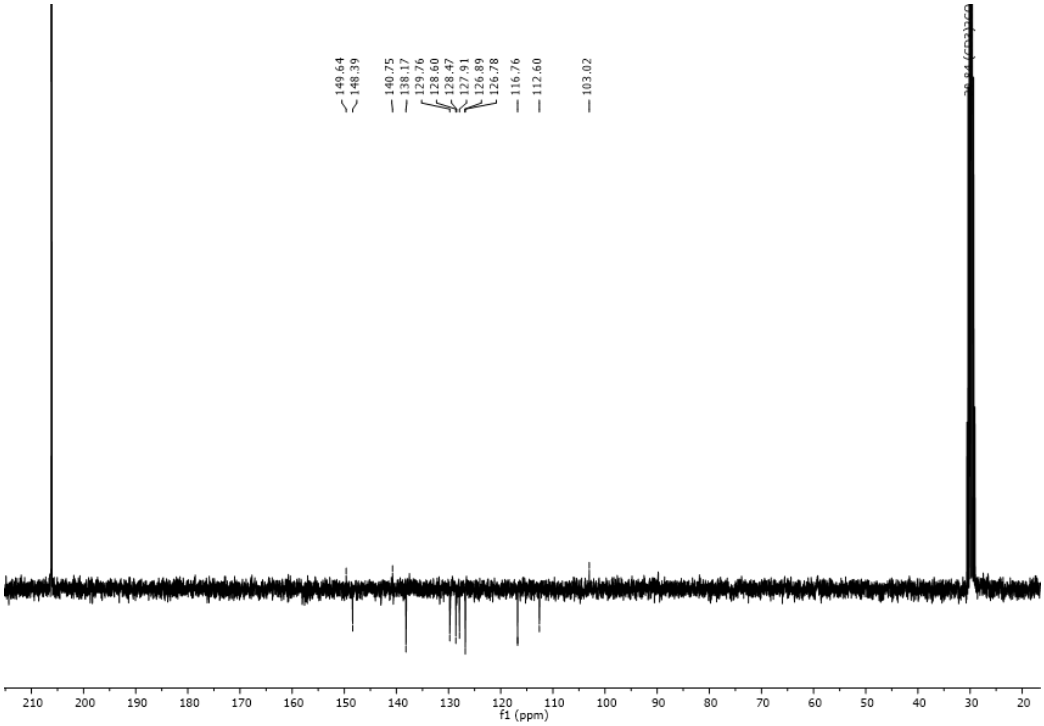

Figure S3.3. APT-NMR spectrum of ligand **L3.1**.

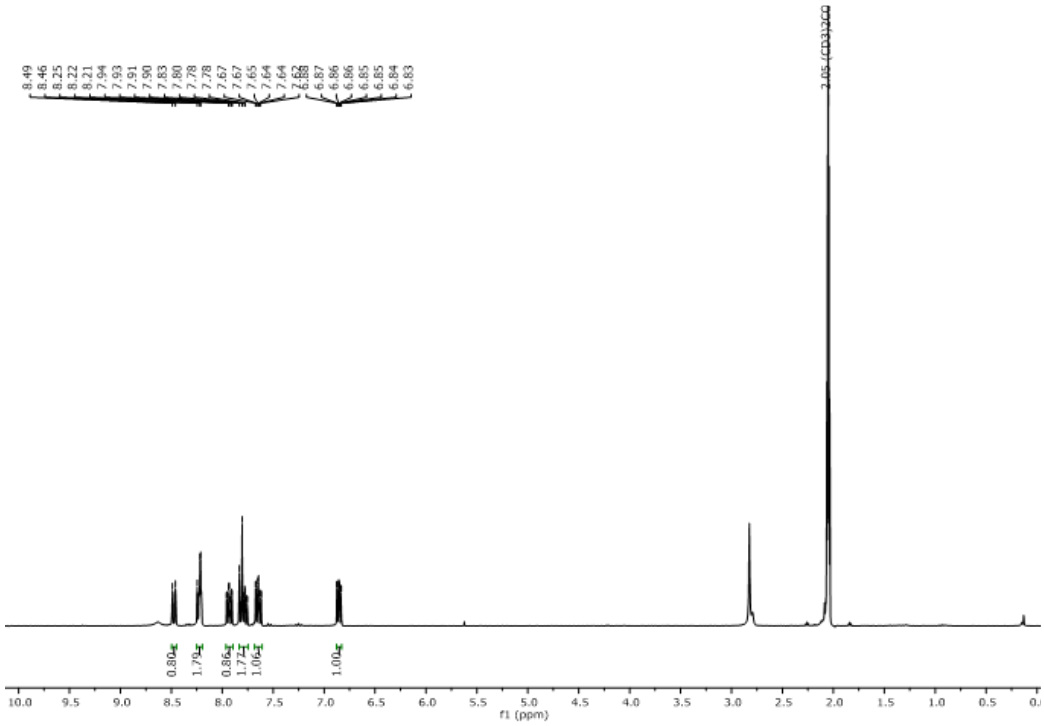

Figure S3.4. [1]H-NMR spectrum of ligand **L3.2**.

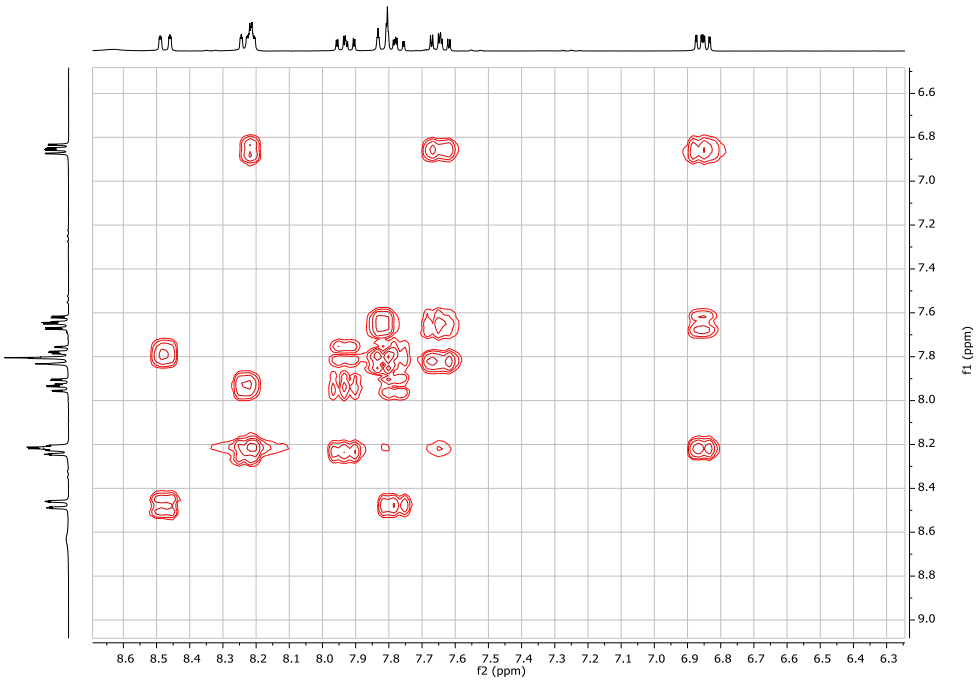

Figure S3.5. COSY-NMR spectrum of ligand **L3.2**.

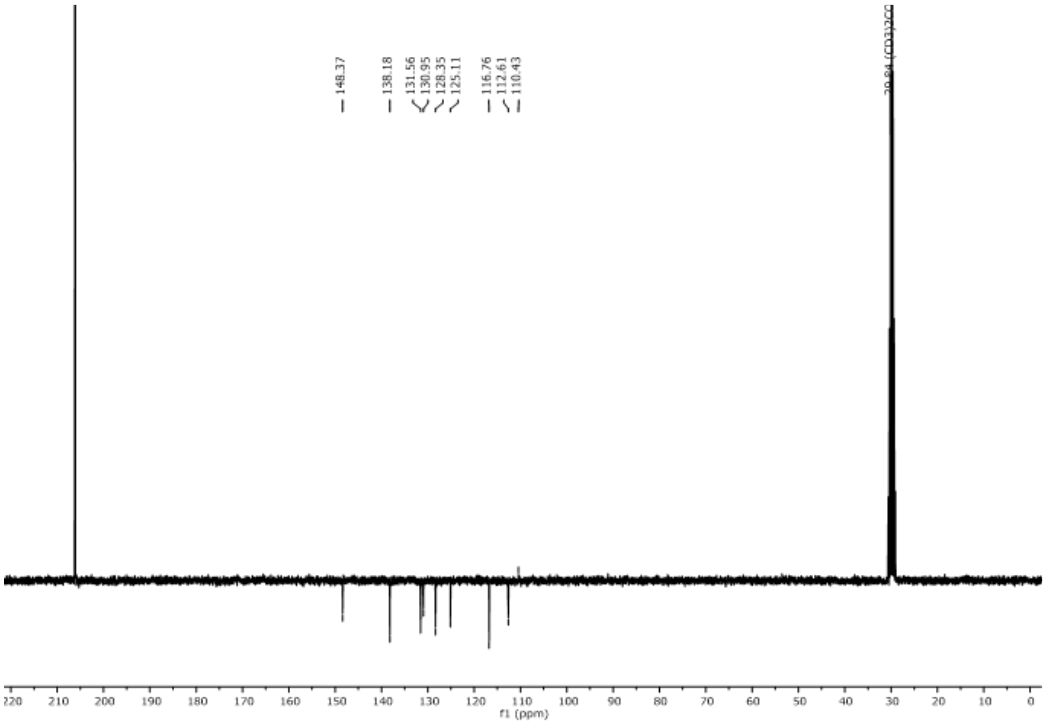

Figure S3.6. APT-NMR spectrum of ligand **L3.2**.

NMR spectra of complexes 3.1-3.4

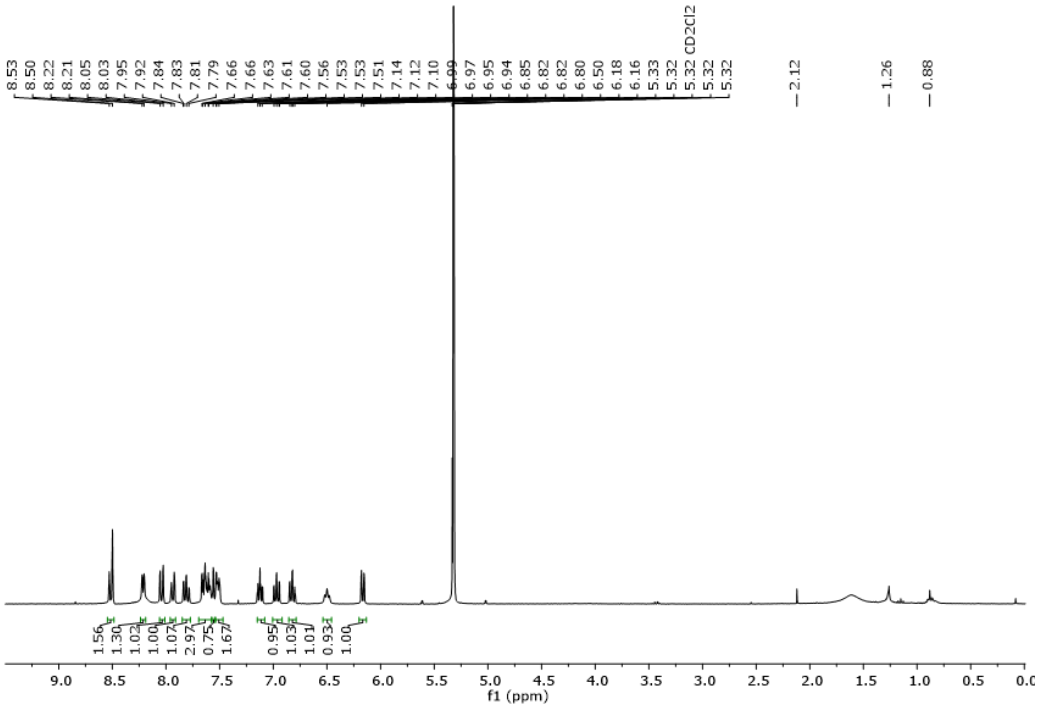

Figure S3.7. ^{1}H-NMR spectrum of complex **3.1**.

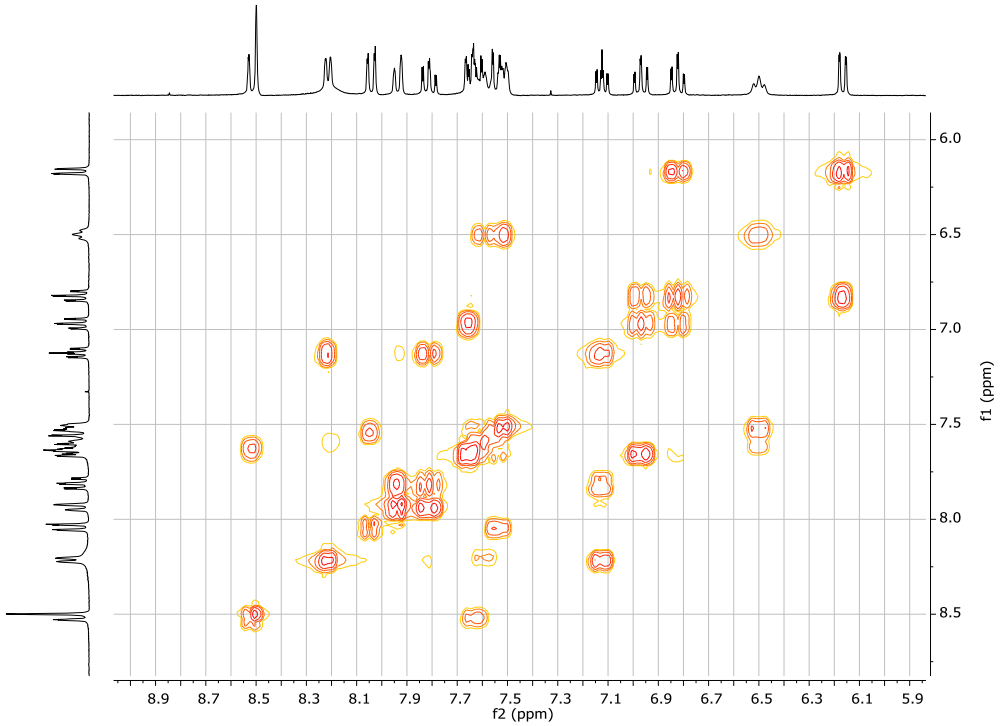

Figure S3.8. COSY-NMR spectrum of complex **3.1**.

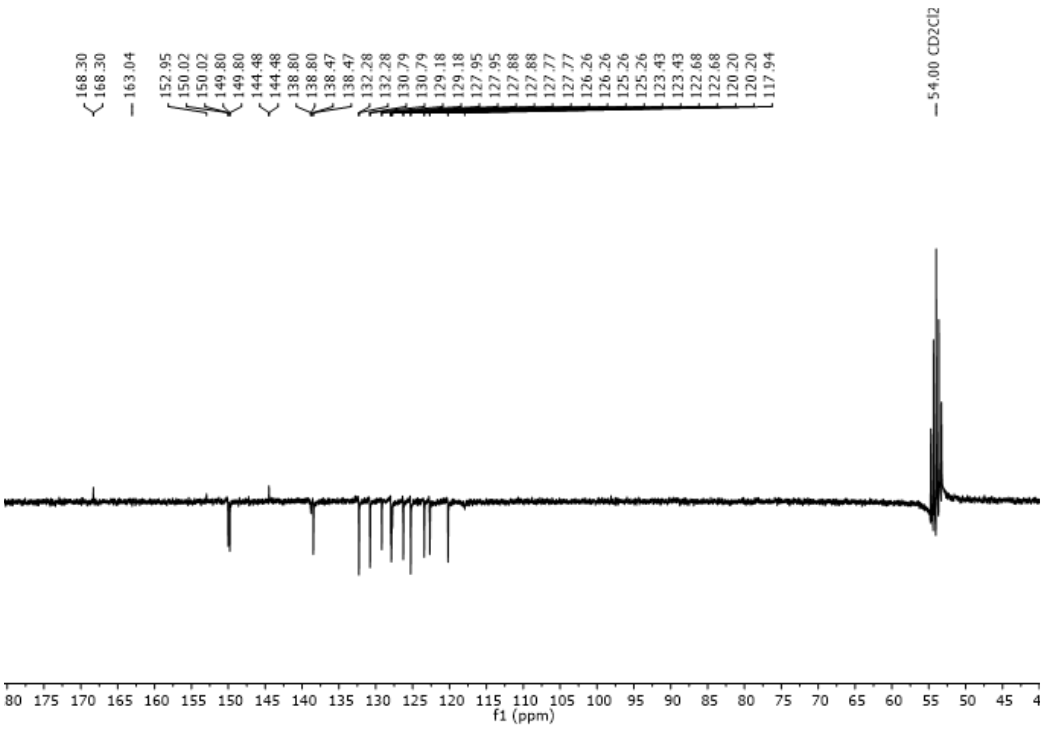

Figure S3.9. APT-NMR spectrum of complex **3.1**.

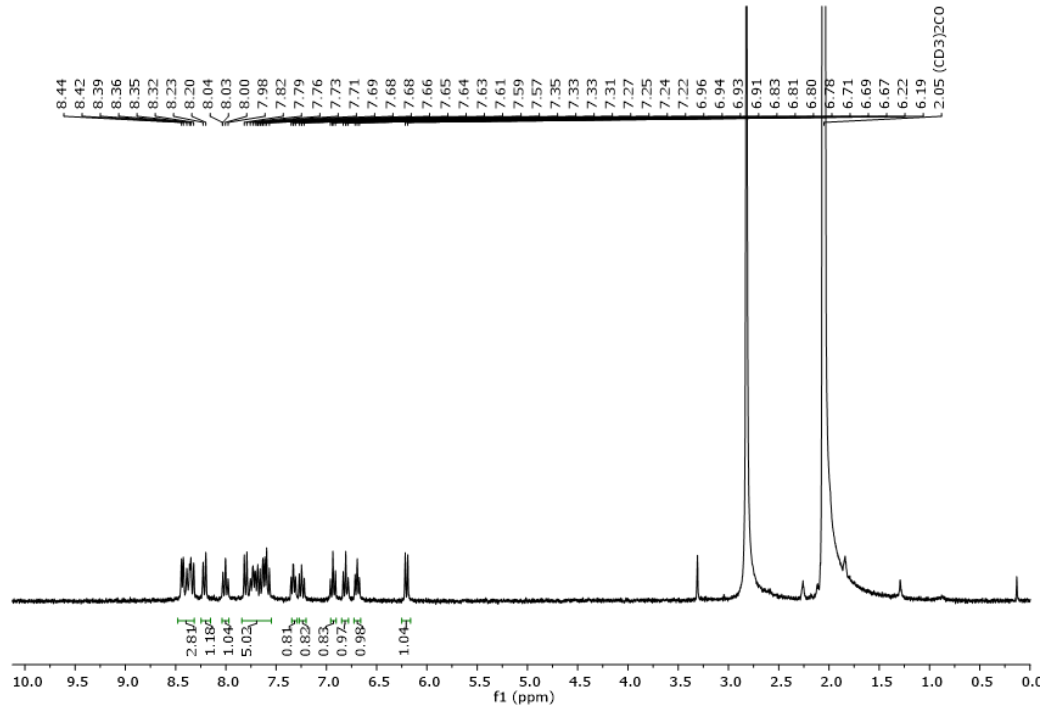

Figure S3.10. ^{1}H-NMR spectrum of complex **3.2**.

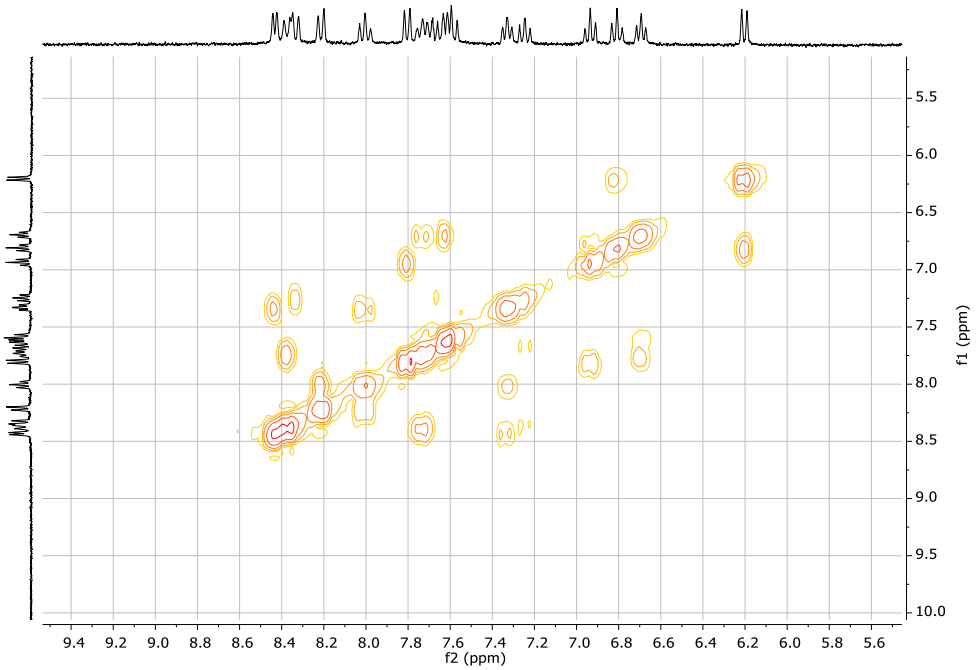

Figure S3.11. COSY-NMR spectrum of complex **3.2**.

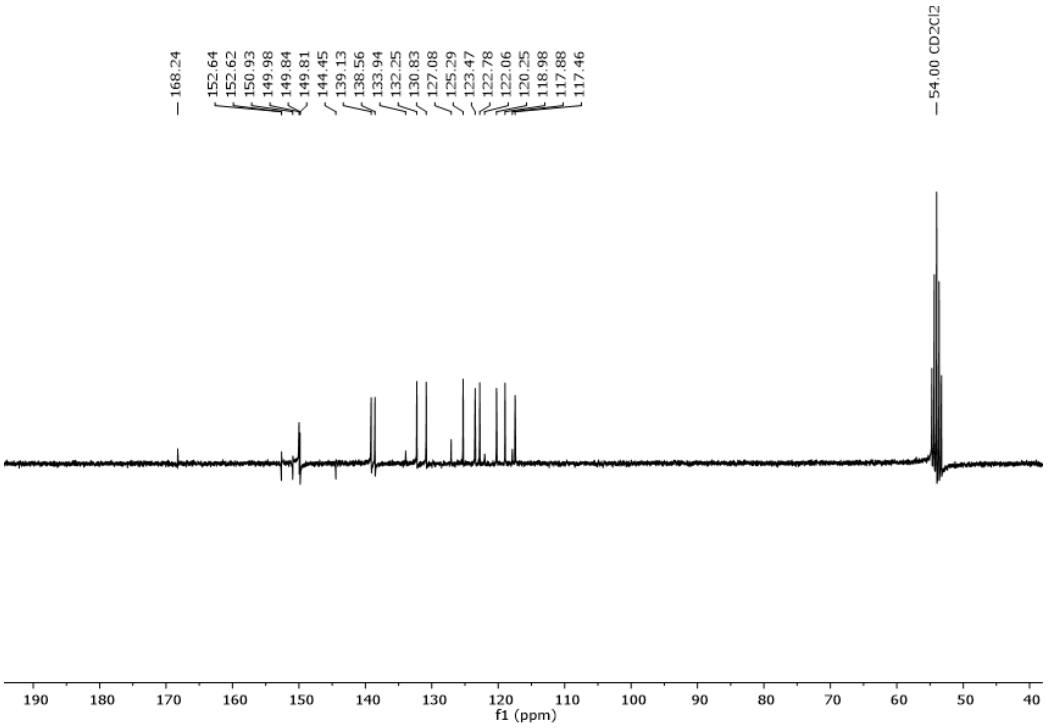

Figure S3.12. APT-NMR spectrum of complex **3.2**.

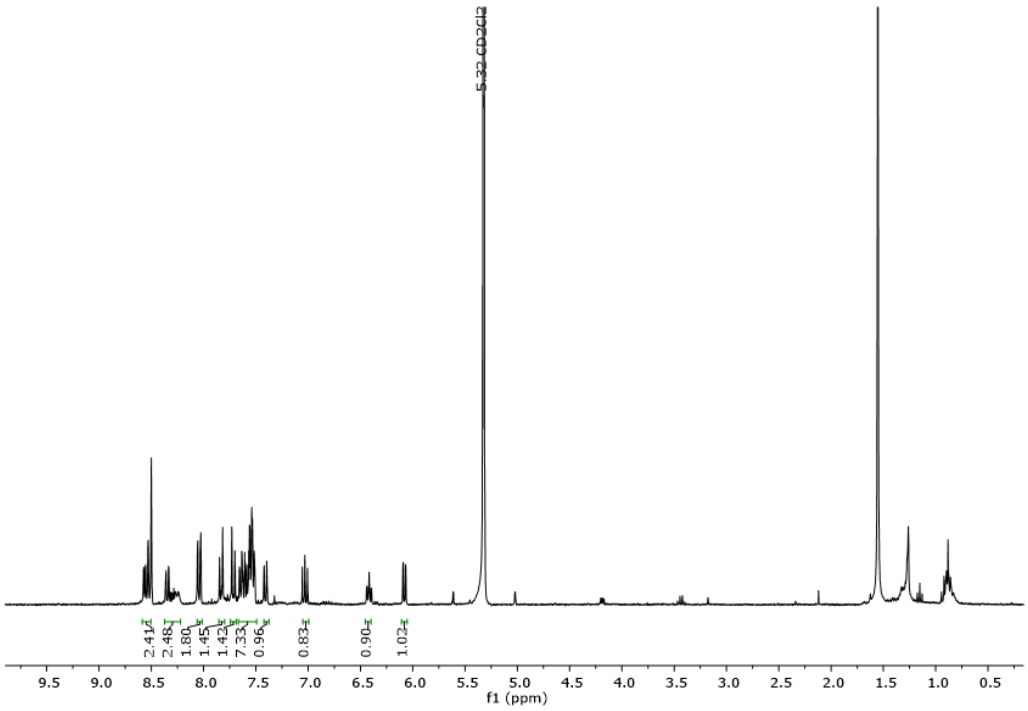

Figure S3.13. ^{1}H-NMR spectrum of complex **3.3**.

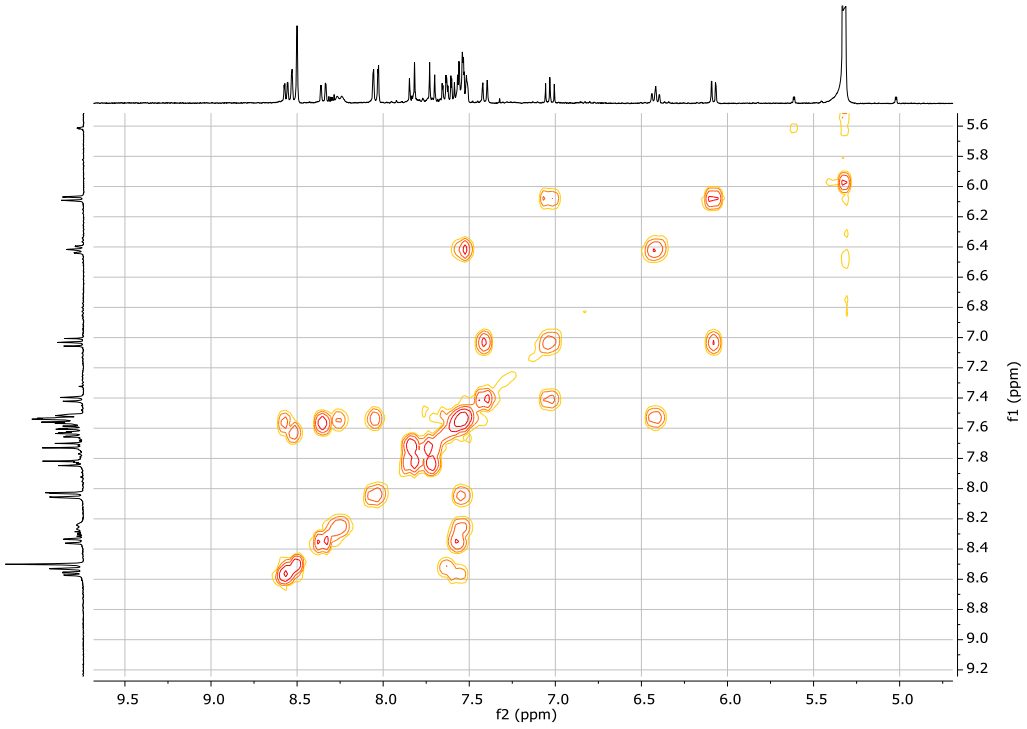

Figure S3.14. COSY-NMR spectrum of complex **3.3**.

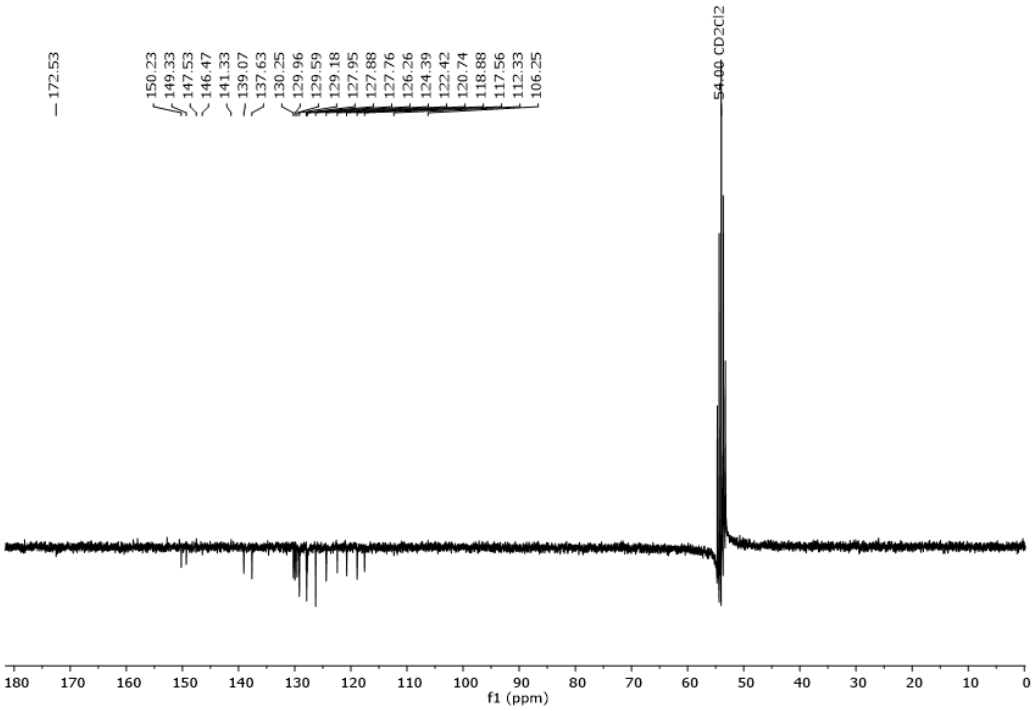

Figure S3.15. APT-NMR spectrum of complex **3.3**.

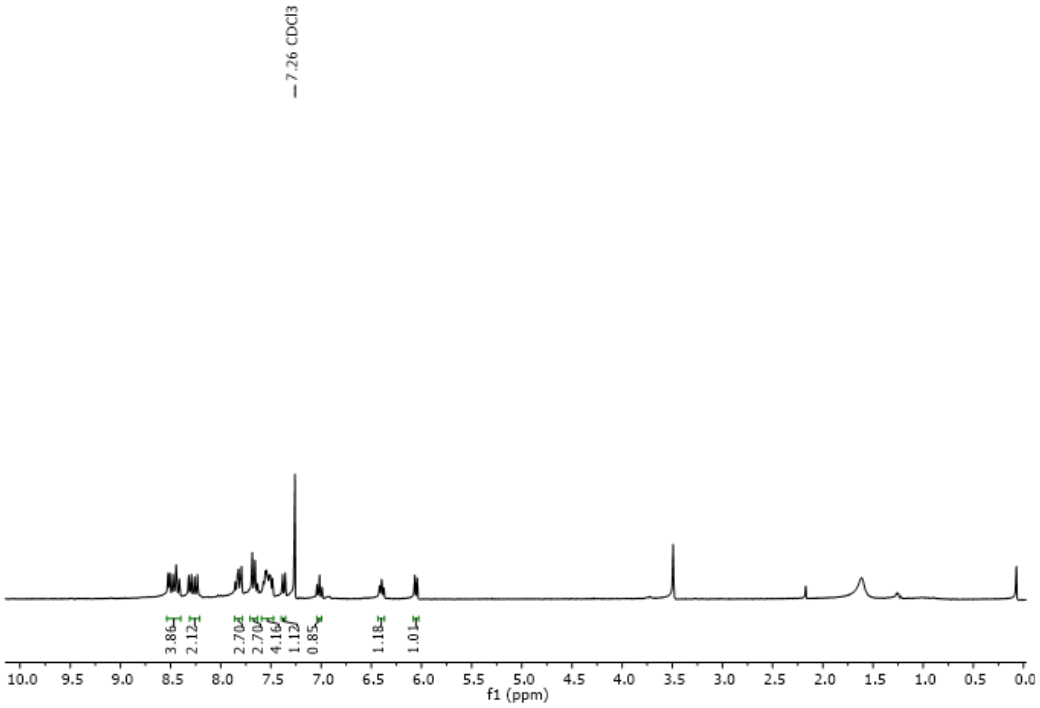

Figure S3.16. ^{1}H-NMR spectrum of complex **3.4**.

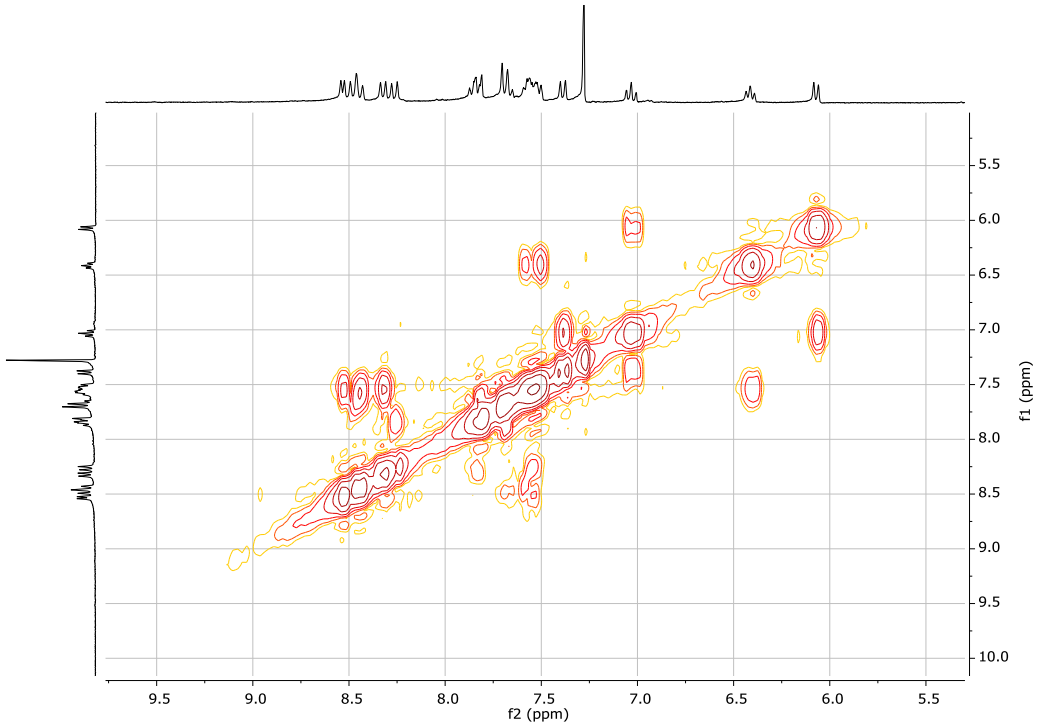

Figure S3.17. COSY-NMR spectrum of complex **3.4**.

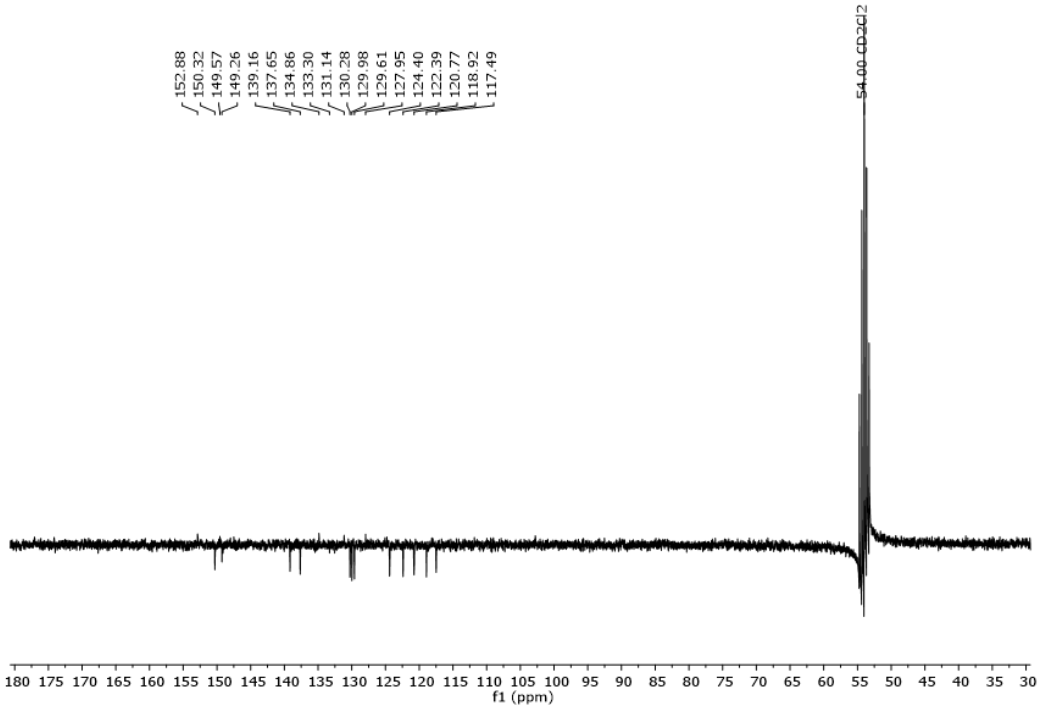

Figure S3.18. APT-NMR spectrum of complex **3.4**.

Mass spectra of L3.2 and complexes 3.2 and 3.4

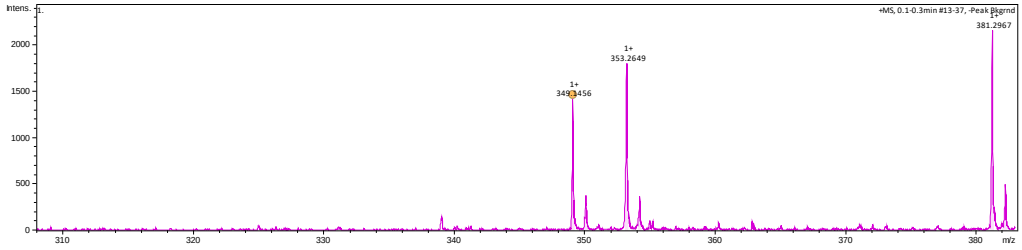

Figure S3.19. ESI-HRMS spectrum of ligand **L3.2**.

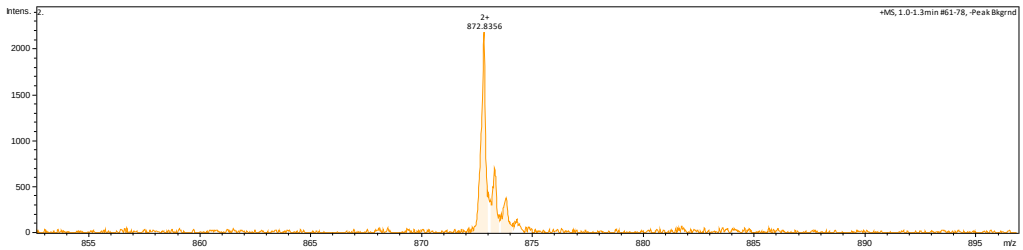

Figure S3.20. ESI-HRMS spectrum of complex **3.2**.

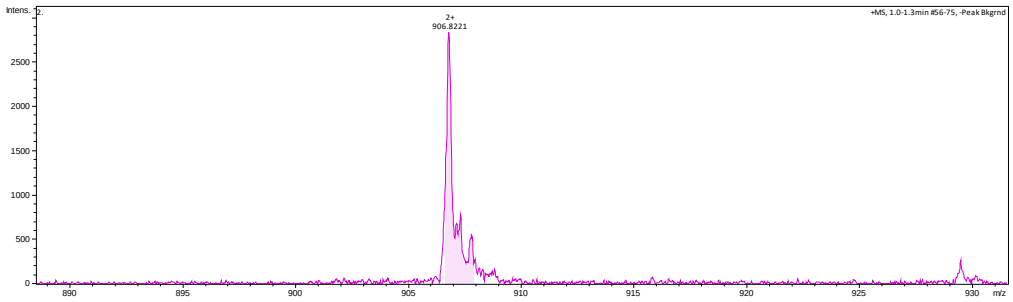

Figure S3.21. ESI-HRMS spectrum of complex **3.4**.

Emission spectra of complexes 3.1-3.4 at different excitation wavelengths

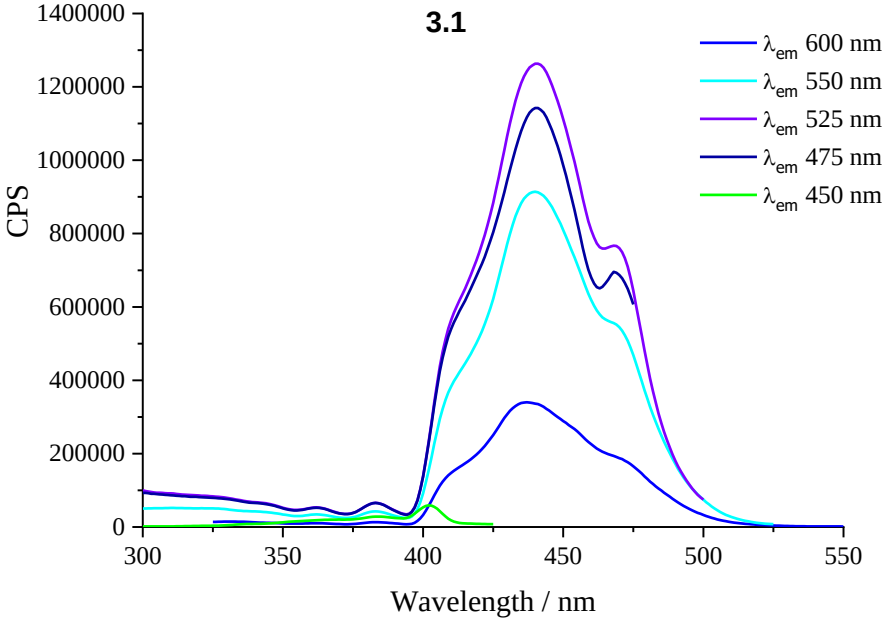

Figure S3.22. Emission-spectra of **3.1** measured in DMSO solution.

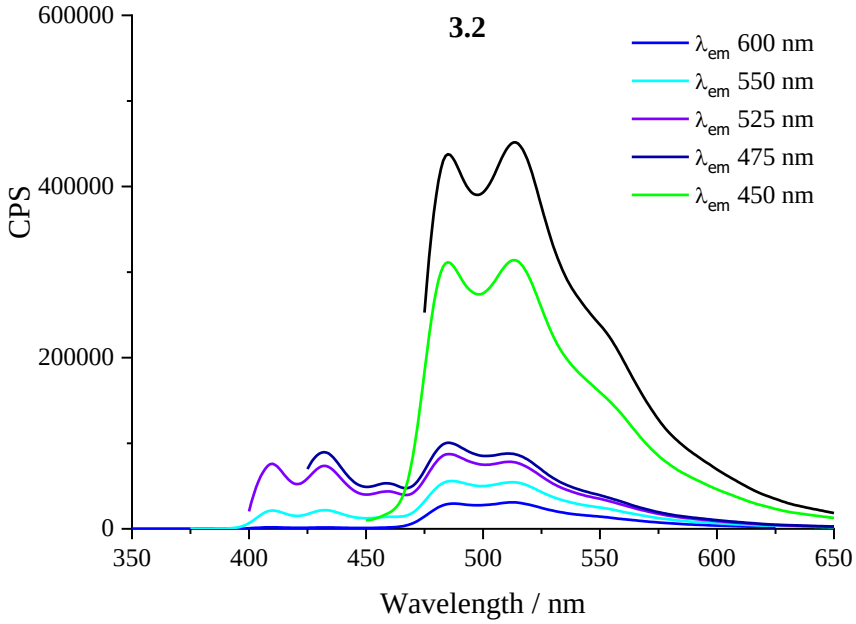

Figure S3.23. Emission-spectra of **3.2** measured in DMSO solution.

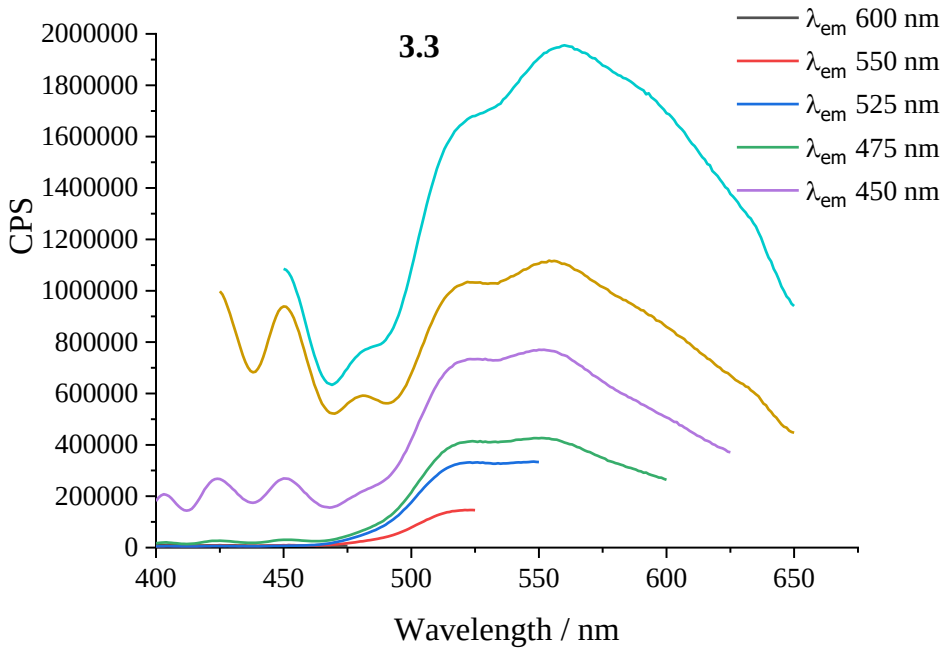

Figure S3.24. Emission-spectra of **3.3** measured in DMSO solution.

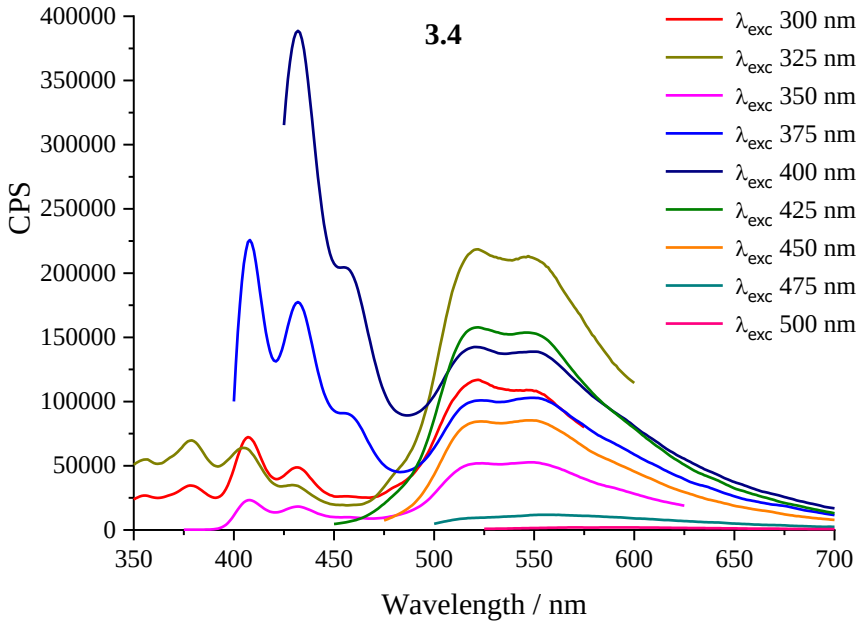

Figure S3.25. Emission-spectra of **3.4** measured in DMSO solution.

Singlet oxygen production of complex 3.4

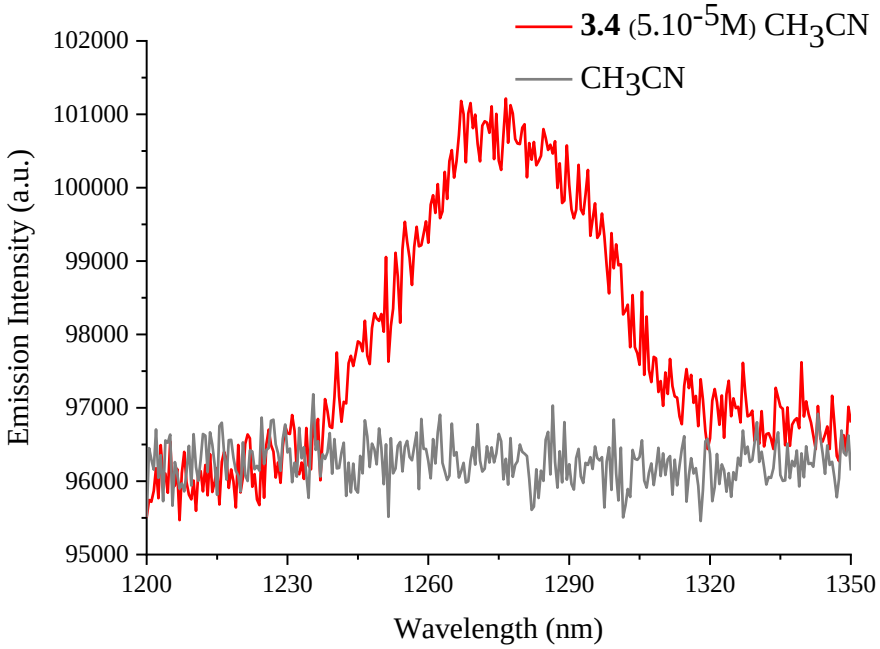

Figure S3.26. Singlet oxygen production of complex **3.4** measured in CH_3CN solution.

Chapter 4

NMR spectra of complexes 4.1-4.8

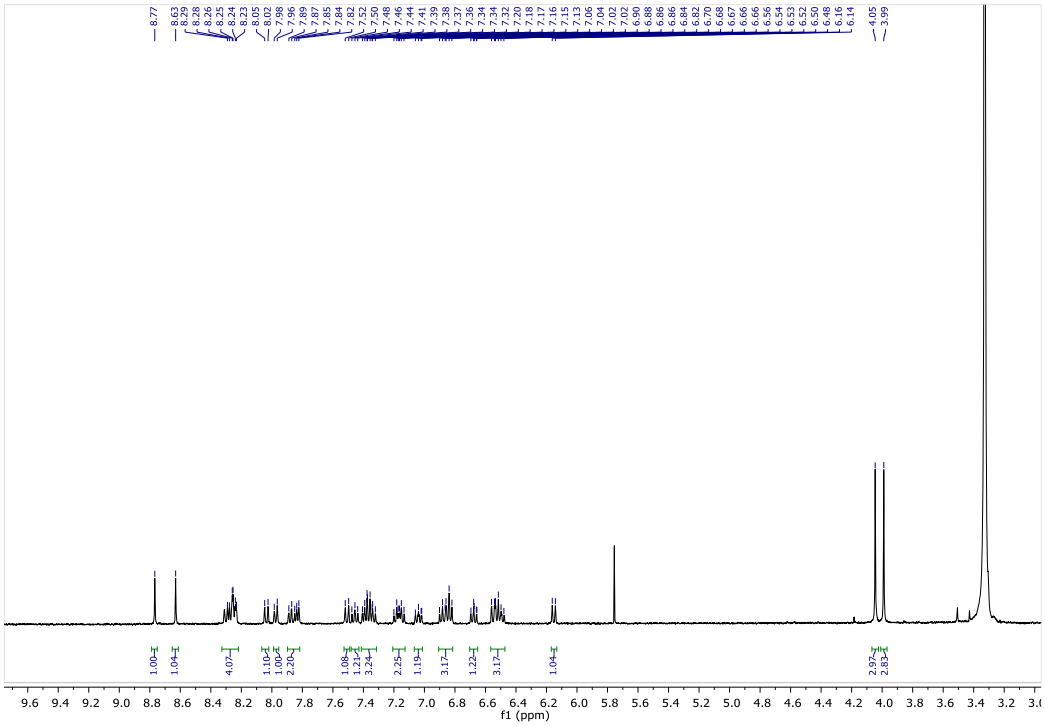

Figure S4.1. ^{1}H-NMR spectrum of complex **4.1**.

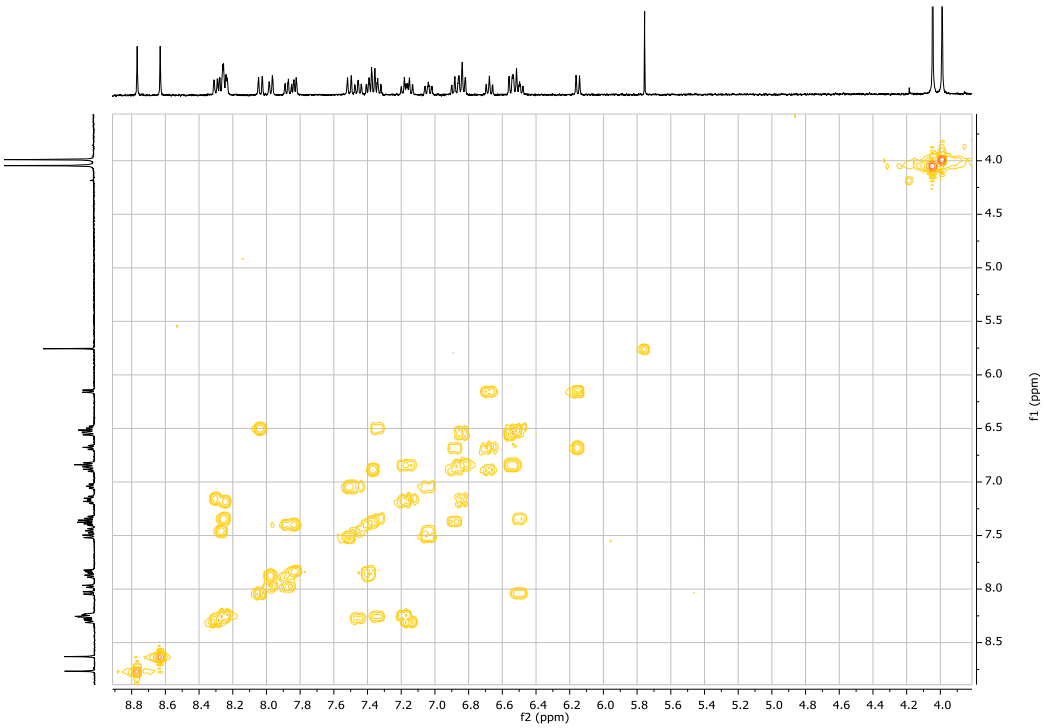

Figure S4.2. COSY-NMR spectrum of complex **4.1**.

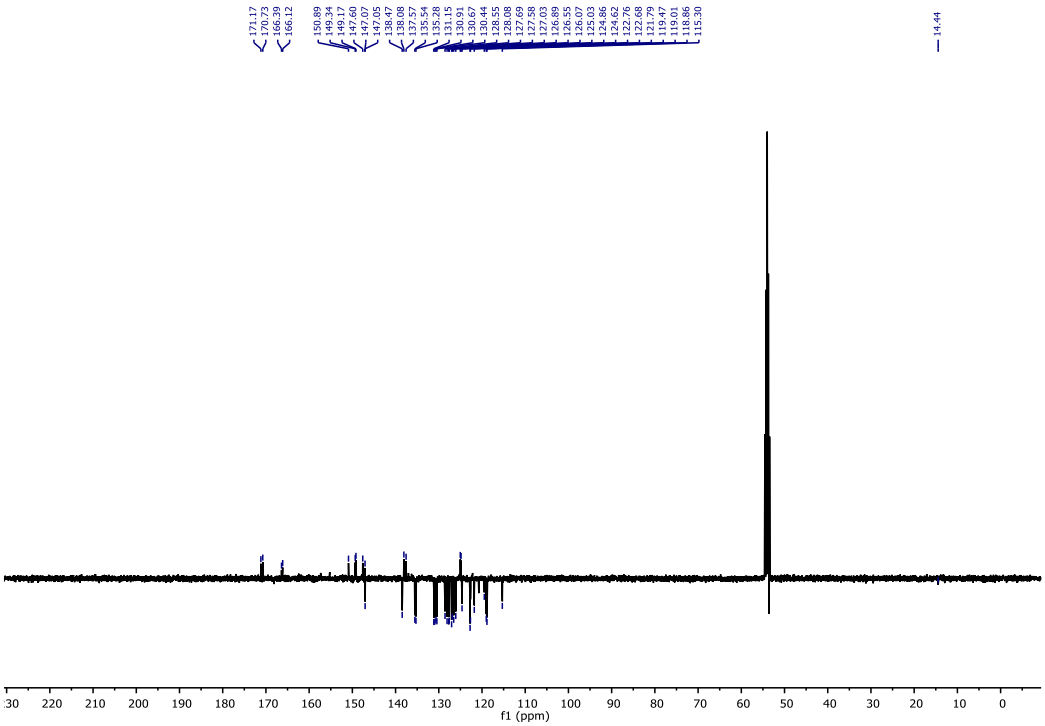

Figure S4.3. APT-NMR spectrum of complex **4.1**.

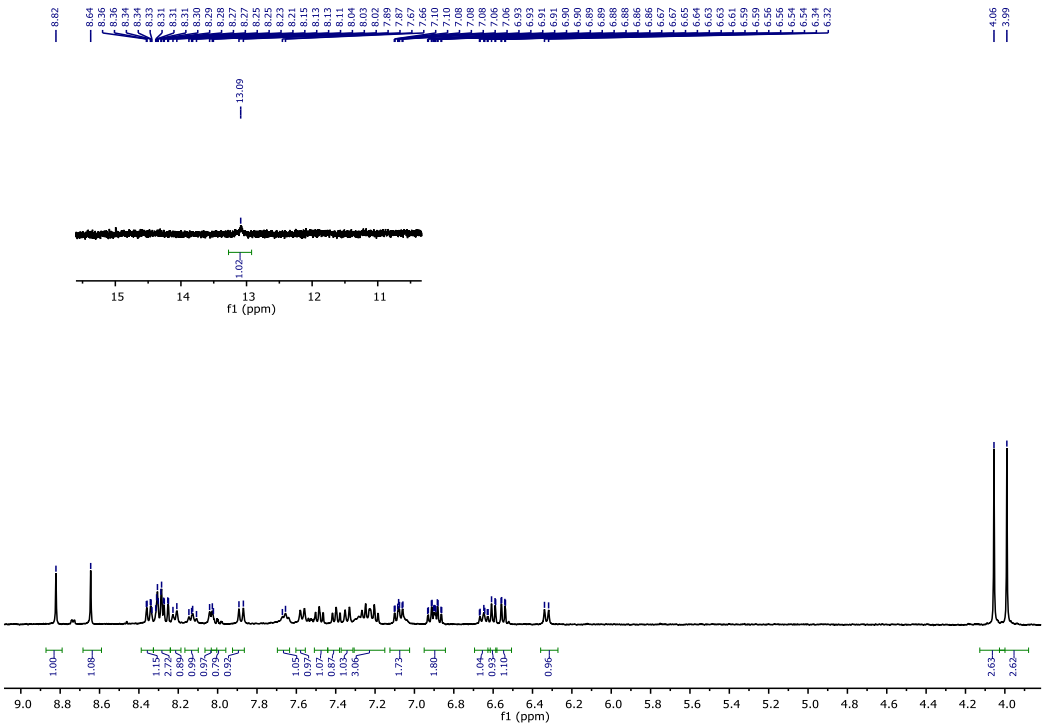

Figure S4.4. ^{1}H-NMR spectrum of complex **4.2**.

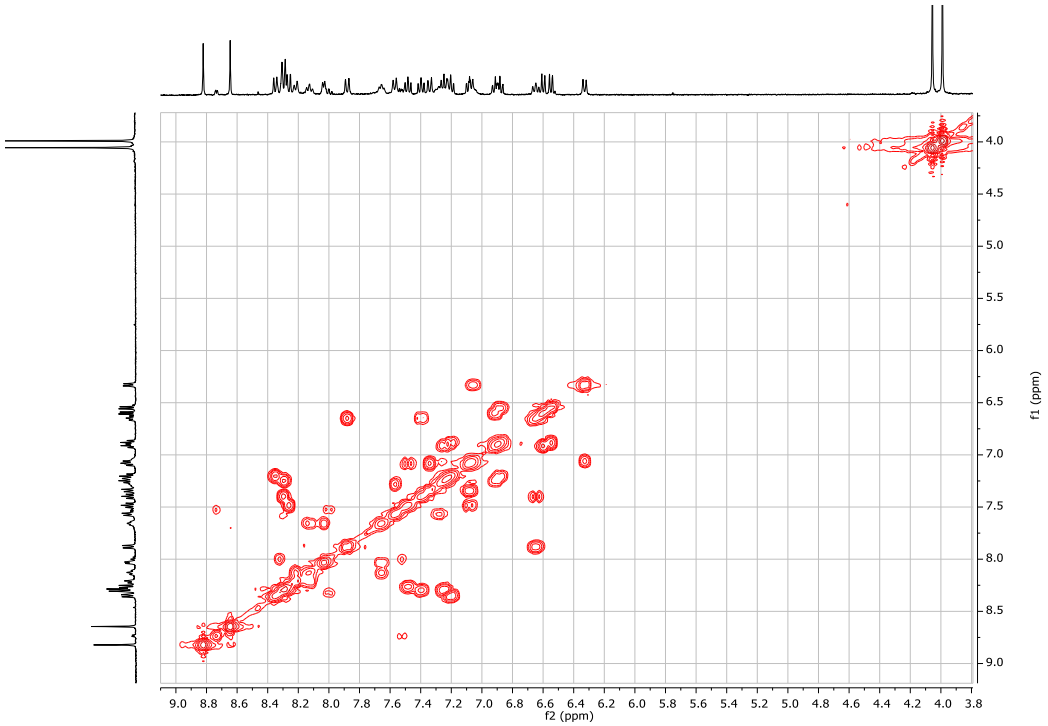

Figure S4.5. COSY-NMR spectrum of complex **4.2**.

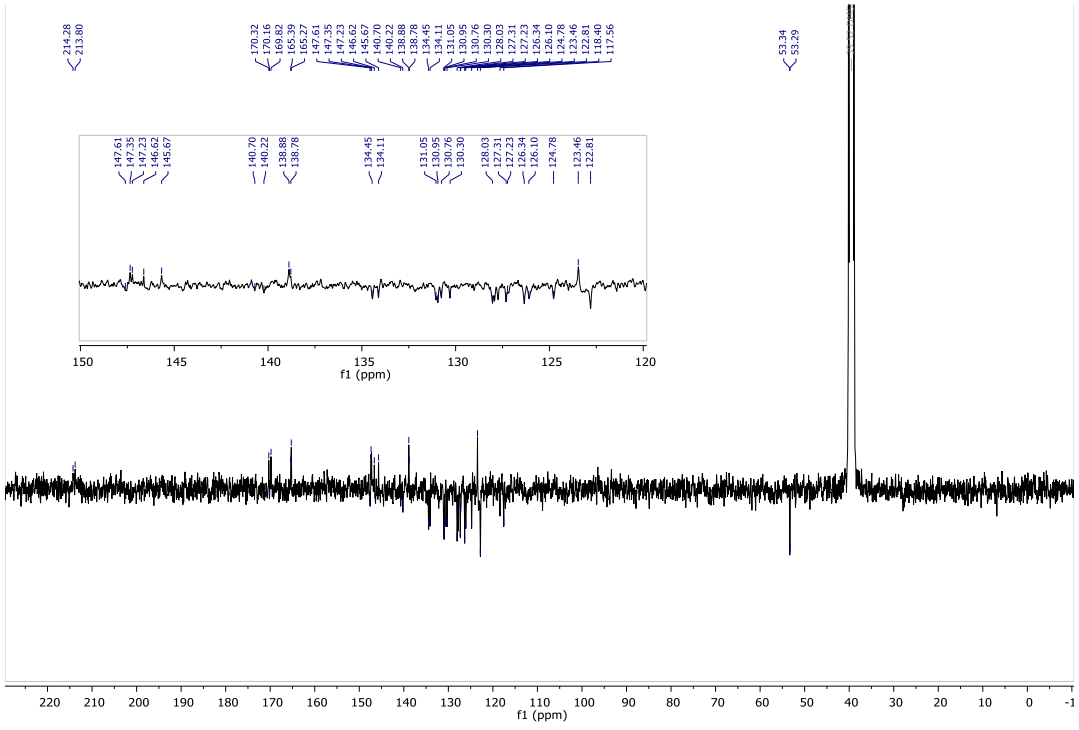

Figure S4.6. APT-NMR spectrum of complex **4.2**.

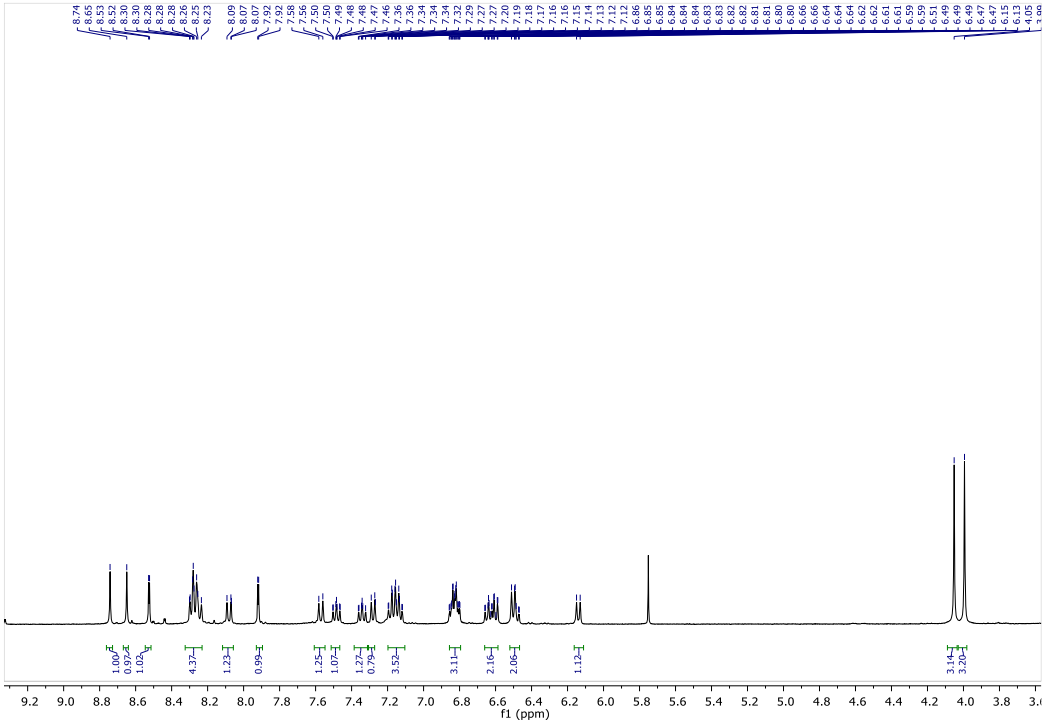

Figure S4.7. ^{1}H-NMR spectrum of complex **4.3**.

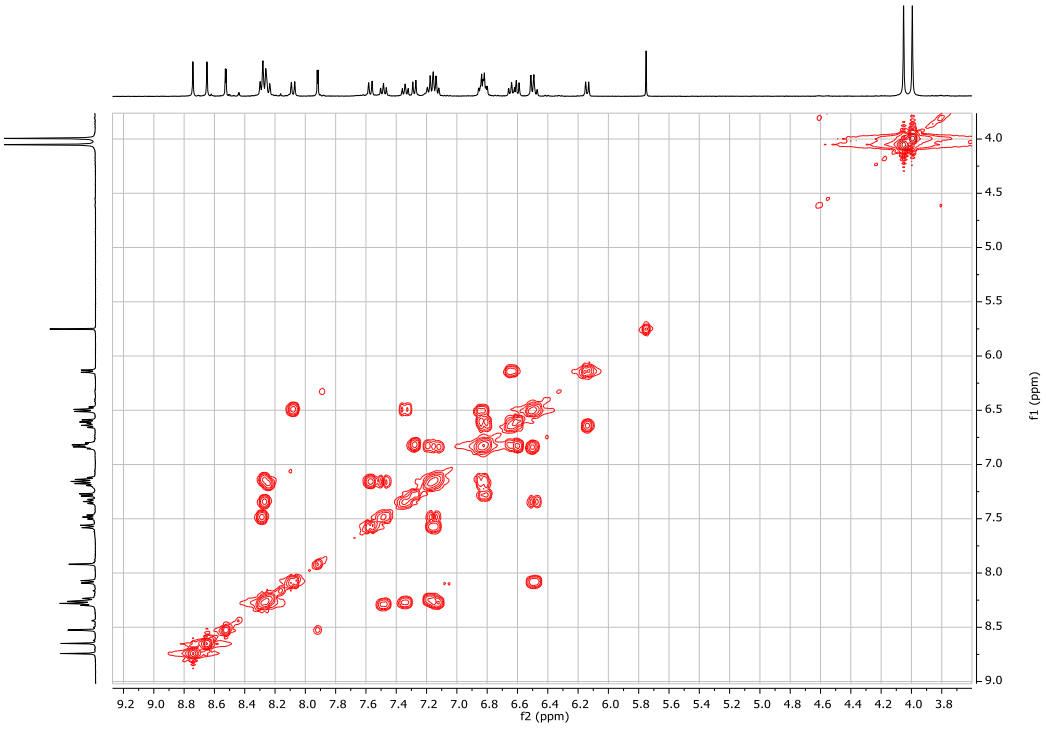

Figure S4.8. COSY-NMR spectrum of complex **4.3**.

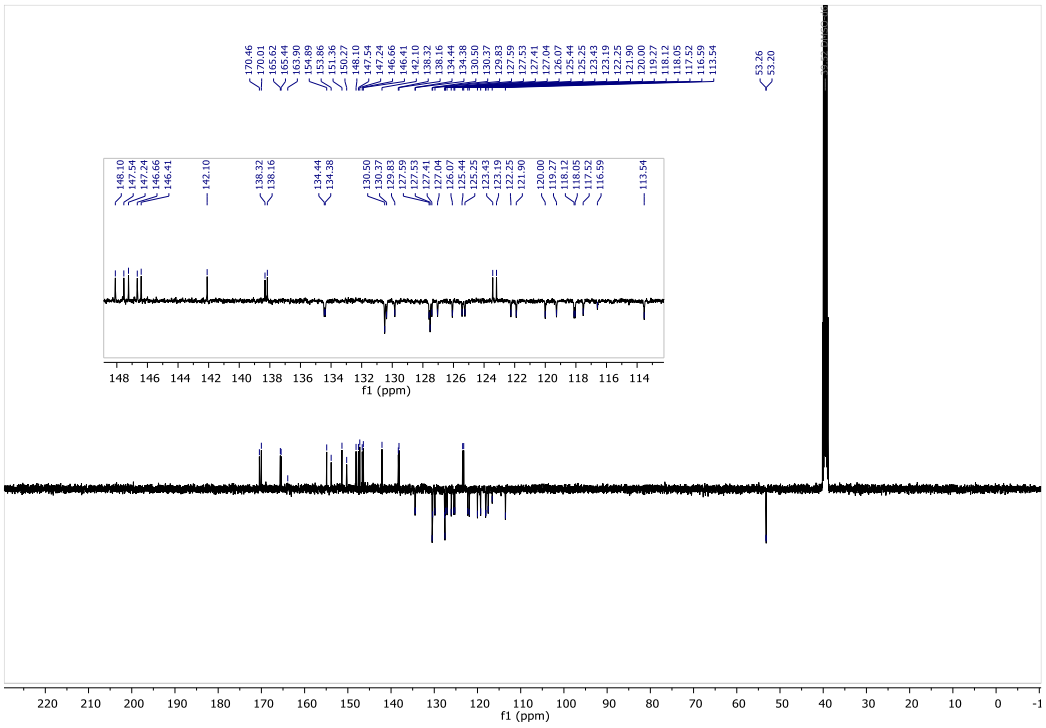

Figure S4.9. APT-NMR spectrum of complex **4.3**.

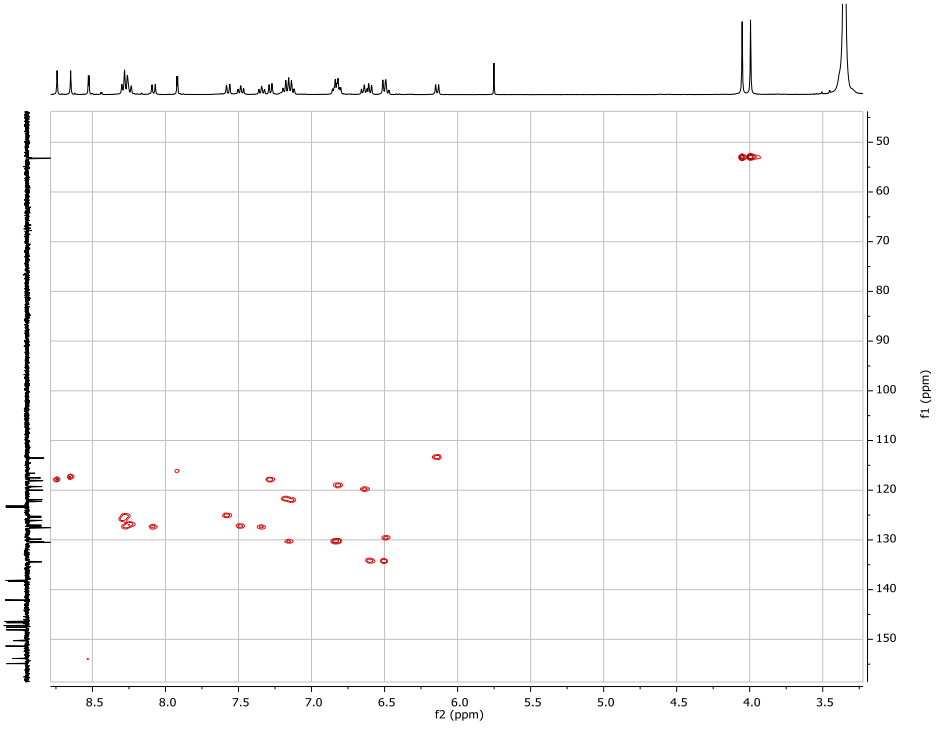

Figure S4.10. HSQC spectrum of complex **4.3**.

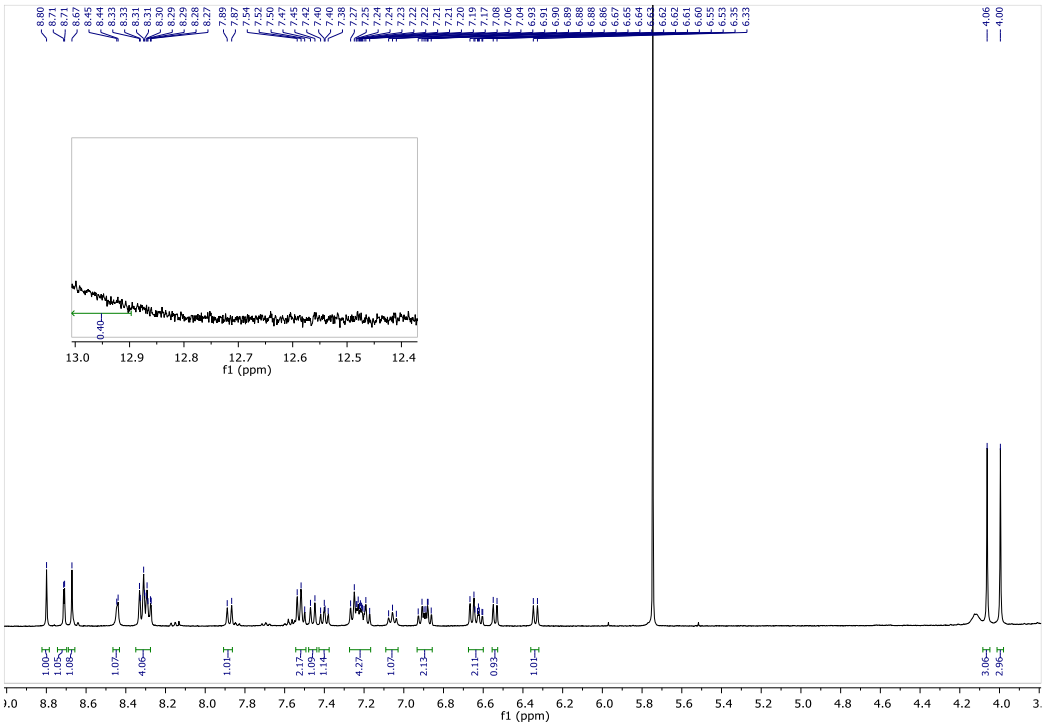

Figure S4.11. ^{1}H-NMR spectrum of complex **4.4**.

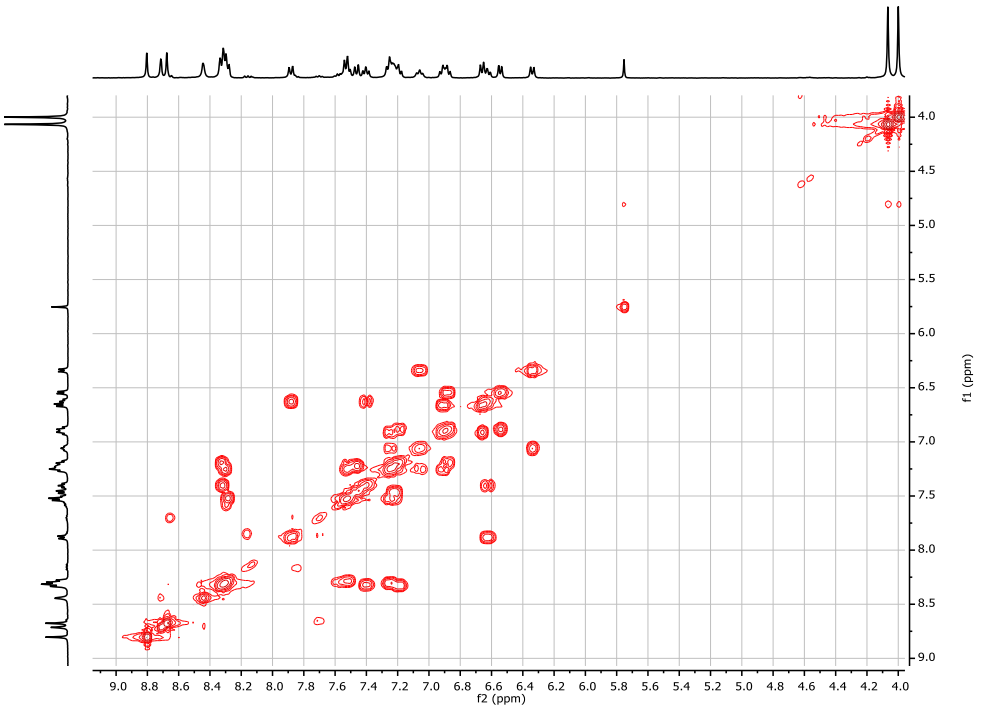

Figure S4.12. COSY-NMR spectrum of complex **4.4**.

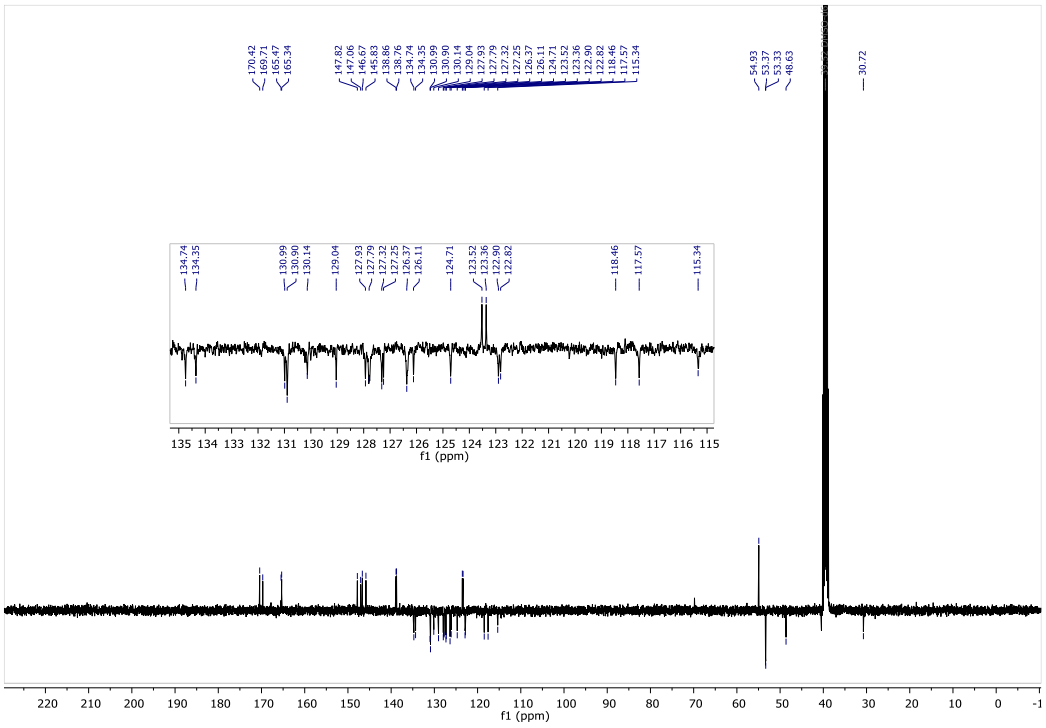

Figure S4.13. APT-NMR spectrum of complex **4.4**.

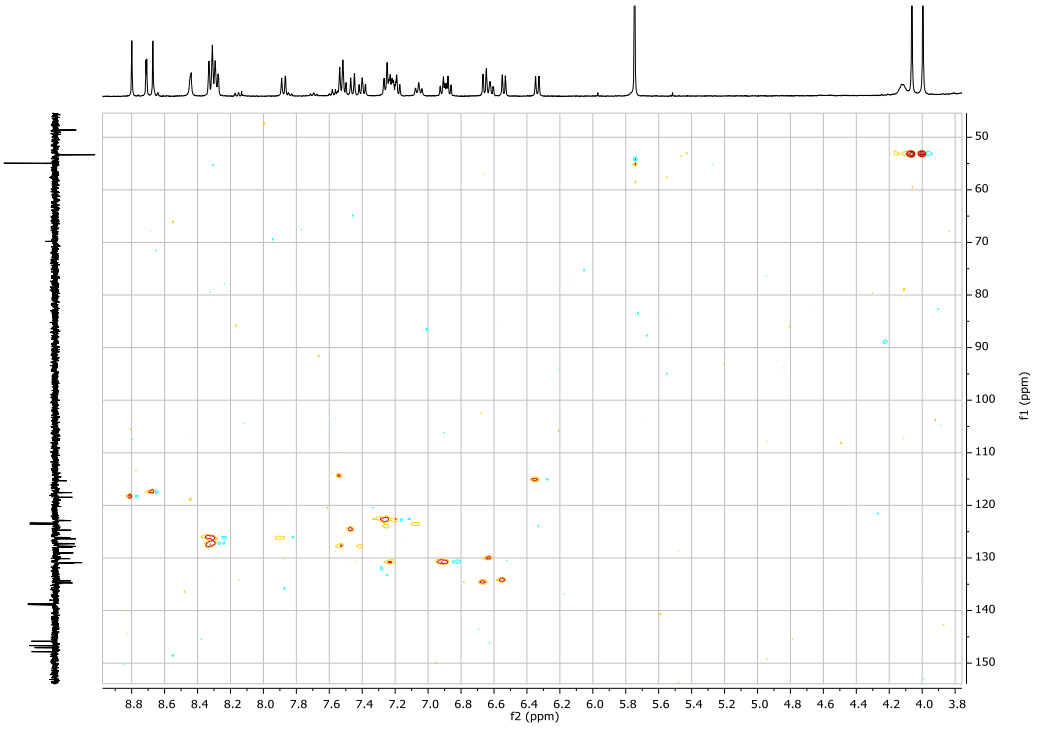

Figure S4.14. HSQC spectrum of complex **4.4**.

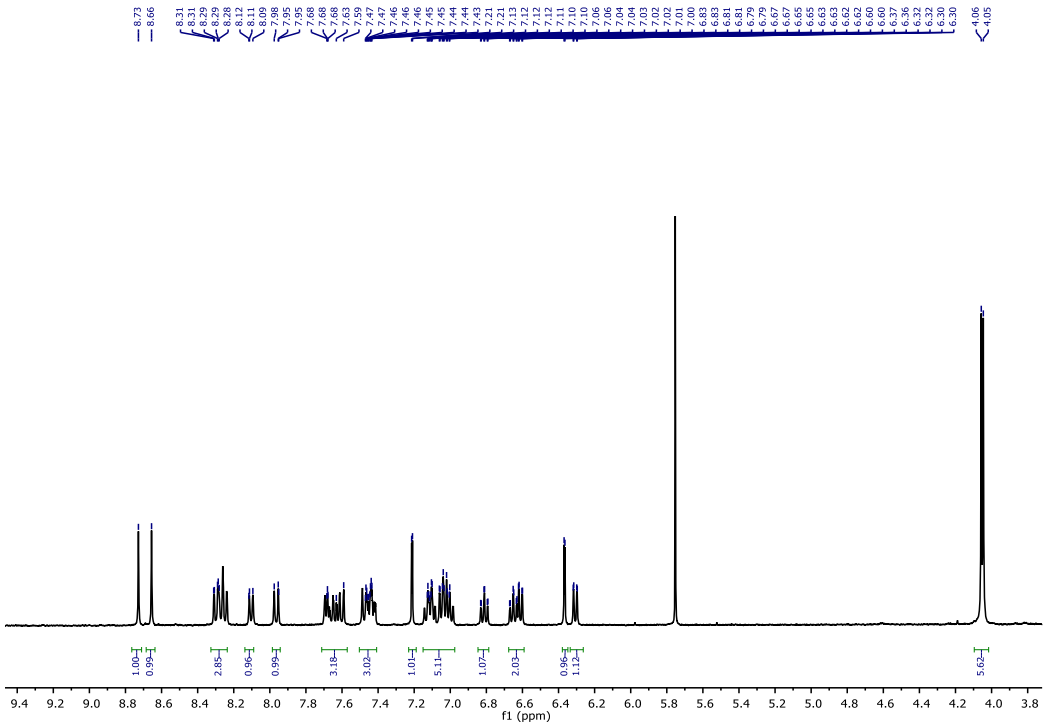

Figure S4.15. ^{1}H-NMR spectrum of complex **4.5**.

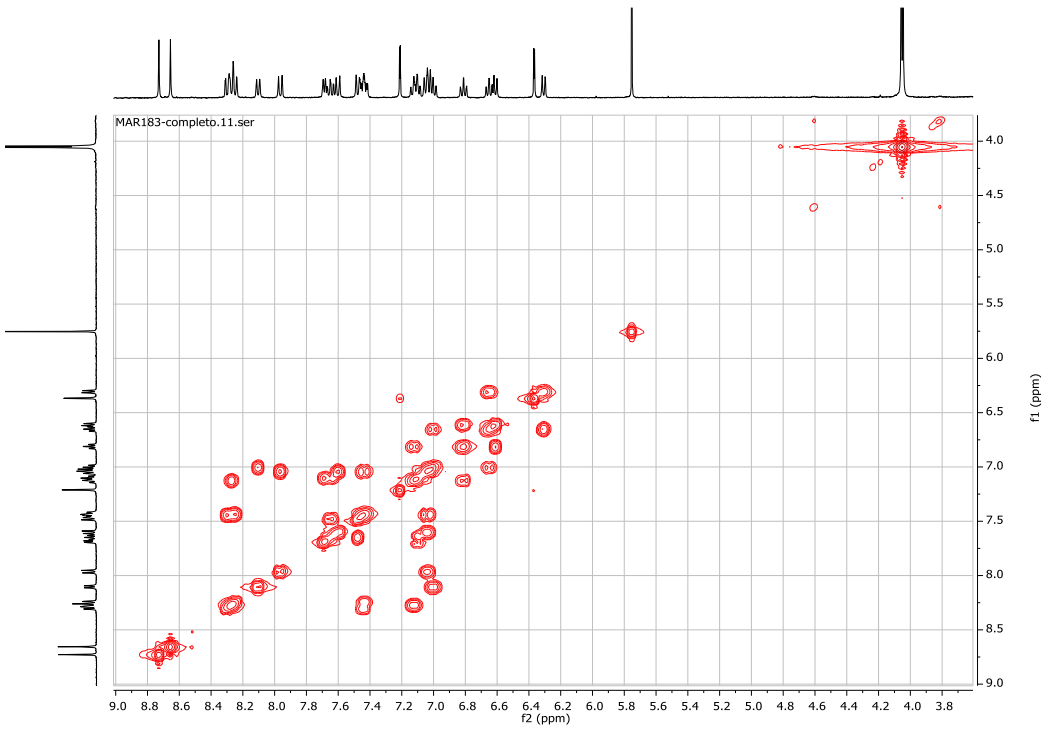

Figure S4.16. COSY-NMR spectrum of complex **4.5**.

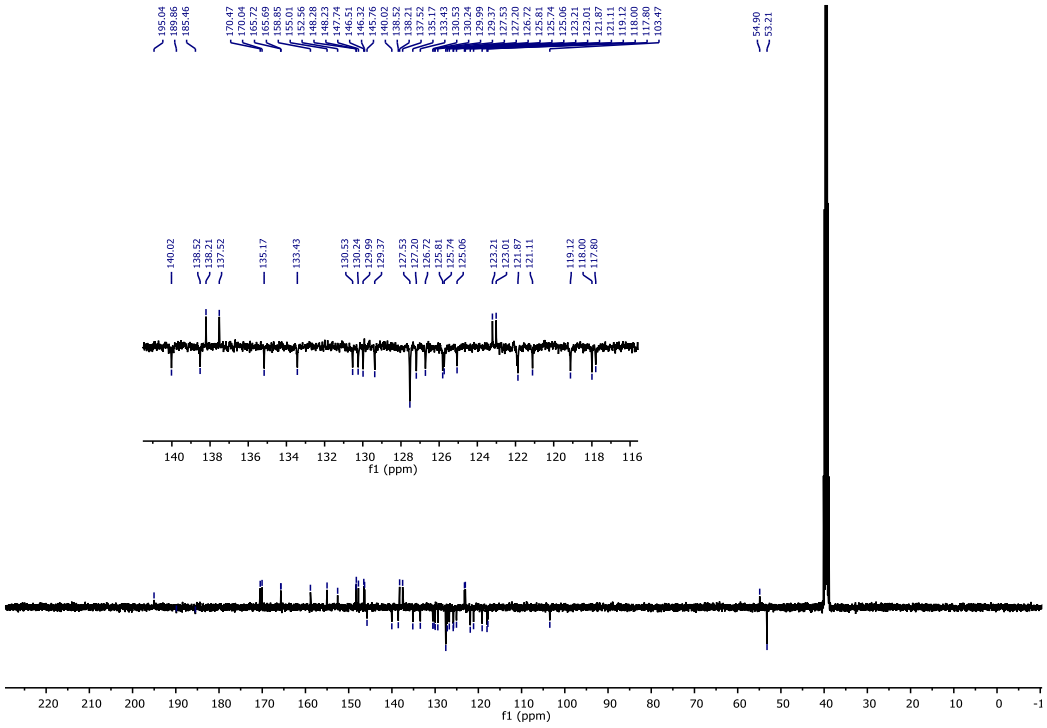

Figure S4.17. APT-NMR spectrum of complex **4.5**.

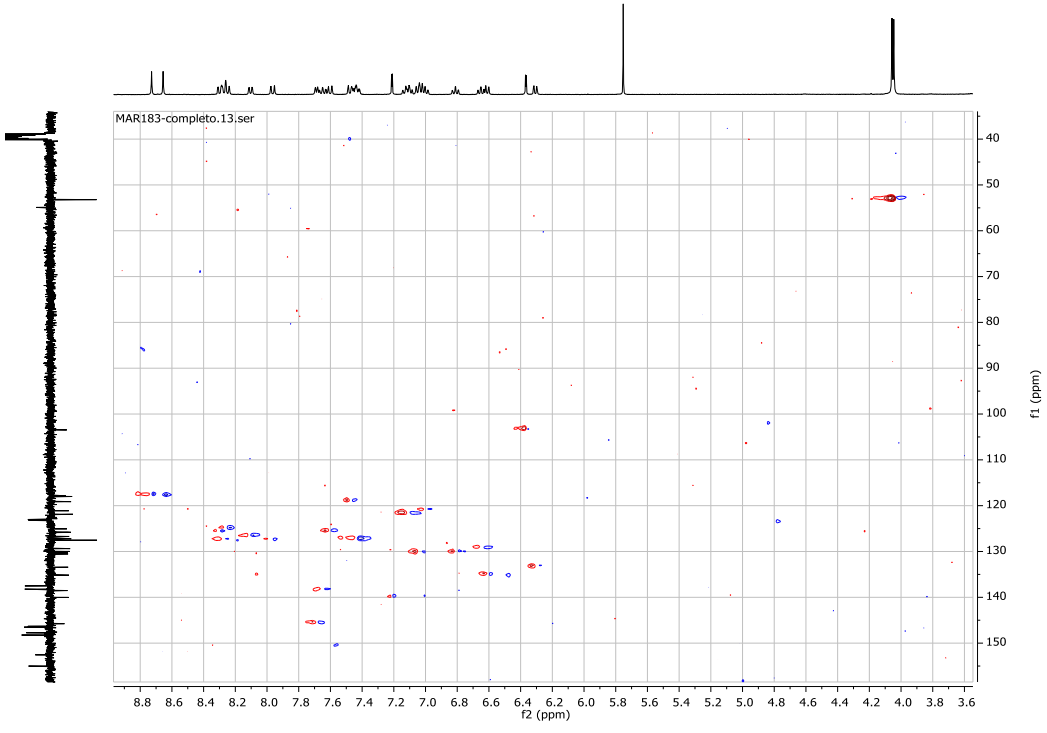

Figure S4.18. HSQC spectrum of complex **4.5**.

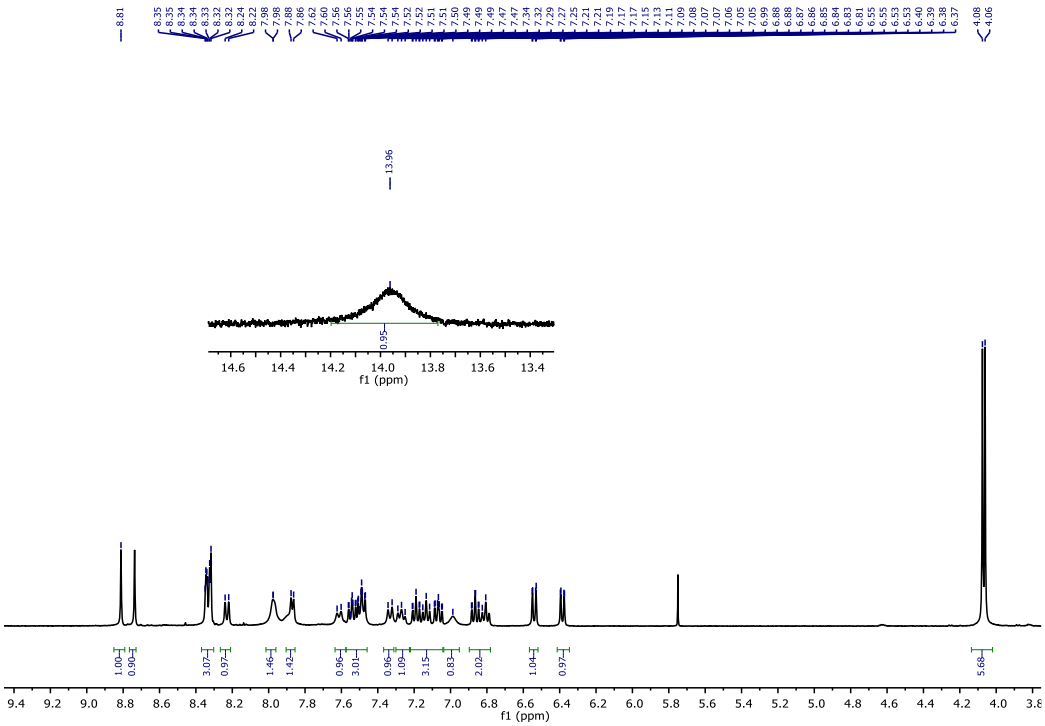

Figure S4.19. [1]H-NMR spectrum of complex **4.6**.

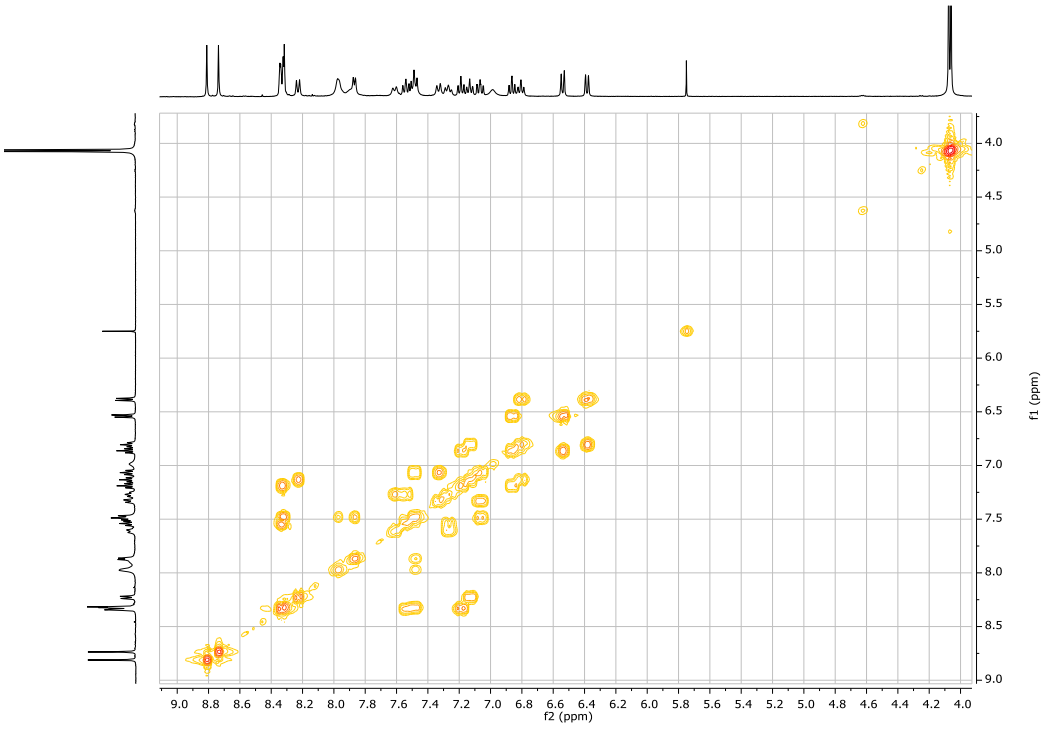

Figure S4.20. COSY-NMR spectrum of complex **4.6**.

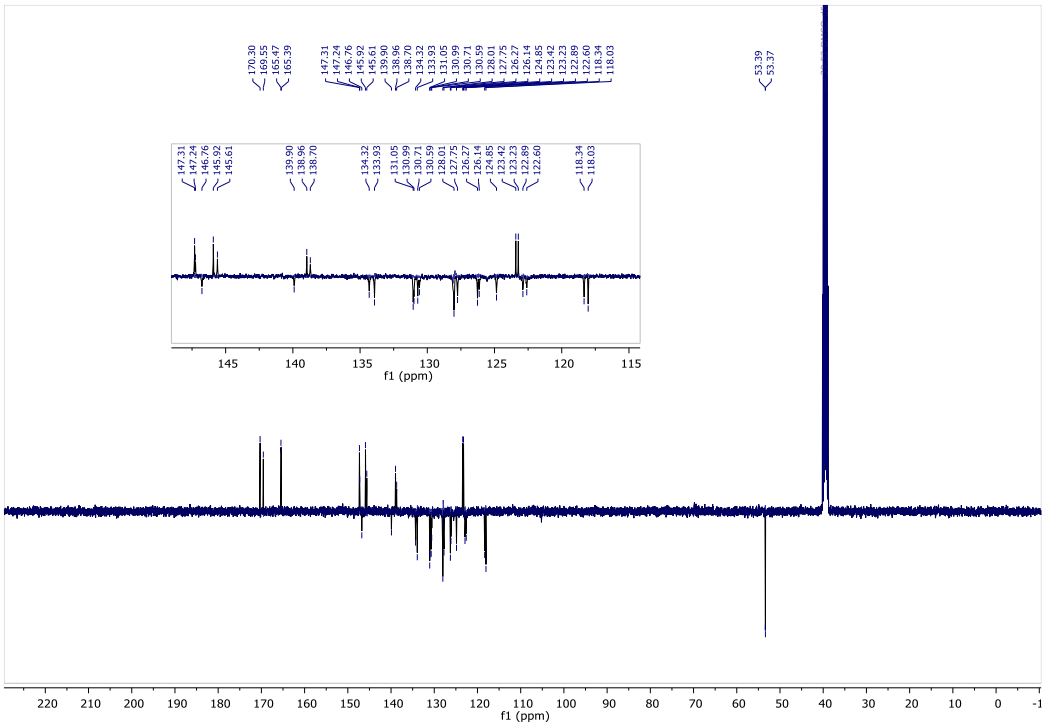

Figure S4.21. APT-NMR spectrum of complex **4.6**.

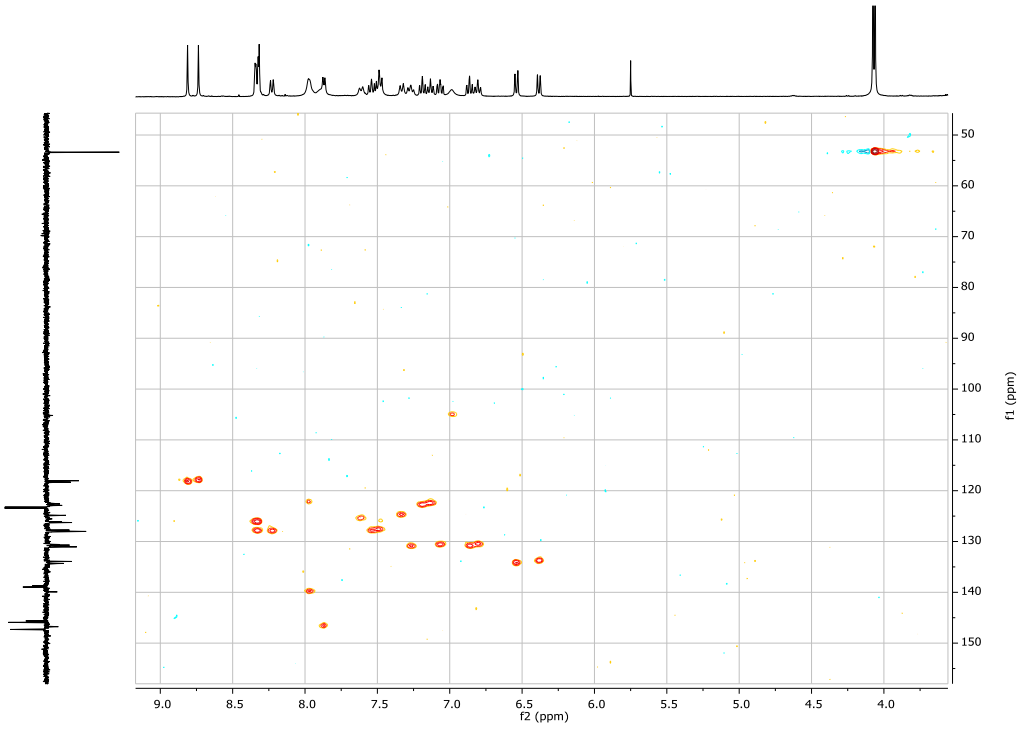

Figure S4.22. HSQC spectrum of complex **4.6**.

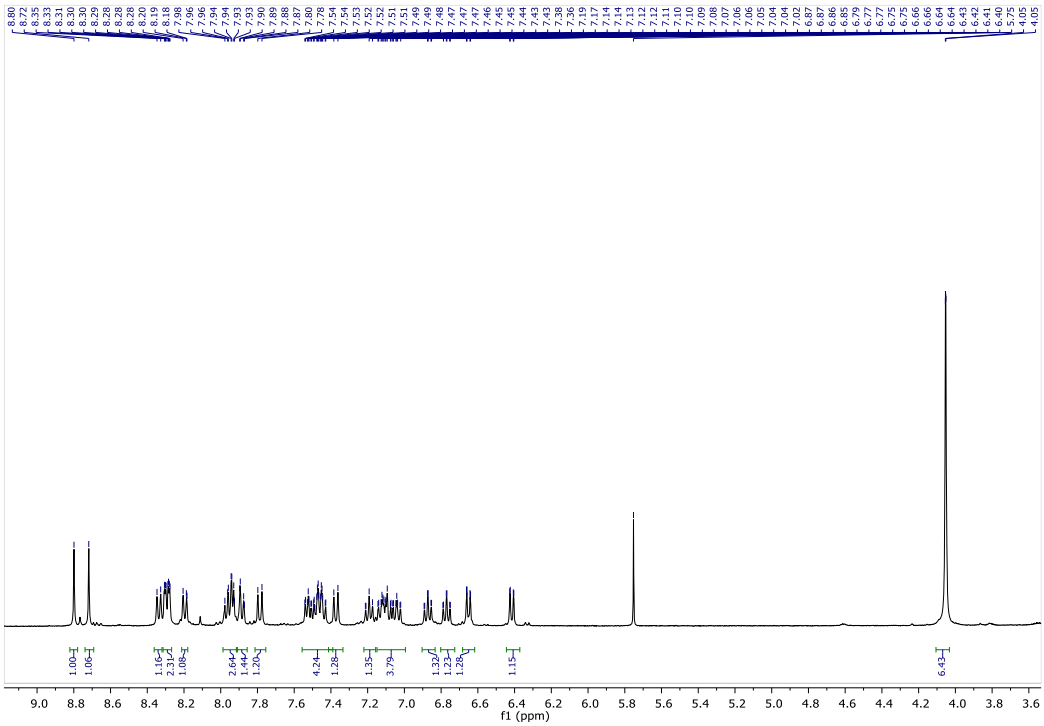

Figure S4.23. ^{1}H-NMR spectrum of complex **4.7**.

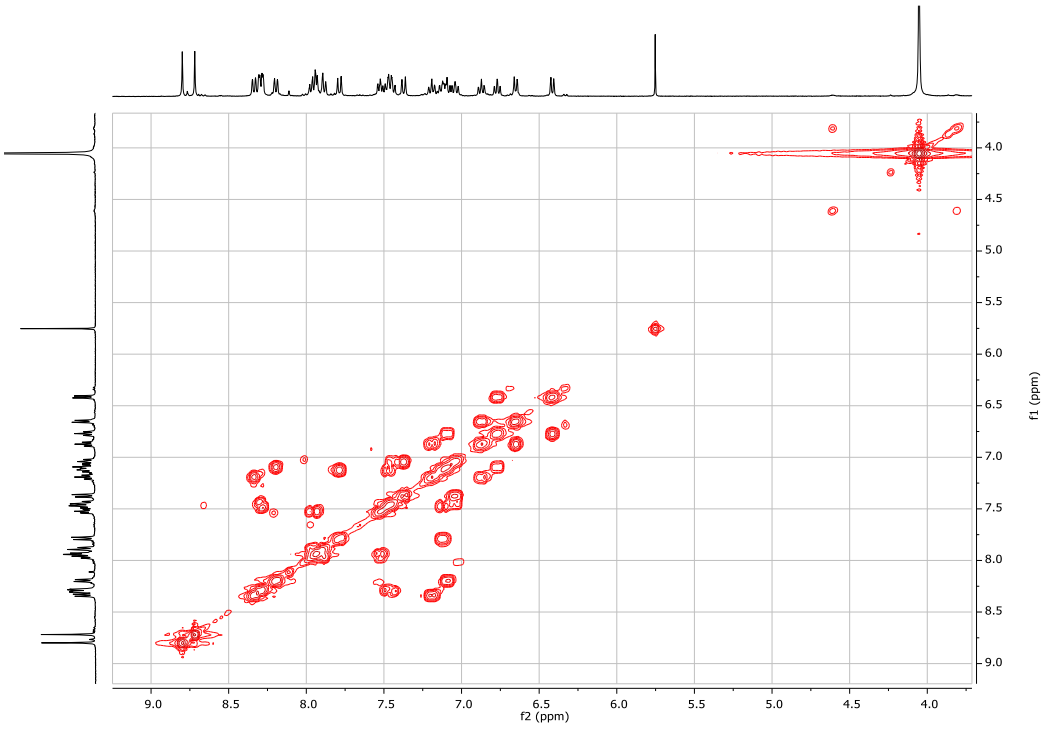

Figure S4.24. COSY-NMR spectrum of complex **4.7**.

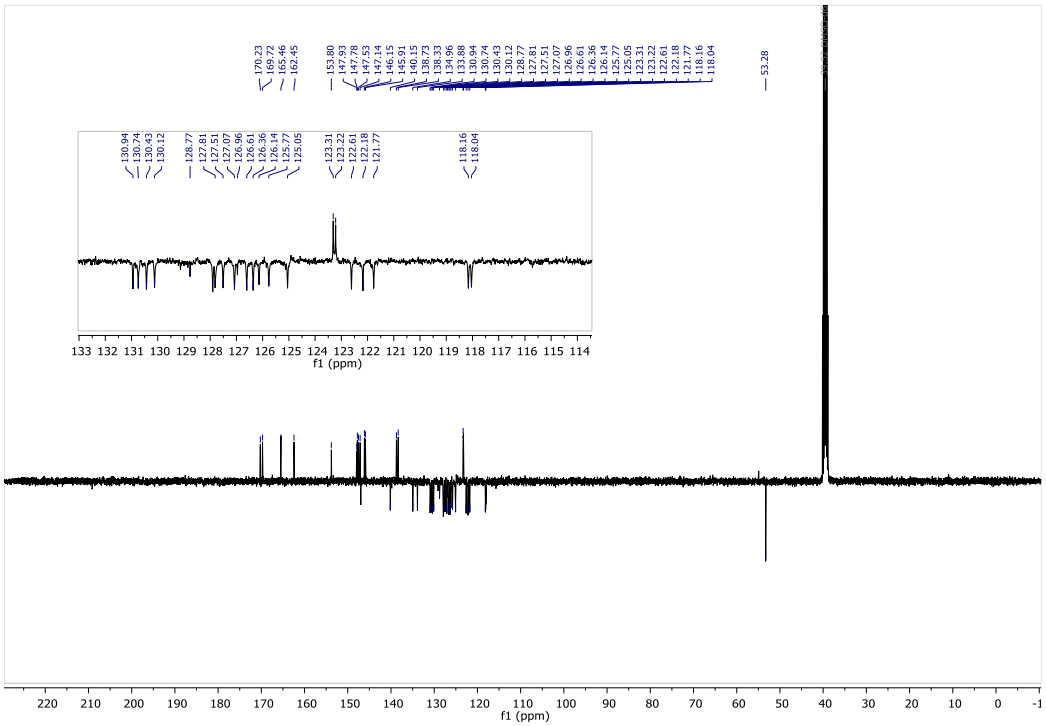

Figure S4.25. APT-NMR spectrum of complex **4.7**.

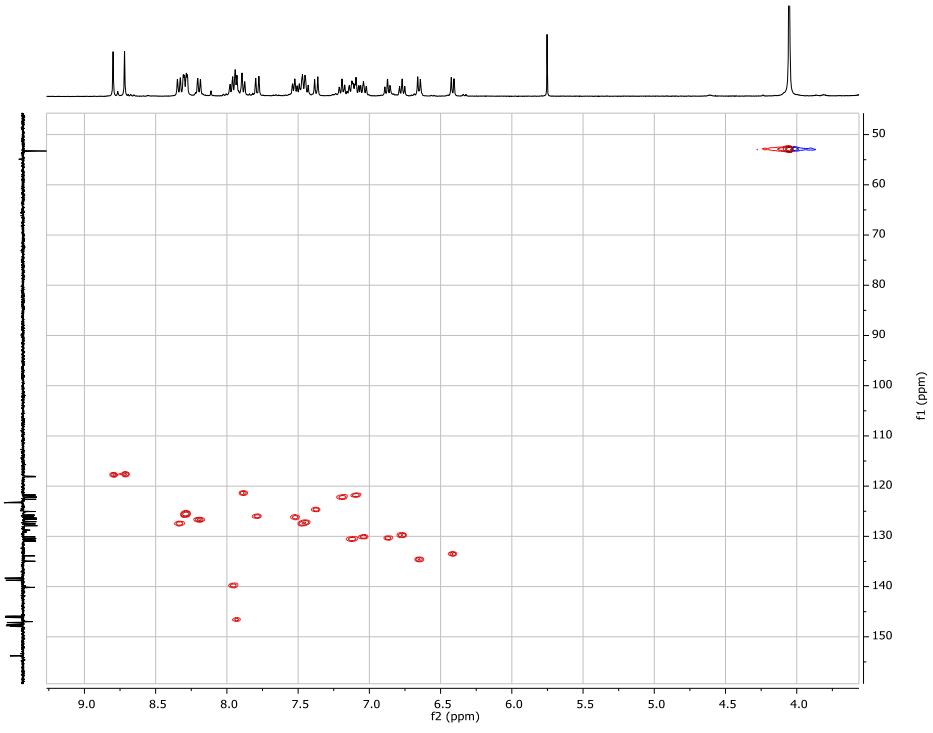

Figure S4.26. HSQC spectrum of complex **4.7**.

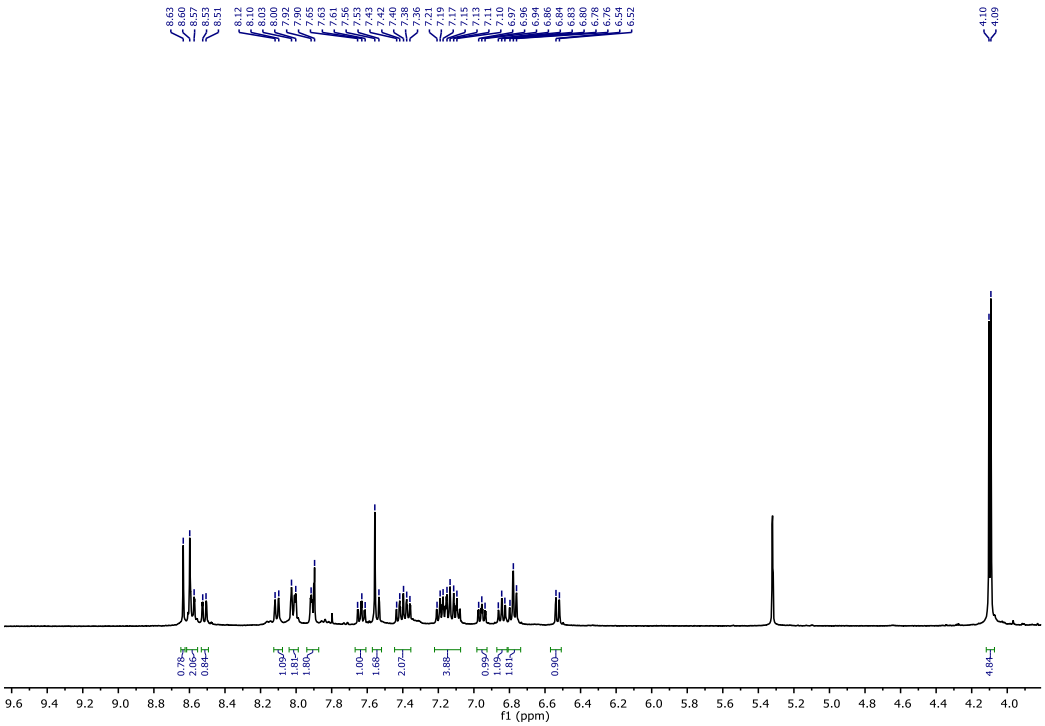

Figure S4.27. ^{1}H-NMR spectrum of complex **4.8**.

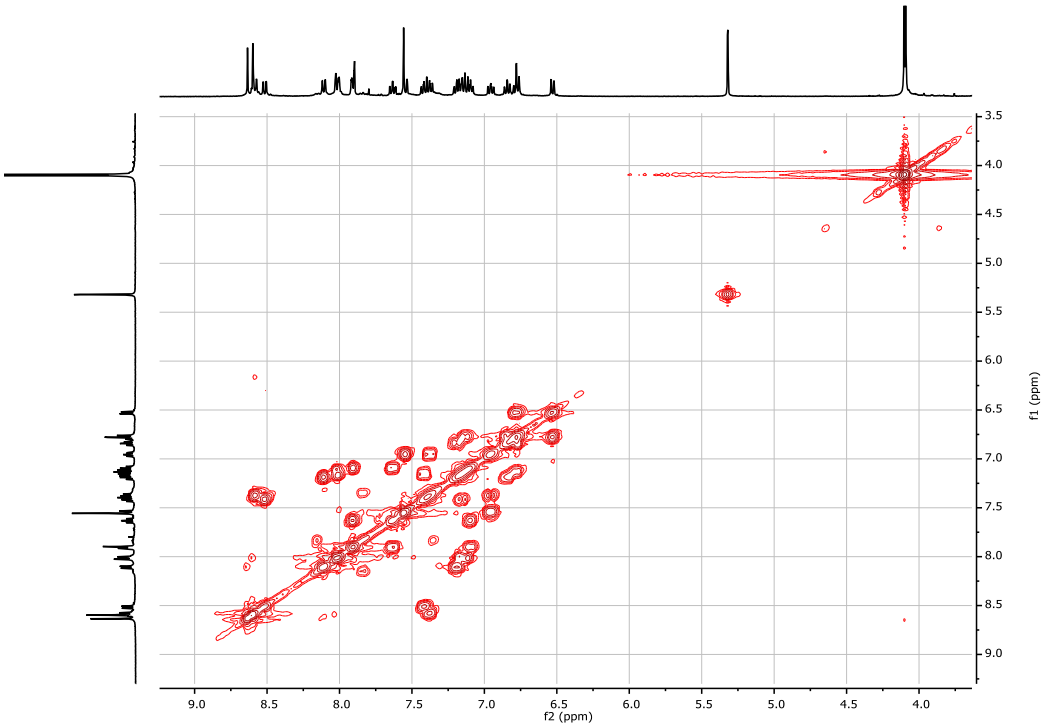

Figure S4.28. COSY-NMR spectrum of complex **4.8**.

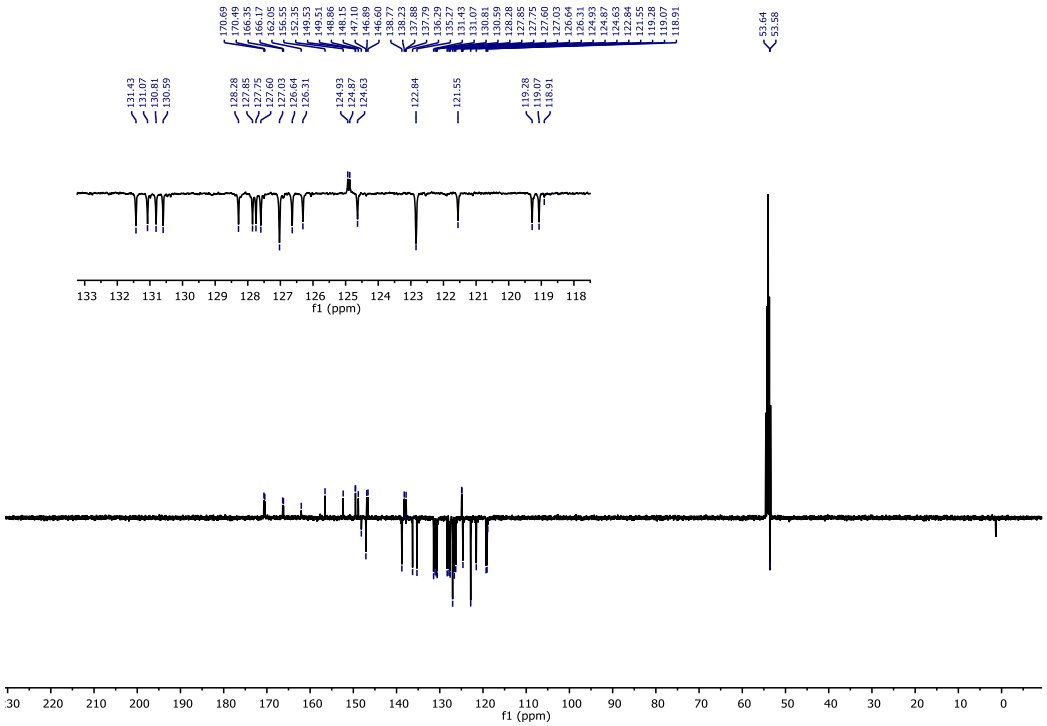

Figure S4.29. APT-NMR spectrum of complex **4.8**.

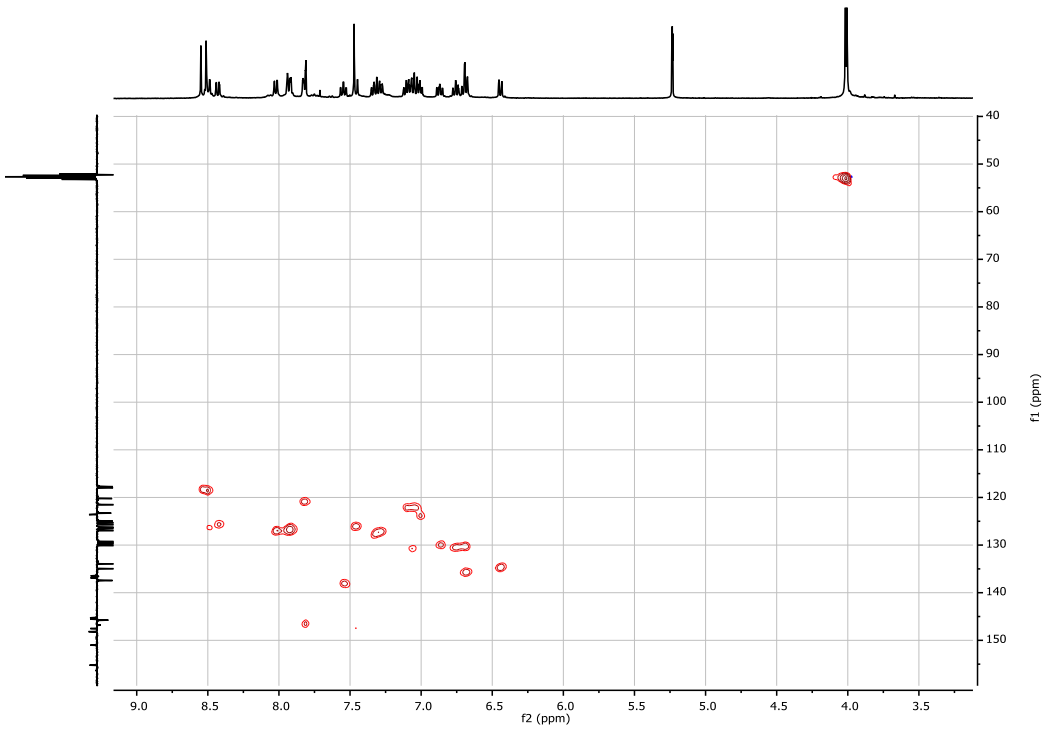

Figure S4.30. HSQC spectrum of complex **4.8**.

Mass spectra of complexes 4.1-4.8

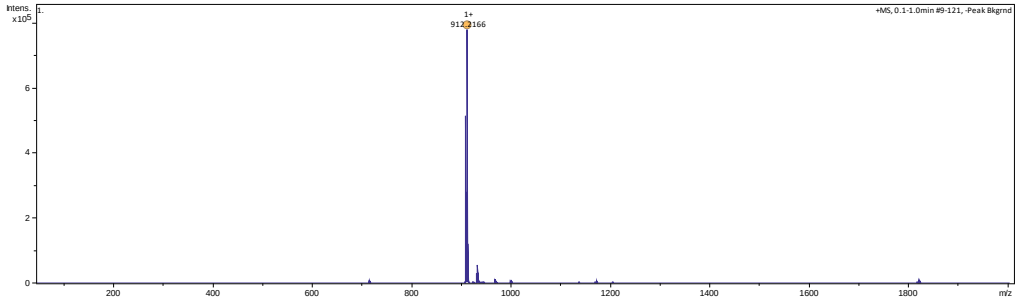

Figure S4.31. ESI-HRMS spectrum of complex **4.1**.

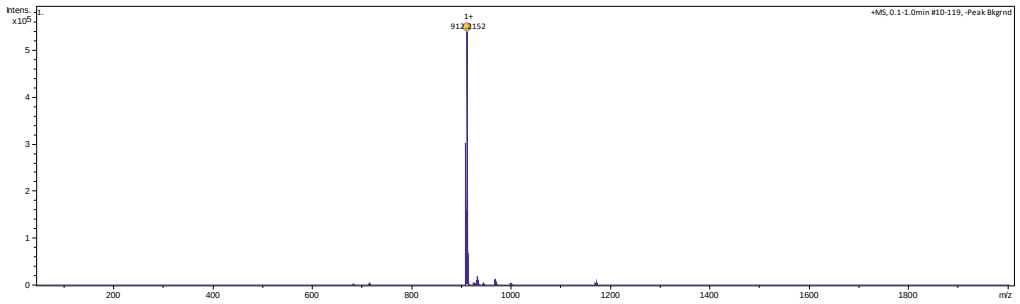

Figure S4.32. ESI-HRMS spectrum of complex **4.2**.

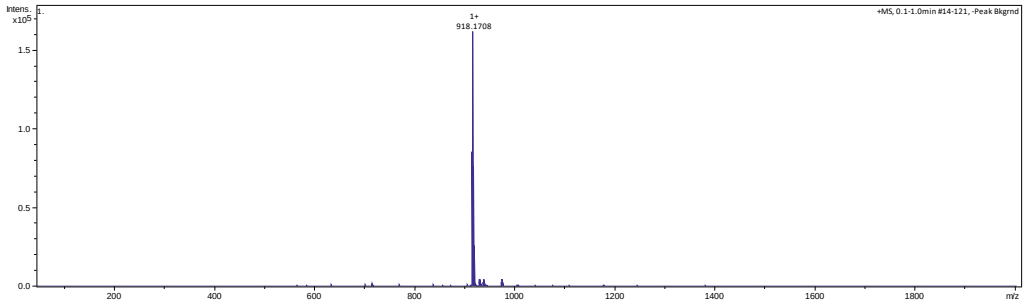

Figure S4.33. ESI-HRMS spectrum of complex **4.3**.

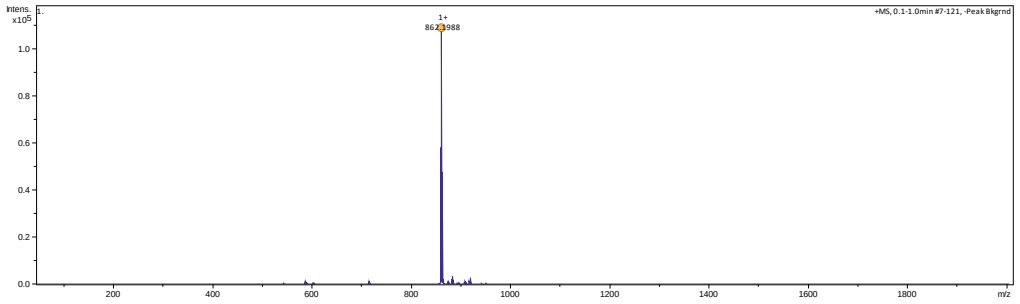

Figure S4.34. ESI-HRMS spectrum of complex **4.5**.

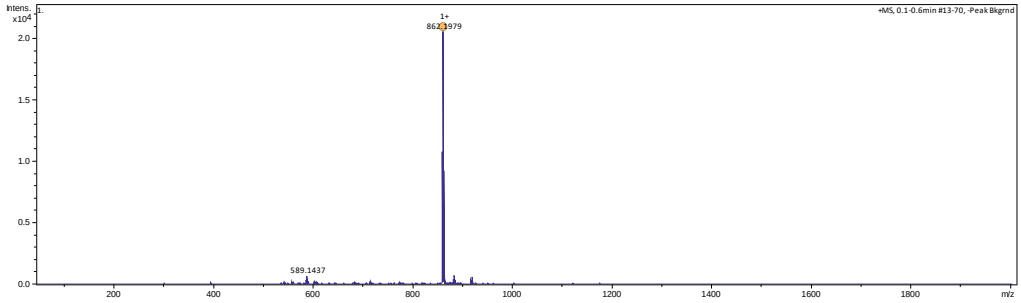

Figure S4.35. ESI-HRMS spectrum of complex **4.6**.

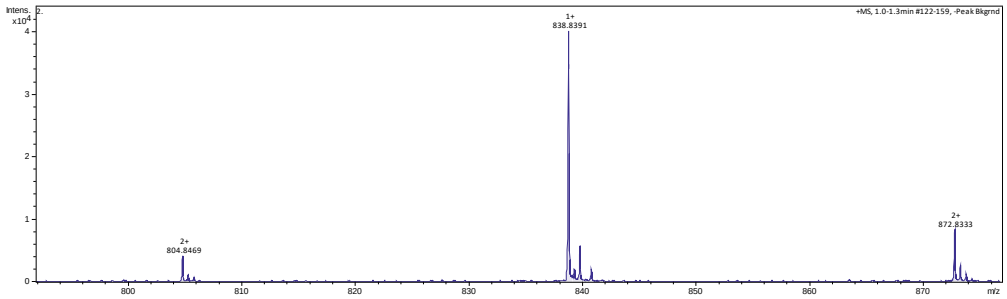

Figure S4.36. ESI-HRMS spectrum of complex **4.7**.

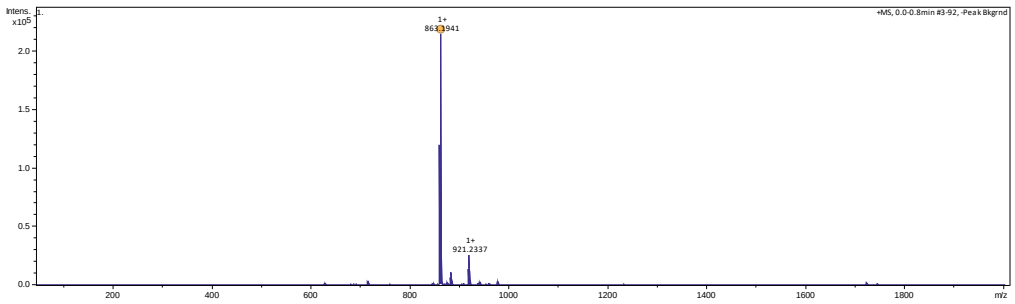

Figure S4.37. ESI-HRMS spectrum of complex **4.8**.

Emission and excitation spectra of complexes 4.1-4.8

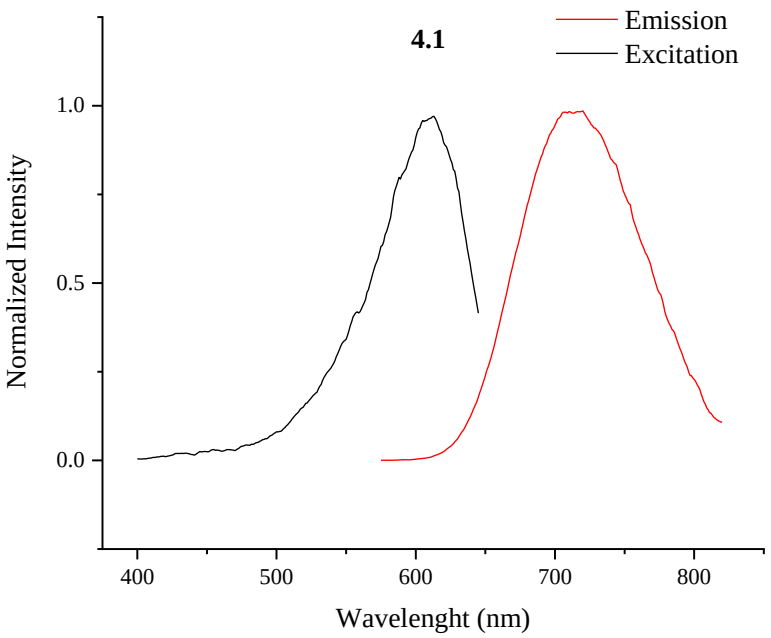

Figure S4.38. Emission-excitation spectra of complex **4.1** measured in DMSO solution.

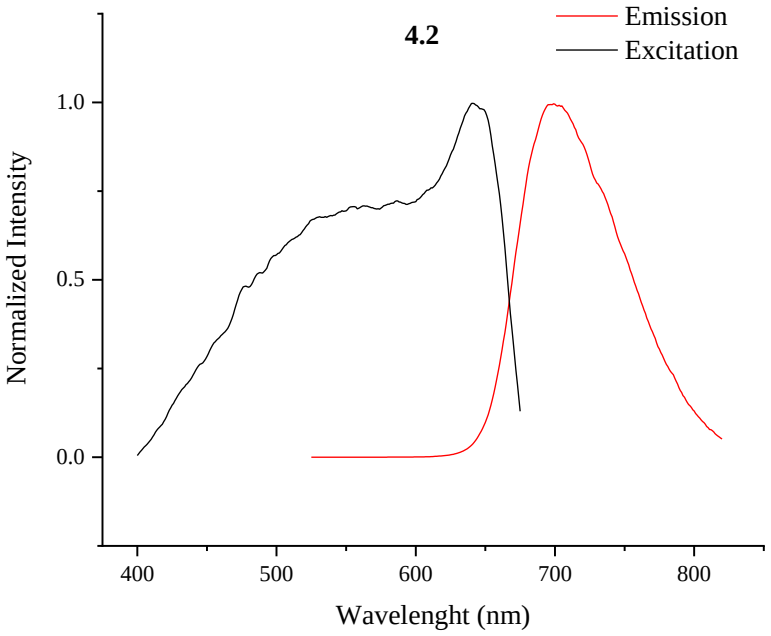

Figure S4.39. Emission-excitation spectra of complex **4.2** measured in DMSO solution.

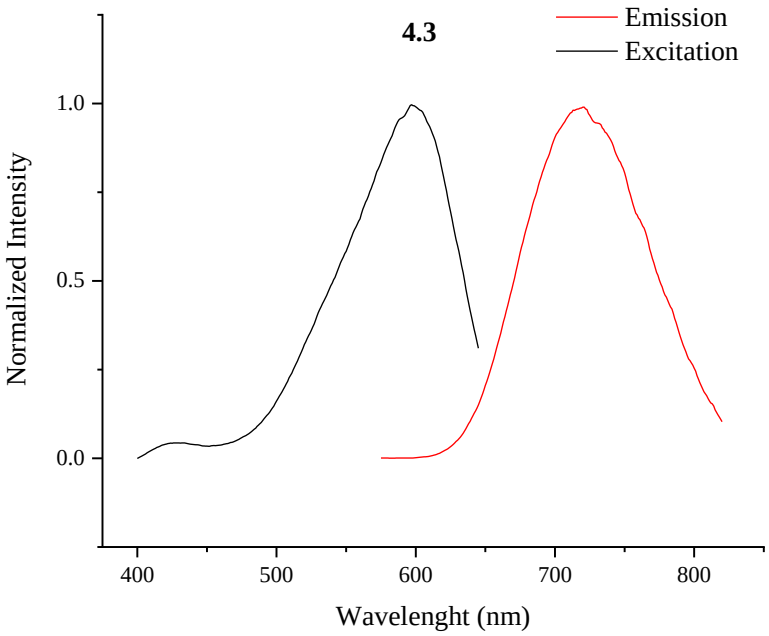

Figure S4.40. Emission-excitation spectra of complex **4.3** measured in DMSO solution.

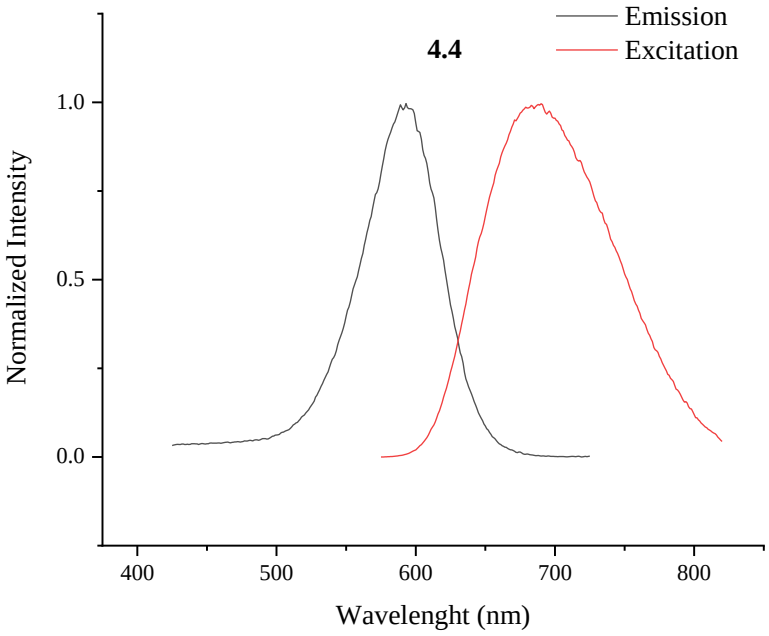

Figure S4.41. Emission-excitation spectra of complex **4.4** measured in DMSO solution.

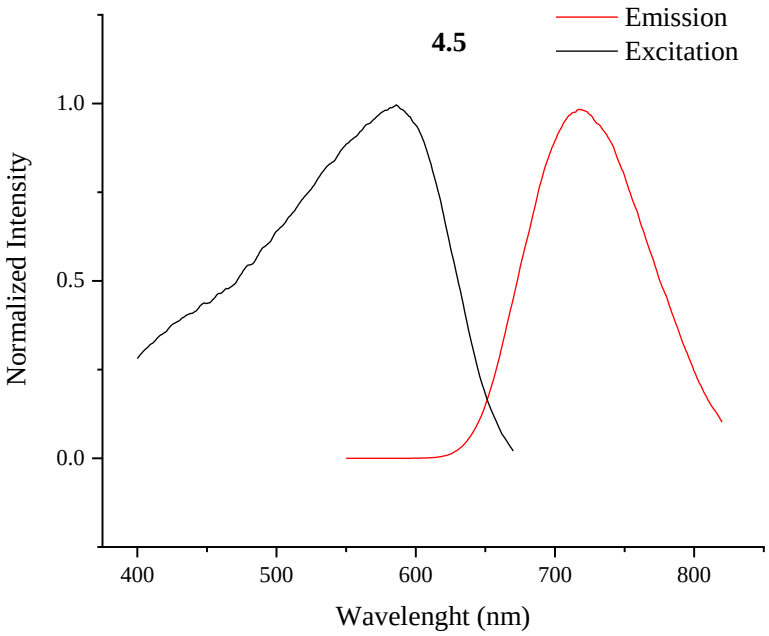

Figure S4.42. Emission-excitation spectra of complex **4.5** measured in DMSO solution.

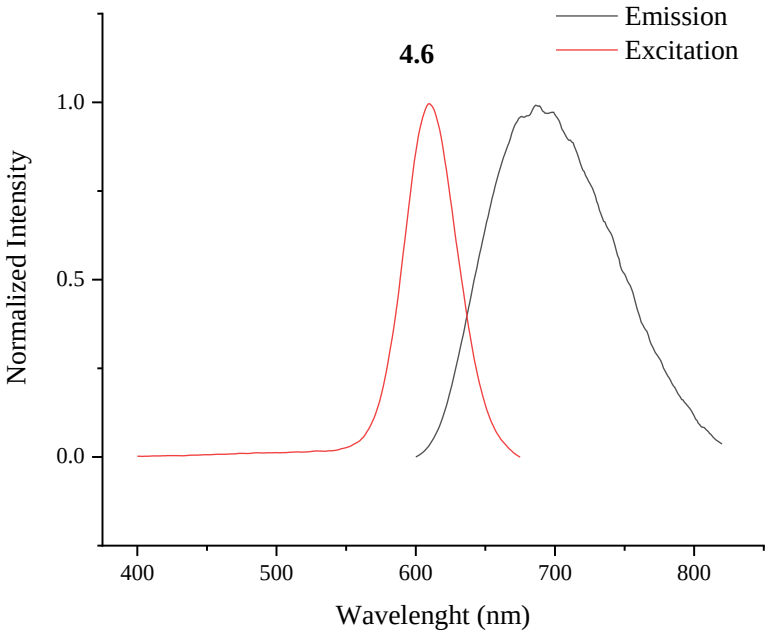

Figure S4.43. Emission-excitation spectra of complex **4.6** measured in DMSO solution.

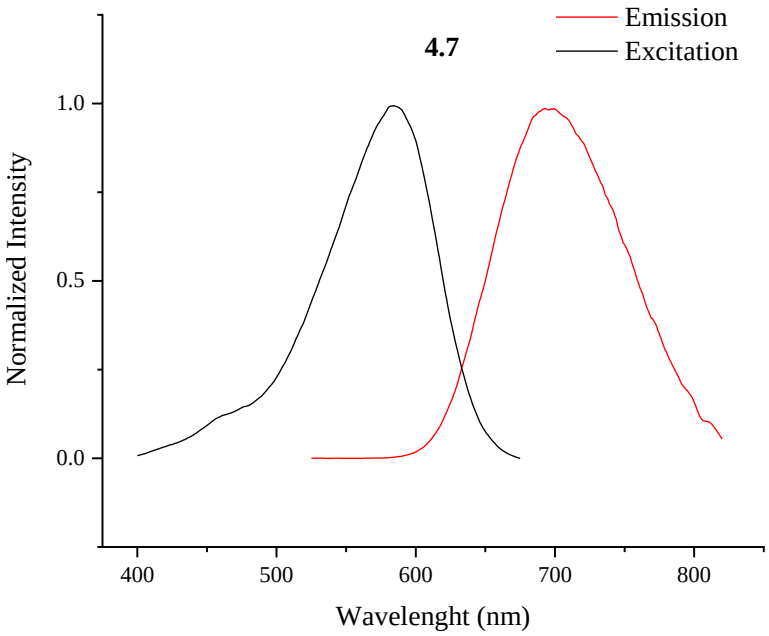

Figure S4.44. Emission-excitation spectra of complex **4.7** measured in DMSO solution.

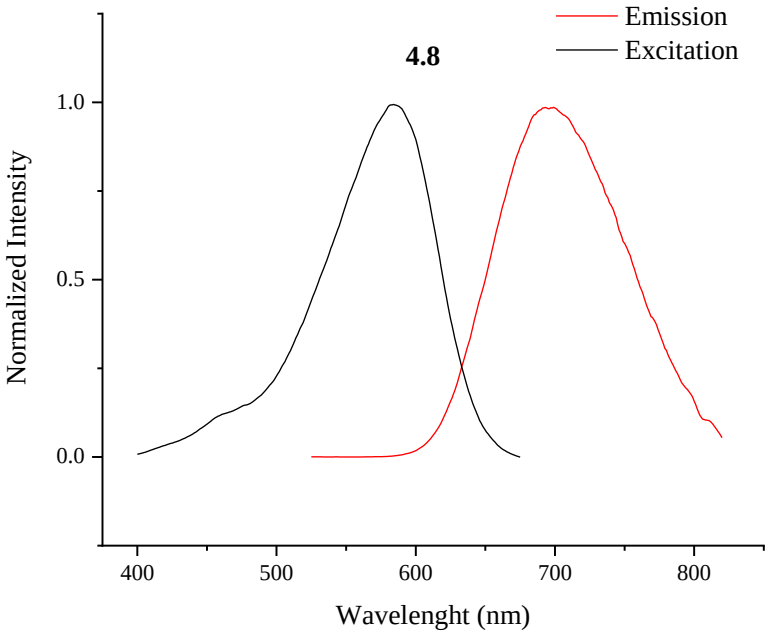

Figure S4.45. Emission-excitation spectra of complex **4.8** measured in DMSO solution.

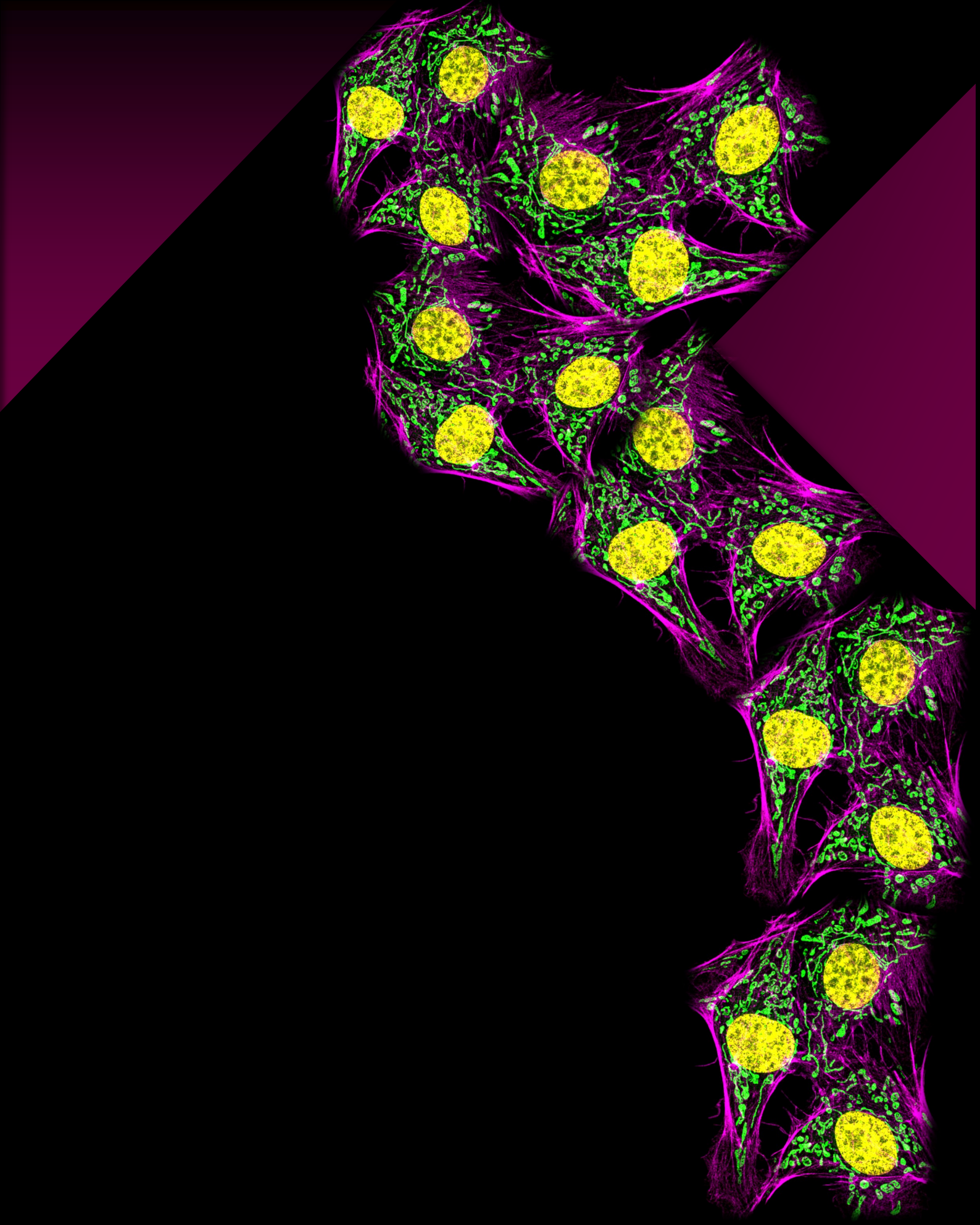

GOBIERNO DE ARAGON

CSIC
Consejo Superior de Investigaciones Científicas

iSQCH
Instituto de Síntesis Química y Catálisis Homogénea